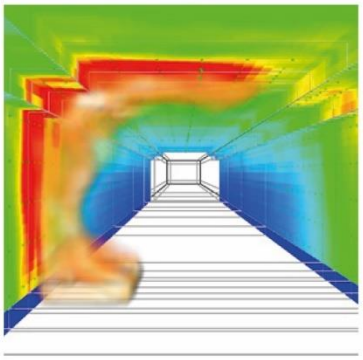
Thermal Exposure in Concrete Tunnels Subjected to Fire

Henrique Neiva Volpini







TU Delft

May 2020

Witteveen + Bos

Thermal Exposure in Concrete Tunnels Subjected to Fire

Thesis
to obtain the degree of Master of Science
in Structural Engineering: Concrete Structures
at the Delft University of Technology,
to be publicly defended online on
Friday May 15, 2020 at 13:00,
via
https://tudelft.zoom.us/j/96018817206
by
Henrique Neiva Volpini





Author: Henrique Neiva Volpini
Student Number: 4748034
Email: hnvolpini@gmail.com

Master thesis committee:

Dr. ir. C.B.M. Blom	Delft University of Technology/Gemeente Rotterdam
Dr. ir. W. Broere	Delft University of Technology
Dr. ir. M.A.N. Hendriks	Delft University of Technology
Dr. ir. B.B.G. Lottman	Witteveen+Bos
Ir. A.J.M. Snel	Witteveen+Bos

An electronic version of this MSc thesis is available at
https://repository.tudelft.nl/

Delft University of Technology
Faculty of Civil Engineering and Geosciences
Stevinweg 1, Delft, The Netherlands

Acknowledgments

Firstly, I would like to thank Kees Blom, not only for proposing the research topic and for recommending me to Witteveen+Bos, but also for the very insightful meetings we had together during the development of this thesis. My gratitude to Max Hendriks and Wout Broere, who promptly accepted the invitation to participate in the assessment committee. I also want to acknowledge the collaboration of Kristina Reinders, who unfortunately had to leave the committee before the end of this work.

I want to express my gratitude to Aryan Snel for providing me the opportunity to temporarily join the Tunnel Safety and Fire Safety Engineering Group in the Department of Underground Infrastructure at Witteveen+Bos as a graduate student. I am also thankful for his clarifying comments and overall guidance. My thanks are extended to Bas Lottman, Thijs Bouwhuis, Lieuwe Hendrik Lei, and Tamara Dolle, my colleagues, who not only enthusiastically received me within the group, but who were also always available to assist me. I am particularly grateful to Thijs for putting extra effort into helping me out with FDS. In special, I wish to express my deep gratitude to Bas, who collaborated almost on a daily basis to the development of this thesis, providing insightful advice and challenging ideas, while also reviewing my work thoroughly, guiding me forward throughout these almost nine months. This project would not be what it is without his profound contribution, for which I simply cannot thank him enough. I also have to acknowledge the contribution of Tunnel Engineering Consultants (TEC), a joint venture between Royal HaskoningDHV and Witteveen+Bos, on providing the data for the case study addressed at the end of this thesis. For that, I am also thankful to Marcel ‘t Hart (Royal HaskoningDHV and TU Delft) for the help he provided me.

My many thanks to all my friends from Brazil, who despite being so far away have still managed to be present in my daily life. I want to extend my gratitude to everyone I have met during these years in Delft, in special to Tommi and Salvo, who restated my long-gone family roots in Italy, and have become brothers to me.

Lastly, I want to acknowledge my family contributions to my personal achievements. I am deeply thankful to my parents, Dalton, and Simone, who never spared sacrifices on my behalf, and have provided me much more than any son could ask for. I also want to thank my aunts, Danuzza and Neila, who since my childhood have treated me as their own sons. My gratitude to my brother Felipe and his wife Raquel, who have just given me my first nephew, little Rafa. Your uncle looks forward to meeting you in person shortly. I also want to thank my girlfriend Mariana, who has been for almost nine years by my side, and that I hope will continue until the rest of my life. I am also grateful to my grandmother, Benvinda, my biggest example that hard work always pays off. Finally, I want to dedicate this accomplishment to my grandfather, Edmar, who unfortunately will not have the opportunity to celebrate with me in person, but will be forever in my heart.

Henrique Neiva Volpini
Delft, May 2020

Abstract

Keywords: fire, adiabatic surface temperature (AST), radiation, RWS curve, concrete tunnels, thermal stresses, Fire Dynamics Simulator (FDS), furnace tests

To date, many fire accidents have occurred in tunnels all over the world. In the worst cases, there were catastrophic consequences with numerous human casualties and significant economic impacts. In the occurrence of such tunnel fires, besides the primary concern of saving human life, ensuring a certain level of structural integrity is also desired. Looking from the latter perspective, this thesis is focused on the fire-induced thermal exposure in concrete tunnels, aiming at coupling numerical simulations of idealized fire scenarios in computational fluid dynamics (CFD) software with the use of FEA for the analysis of structures, moving towards a performance-based approach in replacement of the currently adopted prescriptive approach.

In this sense, fire imposes one of the most hazardous conditions for concrete structures, leading to irreversible chemical and physical changes in the material and characterizing severe thermal degradation of mechanical properties (i.e. compressive strength, tensile strength, and elastic modulus). During fire exposure, steep thermal gradients are formed within the concrete structure. It is shown here that, as a consequence of such temperature distributions within the material, thermal stresses will always develop in concrete structures subjected to fire. Numerous aspects are proven to have an effect on the total state of thermal stresses developed within the structure, namely, elastic modulus, geometry, and supporting conditions. Due to the nature of restrained imposed deformations, in especial the selected curve to describe the thermal degradation of elastic modulus with temperature has shown to have a significant effect on the developed stresses. Accordingly, it is here exposed that the use of Eurocode 2 Part 1-2 [9] to describe normal strength concrete (NSC) might actually lead to unconservative results.

Besides the structural consequences of a fire, this thesis also deeply investigates the interface between a fire and the structure and its consequences to the total thermal exposure imposed by a fire onto the structure. Following this line, the fire-structure interface is rather complex and involves the interaction of three different modes of heat transfer, namely conduction, convection (related to the gas temperatures generated by a fire), and radiation (related to the radiation temperatures generated by a fire). While conduction within the solid phase regulates the amount of heat absorbed by the structure during a fire, radiation overcomes convection and becomes the primary mode of heat supply to the structure. Thus, differently from what most structural engineers usually think, the true gas temperatures achieved by the fire-induced gas phase inside of an enclosure are not necessarily representative to describe the thermal exposure imposed onto the structure. In fact, the only case in which gas temperatures will be representative in describing the thermal exposure generated by a fire is characterized by a scenario in which thermal radiation is emitted at its maximum potential, and thus the gas temperatures equate the radiation temperatures. Other than that, there will always be a gap among these two temperatures, and for those latter cases, the thermal exposure is regulated by the radiation component. Hence, to simplify the matter of dealing with two terms (gas and radiation temperatures) and easy the task of coupling CFD calculations for the fire phase to the structural

analysis in FEA, Wickström [66, 67, 76] introduces the adiabatic surface temperature (AST). Accordingly, AST is a parameter that combines both the radiation and convection contributions to the total heat transfer to the structure into a single term, fully characterizing the thermal exposure induced by a fire onto the structure. Based on this concept, the RWS curve is compared to other fire scenarios reported in the literature (i.e. pool and jet fires), elucidating that the use of this curve according to Eurocode 1 Part 1-2 [75], prescribes, if not the most, one of the most severe fire scenarios encountered in literature, being, at least, as destructive as the most damaging jet fires.

The RWS curve is the result of a test performed by TNO in 1980 [89] for a very narrow and short insulated tunnel of limited height, where oxygen supply was practically unlimited. Even though flames were most likely covering the whole ceiling during the original RWS test, this thesis shows that this curve was derived out of only two gas temperature measurements from this test. However, for the reasons depicted in the previous paragraph, the real thermal exposure achieved during the original test was, as in any fire, governed by the radiation component. Despite all limitations involved in replicating this test numerically, the FDS model developed in this thesis was able to reproduce the original results fairly well. Note that this fire simulation indicates that the real thermal exposure (AST) achieved during RWS test appears to have been considerably smaller than that which is prescribed by the RWS curve.

It does not stop there, as the boundaries of the RWS tunnel were characterized by the use of materials of high *insulation* thermal properties, the temperatures achieved within the tunnel during the RWS test are not representative to describe those which would have been achieved for the same case in a concrete tunnel. In essence, this thesis indicates that due to their thermal properties (in especial, the thermal conductivity), *concrete* and *insulation* behave very differently to the same thermal exposure. Basically, for *insulation* materials, the surface temperature of the solid will tend towards the AST imposed by fire since the beginning of the fire, whereas for *concrete*, there will always be a lag between these two. As a consequence, a *concrete* structure will absorb much more energy from the fire-induced gas phase than the *insulated* one, meaning that more heat will be contained within the gas phase trapped inside an *insulated* tunnel. This difference exposes the main flaw of the prescriptive-based approach. In essence, by using the same time-temperature curve indistinctively among *protected* and *unprotected concrete* tunnels, we are inherently considering two distinct fire scenarios among both. Not only that, but the fire scenario also has to be more severe for the *concrete* case such that the same conditions are achieved in both. As the worst-case fire scenario should not be dependent on whether or not a certain tunnel is protected by passive *insulation*, it becomes clear that the same curve should not be used to represent those cases. In this sense, the results of numerous fire simulations performed in this thesis indicate that, in a prescriptive-based approach, the *hydrocarbon* curve provides a more reasonable choice when dealing with *concrete* tunnels.

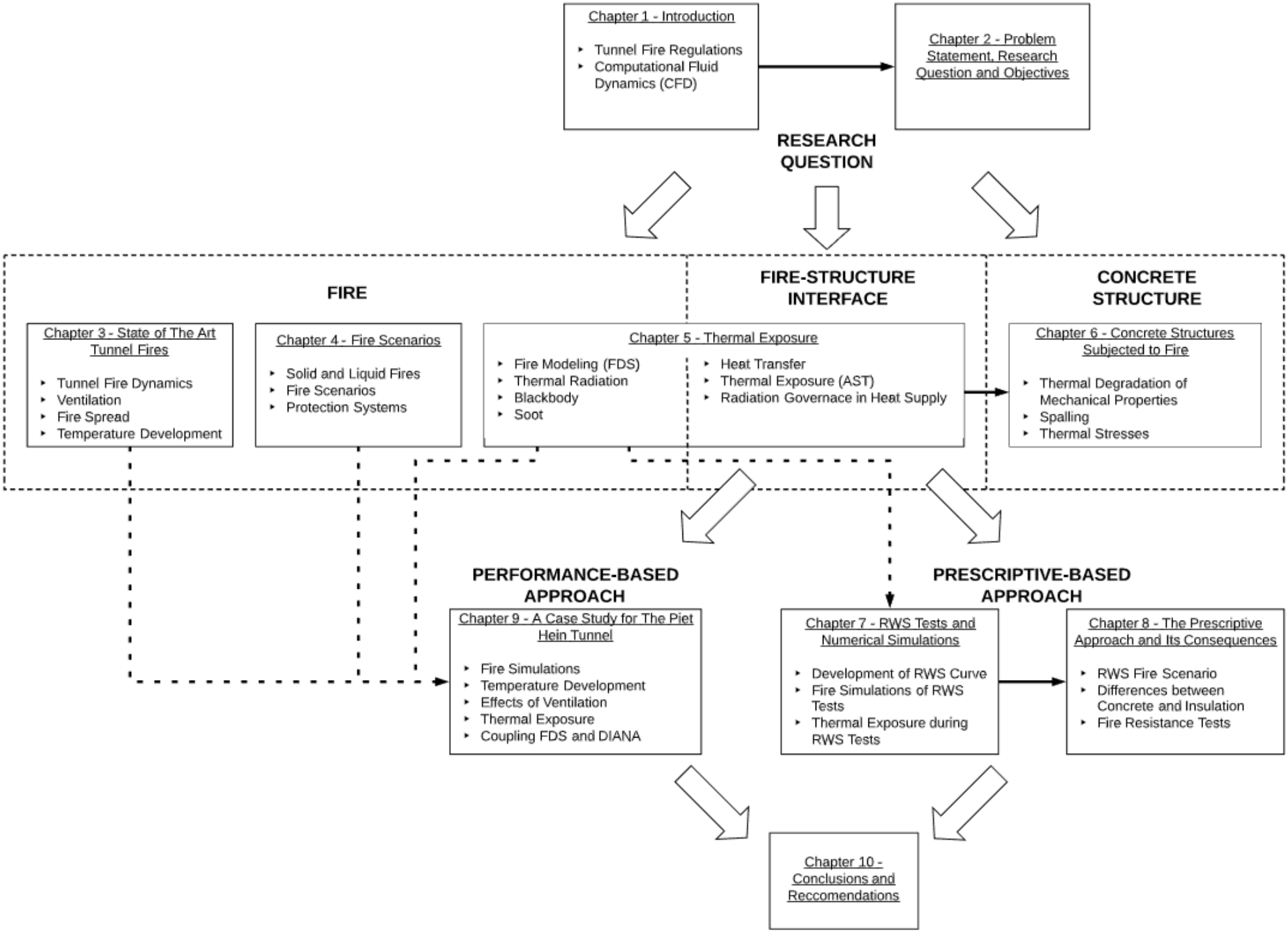
Another problem related to the prescriptive approach refers to the fire resistance furnace tests currently used in the Netherlands to access existing tunnel structures (i.e. the MobiFiRe [108]). It is here proven that this furnace is controlled by temperature measurements of thermocouples which resemble the true gas temperatures within the furnace. Thus, despite the fact that the thermal exposure on the specimen is governed by the radiation component, the furnace is

regulated by the convection contribution. When accounting for the type of fuel used by this furnace and its dimensions, it appears that the thermal exposure imposed on the structure during such tests might not be properly controlled.

At the end of this thesis, a case study is addressed, highlighting the possible benefits one may achieve through a performance-based approach. Here, two different fire scenarios are studied in FDS, namely (1) the idealized RWS pool fire (i.e. a 200 MW gasoline pool fire) and (2) a reduced pool fire (30 MW), while also including the effects of longitudinal ventilation. It is proven that, due to lack of oxygen, the RWS fire scenario is not sustainable within a real tunnel without the use of some extra source of ventilation. It must be noted that this fire scenario achieves its full power for the entire time of simulation (2 hours) even for the minimum level of ventilation currently applied to prevent smoke from spreading upstream the fire source (approximately 3 m/s).

Given the limitations of the study developed here, the use of high longitudinal ventilation has shown to be very beneficial in reducing the overall temperature development within the tunnel. Ventilation promotes mixing with cooler air at the buoyant smoke layer and pushes the flames towards ground level, significantly reducing the thermal exposure imposed on the tunnel as a whole. However, ventilation will not avoid the occurrence of zones of high thermal exposure for sections of the tunnel which are either impinged by flames or located really close to those, where high levels of thermal radiation are inherently being generated by the flames.

Finally, the added benefits gained by a performance-based approach are clearly elucidated when the reduced pool fire is compared to the RWS fire scenario. It is shown, that by selecting a more realistic fire load when considering the allowed traffic within the tunnel, one may achieve a much smaller AST for the structural analysis. In fact, it is also elucidated here that even when considering the idealized RWS fire scenario through a performance-based approach rather than a prescriptive manner, one may expect a significant reduction in the temperature development of the concrete structure exposed to fire.



Schematic overview of the main topics discussed in this thesis

Contents

1 Introduction 3

1.1 Regulations in the Netherlands 5
1.2 Computational Fluid Dynamics (CFD) 6

2 Problem Statement, Research Question and Objectives 10

2.1 Problem Statement 10
2.2 Research Question and Objectives 10

3 Tunnel Fires: State of The Art 12

3.1 Fire Dynamics in Tunnels 12
3.2 Ventilation 16
3.3 Fire Spread 23

4 Fire Scenarios 39

4.1 Fire Load 39
4.2 Parameters affecting HRR 44
4.3 Fire Scenarios 51
4.4 Conclusions 54

5 Thermal Exposure 55

5.1 Mechanisms of Heat Transfer 55
5.2 Heat Transfer in FDS 65
5.3 Thermal Boundary Conditions 74
5.4 Conclusions 79

6 Concrete Structures Subjected to Fire 81

6.1 Introduction 81
6.2 Thermal Degradation of Mechanical Properties 81
6.3 Deformation of Concrete at Elevated Temperatures 86
6.4 Spalling 88
6.5 Thermal Stresses 90
6.6 Thermal Analysis of Concrete Structures Subjected to the RWS curve 93
6.7 Conclusions 107

7 RWS Tests and Numerical Simulations 109

7.1 Introduction 109
7.2 RWS Tests 110
7.3 Temperatures Measured during the RWS Tests 122
7.4 Numerical Simulations of RWS Tests 126
7.5 Variations on the Original RWS Tests 139
7.6 Influence of Selected Concrete's Thermal Properties 157
7.7 Conclusions 159

8 The Prescriptive Approach and its Consequences 161

8.1 The Prescriptive Approach 161
8.2 Thermal Response of Different Materials to the RWS Exposure 178
8.3 Furnace Resistance Tests 186
8.4 Conclusions 199

9 Performance-Based Approach: A Case Study for the Piet Hein Tunnel 201

9.1 Introduction 201
9.2 Model I – RWS Fire Scenario (200 MW) 203
9.3 Model II – Reduced Pool Fire Scenario (30 MW) 223
9.4 Thermal Exposure Imposed on the Piet Hein Tunnel Structure 247
9.5 Coupling FDS and DIANA 253
9.6 Conclusions 260

10 Conclusions and Recommendations 263

10.1 Conclusions 263
10.2 Recommendations 269

11 Appendices 271

12 References 281

1 Introduction

Numerous fire accidents have occurred in road tunnels throughout history. In many cases, those have led to human losses and partial, or even total, collapse of the tunnel lining. Whenever this happens, there are inherent economic impacts for the society and the infrastructure system. Table 1.1 below summarizes a few of those road tunnel fire events and provides a deeper view on the possible outcome of such accidents.

Year	Tunnel	Length	Possible Cause	Fire Duration	Consequences		
					People	Vehicles	Structure
1978	Velsen, The Netherlands	770 m	Front-rear collision	1h20min	5 dead and 5 injured	4 lorries and 2 cars	Serious damage over 30m
1979	Nihonzaka, Shitzuoka (Japan)	2045 m	Front-rear collision	159h	7 dead and 1 injured	127 lorries and 46 cars	Serious damage over 1100m
1982	Caldecott, Oakland (USA)	1028 m	Front-rear collision	2h40min	7 dead and 2 injured	3 lorries, 1 coach and 4 cars	Serious damage over 580m
1993	Serra Ripoli, Bologne-Florence (Italy)	442 m	Collision	2h30min	4 dead and 4 injured	5 lorries and 11 cars	Little damage
1996	Isola Delle Femmine, Palermo (Italy)	148 m	Front-rear collision	-	5 dead and 20 injured	1 tanker, 1 bus and 18 cars	Serious damage, tunnel closed for 2 days
1999	Mont Blanc, France-Italy	11600 m	Oil leakage in the motor	-	39 dead	23 lorries, 10 cars, 1 motorcycle and 2 fire engines	Serious damage, tunnel closed for over 2 years
2001	St. Gotthard, Switzerland	16918 m	Front collision between 2 lorries	2 days	11 dead	13 lorries, 4 vans and 6 cars	Serious damage, tunnel closed for 2 months

TABLE 1.1 – FIRE ACCIDENTS IN ROAD TUNNELS
Adapted from ITA [1]

The recurrent occurrence of fires in tunnels, often leading to catastrophic consequences, brought attention to the matter. This has led to the organization of some major test campaigns around the world. However, such tests always involve high costs, logistical obstacles, and often require the collaboration between several parties (i.e. governments, companies, and institutions). Altogether, those aspects contribute to limit the number of representative large-scale tunnel fire tests performed to date. Not only that, due to insufficient instrumentation, most tests available in literature often lack important data regarding the fire phenomena (Ingason et al. [2]). Out of those tests, there are three in particular which are worth mentioning:

- *EUREKA 'FIRETUN' Test Series (1990-1992) [3]*:

  This test program was performed in an abandoned tunnel in Norway, mainly focused on investigating the fire behavior of different fire sources, such as (1) pool fires; (2) solid fires (i.e. wood cribs); and (3) real rail and road vehicles. In total, 21 large-scale tests were carried out. To date, the results of this test series still constitute a unique database for the heat release rate (HRR) of real vehicles.

- *Memorial Tunnel Fire Ventilation Test Program (1993-1995) [4]*:

  This large-scale test campaign was realized in the United States. The tests were designed to evaluate different ventilation systems and their capabilities of controlling smoke and temperature development during a tunnel fire. The Memorial tests provided important contributions for the design of ventilation systems for tunnels, for which concepts are still largely applied worldwide.

- *Runehamar Tests (2003) [5]*:

  The Runehamar tests were developed in Norway as part of the UPTUN (Upgrading of existing tunnels for fire safety) project. In total, four mockups simulating heavy-goods vehicles (HGV) were tested, proving that burning HGVs could also produce rapidly growing fires with high levels of HRR. This test is particularly important for this thesis because its results are often taken as a confirmation of the occurrence of extremely high temperatures (i.e. similar to those prescribed by the RWS curve) during tunnel fires.

Despite all limitations inherently involved on large-scale tests, they still constitute the basis for technical standards and guidelines used nowadays in tunnel fire safety engineering. In general, those tests created important background on: (1) fire development, spread of heat and smoke, and also on the production of toxic gases; (2) the influence of ventilation systems on smoke control and fire sizes; (3) escape, rescue and fire-fighting possibilities; (4) capabilities of fire detectors; and (5) the use of active protection systems (e.g. sprinklers) and passive protection systems (e.g. fire resistant boards).

Usually, there are mainly three concerns in the occurrence of a tunnel fire. The first, and most important point, is to *save human life*. Here, the primary objective is to provide tunnel users with safe escape conditions. This task involves, among other things, the design of mechanisms for smoke control, which is directly related to: (1) visibility aspects; (2) the level of concentration of toxic gases; and (3) the radiant heat flux towards the floor. The second point often considered during the design of a tunnel with regard to fire safety is to ensure good

firefighting possibilities for the fire brigade. This can be achieved, for instance, by providing firefighters with a clear access to the fire source. A third objective during the design stage is to ensure a certain level of *structural integrity* in case a tunnel fire comes to happen. This can be achieved in several different ways. One common option is to apply protective insulation layers on the tunnel lining, thus limiting the temperature development and thermal stresses developed inside the structure. Another frequent choice consists of the use of water-based systems, commonly known as fixed firefighting systems (FFFS), to control the development of HRR during a fire.

The work developed in this thesis is limited to the last goal described in the previous paragraph (i.e. achieving *structural integrity* during a tunnel fire). Even further, it is mainly focused on *concrete road tunnels* considering the current Dutch practices. In this context, the *structural integrity* of tunnels in the Netherlands is often evaluated according to a prescriptive-based approach, based on the use of the RWS curve (Figure 7.1). Also, most immersed tunnels in the Netherlands are partially protected by some sort of thermal resistant layer attached to their ceiling. Nowadays, this solution is also became more often used in land tunnels.

Powerful tools have emerged in the fire safety engineering field. Computational Fluid Dynamics (CFD) software were developed, allowing the accurate solution of complex fire dynamics flows. CFD has already become popular on the modelling of fire for the assessment of structures, permitting engineers to incorporate the analysis of idealized fire scenarios into the conception of more economically optimal projects. Nonetheless, despite its successful applications in other scenarios, the use of CFD for the evaluation of fires in tunnels is still rather limited, at least with regard to the design of fire safe structures. Therefore, this thesis aims on incorporating CFD modeling of different fire scenarios, accounting for the specific aspects of a particular tunnel, into the structural analysis of this tunnel through the use of finite element software (FEA). This work is hoped to serve as a link between fire safety engineering and structural design of *concrete tunnels*, moving towards a performance-based design. With that in mind, let us briefly cover two important aspects involved in this matter: (1) the regulations binding the structural design of tunnels subjected to fire; and (2) CFD modeling.

1.1 Regulations in the Netherlands

There are no internationally adopted regulations for tunnel fire safety (ITA [1]). In Europe, the Directive 2004/54/EC[1] defines the minimum safety requirements for tunnels in the trans-European road network (TERN). When considering the Dutch context, prescriptive measures are applied at different levels according to the type of tunnel in question, namely (1) *tunnels under open water* or (2) *other tunnels*. The regulations aim on ensuring a minimum level of performance for the tunnel structure in case of fire. The most important aspects are summarized below:

[1] https://eur-lex.europa.eu/legal-content/EN/TXT/HTML/?uri=CELEX:32004L0054&from=EN

- *Fire Regulations:*

For fires in road tunnels, the Dutch Annex of Eurocode 1 Part 1-2 [6] prescribes the use of the RWS fire curve (Figure 7.1). Additional requirements are imposed by Rijkswaterstaat in '*Richtlijnen Ontwerp Kunstwerken*' (ROK 1.4 [7]), and also in '*Landelijke Tunnelstandaard*' (LTS 1.2 [8]). Those are valid for tunnels longer than *250 m* and are applied differently according to the tunnel category:

1) *Tunnels under open water:* The tunnel may not collapse when exposed to a 120 minutes fire according to the RWS curve.

2) *Other tunnels:* New constructions or other tunnels may not collapse for a 60 minutes fire according to the RWS curve. For existing tunnels, the exposure time is reduced to 30 minutes.

An additional requirement often stated in contract is that tunnels must be repairable after the occurrence of a major fire. Thus, when accounting for a certain degree of reparability, the tunnel manager may opt for a higher level of fire protection. In this case, the same requirements for *tunnels under open water* are commonly required.

- *Structural Requirements:*

In the Netherlands, the structural capacity of concrete tunnels under fire must be verified in accordance with Eurocode 2 Part 1-2 [9], considering also the correspondent Dutch Annex [10]. Here, extra requirements are also stated by Rijkswaterstaat in ROK 1.4 [7]. Accordingly:

- *Maximum temperature requirements:*
  - Reinforcement: Must not reach *250 ^{o}C*
  - Concrete: For *immersed tunnels*, the temperature of the concrete surface must not reach *380 ^{o}C*. For *other tunnels*, the temperature of the concrete surrounding the rebars should be limited to *380 ^{o}C*.

- *Spalling:*

Unless specified otherwise in contract, measures must be taken against concrete spalling. Those can be: (1) applying protection to the concrete structure; or (2) making use of a concrete mixture that is insensitive to spalling, possibly achieved by adding polypropylene fibers. In either case, the capacity of the selected method in preventing spalling must be confirmed through fire tests, that are to be developed in accordance with the prescriptions given in '*Fire testing procedure for concrete tunnel linings*' [11].

Note that, at the moment, after several tests performed in previously considered *non-spalling concrete* demonstrated the occurrence of severe progressive spalling in such mixtures (van der Waart and van Gulik [12]), the susceptibility of *unprotected concrete tunnels* to suffer from spalling is a big concern in the Netherlands.

1.2 Computational Fluid Dynamics (CFD)

CFD-based fire models provide numerical solutions for a set of differential equations describing conservation of (1) mass, (2) momentum, and (3) energy within the fire and

surroundings. By performing a fire simulation one will obtain predictions of gas temperatures, gas velocities and gas species concentrations in time, within the control volume (i.e. the domain of simulation). The governing equations are briefly introduced below based on McGrattan and Milles [13]:

- *Conservation of Mass:*

$$\frac{\partial \rho}{\partial t} + \nabla \rho u = 0 \qquad 1.1$$

This equation states that mass will not be created neither destroyed within the domain of simulation. In essence, it prescribes that for every point in the flow field, changes in gas density (ρ) are equal to the net mass flux (ρu) across the boundaries of a small control volume around that correspondent point. As described by McGrattan and Milles [13], in fires, there are several gas species which will be involved in the simulation (e.g. fuel, products of combustion and oxygen). Therefore, equation 1.1 is often rewritten in terms of a set of transportation equations accounting for the mass fractions of each gas species individually. As the idea here is just to introduce the concept of CFD, such formulations will not be presented. Still, it is worth mentioning that the added contribution of all species in the total mass diffusion and production will equal zero.

- *Conservation of Momentum:*

$$\frac{\partial (\rho u)}{\partial t} + \nabla (\rho u u) = -\nabla p + \mathrm{f} + \nabla \tau \qquad 1.2$$

McGrattan and Milles [13] explain that conservation of momentum describes the use of *Newton's Second Law* (i.e. force equals mass times acceleration) for a fluid. Accordingly, the driving force is a combination of pressure gradient (∇p), viscosity generated friction (τ) and external forces (f), such as buoyancy. Equation 1.2 is actually a set of three equations for each velocity component (u) in a three-dimensional geometry.

- *Conservation of Energy:*

$$\frac{\partial (\rho h)}{\partial t} = \nabla (\rho h u) = \frac{Dp}{Dt} + \dot{q}''' - \nabla q + \varepsilon \qquad 1.3$$

Conservation of energy is formulated rather similarly to conservation of mass, and describes that the change of enthalpy (h) at a given point will equal the net energy flux across the boundaries of a small control volume around this point. Energy contributions to gas phase (right-hand side of equation 1.3) are due to: (1) changes in pressure $\left(\frac{Dp}{Dt}\right)$; (2) heat released through combustion ($\dot{q}'''$); (3) radiation and convection heat transfer (∇q); and (4) kinetic energy dissipation (ε). In fire applications, the terms related to pressure and kinetic energy dissipation are negligible, expect for cases in which a compartment is sealed and would therefore lead to a substantial increase in pressure (McGrattan and Milles [13]).

- *Equation of State:*

To close the system of differential equations given by conservation of mass, momentum and energy within a gas body, an equation of state for the gas phase is needed. In fire applications the most common approach is to assume *perfect gas* behavior according to:

$$p = \frac{\rho R T}{\bar{W}} \qquad 1.4$$

where p is the pressure of the gas, ρ is the density, R is the universal gas constant, T is the gas temperature and $\bar{W}$ is the average molecular weight of a gas mixture.

Note that the equation of state relates the pressure of a mass of gas (p) to its enthalpy (h), which is a function of the specific heat at pressure p (c_p) and the temperature (T) of this fluid, as depicted below:

$$h = \int_{T_o}^{T} c_p dT \qquad 1.5$$

1.2.1 Fire Dynamics Simulator (FDS)

FDS is an open-source software, developed by the National Institute of Standards and Technology (NIST) of the United States, which describes low-speed flows, focusing on smoke and heat transport from fires. This CFD code, although still in constant development, is highly recognized by the fire engineering community worldwide and appears to be one of the most used software when performing fire simulations. Ideally, such simulations would be handled by the numerical solution of the governing equations 1.1 to 1.3 through Direct Numerical Simulation (DNS), without the use of any approximation model. However, to be able to capture small-scale diffusive process occurring within the flames and boundary layers near solid obstructions, very small grid sizes (in the order of *1 mm*) are required such that FDS could produce accurate results while operating in DNS mode. Therefore, in real life, it is still impractical to use DNS on solving daily engineering problems related to large-scale fire simulations. To overcome this issue, FDS allows the user to make use of a Large Eddy Simulation (LES) model. McGrattan and Milles [13] explain that through the use of LES, one attempts to resolve the flow field as faithfully as possible to the dynamics of fire while making use of spatial averaging arguments to replace unresolved convection terms by equivalent diffusion terms. This demands the user to pay close attention to the selected grid size, as the accuracy of LES can be severely harmed if there are not enough cells to capture the flow field adequately. Figure 1.1 below provides an illustration of such flow field (right image) and also of the smallest "eddy" (left image) which is captured by the selected grid size, here represented by distance between two consecutive arrows.

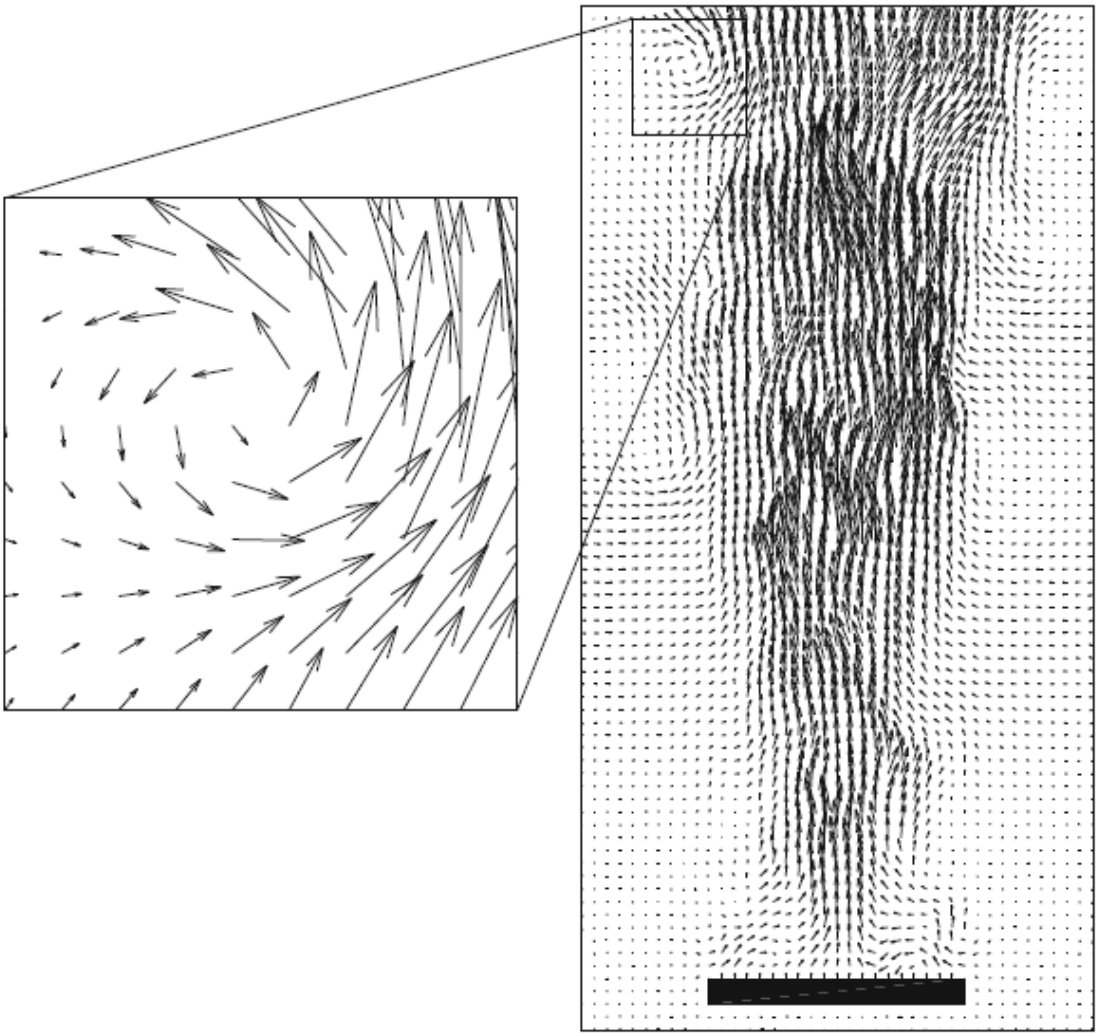


FIGURE 1.1 – FLOW FIELD IN A LES SIMULATION
Retrieved from McGrattan and Milles [13]

2 Problem Statement, Research Question and Objectives

2.1 Problem Statement

As depicted in Chapter 1, the design of concrete tunnels in The Netherlands is currently based on the application of prescriptive measures, relying deeply on the use of the RWS curve (Figure 7.1). This time-temperature curve was established out of tests carried out in the late 70's and early 80's, in a partnership of Rijkswaterstaat and TNO (The Dutch Organization for Applied Scientific Research). As described in ITA [1], a design that is solely based on the extreme high temperatures prescribed by the RWS curve, avoiding to consider the effects of specific conditions of a certain tunnel on fire development (e.g. tunnel geometry, tunnel ventilation and type of traffic allowed in the tunnel), might be overconservative. This raises the question of how conservative this curve can be when arbitrary applied to *concrete tunnels* and elucidates the need for new principles on establishing more optimal designs that account for realistic fire scenarios for each specific situation. In this sense, this thesis is aimed at investigating the possible benefits of incorporating CFD modeling of fire scenarios when for a specific tunnel with the structural analysis of the structure of this tunnel in a FEA software, setting the ground for a performance-based design in replacement of the more commonly adopted prescriptive approach.

2.2 Research Question and Objectives

- Research Question:

Considering the current prescriptive approach, adopted in the structural design of tunnels subjected to fire, how can CFD modeling of different fire scenarios be incorporated together with FEA modeling in the assessment of concrete tunnels, towards a performance-based approach?

- Objectives:

1) To understand: (1) the mechanism behind tunnel fires; (2) the protection systems currently used in tunnel fire safety engineering; and (3) the CFD methodology.

    a) What are the main parameters influencing fire development in tunnels?
    b) How to create realistic fire scenarios?
    c) What are the most used systems to ensure structural integrity in case of a tunnel fire? What kind of effects those systems can have on fire development inside the tunnel?
    d) What is CFD? What are the limitations in the application of CFD for modeling tunnel fires?

2) CFD modeling and validation of the tests on which the development of the RWS curve was based.

    a) What other fire curves are currently used in the design of tunnels worldwide?
    b) How does the RWS curve compare to the results of the RWS tests?
    c) What are the limitations and uncertainties involved on creating CFD models of those tests? How do the CFD models of these tests fit the experimental results?
    d) Is the temperature development inside the tunnel changed in case we alter the conditions originally applied in those tests?

3) To understand the consequences of fire to the structural integrity of the tunnel.

    a) What are the methodologies currently applied to evaluate the occurrence and damage of spalling in a structure?
    b) How does fire affect the mechanical properties of concrete?
    c) What parameters may affect the developed thermal stresses during a fire?
    d) How to describe the interface between fire and structure?

4) Case Study – Coupling CFD with FEA

    a) Does CFD modeling, considering a real fire scenario for the specific tunnel, lead to a smaller time-temperature development than that which is prescribed by the RWS curve?
    b) Can we ensure structural safety of the tunnel through this performance-based approach?

3 Tunnel Fires: State of The Art

There are several parameters which play a role in fire development inside a tunnel. Altogether, they make the phenomenon behind tunnel fires a very complex matter. In this sense, the main purpose of this chapter is to present a comprehensive overview of fire development in tunnels, providing the reader with the most important aspects of tunnel fires. Here, empirical models derived to calculate important parameters (e.g. gas temperatures at the ceiling, flame length and critical velocity) are also presented.

3.1 Fire Dynamics in Tunnels

Ingason [14] gives a full description of fire dynamics in tunnels, where the development of fire is considered to be essentially different than that which is achieved in an open environment. In the latter, burning happens without any enclosure effects, and the supply of air is very often unlimited. On the former, the geometry of the tunnel provides confinement, effectively increasing the heat feedback to the burning vehicles. This leads to a more intense burning, characterized by a higher heat release rate (HRR). Those scenarios are compared in Figure 3.1 below.

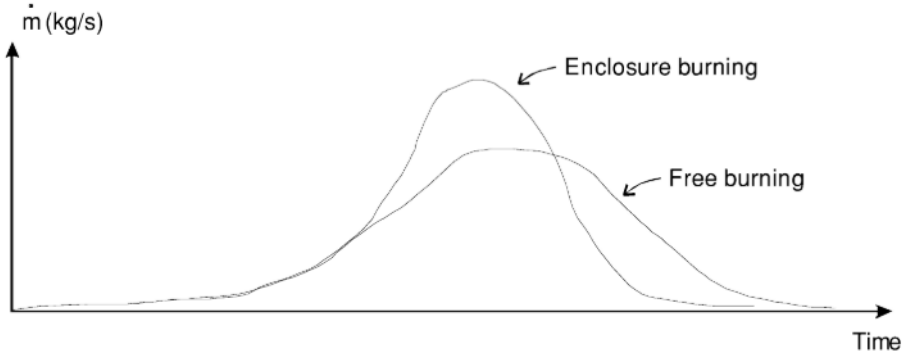


FIGURE 3.1 – ENCLOSURE AND FREE BURNING
Retrieved from Karlsson and Quintere [15]

Tunnel fires are also different from compartment fires. For those latter, the fire size is mainly governed by the area and height of openings located in the enclosure. For tunnels, however, more parameters come into play. In essence, the geometry of the tunnel, the ventilation conditions inside the tunnel, and the thermal properties of the tunnel structure (e.g. rock, concrete, or protection layer) might all have an influence on the development of a tunnel fire.

Compartment fires can be defined into separate stages (Figure 3.2). A fire can be either: (1) *fuel-controlled* (i.e. whenever there is enough oxygen available to combust all fuel vapors in the enclosure), meaning that fire growth is entirely dependent on the mass flow rate of the fuel; or (2) *ventilation-controlled* (whenever there is lack of oxygen to combust all the vaporized fuel), meaning that fire growth will be governed by the inflow of fresh air. Once a fire starts in a compartment, usually a *fuel-controlled* growing phase will take place. If there is lack of fuel, this growing phase will be directly followed by a decay phase. On the other hand, if enough fuel is available, fire will keep on growing, leading to the occurrence of flashover inside the enclosure. The latter is marked by a sudden increase on the HRR, characterizing a stage of extremely rapid fire growth, in which all combustible materials start contributing to fire development. The end of the flashover denotes a period known as fully developed fire, where,

most often, a *ventilation-controlled* fire scenario is achieved. If this is the case, fire development will now be dependent on both air and fuel supply rates, with the efficiency of combustion being governed by the ratio of fuel supply rate relatively to air supply rate. Finally, either fuel or air will cease to exist, and fire will enter a decay phase.

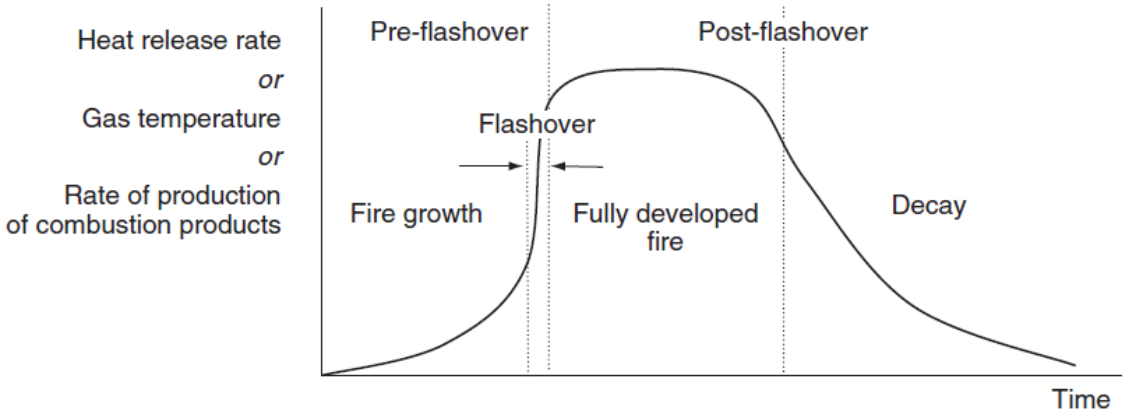


FIGURE 3.2 – COMPARTMENT FIRES
Retrieved from Ingason [14]

In enclosure fires, the heat and smoke are trapped inside the compartment, often making the availability of oxygen to become a limiting factor for fire development. This is generally not the case for tunnel fires, where most often, either due to pressure difference between the portals or through the use of mechanical ventilation systems inside the tunnel, air is continuously supplied thus sustaining fire development. Accordingly, most tunnel fires are expected to be *fuel-controlled*. Also, differently from compartment fires, tunnel fires will not experience flashover. This is due to larger heat losses to the surrounding walls, and also because of lack of fuel in relation to the volume size in which hot fire gases are contained. Although flashover is not achieved, a tunnel fire might develop to become *ventilation-controlled*. Such a scenario can occur in sufficiently large tunnel fires, where several vehicles are burning together. In these cases, the flames emerging from the vehicles burning at the edges of a vehicle line, will act as a barrier for air supply to the center of the fire, making the concentration of oxygen in the center to be significantly reduced. Due to this lack of oxygen, a *ventilation-controlled* fire scenario will be locally achieved. Ingason et al. [2] explains this scenario based on Figure 3.3 below.

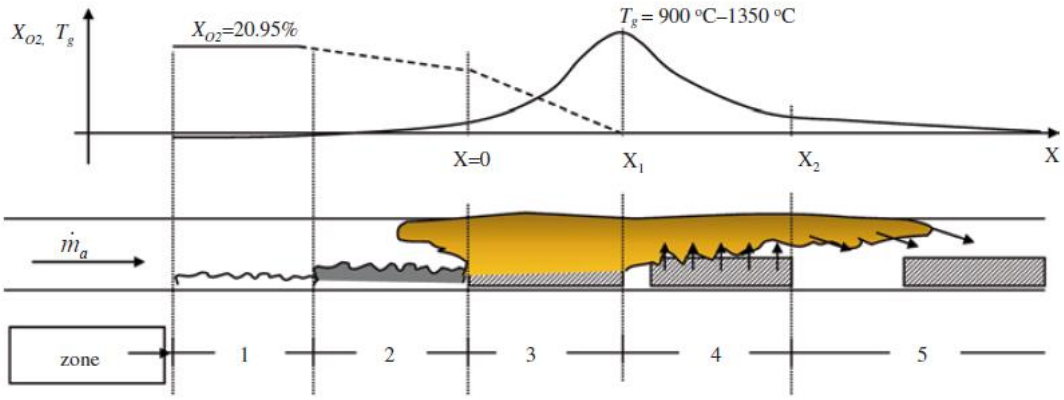


FIGURE 3.3 – VENTILATION-CONTROLLED TUNNEL FIRE
Retrieved from Ingason et al. [2]

Accordingly, there are five zones involved in a *ventilation-controlled* tunnel fire:

1) Burnout cooling zone
2) Glowing ember zone
3) Combustion zone
4) Excess fuel zone
5) Preheating zone

Three of those zones are of special interest for the explanation of a *ventilation-controlled* tunnel fire. There is the *fuel-controlled* combustion zone, which involves all burning vehicles and is marked by $X = 0$, where continuous combustion is achieved, and enough fuel and oxygen are present. From the beginning of the combustion zone and onwards, the gas temperatures increase rapidly to a peak value at $X = X_1$, while oxygen concentration decreases to zero at the same point. This marks the start of the excess fuel zone or, a *ventilation-controlled* zone. Due to high temperatures, fuel is still being vaporized from vehicles within this zone, but as the oxygen was already fully consumed to sustain fire in the previous zone, no combustion will take place here. This zone terminates at $X = X_2$, where the hot gases will cool down below the fuel pyrolysis temperature, and will only be enough to pre-heat further vehicles. Based on Ingason [14], one may define whether a tunnel fire is *fuel* or *ventilation-controlled* according to the air-to-fuel ratio (ϕ):

$$\phi = 3000 \frac{\dot{m}_a}{Q} \qquad 3.1$$

where $\dot{m}_a$ is the mass flow rate of oxygen supply (kg/s) and Q is the HRR (kW).

The equation above is useful in mainly two ways: (1) in case both $\dot{m}_a$ and Q are known, ϕ can be calculated to define whether a fire is *fuel-controlled* ($\phi \geq 1$) or *ventilation-controlled* ($\phi < 1$); (2) for cases where only $\dot{m}_a$ is known, one can set $\phi = 1$ to determine the HRR for which a fire will become *ventilation-controlled*. Note that the latter defines a situation where the amount of oxygen supply is precisely the required to achieve complete combustion, thus characterizing a *'stoichiometric'* condition. Also, according to the author, a good indication that the fire became *ventilation-controlled* is a sudden increase in the concentration of carbon monoxide (CO), a product of incomplete combustion.

3.1.1 Smoke Stratification

Smoke stratification is an important aspect in tunnel fire safety. It is related to several parameters of interest, such as the amount of asphyxiant fire gases, irritating gases and heat released in a fire, as well as the level of visual obscuration. Altogether, those are fundamental aspects when evaluating human escaping conditions during the occurrence of a tunnel fire.

The way smoke spreads is very affected by the ventilation conditions inside the tunnel. Figure 3.4 depicts those scenarios for: (a) natural ventilation; (b) low air velocity (up to *1 m/s*); (c) moderate air velocity (between *1* and *3 m/s*); and (d) high ventilation velocity (*>3 m/s*).

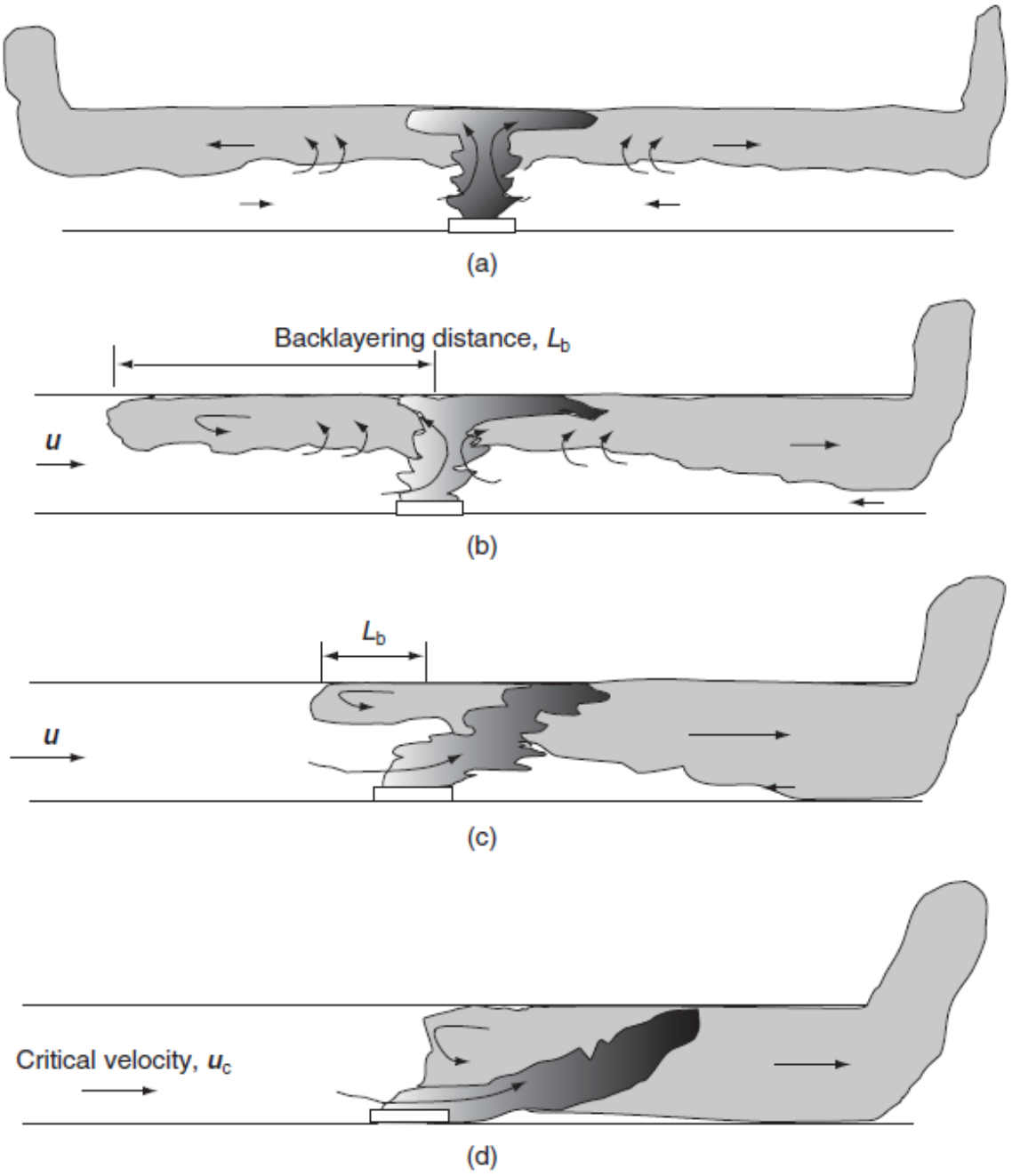


FIGURE 3.4 – SMOKE SPREAD FOR DIFFERENT CONDITIONS
Retrieved from Ingason [14]

The mechanism behind smoke stratification is quite complex. At first, due to buoyancy forces, the hot smoke flows towards the tunnel ceiling. Once it impinges at the top, it starts to flow longitudinally in the tunnel. Due to heat losses to the tunnel structure, and also because of mixing with cool air provided by ventilation, the temperature of the smoke layer decreases with distance from fire source. This lowers the thermal pressure and reduces the level of stratification inside the tunnel. As a result, the depth of the smoke layer will increase and might cover the whole cross section of the tunnel. According to Ingason et al. [2], the solution of a theoretical model to explain all those aspects while also including ventilation effects is too complex, and depends on parameters which cannot be accurately estimated. In this sense, a

simple model proposed by Newman [16] is very often applied to describe the situation in tunnels. Figure 3.5 illustrates the model and a full description of the regions involved on it is provided below:

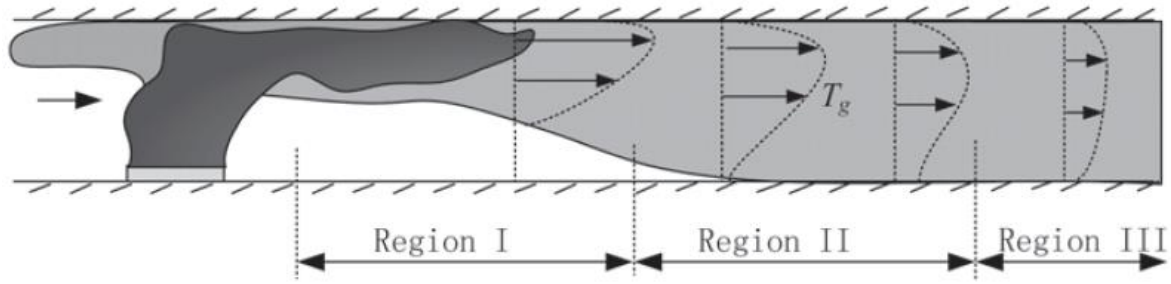


FIGURE 3.5 – SMOKE STRATIFICATION
Retrieved from Nyman and Ingason (2008) [17]

- *Region I* ($Fr < 0.9$): In this region, clear stratification is noticed. This means that buoyancy forces are governing, making the smoke layer to be concentrated at the ceiling. Accordingly, the gas temperatures near the floor are still at ambient conditions.

- *Region II* ($0.9 < Fr < 10$): This region is governed by the interaction between the ventilation velocity and the buoyancy forces. It is controlled by the mixture of fresh air and smoke, making the stratification to be less defined when compared to the previous region.

- *Region III* ($Fr > 10$): This region is marked by insignificant stratification, thus characterizing a homogeneous temperature profile for the smoke layer.

Each region on the model is characterized according to the Froude Number (Fr). The equations related to this parameter are provided in Section 11.1 of this master thesis.

3.2 Ventilation

Ventilation is one of the most important parts of tunnel fire safety. At normal conditions, ventilation systems serve to reduce the concentration of contaminants and heat generated by regular traffic. In case of fire, the ventilation system is also often intended to avoid the spread of smoke upstream of the fire, providing a safe route for evacuation and helping firefighters with their services. Nevertheless, the design of a ventilation system in order to mitigate the consequences of a fire requires great care, as it strongly affects the dynamics of fire itself. Moreover, if the latter is not properly addressed, an opposite desired effect may arise, with ventilation enhancing fire development instead of controlling it. For instance, Ingason et al. [2] describes that sufficiently large ventilation velocities can promote a cooling effect and might even extinguish the fire, but that low ventilation velocities will actually contribute to fire spreading.

There are two types of ventilation systems: (1) *natural ventilation* and (2) *mechanical ventilation* (Ingason et al. [2]). The first is based on environmental conditions and/or on large traffic flows. It is mainly used in very short tunnels, as its applicability to larger ones would require the use of many large shafts. The second kind of system is almost independent of any environmental conditions, making it more reliable, and thus widely used. Mechanical

ventilation is applied either in longitudinal ventilation systems or in transversal ventilation systems. Usually, the first kind of mechanical ventilation is preferred due to the simplicity and relatively low cost for the installation of jet fans.

3.2.1 Longitudinal Ventilation

These systems are generally based on the use of jet fans to create a longitudinal airflow inside the tunnel. This flow serves only to push the contaminants further ahead down the tunnel, and not to eliminate them. As a consequence, the concentration of pollutants will increase in distance from the entrance of the tunnel. This can lead to the occurrence of unacceptable concentration levels of contaminants in very long tunnels. If that is the case, then the use of shafts along the tunnel will be required to provide exchange of the polluted air with fresh air. Figure 3.6 below, provides illustration of longitudinal ventilation systems during normal conditions, while Figure 3.7 depicts their applicability on controlling smoke in case of a fire. Section 4.2.2 provides a deeper description of other effects that longitudinal ventilation can have on a tunnel fire.

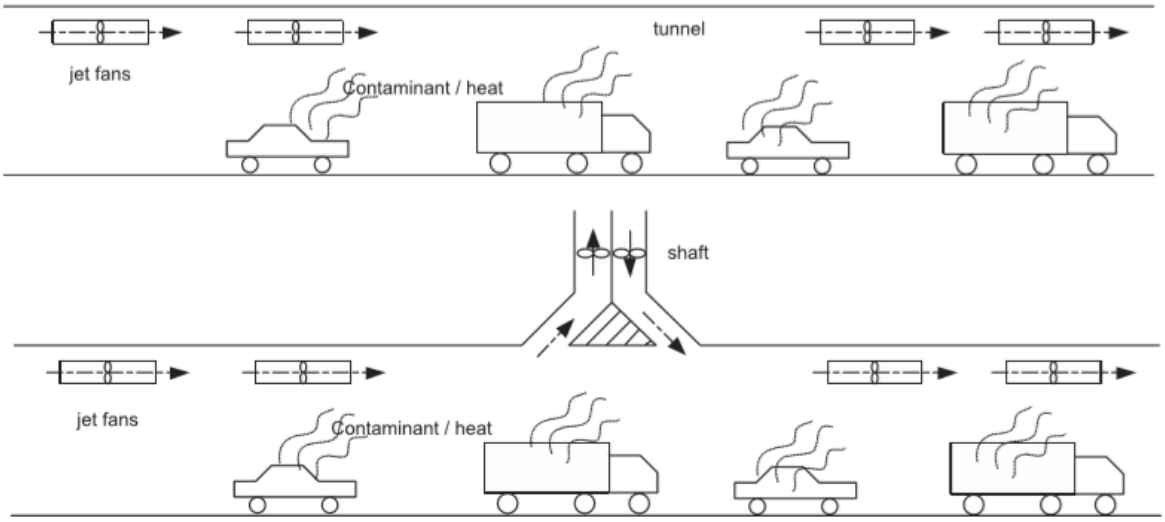


FIGURE 3.6 – LONGITUDINAL SYSTEMS
Retrieved from Ingason [14]

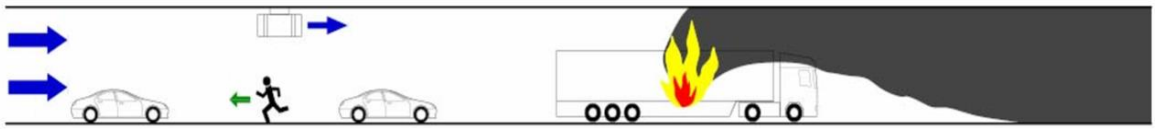


FIGURE 3.7 – SMOKE CONTROL WITH LONGITUDINAL SYSTEMS [2]

3.2.1.1 Backlayering Length

The use of longitudinal ventilation systems is also aimed on controlling backlayering of smoke in the upstream direction. This is an important task on ensuring a safe escape route for people inside the tunnel, and also on providing firefighters with direct access to the fire source.

[2] http://www.cetu.developpement-durable.gouv.fr/

Backlayering of smoke during a fire will occur in case the longitudinal ventilation inside the tunnel is below a certain critical velocity (Section 0). Figure 3.8 illustrates this scenario.

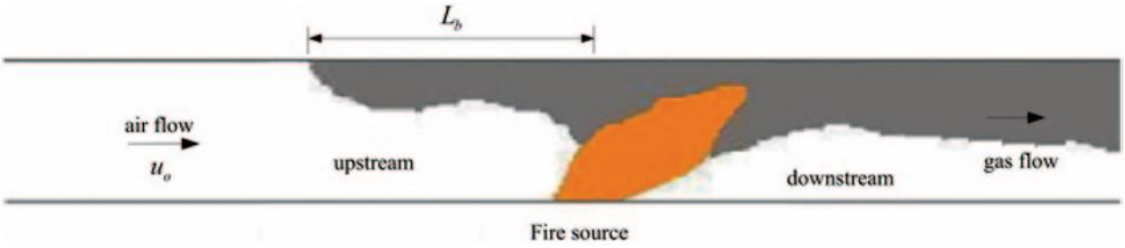


FIGURE 3.8 – BACKLAYERING IN A TUNNEL FIRE
Retrieved from Ingason [14]

Several models to calculate the backlayering length were found in literature:

1) Thomas [18]:

Thomas was the first author to propose an equation to estimate the backlayering length L_b (m). His work considers theoretical correlations between the hot plume above fire and the backflow of hot gases in a longitudinal flow, making a correlation of the critical velocity and the Froude Number. Accordingly:

$$\frac{L_b}{H} = 0.6\left(\frac{2gHQ}{T_0\rho_a c_p u^3 A} - 5\right) \qquad 3.2$$

where T_0 is the average fire temperature (K), H is the tunnel height (m), Q is the HRR (kW), g is the gravitational acceleration (m/s^2), ρ_a is the ambient air density (kg/m^3), c_p is the heat capacity (kJ/kgK), u is the longitudinal velocity (m/s) and A is the cross section area of the tunnel (m^2).

2) Vantelon et al. [19]:

Differently from Thomas [18], the authors proposed a formulation in which backlayering length is proportional to a modified Richardson Number:

$$\frac{L_b}{R} \sim \left(\frac{gQ}{T_0\rho_a c_p u^3 R}\right)^{0.3} \qquad 3.3$$

where R is the tunnel radius (m) and the other parameters are the same as stated in equation 3.2.

3) Li et al. [20]:

This study reports on a correlation between the ratio of ventilation velocity by critical velocity, namely dimensionless confinement velocity (V^{**}), and the ratio of backlayering length by tunnel height or, the dimensionless backlayering length ($L_b{}^*$). Based on experimental results, the following formulation to estimate the backlayering length is proposed:

$$\frac{L_b}{H} = L_b^{\ *} = \begin{cases} 18.5\, ln\left(0.81\frac{Q^{*\frac{1}{3}}}{u^*}\right), Q^* \leq 0.15 \\ 18.5\, ln\left(\frac{0.43}{u^*}\right), Q^* > 0.15 \end{cases} \quad \textbf{3.4}$$

with

$$Q^* = \frac{Q}{T_a \rho_a c_p g^{\frac{1}{2}} H^{\frac{5}{2}}};\ u^* = \frac{u}{\sqrt{gH}}$$

where L_b is the backlayering length (m), and H is the tunnel height (m). Also, in the above equation, Q^* is the dimensionless HRR, u^* is the dimensionless longitudinal velocity, T_a is the ambient temperature (K), H is the tunnel height (m), Q is the HRR (kW), g is the gravitational acceleration (m/s^2), ρ_a is the ambient air density (kg/m^3), c_p is the heat capacity (kJ/kg.K) and u is the longitudinal velocity (m/s).

This relation confirms the dependency of the backlayering length on the modified Richardson Number, but with a different coefficient than the one proposed by Vantelon et al. [19]. At higher HRRs, the backlayering length has shown to be dependent only on the ventilation velocity. The authors have also pointed out that the backlayering length is likely to reduce in case there is vehicle obstruction upstream the fire source, meaning that any small change in ventilation velocity yields in greater change of the backlayering length. Gannouni and Maad [21] CFD simulations prove this previous claim and show that the backlayering length is significantly smaller in case there is an obstruction upstream the fire.

4) Meng et al. [22]:

The authors evaluated the effects of blockage ratio on backlayering length of longitudinally ventilated tunnel fires. The model depicted by equation 3.4 was used to study model-scale test results, performing accurately on estimating the backlayering length in empty tunnels, but failing when accounting for the effects of vehicular blockage upstream the fire source. Thus, a new correlation considering the blockage ratio (ϕ) (i.e. the percentage of the tunnel that is blocked by an obstacle upstream the fire source) was proposed:

$$L_b^{\ *} = \begin{cases} [16.12 + ln(4.689(1-\phi) - 3.436)]\, ln\left(\frac{Q^{*\frac{1}{3}}}{u^*}\right) - 3.5(1-\phi) - 1.512 & , \phi < 0.39 \\ [8.5(1-\phi) + 0.525]\, ln\left(\frac{Q^{*\frac{1}{3}}}{u^*}\right) - 5.617(1-\phi) + 2.192 & , \phi \geq 0.39 \end{cases} \quad \textbf{3.5}$$

where $L_b^{\ *}$ is the dimensionless backlayering length or, the ratio between the backlayering length L_b by the tunnel height H; Q^* is the dimensionless HRR and u^* is the dimensionless longitudinal velocity, as in equation 3.4; and ϕ is the blockage ratio.

3.2.1.2 Critical Velocity

Critical velocity is defined as the minimum longitudinal velocity required to avoid any backlayering of smoke in the upstream direction during a tunnel fire. It is an important parameter at hand of tunnel designers to decide upon mechanical ventilation systems, and thus provide a clean escape route for people upstream the fire, while also helping firefighters to

procced their job. According to Ingason [23], this is the most well investigated parameter in tunnel fire research. Numerous studies proposed formulations to predict the critical velocity in a tunnel. The most well-known models are shortly described below:

1) Thomas [18, 24]:

Once again, Thomas was the first author to propose a correlation to estimate the critical velocity. Based on the assumption of immediate full mixing of heat and incoming air at the fire source, he suggested a dependency of critical velocity on a critical Froude Number:

$$u_c = \left(\frac{gQ'}{\rho_a c_p T_a}\right)^{1/3} \qquad \textbf{3.6}$$

where u_c is the critical velocity (m/s), g is the gravitational acceleration (m/s^2), Q' is the convective heat release rate per unit width of the tunnel (kW/m), ρ_a is the ambient air density (kg/m^3), c_p is the heat capacity (kJ/kg.K), and T_a is the ambient temperature (K).

2) Oka and Atkinson [25]:

This is the first study which reported on the independency of the critical velocity on the HRR for large fires. Based on a series of model-scale tests they formulated equations to estimate the critical velocity for small and large fires. In their proposition, the critical velocity is taken to be independent on the tunnel width. For small fires it should decrease for increasing tunnel heights, whereas an opposite effect is expected for large fires. Accordingly:

$$\frac{u_c}{\sqrt{gH}} = u_c^* = \begin{cases} 0.7\, Q^{*1/3} & Q^* \leq 0.124 \\ 0.35, Q^* & Q^* > 0.124 \end{cases} \qquad \textbf{3.7}$$

with

$$Q^* = \frac{Q}{\rho_a c_p T_a g^{1/2} H^{5/2}}$$

where u_c is the critical velocity (m/s), g is the gravitational acceleration (m/s^2), H is the tunnel height (m), Q is the heat release rate (kW), ρ_a is the ambient air density (kg/m^3), c_p is the heat capacity (kJ/kg.K) and T_a is the ambient temperature (K).

3) Wu and Bakar [26]:

Based on experimental results, the authors proposed a correlation of critical velocity on the hydraulic diameter, incorporating the effects of tunnel width into Oka and Atkinson [25]. According to their model, for small fires the critical velocity should reduce for increasing tunnel width, whereas for larger fires an opposite effect is expected, and the critical velocity becomes proportional to the width of the tunnel.

$$\frac{u_c}{\sqrt{g\bar{H}}} = u_c^* = \begin{cases} 0.68\, Q^{*1/3} & Q^* \leq 0.2 \\ 0.40 & Q^* > 0.2 \end{cases} \qquad \textbf{3.8}$$

with

$$Q^* = \frac{Q}{\rho_a c_p T_a g^{1/2} \bar{H}^{5/2}}$$

where u_c is the critical velocity (m/s), g is the gravitational acceleration (m/s^2), $\bar{H}$ is the hydraulic diameter of the tunnel (m), Q is the heat release rate (kW), ρ_a is the ambient air density (kg/m^3), c_p is the heat capacity (kJ/kg.K) and T_a is the ambient temperature (K).

4) Kunsch [27]:

Differently from the previous studies under the matter, the author approached the problem through a theoretical analysis over ceiling jets under unconfined ceilings, also proposing a formulation to estimate the critical velocity. Despite its weakness on describing large fires, his work serves as the basis for further improvements of models based on this methodology (Ingason [23]). Kunsch's proposal is given by the equation below:

$$\frac{u_c}{\sqrt{gH}} = u_c^* = 1.52 \frac{Q^{*\frac{1}{3}} \sqrt{C_1 + (C_1 - C_2)\, 6.13\, Q^{*\frac{2}{3}}}}{1 + 6.13\, Q^{*\frac{2}{3}}} \qquad \textbf{3.9}$$

with

$$Q^* = \frac{Q}{\rho_a c_p T_a g^{1/2} H^{5/2}}$$

where u_c is the critical velocity (m/s), g is the gravitational acceleration (m/s^2), H is the tunnel height (m), Q is the heat release rate (kW), ρ_a is the ambient air density (kg/m^3), c_p is the heat capacity (kJ/kg.K), T_a is the ambient temperature (K). C_1 and C_2 are two constants which are calculated according to the tunnel geometry (i.e. tunnel height and width).

5) Li et al. [20] and Li and Ingason [28]:

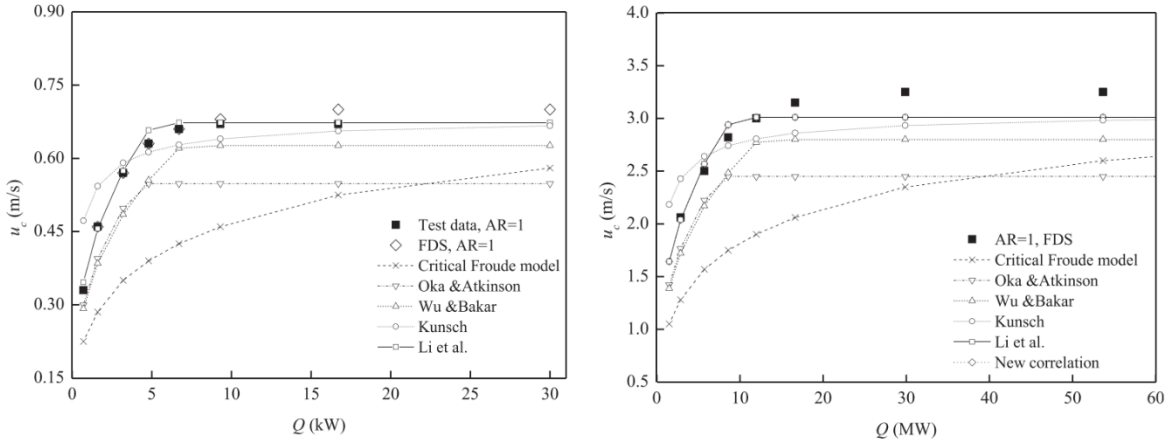
Li et al. [20] carried out theoretical and model analysis to predict the critical velocity in tunnel fires. They have confirmed that an upper limit for the critical velocity exits for growing HRR, but greater coefficients than the ones proposed by Oka and Atkinson [25] and Wu and Bakar [26] were found. Reason is made to the fact that these previous experiments erroneously applied water sprays to cool off the walls, thus changing considerably fire dynamics inside the tested tunnels. This study was later updated by Li and Ingason [28] through numerical simulations and model-scale tests, and includes the effects of tunnel width on the formulation to predict critical velocity. Results have shown that for small fires (up to 20 MW) the critical velocity decreases for increasing tunnel width, while for large fires, the critical velocity becomes independent on the tunnel width. It was also shown that the effects of tunnel height are more dominant than the effects of tunnel width, what explains the already good predictions previously obtained by the application of the first model which excluded the width effect. Figure 3.9 presents a comparison of all models described in this thesis with model-scale test results and also with large-scale CFD simulations. It is interesting to notice that at a longitudinal velocity of approximately *3 m/s*, independent of the level of HRR, no backlayer smoke will exist inside the tunnel. Also, keep in mind that that the line entitled '*New correlation*' refers to the model proposed by Li and Ingason[28]:

$$u_c{}^* = \frac{u_c}{\sqrt{gH}} = \begin{cases} 0.81\,\varphi^{-\frac{1}{12}}\,Q^{*\frac{1}{3}} & Q^* \le 0.15\varphi^{-\frac{1}{4}} \\ 0.43 & Q^* > 0.15\varphi^{-\frac{1}{4}} \end{cases} \qquad \textbf{3.10}$$

with

$$Q^* = \frac{Q}{\rho_a c_p T_a g^{1/2} H^{5/2}} \; ; \; \varphi = \frac{W}{H}$$

where u_c is the critical velocity (m/s), g is the gravitational acceleration (m/s^2), H is the tunnel height (m), W is the tunnel width (m), Q is the heat release rate (kW), ρ_a is the ambient air density (kg/m^3), c_p is the heat capacity (kJ/kg.K) and T_a is the ambient temperature (K).



(a) model scale tests (b) full scale simulations

FIGURE 3.9 – CRITICAL VELOCITY MODELS
Retrieved from Li and Ingason [28]

There are also numerous studies on critical velocity which are based on CFD calculations. The main findings are provided below:

a) Hwang and Edwards [29]:

Through numerical simulation the authors confirmed that the critical velocity levels-off for large HRR, relating this fact to the achievement of a maximum temperature above the fire source. They have also reported in a non-linear effect of tunnel inclination on the critical velocity.

b) Vauquelin and Wu [30]:

The authors evaluated the effect of tunnel width on the critical velocity and concluded that the backflow should be easily prevented for both rather narrow and quite wide tunnels.

c) Tsai et al. [31]:

This study investigated on the critical velocity in case of multi-source tunnel fires. According to it, if the distance between two adjacent fires is rather small, then the critical velocity should be the same of that for a single case with added HRR from both fires. In case the fire sources are enough apart from each other, then the critical velocity is determined by the HRR of the

single greater fire. Finally, for identical fires, the critical velocity should decrease for greater distances between the two sources.

d) Gannouni and Maad [21]:

The authors proved based on CFD models that the critical velocity decreases with the presence of obstructions upstream the fire source. This effect is reported to increase even further if the obstruction is placed at higher levels relatively to the floor.

3.2.2 Transverse Ventilation

Transverse ventilation systems are the ones where air flows transversely from supply vents into exhaust vents. For such a system to function, many vents positioned longitudinally along the tunnel are required to ensure constant supply of fresh air and exhaustion of contaminants (Figure 3.10). This system is often used to control smoke propagation in tunnels with traffic flows running in both directions (Figure 3.11).

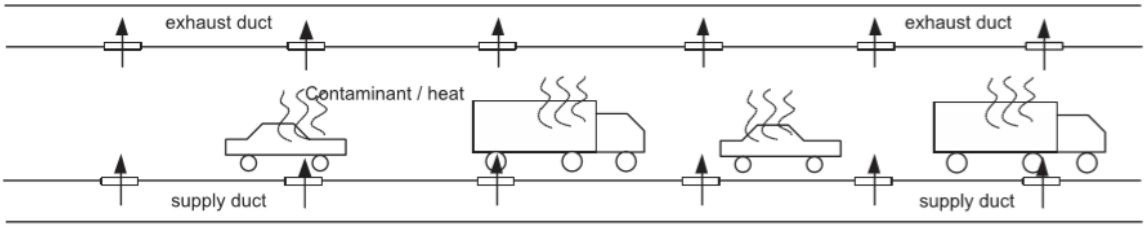


FIGURE 3.10 – TRANSVERSE VENTILATION SYSTEM
Retrieved from Ingason [14]

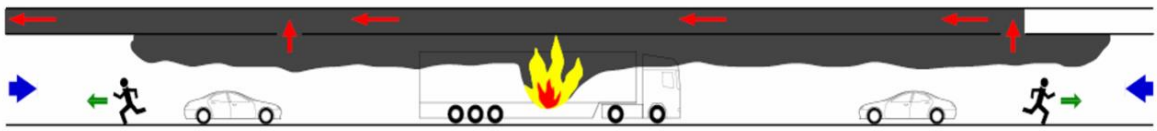


FIGURE 3.11 – SMOKE PROPAGATION IN TRANSVERSE SYSTEMS [3]

3.3 Fire Spread

A serious tunnel fire scenario is often achieved when fire spreads to adjacent vehicles. Whenever this happens, fire grows in size, yielding in a hazard condition for evacuees and also reducing the possibilities for firefighters. Situations in which fire spread between several vehicles led to the most severe tunnel fire accidents reported to date, with catastrophic outcome. This was the case for the Mont Blanc tunnel between France and Italy, where a tunnel fire in 1999 led to the death of 39 people.

Ingason et al. [2] describes the main mechanisms of fire spread in a tunnel:

1) *Flame impingement:* Direct impingement of flame or hot smoke layer in an adjacent vehicle.

[3] http://www.cetu.developpement-durable.gouv.fr/

2) *Flame surface spread*: Flame spread across the surface of the fire load.

3) *Spontaneous ignition*: Due to high temperatures along the tunnel, a vehicle that is not very close to the fire source might absorb enough heat and simply ignite.

4) *Fuel transfer*: Leaking may lead to liquid fuels to spread and reach further vehicles.

5) *Explosion*: Explosion, for instance of a fuel tanker, may spread burning fuel to nearby vehicles.

In case of tunnel fires, flame impingement and spontaneous ignition are of special interest. In the former, flame impinges on the ceiling thus spreading longitudinally, and may, therefore, reach vehicles in the vicinity of the fire or even further away, leading those to piloted ignition. Carvel et al. [32] determined the probability of fire impingement on other vehicles for different fire scenarios. According to the authors, small car fires (limited to 8 MW) produce flames that can probably impinge on another vehicle located up to *5 m* away, while large HGV fires (greater than 64 MW) will most certainly produce flames that are able to reach another HGV within a *20 m* range. Hence, this mechanism might be the governing situation for fire spread to larger targets (e.g. HGVs) around the fire source.

Spontaneous ignition is also likely to occur in a tunnel fire. In that case, the heat transfer, either through radiation or convection, is of such magnitude that a target located away from the fire source just spontaneously ignite. Figure 3.12 below provides illustration of the two main mechanisms described here. According to Lönnemark and Ingason [33], when added together, these mechanisms make flame length and plume temperatures to be the most important parameters in the assessment of fire spread. Those are further investigated on Sections 3.3.1 and 3.3.2, respectively.

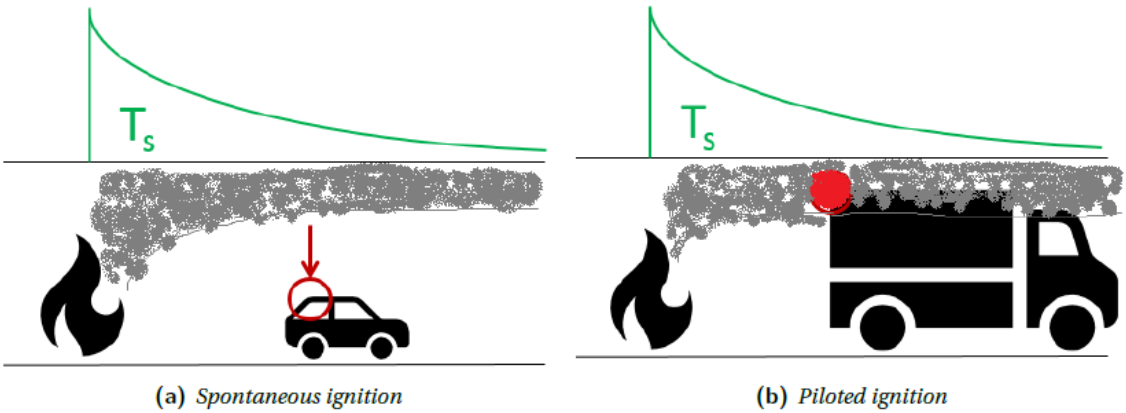


FIGURE 3.12 – MECHANISMS FOR FIRE SPREAD IN TUNNELS
Retrieved from de Poli [34]

It is important to highlight the differences between the two ignition modes described previously, namely (a) spontaneous ignition and (b) piloted ignition (Figure 3.12). Thus, a certain object only ignites when attaining a critical temperature, which is dependent on the mode of ignition and varies per material. Considering the materials that are often involved in tunnel fires, Ingason [14] estimates this critical temperature according to the mode of ignition:

1) *Spontaneous Ignition:*
   - 600 ºC if exposed to radiant heat
   - 500 ºC if exposed to convective heat

2) *Piloted Ignition:*
   - 300 – 410 ºC for radiant heat
   - 450 ºC for convective heat

3.3.1 Flame Length

On a literature review over tunnel fire dynamics, Ingason [23] reported that despite its importance when addressing tunnel fires, studies regarding flame length are rather limited, highlighting the urgent need for new researches over the topic. A summary of the main models used to estimate the flame length in tunnel fires is provided below. In the end, a study describing blockage effects on flame length is also presented:

1) Rew and Deaves [35] :

Based on the results of well-known large-scale tests in the Channel Tunnel (connecting France to the United Kingdom), the authors proposed the first correlation to predict the flame length of a tunnel fire. Accordingly:

$$l_f = 0.02\left(\frac{Q}{120}\right)\left(\frac{u}{10}\right)^{-0.4} \qquad 3.11$$

where l_f is the flame length (m), Q is the HRR (kW) and u is the longitudinal ventilation velocity (m/s).

Here, the total flame length was defined as the *horizontal distance from the center of the fire source to a 600 ºC contour*. More recent studies under the matter still follow this definition on the derivation of new models.

2) Lönnermark and Ingason [33]:

The authors used the model developed by Rew and Deaves [35] to address the results of large-scale tests in the Runehamar Tunnel (Norway). Apparently, as their model fails to account for the geometry of the tunnel, its applicability on describing the flame length achieved inside other tunnels (i.e. with a different geometry than that of the Channel Tunnel) is rather limit. In this sense, a new correlation was proposed by Lönnermark and Ingason [33], in which the effects of tunnel height were included:

$$l_f = \frac{1370 Q^{0.8} u^{-0.4}}{\left(T_f - T_a\right)^{3/2} H^{3/2}} \qquad 3.12$$

where l_f is the flame length (m), T_f is the flame tip temperature (K), T_a is the ambient temperature (K), H is the tunnel height (m)), Q is the HRR (kW) and u is the longitudinal velocity (m/s).

3) Ingason and Li [36] and Ingason et al. [2]:

Ingason and Li (2010) [36] defined a dimensionless flame length ($l_f{}^*$) as the ratio of the flame length (l_f) by the tunnel height (H), and noted a linear relationship of this parameter with a

dimensionless HRR (Q_f^*). In a later stage, Ingason et al. [2] updated the previous work and proposed a simple model to evaluate the flame length of large tunnel fires, for which different scenarios can be achieved according to the longitudinal velocity in the tunnel. Basically, for rather small velocities, flames shall propagate both upstream and downstream the fire source (Figure 3.13). For higher velocity levels, a different scenario is expected, in which flames shall only propagate downstream of the fire source (Figure 3.14).

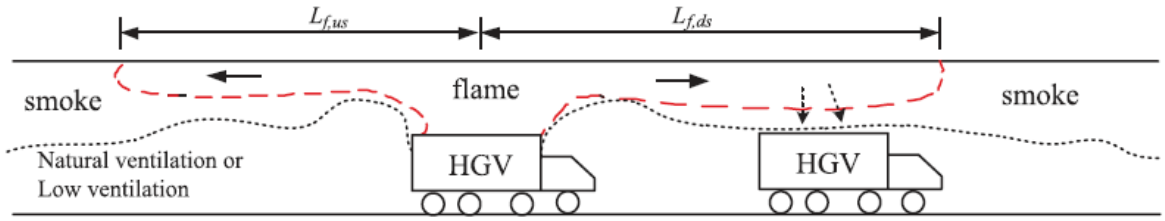


FIGURE 3.13 - FLAME LENGTH FOR LOW LONGITUDINAL VENTILATION
Retrieved from Ingason et al. (2015) [2]

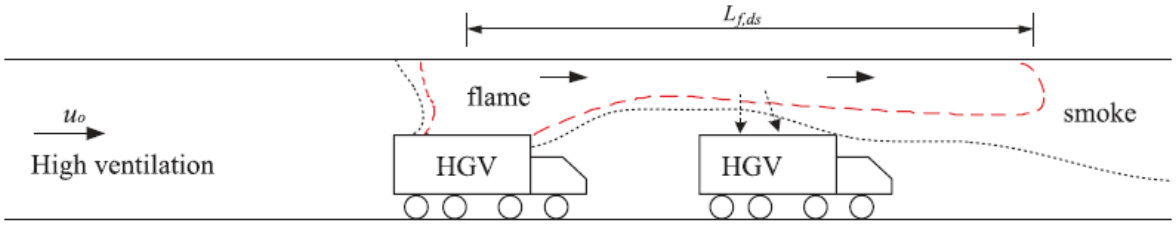


FIGURE 3.14 – FLAME LENGTH AT RELATIVELY HIGH LONGITUDINAL VENTILATION
Retrieved from Ingason et al. [2]

A transition velocity defining the limit between those scenarios is defined according to large-scale test results, and is given by $u_{tp}{}^* = 0.30$. Thus, based on the calculation of the dimensionless velocity as in equation 3.4, one may define which one of the two conditions (depicted in Figure 3.13 and Figure 3.14) is expected to occur. Accordingly, the model described below can be used to estimate the flame length:

- *Flame length downstream the fire source:*

$$\frac{l_{f,ds}}{H} = 5.5\, Q_f^* \qquad \textbf{3.13}$$

with

$$Q_f^* = \frac{Q}{\rho_a c_p T_a g^{\frac{1}{2}} A H_{ef}{}^{\frac{5}{2}}}$$

where $l_{f,ds}$ is the flame length downstream the fire (m), H is the tunnel height (m), Q is the HRR (kW), ρ_a is the ambient air density (kg/m^3), c_p is the specific heat capacity of air (kJ/(kg K)), T_a is the ambient temperature (K), A is the cross-sectional area of the tunnel (m^2), g is the gravitational acceleration (m/s^2), and H_{ef} is the height from the surface of the fire to the ceiling (m).

- *Maximum total flame length:*

Note that the maximum flame length is given by a situation without the use of longitudinal ventilation in the tunnel. According to the author, it is approximately twice the value of the total length in a tunnel under high ventilation velocity.

$$\frac{l_{f,mt}}{H} = 10.2\ Q_f^* \qquad \textbf{3.14}$$

where $l_{f,mt}$ is the maximum achievable flame length (m), H is the tunnel height (m) and Q_f^* is given by equation 3.13.

Equations 3.13 and 3.14 depicted above can be used to estimate the flame length for both scenarios, namely *low* and *high longitudinal ventilation.* For the former case, flame will propagate in both directions and equation 3.13 will provide the flame length downstream of the fire source, while equation 3.14 will give the total flame length. Thus, the flame length upstream the fire source is simply the difference between both terms. For the latter case, flame will only exist in downstream direction, and its length is given according to equation 3.13.

Note that despite considering the level of ventilation on the tunnel to define which scenario is likely to occur, the model avoids to account for the influence of ventilation on the total flame length. In reality, this is clearly not the case, as the flame length in known to be considerably reduced by the use of high ventilation velocities. Thus, the model presented here shall be understood as providing the boundaries of the *maximum achievable flame length* inside a tunnel for a given HRR.

4) Qiu et al. [37]:

In a more recent study, Qiu et al. performed model-scale tests accounting for various HRRs, several source to ceiling heights, different levels of longitudinal ventilation and different burner sizes to evaluate the flame length. Their study shows that the flame length: (1) increases for higher HRR; (2) decreases if the distance between the fire source and the ceiling is increased; (3) is reduced in wider tunnels; and (4) is significantly reduced by the use of longitudinal ventilation, even for low ventilation velocities. The authors have also proposed two models to calculate the flame length for situations *with* and *without longitudinal ventilation*, which assume that air entrainment on the impinged ceiling flow consumes unburnt fuel inside the buoyant plume. As the formulation is quite extensive, their model is given in Section 11.2.

5) Wang [38]:

The author investigated through CFD models the effects of blockage both upstream and downstream the fire source by comparing the scenarios with a situation without blockage (Figure 3.15). Note that all simulations included longitudinal ventilation. For upstream blockage (b), an increase on the flame length was noted. This could lead to shorter spontaneous ignition of objects downstream the fire, thus favoring fire spread. For the case of downstream blockage (c), the flame length was shortened. Nonetheless, in this situation fire became *under-ventilated*, what in reality would mean a significant increase on the production of carbon monoxide (CO), thus leading to dangerous conditions for tunnel users located downstream the

fire source. Therefore, according to the authors the presence of obstructions, both downstream and upstream a fire, shall increase the potential risk of a tunnel fire.

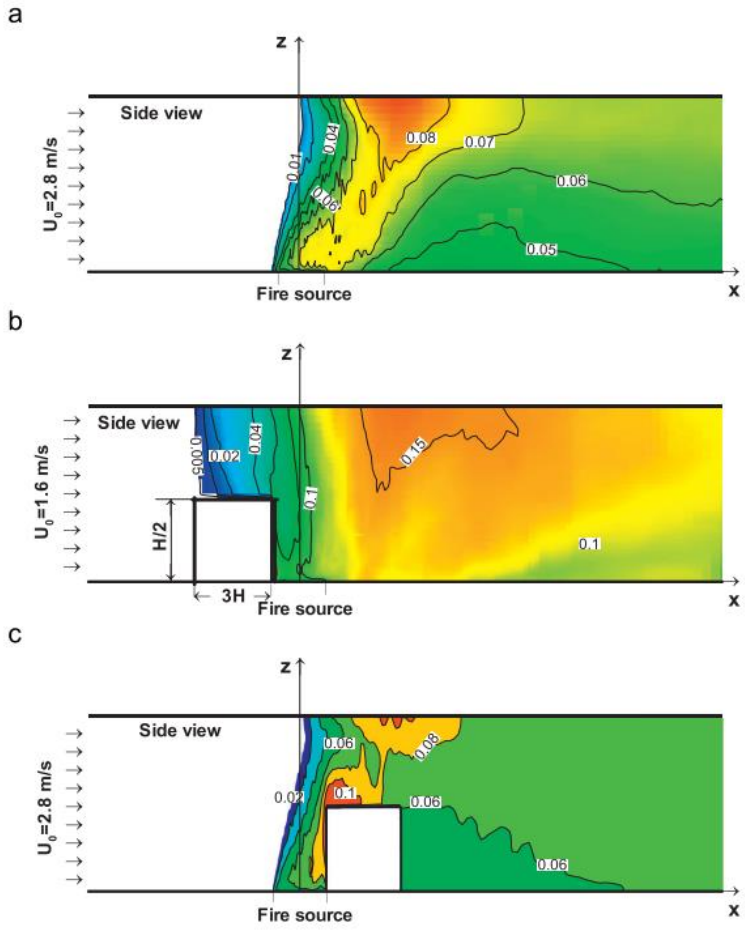


FIGURE 3.15 – EFFECTS OF OBSTRUCTION ON TOTAL FLAME LENGTH
Retrieved from Wang [38]

3.3.2 Gas Temperatures

The temperatures reached by the hot gases on the buoyant plume is of great importance in the context of tunnel fire safety. Not only it defines the heat exposure imposed on tunnel users and on the structure, as it is also fundamental on the assessment of fire detection and fire spread. Therefore, gas temperatures can be related to escape and stability conditions, to firefighting possibilities, and also to the likelihood of achieving a large tunnel fire involving several vehicles.

For the scope of this thesis, only the stability of the tunnel structure is of concern. Conservatively, most designs are still mainly based on the use of standardized time-temperature curves. Those latter, define the heat flux towards the tunnel lining, allowing the calculation of a temperature profile inside the structure, as a function of the distance from the exposed surface. For a concrete tunnel, the time to collapse is often assumed as the time needed for the reinforcement to reach a critical temperature, in which its mechanical properties start to degrade. Therefore, if a performance-based design is to be achieved, a model to calculate the gas temperatures including the effects of the tunnel geometry, HRR and ventilation conditions is needed (Li and Ingason [39]).

3.3.2.1 Maximum Temperature at the Ceiling

This section provides studies and formulations to estimate the maximum temperature at the ceiling during a tunnel fire. Accordingly:

1) Kurioka et al. [40]:

Based on empirical correlations, the authors proposed a model to calculate the maximum gas temperature at the ceiling. According to their proposition, the maximum temperature obtained in a tunnel fire is a function of the HRR and the Froude Number:

$$\frac{\Delta T_{C,max}}{T_a} = \gamma \left(\frac{Q^{*\frac{2}{3}}}{Fr^{\frac{1}{3}}} \right)^{\varepsilon} \rightarrow \begin{cases} \dfrac{Q^{*\frac{2}{3}}}{Fr^{\frac{1}{3}}} < 1.35 \rightarrow \gamma = 1.77;\ \varepsilon = 6/5 \\ \dfrac{Q^{*\frac{2}{3}}}{Fr^{\frac{1}{3}}} \geq 1.35 \rightarrow \gamma = 2.54;\ \varepsilon = 0 \end{cases} \quad \textbf{3.15}$$

with

$$Fr = \frac{u^2}{g H_{ef}}\ ;\ Q^* = \frac{Q}{T_a \rho_a c_p g^{\frac{1}{2}} H_{ef}^{\frac{5}{2}}}$$

where $\Delta T_{C,max}$ is the maximum ceiling temperature (K), T_a is the ambient air temperature (K), u is the longitudinal velocity (m/s), H_{ef} is the height from the surface of the fire to the ceiling (m), T_a is the ambient temperature (K), ρ_a is the ambient air density (kg/m^3), c_p is the specific heat capacity of air (kJ/(kg K)), g is the gravitational acceleration (m/s^2), and Q is the HRR (kW).

Hu et al.[41] reports that this model compares fairly well with the results of full-scale tests performed in their own study, and also with CFD simulations of those tests. Some small deviations were assigned to the inclination of the tunnel, as the slope effect is not included in equation 3.15.

2) Li and Ingason [39, 42] and Li et al. [43]:

Li and Ingason [39] claim that the previous model (1) cannot predict the maximum temperature below the ceiling for low ventilation velocities, as those would lead to very small values of Froude Number, yielding in an infinitely large maximum temperature. They have also pointed out that, in general, model (1) should overestimate the maximum temperature for tunnel fires, as thick fire proof blankets were used on the tests that based the development of the model. Moreover, adiabatic boundaries where achieved, thus probably underestimating the heat losses near the fire source when compared to that of a real tunnel fire. Mention is also made to the work of Hu et al. [41]. Apparently, the good correspondence between their tests and Kurioka et al. [40] equation was only obtained because very low HRRs were used by Hu et al. [41] when performing their tests. Thus, based on theoretical analysis of axisymmetric fire plumes and on empirical coefficients, calculated out of experimental data collected during quasi-state conditions, Li and Ingason [39] proposed a new model that can be used to estimate the maximum excess temperature (not the maximum temperature) for *small* and *large fires*. It is depicted below:

- *Region I* ($V' < 0.19$):

$$\Delta T_{C,max} = \begin{cases} 17.5\dfrac{Q^{2/3}}{H_{ef}^{5/3}}, & 17.5\dfrac{Q^{2/3}}{H_{ef}^{5/3}} < 1350 \\ 1350, & 17.5\dfrac{Q^{2/3}}{H_{ef}^{5/3}} \geq 1350 \end{cases} \quad \textbf{3.16}$$

- *Region II* ($V' \geq 0.19$):

$$\Delta T_{C,max} = \begin{cases} \dfrac{Q}{u\, b_{f0}^{1/3} H_{ef}^{5/3}}, & \dfrac{Q}{u\, b_{f0}^{1/3} H_{ef}^{5/3}} < 1350 \\ 1350, & \dfrac{Q}{u\, b_{f0}^{1/3} H_{ef}^{5/3}} \geq 1350 \end{cases} \quad \textbf{3.17}$$

with

$$V' = \frac{u}{\left(\dfrac{gQ}{b_{f0}\rho_0 c_p T_a}\right)^{\frac{1}{3}}}$$

where u is the longitudinal velocity in the tunnel (m/s), Q is the HRR (kW), ρ_0 is the ambient air density (kg/m^3), c_p is the heat capacity of air (kJ/(kg K)), T_a is the ambient temperature (K), H_{ef} is the vertical distance from the bottom of the fire source to the tunnel ceiling (m), g is the gravitational acceleration (m/s^2), and b_{f0} is the radius of the fire source (m). In case the fire source has a different shape than a circle, Ingason et al. [2] proposes the use of an equivalent circular radius given by $\sqrt{4A/\pi}$, with A being the area of the fuel source (m^2).

For *small tunnel fires* under high ventilation ($V' \geq 0.19$), the maximum excess gas temperature increases linearly with the HRR and is inversely proportional to the longitudinal ventilation velocity. For low velocities ($V' < 0.19$), it varies with two-thirds power of the HRR and is independent on the ventilation. When addressing *large tunnel fires*, situations in which flames can impinge on the ceiling, it is expected that the maximum excess gas temperature will approach a constant value, no matter the level of ventilation. Nonetheless, despite being described as a universal constant in equations 3.16 and 3.17, for which the upper limit of *1350 ^oC* was chosen as the highest maximum temperature ever measured in a full-scale test, it actually varies according specific conditions of a given tunnel. For instance, when addressing model-scale tests, this limit is apparently reduced to *1100 ^oC*.

Note that the maximum ceiling temperature is independent of the tunnel width (Lönnermark and Ingason [44]). Also, despite requiring the value of the longitudinal ventilation in order to determine what region one should use in the calculation, the model can also accurately estimate the ceiling temperature for *natural ventilated* or *transversally ventilated* tunnels. The longitudinal velocity in those cases is typically low, and they should fit in the first region of the model or, equation 3.16. This assumption is validated through the good correlation between the Memorial test results and the proposed equation. Also, the authors have pointed out on the use of the same model to estimate the HRR of a tunnel fire in case the temperature development in time is given. Note that this is always the case whenever standardized time-temperature

curves are used, meaning that the model presented here can become a powerful tool on converting such curves into a specific fire scenario, characterized by the HRR development in time. If so, the HRR curve found is to be understood as the minimum HRR necessary to generate such temperatures.

Figure 3.16 gives a comparison between the proposed model (dashed line) with the results of the model-scale tests (white marks) and the results of important full-scale tests (black marks). As it can be seen, the model is able to give good predictions of the results obtained in both cases. Once again, mention is made that in case of a model-scale test, the constant plateau is at lower level (*1100 ºC*), which is not highlighted in Figure 3.16.

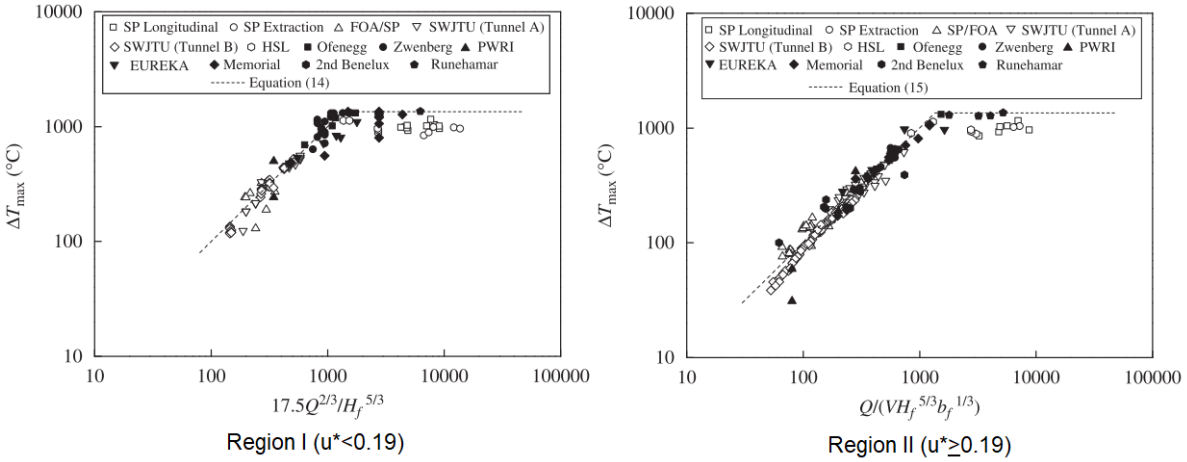


FIGURE 3.16 – COMPARISON WITH MODEL AND FULL-SCALE TEST RESULTS
Retrieved from Li et al. [39]

3) Ji et al. [45]:

Most studies regarding tunnel fires are developed considering a scenario in which the fire source is located at the center of the cross-section of the tunnel. Nevertheless, in realistic cases, a fire might occur at any position inside of a tunnel. In this sense, the authors investigated, through model-scale experiments of different pool fires, possible changes in the maximum ceiling temperature due to different transverse locations (from centerline fires up to wall fires) for the fire.

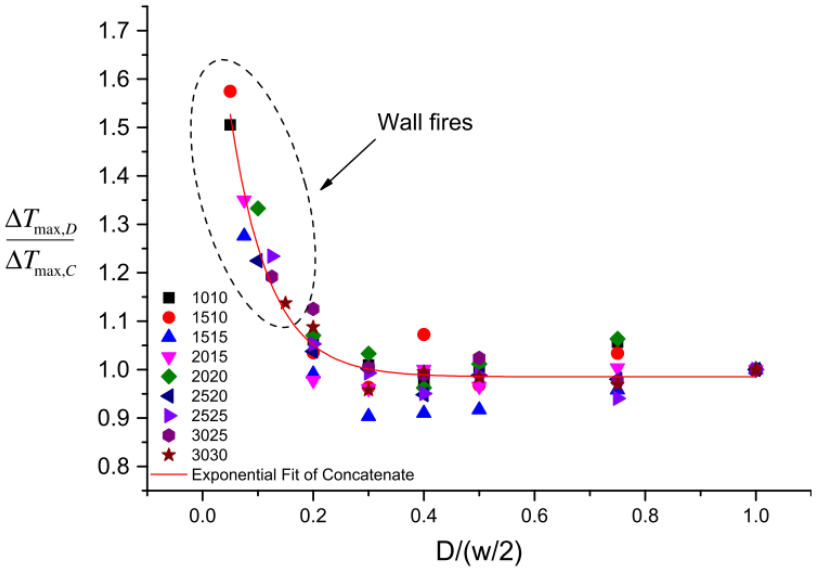


FIGURE 3.17 – EFFECT OF DIFFERENT TRANSVERSE LOCATIONS ON MAXIMUM CEILING TEMPERATURE
Retrieved from Ji et al. [45]

Figure 3.17 summarizes the findings of their work. In this figure, $\Delta T_{max,C}$ is the maximum temperature rise for fire located at the centerline of the tunnel, $\Delta T_{max,D}$ is the maximum temperature rise for different transverse locations, with D being the distance between the center of the fire and the wall and w being the width of the tunnel. From those results, we can infer that whenever fire is located *within 10% of the width of the tunnel* from the wall (wall fires in Figure 3.17), one can expect a considerable increase on the maximum temperature at the ceiling due to a tunnel fire. Based on an exponential fit of those results (red line in Figure 3.17), the authors proposed a model to compute the maximum ceiling temperature for fires located in any transverse position along the tunnel:

$$\Delta T_{max,D} = 17.9 \frac{Q^{2/3}}{H_{ef}^{5/3}} \left(1.096 e^{-\frac{14.078D}{\frac{w}{2}}} + 1 \right) \qquad \textbf{3.18}$$

where Q is the HRR (kW), H_{ef} is the vertical distance from the bottom of the fire source to the tunnel ceiling (m), D is the distance between the fire and the wall (m), and w is the width of the tunnel (m).

An important remark here is that this study, conclusively shows that different fire locations affect only the maximum temperatures near the fire source. Moreover, with enough distance from the fire source, the temperature at the ceiling becomes the same for both centerline and wall fires and the models described in Section 0 to predict the longitudinal temperature distribution at the ceiling should still be valid to address *wall fires*.

4) Fan et al. [46]:

This study described experiments to investigate the effect of tunnel cross-section on the maximum gas temperature at the ceiling. Model-scale tests of tunnels of varied width and height were used. The widths were *0.3*, *0.45*, and *0.6 m* or *6*, *9*, and *12 m* when converted to real scale. The tunnels were constructed in two different heights (*0.25* and *0.4 m*),

corresponding to *5* and *8 m* in reality. The results of this work (Figure 3.18) clearly show that the maximum ceiling temperature is not completely independent on the tunnel width, thus going against the findings of Lönnermark and Ingason [44]. However, the authors have also confirmed that the maximum temperature at the ceiling is indeed more affected by the tunnel height. Therefore, despite not including any effects of tunnel width on the maximum ceiling temperature, the models described earlier in this section (equations 3.16 and 3.17) should still provide reliable estimates.

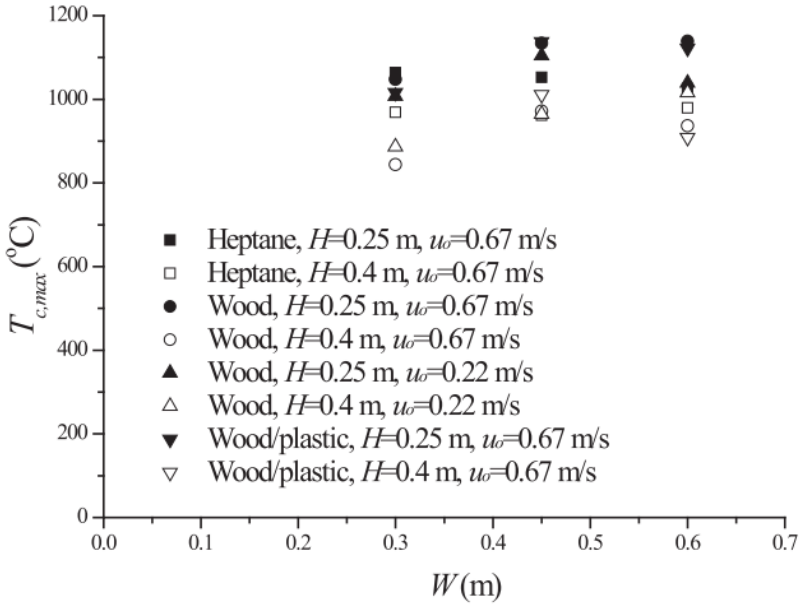


FIGURE 3.18 – MAXIMUM CEILING TEMPERATURE AS A FUNCTION OF TUNNEL GEOMETRY
Retrieved from Fan et al. [46]

3.3.2.2 Position of Maximum Ceiling Temperature

Ingason et al. [2] proposed a model (equation 3.19) to calculate the position of the maximum ceiling temperature from center of the fire source (L_{MT}) for a tunnel with longitudinal air flow. Figure 3.19 below depicts the situation.

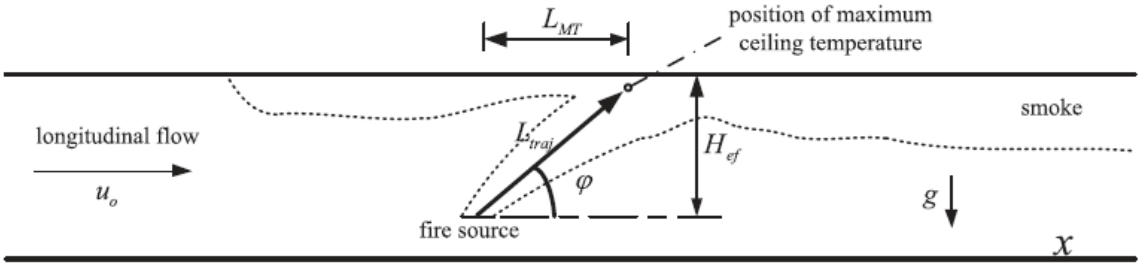


FIGURE 3.19 – POSITION OF MAXIMUM CEILING TEMPERATURE
Retrieved from Ingason et al. [2]

$$sin\,\varphi = \frac{H_{ef}}{L_{traj}} = \begin{cases} 1 & V' \leq 0.19 \\ (5.26V')^{-\frac{3}{5}} & V' > 0.19\ and\ Q^* \leq 0.15 \\ 0.25\left(\frac{b_{f0}u^*}{H}\right)^{-\frac{1}{5}} & V' > 0.19\ and\ Q^* > 0.15 \end{cases} \quad \textbf{3.19}$$

with

$$V' = \frac{u}{\left(\frac{gQ}{b_{f0}\rho_0 c_p T_a}\right)^{\frac{1}{3}}}\ ;\ Q^* = \frac{Q}{T_a\rho_a c_p g^{\frac{1}{2}} H_{ef}{}^{\frac{5}{2}}}\ ;\ u^* = \frac{u}{\sqrt{gH}}$$

where φ is the flame angle (rad), u is the longitudinal velocity in the tunnel (m/s), Q is the HRR (kW), ρ_0 is the ambient air density (kg/m^3), c_p is the heat capacity of air (kJ/(kg K)), T_a is the ambient temperature (K), H_{ef} is the vertical distance from the bottom of the fire source to the tunnel ceiling (m), H is the tunnel height (m), g is the gravitational acceleration (m/s^2), and b_{f0} is the radius of the fire source (m). In case the fire source has a different shape than a circle, Ingason et al. [2] proposes the use of an equivalent circular radius given by $\sqrt{4A/\pi}$, with A being the area of the fuel source (m^2).

Once the flame angle is known, one can calculate L_{MT} through simple trigonometrical relations:

$$L_{MT} = H_{ef}\,cot\,\varphi \quad \textbf{3.20}$$

where L_{MT} is the position of maximum ceiling temperature (m),), H_{ef} is the vertical distance from the bottom of the fire source to the tunnel ceiling (m) and φ is the flame angle (rad).

3.3.2.3 Temperature Distribution along the Tunnel

A tunnel designer must have at hand models to predict the temperature distribution along the tunnel in the occurrence of a fire. This information supports the decision over the location of fire detectors (Nyman and Ingason [17]), which is directly related to the time of activation of the fixed fire-fighting systems (FFFS). Not only that, but it is also a fundamental tool on the calculation of heat fluxes towards the floor, which is essential for analyzing escape conditions.

- *Longitudinal Temperature Distribution:*

Three different models were found in literature for the calculation of the longitudinal temperature distribution at the ceiling during a tunnel fire. Thus:

1) Ingason and Li[36] and Ingason et al. [2]:

Ingason and Li [36] performed model-scale tests and formulated a dimensionless correlation to calculate the ceiling gas temperature distribution downstream the fire source based on theoretical analysis of stratified smoke flows at a quasi-steady state. The primary mechanisms for the decrease of smoke temperature while spreading longitudinally in the tunnel are the heat losses to the tunnel structure and to the ambient air. Nevertheless, whenever there is a *large fire* inside the tunnel, flames will impinge on the ceiling and will continuously release heat along it. This introduces a large amount of heat on the smoke flow, indicating that the temperature decay at the vicinity of a *large fire* will not happen as fast as in Ingason and Li [36]. Therefore, the effects of a *virtual origin* were introduced by Ingason et al. [2]:

$$\frac{\Delta T_C(x)}{\Delta T_{C,max}} = 0.57e^{-\left(0.143\frac{x-x_v}{H}\right)} + 0.45e^{-\left(0.024\frac{x-x_v}{H}\right)} \quad \textbf{3.21}$$

with

$$x_v = \begin{cases} L_f - 10H, & L_f > 10H \\ 0, & L_f \leq 10H \end{cases}$$

where $\Delta T_{C,max}$ is the maximum excess gas temperature beneath the ceiling (K), $\Delta T_C(x)$ is the ceiling temperature at the position x, which is the downstream distance from the fire source (m), H is the tunnel height (m), x_v is the virtual origin (m), and L_f is the flame length (m) calculated as in equation 3.13.

Figure 3.20 shows that, despite being based on results of model-scale tests, equation 3.21 (black line) has performed fairly well on describing data measured in large-scale test campaigns.

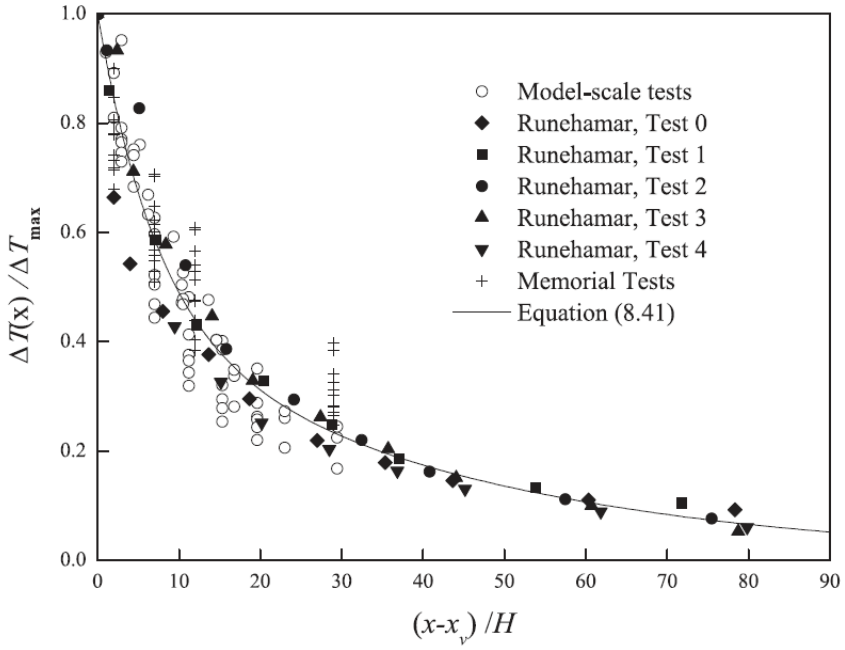


FIGURE 3.20 – COMPARISON BETWEEN MODEL PREDICTIONS AND TEST RESULTS
Retrieved from Ingason et al. [2]

2) Fan et al. [46]:

In this study the authors used the model presented in equation 3.21 in a comparison of model-scale tests of heptane pool fires, wood crib fires and a combination of wood and plastic fires for different tunnel cross-sections. Model (1) slightly overpredicted the temperatures measured during their tests. Apparently, by neglecting any effect of the maximum HRR, the model fails to predict the temperature development of *large fires*. Thus, a new formulation is proposed to address such fires ($Q^* > 0.75$). Accordingly:

$$\frac{\Delta T_C(x)}{\Delta T_{C,max}} = e^{-0.2Q^{*-0.52}\left(\frac{x-x_{max}}{H}\right)} \quad \textbf{3.22}$$

with

$$Q^* = \frac{Q}{T_a \rho_a c_p g^{\frac{1}{2}} H^{\frac{5}{2}}}$$

where Q is the HRR (kW), ρ_0 is the ambient air density (kg/m^3), c_p is the heat capacity of air (kJ/(kg K)), T_a is the ambient temperature (K), H is the tunnel height (m), g is the gravitational acceleration (m/s^2), and x_{max} is the position of the maximum ceiling temperature (m) calculated as in Section 3.3.2.2.

3) Zhao et al. [47]:

In case the combustion zone extends to multiple fire sources, the authors claim there will exist three different regions for the calculation of the longitudinal temperature distribution (Figure 3.21). The first region is fuel rich, but lacks oxygen to achieve complete combustion, attaining an almost constant temperature. In the second region, there is air entrainment, which enhances combustion and increases the ceiling temperatures up to a maximum, setting the start of the third region. At the latter, the temperature function decreases with the distance from the center of the fire source. Note that this scenario is representative for fires involving multiple vehicles, where an *under-ventilated* condition is locally achieved at the center of the burning zone.

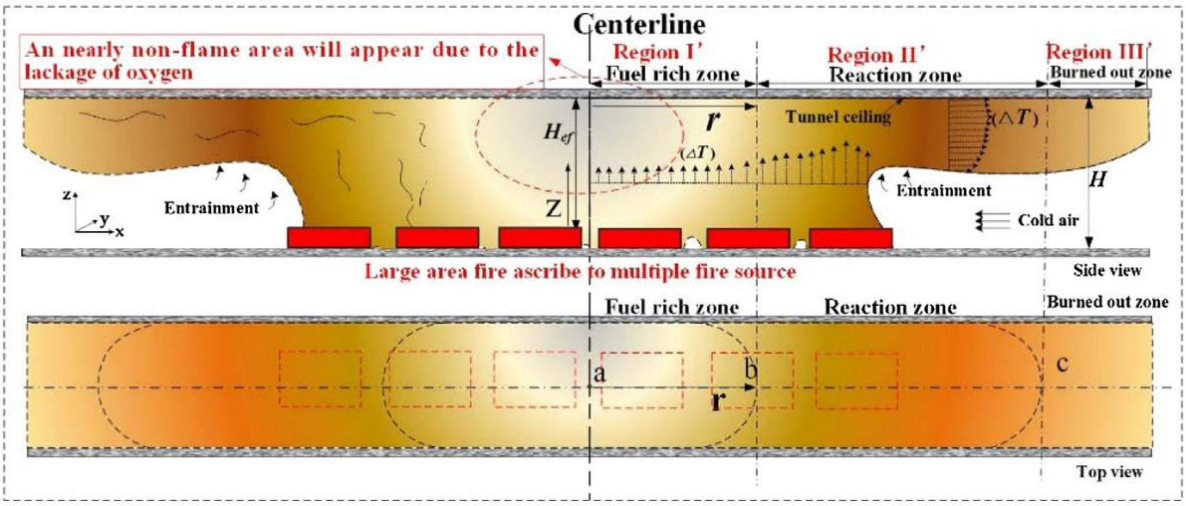


FIGURE 3.21 – TEMPERATURE DISTRIBUTION IN CASE OF MULTIPLE FUEL SOURCES
Retrieved from Zhao et al. [47]

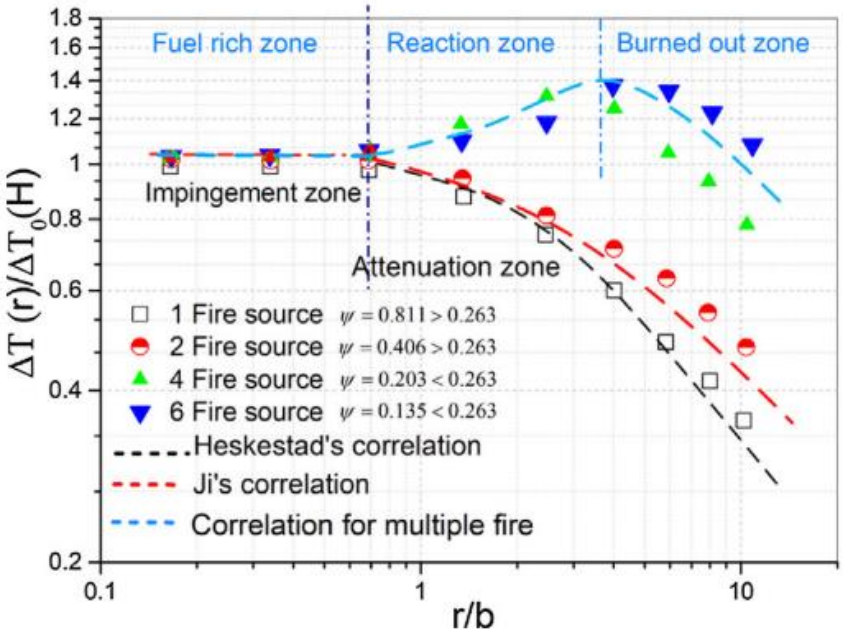


FIGURE 3.22 – LONGITUDINAL TEMPERATURE PROFILE FOR MULTIPLE BURNING FIRES
Retrieved from Zhao et al. [47]

In this case, the models presented previously are not able to accurately prescribe the longitudinal temperature distribution. Therefore, based on experimental results, Zhao et al. [47] proposed a new model to be used in such conditions:

- *Region I – Continuous Flame Zone* $\left(\frac{x-x_0}{2b_{f0}Q^{*\frac{2}{5}}} \leq 1.47\right)$:

$$\frac{\Delta T_C(x)}{T_a} = 3.27 \qquad 3.23$$

- *Region II – Intermittent Flame Zone* $\left(1.47 < \frac{x-x_0}{2b_{f0}Q^{*\frac{2}{5}}} \leq 5.36\right)$:

$$\frac{\Delta T_C(x)}{T_a} = 3.882\left(\frac{x-x_0}{2b_{f0}Q^{*\frac{2}{5}}}\right)^{-1/5} \qquad 3.24$$

- *Region III – Buoyant Plume Zone* $\left(\frac{x-x_0}{2b_{f0}Q^{*\frac{2}{5}}} > 5.36\right)$:

$$\frac{\Delta T_C(x)}{T_a} = 6.15\left(\frac{x-x_0}{2b_{f0}Q^{*\frac{2}{5}}}\right)^{-2/3} \qquad 3.25$$

with

$$x_0 = 0.083\, Q^{*\frac{2}{5}} - 2.04\, b_{f0}\ ;\ Q^* = \frac{Q}{T_a \rho_a c_p g^{\frac{1}{2}} H^{\frac{5}{2}}}$$

where Q is the HRR (kW), ρ_0 is the ambient air density (kg/m^3), c_p is the heat capacity of air (kJ/(kg K)), g is the gravitational acceleration (m/s^2), T_a is the ambient temperature (K), H is the tunnel height (m), x is the distance from the center of the fire source (m) and b_{f0} is the radius of the fire source (m). In case the fire source has a different shape than a circle, Ingason et al. [2] proposes the use of an equivalent circular radius given by $\sqrt{4A/\pi}$, with A being the area of the fuel source (m^2).

- *Transversal Distribution:*

Fan et al. [48] studied the transverse decay of temperature (Figure 3.23) based on the experiments performed by Ji et al. [45]. According to their study, the transverse decay rate of ceiling temperature is larger than the longitudinal one, due to a blocking effect of the tunnel sidewall. This can be an important information when defining the locations in which fire detectors should be installed. A model to evaluate the transversal temperature distribution accounting for different fire positions in a tunnel was proposed:

$$\Delta T_{max,d_f} = 17.9 \frac{Q^{2/3}}{H_{ef}^{5/3}} \left(1.096 e^{-\frac{14.078D}{\frac{w}{2}}} + 1\right)\left(0.893 e^{-\frac{3.745 d_f}{w}} + 0.107\right) \qquad \textbf{3.26}$$

where $\Delta T_{max,d_f}$ is the maximum smoke temperature at a certain transverse location (K) and d_f is the transverse distance from the center of the fire source (m), D is the distance between the fire source and the wall (m), w is width of the tunnel (m) and d_f is the location of the where the temperature is to be estimated.

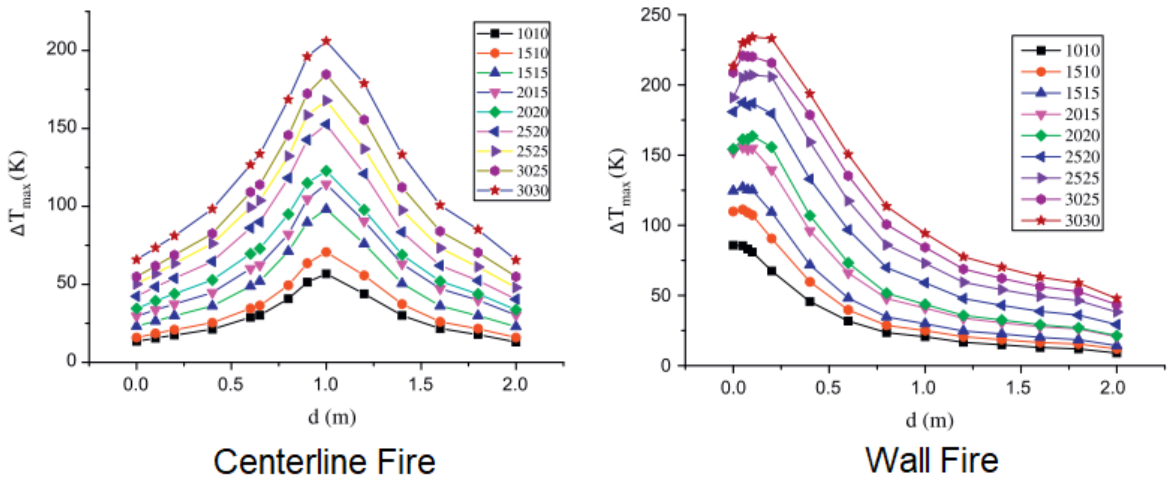


FIGURE 3.23 – TRANSVERSAL TEMPERATURE DISTRIBUTION
Retrieved from Fan et al. [48]

4 Fire Scenarios

This chapter is aimed at the process of deriving fire scenarios, specially focusing on tunnel fires. In this sense, a distinction between solid fires and liquid fires is made, and the main differences between them are exposed. Here, it will also become clear how fire loads are constructed, and how physical conditions of the tunnel are assumed to affect fire development. The concepts and data provided in this chapter are fundamental to the development of a performance-based approach to assess the structural integrity of tunnels in case of fire.

4.1 Fire Load

The heat release rate (HRR) of a fire dictates the temperature development inside an enclosure, which is used in the evaluation of the structural integrity of the tunnel lining during a tunnel fire. Thus, it becomes fundamental to understand how to characterize fire loads, and also to understand the types are likely to occur in a tunnel. In this sense, a fire load is often described in terms of the development of the HRR in time, as exemplified in Figure 4.1 with several large-scale test results of simulated heavy-good vehicle (HGV) fires. From this figure, especially for the case of solid fires (Section 4.1.1.1), we can note that fire development can vary considerably even between similar cases. This makes it a hard task to predict the real HRR development produced by a known fire load (e.g. a car). Thus, in order to evaluate the consequences of a fire in the design stage, a fire load is more often described based on simpler linear functions in triangular or trapezoidal shapes (Figure 4.2). Note that if the decay phase of a fire is not considered, the development of HRR will usually be represented by a bilinear curve, rising linearly to a maximum which is followed by a constant plateau. In case a more realistic description of the HRR in time is pursued (Figure 4.1), one may apply a model based on a single exponential curve description (Ingason [49] and Hansen and Ingason [50]).

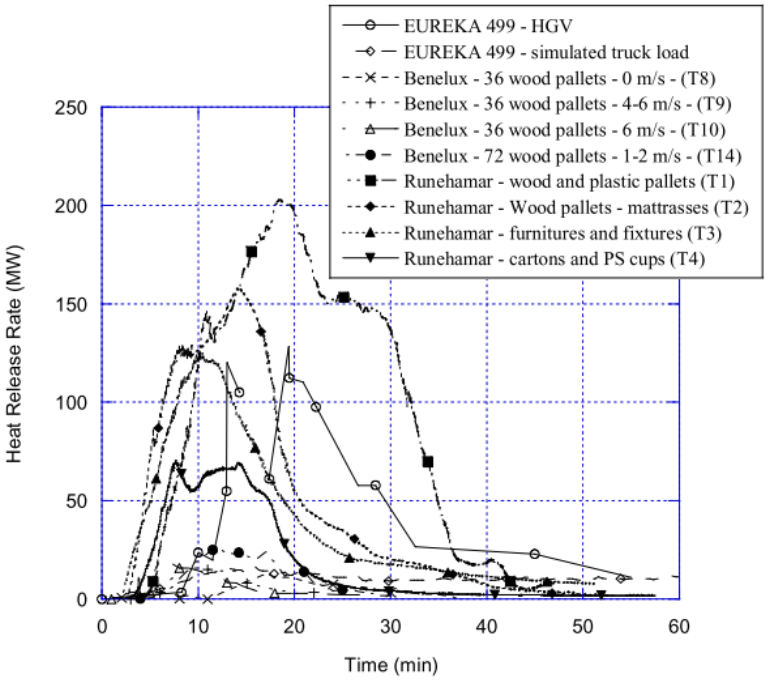


FIGURE 4.1 – HRR FOR HGV FULL-SCALE TESTS
Retrieved from Ingason [23]

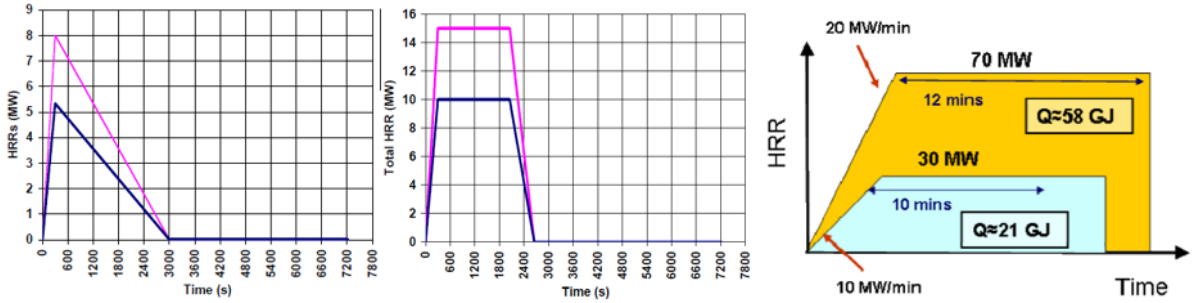


FIGURE 4.2 – HRR LINEAR PROFILES
Retrieved from UPTUN [51, 52]

Figure 4.3 below provides valuable examples of fire loads, which can be used to represent likely fire scenarios for a given tunnel. Note that, no matter the type of curve selected on resembling fire loads, the HRR will be characterized based on three parameters: (1) the peak HRR (Section 4.1.1), which describes how large a fire is; (2) the time to reach the peak HRR (Section 4.1.2), which provides information about how fast a fire grows; and (3) the energy content (Section 4.1.3), which defines the total duration of a fire.

Parameter	Clearance of the tunnel				
	height < 2,7 m	**height 2,7 m to 3,5 m**	**height > 3,5 m no dangerous goods allowed**	**height > 3,5 m DGs or no DGs allowed**	**height > 3,5 m dangerous goods allowed**
typical fire	2 - 3 cars	1 van (loaded)	1 HGV	1 HGV with high calorific potential	1 petrol tanker
heat release rate [MW]	8	15	30	100	200
smoke flow rate [m^3/s]	30	50	80	?	300[1)]
growth time t_g [min]	5	5	10	10	10
peak duration t_{max} [min]	20	30	60	60	60
decline time t_d [min]	20	20	30	20	30
released energy [GJ]	18	63	125	450	960

FIGURE 4.3 – FIRE LOAD ACCORDING TO THE NEW FRENCH REGULATION
Retrieved from UPTUN [51]

4.1.1 Peak HRR

As described before, HRR is the most important parameter when addressing the consequences of a tunnel fire. It correlates the mass burning rate of the fuel to the heat, smoke, and gas production. Here, a distinction is made between solid fires (Section 4.1.1.1) and liquid fuels, which form pool fires (Section 4.1.1.2). According to Ingason et al. [2], peak HRR values are often based on measurements realized in large-scale tests. Nevertheless, not only real measurements are rather limited, but they are also characterized by a large error range (15% to 25%). The latter, allied to the fact that this parameter is affected by several conditions during

a test (Section 4.2), highlights that the use of tabulated HRR in describing tunnel fires requires extra care.

4.1.1.1 Solid Fires

In tunnels, solid fires are characterized by burning vehicles (i.e. cars, vans, buses, heavy-good vehicles (HGV) and dangerous-good vehicles (DGV)). The maximum HRR in these cases is given by:

$$\dot{Q}_{max} = \dot{m}''_{f,max} A_f \chi \Delta H_c \quad \textbf{4.1}$$

where $\dot{Q}_{max}$ is the maximum HRR (MW), $\dot{m}''_{f,max}$ is the maximum fuel burning rate per unit area (kg/(m^{2}s)), A_f is the exposed fuel surface (m^2), χ is the combustion efficiency and ΔH_c is the heat of combustion (MJ/kg). The product $\chi \Delta H_c$ is also known as the effective heat of combustion.

Several regulations and authors reported on values of maximum HRR for different types of vehicle. This information is based on large-scale test results realized through the years. A full description of the expected values is given by Ingason et al. [2] and is summarized below:

1) *Passenger vehicles:*
   - Single cars = 5 MW.
   - Two vehicles = 10 MW.
   - Three vehicles = Up to 16 MW.

2) *Buses:* Up to 30 MW, but data over the peak HRR in this case is very limited.

3) *HGV:* 13 to 202 MW.
   There is a big variation in the measurements for the peak HRR in HGV tests. In most cases, those are based in simulated HGV fires through the use of mock-ups, often made of wooden pallets, or of a combination of those with plastics. The large range of values rely on the fact that HRR is dependent on the exposed surface area. Thus, an open cargo test provides different results than an enclosed one. Also, a fire might be very affected by the ventilation conditions in the vicinity of the fire source.

4) *DGV*: Tanker fires are often addressed as leading to the formation of pool fires (Section 4.1.1.2).

As shown by the values provided above, test results yield in a broad range of peak HRR for the same type of vehicle, making it difficult to compare similar cases. Thus, Ingason et al. [2] proposes the adoption of the heat release rate per unit area (HRRPUA), which provides a narrower range of values and supports more reliable decisions. Accordingly, the HRRPUA of *passenger cars* is around *0.3* to *0.4 MW/m^2*. For *HGV fires*, expected HRRPUA are in between *0.2* to *0.5 MW/m^2*. Therefore, by estimating the exposed area of a certain vehicle, fair estimations on the peak HRR shall be achieved. This also highlights the importance of the geometry of the fuel, as the total exposed surface defines the maximum fire size.

In a different manner, Lönnermark [53] addressed the maximum HRR in terms of the energy content. Through linear regression of several test results, he proposed ratios of *0.868 MW/GJ* for *passenger cars* and *0.866 MW/GJ* for *HGVs* to estimate the maximum HRR based on the

total energy content of a certain vehicle. Note that these values are referring to *fuel-controlled* fire scenarios (Section 3.1).

4.1.1.2 Pool Fires

A pool fire may form within tunnels in case there is leakage of liquid fuels from vehicles. Pool fire are also very often used as a form of fire load in both large-scale and model-scale tests. Karlsson and Quintiere [15] describe that for free burning conditions, the burning rate of a pool fire will quickly reach a constant value, which is mainly dependent on the diameter of the spill (Figure 4.4). Note that this gives a very different situation when compared to the previous case (Section 4.1.1.1). For solid fuels, not only the exposed burning area varies in time but also the burning rate of the material itself will not be constant. As a consequence, the HRR curve resulting from those fires usually grows to a peak value, decaying right after (Figure 4.1). For pool fires, however, the HRR is expected to rise rapidly to a peak value, remaining almost unchanged at its maximum capacity for the total burning period (i.e. assuming that the burning area is kept the same).

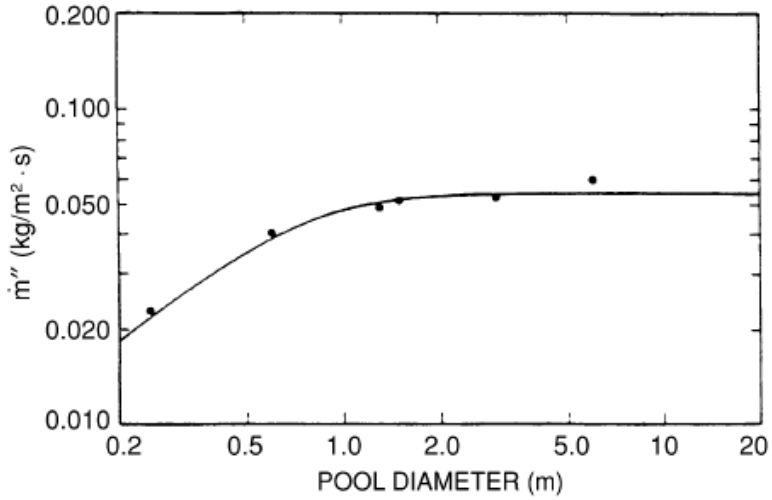


FIGURE 4.4 – BURNING RATE FOR GASOLINE POOLS ACCORDING TO THE DIAMETER
Retrieved from Karlsson and Quintiere (2000) [15]

The peak HRR of pool fires can be estimated by:

$$\dot{Q}_{max} = \dot{m}''_{\infty}\left(1 - e^{-k\beta D}\right) \chi \, \Delta H_c \, A_f \qquad 4.2$$

where $\dot{Q}_{max}$ is the maximum HRR (MW), $\dot{m}''_{\infty}$ is the highest value for the mass burning rate (kg/(m²s)), D is the pool diameter (m), ΔH_c is the heat of combustion (MJ/kg), χ is the combustion efficiency, A_f is the pool area (m²) and $k\beta$ is the product of the extinction-absorption coefficient of the flame k (1/m) and the mean beam-length corrector β.

The product $k\beta$ is a function of the radiative heat flux from the flame towards the fuel surface and is particular for every fuel. The equation above can also be applied to pool fires of non-circular geometry. In that case, an equivalent diameter may be calculated by assuming a circular pool of equivalent area. According to Karlsson and Quintiere [15], alcohols burn with flames containing very little soot, making the combustion efficiency (χ) to be close to a unity. For the case of sootier flames, such as the ones involved in oil burnings, the combustion efficiency is

reduced to approximately 60 to 70%. Figure 4.5 provides values for the constants required in equation 4.2.

Data for Large Pool ($D > 0.2$ m) Burning Rate Estimates

Material	Density (kg/m³)	$\dot{m}''_\infty$ (kg/m²s)	ΔH_c (MJ/kg)	$k\beta$ (m⁻¹)
Cryogenics				
Liquid H_2	70	0.017	120.0	6.1
LNG (mostly CH_4)	415	0.078	50.0	1.1
LPG (mostly C_3H_8)	585	0.099	46.0	1.4
Alcohols				
Methanol (CH_3OH)	796	0.017	20.0	[a]
Ethanol (C_2H_5OH)	794	0.015	26.8	[b]
Simple organic fuels				
Butane (C_4H_{10})	573	0.078	45.7	2.7
Benzene (C_6H_6)	874	0.085	40.1	2.7
Hexane (C_6H_{14})	650	0.074	44.7	1.9
Heptane (C_7H_{16})	675	0.101	44.6	1.1
Xylene (C_8H_{10})	870	0.09	40.8	1.4
Acetone (C_3H_6O)	791	0.041	25.8	1.9
Dioxane ($C_4H_8O_2$)	1035	0.018	26.2	5.4[b]
Diethyl ether ($C_4H_{10}O$)	714	0.085	34.2	0.7
Petroleum products				
Benzine	740	0.048	44.7	3.6
Gasoline	740	0.055	43.7	2.1
Kerosine	820	0.039	43.2	3.5
JP-4	760	0.051	43.5	3.6
JP-5	810	0.054	43.0	1.6
Transformer oil, hydrocarbon	760	0.039[b]	46.4	0.7[b]
Fuel oil, heavy	940–1000	0.035	39.7	1.7
Crude oil	830–880	0.022–0.045	42.5–42.7	2.8
Solids				
Polymethylmethacrylate $(C_5H_8O_2)_n$	1184	0.020	24.9	3.3
Polypropylene $(C_3H_6)_n$	905	0.018	43.2	
Polystyrene $(C_8H_8)_n$	1050	0.034	39.7	

[a] Value independent of diameter in turbulent regime.
[b] Estimate uncertain, since only two points available.

Source: Babrauskas, V., in *SFPE Handbook of Fire Protection Engineering*, 2nd ed., National Fire Protection Association, Quincy, MA, 1995. With permission.

FIGURE 4.5 – EMPIRICAL CONSTANTS
Retrieved from Karlsson and Quintiere [15]

Equation 4.2 is very accurate to describe cases of pool fires burning in the open environment, especially when ventilation does not affect the HRR. Nonetheless, as described by Ingason et al. [2], the burning conditions of pool fires in tunnels are changed considerably. Firstly, in real pool fires, the thickness of the pool shall be only of a few millimeters, differently from the deep pools which are often used in tests. This significant difference in the depth of the pool might reduce the HRR of a real pool fire in 70% if compared to the maximum HRR measured in tests of pool fires confined in deep pans. Another important aspect altering the HRR of pool fires in

tunnels is the presence of longitudinal ventilation. As explained by Ingason [54], the burning rate of pool fires tends to decrease for increasing ventilation velocities. Therefore, it is hard to assume a unique value for the maximum HRR of pool fires in tunnels, but some HRRPUA are given in Figure 4.6. Considering the same figure, one may note that the HRRPUA of *liquid fires* can be over five times greater than that of the worst case for *solid fuels* (i.e. *0.5 MW/m²* for an HGV fire).

Type of fuel	Test series	Exposed fuel area (m^2)	Maximum heat release rate per square meter exposed fuel area MW/m^2
Liquid			
Gasoline	Ofenegg, Zwenberg, No.3 Shimizu	6.6, 47.5, 95	0.35 – 2.6
Kerosine	Glasgow	1.44	1.4
n-Heptane	Eureka	1, 3	3.5
n-60 % heptane/40% toulene	2nd Benelux	3.6, 7.2	1.1 – 1.6
Low-sulfur No 2 fuel oil	Memorial	4.5, 9, 22.2, 44.4	1.7 – 2.5

FIGURE 4.6 – HRRPUA OF LIQUID FIRES
Retrieved from Ingason [23]

4.1.2 Time to peak HRR

The time to peak HRR is more often addressed in terms of the fire growth rate. Some studies (Carvel et al. [55] and Ingason and Li [36]) reported that the fire growth rate is increases for higher longitudinal velocities, highlighting the importance of this parameter on the early stages of fire development. In this sense, a simple theoretical model was proposed by Li and Ingason [56], which can even be used to address the situation in which different fuels are involved on a same fire. According to their work, the fire growth rate increases linearly with the ventilation velocity.

4.1.3 Energy Content

This parameter defines the total duration of a fire scenario and equals the area of the HRR curve in time. As the heat of combustion for any given fuel is assumed to be constant, the total energy content is solely a function of the summation of all available fuels.

4.2 Parameters affecting HRR

The fire size is a consequence of heat balance between all contributing factors involved in the development of fire. Those are the radiations from: the flame, the hot gases, the surrounding structure, and the reradiation loss from fuel surface. There are several parameters in a tunnel which can influence some terms of this heat balance, and thus alter fire development. This section aims to investigate the possible effects of the geometry of the tunnel, the ventilation, the position of fire within the tunnel, and also of protection systems on the HRR development in time.

4.2.1 Geometry of the tunnel

Several studies regarding the effects of tunnel geometry on fire development were found. A summary of those is provided below:

1) Carvel et al. [57]:

The authors were the first ones to report on the influence of tunnel geometry on the HRR. A Bayesian approach was used to assess the results of several available tests (cars, wooden cribs, and pool fires) in order investigate which geometrical parameters (i.e. tunnel height, tunnel width, blockage ratio, and hydraulic diameter) would alter the HRR. Conclusion was made that only the *tunnel width* would potentially have an influence. An empirical equation accounting for those findings was developed, where the HRR of a tunnel fire is evaluated based on the HRR of an identical fire burning in the open:

$$\dot{Q}_{tunnel} = 24\dot{Q}_{open}\left(\frac{W_F}{W_T}\right)^3 + \dot{Q}_{open} \qquad 4.3$$

where $\dot{Q}_{tunnel}$ is the HRR of a tunnel fire, $\dot{Q}_{open}$ is the HRR of that same fire in the open, W_F is the width of the fire object, and W_T is the width of the tunnel.

2) Lönnermark and Ingason [44]:

According to their work, both the *width* and the *height* would affect the HRR, but those effects would actually rely on the starting conditions and on the type of fuel involved on a fire. For instance, a pool fire within a tunnel of relatively small height or width, would increase in size for increasing tunnel dimensions. On the other hand, for the case of larger initial dimensions, a further increase on the size of the tunnel would actually lead to a reduction of the HRR of the pool. When considering wood crib fires, the results of the tests have shown that the relations are the opposite of those for pool fires.

3) Li et al. [58]:

The authors used the results of model-scale tests (Lönnermark and Ingason [44]) and the equation developed by Carvel et al. [57] to address the effects of width and height on tunnel fires. Equation 4.3 was reported to be inaccurate, as it was developed based on rather small data over low HRR fires. In their study they have found that, for *fuel-controlled* pool fires, the HRR is independent on the tunnel width and slightly increases for lower heights. *Ventilation-controlled* fires (e.g. a large pool fire in a tunnel with low ventilation velocity) are apparently not sensitive to the tunnel geometry, and the HRR of such will be dictated by the ventilation conditions inside the tunnel.

Li et al. [58] also investigated the effect of the tunnel geometry on the fire size of solid fuels. Once again, in case of *fuel-controlled* fires, the dimensions of the tunnel shall not affect the HRR (Figure 4.7). *Ventilation-controlled* solid fires have also shown to be independent on variations of the geometry of the tunnel. In those cases, as there might be a lack of air supply to achieve complete combustion, the HRR could even be reduced when compared to that of a same fire in the open (Figure 4.8). Thus, no matter the kind of fuel that is burning, the effects of tunnel geometry were shown to be practically neglectable. Note that this does not mean that the HRR of tunnel fires will be the same as that of equivalent fires burning in the open. In essence, the HRR of *fuel-controlled* fires will be largely increased due to the confinement provided by the tunnel (Figure 4.7), but further changes in the aspect ratio of the tunnel (at least for a range of *0.75* to *2.4*) should not generate extra effects.

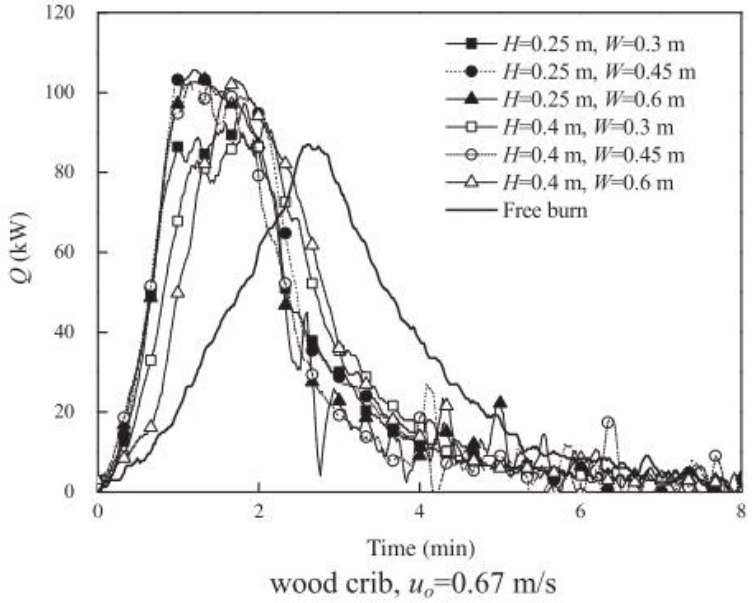


FIGURE 4.7 – EFFECT OF TUNNEL GEOMETRY ON THE HRR OF FUEL-CONTROLLED FIRES
Retrieved from Li et al. [58]

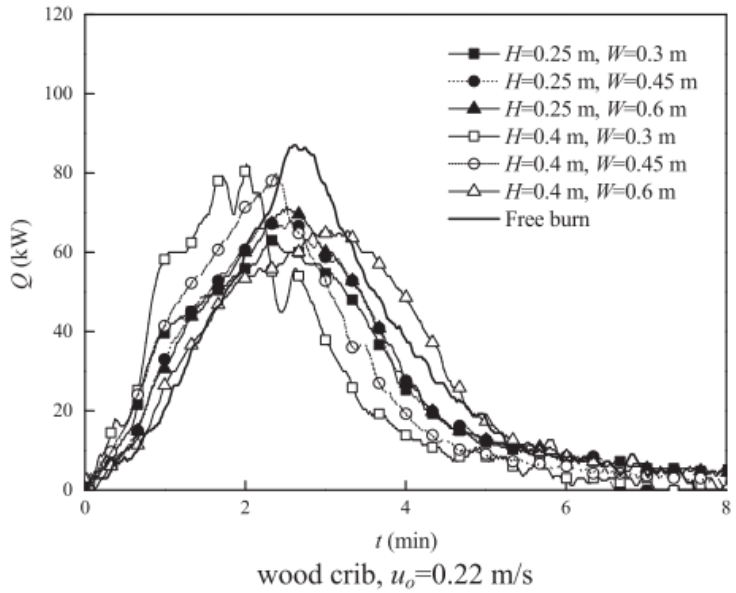


FIGURE 4.8 – EFFECT OF TUNNEL GEOMETRY ON THE HRR OF VENTILATED-CONTROLLED FIRES
Retrieved from Li et al. [58]

4.2.2 Ventilation

The level of ventilation defines the amount of fresh air that is available inside the tunnel and regulates the degree of vitiation in the vicinity of the fire. In most cases, there is enough air flowing through the fire and full combustion is achieved within the tunnel. However, for large fires in very long tunnels with low ventilation velocities, there might be lack of fresh air to sustain combustion and a *ventilation-controlled* condition might be achieved. For those cases, increasing the ventilation velocity might have an important effect on fire development. Thus, as ventilation is very often adopted on controlling smoke of a tunnel fire, it is of interest to better understand its effects on the HRR of a tunnel fire. The main findings are given below:

1) Carvel et al. [55] and Carvel et al. [32]:

The first study under the influence of longitudinal ventilation in fire development was made by Carvel et al. [55]. Making use of a Bayesian approach to address rather limited data, the authors reported on the enhancement of fire for different ventilation velocities. Accordingly, at a ventilation velocity of *3 m/s*, an HGV fire might be up to five times as larger as that in the same case under natural ventilation. If the velocity is increased to *10 m/s* the effects grow even further, and the fire is likely to grow up to ten times. For liquid fires, different behaviors are expected according to the size of the pool. In case of a large pool fire, velocities of *10 m/s* will probably increase the HRR by 50%, whereas for small pools the ventilation is actually expected to reduce the fire size.

This study was later updated by Carvel et al. [32] to include data of two large-scale tests, realized in the 2nd Benelux Tunnel (The Netherlands, 2002) and in the Runehamar Tunnel (Norway, 2003). Accordingly, the HRR of an HGV fire would probably grow about three times for longitudinal velocities in the range of *2* to *4 m/s*, and about eight times for a ventilation velocity of *10 m/s*. Another important discovery was that the likelihood of fire spreading to an adjacent HGV downstream the tunnel is actually reduced for such high levels of ventilation.

2) Ingason and Li [36]:

The authors investigated the effects of ventilation velocities in the range of *2* to *5 m/s* when converted to full-scale conditions. According to them, the work presented previously (1) might be correct in describing *ventilation-controlled* tunnel fires. On the other hand, *fuel-controlled* fires, although increased in the order of *1.4* to *1.55* times that of an equivalent fire burning in the open, are not expected to be further affected by ventilation conditions inside the tunnel. Note that this finding is also in line with Lönnermark and Ingason [44] or, in other words, that the influence of the ventilation velocity on fire growth rate is much larger than that on the maximum HRR achieved by a fire.,

3) Li et al. [59]:

Based on Roh et al. [60] experiments on model-scale pool fires, the authors proposed a correlation for the relative increment of HRR of tunnel fires according to the level of longitudinal velocity applied in the tunnel:

$$k = C\,\frac{uA}{g^{\frac{1}{2}}\,r^{\frac{5}{2}}} \qquad 4.4$$

In the above equation, k is the relative increment of HRR, u is the longitudinal ventilation velocity (m/s), A is the cross sectional area of the tunnel (m^2), g is gravity acceleration (m/s^2), r is the equivalent radius of fire source (m) and C is a proportionality coefficient that accounts for the type of fuel. The proportionality between the increase of HRR and the second term of the righthand side of the equation is reported to hold for any fuel.

4) Li et al. [58]:

The authors claim that the burning rate of pool fires is highly affected by the scale of the pans. Thus, equation 4.4 might not be applicable to describe large pool fires. In their study, they have also investigated the effects of longitudinal velocity for sets of wood cribs, and for a

combination of those with plastics. According to their work, the maximum HRR is independent on the ventilation velocity for *fuel-controlled* fires, as depicted by the continuous line above the dashed line in Figure 4.9. Note that this does not mean that the HRR for the tunnel fire will be the same as that of on an identical fire burning in the open. As explained by the authors, the maximum HRR achieved inside a tunnel is expected to increase in approximately 25% when compared to that of the same fire in the open. For *ventilation-controlled* fires, the peak HRR becomes directly dependent on the ventilation conditions inside the tunnel.

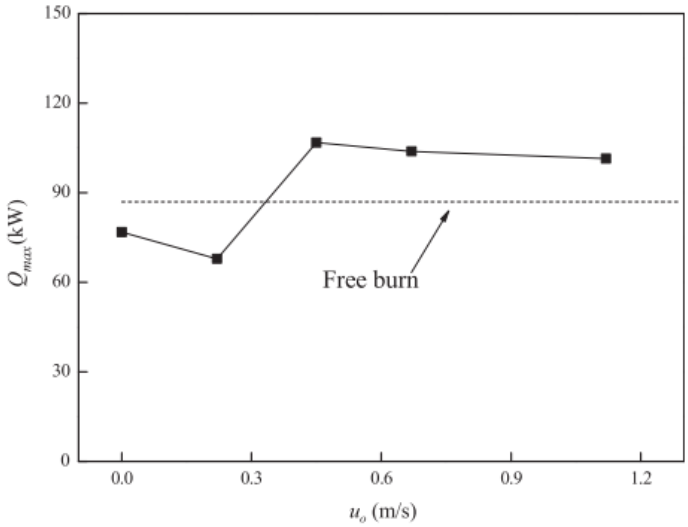


FIGURE 4.9 - MAXIMUM HRR FOR DIFFERENT VENTILATION VELOCITIES
Retrieved from Li et al. [58]

4.2.3 Location of the fire source inside the tunnel

Most tunnel fire tests are performed with the fire source being placed at the centerline of the tunnel. Nonetheless, in realistic cases, a fire might occur anywhere within the tunnel. No previous studies were found about the influence of the fire location on the development of HRR. However, Ji et al. [45] studied the effect of different transverse fire locations on the maximum ceiling temperatures. Their findings are explained in Section 3.3.2.1.

4.2.4 Protection Systems

Protection systems can be divided in two groups, namely: (1) passive systems (Section 4.2.4.1); and (2) active systems (Section 4.2.4.2). The first ones are based on the application of insulation layers on the surface of the tunnel structure. The second type refers to the so-called Fixed Fire Fighting Systems (FFFS). Both types of protection systems, and their possible influences in the total HRR achieved by a tunnel fire, are discussed in more detail in the next subsections.

4.2.4.1 Passive Systems

According to Davidson et al. [61], these systems are intended to provide the structure with the ability to resist the rapid-fire growth and to insulate the underlayer material, thus limiting the maximum temperature achieved by the structure. If correctly designed, the use of such systems avoids the occurrence of spalling and the degradation of mechanical properties of concrete, and also of its reinforcements, thus ensuring structural integrity during a fire. Davidson et al. [61] summarizes the types of passive systems that are currently applied to tunnels:

1) *Cladding*: This system consists of the application of rigid panel boards made of fire-resistant components (i.e. calcium silicates) on the tunnel lining. They are anchored to the surface of the tunnel adjacently to each other, forming a homogeneous protective layer over the concrete structure (Figure 4.10).

2) *Spray-Applied Refractory Cements:* Refractory cements contain inert materials as vermiculite, which makes them able to undertake extremely high temperatures without burning, producing smoke, or releasing toxic gases. They are uniformly sprayed to the surface of the tunnel lining forming a protective layer, which can be as thick as needed.

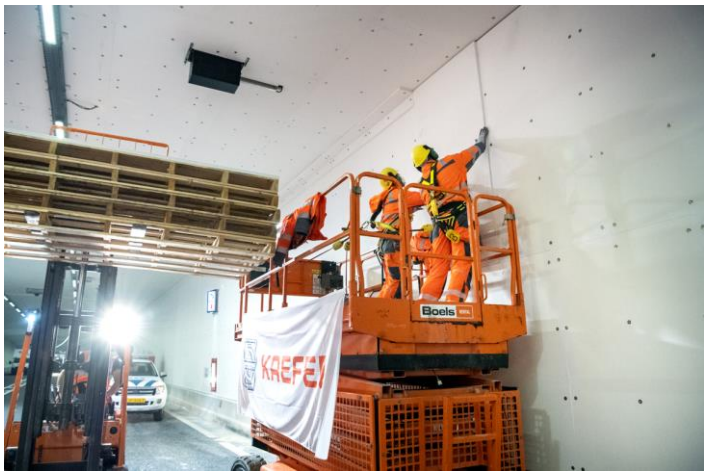


FIGURE 4.10 – CLADDING[4]

As depicted by Tomar and Khurana [62], the effects of passive systems on the peak HRR are not well understood and should be further investigated. Nonetheless, due to the thermal properties of such materials, there is an expectation, confirmed in limited scale by a few studies, that they will lead to an increase of the HRR achieved by tunnel fire. This possibility is explained by: (a) *higher emissivity* of such materials when compared to that of concrete, meaning that the heat feedback of the protection system back to the enclosure is larger than that of concrete; (b) *lower thermal inertia*, so it suffers a faster increase in surface temperature, and thus starts contributing to the fire in a shorter period than concrete; and (c) *lower thermal conductivity*, making the heat to be more trapped inside the tunnel environment as it takes more time to spread through the walls.

4.2.4.2 Active Systems

Active systems are the ones that are used to effectively control or suppress a tunnel fire. They are known as Fixed Fire Fighting Systems (FFFS) and include all kinds of water-based and foam-based systems. Ingason et al. [2] describes that such systems can be aimed at three

[4] https://bezoekerscentrum.rijkswaterstaat.nl/SchipholAmsterdamAlmere/news/laatste-hittewerende-plaat-in-gaasperdammertunnel-geplaatst/#.Xrc_0GgzaUk

different levels (Figure 4.11): (1) *fire suppression*, where the maximum HRR is effectively reduced, and fire growth is significantly affected in a short period after the beginning of operation; (2) *fire control*, where the objective is to control the fire by limiting the maximum level of HRR without necessarily reducing the total amount of energy released from a fire; and (3) *fire extinction*, when the goal is to completely eliminate a fire shortly after the activation of the system.

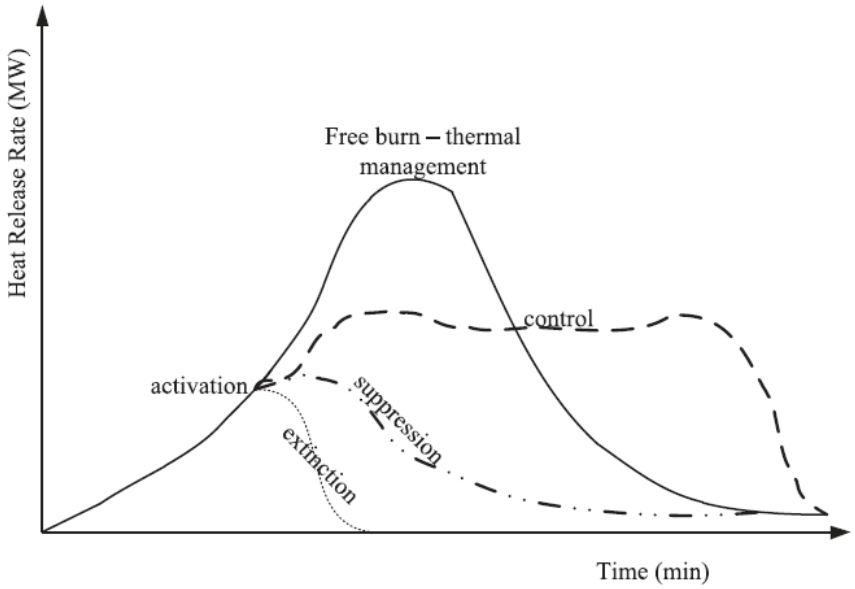


FIGURE 4.11 - PERFORMANCE OF WATER-BASED FFFS
Retrieved from Ingason et al. [2]

In case of a tunnel fire, the goal is usually to achieve suppression, as extinction is hardly reached due to its large requirements of water supply. In essence, the flame volume is to be controlled, making the heat feedback to be immediately reduced. The systems applied to tunnels are mostly water-based and can be divided into two categories:

1) *Deluge Systems:* Consist of several deluge zones positioned adjacent to each other. The water supply is designed to suffice the simultaneous operation of at least two zones and is based on atmospheric pressure.

2) *Water Mist Systems:* Are similar to deluge systems but require significantly less water storage, as they operate under higher pressure. There are also two kinds of water mist systems, the ones which are based in lower pressures (up to 10 bar) and the ones based on high pressure (up to 120 bar).

Ingason et al. describes that the deluge systems are based on a water flow rate of *10* to *12.5mm/min* and suppress a fire through fuel surface cooling. On the other hand, water mist systems apply a rate of *1* to *4mm/min* and achieve fire suppression through dilution of the concentration of pyrolysis gases in the air and also by cooling the gas phase of a fire. Those systems are able to reduce the HRR and to avoid fire spread, but the time of activation is an important parameter for successfully achieving this task. The effects of water based fixed systems have even be included in the NFPA 502, a standard developed by the National Fire Protection Association (NFPA) and depicted in Figure 4.12 below. In the absence of data,

Tomar and Khurana [62] report that many designers consider that the use of FFFS leads to a reduction of 50% of the total HRR.

Fire data for typical vehicles, NFPA 502 (National Fire Protection Association USA, NFPA 502, 2017).

Vehicle	Experimental HRR (MW)	Time to peak HRR	Experimental HRR with fixed water based fire protection system (MW)	Time to peak HRR
Car	5–10	0–54 min	–	–
Multiple passeger car	10–20	10–55 min	10–15	35 min
Bus	25–34	7–14 min	20	–
HGV	20–200	7–48 min	15–90	10–30 min
Petrol tanker	200–300	–	10–200	–

FIGURE 4.12 - EFFECT OF WATER BASED FFFS IN HRR
Retrieved from Tomar and Khurana (2019) [62]

4.3 Fire Scenarios

Different fire scenarios are compared in order to define upon the worst-case possible. The latter is the basis for setting a design fire, which is afterwards converted into standards and regulations. From a structural point of view, those are very often represented in the form of time-temperature curves (Chapter 8). Those prescriptive curves are very generic and avoid any consideration over the specific characteristics of a given tunnel. In case an improved design is pursued, one may follow a performance-based approach (Chapter 9) to account for how the physical aspects of a tunnel may really affect fire development. Therefore, it is fundamental to understand what parameters are involved in developing different fire scenarios and how they relate to each other. Only then, a solid decision over the worst-case scenario for a specific tunnel can be made, allowing a more optimum design.

According to Kim et al. [63], a tunnel fire might occur for several different reasons, such as: collisions, fuel leakage, overheating of the breaks or electrical failure in the engine. Focusing on achieving effective firefighting operations, the authors studied data from 69 tunnel fires and classified them into most common incident categories for tunnel fires. Those categories were later related to four model classes which could be used to describe the most likely fire scenario for a certain tunnel. Accordingly:

- *Incident Categories (IC):* Indicate the type of initial incident.

  - *IC1:* Single fires that do not propagate to other vehicles (63%)
  - *IC2:* Single fires that propagate to other vehicles (7%)
  - *IC3:* Collision fires limited to vehicles involved in the collision (10%)
  - *IC4:* Collision fires that spread to other vehicles (19%)

- *Classes:*

  1) *Class I:* Tunnels with restricted transit of heavy good vehicles (HGV) and dangerous good vehicles (DGV) (IC1)
  2) *Class II:* Tunnels with high fire load traffic as HGV and DGV (IC1 to IC4)
  3) *Class III:* Unidirectional tunnels with reduced flow of vehicles (IC1 or IC2)
  4) *Class IV:* Congested or bidirectional tunnels (IC2 or IC4)

A framework, relating classes and categories was proposed (Figure 4.13). Based on it, one should consider the type of vehicles passing through the tunnel, the time response of the fire

brigade, the direction of traffic flow and the likelihood of congestion inside the tunnel, to classify a given tunnel into one of the four classes described above.

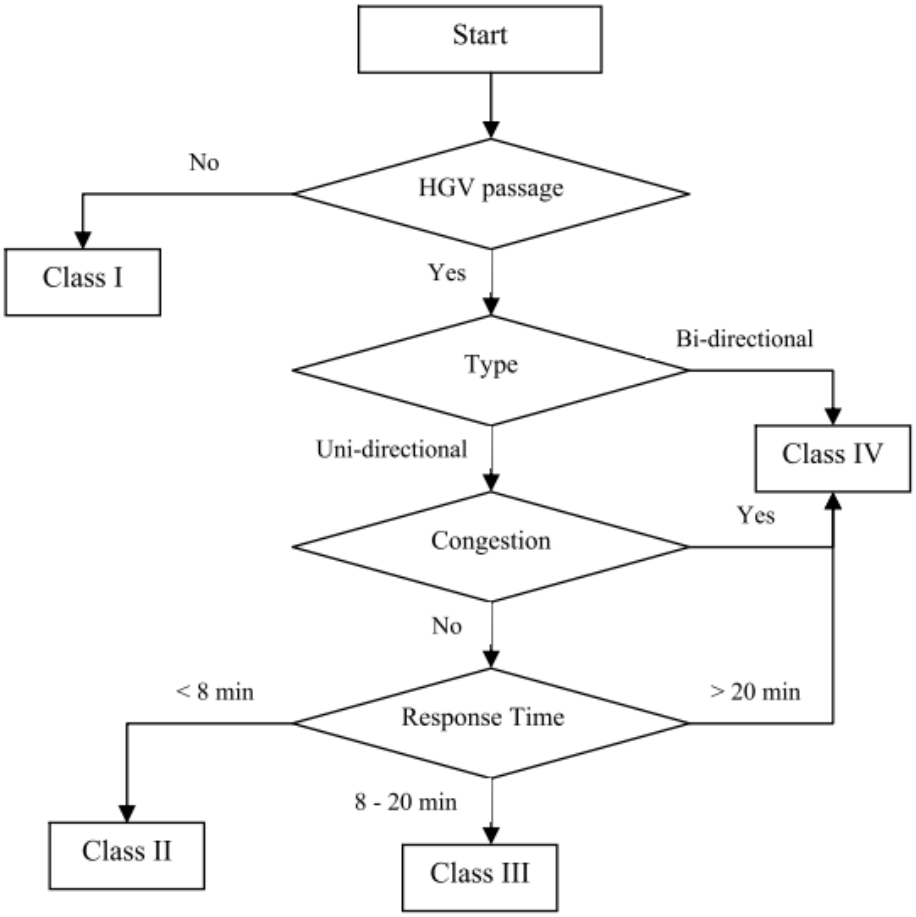


FIGURE 4.13 – FRAMEWORK FOR DECIDING UPON A MODEL FOR ROAD TUNNELS
Retrieved from Kim et al. [63]

The work presented here is solely focused on helping fire brigades to proceed with their job. Despite not being directly related to the scope of this thesis, in which focus is only on the structural integrity during tunnel fires, this type of approach can still be useful, as it highlights the methodology of deriving possible fire scenarios in a tunnel. In a similar manner, one might consider applying the same concepts presented here to idealize what kind of fire events would be likely to occur within a certain tunnel. Thus, among several likely fire scenarios, one can opt for a worst-case and develop a more realistic time-temperature curve for that specific tunnel, rather than just applying the prescribed RWS curve. The starting point for the use of such an approach is to classify the tunnel according to the type of traffic allowed within it (Section 4.3.1). From that, one can determine which fire scenarios are likely to occur inside this tunnel. Once those are known, one can decide upon the worst-case for this specific tunnel. This is illustrated in Figure 4.14 below, where different types of tunnels are linked their most dangerous fire events.

Type of tunnel	Triggering event for a fire scenario to be evaluated in the Specific Hazard Study
A) Road tunnel open HGVs, transportation of dangerous goods (DGs) not allowed	a) Fire on a truck
	b) Fire on a large truck carrying combustible liquid or easily melting solid with high calorific value
B) *Road tunnel open HGVs, including transportation of (DGs)*	a) Fire on a large truck
	b) Fire on a petrol tanker (carrying 20 tons of fuel)
C) *Tunnels with limited clearance between 2 m and 3.5 m*	a) Fire involving a van loaded with flammable liquids, without outside spill
	b) Fire on a small truck
D) *Tunnels with clearance below or equal to 2 m*	a) Fire on a passenger car with propagation to one or two other cars
	b) Fire involving a van loaded with flammable liquids, without outside spill

FIGURE 4.14 – FIRE SCENARIOS ACCORDING TO THE NEW FRENCH REGULATION
Retrieved from UPTUN [51]

4.3.1 Tunnel Categories in the Netherlands

As described previously, the fire load in a tunnel is consisted either of vehicles or pool fires, which are formed from leaking vehicles. Thus, it becomes essential to understand how tunnels are classified in the Netherlands with respect to allowed traffic, as this inherently defines the possible fire events that can occur within a given tunnel. In the Netherlands, hazardous substances may not be transported through every tunnel. In this sense, tunnels are classified into five categories [64], which impose specific traffic restrictions for the tunnel:

- *Tunnel Category A:* No restrictions for the transport of dangerous goods.
- *Tunnel Category B:* Restriction for dangerous goods which can: (1) generate very large explosions.
- *Tunnel Category C:* Restriction for dangerous goods which can: (1) generate very large explosions; (2) generate a large explosion; and (3) release a large quantity of toxic substances.
- *Tunnel Category D:* Restriction for dangerous goods which can: (1) generate very large explosions; (2) generate a large explosion; (3) release a large quantity of toxic substances; and (4) can generate a large fire. Note that this is the category of the Piet Hein tunnel (Chapter 9), which is selected as the case study for this thesis.
- *Tunnel Category E:* Allows only the transportation of very few kinds of dangerous goods.

4.4 Conclusions

The following conclusions are drawn with respect to the work developed in this chapter:

1) A fire is described in terms of the development of HRR in time, which is related to the product between the mass loss rate of fuel ($\dot{m}_f''$ in equation 4.1) and the total burning area (A_f in equation 4.1). Pool fires burn with constant $\dot{m}_f''$ (Figure 4.4), making the development of HRR to be fully quantifiable in terms of the area of the pool. Thus, if the surface area of the pool is kept constant during the combustion of fuel then the HRR will also be constant in time.

2) This scenario is changed when dealing with solid fires. For those, both the burning rate of the material ($\dot{m}_f''$ in equation 4.1) and the burning area of fuel (A_f in equation 4.1) will vary in time, hardening the task of predicting the development of HRR for such fires (Figure 4.1). As a consequence, solid fires are more often described in terms of their peak HRR, which is calculated theoretically based on the maximum burning rate and maximum exposed area.

3) There are two types of protections systems that are applied to tunnels, namely *passive* and *active* systems. The former consists of the use of insulation materials to limit the temperature development of the tunnel lining during a fire, thus ensuring structural integrity. The latter is based on the application of FFFS, mainly water-based, which protect the tunnel structure by effectively changing fire dynamics and thus reducing the development of HRR (Figure 4.11 and Figure 4.12). The use of insulation is of particular importance for the work developed in this thesis, and will be further addressed in Chapters 7 and 8, where the origin of the RWS curve and its use in tunnel fire safety engineering are deeply discussed.

4) The effects of the geometry of the tunnel in the HRR of a fire vary in the literature (Section 4.2.1). Apparently, due to heat feedback from the tunnel structure, the HRR of a *fuel-controlled* fire is expected to increase when compared to that of the same case burning in the open environment. However, further changes in the geometry of the tunnel do not seem to generate extra effects on the HRR (Figure 4.7).

5) The effects of ventilation on the size of tunnel fires also vary in the found literature (Section 4.2.2). Generally speaking, the development of *fuel-controlled* tunnel fires is independent of the ventilation conditions inside the tunnel. The opposite behavior is expected for *ventilation-controlled* tunnel fires, and the HRR of such might be largely affected by the use of ventilation.

5 Thermal Exposure

This chapter provides the reader with fundamental concepts of fire and the interface between fire and structure. At first, the mechanisms of heat transfer between a fire and a structure are presented. Then, important aspects on the use of FDS in performing fire simulations are highlighted. After that, thermal boundary conditions used to describe the interface between fire and structure in heat transfer calculations are given, highlighting a simple way of coupling CFD calculations for the fire phase with the FEA of structures.

5.1 Mechanisms of Heat Transfer

There are three modes of heat transfer, namely conduction, convection, and radiation. In the analysis of structures subjected to fire, each one of these mechanisms will play a role. In essence, conduction determines the rate of heat that will flow into the solid during a fire or, in other words, it regulates the amount of thermal energy which is absorbed by the structure. Convection and radiation, on the other hand, are the means through which heat will be exchanged between the source (i.e. a fire) and the receiver (i.e. a structure). In the very early stages of a fire convection will be of importance. However, the levels of emitted thermal radiation will grow considerably as soon as high temperatures are achieved within the flames and/or enclosure. As a result, radiation will take control over convection thus becoming the dominant mechanism of heat transfer to the structure (Drysdale [65]). This radiation governance in fires is later discussed in Section 5.1.3.2. For now, the focus will be to present the basic concepts and governing equations of each mode of heat transfer with an emphasis on their application to fire safety engineering. In this sense, the total heat transferred to a structure during a fire event is given by the added contribution of convection and radiation according to:

$$\dot{q}''_{tot} = \dot{q}''_{con} + \dot{q}''_{rad} \qquad 5.1$$

where $\dot{q}''_{tot}$ is the total heat flux to a surface (W/m^2), $\dot{q}''_{con}$ is the convection heat flux (W/m^2) and $\dot{q}''_{rad}$ is the net radiation heat flux (W/m^2).

However, before addressing the mechanisms through which a structure absorbs energy, namely convection (Section 5.1.2) and radiation (Section 5.1.3), the following section will describe how heat is conducted in a solid.

5.1.1 Conduction

Conduction heat transfer is only possible within a state of matter. Although it can also occur in gases and liquids, conduction is more often associated with solids. It is the result of energy transferred through collisions from particles at higher temperatures (thus having higher molecular energy) to particles at a lower energy state (Wickström [66]). *Fourier's law* of heat conduction implies that heat flux in the solid is proportional to the thermal gradient through a constant known as thermal conductivity. It is depicted below for a one-dimensional case:

$$\dot{q}''_x = -k\frac{dT}{dx} \qquad 5.2$$

where $\dot{q}''_x$ is the heat flux (W/m^2), k is the thermal conductivity (W/(m.K)), dT is the temperature difference (K) over a distance dx (m).

The steady state solution of *Fourier's equation*, illustrated by Figure 5.1, is obtainable by simple integration and is given below for cases in which the thermal conductivity can be assumed as temperature independent:

$$\dot{q}_x'' = \frac{k}{L}(T_1 - T_2) \qquad 5.3$$

where $\dot{q}_x''$ is the heat flux (W/m²), k is the thermal conductivity (W/(m.K)), L is the wall thickness (m), (m) and $(T_1 - T_2)$ is the temperature difference between the wall surfaces (K).

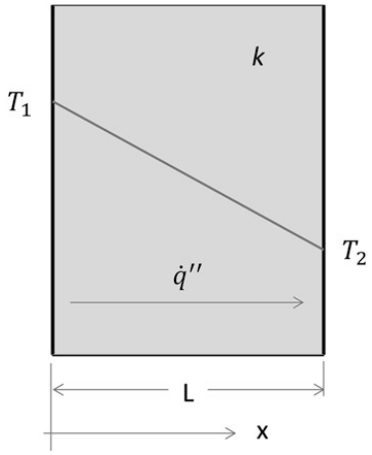


FIGURE 5.1 – HEAT FLUX THROUGH A WALL
Retrieved from Wickström [66]

The study of structures subjected to fire will require a more complex formulation of conduction heat transfer. Due to the transient nature of fires, *Fourier's law* has to be rewritten in terms of time and spatial derivatives. For a simple one-dimensional analysis, conduction will be evaluated through the solution of the differential equation below:

$$\rho_s c_s \frac{\partial T_s(x,t)}{\partial t} = \frac{\partial}{\partial x}\left(k_s \frac{\partial T_s(x,t)}{\partial x}\right) \qquad 5.4$$

where ρ_s is the solid's density (kg/m³), c_s is the solid's specific heat (kJ/(kg.K)), k_s is the solid's thermal conductivity (W/(m.K)) and $T_s(x,t)$ is the temperature development of the solid in time at a depth x, where x=0 represents the surface of the solid which is exposed to fire.

Note that the equation above ensures conservation of energy within the structure. Essentially, it tells us that all the energy absorbed by the solid phase during a fire will be split between: (1) a parcel which is stored within the body in terms of internal energy (characterized by the left-hand side of equation 5.4), and thus responsible for any temperature increase of the structure; and (2) energy that is in transit through the material (given by the right-hand side of equation 5.4), for which case we call it heat. The product between the density ρ_s and the specific heat of the solid c_s is known as the volumetric heat capacity and indicates the amount of energy required to increase a volume of *1 m^3* by a temperature of *1 K*. For most materials, both the specific heat c_s and the thermal conductivity k_s are temperature dependent. Not only that, for certain cases the density of the solid will also vary with temperature (e.g. combustible materials, due to moisture evaporation within the structure, or even due to dehydration process at microstructure level). Altogether, these contribute to make the solution of a thermal transient analysis to be rather complex, often requiring the use of numerical procedures.

5.1.2 Convection

Convection is the mode of heat transfer associated with the motion of a fluid. In fires, it may arise naturally through buoyancy-driven flows, where the hot gases generated by combustion will rise being replaced by colder masses of air, or it might also be induced by some external source (e.g. wind generated by a fan during a tunnel fire). In the former case we refer to *natural convection*, whereas for the latter we nominate it *forced convection*. No matter the type of convection prevailing in a fire scenario, Wickström [67] describes that for most fire engineering cases this mode of heat transfer can be simplified into the equation below:

$$\dot{q}''_{con} = h(T_g - T_{surface}) \qquad 5.5$$

where $\dot{q}''_{con}$ is the convective heat flux (W/m^2), h is the convective heat transfer coefficient (W/(m^2.K)), T_g is the gas temperature at the vicinity of the exposed surface (K), and T_s is the absolute surface temperature of the structure (K).

Hence, convection is proportional to the temperature difference between that of the surrounding gases and that of the surface of the structure through a convective heat transfer coefficient. This coefficient is mainly dependent on the flow conditions (i.e. laminar or turbulent flow) at the vicinity of the structure. In essence, the type of flow defines the thickness of the thermal boundary layer which is formed close to the surface (represented by δ in Figure 5.2). According to Drysdale [65], typical values for the heat transfer coefficient are in the range of *5 – 25 W/m^2.K* for *natural convection* and *10 – 500 W/m^2.K* for *forced convection* in air. This coefficient actually varies during a fire event. However, it is common practice in fire safety engineering to assume it as a constant, and rather conservative, parameter. Such choice usually has no major influence into the thermal analysis of structures exposed to fire. This is the case because the convection contribution to the total amount of heat transferred to a structure during a fire is quite limited when compared to the thermal exposure induced by incident radiation (Section 5.1.3.2). Thus, provided that radiation is correctly accounted for in the thermal analysis of a structure subjected to fire, the effects of assuming larger values for the convection heat transfer coefficient will be minimum.

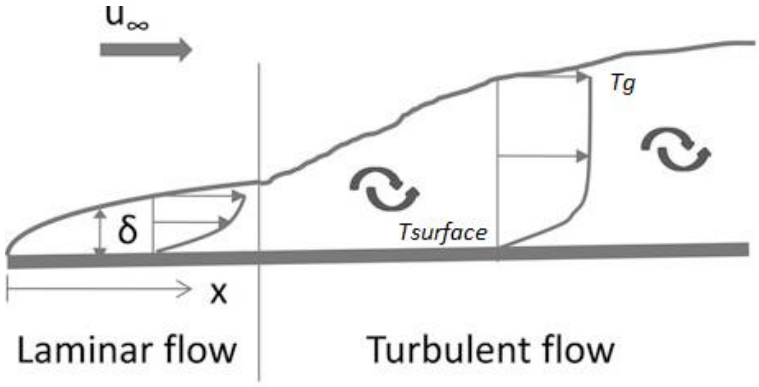


FIGURE 5.2 – GAS VELOCITY PROFILE IN THE VICINITY OF THE SURFACE
Adapted from Wickström [66]

5.1.3 Radiation

Differently from conduction and convection, radiation is a mode of heat transfer that does not require any intervening medium to occur. As explained by Tien et al. [68], thermal radiation

relies on the theory of electromagnetic waves, which is the basis of quantum mechanics. In essence, all objects with a finite temperature emit energy packages (known as photons) due to electron oscillations within the body. If the absolute temperature increases, these oscillations become more rapid and will lead to higher levels of emitted thermal radiation ($\dot{q}''_{emi}$ in Figure 5.3). As all bodies generate thermal radiation, every object in space is also subjected to an incident amount of radiation ($\dot{q}''_{inc}$ in Figure 5.3), which is originated from other emitting bodies. Part of this incident radiation is reflected back to the environment at the surface of the object of interest ($\dot{q}''_{ref}$ in Figure 5.3), whereas the remaining parcel is absorbed by the body ($\dot{q}''_{abs}$). In fire safety engineering we are interested in the net difference between the levels of incoming and outgoing thermal radiation in a structure ($\dot{q}''_{rad}$ in Figure 5.3), which is actually what characterizes the radiation heat transfer between two sources at different temperatures or, in our case, a fire and the structure. Thus, based on Wickström [67], the net radiation heat flux entering a structure is given by:

$$\dot{q}''_{rad} = \dot{q}''_{abs} - \dot{q}''_{emi} = \left(\dot{q}''_{inc} - \dot{q}''_{ref}\right) - \dot{q}''_{emi} \qquad 5.6$$

where $\dot{q}''_{rad}$ is the net radiant heat flux (W/m^2), $\dot{q}''_{abs}$ is the radiant heat flux absorbed by the structure (W/m^2) which is equal to $\left(\dot{q}''_{inc} - \dot{q}''_{ref}\right)$ or, in other words, the difference between incident radiation ($\dot{q}''_{inc}$) and the amount of radiation which is reflected back to the environment at the surface of the structure ($\dot{q}''_{ref}$). Finally, $\dot{q}''_{emi}$ is the amount of thermal radiation which is emitted by the structure (W/m^2) according to its own absolute temperature.

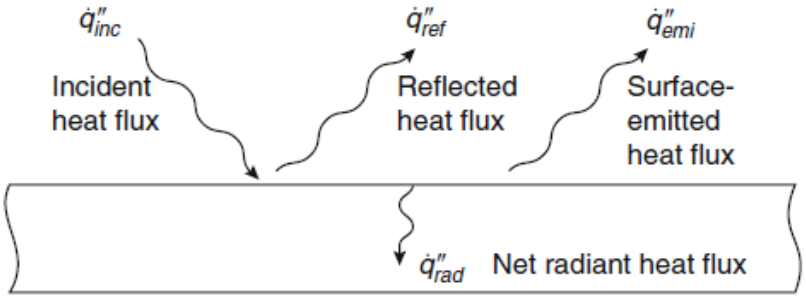


FIGURE 5.3 – RADIATION HEAT TRANSFER
Retrieved from Wickström [67]

In principle $\dot{q}''_{abs}$ and $\dot{q}''_{emi}$ are independent of each other. This means that a body will always absorb and emit radiation. The amount of heat absorbed by the structure equals the difference between $\dot{q}''_{inc}$ and $\dot{q}''_{ref}$, but is often simplified in terms of the surface absorptivity coefficient α_s. The physics behind this parameter will be left for the discussion over $\dot{q}''_{emi}$. For now, it is important to mention that the absorptivity will assume a value between *0* and *1* and will define the percentage of $\dot{q}''_{inc}$ that is actually absorbed by the structure. Therefore:

$$\dot{q}''_{abs} = \alpha_s \, \dot{q}''_{inc} \qquad 5.7$$

where $\dot{q}''_{abs}$ is the radiation absorbed by the body (W/m^2), $\dot{q}''_{inc}$ is the incident radiation at the surface (W/m^2) and α_s is the surface's absorptivity.

A much more complex issue is to address the emissions of thermal radiation from a body. As described earlier, thermal radiation refers to the propagation of electromagnetic waves travelling in the speed of light (i.e. photons). Essentially, the amount of energy which is carried

by each one of those particles is inversely proportional to the wavelength (λ) at which those photons are travelling in space. A body will always emit packages of thermal radiation in several wavelengths, but the maximum emitted spectrum of radiation is known, and can be calculated based on *Planck's distribution law* according to the absolute temperature of the object. To limit the discussion to the applicability of radiation heat transfer in fire safety engineering this law is omitted here, but such spectrums of radiation (i.e. *Planck's distributions*) are exemplified in Figure 5.4 together with the illustration of a *blackbody*. Accordingly, a *blackbody* is characterized as a *perfect diffusive emitter* or, in other words, an idealized surface which emits the maximum possible thermal radiation at every wavelength and with no directional dependency (Tien et al. [68]). An important remark here is that a *blackbody* also exhibits *continuous absorption*, meaning that this body will absorb all the thermal radiation incident on its surface independent on wavelength or direction (i.e. α_s=1 in equation 5.7)or, in other words, that $\dot{q}''_{abs} = \dot{q}''_{inc}$ and $\dot{q}''_{ref} = 0$. The total amount of thermal radiation emitted by a *blackbody*, which is kept at a static absolute temperature, is given by the integral of the spectral emissive power at this temperature over all wavelengths. The result of this integral is known as the *Stefan-Boltzmann law*:

$$\dot{q}''_{emi,blackbody} = \sigma \, T^4_{blackbody} \qquad \textbf{5.8}$$

where $\dot{q}''_{emi,blackbody}$ is the thermal radiation emitted by a blackbody (W/m²), σ is the Stefan-Boltzmann constant (5.67 x 10⁻⁸ W/(m²K⁴)) and $T_{blackbody}$ is the absolute surface temperature of a blackbody (K).

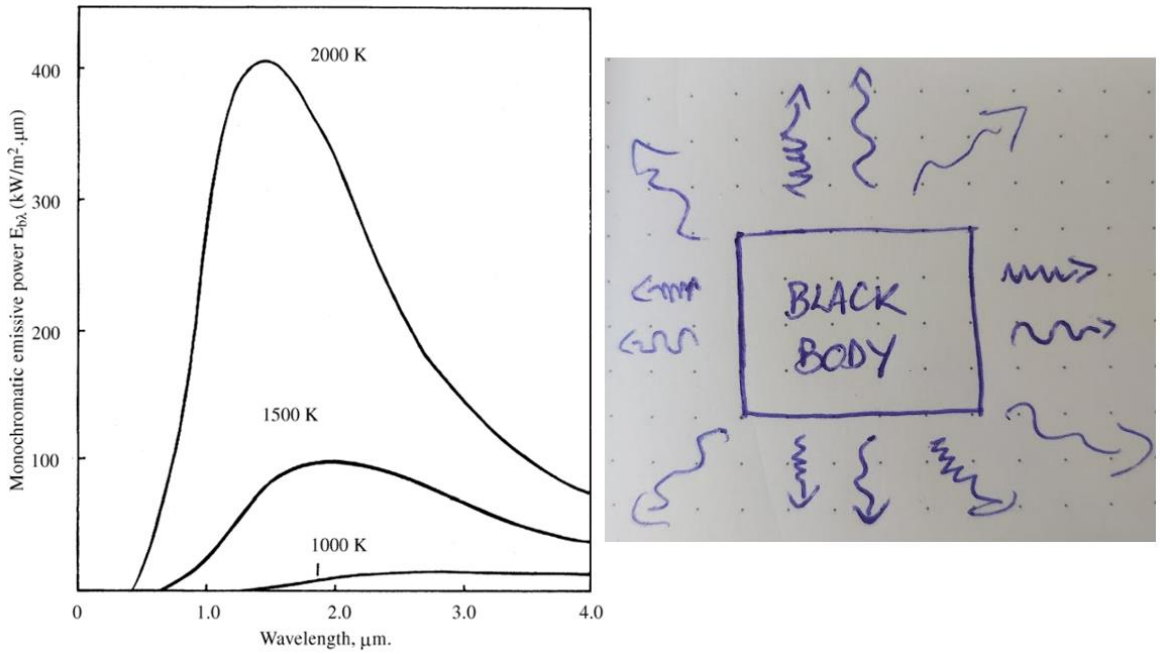


FIGURE 5.4 – ENERGY SPECTRUM OF RADIATION EMITTED BY A BLACKBODY
Adapted from Drysdale [65]

In real life though, differently from *blackbodies*, most surfaces will not emit thermal radiation at their maximum levels (Figure 5.5). Still, in fire engineering practice, surfaces are assumed to behave as *diffusive grey bodies* (Drysdale[65]). This means that despite not emitting the maximum levels of thermal radiation at all wavelengths, the intensity of emitted radiation is considered to be independent of wavelength. Also, thermal radiation is assumed to be equally

emitted in all directions. Although this is an approximation (Figure 5.5), it allows the use of the *Stefan-Boltzmann law* (equation 5.8) by simply introducing a surface's emissivity ε_s, which relates the percentage of radiation emitted by a body in comparison to that of a *blackbody*. For instance, if a structure has a surface emissivity of *0.75* (as sown in Figure 5.5), then the amount of radiation emitted by this surface is equal to *75%* of that of a *blackbody* kept at the same absolute temperature. Therefore, a *modified Stefan-Boltzmann* equation is used in fire safety engineering:

$$\dot{q}''_{emi} = \varepsilon_s \sigma T^4_{surface} \qquad 5.9$$

where $\dot{q}''_{emi}$ is the total radiation heat flux emitted by the surface of the structure (W/m^2), ε_s is the surface's emissivity, σ is the Stefan-Boltzmann constant (5.67 x 10^{-8} W/(m^{2}K^4)), and $T_{surface}$ is the absolute surface temperature of the structure (K).

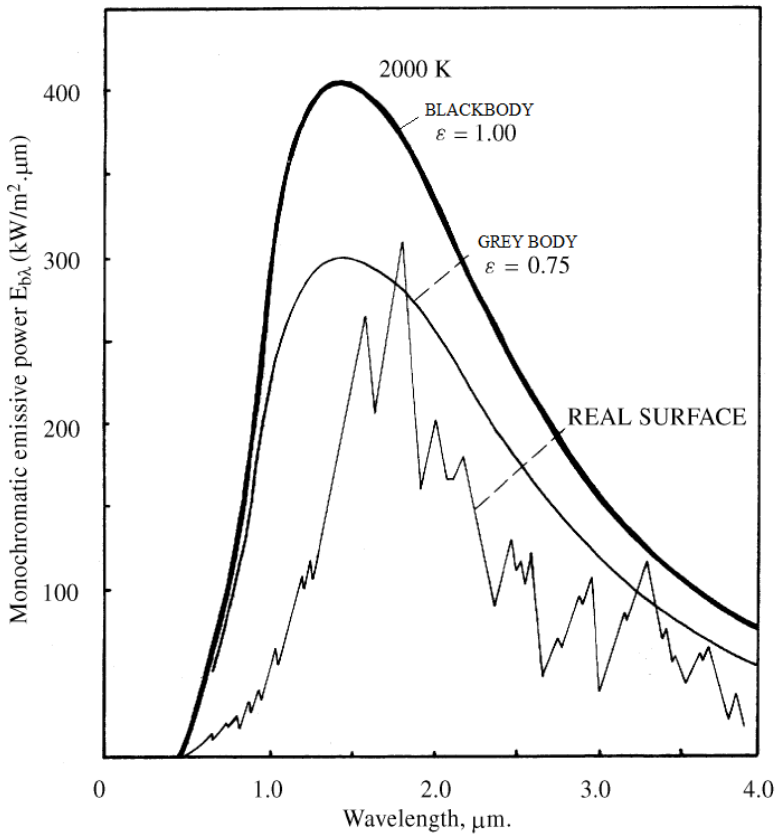


FIGURE 5.5 – ENERGY SPECTRUM OF RADIATION EMITTED BY A REAL SURFACE
Retrieved from Drysdale [65]

Kirchoff's law states that if a body is able to maintain thermal equilibrium (such that it can be kept at a constant absolute temperature), then its absorptivity α_s and its emissivity ε_s have to equal each other (Tien et al. [68]). Wickström [66] describes that this *law* does not hold when the source (emitting radiation to a surface) and the target itself, have very different temperatures. However, as α_s and ε_s vary only marginally with temperature for most building materials, the use of *Kirchoff's law* is also a reasonable approximation when addressing structures subjected to fire. Note that the use of this law is also only valid for the so-called *blackbodies* and/or *grey bodies*, as those are assumed to emit and absorb radiation equally in every direction and independent of the wavelength. So, by making use of *Kirchoff's law* and

replacing equations 5.7 and 5.9 into equation 5.6, we get a new equation for the net radiant heat flux to the structure:

$$\dot{q}''_{rad} = \varepsilon_s(\dot{q}''_{inc} - \sigma T^4_{surface}) \qquad \textbf{5.10}$$

where $\dot{q}''_{rad}$ is the net radiant heat flux (W/m²), $\dot{q}''_{inc}$ is the incident radiation at the surface of the structure (W/m²), ε_s is the surface's emissivity, σ is the Stefan-Boltzmann constant (5.67 x 10^{-8} W/(m²K⁴)) and $T_{surface}$ is the absolute surface temperature of the structure (K).

During a fire, the incident radiation in a structure is the added contribution of radiation emitted from several different sources (e.g. the surrounding flames and smoke, and/or other surfaces present within an enclosure), making it quite complex to be assessed in reality. However, if the thermal exposure of a structure is to be evaluated, then the amount of incident radiation at the surface of this structure has to be known in advance. In practical terms $\dot{q}''_{inc}$ is either: (1) directly or indirectly prescribed by codes, which are often based on measurements collected during fire tests; or (2) obtained through fire simulations in CFD software (e.g. FDS). The levels of incident radiation which are expected to occur in different fire scenarios are described in Chapter 8 of this thesis. Here, the focus is on the numerical solution of transient thermal problems. In this sense, it is very often convenient to translate $\dot{q}''_{inc}$ in terms of a hypothetical radiation temperature T_r, as illustrated in Figure 5.6. Basically, the *Stefan-Boltzmann law* (equation 5.8) is used to represent $\dot{q}''_{inc}$ through the absolute temperature of a *blackbody* (T_r) emitting an equivalent amount of thermal radiation, such that $\dot{q}''_{emi,blackbody} = \dot{q}''_{inc}$. Thus:

$$T_r = \sqrt[4]{\frac{\dot{q}''_{inc}}{\sigma}} \qquad \textbf{5.11}$$

where T_r is the hypothetical radiation temperature (K), $\dot{q}''_{inc}$ is the incident radiation at the surface of the structure (W/m²) and σ is the Stefan-Boltzmann constant (5.67 x 10^{-8} W/(m²K⁴)).

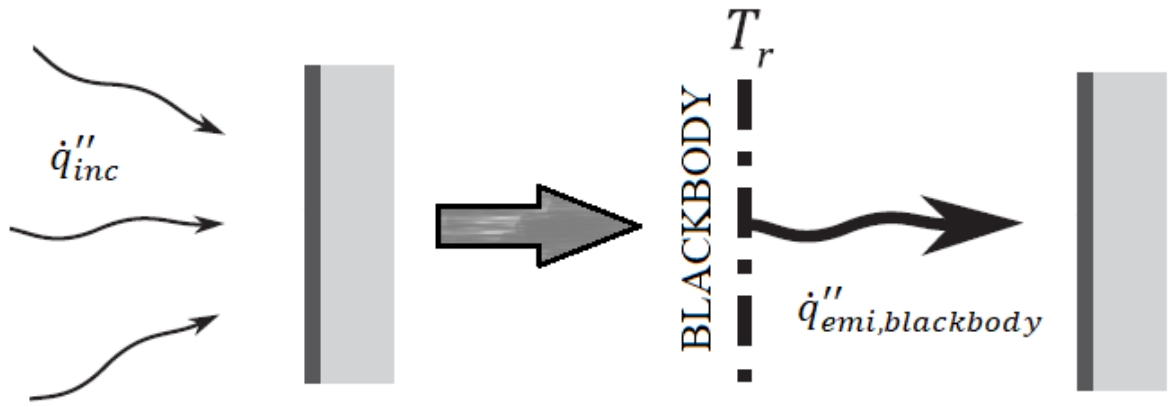


FIGURE 5.6 – RADIATION TEMPERATURE

Based on this concept, the net radiant heat flux $\dot{q}''_{rad}$ to the structure can be rewritten in terms of the equation below:

$$\dot{q}''_{rad} = \varepsilon_s \sigma (T_r^4 - T_{surface}^4) \quad \textbf{5.12}$$

where ε_s is the surface emissivity, σ is the Stefan-Boltzmann constant (5.67 x 10^{-8} W/(m^2K^4)), T_r is the radiation temperature (K) and $T_{surface}$ is the absolute surface temperature (K). Wickström [67] describes that the emissivity can be taken as 0.8 for most building materials.

5.1.3.1 Radiation from Hot Gases and Flames

The amount of thermal radiation emitted by hot gases and flames is also treatable based on the *modified Stefan-Boltzmann* equation presented in the previous Section 5.1.3. This equation is provided here in a different manner to fundament the discussion developed in this topic. Accordingly:

$$\dot{q}''_{emi,f} = \varepsilon_f \sigma T_f^4 \quad \textbf{5.13}$$

where $\dot{q}''_{emi,f}$ is the radiation heat flux emitted by the flames (W/m^2), ε_f is the flame's emissivity, σ is the Stefan-Boltzmann constant (5.67 x 10^{-8} W/(m^2K^4)), and T_f is the flame's temperature (K). Note that the equation above is also valid to describe a hot gas body. In this case, the subscript f (i.e. flames) should be replaced by g (i.e. gas) and all the terms which are referring to the characteristics of the flame will now be related to a gas body.

Drysdale [65] explains that not all gases will interact with electromagnetic radiation in the thermal region of the spectrum (Figure 5.7). For instance, gases such as N_2, O_2 and H_2 are completely transparent to thermal radiation and will neither absorb nor emit radiation at this specific range of the spectrum. Only gases with heteronuclear molecules (e.g. CO, CO_2 and H_2O) are susceptible to interact with thermal radiation. Even so, such species do not exhibit the characteristic behavior of a *blackbody* or a *grey body*. This means that those gases are only affected by thermal radiation at certain wavelengths intervals and not on the total spectrum range (Figure 5.7), hardening the task of accurately accessing thermal radiation in such gas bodies. Effectively, engineering calculations hardly ever require such a high resolution of the emissivity spectra of those gases (Tien et al.[68]), thus a volume of gas is often evaluated in terms of an *equivalent grey body* (Drysdale [65]). In practical terms, this has two major consequences: (1) the heat absorbed or emitted by clean air is considered negligible (Wickström [66]); and (2) *non-luminous flames* (i.e. flames which burn without yielding in high levels of products of incomplete combustion) have very low emissivities (Drysdale [65]), and hence despite reaching high absolute temperatures will generate rather low levels of thermal radiation (see equation 5.13).

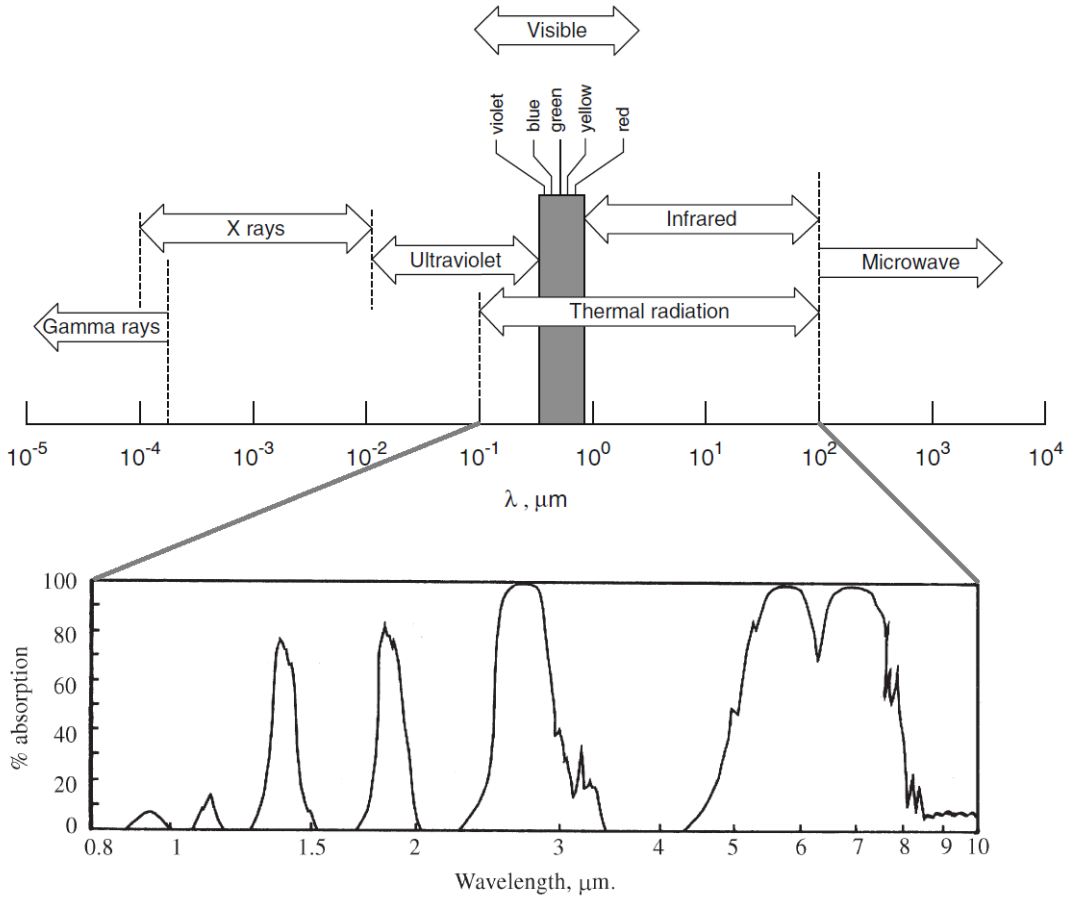


FIGURE 5.7 – ABSORPTION SPECTRA OF WATER VAPOR IN COMPARISON WITH THE TOTAL SPECTRUM OF THERMAL RADIATION
Adapted from Drysdale [65] and Tien et al. [68]

Most fires, however, do generate high levels of thermal radiation. Somehow, there seems to be a gap in between this evidence and the discussion presented in the previous paragraph. This gap is filled by the fact that a fire hardly ever burns without generating considerable levels of products of incomplete combustion, known as soot (i.e. minute carbonaceous particles). According to Drysdale [65], soot particles are formed within the flame and while still inside the flame body will achieve high temperatures and act as a minute *black* or *grey bodies*. If those soot particles are not entirely consumed while travelling through the oxidative regions of the flame, they will escape from the top parts to produce smoke (Figure 5.8). It is the presence of soot which provides flames their characteristic yellow luminosity, and thus differentiates *luminous* from *non-luminous flames* (Figure 5.9). Due to soot generation, the radiation emanating from *luminous flames* or smoke layers can be treated as independent of wavelength. The total emissive capacity of the flame (represented by ε_f in equation 5.13) becomes a function of soot concentration and of the mean beam length (L), a parameter related to the thickness of a flame body. For *thick luminous flames* (i.e. hydrocarbon flames with $L > 1\ m$) it is common procedure in fire safety engineering to assume a *blackbody* behavior (i.e. $\varepsilon_f = 1$ in equation 5.13). The practical consequences of this choice are exposed in Chapter 8. A final remark here is that as soot particles provide the main mechanism for radiative heat loss in fires, highly sooty flames appear to achieve lower average flame temperatures.

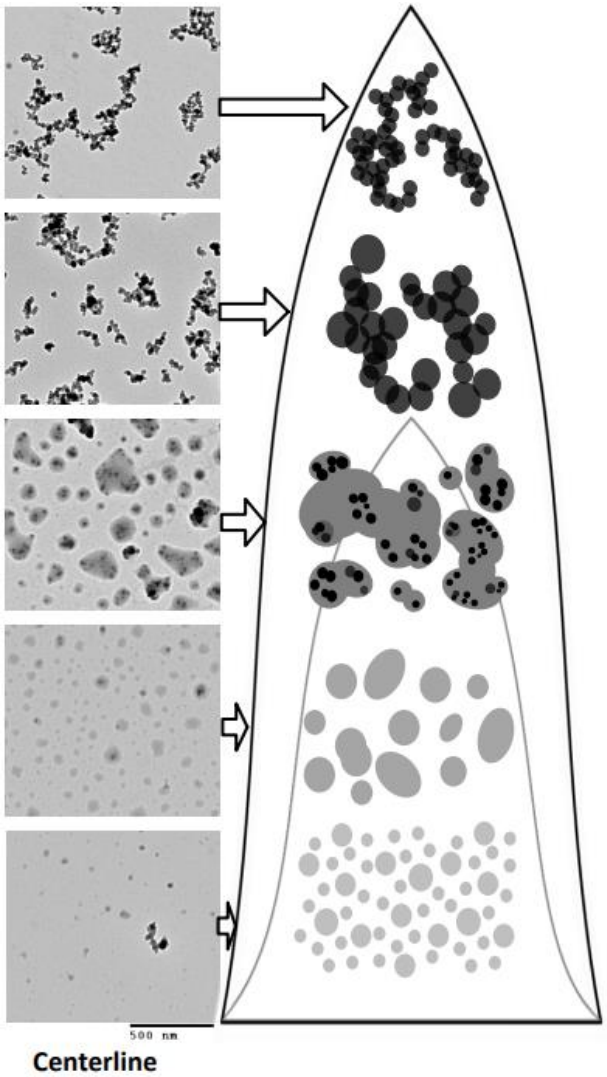


FIGURE 5.8 – SCHEMATIC EVOLUTION OF SOOT PARTICLES WITHIN THE FLAME CORPSE
Adapted from Kholghy [69]



FIGURE 5.9 – LUMINOUS AND NON-LUMINOUS FLAMES

5.1.3.2 Radiation Governance in Fires

From Section 5.1 we know that heat is transferred to the structure through radiation and convection. The radiation contribution depends on temperatures to the fourth power (equation 5.12), while convection relies on temperatures to the power of one (equation 5.5). This different dependency on temperature is the reason why radiation becomes the governing mode of heat transfer to a structure subjected to fire. Figure 5.10 illustrates this behavior by comparing the radiation and convection contributions to the total heat flux to structures, which are fixed at three different reference temperatures (Section 11.4). As we can see, convection will govern the total heat flux to the structure only at the early stages of a fire. Essentially, as soon as temperatures rise to higher levels, radiation will overcome convection and will become the main source of heat supply to the structure. Note that even for a very low surface emissivity (i.e. $\varepsilon_s = 0.2$), thermal radiation will still surpass convection for temperatures above 1000 ^{o}C (look at the graph of $T_{surface} = 500$ ^{o}C in Figure 5.10). This radiation dominance appears to be even more pronounced when considering concrete structures (i.e. $\varepsilon_s = 0.7$) subjected to tunnel fires, in which temperatures above 1100 ^{o}C are expected to occur (Figure 8.4 and Figure 8.5).

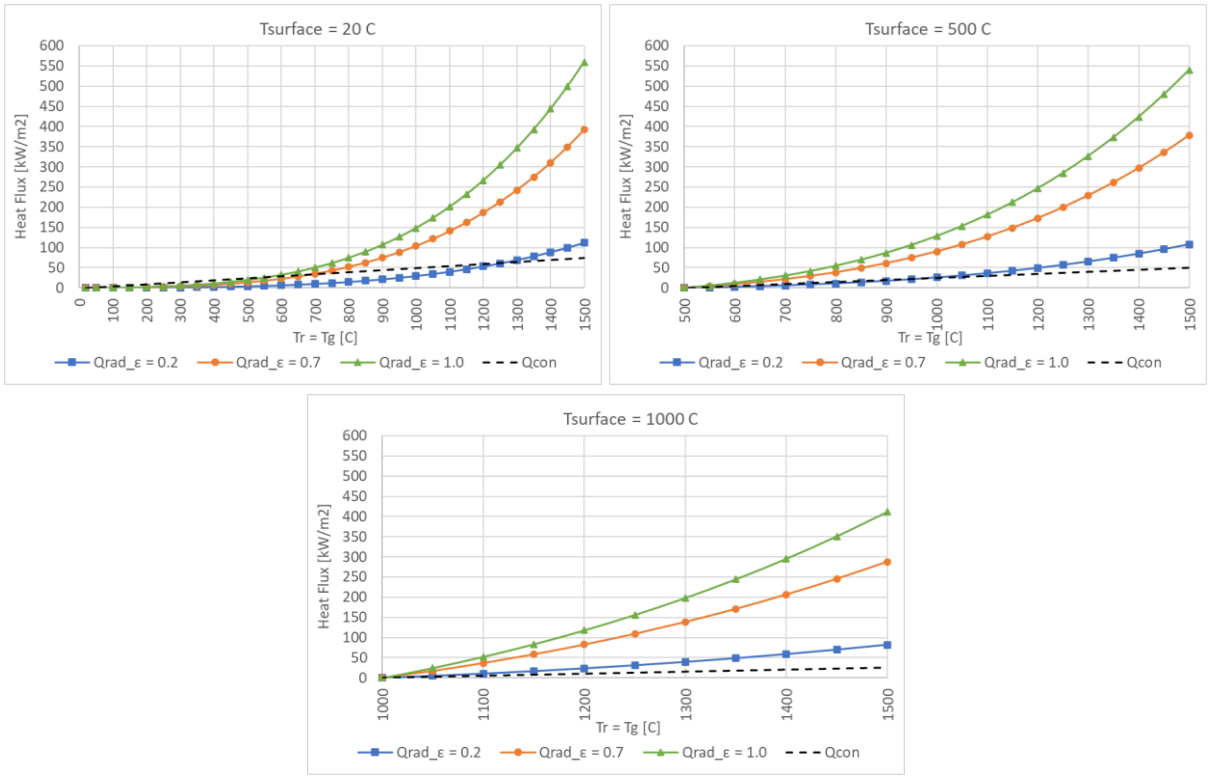


FIGURE 5.10 – RADIATION AND CONVECTION CONTRIBUTIONS TO THE TOTAL HEAT FLUX FOR STRUCTURES AT DIFFERENT REFERENCE TEMPERATURES

5.2 Heat Transfer in FDS

As FDS will be used to perform numerous fire simulations in this thesis, it is also essential to understand how FDS applies the different heat transfer mechanisms (i.e. conduction, convection, and radiation). Therefore, this topic is focused on presenting the governing equations and the fundamental assumptions which are used in this software.

5.2.1 Conduction in FDS

At solid obstructions, FDS applies a one-dimensional heat conduction model according to the equation below (*FDS Technical Reference Guide* [70]):

$$\rho_s c_s \frac{\partial T_s(x,t)}{\partial t} = \frac{\partial}{\partial x}\left(k_s \frac{\partial T_s(x,t)}{\partial x}\right) + \dot{q}_s''' \qquad 5.14$$

where ρ_s is the solid's density (kg/m^3), c_s is the solid's specific heat (kJ/(kg.K)), k_s is the solid's thermal conductivity (W/(m.K)) and $\dot{q}_s'''$ is a source term which can accounts for radiative absorption and emission in depth and/or chemical reactions within the solid. Heat is conducted only in the direction of x pointing into the solid, where x = 0 represents the surface.

For the simulations performed in this thesis, radiation absorption and emission in depth are not considered. Also, the solid materials used during the simulations are not prescribed to suffer any chemical reactions (e.g. combustion or water evaporation). Therefore, $\dot{q}_s'''$ is vanished in equation 5.14 and the formulation of heat conduction becomes identical to what is described in Section 5.1.1. Evidently, heat is conducted in more than one dimension within a solid. However, when considering the thermal exposure of structures subjected to tunnel fires, this one-dimensional heat conduction model is expected to provide accurate results. Moreover, the walls and ceiling of both tunnels studied in this thesis (i.e. the tunnel used during the RWS tests which is described in Chapter 7 and the Piet Hein tunnel used in the case study developed in Chapter 9) are composed of large flat surfaces. For those cases, the maximum exposure is expected to cover sufficiently large areas uniformly, making the one-dimensional heat conduction model to accurately predict the temperature development within the solid located in such areas.

Coupling between the gas phase and the solid phase is achieved through a boundary condition assigned to the front surface of the obstruction according to the equation below:

$$-k_s \frac{\partial T_s(0,t)}{\partial x} = \dot{q}_{con}'' + \dot{q}_{rad}'' \qquad 5.15$$

where k_s is the solid's thermal conductivity (W/(m.K)), $T_s(0,t)$ is the solid's surface temperature (K), $\dot{q}_{con}''$ is the convective heat flux (W/m^2) and $\dot{q}_r''$ is the net radiative heat flux (W/m^2).

Note that the boundary condition described in the equation above, ensures conservation of energy. For the solid phase side, given by the left-hand side of equation 5.15, heat is transferred through conduction. On the gas phase side, given by the right-hand terms on the same equation, heat fluxes are due to convection and radiation.

5.2.2 Convection in FDS

In FDS, convection heat transfer to a solid obstruction is also evaluated based on equation 5.5. For fire simulations developed in LES (Section 1.2.1), the convective heat transfer coefficient (h in equation 5.5) for planar surfaces is evaluated based on a combination of *natural* and *forced convection* correlations and is obtained according to the equation below:

$$h = max\left[C\left(T_g - T_{surface}\right)^{\frac{1}{3}};\ k_g Nu\ ;\ \frac{k_g}{\delta_n/2}\right] \qquad 5.16$$

where h is the convective heat transfer coefficient (W/(m^2.K)), T_g is the gas temperature at the center of the first gas phase cell in the interface with the obstruction (K), $T_{surface}$ is the solid's surface temperature (K), C is an empirical coefficient for natural convection (1.52 for a horizontal plate and 1.31 for a vertical plane), k_g is the thermal conductivity of the gas (W/(m.K)), Nu is the Nusselt number, and δ_n is the normal grid space (m).

5.2.3 Radiation in FDS

For the simulations performed here the thermal radiation from the surrounding gases is assumed to be absorbed within an infinitely thin layer at the surface of the solid obstruction (i.e. there is no absorption in depth of the solid obstruction). Therefore, the net radiative heat flux is given by:

$$\dot{q}''_{rad} = \dot{q}''_{rad,incoming} - \dot{q}''_{rad,outgoing} \qquad 5.17$$

where $\dot{q}''_{rad,incoming}$ is the total amount of radiation heat flux arriving at the surface of the solid obstruction (W/m^2) and $\dot{q}''_{rad,outgoing}$ is the radiative heat flux which is emitted by the solid obstruction (W/m^2). Note that $\dot{q}''_{rad,outgoing}$ is calculated according to equation 5.9.

In FDS, $\dot{q}''_{rad,incoming}$ is computed as the added contribution of radiation transported from every point within the domain of simulation to the surface in question. As explained in *FDS User's Guide* [71], most large-scale fire simulations are performed in LES (Section 1.2.1) due to limited computational capacity. The practical consequence of this is that the grid sizes which are commonly used in such fire simulations (i.e. tens of centimeters in size) are relatively coarse to reliably solve the flame sheet. In essence, while the average cell gas temperature is usually well predicted outside the combustion zone (provided enough grid resolution is applied in the simulation), flame temperatures are not (i.e. the average cell gas temperatures within the reacting zone). During a fire, the flame zone is the primary source of thermal radiation to the environment in question. As we know, the levels of thermal radiation generated by a flame body (i.e. $\dot{q}''_{emi,f}$ in equation 5.13) are proportional to the fourth power of flame temperature (i.e. T_f in equation 5.13). Hence, if the radiation field achieved during a fire is to be accurately solved, not having well-resolved flame temperatures becomes an important issue in fire simulations. To overcome this problem and achieve enough resolution of the thermal radiation field, FDS corrects the radiation emissions within the combustion zone through the application of a *radiative fraction* (χ_r). In essence, this means that a percentage χ_r of the HRR generated during a fire will be directly converted into radiative heat flux. Therefore, this *radiative fraction* is of fundamental importance when using FDS in a performance-based approach. To have a better understanding of the use of this parameter, we first have to address the combustion process (i.e. the means through which heat is generated during a fire).

5.2.3.1 Combustion Process

As depicted in *FDS User's Guide* [71], there are several types of combustion modes which can be applied in a FDS simulation. All models developed in this thesis make use of the entitled *'Single-Step, Mixing-Controlled Combustion'*. This type of combustion is based on the chemistry below:

$$C_x H_y O_z N_v + \nu_{O_2} O_2 \rightarrow \nu_{CO_2} CO_2 + \nu_{H_2O} H_2O + \nu_{CO} CO + \nu_{Soot} Soot + \nu_{N_2} N_2$$

The user is responsible to define the combustion process that will be used during the simulation. In its simplest form, this is done by selecting a fuel ($C_x H_y O_z N_v$) and setting the yields of *CO* and *Soot* (i.e. products of incomplete combustion) which are to be produced by the fire. FDS then uses this information to calculate the stoichiometric coefficients ν for the combustion reaction. Another important parameter here is the *heat of combustion* (kJ/kg). It defines the amount of energy that will be released in the domain of simulation whenever combustion takes place. FDS has a list of tabulated fuels in which the *heat of combustion* is already included for cases of complete combustion (i.e. no *CO* and *Soot* generation). However, if the yields of those products of incomplete combustion are defined by the user during a fire simulation, FDS will automatically recalculate an *effective heat of combustion* based on the stoichiometric coefficients of the combustion reaction.

The user is also responsible to define the fire scenario. For the work developed in this thesis, this is done by prescribing a certain area within the domain of simulation as a fire source. Then, either a HRRPUA (heat release rate per unit area) or a MLRPUA (mass loss rate per unit area) is prescribed to this area. In the first case, FDS will divide the defined HRRPUA by the *effective heat of combustion* to obtain the correspondent MLRPUA, while for the latter case this value is already provided by the user. In either case, FDS will assign a boundary condition to this specific area in which gasified fuel is going to be constantly released into the domain according to the chosen/calculated MLRPUA. Also, through the use of this boundary condition, the fire development itself will not affect the availability of fuel within the domain.

Once the simulation is started, whenever fuel enters the domain of simulation and encounters enough O_2 (according to the prescribed combustion chemistry), it will just combust immediately, thus releasing energy. If there is lack of O_2 inside the gas cells where fuel is entering the domain, it will not combust. In this case, this unburned vaporized fuel will just travel as any other gas species inside the boundaries of simulation. Once/if it then encounters enough O_2 somewhere else, then it will just combust immediately at that specific location. Note that in this *'Single-Step, Mixing-Controlled Combustion'* model, once fuel reacts with O_2 leading to the formation of the products of combustion, no further reaction will take place. In other words, the products of incomplete combustion, namely *CO* and *Soot*, will not further react with O_2. Therefore, gas species grid cells will be divided into: (1) cells that will experience combustion of fuel, being referred here as part of the *reacting zone* (i.e. the so-called *flame zone*); and (2) cells that will not experience any combustion of fuel and thus only carry different gas species (i.e. air; products of combustion; or, most often, a mix of both). Those will be named as cells *outside the flame zone*.

Heat is released inside the domain by the combustion of fuel within cells. The heat release rate per unit volume achieved in each one of those cells is given by:

$$\dot{q}''' = -\sum_{\alpha} \dot{m}_{\alpha}''' \, \Delta h_{f,\alpha} \qquad 5.18$$

where $\dot{q}'''$ is the heat release rate per unit volume, $\dot{m}_{\alpha}'''$ are the mass fraction of each species involved in the combustion process (i.e. reactants and products), and $\Delta h_{f,\alpha}$ are the heats of formation correspondent to those species.

A final remark here refers to the two distinct types of gas cells, namely *flame zone* and *outside flame zone*. In essence, FDS does not know how to differentiate flame from no flame zones. For instance, in a real fire there are regions within the flame in which oxygen concentration is quite low. In FDS, the grid cells composing such regions will not actively participate in the combustion process, meaning that they will not release heat. Therefore, such cells are treated as if they were *outside the flame zone* (Figure 5.11), although, in reality, they would also be part of the flame body. With this in mind, the following distinction holds:

$$\begin{cases} Outside\ flame\ zone \rightarrow \ \dot{q}''' = 0 \\ Reacting\ zone\ or\ "Flame\ zone" \rightarrow \dot{q}''' > 0 \end{cases} \qquad 5.19$$

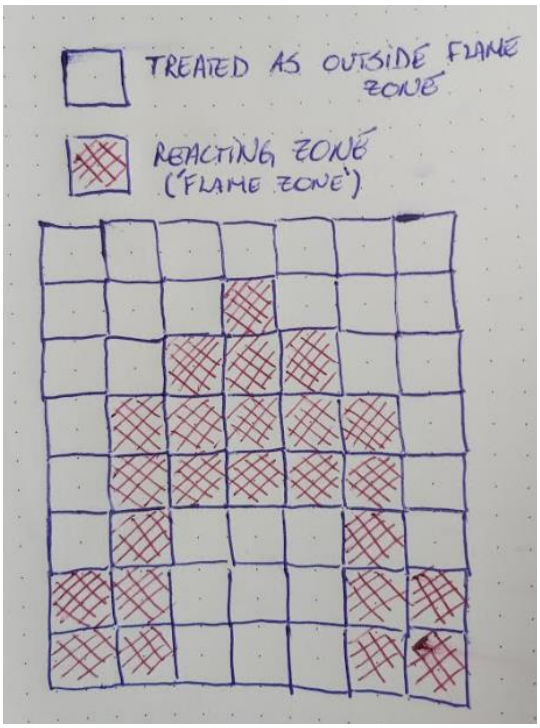


FIGURE 5.11 – FLAME ZONE IN FDS

5.2.3.2 Radiative Fraction

As described previously in Section 5.2.3, to ensure that the radiation field in a fire simulation will not be harmed by the poor resolution of flame temperatures, FDS will correct the radiation emitted for most cells within the *reacting zone* (equation 5.19) based on a *radiative fraction* (χ_r). In essence, this correction is done for every cell in which:

$$\chi_r \, \dot{q}''' > 10 \ kW/m^3 \qquad 5.20$$

where χ_r is the radiative fraction and $\dot{q}'''$ is the heat release rate per unit volume (kW/m^3).

The procedure ensures that the net radiative emission from each cell in the *reacting zone* will correspond to the specified radiative fraction χ_r times the total combustion energy generated in this region. This process is exemplified by the equation below:

$$\iiint \chi_r \, \dot{q}''' = \iiint (\dot{q}'''_{rad,abs} - C\dot{q}'''_{rad,emi}) \qquad \textbf{5.21}$$

where χ_r is the radiative fraction, $\dot{q}'''$ is the heat release rate per unit volume of each gas cell (kW/m³), $\dot{q}'''_{rad,abs}$ is the amount of radiation absorbed per unit volume by each gas cell (kW/m³), $\dot{q}'''_{rad,emi}$ is the amount of radiation per unit volume which is emitted by each gas cell (kW/m³) and C is a constant applied by FDS to ensure the radiative fraction is achieved within the combustion zone.

The right-hand side of equation 5.21 represents the volume integral of the net radiative heat flux of each gas cell within the *reacting zone* or, in other words, the total energy transferred through radiation in that cell. The radiation heat flux absorbed by the gas body ($\dot{q}'''_{rad,abs}$) is defined based on the gas absorption coefficient (calculated by FDS for each gas cell) and on the incident amount radiation in that cell. In essence, this process is similar to what is exemplified in equation 5.7 for a solid surface, although the mathematics are much more complex as FDS deals with volumes instead of areas. The radiation heat flux emitted by each gas cell ($\dot{q}'''_{rad,emi}$) relies on the *modified Stefan-Boltzmann law* (given by equation 5.9 for a solid surface), thus being calculated according to the absorption coefficient for the gas and proportionally to the average gas temperature of the cell to the fourth power. As we know, the gas temperature of cells participating in the combustion of fuel are not accurately predicted in a fire simulation. Therefore, FDS inserts the constant C to correct the emission term in equation 5.21. Basically, this constant is computed at each time step of the simulation to ensure that the volume integral over the entire *reacting zone* (i.e. right-hand side of equation 5.21) will equal the volume integral of $\chi_r \, \dot{q}'''$ (right-hand side of equation 5.21) over the same region, thus ensuring that the net radiative emissions from the fire will be exactly what is specified by χ_r (Figure 5.12).

Note that gas cells located elsewhere inside the domain (i.e. cells *outside the flame zone*, as described by equation 5.19) will emit and absorb thermal radiation according to their absolute temperature and absorption coefficient (computed based on *grey gas* assumption). Due to this, the absolute value of radiative energy transported within the domain is not necessarily equal to the volume integral of $\chi_r \, \dot{q}'''$. In essence, conservation of energy (equation 1.3) is ensured within the whole domain of simulation, but energy can still be converted or stored within the gas and solid phases. Therefore, while the radiation emissions from the fire source are corrected to correspond to the *radiative fraction*, once energy is released inside the domain in form of thermal radiation it can be converted into other forms of energy. For instance, radiation can be reabsorbed by colder combustion products (e.g. smoke and water vapor), which would decrease the total amount of energy transported through radiation. Or, it can also be that the hot smoke layer heats up and becomes a source of radiation in itself, thus increasing the amount of thermal radiation which is transported within the domain. Keep this in mind for now, we will come back to this point in Chapter 9 when addressing the effects of ventilation into the heat exposure of a concrete structure during a tunnel fire.

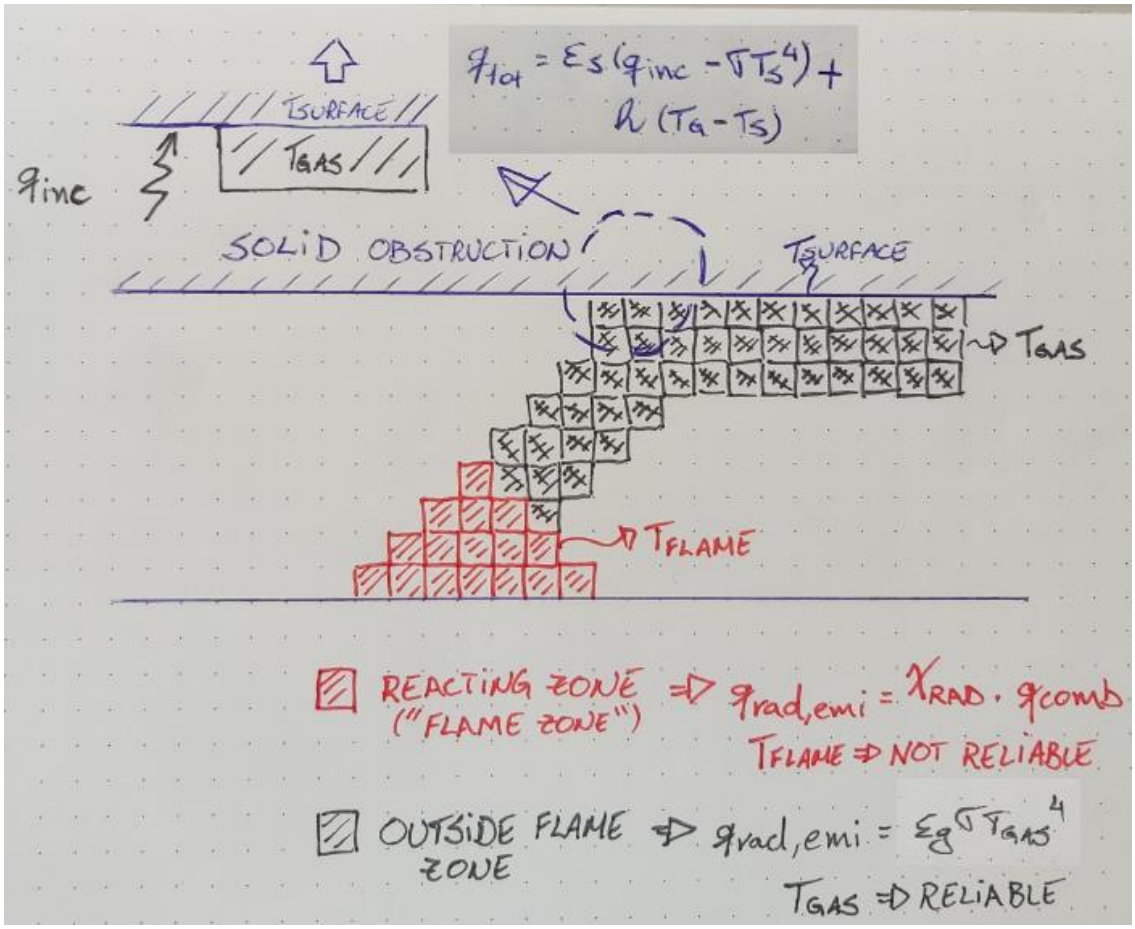


FIGURE 5.12 – RADIATION EMISSIONS AND HEAT TRANSFER TO SOLID OBSTRUCTIONS

Now, let us go back to the discussion about the *radiative fraction* and consider the numerical results obtained in fire simulations. In FDS, gas temperatures are more accurately predicted away from the fire source. However, provided a *radiative fraction* is correctly specified by the user, one may expect a reliable resolution of the radiation field which is conceived by a fire. As radiation governs the heat exposure of structures subjected to fire (Section 5.1.3.1), this parameter becomes fundamentally important for the scope of this thesis. Once again, the *radiative fraction* is the percentage of the total HRR of a fire which is released through thermal radiation. According to *FDS User's Guide* [71], this fraction is a function of the fire size, flame temperature, and chemical composition of both fuel and products involved in the combustion reaction. FDS default values of χ_r are provided in Figure 5.13. Those values are based on measurements performed on relatively small flames, and there is no single value of χ_r which is representative for every fire scenario involving a given fuel.

Species	χ_r
ACETONE	0.27
ACETYLENE	0.49
BENZENE	0.60
BUTANE	0.30
DODECANE	0.40
ETHANE	0.25
ETHANOL	0.25
ETHYLENE	0.25
HYDROGEN	0.20
ISOPROPANOL	0.29
METHANE	0.20
METHANOL	0.16
N-DECANE	0.40
N-HEPTANE	0.40
N-HEXANE	0.40
N-OCTANE	0.40
PROPANE	0.30
PROPYLENE	0.37
TOLUENE	0.40
All other species	0.35

FIGURE 5.13 – DEFAULT RADIATIVE FRACTIONS IN FDS
Retrieved from *FDS User's Guide* [71]

Ideally, the amount of thermal radiation released by a fire could be evaluated based on equation 5.13 according to the absolute temperature achieved by a flame body. In reality, however, gas temperatures will vary all over the flames. Soot concentration will also not be uniform within the flame body (Figure 5.8), meaning that the flame emissivity (ε_f in equation 5.13) is not necessarily always equal to *1* or, in other words, that the assumed *blackbody* behavior is not achieved for the whole flame corpse. When these facts are added together, it becomes clear that the emissions of thermal radiation are also not uniform within the flame (Figure 5.14).

According to Beyler [72], this makes the behavior of large pool fires to be significantly different than that of smaller flames. Basically, in large flame bodies, the outer layer will be at a lower temperature than the *luminous* inner core. Therefore, the cooler soot located in the outside perimeter will obscure the thermal radiation emitted from the hotter regions within. In essence, reabsorption of thermal radiation by the flame body itself will contribute to reduce the *radiative fraction* of large flames when compared to that of smaller flames (i.e. $D < 1m$ in Figure 5.15). Although this non-uniformity of temperatures inside the flame hardens the task of accurately modelling thermal radiation from large pool fires (Drysdale [65]), the use of the upper bound *radiative fractions* (Figure 5.13) when modeling large-scale fires should, at least in theory, provide conservative results. With this is mind, all the fire simulations performed in this thesis, even those for really large fires (Chapter 9), are executed according to the *radiative fractions* given in Figure 5.13. Note that those are considered to be the maximum limits of *radiative fraction* for each correspondent fuel. This is the case because they were determined

for small flame bodies, for which the temperature difference between the outer layer and the inner core is significantly reduced when compared to that of larger fires, thus reducing significantly the radiation reabsorption within the flame body.

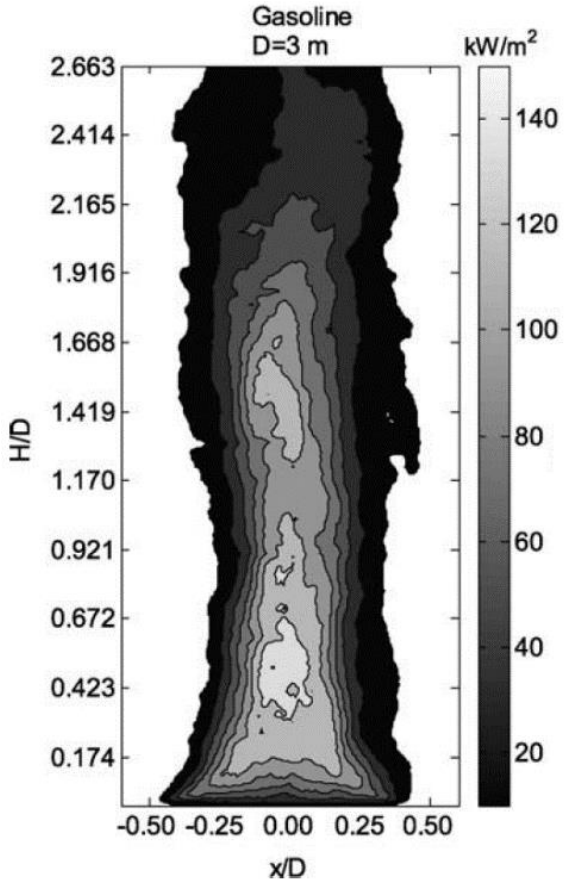


FIGURE 5.14 – MEAN FLAME EMISSIVE POWER OF A GASOLINE POOL FIRE
Retrieved from Munoz et al. [73]

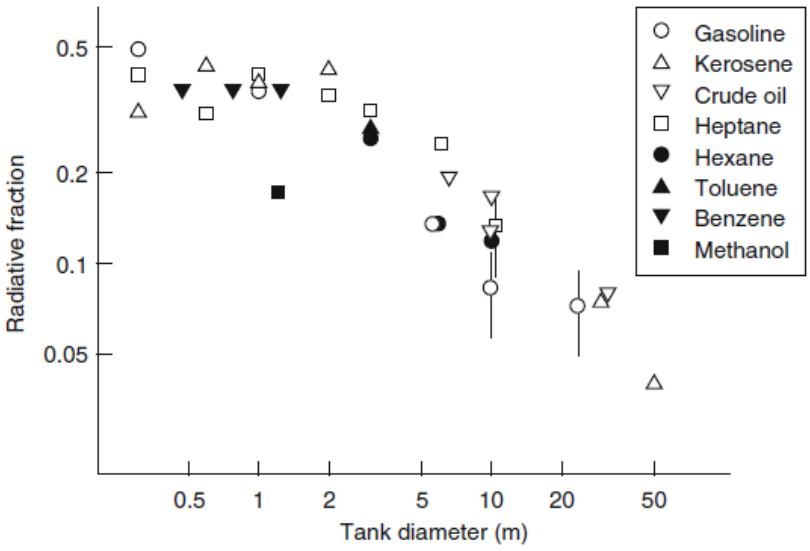


FIGURE 5.15 – RADIATIVE FRACTION MEASURED FOR POOL FIRES OF DIFFERENT DIAMETERS
Retrieved from Beyler [72]

5.3 Thermal Boundary Conditions

In order to evaluate the temperature evolution within a structure during fire (i.e. transient solution of equation 5.4), we have to assign a boundary condition to describe the interface between the source of energy (i.e. a fire) and the receiver (i.e. the structure). In a transient thermal analysis, Wickström [66] explains that there are three kinds of boundary conditions which can applied: (1) prescribed surface temperature; (2) prescribed surface heat flux; and (3) the so-called *natural boundary condition*. The third kind of boundary condition accounts for temperature differences between the solid phase and the fire phase and can be used in three different ways: (a) by prescribing a gas temperature function (i.e. considers convection only); (b) by prescribing the development of a fire temperature (i.e. considers both convection and radiation with $T_r = T_g = T_f$); and (c) by prescribing the contribution of radiation and convection individually, such that $T_r \neq T_g$. The different types of thermal boundary conditions are summarized in Figure 5.16 and will be treated individually in the next sections.

No	Kind of boundary condition	Formula
1	Prescribed surface temperature	$T_{x=x_0} = T_s$
2	Prescribed surface heat flux	$-k\frac{\partial T}{\partial x}\Big\|_{x=0} = \dot{q}''_s$
(3a)	Natural boundary condition (prescribed convection)	$-k\frac{\partial T}{\partial x}\Big\|_{x=0} = h\left(T_g - T_s\right)$
(3b)	Natural boundary condition (prescribed convection and radiation, equal radiation and gas temperatures)	$-k\frac{\partial T}{\partial x}\Big\|_{x=0} = \varepsilon\sigma\left(T_f^4 - T_s^4\right) + h_c\left(T_f - T_s\right)$
(3c)	Natural boundary condition (prescribed convection and radiation conditions, different radiation and gas temperatures)	$-k\frac{\partial T}{\partial x}\Big\|_{x=0} = \varepsilon \cdot \sigma\left(T_r^4 - T_s^4\right) + h_c\left(T_g - T_s\right)$ or $-k\frac{\partial T}{\partial x}\Big\|_{x=0} = \varepsilon\left(\dot{q}''_{inc} - \sigma T_s^4\right) + h_c\left(T_g - T_s\right)$

FIGURE 5.16 – THERMAL BOUNDARY CONDITIONS
Adapted from Wickström [66]

5.3.1 Prescribed Surface Temperature

The first type of boundary condition implies that the surface temperature of the structure is to be prescribed instead of calculated. For this reason, it is hardly ever applied in fire safety engineering, although for some materials (e.g. insulation) it may still provide reliable results (Section 8.2).

5.3.2 Prescribed Surface Heat Flux

In nature, the second kind of boundary condition can rarely be specified in fire problems. However, although it is not a common practice in the building industry, which more often relies on fire curves to define thermal loads (as exemplified in Figure 8.3 for tunnel fires), other fields (e.g. oil industry) commonly describe the thermal exposure imposed on structures in terms of *heat flux* (see for instance Sections 8.1.2.1 and 8.1.2.2). Wickström [66] explains that for those cases, the so-called *heat flux* is to be understood as the total heat flux to a surface which is kept at ambient temperature. This is translated into the equation below:

$$\dot{q}''_{tot} = \alpha_s \dot{q}''_{inc} - \varepsilon_s \sigma \left(T^4_{surface} - T^4_a\right) - h(T_{surface} - T_a) \qquad 5.22$$

where $\dot{q}''_{tot}$ is the total heat flux to the structure (W/m^2), $\dot{q}''_{inc}$ is the incident heat flux prescribed to the structure (W/m^2), α_s is the surface absorptivity, ε_s is the surface emissivity, σ is the Stefan-Boltzmann constant (5.67 x 10^{-8} W/(m^{2}K^4)), $T_{surface}$ is the development of the surface temperature in time (K), T_a is the ambient temperature (K) and h is the convective heat transfer coefficient (W/(m^2.K)).

Therefore, the second type of boundary condition is rewritten in terms of equation 5.23 and will actually become very similar to a *natural boundary condition*, as now the amount of energy which will be absorbed by the structure also becomes dependent on the surface temperature of the structure itself.

$$-k_s \left.\frac{\partial T}{\partial x}\right|_{x=0} = \dot{q}''_{tot} \qquad 5.23$$

where $\dot{q}''_{tot}$ is the total heat flux to the structure (W/m^2), k_s is the thermal conductivity of the solid (W/(m.K)) and $\left.\frac{\partial T}{\partial x}\right|_{x=0}$ is the development of the surface temperature in time (K).

Based on this concept, Maluk [74] proposed an innovative fire testing methodology, providing a better controlling mechanism of the thermal exposure imposed on the structure during fire tests (Figure 8.39). We will come back to this in Section 8.3.3 where this test will be briefly explained.

5.3.3 Natural Boundary Condition

As explained previously, this is the most commonly adopted type of thermal boundary condition when addressing structures subjected to fire. This is the case because it better translates the governing physics behind fires. Moreover, in its complete form (i.e. type 3c in Figure 5.16), the *natural boundary condition* considers the transient and independent contributions of both convection and radiation to the total heat flux to the structure. It is however important to differentiate the use of the *natural boundary condition* in each one of its forms.

5.3.3.1 Type (a): Convection Only

In its simplest form, the *natural boundary condition* accounts only for the convection contribution to the total heat transfer to the structure. If considered the use of the RWS curve in tunnel fires, this boundary condition would be written in terms of the following equation:

$$-k_s \left.\frac{\partial T}{\partial x}\right|_{x=0} = h(T_{RWS} - T_{Surface}) \qquad 5.24$$

where k_s is the thermal conductivity of the solid (W/(m.K)), $\left.\frac{\partial T}{\partial x}\right|_{x=0}$ and $T_{Surface}$ described the development of the surface temperature in time (K), h is the convective heat transfer coefficient (W/(m^2.K)) and T_{RWS} is the gas temperatures given by the use of the RWS curve (Figure 7.1). Note that the term on the left-hand side of the equation above is equivalent to $\dot{q}''_{tot}$ or, the total heat flux to the structure (W/m^2).

Most thermal problems in structural engineering are limited to: (a) cases where the developed thermal gradients are evaluated solely in the steady state, such as the study of thermally induced stresses when there is a known temperature difference between the outer and the inner part of

a structure (e.g. reservoir); or (b) cases where convection is the dominant mode of heat transfer, for instance, in a transient analysis of thermal stresses generated by a young warm concrete which is hardening in ambient temperature. As a consequence, it appears that most structural engineers are often unaware of the fact that radiation is the governing mode to the total amount of heat transferred to structures during a fire (Section 5.1.3.2). For this reason, the convection boundary condition is quite regularly the selected option to perform thermal analysis of structures subjected to fire. This is for instance what is proposed by the use of *PCTempflow*[5], a nice freeware which appears to be commonly used in the Netherlands to evaluate time dependent temperature distributions of one-dimensional layered structures. The consequences of such choice are exposed in Section 6.6.3.

5.3.3.2 Type (b): Fire Curves

This type of *natural boundary condition* presupposes an uniform fire temperature, meaning that the radiation temperature (i.e. T_r in equation 5.12) is assumed equal to the absolute gas temperature (i.e. T_g in equation 5.5) achieved during a fire. This will be valid for most standards that are based on the use time-temperature fire curves to define the thermal exposure to the structure. In essence, this assumption characterizes a *blackbody* behavior for the fire phase (Section 5.1.3). Note that, at least when considering the results of the simulations of the RWS tests in Chapter 7, this is a conservative assumption (compare gas and radiation temperatures in Figure 7.38). Therefore, considering what is prescribed by Eurocode 1 Part 1-2 [75], the boundary condition for the use of the RWS curve to evaluate tunnel structures becomes:

$$-k_s \left.\frac{\partial T}{\partial x}\right|_{x=0} = \varepsilon_s \sigma \left(T_{RWS}^4 - T_{surface}^4\right) + h\left(T_{RWS} - T_{surface}\right) \qquad 5.25$$

where k_s is the thermal conductivity of the solid (W/(m.K)), $\left.\frac{\partial T}{\partial x}\right|_{x=0}$ and $T_{Surface}$ describe the development of the surface temperature in time (K), σ is the Stefan-Boltzmann constant (5.67 x 10^{-8} W/(m^{2}K^4)), T_{RWS} is the temperature development prescribed by the use of the RWS curve (K), h is the convection heat transfer coefficient which is assumed to be equal to 50 W/(m^2.K), and ε_s is the surface emissivity which is assumed equal to 0.7 for concrete structures. Note that the term on the left-hand side of the equation above is equivalent to $\dot{q}''_{tot}$ or, the total heat flux to the structure (W/m^2).

5.3.3.3 Type (c): Adiabatic Surface Temperature (AST)

In reality, the radiation temperature induced by a fire is not necessarily equivalent to the achieved gas temperatures. As explained in Section 5.1.3.1, the emissivities of hot gases and flames (i.e. ε_f in equation 5.13) are dependent on soot concentration. It could also be that the radiation temperature is higher than the gas temperature for certain locations of interest. Take a look for instance in Figure 3.4a and think of an object located at ground level, below the smoke layer. In this situation, while the gas surrounding this object is essentially at ambient temperature, due to the high levels of thermal radiation which are emitted from the hot smoke

[5] http://members.ziggo.nl/wolsink/PCTempFlow.htm

layer above, the radiation temperature will certainly be above this level (look at equation 5.11). Therefore, for a realistic case, the *natural boundary condition* can be written in terms of:

$$-k_s \frac{\partial T}{\partial x}\Big|_{x=0} = \varepsilon_s \sigma \left(T_r^4 - T_{surface}^4\right) + h(T_g - T_{surface}) \qquad \textbf{5.26}$$

where k_s is the thermal conductivity of the solid (W/(m.K)), $\frac{\partial T}{\partial x}\Big|_{x=0}$ and $T_{Surface}$ describe the development of the surface temperature in time (K), ε_s is the surface emissivity, σ is the Stefan-Boltzmann constant (5.67 x 10^{-8} W/(m^2K^4)), T_r is the hypothetical radiation temperature (K), h is the convection heat transfer coefficient and T_g is the absolute gas temperature (K). Note that the term on the left-hand side of the equation above is equivalent to $\dot{q}''_{tot}$ or, the total heat flux to the structure (W/m^2).

Nowadays, based on fire simulations in CFD software (e.g. FDS), we are able to prescribe this type of boundary condition to the structure more often. To facilitate the task of incorporating CFD-based calculations into thermal structural analysis through FEA software, Wickström [66, 67, 76] proposed the concept of AST (Figure 5.17). Accordingly, AST is defined as the hypothetical temperature (T_{AST}) the surface of a structure would achieve in case that structure was made of a perfect insulator material. Accordingly, one may think of AST as the equilibrium surface temperature in which no heat is absorbed nor lost by the surface to the enclosure. Thus, T_{AST} is obtained when the total heat flux to the surface equals zero ($\dot{q}''_{tot} = 0$ in equation 5.1), and is given by the solution of the equation below:

$$\varepsilon_s \sigma (T_r^4 - T_{AST}^4) + h\left(T_g - T_{AST}\right) = 0 \qquad \textbf{5.27}$$

where ε_s is the surface emissivity, σ is the Stefan-Boltzmann constant (5.67 x 10^{-8} W/(m^2K^4)), T_r is the hypothetical radiation temperature (K), T_{AST} is the adiabatic surface temperature (K), h is the convection heat transfer coefficient and T_g is the absolute gas temperature (K).

Hence, in possession of the evolution of T_r and T_g in time, a single effective temperature development (T_{AST}) can be calculated based on equation 5.27. Alternatively, T_{AST} can directly be outputted from any FDS simulation. Once this T_{AST} is known, it can be used to represent an equivalent boundary condition to that given by equation 5.26, according to:

$$-k_s \frac{\partial T}{\partial x}\Big|_{x=0} = \varepsilon_s \sigma \left(T_{AST}^4 - T_{surface}^4\right) + h(T_{AST} - T_{surface}) \qquad \textbf{5.28}$$

where k_s is the thermal conductivity of the solid (W/(m.K)), $\frac{\partial T}{\partial x}\Big|_{x=0}$ and $T_{Surface}$ describe the development of the surface temperature in time (K), ε_s is the surface emissivity, σ is the Stefan-Boltzmann constant (5.67 x 10^{-8} W/(m^2K^4)), T_{AST} is the adiabatic surface temperature (K) and h is the convection heat transfer coefficient (W/(m^2.K)). Note that the term on the left-hand side of the equation above is equivalent to $\dot{q}''_{tot}$ or, the total heat flux to the structure (W/m^2).

A final remark here is that T_{AST} will always assume a value between T_r and T_g.

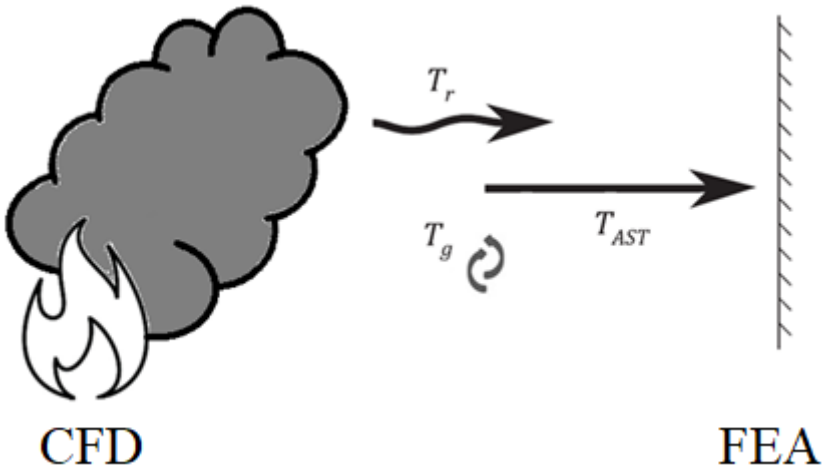


FIGURE 5.17 – AST

Here, one important remark is that in cases where a fire generates hazardous conditions to a structure, meaning that very high gas temperatures are achieved inside an enclosure, T_{AST} will always be governed by the radiation component. Note that the behavior is the opposite for low values of T_r, where T_{AST} will actually tend towards T_g. Figure 5.18 highlights both behaviors by providing a comparison between T_{AST} and T_r for four different levels of T_g. In this figure, the dashed black line defines $T_{AST} = T_r$. The derivation of this figure is given in Section 11.3, but it is worth to mention that the emissivity ε_s and the convection heat transfer coefficient h are taken as equal to the values prescribed in Eurocode 1 Part 1-2 [75] for concrete tunnels subjected to fire.

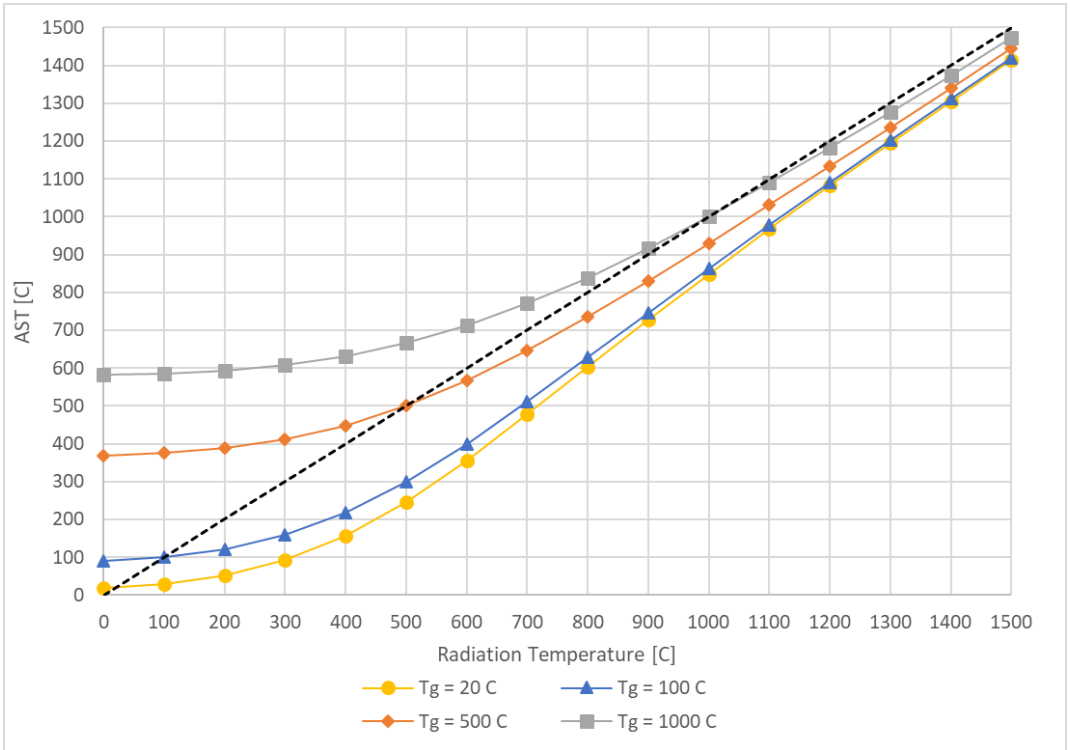


FIGURE 5.18 – AST VS RADIATION TEMPERATURE FOR DIFFERENT GAS TEMPERATURES

5.4 Conclusions

This chapter covered fundamental aspects with respect to: (1) fire and CFD-based fire simulations and (2) the interaction between fire and structure. The main conclusions are summarized here according to each topic:

- *Fire and CFD-based fire simulations:*

1) Heat is lost from a fire through convection and radiation. The latter becomes the most important mechanism of heat transfer when addressing fire exposed structures. Ideally, the amount of thermal radiation emitted by a fire could be evaluated based on the achieved flame body temperature through the use of equation 5.13. In reality, however, gas temperatures will vary all over the flame corpse (Figure 5.14), and thus, so will the levels of emitted thermal radiation.

2) For this reason, the amount of radiation generated by a fire is often translated in terms of a radiative fraction, which describes the total percentage of the HRR of a fire that is released through radiation. In hydrocarbon fires, this radiative fraction is limited to 0.5 for rather small pool fires (i.e. *diameter* < *1 m* in Figure 5.15).

3) Flames are often assumed to behave as *blackbodies* (i.e. ε_f. equal 1 in equation 5.13). Nevertheless, the flame emissivity is tied to the amount of soot produced within the flame body itself. High levels of soot generation will characterize *luminous flames* (Figure 5.9), for which a *blackbody* behavior might be achieved.

4) Soot formation is also the reason why the radiative fraction will decrease for increasing fire sizes (Figure 5.15). In essence, cooler soot located at the outer layer of the flame body will reabsorb thermal radiation emitted by the hotter regions within. As a consequence, the total percentage of the HRR released by radiation decreases significantly for very large fires.

5) If soot is not fully consumed within the flame corpse, then, it will eject from the top parts of the flame to form what we know as smoke. As the interaction of pure air and products of complete combustion (i.e. H_2O and C_2O) with thermal radiation is rather limited (Figure 5.7), it is the presence of soot in smoke bodies which allows us to assume *grey* or *blackbody* behavior for such gas masses.

6) When performing fire simulations with FDS, gas temperatures within the flame zone (Figure 5.12) are not reliably calculated. This is due to the grid sizes currently used in large-scale fire simulations, which are limited by the calculation capacity of computers. As thermal radiation is related to the fourth power of the achieved gas temperatures (equation 5.13), underestimating/overestimating such temperatures would seriously harm the results of a fire simulation. To overcome this issue, FDS applies a radiative fraction, according to the type fuel used in the simulation (Figure 5.13), to correct the radiation source term within the reacting zone (equation 5.21). Therefore, although the gas temperatures near the fire source are not correctly predicted, we should still obtain

reliable results to characterize the thermal exposure of the structure also for locations in the vicinity of the reacting zone (Figure 5.11), provided a correct radiation fraction is selected in the simulation.

- *Fire-structure interaction:*

1) Heat is transferred from a fire to the structure through convection and radiation. Due to the fourth power dependence on temperatures, the latter will become the primary mode of heat supply to the structure as soon as high temperatures are generated by a fire (Figure 5.10).

2) One may make use of CFD-based fire simulations to describe more realistically the thermal exposure which is imposed on the structure by a certain fire scenario. If that is the case, then AST (equation 5.27) should be used to link the CFD calculations for the fire phase to the structural fire analysis in a FEA software. This parameter has the added benefit of combining the effects of radiation and convection into a single term, fully describing the fire-phase in the analysis, and thus easing the task of exchanging information between CFD and FEA.

3) Note also that as AST fully characterizes the thermal exposure imposed on the structure, it will also represent the maximum temperature that could ever be achieved by this structure during a given fire scenario.

6 Concrete Structures Subjected to Fire

This chapter is aimed at the numerous consequences of fire to the concrete structure. In this sense, the thermal degradation of mechanical properties, the deformation of concrete at elevated temperatures and the occurrence of spalling are briefly described. Then, the development of thermal stresses is addressed and the influence of some parameters (i.e. the support conditions, the elastic modulus, the thermal boundary condition, and the thickness of the specimen) into the total thermal stress state within the structure is studied.

6.1 Introduction

Fire imposes one of the most critical conditions to any structure. Generally speaking, when compared to other building materials (e.g. steel and wood), concrete is known to provide high fire resistance (Kodur [77] and Buchanan and Abu [78]). Moreover, concrete is non-combustible and ally relatively low thermal conductivity (i.e. k_s in equation 5.4) with high volumetric heat capacity (i.e. the product $\rho_s c_s$ in equation 5.4), which slows the rate of heat transfer within the material. As a consequence, the core region of an exposed concrete element will remain cool for a relatively long period, fully retaining its strength capacity. Not only that, provided enough cover is applied to the reinforcements, concrete will also serve as an effective heat barrier, limiting the temperature achieved by the reinforcing bars during a fire.

On the downside, at such high temperatures, concrete suffers irreversible physical and chemical changes in its composition which leads to permanent and significant loss of mechanical properties (Section 6.2). Also, increased temperatures will lead to the development of different strain components in a concrete structure (Section 6.3). In especial, thermal expansion will lead to the development of high thermal stresses, as steep thermal gradients are formed within the depth of the structure. Allied with high pore pressure, such stresses might cause the occurrence of explosive spalling (Section 6.4). That being said, this chapter will cover all those fire-related issues for the concrete structure, focusing, in particular, in the development of thermal stresses (Section 6.5) and on the influences of certain parameters in the levels of such stresses (Section 6.6).

6.2 Thermal Degradation of Mechanical Properties

At high temperatures, several physical and chemical changes will occur within a concrete structure. Fletcher et al. [79] explain that at *100 ^oC*, water begins to vaporize within the concrete and that this process might be extended up to *140 ^oC*, due to pressure effects. Beyond moisture loss, calcium hydroxide in the cement paste will start to dehydrate at *400 ^oC*. The aggregate phase will also suffer changes, but the temperature related to those will be dependent on the aggregate type. For instance, quartz-based aggregates will increase in volume at approximately *575 ^oC*, while limestone aggregates start to decompose at *800 ^oC*. Altogether, these effectively reduce the strength of the material as whole, characterizing the softening behavior of concrete at elevated temperatures (Figure 6.1). The temperature for which a significant strength reduction can be expected is *~660 ^oC* for concrete mixtures with carbonate aggregates and *~430 ^oC* for siliceous aggregates (Fletcher et al. [79]). Note that as those changes take place in chemical level, they are not reversible. As a consequence, a concrete structure might be significantly weaker after being exposed to fire.

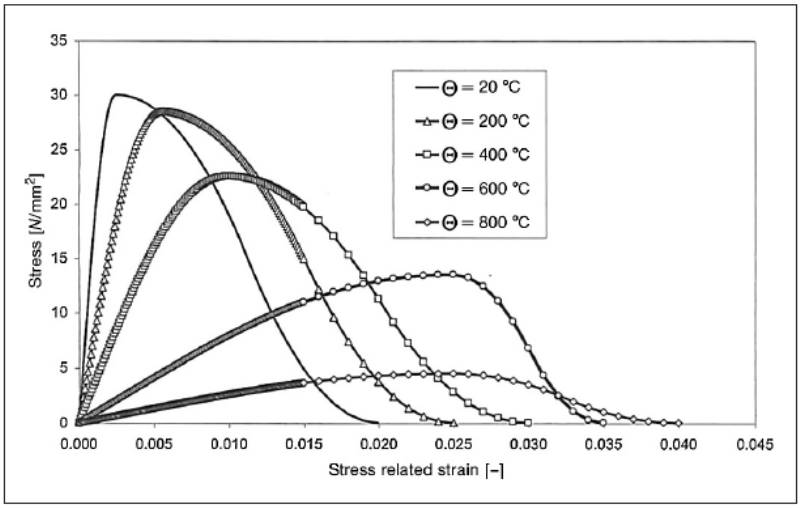


FIGURE 6.1 – CONCRETE'S STRESS-STRAIN RELATIONSHIPS AT ELEVATED TEMPERATURES
Retrieved from Model Code 2010 [80]

6.2.1 Compressive Strength

As shown in Figure 6.2, normal strength concrete (NSC) and high strength concrete (HSC) behave differently when exposed to fire. Kodur [77] explains that test data over NSC, despite having large scatter, show a uniform pattern for the variation of concrete's compressive strength with temperature. Apparently, as NSC is highly permeable, the pore pressure generated by water vapor is easily diffused within the material. As a consequence, the compressive strength of NSC is only marginally affected up to a temperature of *400 ºC*. This is not the case for HSC, where the use of higher percentages of special binders (e.g. slag and silica fume) lead to a very dense and highly impermeable microstructure. Thus, once water vaporizes, pore pressure levels will raise rapidly in HSC, promoting the formation of inner microcracks within the specimen. As a consequence, HSC appears to experience a faster strength deterioration in the early stages of fire (up to *200 ºC*) when compared to NSC. Still, for both types of concrete, once extremely high temperatures are achieved (above *800 ºC*), most of the compressive strength is lost.

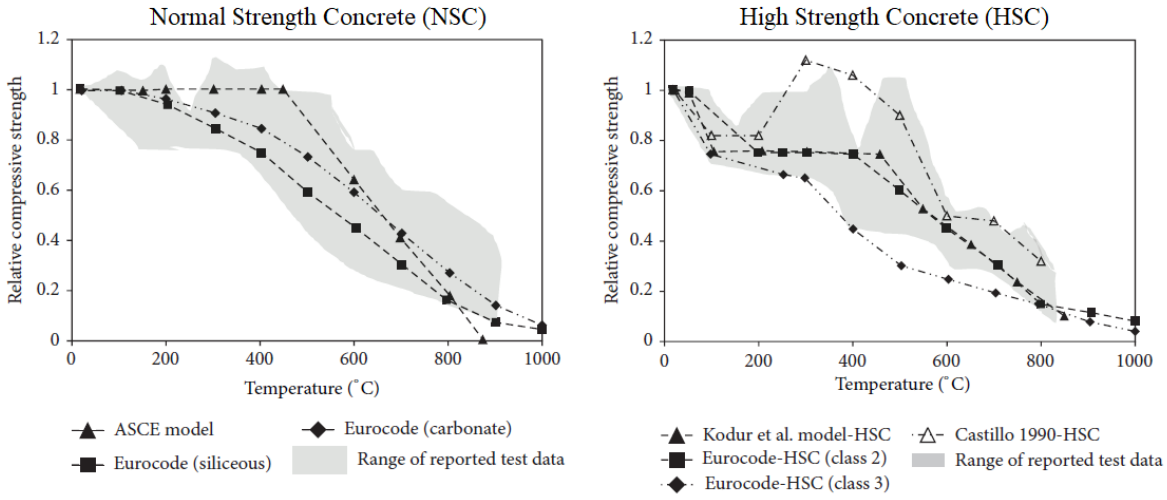


FIGURE 6.2 – VARIATION IN COMPRESSIVE STRENGTH AS A FUNCTION OF TEMPERATURE
Retrieved from Kodur [77]

A final remark here concerns the reported test data for HSC. Note that it varies significantly up to *500 °C*, but above this temperature, as fewer test results are available for HSC, the scatter is quite small if compared to that of NSC (Figure 6.2). According to Kodur [77], this is probably due to the occurrence of spalling in HSC. Basically, as NSC appears to be less susceptible to this type of failure, more data points are available in literature above *500 °C*, explaining the higher variability for this type of concrete.

6.2.2 Tensile Strength

Figure 6.3 provides the thermal degradation of concrete's tensile strength. Note that Eurocode 2 Part 1-2 [9] assume the same behavior for NSC and HSC. As the tensile strength of concrete is much lower than the correspondent compressive strength, we often neglect it when designing reinforced concrete structures is normal conditions. However, when analyzing concrete structures subjected to fire, this parameter may play an important role to understand the propagation of cracks involved in the occurrence of spalling (Kodur [77]).

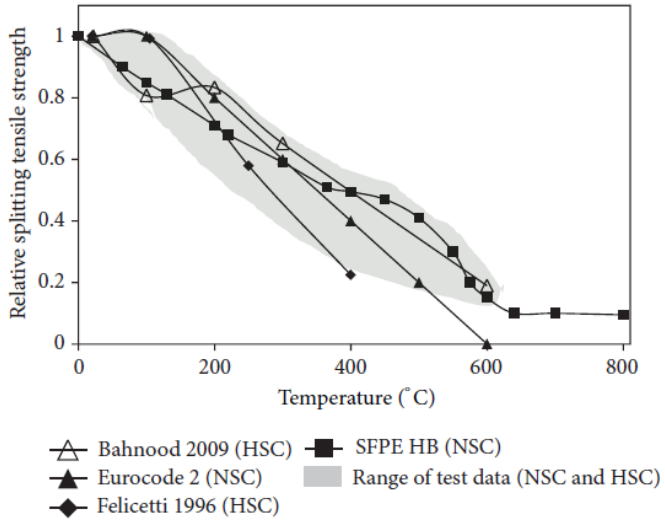


FIGURE 6.3 – VARIATION IN TENSILE STRENGTH AS A FUNCTION OF TEMPERATURE
Retrieved from Kodur [77]

6.2.3 Elastic Modulus

For NSC, Eurocode 2 Part 1-2 [9] does not directly provide the evolution of concrete's elastic modulus with temperature. However, it can be indirectly calculated based on the coefficient of reduction of compressive strength with temperature ($k_{c,T}$) and on the strain corresponding to the compressive strength at that temperature ($\varepsilon_{c1,T}$). Accordingly:

$$f_{c,T} = k_{c,T} f_{ck} = E_{c,T} \varepsilon_{c1,T} \qquad 6.1$$

where $f_{c,T}$ is concrete's compressive strength for a temperature T (MPa), $k_{c,T}$ is the coefficient of strength reduction at temperature T (which is provided in EN 1992-1-2), f_{ck} is concrete's compressive strength at a reference temperature of 20 °C, $E_{c,T}$ is concrete's elastic modulus at a temperature T (MPa), $\varepsilon_{c1,T}$ is the strain corresponding to $f_{c,T}$ (which is also provided in EN 1992-1-2).

Therefore, if one assume $E_{c,T} = k_{E,T}E_c$ or, that concrete's elastic modulus at a given temperature ($E_{c,T}$) is equal to the product between a hypothetical coefficient of reduction of elastic modulus with temperature ($k_{E,T}$) and the elastic modulus of concrete at 20 ºC (E_c), then:

$$k_{c,T}f_{ck} = k_{E,T}\left(\frac{f_{ck}}{\varepsilon_{c1,20}}\right)\varepsilon_{c1,T} \rightarrow k_{E,T} = \frac{k_{c,T}\,\varepsilon_{c1,20}}{\varepsilon_{c1,T}} \qquad 6.2$$

where $k_{c,T}$ is the coefficient of strength reduction at temperature T, f_{ck} is concrete's compressive strength at a reference temperature of 20 ºC, $\left(\frac{f_{ck}}{\varepsilon_{c1,20}}\right)$ is equal to concrete's elastic modulus at a reference temperature of 20 ºC (i.e. E_c), $\varepsilon_{c1,T}$ is the strain corresponding to $f_{c,T}$, and $k_{E,T}$ is the coefficient of reduction of concrete's elastic modulus with temperature.

Based on this, Figure 6.4 provides the comparison between the evolution of NSC elastic modulus with temperature (indirectly calculated according to Eurocode 2 Part 1-2 [9]) and several test results. As it can be seen, equation 6.2 provides lower values than the real measurements. This is not necessarily conservative, as one might think when looking at this figure. From one side, it reduces the capacity of the structure in carrying external loads, which is indeed conservative. From another, it also reduces the levels of thermal stresses generated in the structure due to restrained deformations. Therefore, from a fire resistance point of view, the selected values are actually not conservative. These will be better explained in Section 6.2.3.

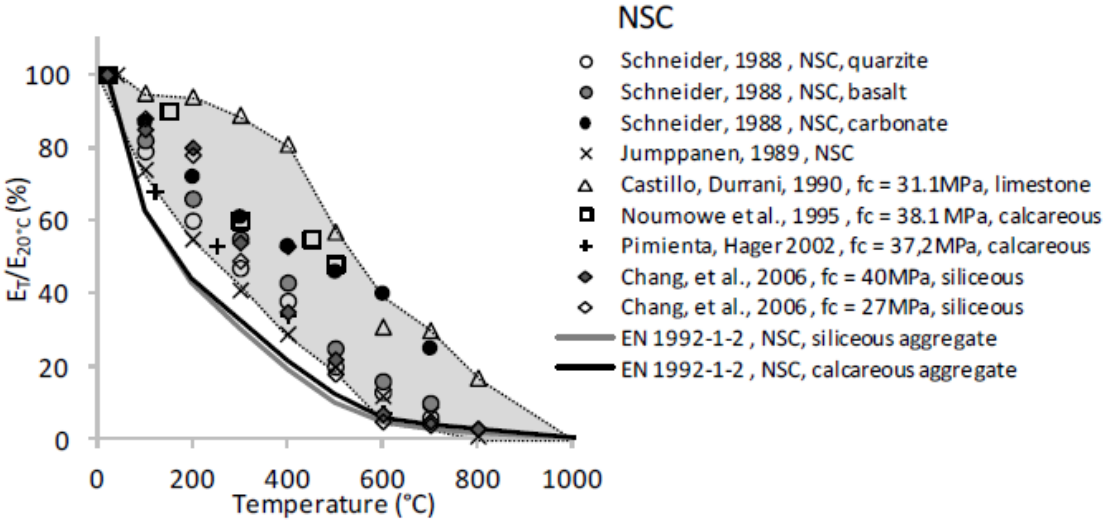


FIGURE 6.4 – VARIATION OF CONCRETE'S ELASTIC MODULUS WITH TEMPERATURE (NSC)
Retrieved from Hager and Krzemień [81]

For HSC, Eurocode 2 Part 1-2 [9] directly prescribes a coefficient of reduction to describe the evolution of the elastic modulus with temperature. This parameter is calculated through the equation below:

$$k_{E,T} = k_{c,T}^2 \qquad 6.3$$

where $k_{c,T}$ is the coefficient of compressive strength reduction at temperature T (which is provided in EN 1992-1-2) and $k_{E,T}$ is the correspondent reduction coefficient of elastic modulus.

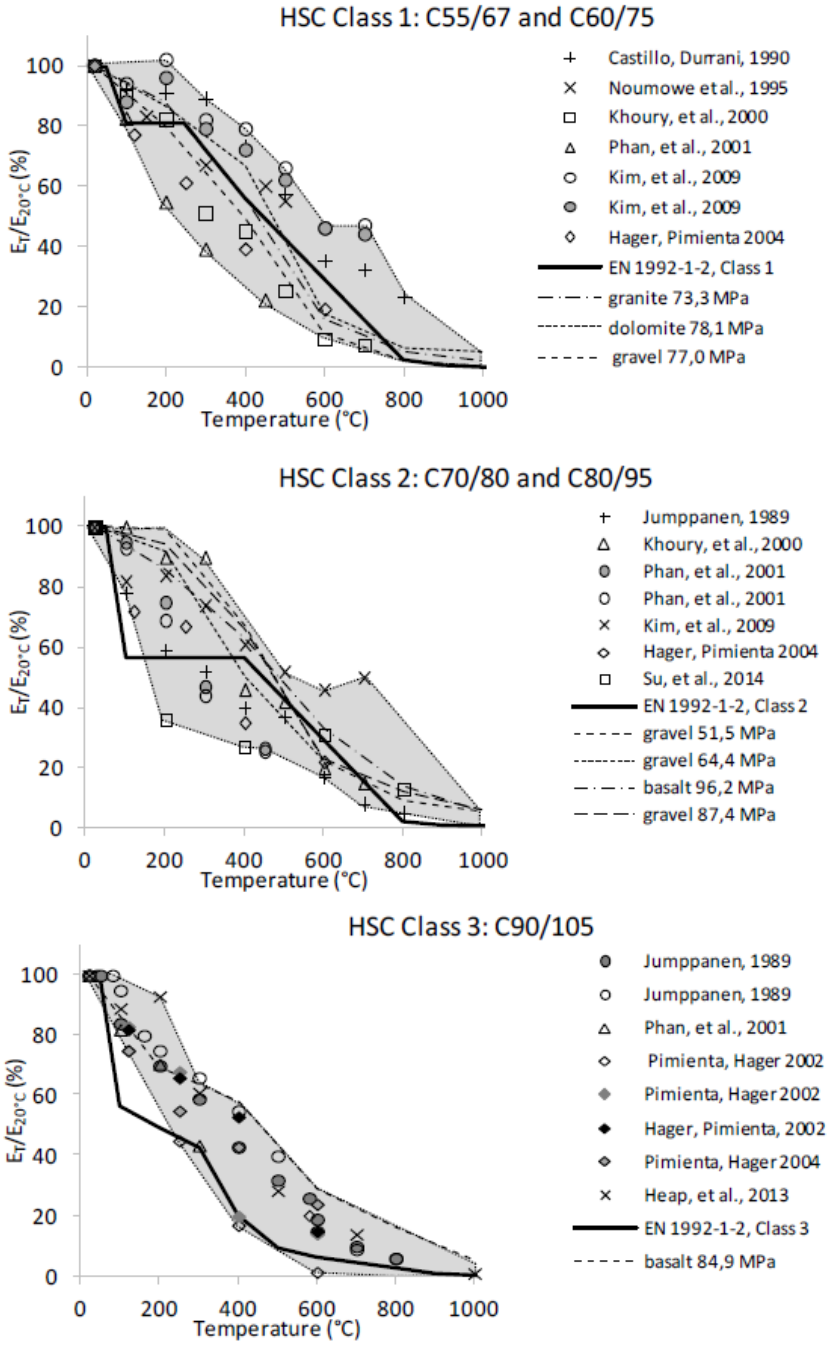


FIGURE 6.5 - VARIATION OF CONCRETE'S ELASTIC MODULUS WITH TEMPERATURE (HSC)
Retrieved from Hager and Krzemień [81]

Figure 6.5 provides a comparison of the values obtained through equation 6.3 with several test results according to the correspondent HSC class. Differently from NSC, Eurocode's choice for the thermal degradation of HSC elastic modulus is now more in line with test measurements encountered in literature, especially when considering classes 1 and 2. However, it must be pointed out that the constant plateau adopted in these classes (i.e. from *100 °C* to *250 °C* in HSC Class 1 and from *200 °C* to *400 °C* in HSC Class 2) does not seem to represent the real evolution at those specific temperature ranges, since all test data seems to indicate a continuous decay.

A much simpler function to evaluate the coefficient of reduction for the elastic modulus is described in Buchanan and Abu [78], based on the old British standard (BS 8110) for the design of reinforced concrete structures. Accordingly, the reduction coefficient is given by equation 6.4, and is plotted in Figure 6.6 together with the propositions of Eurocode 2 Part 1-2 [9] for NSC Siliceous and HSC Class 1. This curve, here entitled as *Buchanan and Abu*, will be later used in Section 6.2.3 to highlight the importance of the elastic modulus into the evaluation of the thermal stresses that are imposed to concrete structures during fire.

$$\begin{cases} k_{E,T} = 1.0 & T < 150℃ \\ k_{E,T} = \dfrac{700 - T}{550} & 150℃ \leq T < 645℃ \\ k_{E,T} = 0.1\left(\dfrac{1000 - T}{355}\right) & 645℃ \leq T < 1000℃ \end{cases} \quad 6.4$$

where $k_{E,T}$ is the linear coefficient of reduction of elastic modulus at temperature T.

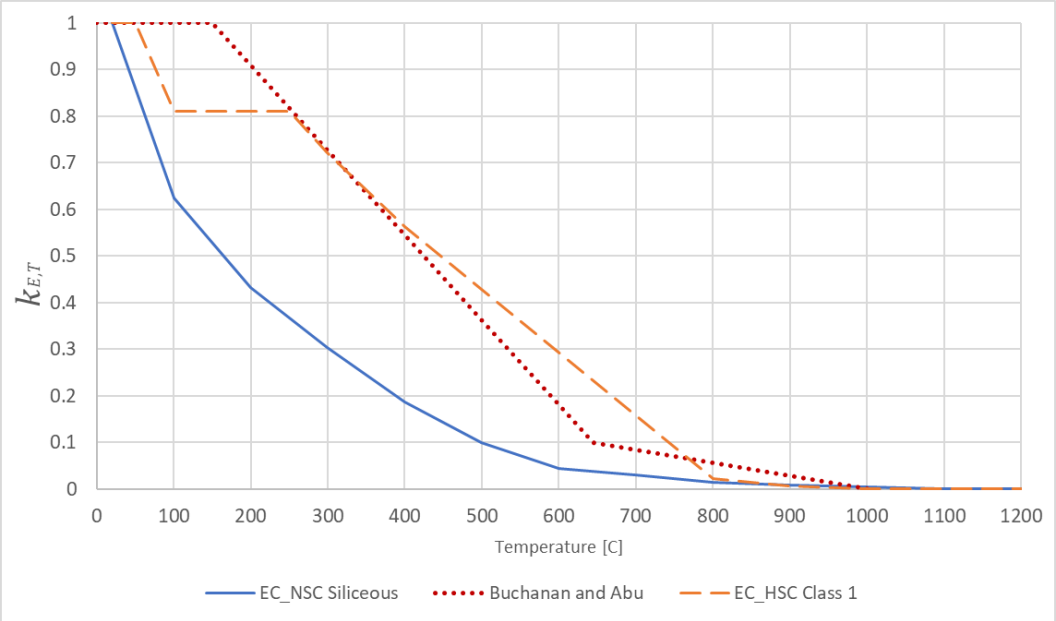


FIGURE 6.6 – EVOLUTION OF YOUNG'S MODULUS IN TEMPERATURE

6.3 Deformation of Concrete at Elevated Temperatures

Buchanan and Abu [78] explain that the deformation of concrete at elevated temperatures is composed of four terms:

$$\varepsilon = \varepsilon_{th}(T) + \varepsilon_{\sigma}(\sigma, T) + \varepsilon_{cr}(\sigma, T, t) + \varepsilon_{tr}(\sigma, T) \quad 6.5$$

where ε is the total strain, $\varepsilon_{th}(T)$ is the thermal strain, $\varepsilon_{\sigma}(\sigma, T)$ is the strain resulting of the applied external load, $\varepsilon_{cr}(\sigma, T, t)$ is the creep strain and $\varepsilon_{tr}(\sigma, T)$ is the transient strain.

The stress related strain (ε_{σ}) is merely a function of the applied load and the reduction of elastic modulus with temperature. Thermal strain (ε_{th}) is the result of the expansion of the material, due to an increase in temperature. Considering its importance for the development of thermal stresses, it will be treated separately in Section 6.3.1. Creep strain (ε_{cr}) is well studied at ambient temperature and accounts for the increase in concrete's deformation in time due to a

sustained load. As a result of moisture movement out of the concrete matrix, this phenomenon is known to be enhanced at elevated (Kodur [77]). Transient strain (ε_{tr}) only occurs during the first heating of a concrete structure. It is the result of a complex process involving chemical changes in concrete's composition and differences in the total thermal expansion of the cement paste and aggregates, which lead to the development of internal stresses and microcracking. According to Kodur [77], limited information is available in literature over ε_{cr} and ε_{tr} at elevated temperatures, especially when considering HSC. For this reason, and accounting for the complex nature of both terms, measuring, stating, and using these strains stretch beyond the scope of this thesis. Thus, they will not be further investigated here.

6.3.1 Thermal Strain

The thermal strain (ε_{th}) describes how concrete expands while increasing its own temperature. This component of strain has a fundamental role when evaluating the thermal stresses imposed due to restrained deformations (Section 6.5). Eurocode 2 Part 1-2 [9] differentiates ε_{th} according to the type of aggregate (i.e. siliceous or carbonate), as they are the main source main source behind the thermal expansion behavior of concrete. The adopted ε_{th} functions are provided in Figure 6.7 in comparison with the range of available test data in literature. As we can see, the values selected are in line with test results.

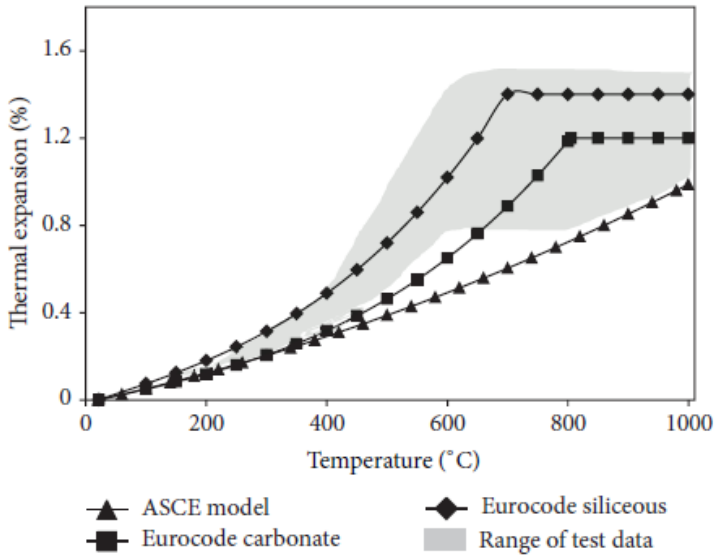


FIGURE 6.7 – CONCRETE'S THERMAL EXPANSION
Retrieved from Kodur [77]

The thermal strain is quite often used in terms of a coefficient of thermal expansion (α_T). The development of this coefficient in temperature is illustrated in Figure 6.8 for a *Siliceous Concrete*. Note that α_T is calculated according to the equation below for a reference temperature of 20 °C (Eurocode 2 Part 1-2 [9]):

$$\alpha_T = \frac{\varepsilon_{th,T}}{(T - 20)} \qquad 6.6$$

where α_T is the coefficient of thermal expansion (1/°C) at a temperature T, $\varepsilon_{th,T}$ is the thermal strain at the correspondent temperature T (illustrated in Figure 6.7), and T is the temperature achieved by the concrete specimen (°C).

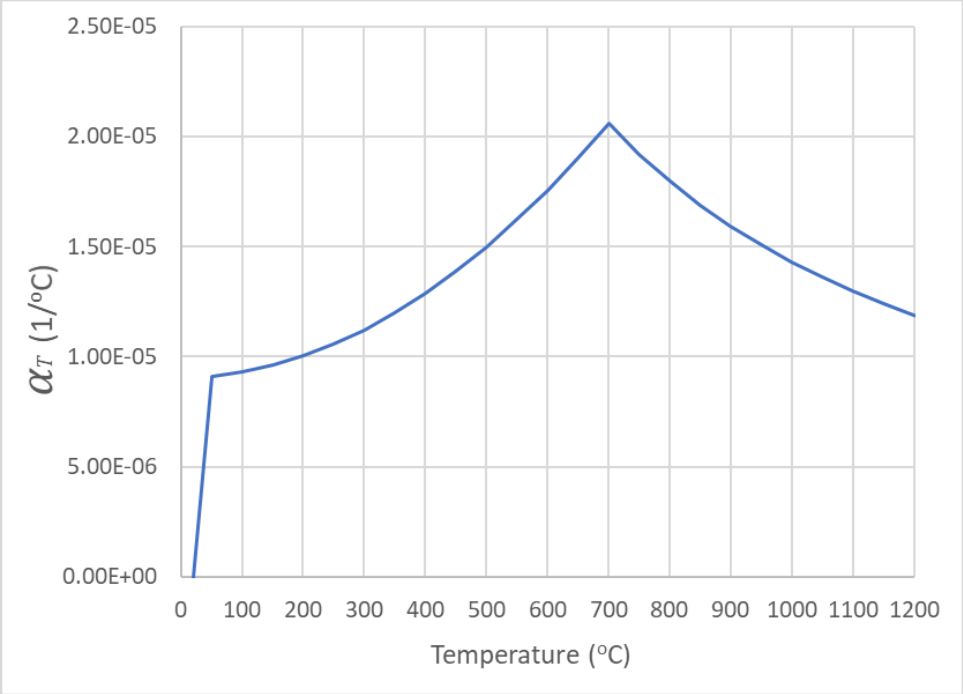


FIGURE 6.8 – COEFFICIENT OF THERMAL EXPANSION FOR SILICEOUS CONCRETE

6.4 Spalling

Another concern for concrete structures subjected to fire is the occurrence of spalling, a type of failure in which layers of concrete are removed from the surface of a structural element (Figure 6.9). In its most extreme form (i.e. explosive spalling), this process occurs violently and results in serious loss of material (Khoury and Anderberg [82]), reducing the thickness of the element significantly and exposing the reinforcements to fire. Depending on the extent of such damage, explosive spalling could even lead to structural failure.



FIGURE 6.9 – SPALLING
Retrieved from Lottman [83]

There are two main theories which are used to explain the spalling mechanism:

1) *Pore pressure spalling:* In this theory, spalling is assumed to be a consequence of the build-up of pore pressure within the material during heating (Harmathy [84]). The rapid evaporation of liquid water in concrete structures subjected to fire leads to the

occurrence of pore pressure inside the concrete specimen. In case the formed pore pressure has no route to escape, it will build-up significantly. Then, the mechanism for spalling will be formed when the pore pressure peak overcomes the tensile strength of concrete. Here, the higher spalling susceptibility of HSC when compared to NSC, is described in terms of concrete's permeability. As HSC has a much denser microstructure than NSC, higher pore pressures will be formed within this type of concrete. Therefore, the lower the permeability of concrete, the greater the fire induced spalling.

2) *Thermal stress spalling:* Here, spalling is perceived as a consequence of the thermal stress state achieved during a fire (Dougill [85]). The resultant steep thermal gradients allied with restrained imposed deformations will lead to the development of compressive stresses close to the heated surface and tensile stresses in the cooler regions within. Spalling is then perceived as the release of the compressed surface layer in a brittle fracture failure. This process might be potentialized by the development of pore pressure and/or due to the applied external loads. However, those are not perceived as the driving mechanism of the occurrence of spalling.

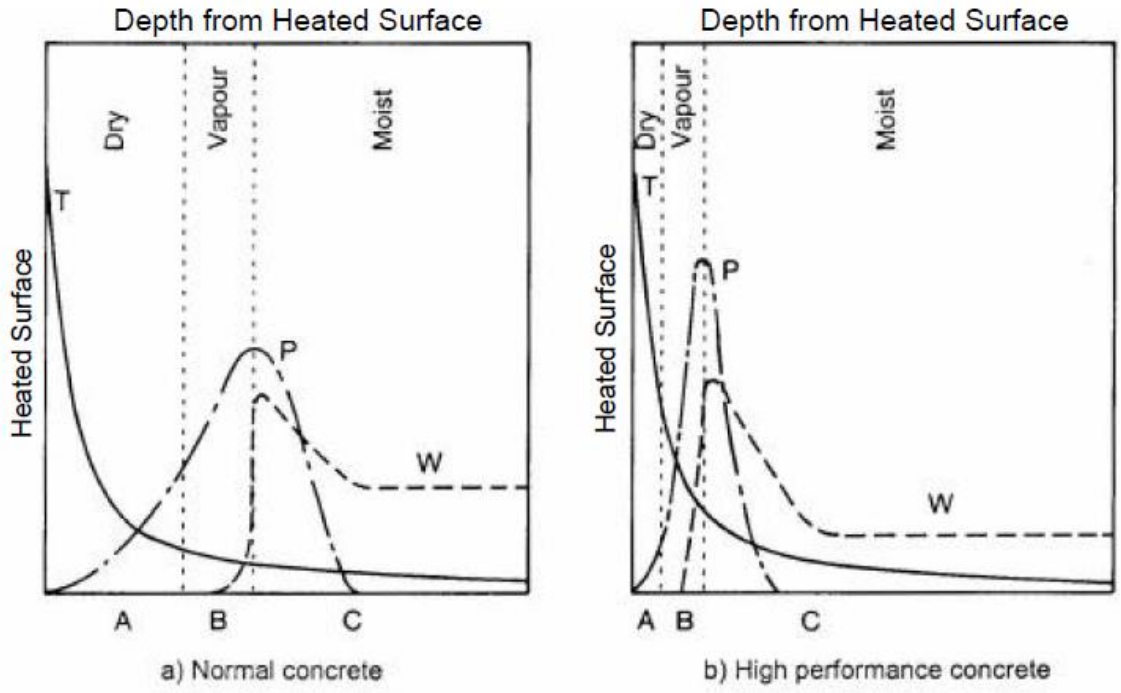


FIGURE 6.10 – PORE PRESSURE SPALLING
Retrieved from Khoury and Anderberg [82]

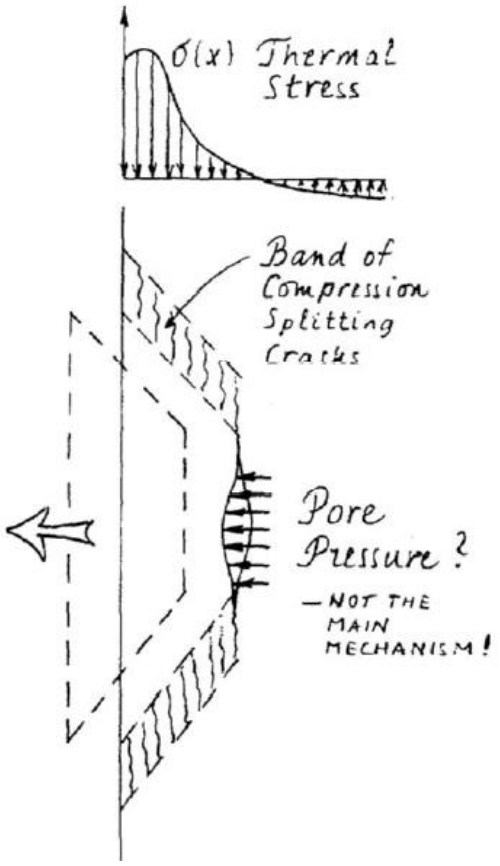


FIGURE 6.11 – THERMAL STRESS SPALLING
Retrieved from Maluk [74]

In this thesis, spalling will be looked at from the perspective of induced thermal stresses. In this sense, the next section will describe how thermal stresses develop and evolve according to the thermal gradients formed within the structure during fire exposure. After that, Section 6.6 investigate a few parameters which can play a role into the total thermal stress state induced in the structure. Finally, Section 6.7 will discuss a few challenges involved in modelling spalling.

6.5 Thermal Stresses

During a fire, nonlinear thermal gradients will be formed within the concrete structure (Figure 7.19). Such temperature distribution will always generate eigen temperatures (Section 6.5.3), which will inevitably lead to the development of thermal stresses on concrete structures subjected to fire. However, the magnitude of such stresses is governed by the extent to which those thermal deformations are restrained within the structure. In this sense, the support conditions of the concrete structure (Section 6.6.1), as well as the cross-sectional dimensions (Section 6.6.4) will play a fundamental role into the stress state which is to be expected. Nonetheless, before addressing those issues, let us understand the nature behind the development of thermal stresses. Following this line, van Breugel [86] explains that a temperature gradient ($T(x)$ in Figure 6.12) can always be subdivided into three temperature components, namely (1) mean temperature (ΔT_{ave} in Figure 6.12); (2) temperature difference (ΔT_b in Figure 6.12); and (3) eigen temperature (ΔT_e in Figure 6.12). Each one of these temperature components will induce a certain type of thermal expansion to the structure. If the correspondent thermal deformation is for some reason restrained, then it will lead to the

development of internal stresses. When those stress components are added together, we get the total thermal stress distribution for the structure in analysis.

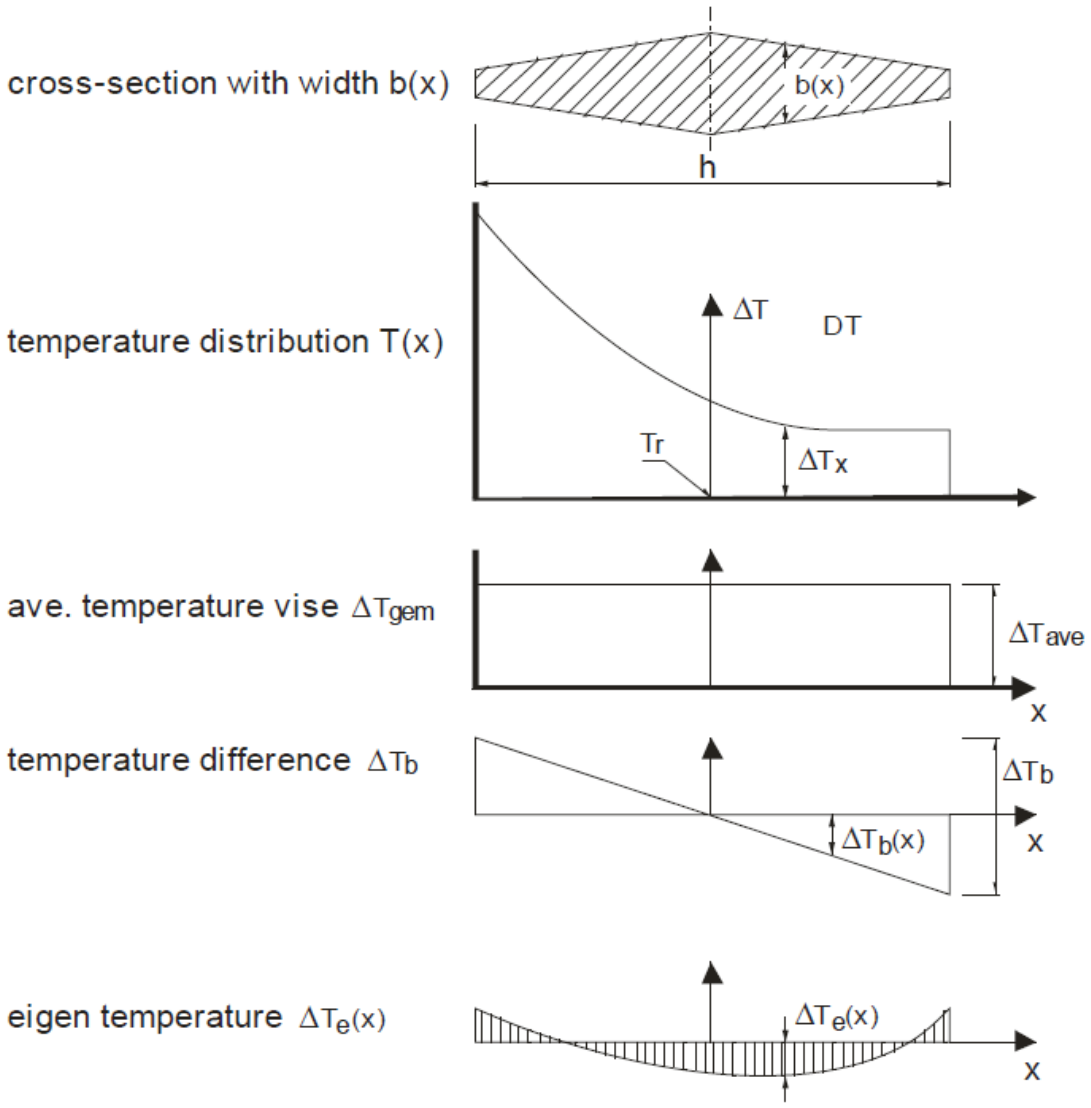


FIGURE 6.12 – SUBDIVISION OF AN ARBITRARY TEMPERATURE DISTRIBUTION
Retrieved from van Breugel [86]

6.5.1 Mean Temperature

As shown in Figure 6.12, the mean temperature (ΔT_{ave}) characterizes a constant temperature distribution over the cross section. It is calculated according to the equation below:

$$\Delta T_{ave} = \frac{1}{A_c}\int_{x_1}^{x_2} \Delta T(x)\, b(x) dx \qquad 6.7$$

where A_c is the cross sectional area (m^2), $\Delta T(x)$ is the arbitrary temperature distribution, $b(x)$ is the cross sectional width (m), and $x_{1,2}$ are the coordinates in the thickness direction of the cross section (m) considering x=0 at the center of the specimen.

The mean temperature will promote shortening or lengthening of the total cross section in the longitudinal direction (i.e. perpendicular to the plane defining the cross section). In case this

deformation is to be restricted at the supports of the structure, then ΔT_{ave} will induce a constant thermal stress in the structure, which is given by the equation below:

$$\sigma_{\Delta T_{ave}} = -\alpha_T \, \Delta T_{ave} \, E_c \qquad 6.8$$

where $\sigma_{\Delta T_{ave}}$ is the thermal stress due to mean temperature; α_T is the coefficient of thermal expansion; ΔT_{ave} is the mean temperature; and $E_{c,T}$is concrete's elastic modulus. The negative sign indicates that a positive mean temperature will generate compression.

6.5.2 Temperature Difference

The temperature difference (ΔT_b) yields in a linear temperature distribution over the cross section and is calculated according to:

$$\Delta T_b = \frac{h}{I_c} \int_{x_1}^{x_2} \Delta T(x) \, b(x) \, x \, dx \qquad 6.9$$

where h is the total thickness of the cross section (m), I_c is the moment of inertia around the y-axis (m^4), $\Delta T(x)$ is the arbitrary temperature distribution, $b(x)$ is the cross sectional width (m), and $x_{1,2}$ are the coordinates in the thickness direction of the cross section (m) considering x=0 at the center of the specimen.

Once ΔT_b is known, the linear temperature distribution $\Delta T_b(x)$ can be obtained through:

$$\Delta T_b(x) = \frac{\Delta T_b}{h} x \qquad 6.10$$

The temperature difference (ΔT_b) induces a curvature ($\kappa_{\Delta T_b}$) in the specimen:

$$\kappa_{\Delta T_b} = \frac{\Delta T_b \alpha_T}{h} \qquad 6.11$$

In case the curvature is fully restrained by the supports of the structure (e.g. a double clamped beam), a constant bending moment will be imposed to the specimen:

$$M_{\Delta T_b} = \kappa_{\Delta T_b} \, I_c \, E_c \qquad 6.12$$

where $M_{\Delta T_b}$ is the constant bending moment generated by ΔT_b for a fully restrained beam; $\kappa_{\Delta T_b}$ is the curvature imposed by the temperature difference ΔT_b; I_c is the moment of inertia around the y-axis; and E_c concrete's elastic modulus. A negative ΔT_b indicates compression on the fire exposed side.

6.5.3 Eigen Temperature

The resulting eigen temperature distribution $\Delta T_e(x)$ reveals a temperature profile in which the temperature summation of over the entire cross section of the element is equal to zero. As they are in self equilibrium, eigen temperatures do not generate thermal expansion or curvature in the structural element. For this reason, whenever they occur within a structure, they will always impose internal stresses to the cross section. In essence, this is the reason why thermal stresses will always occur in concrete structures subjected to fire. As concrete has rather low thermal conductivity, heat does not flow easily through the material. This yields in the formation of steep thermal gradients within the structure during a fire, and those nonlinear temperature distributions will always lead to the development of eigen temperatures. That being said, the eigen temperature distribution is calculated according to the equation below:

$$\Delta T_e(x) = \Delta T(x) - [\Delta T_{ave} + \Delta T_b(x)] \quad \textbf{6.13}$$

where $\Delta T_e(x)$ is the eigen temperature distribution, $\Delta T(x)$ is the arbitrary temperature distribution, ΔT_{ave} is the mean temperature distribution (equation 6.9) and $\Delta T_b(x)$ is the linear temperature distribution (equation 6.10).

The equivalent eigen stresses follow directly from the eigen temperature and are depicted below:

$$\sigma_{\Delta T_e(x)} = -\alpha_T \, \Delta T_e(x) \, E_c \quad \textbf{6.14}$$

where $\sigma_{\Delta T_e(x)}$ is the eigen stress at location x; α_T is the coefficient of thermal expansion; $\Delta T_e(x)$ is the eigen temperature at location x of interest; and E_c is concrete's elastic modulus. The negative sign indicates that a positive eigen temperature generates a compression stress.

6.6 Thermal Analysis of Concrete Structures Subjected to the RWS curve

The first step when evaluating the structural response of an element subjected to fire is to perform a transient thermal analysis to determine the thermal gradients that will be formed within the structure. Ideally, this could be achieved analytically by solving the heat conduction problem, formulated in equation 5.4, through the use of a thermal boundary condition to describe the interface between fire and concrete (Section 5.3). In reality, however, the thermal properties of concrete are temperature dependent and will vary with time (Section 11.5), elevating the level of complexity involved on the mathematical solution of the heat conduction problem. Therefore, in engineering practice, the use of numerical methods is often favored to achieve a solution for such type of transient analysis. Following this line of thinking, DIANA FEA is selected in this thesis as the numerical tool to perform both transient thermal analysis and structural analysis. Here, the interest is to understand what factors can have an influence in the development of such stresses. Thus, this section investigates the effects of (1) support conditions; (2) elastic modulus; (3) type of thermal boundary condition; and (4) specimen thickness, for a concrete structure subjected to the RWS curve. However, before addressing those issues, let us introduce the simple FE model that will serve as the starting point for the study developed in this topic.

Accordingly, this model consists of a quite simple two-dimensional simply-supported concrete slab (Table 6.1). Although the model is two-dimensional, fire is uniformly applied to the bottom edge of this slab (Figure 6.13). This characterizes a homogenous development of temperature in depth. In practical terms, the solution of the transient thermal analysis obtained here should be almost identical to that of a one-dimensional case (equation 5.4), provided enough grid resolution is used and small time steps are selected. To ensure the thermal transient analysis yields accurate results, the mesh size and time step selected here were calibrated according to what is described in Section 11.5. Once the thermal transient analysis is over, a nonlinear structural analysis is performed to calculate the correspondent thermal stresses (Table 6.2). As the concrete slab used here is simply-supported, there are no restrictions to the deformations imposed by the mean temperature (Section 6.5.1) and by the temperature difference (Section 6.5.2). Hence, the thermal stresses calculated by DIANA are effectively representing the resulting eigen stresses (Section 6.5.3).

Thermal Properties (EC 1992-1-2)	
Conductivity	EC Lower Limit (Figure 11.2)
Specific Heat	u = 0% (Figure 11.3)
Density	2300 kg/m3
Convection Heat Transfer Coefficient	50 W/m2.K
Emissivity	0.7
Geometry	
Length	9.3 m
Thickness	0.9 m
Boundary Conditions	
Bottom Edge	Exposed to RWS Curve (Equation 5.25)
Other Edges	$\dot{q}''_{tot} = 0$ in Equation 5.23
Initial Body Temperature	20 ^{o}C
Numerical Solution	
Mesh Size	0.1 m x 0.01 m up to a thickness of 0.3 m (green section in Figure 6.13); 0.1 m x 0.1 m for the remaining thickness (yellow section in Figure 6.13)
Time Step	10 seconds
Iteration Process	Newton-Raphson
Convergence Tolerance	1E-6

TABLE 6.1 – THERMAL TRANSIENT ANALYSIS OF A CONCRETE STRUCTURE SUBJECTED TO THE RWS CURVE

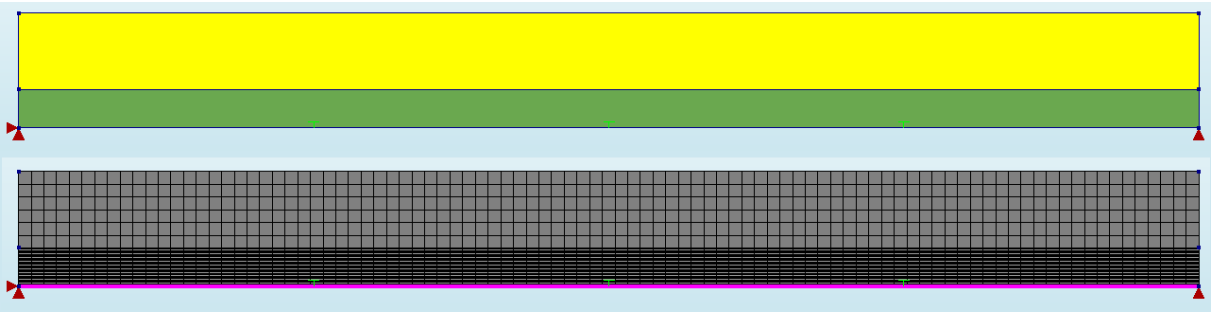


FIGURE 6.13 – GEOMETRY AND MESH

Mechanical Properties (EC 1992-1-2)	
Concrete Class	C55/65
Initial Elastic Modulus	3.82E+10 N/m^2
Thermal Degradation of Elastic Modulus	EC_NSC Siliceous (Figure 6.6)
Poisson's Ratio	0.15
Coefficient of Thermal Expansion	Figure 6.8
Numerical Solution	
Time Step	300 seconds
Iteration Process	Regular Newton-Raphson
Convergence Norm	Displacement/Force
Convergence Tolerance	1E-6
Finite Element	
Element Type	Plane Stress
Interpolation	Quadratic

TABLE 6.2 – NONLINEAR STRUCTURAL ANALYSIS

Figure 6.14 provides the evolution of the temperature distribution in depth for a concrete structure uniformly exposed to the RWS curve. As we can see, concrete's temperature at a depth of *140 mm* is limited to approximately *100 ^{o}C* after two hours of fire exposure. At a depth of *200 mm*, temperature variations are already limited to less than *20 ^{o}C*. Note that if the

minimum provision for the maximum allowable reinforcement temperature is to be achieved in design (i.e. *250 °C* as depicted in Section 1.1), then the minimum concrete cover for a two-hours exposure to the RWS curve should be approximately equal to *90 mm*, provided spalling is not a concern. Figure 6.15 provides the correspondent thermal stresses which are generated within the structure due to the formed thermal gradients. Here, the nature of eigen stresses is exposed together with the softening behavior of the material (characterized by a stiffness reduction at high temperatures). As this temperature distribution is self-equilibrating, it will not deform the cross section, which will inherently induce both compression and tensile stresses into the structure. When considering the evolution of thermal stresses in time, note that the maximum peak compressive stresses are only slightly altered, whereas the maximum peak tensile stresses actually grow tremendously. On one hand, this indicates that the risk of compression failure should reduce in time, as the thickness available to carry approximately the same level of stress is actually growing while the compression stresses are reducing due to softening of the material. On the other, as concrete has rather limited tensile strength, the risk of developing internal cracks is severely increased in time. If the mechanism for compressive failure of the outer concrete layer has already been formed, then the development of internal cracking might provide the conditions for spalling to occur (Section 6.4).

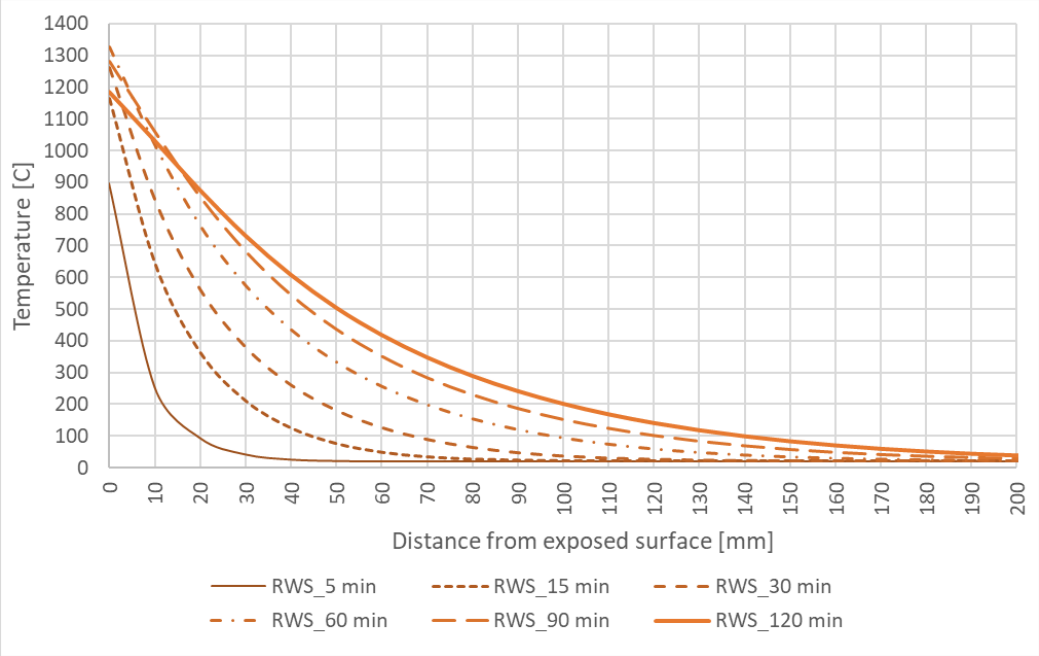


FIGURE 6.14 – EVOLUTION OF TEMPERATURE DISTRIBUTION IN TIME

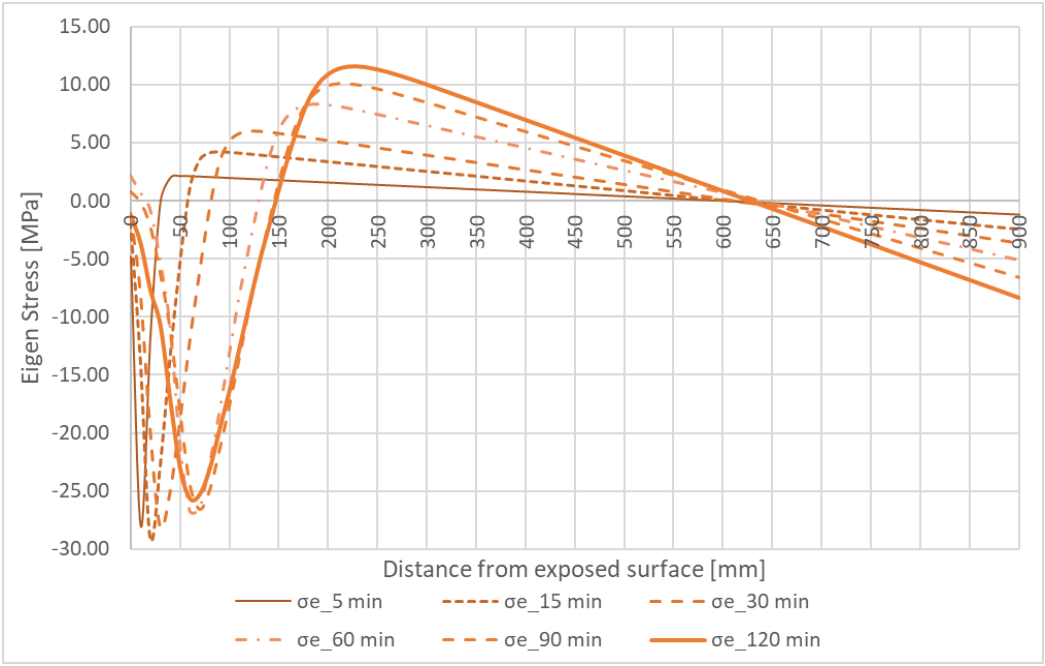


FIGURE 6.15 – EVOLUTION OF EIGEN STRESSES IN TIME

6.6.1 Type of Support

The geometry of the model (Table 6.1) was selected according to the minimum thickness and approximate span for one section of the ceiling of the Piet Hein tunnel, which is the case study of this thesis (Chapter 9). Here, the effects of support conditions into the developed thermal stresses are investigated. In total, four scenarios are studied: (1) simply supported slab (Figure 6.13); (2) double clamped slab (Figure 6.16); (3) slab connected to 0.5 m thick walls (Figure 6.17); and (4) slab connected to 1.0 m thick walls (Figure 6.17). Cases 3 and 4 represent intermediate levels of support stiffness between a simply supported slab (i.e. zero stiffness) and a double clamped slab (i.e. infinite stiffness). Note that the selected wall thicknesses are respectively equal to the minimum and maximum thicknesses of the Piet Hein tunnel walls. For both cases, the distance from the bottom of the slab to the fixed supports at the bottom of the walls (Figure 6.17) is equal to *5 m*, which is approximately equal to the real height of such walls. The span of the slab in between the center line of the walls is kept equal to *9.3 m*, as depicted in Table 6.1. A final remark here is that fire was only applied to the bottom edge of the slab which is located in between the inner edges of the walls.



FIGURE 6.16 – DOUBLE CLAMPED SLAB

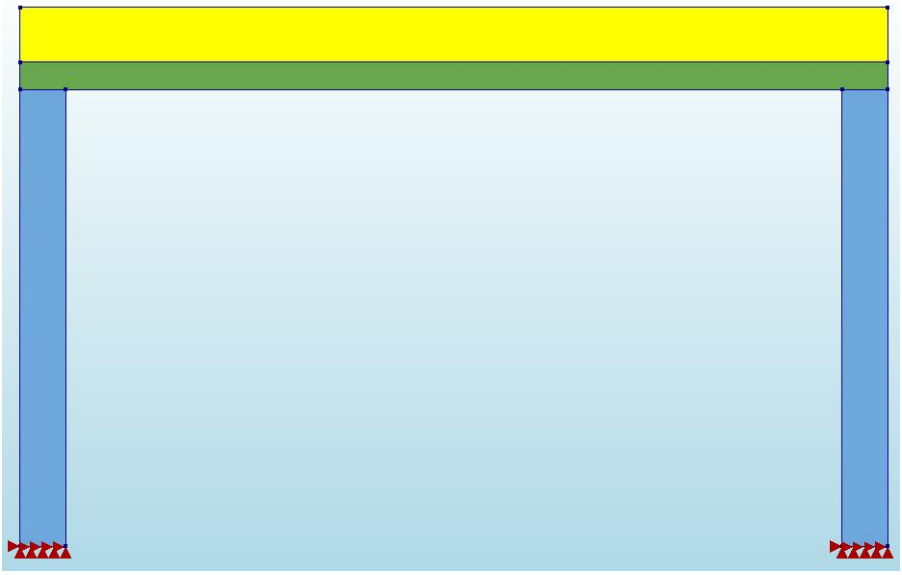


FIGURE 6.17 – MODEL WITH WALLS

Figure 6.18 provides the thermal stresses for all cases studied here (evaluated at midspan). As described in the previous topic, for the simply supported slab (red line in Figure 6.18), only eigen stresses are generated. For a double clamped slab (orange line in Figure 6.18), thermal deformations imposed by mean temperature and temperature difference are fully restrained (Section 6.5). As a consequence, they will also contribute with thermal stresses to the structure. For such cases, the thermal stresses shown in Figure 6.18 actually represent the superposition of the individual stress contributions of each one of those temperature distributions (i.e. mean, difference and eigen temperature). For cases 3 and 4 (blue and green lines in Figure 6.18, respectively), thermal deformations imposed by mean temperature and temperature difference are only partially restrained, limiting to certain level, their thermal stress contributions. All that being said, let us evaluate the effects of supporting conditions in the achieved thermal stress state. From Figure 6.18, we can clearly see that the supporting conditions actually have a fundamental role in the consequences of a fire to the concrete structure. In essence, the thermal stresses generated by mean temperature and temperature difference might even be beneficial from a structural point of view. Basically, for cases which compression failure is not a concern, the contribution of these temperature components might lead to significant reductions on the maximum peak tensile stresses achieved during a fire.

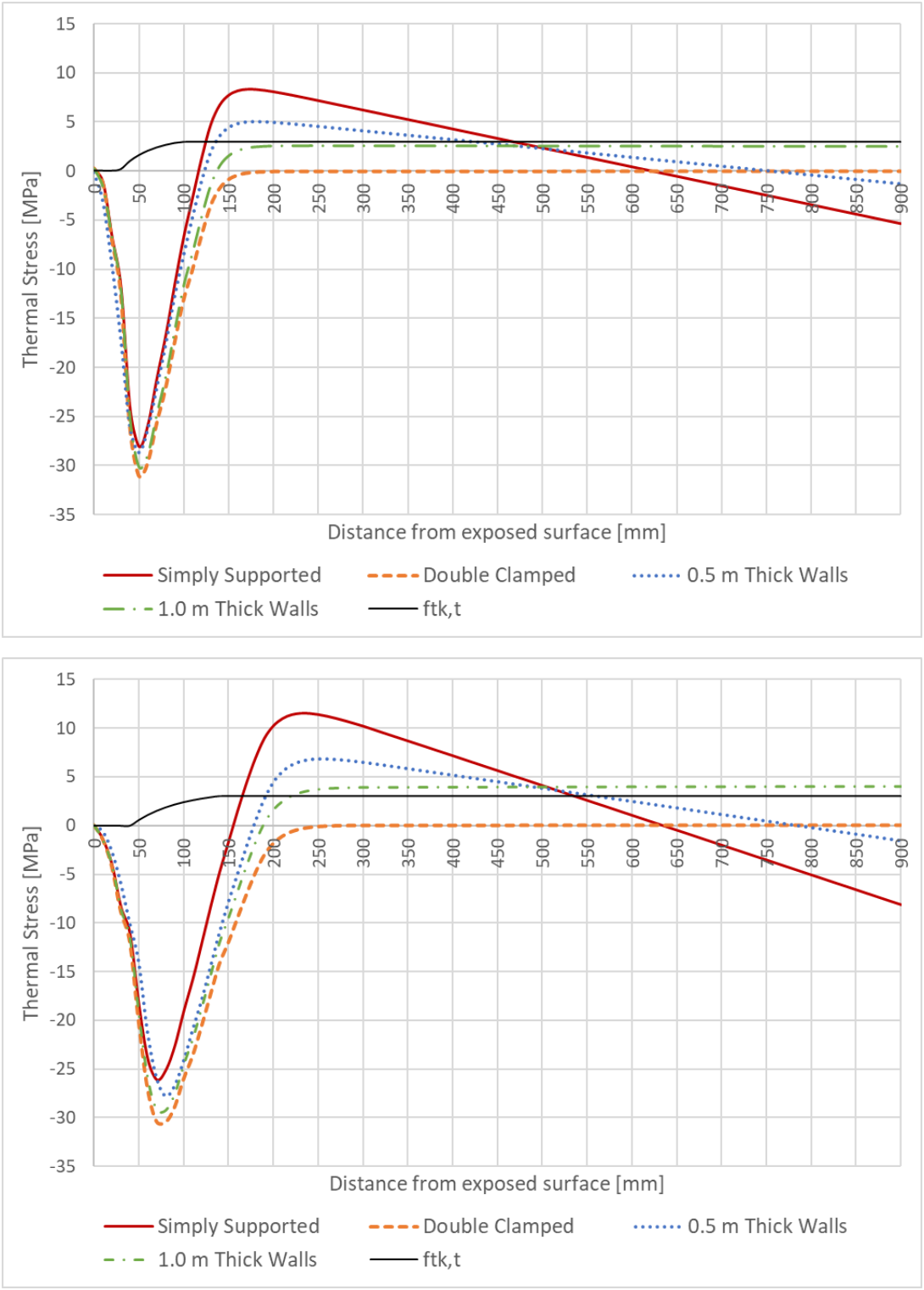


FIGURE 6.18 – THERMAL STRESSES FOR DIFFERENT SUPPORT CONDITIONS
(Top Image: After 1 hour / Bottom Image: After 2 hours)

6.6.2 Elastic Modulus

From Figure 6.6, we see that Eurocode 2 Part 1-2 [9] treats NSC and HSC very differently when considering the thermal degradation of elastic modulus, adopting a much higher decay rate for NSC than for HSC. After tests, the concrete of the Piet Hein tunnel (Chapter 9) was classified as C55/65, which is also the first strength class to be classified as HSC in Eurocode 2 Part 1-2 [9]. Hence, this topic compares the thermal stresses achieved in a concrete structure subjected to the RWS fire for two choices of elastic modulus: (1) EC_NSC Siliceous (Figure 6.6); and (2) Buchanan and Abu (Figure 6.6), which is here used in replacement of EC_HSC Class 1 (Figure 6.6) as it appears to describe the test results obtained for this type of concrete more faithfully (look at HSC 1 in Figure 6.5).

Figure 6.19 compares the thermal stresses achieved after a one-hour exposure to the RWS curve considering two different support conditions: (a) double clamped slab (Figure 6.16); and (b) simply supported slab (Figure 6.13). It becomes clear that the choice of elastic modulus has a significant influence in the structural analysis of concrete structures subjected to fire. By selecting a curve with rapid thermal degradation of elastic modulus, such as EC_NSC Siliceous, one might be extremely underestimating the level of thermal stresses generated in the structure during a fire. In fact, when looking at Figure 6.4, it appears that the use of Eurocode 2 Part 1-2 [9] to described the thermal degradation of NSC is actually unconservative, as it describes a faster decay than that which appears to be achieved in reality. Note, for instance, that for the case of a double clamped slab, selecting the elastic modulus according to EC_NSC Siliceous would indicate no possibility of structural failure during a fire, as the generated thermal stresses are fully comprised within the strength limits of the material (Figure 6.19). In reality however, if concrete's thermal degradation does not occur so rapidly, then compressive failure of the outer layer of the structure is actually likely to happen (look at red line in the left image of Figure 6.19). Such difference exposes the nature of restrained imposed deformations. As structural engineers, we are more often used to assess the structural response of an element to applied forces. In such cases, the stiffer the structure is, the lower the stresses will be. However, we cannot forget that this plot is reverted when dealing with imposed deformations. For those cases, the stiffer the structure the higher the stress level.

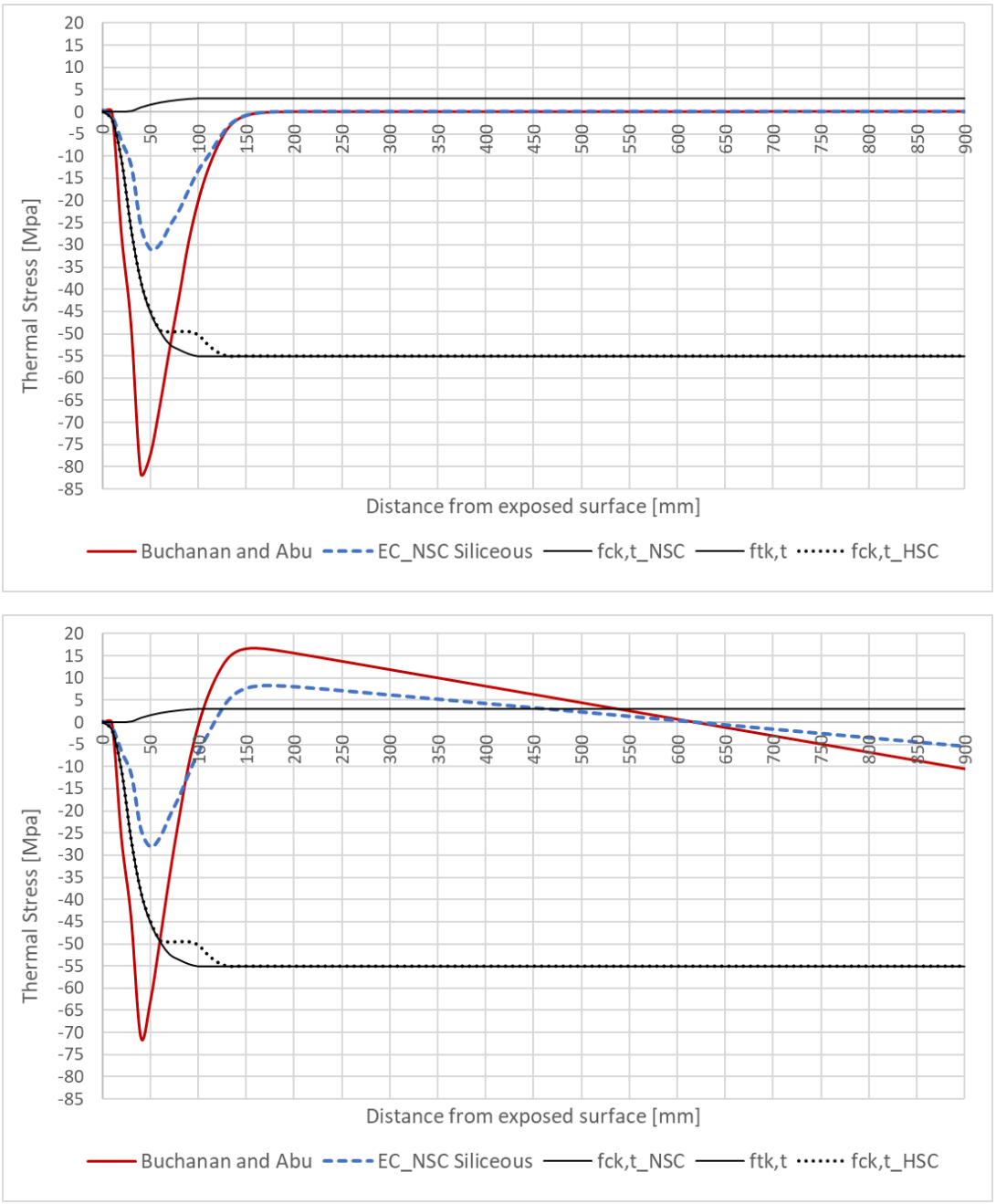


FIGURE 6.19 – THERMAL STRESS ACCORDING TO ELASTIC MODULUS (SIMPLY SUPPORTED SLAB)

(Top Image: Double Clamped Slab / Bottom Image: Simply Supported Slab)

Before moving further to the next topic we will have a look on the thermal stress evolution for HSC (here entitled as Buchanan and Abu), which is provided in Figure 6.20. Generally speaking, the behavior is similar to that which was described for the same simply supported slab case when considering EC_NSC Siliceous (Figure 6.15). Basically, the compressive stress peak is reduced with time (due to the softening of the material), whereas the tensile stresses are increased. The major difference here is that the maximum peak compressive stress at the early stage is significantly reduced after longer periods of fire exposure (Figure 6.20). Finally, look at the thermal stress state achieved after 5 minutes of exposure and compare it to the initial

compressive and tensile strength of concrete. If spalling is really driven by the occurrence of thermal stresses, then this clearly indicates the susceptibility of HSC to this type of failure.

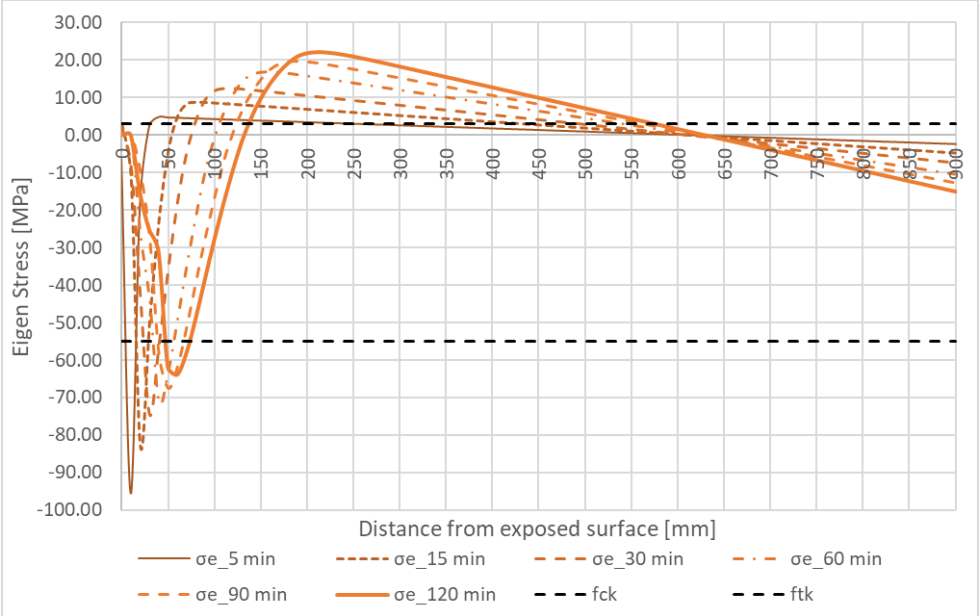


FIGURE 6.20 – EVOLUTION OF EIGEN STRESSES IN TIME (SIMPLY SUPPORTED SLAB)
(Thermal Degradation of Elastic Modulus = Buchanan and Abu)

6.6.3 Type of Thermal Boundary Condition

Section 5.3.3 introduced the so-called natural boundary conditions, used to define the interface of heat transfer between fire and concrete. In Section 5.3.3.1, it was described that a purely convective boundary condition (equation 5.24) appears to be quite often used by structural engineers when performing fire analysis, even though the total heat transferred to a structure during a fire is actually governed by the radiation component (Section 5.1.3.2). Therefore, this topic is intended to compare the results of the use of these two different types of thermal boundary condition, here entitled as: (a) Convection (equation 5.24); and (b) RWS (equation 5.25). At first, we will address the differences in the solution of equation 5.4 in time or, in other words, how the thermal transient analysis is affected by avoiding to include the radiation contribution. Then, we will look at the correspondent thermal stresses.

Figure 6.21 provides the evolution of concrete's surface temperature in time for both types of boundary condition, while Figure 6.22 compares the temperature evolution in depth. As we can see, the results of a transient thermal analysis are completely altered if radiation is not considered. Basically, the heat supply to the structure will occur at a much faster rate when radiation is included in the analysis (Figure 6.23). This is explained by the fact that convection heat transfer occurs according to the simple difference of gas temperature and concrete's surface temperature (equation 5.5), while the rate of radiation heat transfer is dependent on temperatures to the fourth power (equation 5.12). As a consequence, the temperature development of the structure is seriously underpredicted when only convection is used to describe the interface between fire and concrete. As both mechanical and deformation properties are temperature dependent (Figure 6.6 and Figure 6.8 respectively), in the next paragraph we will investigate whether such underestimation of the temperature development of the cross section also leads to major structural consequences.

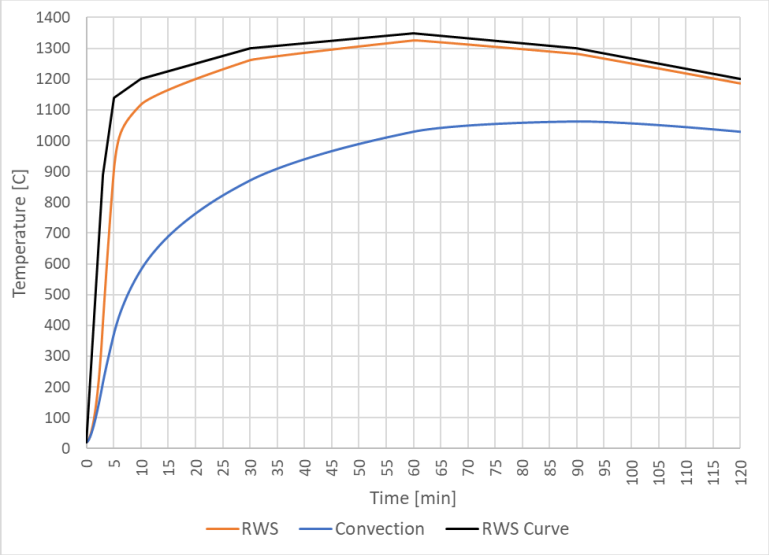


FIGURE 6.21 – EVOLUTION OF CONCRETE'S SURFACE TEMPERATURE IN TIME

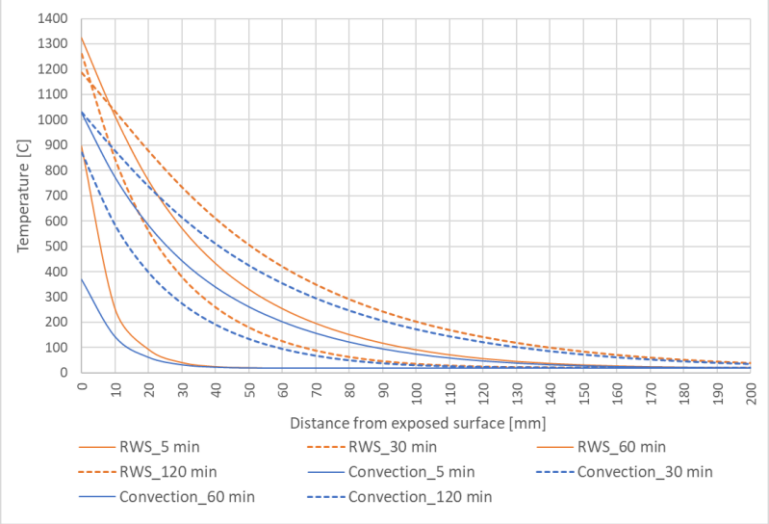


FIGURE 6.22 – EVOLUTION OF TEMPERATURE DISTRIBUTION IN TIME

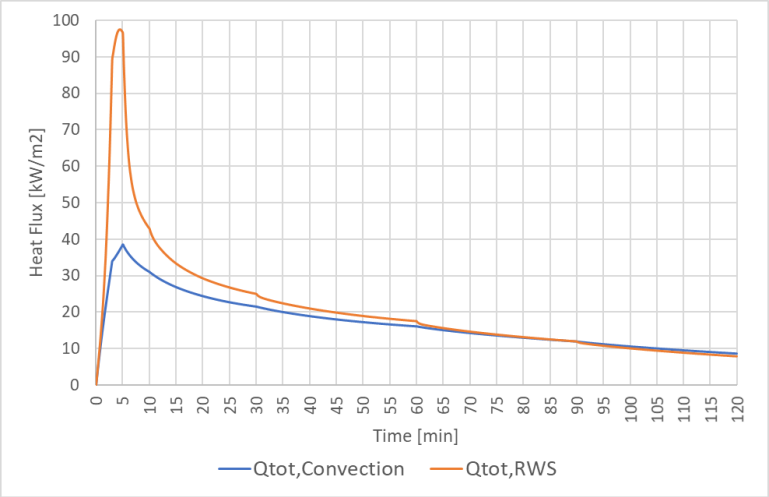


FIGURE 6.23 – TOTAL HEAT FLUX TO THE STRUCTURE

Figure 6.24 compares the thermal stress evolution in time for both types of boundary condition. The stresses are evaluated at midspan of a simply supported concrete slab (Figure 6.13) when considering the elastic modulus according to Buchanan and Abu (Figure 6.6). Apparently, there is no significant difference in the stress state achieved for both cases. Moreover, the peak stresses will occur at a smaller depth in the cross section when considering only the convection boundary condition (equation 5.24), but the stress magnitude is only slightly altered and the total stress pattern is kept nearly identical.

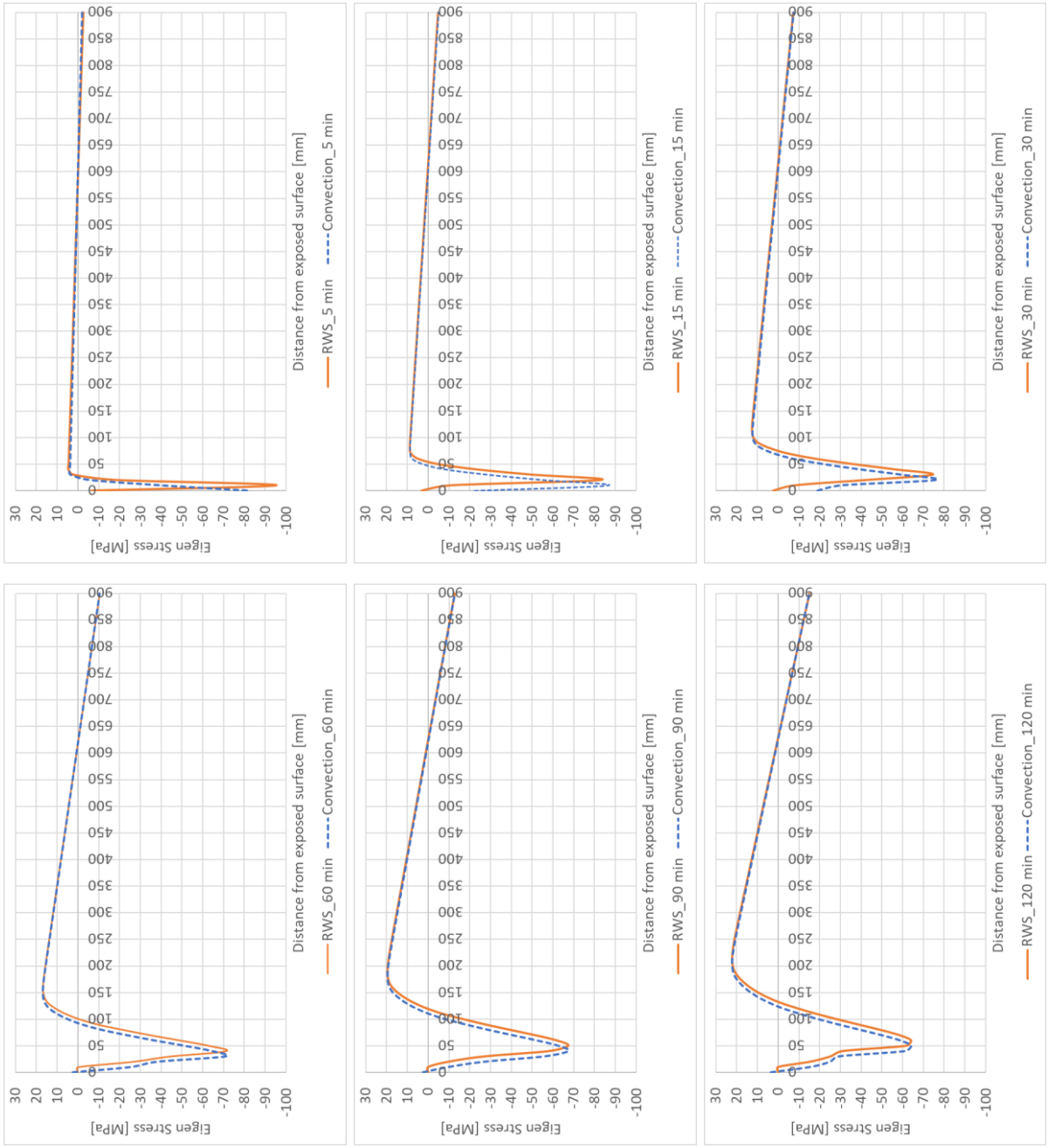


FIGURE 6.24 – COMPARISON OF THE EVOLUTION OF THERMAL STRESSES IN TIME

The similarity between the thermal stresses for the two cases studied here is rather unexpected, if considered that the developed thermal gradients are completely different between the two types of boundary condition (Figure 6.22). This indicates that the explanation behind the

analogous level of thermal stresses lies over the material itself. In fact, we can understand this behavior by looking at the development of concrete's mechanical and deformation properties with temperature (i.e. Figure 6.6 and Figure 6.8, respectively). On one hand, the thermal expansion coefficient grows continuously until its peak value at a temperature of 700 ºC, then starts decaying as the thermal strain is kept constant for any temperature above that (Figure 6.7). On the other, the elastic modulus of concrete is reduced to 10% of its original value already at a concrete temperature of 645 ºC, this contributes to reduce the magnitude of thermal stresses achieved in the structure at extremely high temperatures. In this sense, Figure 6.25 combines the effects of mechanical and deformation properties of concrete and provides the evolution of thermal stresses according to the temperature which is reached by a concrete structure. As we can see, differently from one often idealizes, extremely high temperatures will not necessarily maximize the levels of stress. In fact, the material becomes so soft at such temperatures that the induced thermal stresses appear to be minimized. Here, it also becomes clear the consequences of adopting such a fast thermal degradation for the elastic modulus of the material, as that indirectly adopted by the use of Eurocode 2 Part 1-2 [9] when dealing with NSC.

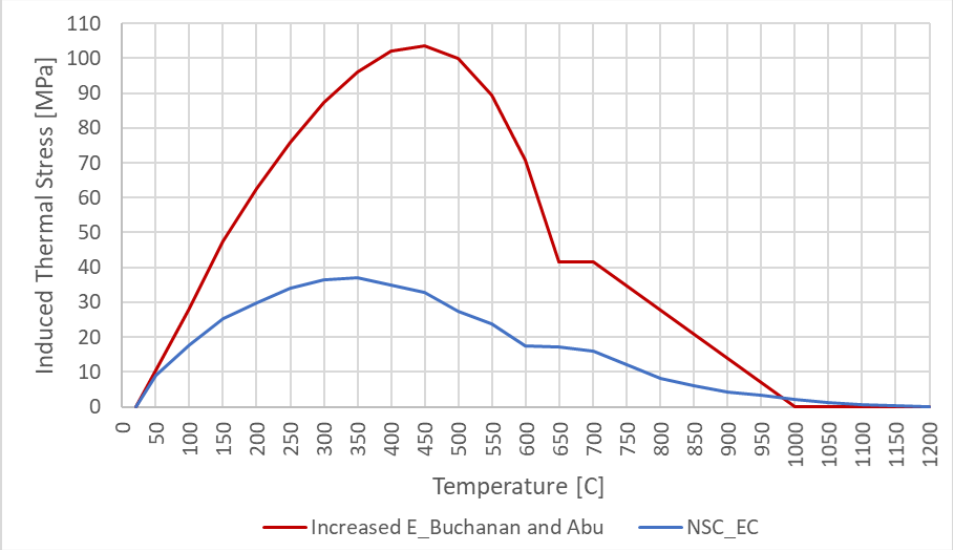


FIGURE 6.25 – THERMAL STRESSES ACCORDING TO ACHIEVED CONCRETE TEMPERATURE[6]

Finally, note that the study presented in this topic should not be seen as proof that by selecting a purely convective boundary condition (equation 5.24) one will achieve the same structural results as that which is obtained by the use of the full thermal boundary condition (equation 5.25). What we effectively take out of this study is that without including other types of physical nonlinearities (e.g. crushing and cracking) in the FE model, we cannot have a definitive position about the influences of the selected thermal boundary condition in the structural response of the specimen.

[6] $\sigma = \alpha_T \, \Delta T E_c$, where the thermal expansion coefficient (α_T) is given by Figure 6.7; the evolution of the elastic modulus (E_c) is calculated according to Figure 6.6; and ΔT is based on a reference temperature of 20 ºC.

6.6.4 Thickness of Specimen

If two concrete structures have identical thermal properties (i.e. density, specific heat, thermal conductivity and emissivity) and are subjected to a same fire then, they shall experience an identical temperature evolution, provided that the structure can be thermally treated as semi-infinite (meaning that heat does not penetrate through the whole thickness of the specimen). In such cases, the thickness of the structural element will have an effect on the achieved eigen temperature distribution, as it contributes to reduce the mean temperature distribution (equation 6.7) and the temperature difference distribution (equation 6.9) in thicker elements. Hence, this section investigates the thermal stresses formed in a simply supported slab exposed to the RWS curve for three different slab thicknesses: (1) *0.9 m* (minimum ceiling thickness for the Piet Hein tunnel); (2) *0.5 m* (minimum wall thickness for the Piet Hein tunnel); and (3) *0.3 m*, which is approximately the minimum thickness for which a concrete slab can be treated as semi-infinite when exposed for two hours to the RWS curve.

Figure 6.26 provides the evolution of thermal stresses in time for all cases studied here. It can be seen that thinner elements will experience a considerable reduction in the maximum peak compression stresses (especially for the case of a *0.3 m* thick slab), but will also suffer from significantly higher tensile stresses. It also appears that really thick elements are highly susceptible to suffer from compressive failure at the outer layer. Depending on the supporting conditions (Figure 6.18) and also on the interaction with externally applied loads, such thick slabs might also be affected by the development of internal cracks. For thinner elements, such high tensile thermal stresses as those obtained here (maximum peak values of approximately *30 MPa* for *0.3 m* and *0.5 m* thick slabs) seem to indicate that even extremely stiff support conditions might not be enough to avoid the development of internal cracks.

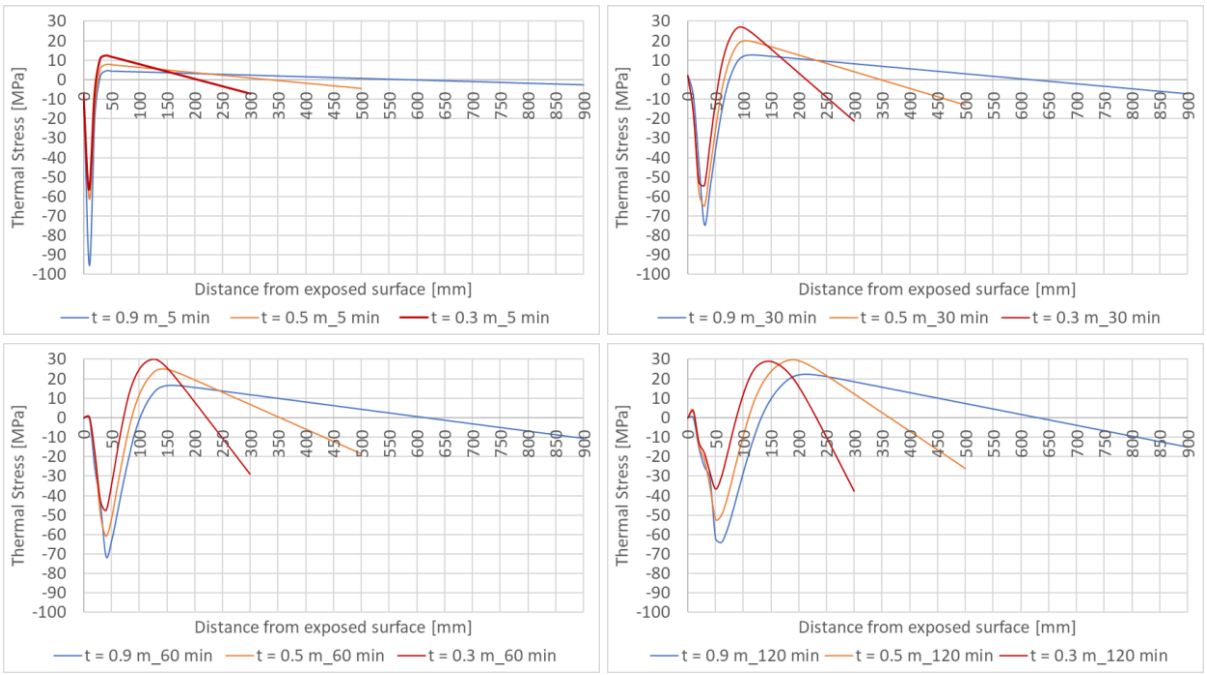


FIGURE 6.26 – EVOLUTION OF THERMAL STRESS IN TIME FOR DIFFERENT SLAB THICKNESSES

6.6.5 Plane Stress Versus Plane Strain

All FE models studied in Section 6.6 were developed considering a *plane stress* state. The latter is often used to describe thin elements loaded in-plane, where there are no restrictions to the out-of-plane deformation. Thus, only in-plane stresses will develop in such models, which are assumed constant across the thickness of the element. This *plane stress* state is defined below based on Timoshenko and Goodier [87]:

$$\begin{bmatrix}\sigma_{xx}\\ \sigma_{yy}\\ \sigma_{xy}\end{bmatrix} = \frac{E}{1-\nu^2}\begin{bmatrix}1 & \nu & 0\\ \nu & 1 & 0\\ 0 & 0 & (1-\nu)/2\end{bmatrix}\begin{pmatrix}\varepsilon_{xx}\\ \varepsilon_{yy}\\ \gamma_{xy}\end{pmatrix} \qquad 6.15$$

with

$$\sigma_{zz} = 0 \qquad \sigma_{zx} = \sigma_{yz} = 0$$
$$\varepsilon_{zz} = -\frac{\nu}{E}(\sigma_{xx} + \sigma_{yy}) \qquad \gamma_{yz} = \gamma_{zx} = 0$$

For tunnels, however, the dimension in z-direction is exceptionally large. This characterizes a different stress state, known as *plane strain*. For this case, the out-of-plane strains are assumed fully restricted, meaning that stresses will also develop in z-direction. This *plane strain* state is expressed by the equation below (Timoshenko and Goodier [87]):

$$\begin{bmatrix}\sigma_{xx}\\ \sigma_{yy}\\ \sigma_{xy}\end{bmatrix} = \frac{E}{(1+\nu)(1-2\nu)}\begin{bmatrix}1-\nu & \nu & 0\\ \nu & 1-\nu & 0\\ 0 & 0 & (1-2\nu)/2\end{bmatrix}\begin{pmatrix}\varepsilon_{xx}\\ \varepsilon_{yy}\\ \gamma_{xy}\end{pmatrix} \qquad 6.16$$

with

$$\varepsilon_{zz} = 0 \qquad \gamma_{yz} = \gamma_{zx} = 0$$
$$\sigma_{zz} = \nu\,(\sigma_{xx} + \sigma_{yy}) \qquad \sigma_{yz} = \sigma_{zx} = 0$$

Lottman [83] has shown that the *plane strain* schematization contributes to increase the level of thermal stresses in structures subjected to fire (Figure 6.27). This indicates that the stresses obtained in the study performed in Sections 6.6.1 to 6.6.4 are, in fact, even higher than that which was shown. However, this does not invalidate the qualitative conclusions about the effects of (1) supporting conditions, (2) selected elastic modulus thermal degradation, (3) type of thermal boundary condition and (4) element thickness on the developed thermal stresses in concrete structures subjected to fire.

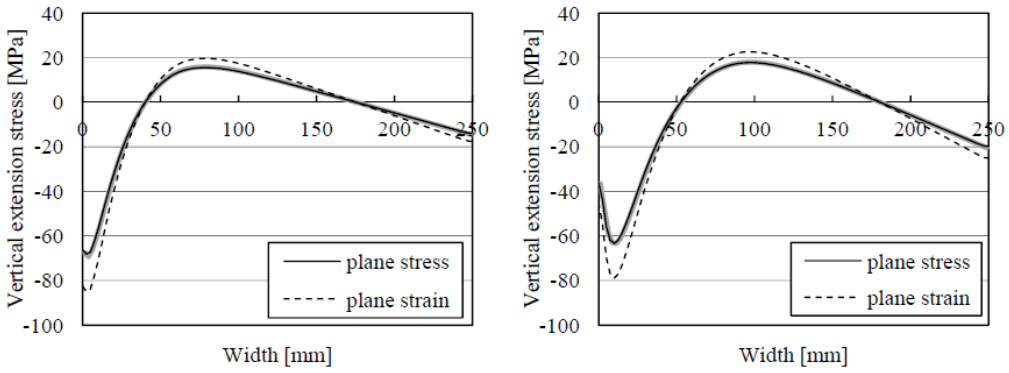


FIGURE 6.27 – INFLUENCE OF SELECTED STRESS STATE IN THERMAL STRESSES
Retrieved from Lottman [83]

6.7 Conclusions

The main conclusions regarding the work developed in this chapter are summarized below:

1) Concrete will suffer irreversible chemical and physical changes due to the high temperatures achieved during a fire. Those changes characterize severe thermal degradation of compressive strength (Figure 6.2), tensile strength (Figure 6.3) and elastic modulus (Figure 6.6), which differ according to the type of concrete (i.e. NSC or HSC).

2) Steep thermal gradients are formed within the concrete structure during a fire (Figure 6.14). Such gradients can be subdivided into three temperature components, namely mean temperature (Section 6.5.1), temperature difference (Section 6.5.2) and eigen temperature (Section 6.5.3). The first two will impose thermal deformations to the structure (i.e. elongation and curvature, respectively). If those deformations are restrained, then thermal stresses will arise in the cross section. The eigen temperature, by definition, will not deform the structure and will always impose thermal stresses. As nonlinear thermal gradients are formed within the concrete structure during a fire, eigen temperatures will always develop, meaning that thermal stresses will inherently occur in concrete structures subjected to fire.

3) As eigen temperatures are self-equilibrating they always impose compression and tensile stresses to the structure (Figure 6.15). The support conditions will define to what extent deformations imposed by mean temperature and by temperature difference are restrained, which defines their contributions to the total thermal stress state. Generally speaking, by increasing the degree of restriction to imposed deformations we reduce the maximum tensile stress while increasing the compressive peak (Figure 6.18).

4) The function selected to represent the thermal degradation of elastic modulus in time (Figure 6.6) has tremendous influence on the achieved thermal stress state (Figure 6.19). In essence, due to the nature of imposed deformations, the stiffer the structure the higher the induced thermal stresses. Therefore, assuming a faster decay rate than that which is actually achieved in reality can be severely misleading. In this sense, the use of Eurocode 2 Part 1-2 [9] to describe the behavior for NSC might lead to unconservative results (Figure 6.4).

5) Using a purely convective boundary condition (equation 5.25) to describe the interface of heat exchange between a fire and a structure will result in severe underestimation of the temperature development of the structure (Figure 6.21 and Figure 6.22). Hence, the correct type of boundary condition when making use of standard fire curves is given by equation 5.26 and considers the combined effect of convection and radiation into the total amount of heat transferred to the structure.

6) It is no simple task to evaluate the structural response of a concrete structure subjected to a tunnel fire. Numerous factors influence the structural behavior of a

fire exposed member (e.g. mechanical properties, thermal properties, support conditions and geometry of the structure). Generally speaking, the occurrence of high compression stresses on the outer layer of the exposed side of the structure is expected (Figure 6.19 and Figure 6.20). Also, according to the support conditions, high tensile stresses might occur (Figure 6.18). This indicates that other types of physical nonlinearities (e.g. crushing and cracking) and even geometrical nonlinearities have to be included in the analysis if the fire damage is to be truly assessed.

7) When analyzing tunnel structures in 2D models, a *plane strain* state should be selected. If a *plane stress* state is chosen instead, one will underestimate the thermal stresses developed within the structure during a tunnel fire.

8) The matter gets much more complex if spalling has also to be numerically quantified. Besides all complexities involved on modelling the phenomenon in itself (e.g. buckling failure, crack propagation and possible pore pressure effects), a new thermal boundary condition will be formed as soon as a piece of the structure spalls (Figure 6.28). To understand why this happens, have a look at equation 5.25. As you can see, the rate of heat supply to the structure is dependent on the surface temperature of the structure itself. Assuming the fire conditions are kept unchanged, once a piece is spalled from the structure, a new surface, at a cooler temperature, will be exposed to fire. As a consequence, the temperature difference between the fire phase and the structure increases and heat absorption will be once again enhanced. Therefore, the driving "force" behind the occurrence of spalling is somehow renewed every time a piece of the structure is spalled, which might explain the continuous nature of the phenomenon.

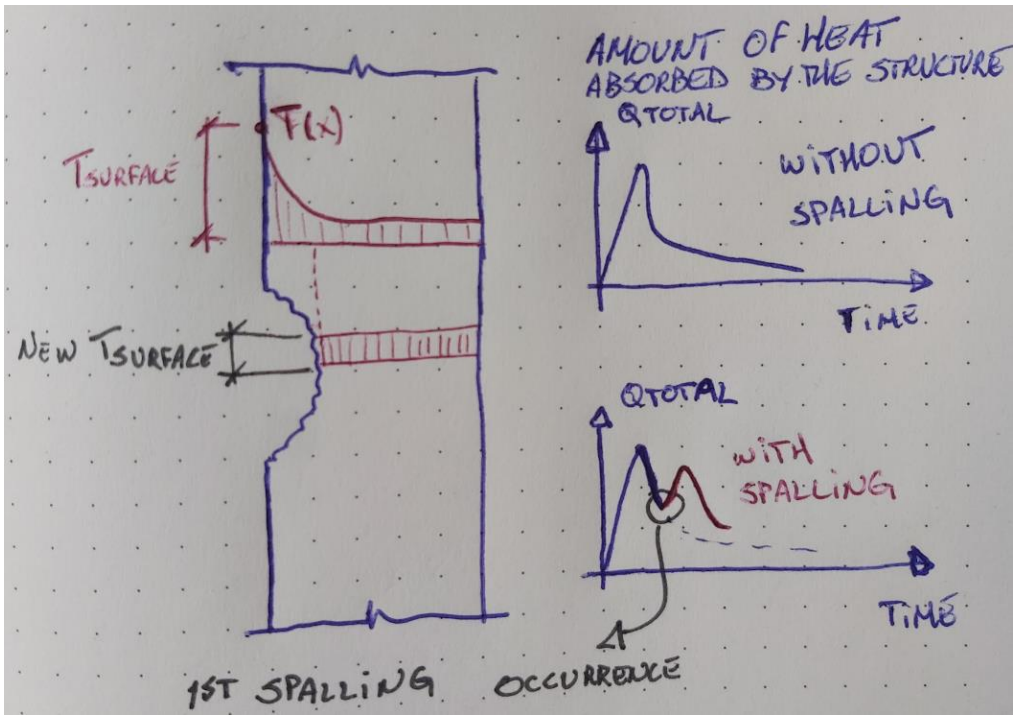


FIGURE 6.28 – CHANGE IN THERMAL BOUNDARY CONDITION DUE TO SPALLING

7 RWS Tests and Numerical Simulations

This chapter aims at investigating the tests which based the development of the RWS fire curve. At first, a full description of the original test setup is provided, and the results are analyzed. Then, a numerical simulation of this test, performed by RWS itself, is discussed. Finally, the FDS models developed in this thesis, also to simulate the RWS test, are explained together with the limitations and assumptions involved in developing those models.

7.1 Introduction

In 1979, the *Ministerie van Infrastructuur en Waterstaat* (RWS) hired TNO (the Netherlands Organization for Applied Scientific Research) to verify the capability of two insulation materials in protecting concrete during a severe gasoline fire [88]. In 1980, once again by order of RWS, TNO repeated this first test in order to confirm the efficiency of one of the previous types of insulation, and also to verify the capacity of a third insulation material [89]. From now on, those tests will be referred to as RWS 1979 [88] and RWS 1980 [89], respectively. The RWS fire curve (Figure 7.1) was developed based on temperature measurements of those tests, and is expected to represent a severe fire due to a leaking gasoline tanker truck. A simple description of this intended fire scenario is given by RWS 2003 [90]:

- Assume a *50 m^3* gasoline tanker truck loaded at *90%* of its full capacity. This would yield in a total fire load of *45 m^3* of gasoline.
- The specific density of gasoline is: $\rho_{gasoline} = 720\ \mathrm{kg/m^3}$
- The effective heat of combustion of gasoline is: $\Delta H_{c,gasoline} = 43.5\ \mathrm{MJ/kg}$

Now, if an average fire capacity of 200 MW is considered then, the total burning time (t_b) would be equal to:

$$t_b = \frac{45\ x\ 720\ x\ 43.5}{200} = 7047\ sec \rightarrow t_b = 118\ min$$

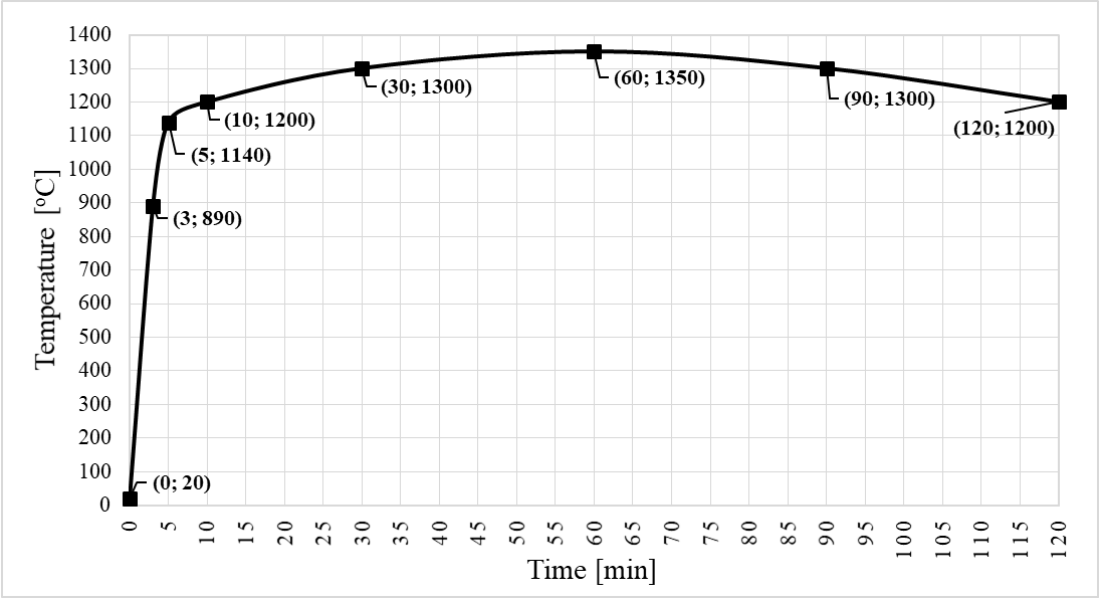


FIGURE 7.1 – RWS CURVE

7.2 RWS Tests

7.2.1 RWS 1979

As previously described, in 1979, TNO was hired by RWS to examine whether the insulation materials HOECO FII/I and CAFCO D C/F would be able to protect concrete tunnels against gasoline fires. A simple description of these materials is given below:

5) *HOECO FII/I:* This is a fire coating consisted of mineral fibers and binding agents which also contains surcharges that react at high temperatures, thus preventing segregation. It is applied in a single sprayed layer, up to the required thickness.

6) *CAFCO D C/F:* This is a cladding material that consists of mineral fibers and binders, and also includes surcharges that prevent unmixing and improve processing. It is applied entirely mechanically in two separate layers. The first one serves as an adhesive layer, while the second represents the real insulation layer. The latter is sprayed on top of the adhesive layer in a single process.

7.2.1.1 Tunnel

A tunnel of limited dimensions was constructed for the test (Figure 7.2). It was 8 m long and had a squared cross section of 2 m *x* 2 m (internal dimensions). On one side, the tunnel had an open end of approximately 1.5 m outside the building. On the other side, it ended in a room of internal dimensions of 3 m *x* 3 m *x* 2.5 m (length *x* width *x* height), connected in the end to a corridor of 2 m *x* 1 m *x* 2 m. The corridor also had an open end of about 1.5 m outside the building. Therefore, the tunnel had both ends directly in contact with the open environment.

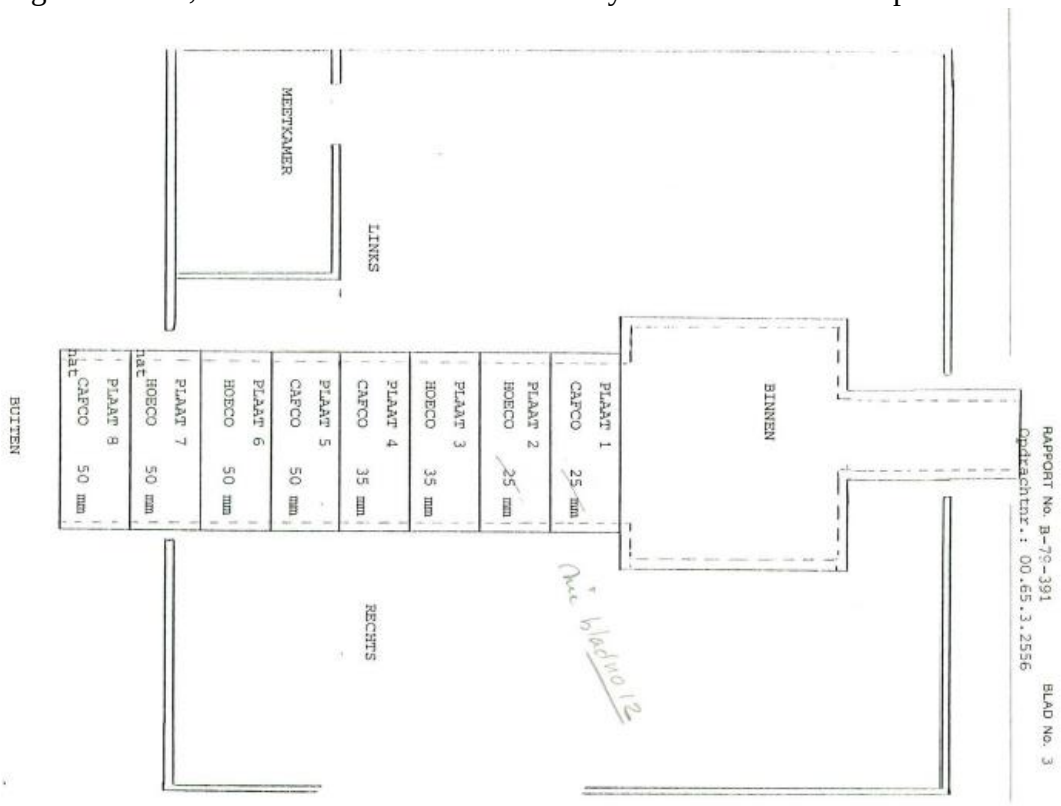


FIGURE 7.2 – TOP VIEW OF RWS 1979 TEST SETUP
Retrieved from RWS 1979 [88]

The tunnel ceiling was composed of eight 150 mm thick concrete slabs of 2.5 m *x* 1 m (width *x* length). Each one of those slabs was covered by a single insulation material, whose thicknesses varied per slab (Figure 7.2). The tunnel walls were made of 240 mm thick concrete gas-block bricks. To ensure sufficient air would always be available for combustion, *30 openings* at a height of 0.5 m were created on the right wall (Figure 7.3). Each one of those openings had an area of 150 mm *x* 100 mm (width *x* height).



FIGURE 7.3 – SIDE VIEW OF THE RWS TUNNEL

7.2.1.2 Fire Load

During the test, regular gasoline was constantly and uniformly supplied to four identical 70 mm deep steel containers (Figure 7.4). These trays had a squared bottom of 800 mm *x* 800 mm, which ended in sloping edges at an angle of 45 degrees. Accordingly, the area of the containers increased in height up to a maximum of 940 mm *x* 940 mm. Therefore, if the supply of fuel would increase during the test, then, the amount of fuel being burned would also increase, avoiding any overflowing of unburned fuel from the steel bins.

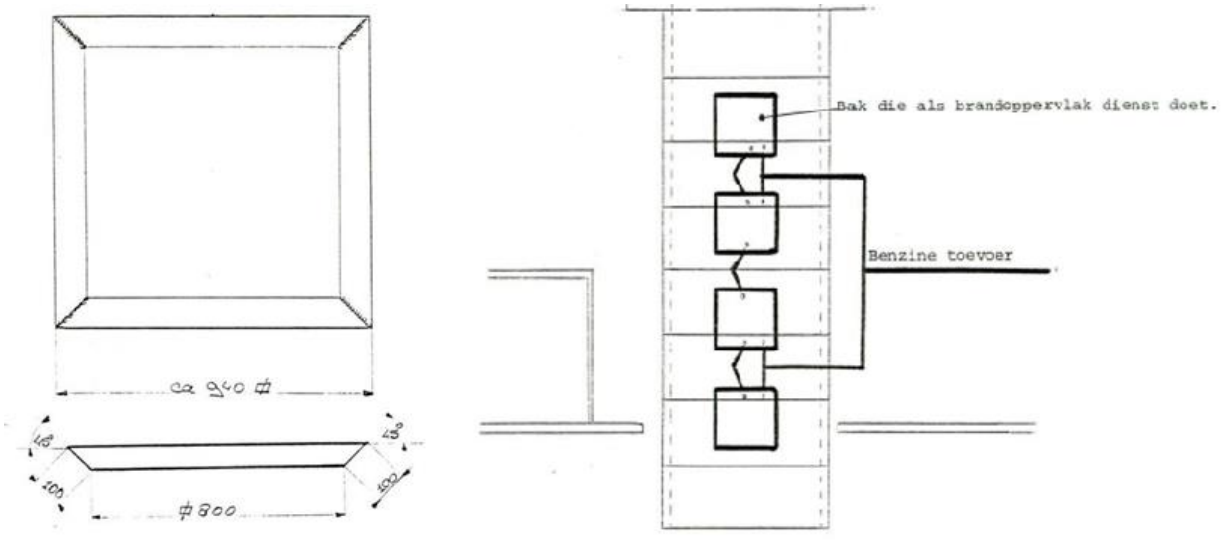


FIGURE 7.4 – STEEL CONTAINERS AND ARRANGEMENT IN THE TUNNEL
Retrieved from RWS 1979 [88]

The four containers were centrally installed in the tunnel at a height of approximately 0.5 m from the floor, and with a gap of approximately 0.65 m between each other (Figure 7.4). In total *1500 liters* of gasoline were burned in *115 minutes*, yielding in an average consumption of approximately *3.26 l/min per bin*. Figure 7.5 below highlights one of the pool fires achieved during the test.



FIGURE 7.5 – POOL FIRE DURING THE RWS TEST
Retrieved from RWS 1979 [88]

7.2.1.3 Temperature Measurements

Nine thermocouples were installed inside the tunnel to record the temperatures achieved during the test (Figure 7.6). Thermocouples 1 to 8 were positioned 0.3 m away from the walls, and 0.1 m below the ceiling. Thermocouple 9 was positioned inside a cable duct located in the middle of the tunnel and is not of interest for the scope of this thesis. The measurement range of these thermocouples was limited to *1200 ºC*.

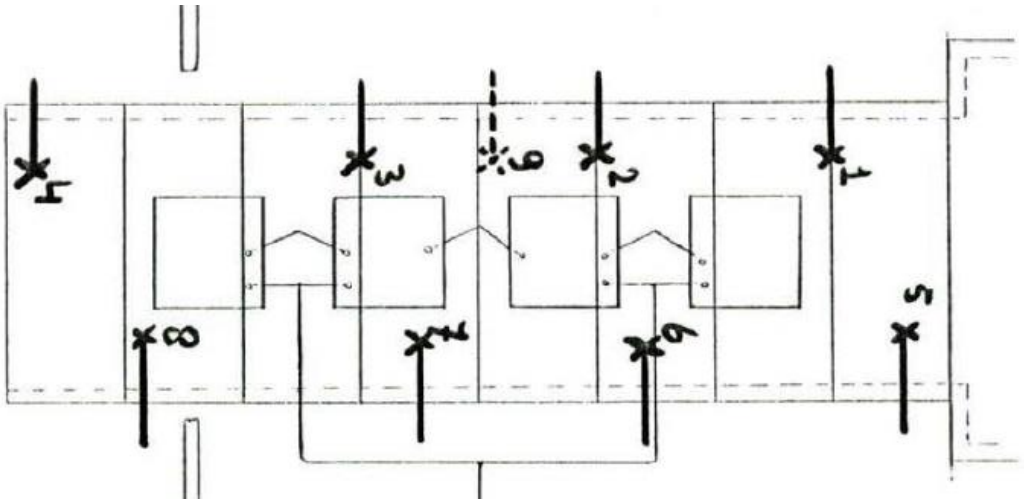


FIGURE 7.6 – LOCATION OF THERMOCOUPLES IN THE RWS 1979 TEST
Retrieved from RWS 1979 [88]

No mention was made about the kind of thermocouples used to collect temperatures inside the tunnel. Nonetheless, based on Figure 7.7, *wire thermocouples* appear to have been used during the RWS tests. Figure 7.8 provides the working principle of this type of thermocouple. According to Goldstein et al. [91], this device consists of a thermoelectric system, formed by

a reference junction and a measuring junction. The electrical circuit is created by the use of two dissimilar metals. An electromotive force is generated whenever a temperature difference exists between these two junctions. As the temperature in the reference junction is known, the temperature at the measuring junction becomes only a function of the formed electrical circuit. The latter is governed by the thermal properties of the metals used at the junction, which also defines the level of accuracy of the measurements. The use of *wire thermocouples* is an important aspect about the RWS tests and will be further discussed in Section 7.3.

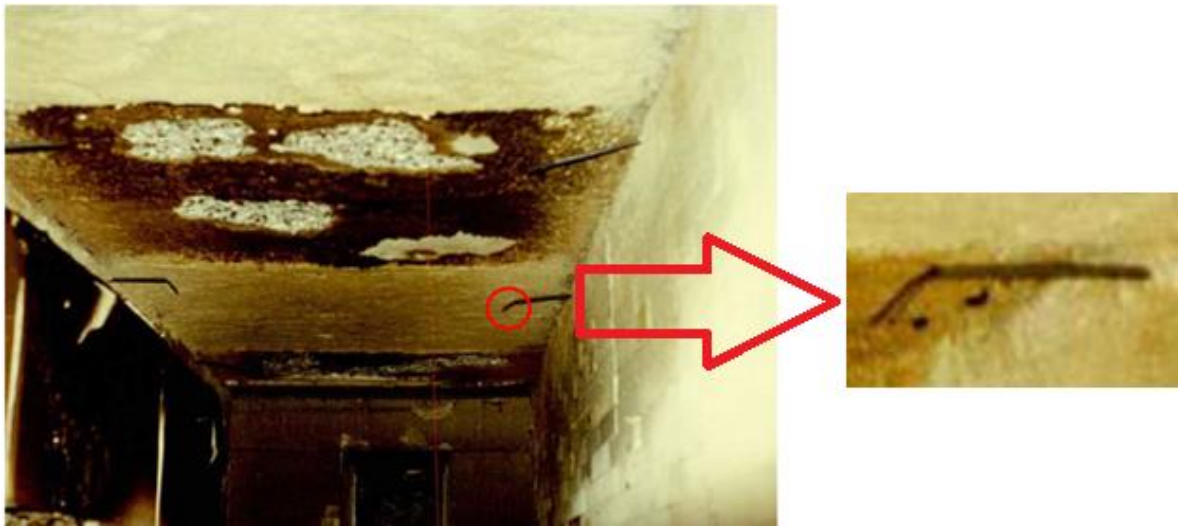


FIGURE 7.7 – WIRE THERMOCOUPLES
Retrieved from RWS 1979 [88]

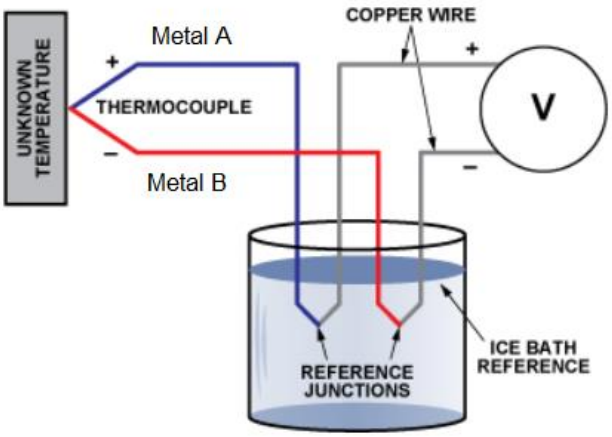


FIGURE 7.8 – WORKING PRINCIPLE OF WIRE THERMOCOUPLES[7]

The temperature measurements recorded by thermocouples 1 to 8 (Figure 7.6) during the test are provided by Figure 7.9 in comparison with the RWS curve. It is important to highlight that thermocouple 4 failed during the test, so its measurements were not included in the original report [88]. Also, note that the temperature measurements obtained by most thermocouples in

[7] https://www.analog.com/en/analog-dialogue/articles/measuring-temp-using-thermocouples.html

this test were limited by the upper capacity of the thermocouples (*1200 °C*). This is the reason why RWS performed a similar test in 1980 (Section 7.2.2).

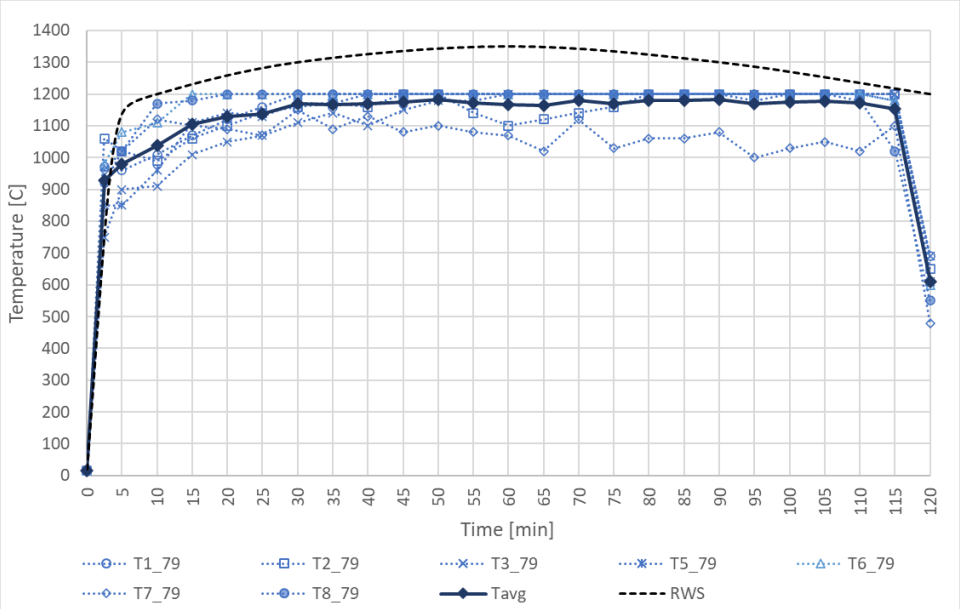


FIGURE 7.9 – GAS TEMPERATURE MEASUREMENTS IN RWS 1979 TEST
Derived from RWS 1979 [88]

Besides the thermocouples described above (T1 to T8), which were used to record gas temperatures in the tunnel, there were also thermocouples placed inside the concrete slabs to monitor the temperature profile of the tunnel ceiling (Figure 7.10). In total, there were eleven thermocouples embedded inside each slab: (1) three were located on the bottom interface between concrete and insulation; (2) three were placed 2.5 cm inside concrete, against the bottom slab reinforcement; (3) three were placed 10 cm inside concrete; and (4) two were placed on top of each slab. Those measurements were of importance in the evaluation of the performance of the tested insulation materials, but are not relevant for the scope of this thesis as the interface between the gas phase generated by the pool fires and the ceiling is describe by the thermal properties of the insulation materials used to protect the concrete slab. Thus, the measurements of the thermocouples located inside the concrete ceiling are omitted here.



FIGURE 7.10 – THERMOCOUPLES INSIDE CONCRETE SLAB
Retrieved from RWS 1979 [88]

7.2.2 RWS 1980

In 1980, TNO repeated the same test described in Section 7.2.1. The test setup was kept nearly identical, but a few changes apply:

1) As CAFCO D C/F insulation failed considerably in RWS 1979 [88], it was substituted by a different insulation material (PYROK) in RWS 1980 [89]. Accordingly:

a. PYROK: This is a spray plaster applied mechanically in several layers. Each layer involves a separate treatment in which a special adhesive made of a cement-rich mortar is applied in a layer of approximately 2 mm, between two insulation layers with a maximum thickness of 7 mm each. The process is repeated until the desired total insulation thickness is reached.

2) In this new test, one of the slabs (number 8 in Figure 7.11) was kept partially unprotected. Moreover, the thermocouples on the bottom of this slab were recording the surface temperature of concrete in direct contact with the hot gases at the ceiling.

3) The same amount of fuel was burned (*1500 liters* of gasoline), but in RWS 1980 [89] the total burning time was reduced to *100 minutes*. This gives an average burning rate of *3.75 l/min per bin*, which is ~15% higher than in the first test.

4) Nine thermocouples were placed on the ceiling to monitor gas temperatures inside the tunnel. They are once again located 0.3 m away from the walls and 0.1 m below the ceiling. There was no reference about the range of operation of the thermocouples used in this new test, but temperatures above *1200 ^{o}C* were measured.

5) Thermocouples 4 and 5 were placed side by side (Figure 7.11), with thermocouple 5 being a digital recorder that was immediately readable during the whole test. Thermocouple 3 was placed inside a cable duct and is not of interest for this thesis.

6) As depicted by the red circles in Figure 7.12, only three thermocouples were kept in the same position as in RWS 1979 [88].

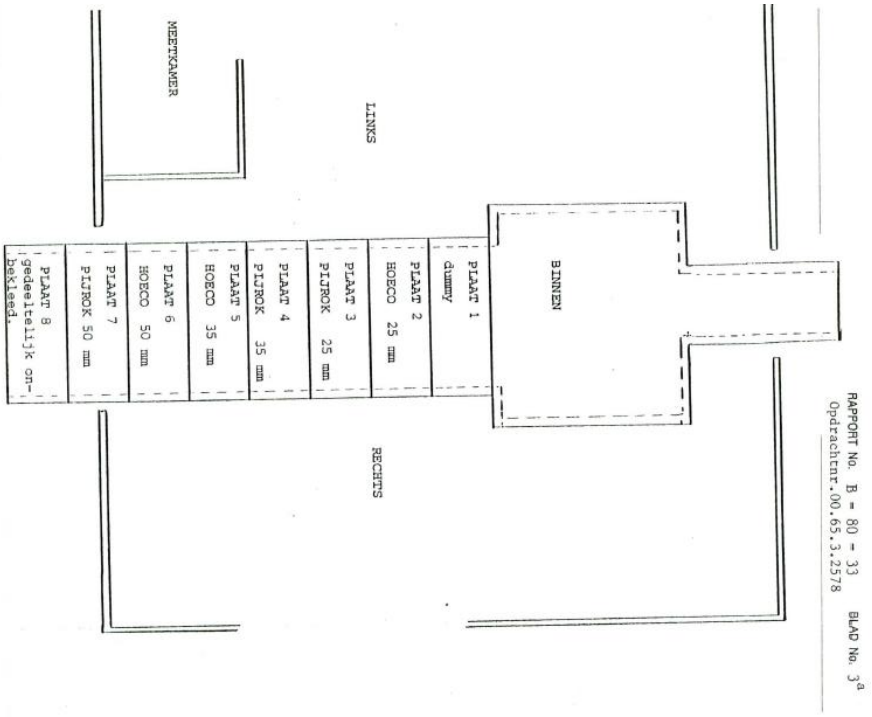


FIGURE 7.11 – RWS 1980 TEST SETUP
Retrieved from RWS 1980 [89]

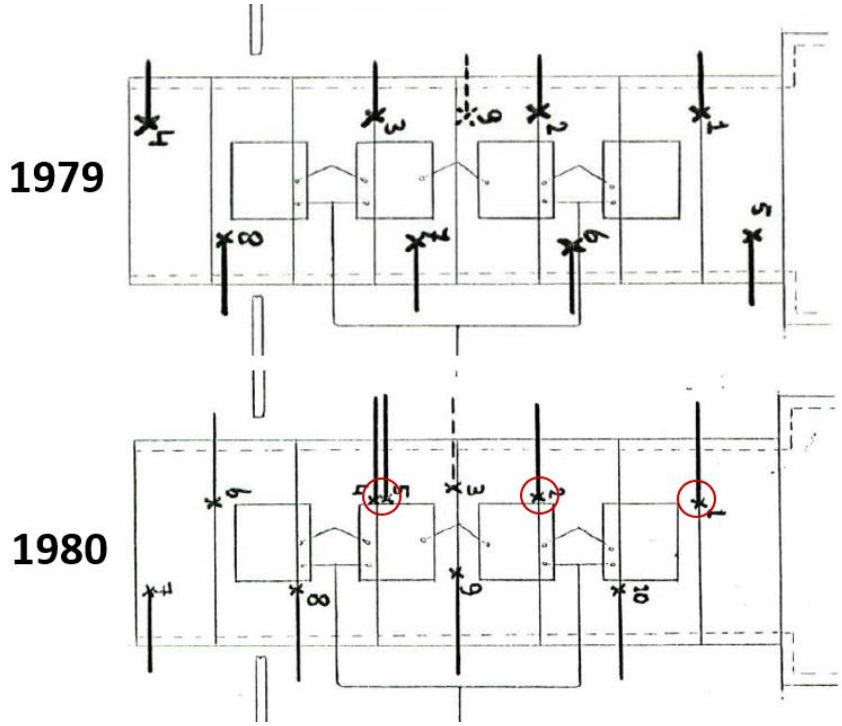


FIGURE 7.12 – COMPARISON OF THERMOCOUPLES IN RWS 1979 AND 1980
Adapted from RWS 1979 and 1980 [88, 89]

7.2.2.1 Temperature Measurements

Figure 7.13 below depicts the gas temperature measurements of RWS 1980 in comparison with the RWS fire curve.

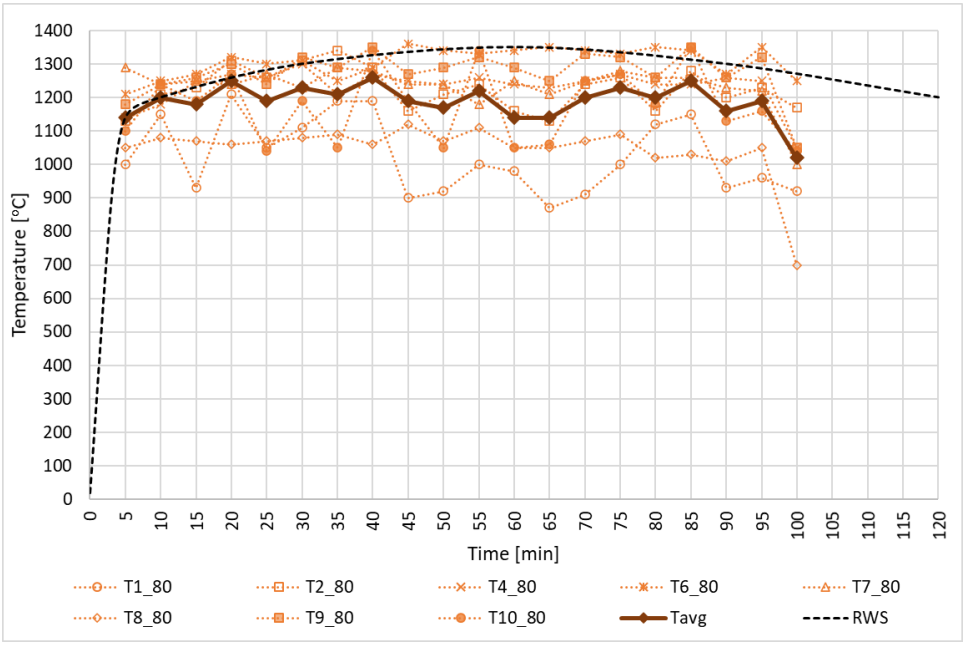


FIGURE 7.13 – GAS TEMPERATURE MEASUREMENTS IN RWS 1980 TEST
Derived from RWS 1980 [89]

When Figure 7.9 and Figure 7.13 are compared against each other, it is clear that the RWS curve is a result of temperature measurements obtained during RWS 1980 [89]. Not only that,

as shown by Figure 7.14, it appears to be derived out of temperature measurements of only two thermocouples, namely T6 and T9 in Figure 7.12. Note that the average temperature obtained in RWS 1980 [89] is clearly around *1200 ºC* (Figure 7.13). This certainly raises the question of how representative the curve really is on describing the results obtained during the test itself.

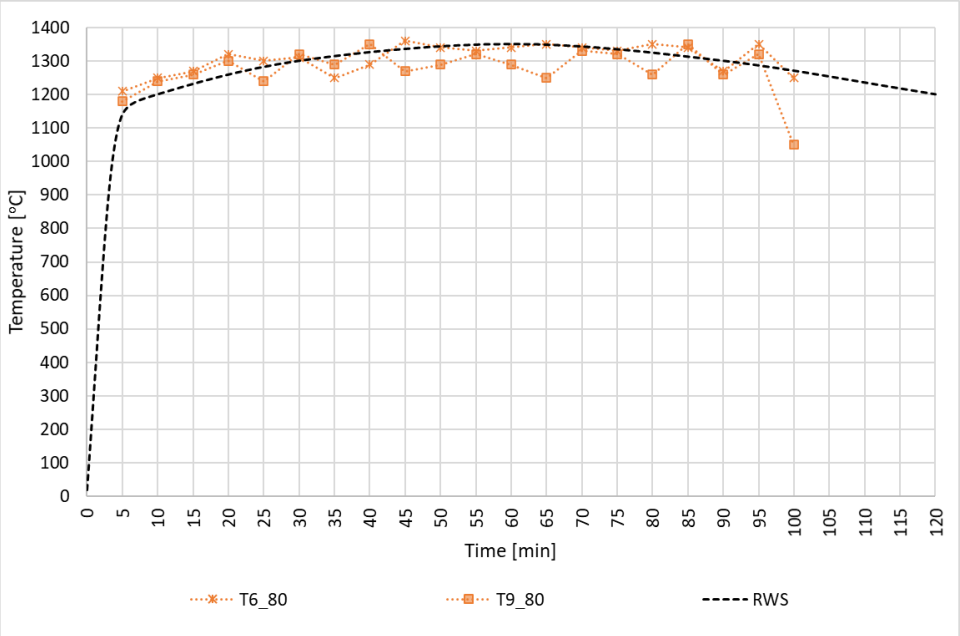


FIGURE 7.14 – POSSIBLE RWS CURVE DERIVATION
Derived from RWS 1980 [89]

7.2.3 Comparison between RWS 1979 and RWS 1980

As explained previously in Section 7.2.2, only three thermocouples in RWS 1980 [89] were positioned in the same place as in RWS 1979 [88]. Figure 7.15 provides a comparison between those measurements in both tests, and also between the average temperature development in time. Clearly, the beginning of fire was more pronounced in RWS 1980, where higher temperatures were achieved specially during the first *30 minutes*. This might indicate that in RWS 1980 more fuel was burned during this first stage, and that could be the reason for a reduction in the total burning time achieved for the second test (*100 minutes* against *115 minutes* in the former). After this first stage, the results become rather similar between both tests, excluding those of thermocouple T1. This comparison is of course limited by the fact that in RWS 1979 [88], the thermocouple measurement capacity was limited to *1200 ºC*.

The difference between the results for measurements of thermocouple T1 in 1979 and in 1980 are, according to the report of RWS 1980 [89], due to wind effects. As depicted in the same report, the burning conditions were virtually the same for both tests, but in the second one the wind direction was more focused from the back of the tunnel to the front or, in other words, from thermocouple T1 to thermocouple T6 (Figure 7.12). This is also assumed to explain the smaller temperatures measured by T1 and the higher temperatures measured by T6 during the second test (Figure 7.16).

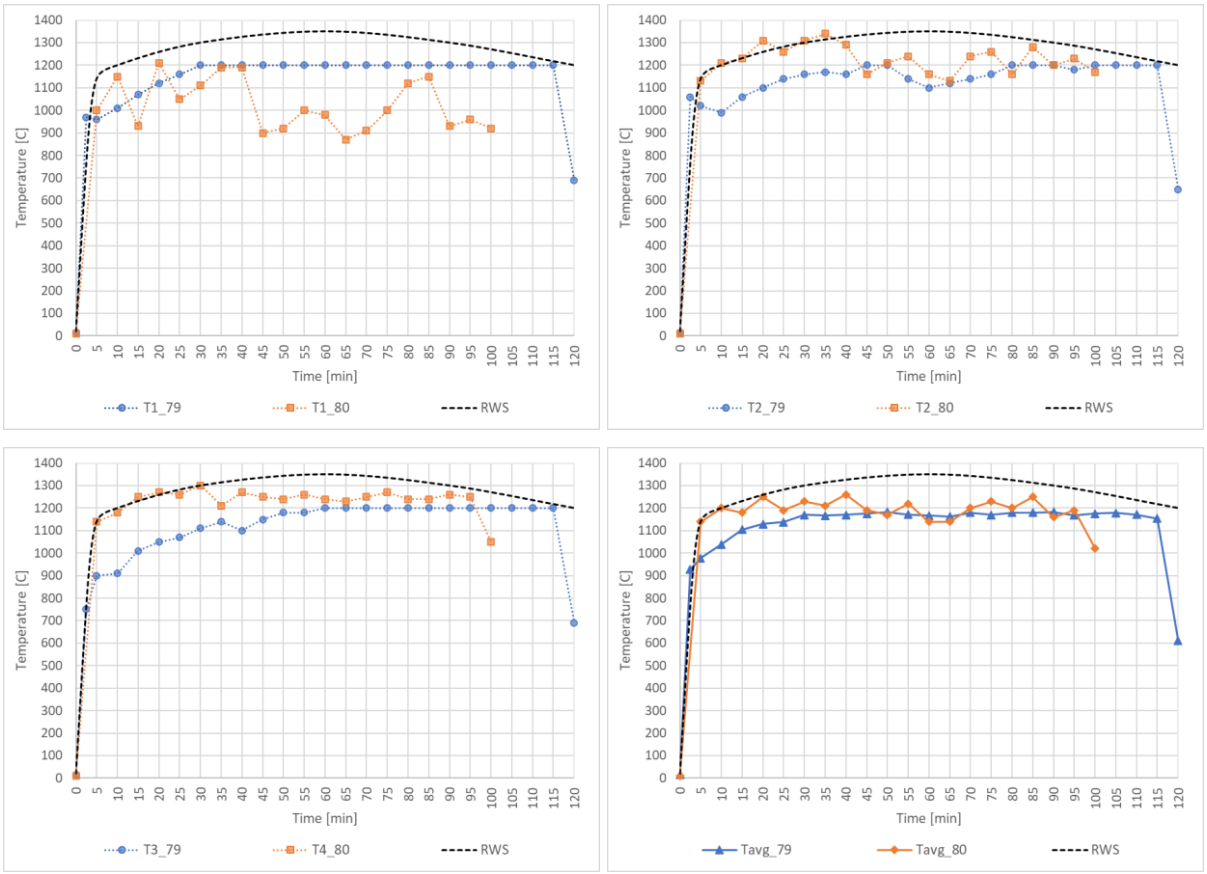


FIGURE 7.15 – COMPARISON OF MEASUREMENTS IN RWS 1979 AND 1980
Derived from RWS 1979 and RWS 1980 [88, 89]

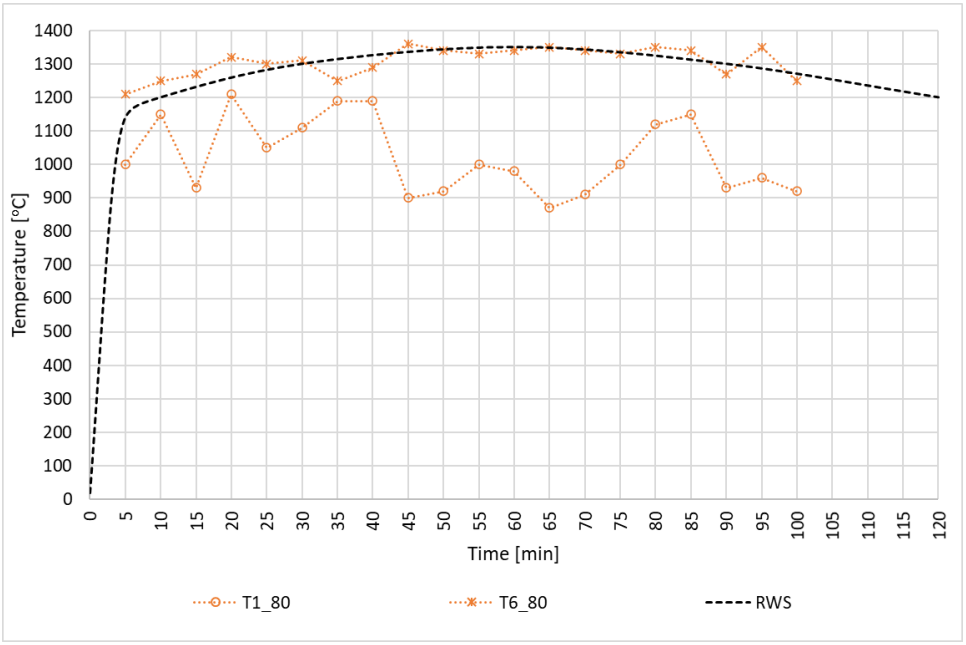


FIGURE 7.16 – T1 AND T6 IN RWS 1980
Derived from RWS 1980 [89]

7.2.4 Numerical Simulation of RWS Test by RWS

In 2003, RWS carried out CFD calculations to predict and assess the results of fire tests performed in the 2nd Benelux tunnel [90]. During this study, the RWS tests described previously (Sections 7.2.1 and 7.2.2) were also modeled. Figure 7.17 shows the FDS model used in this simulation. A brief description of the information available in RWS 2003 [90], together with the related uncertainties about this model are given below:

1) *Fire Load:* The source was simulated by four pans of 800 mm *x* 800 mm each or, the smallest area of the steel containers used during the RWS tests (Section 7.2.1.2). The type of fuel used in the simulation was not mentioned. The report also lacks information about the boundary condition used to prescribe the amount of fuel supplied into the domain during the fire simulation.

2) *Tunnel geometry*: The full test setup described in Section 7.2.1.1 was included in the simulation. Nonetheless, the ceiling of the tunnel was simulated only by the heat-resistant cladding material, meaning that the model did not include a concrete slab on top of the insulation. No information is provided regarding the thermal properties assigned to the ceiling or to the walls of the RWS tunnel.

3) *Domain of Simulation:* At least with regard to Figure 7.17, it appears that the simulation domain was limited to the outer edges of the tunnel. Also, it seems that *open* boundary conditions were assigned to the top and sides of the computational domain.

4) *Measurements:* Also based on Figure 7.17, it is possible to notice that the thermocouples were simulated through devices placed inside the domain of simulation. In FDS, those can be: (1) devices which collect mean cell gas temperatures; or (2) special devices that simulate a thermocouple, and thus collect the temperature in time of a small nickel sphere located at the assigned position. Either way, the temperatures generated by the simulation should be comparable to the gas temperature measurements achieved during the RWS tests (Section 7.2.1.3).

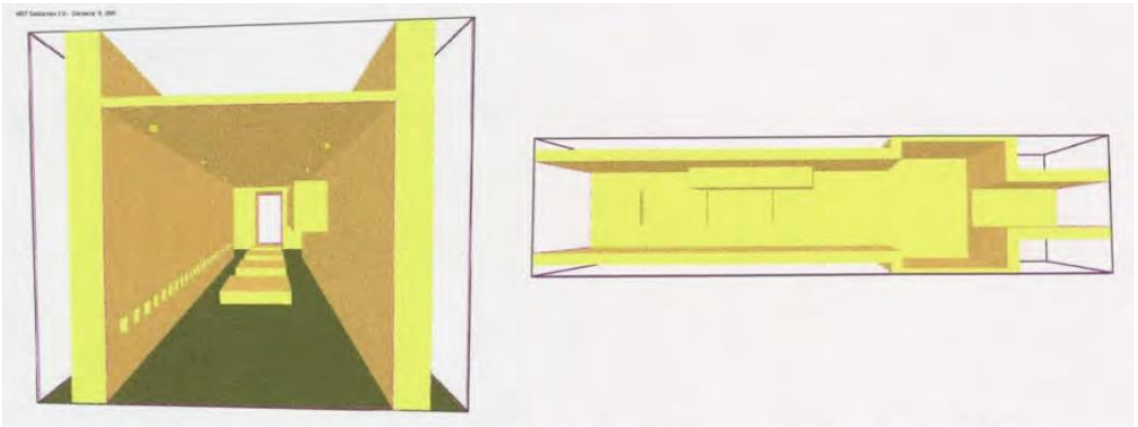


FIGURE 7.17 – FDS MODEL OF RWS TEST
Retrieved from RWS 2003 [90]

7.2.4.1 HRR

Figure 7.18 shows that the HRR obtained in this simulation reached a maximum fire power of 6 MW almost immediately. After that, it appears to be kept nearly constant through the whole simulation. Also, approximately half of the energy released in the simulation was transferred inside the domain through radiation.

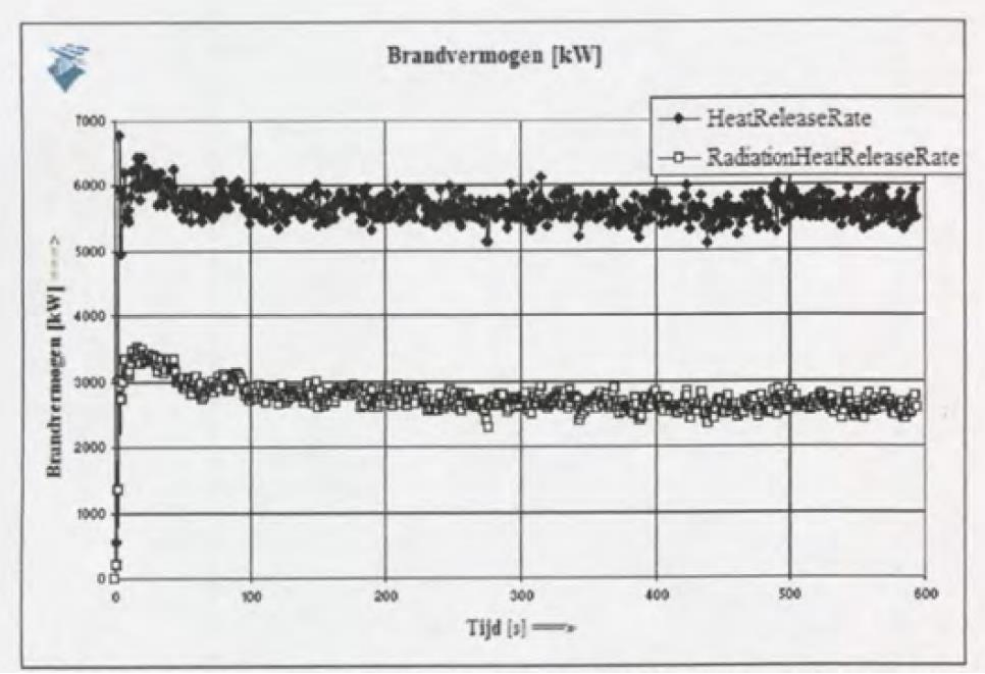


FIGURE 7.18 – HRR (WITH HOLES)
Retrieved from RWS 2003 [90]

7.2.4.2 Temperature Measurements

Figure 7.19 gives the temperature development of the simulated thermocouples in time. It can be seen that after *100 seconds* the temperatures in the tunnel are nearly constant at *1200 ^oC* until the end of the simulation at *600 seconds*, or *10 minutes*. Note that thermocouple 3 is located below the cable duct and is not of interest for this thesis.

Considering the total time of fire simulation, the measured temperatures in RWS 1979 [88] average for nearly *1000 ^oC* (Figure 7.9). When compared to the results of RWS 1980 [89], the simulation performs quite well, as the measurements obtained during the test are indeed averaging for *1200 ^oC* after *10 minutes* of fire (Figure 7.13). Nonetheless, one should keep in mind that the fire power inputted into this simulation might have had an important role in the obtained results. Basically, based on Figure 7.18 we can conclude that during the simulation, fire was almost instantaneously introduced with full power into the domain, and rather steady state conditions were already reached after *5 minutes* of fire. In reality this was clearly not the case. The results of RWS 1980 [89] lack data about the development of HRR in time at the early stage of fire development, since the first temperature measurements are given only after *5 minutes* of the beginning of the test. This makes it impossible to infer conclusions on how fast fire actually grew in reality. Even so, it is clear that temperatures were still rising after *10 minutes* of fire (Figure 7.13).

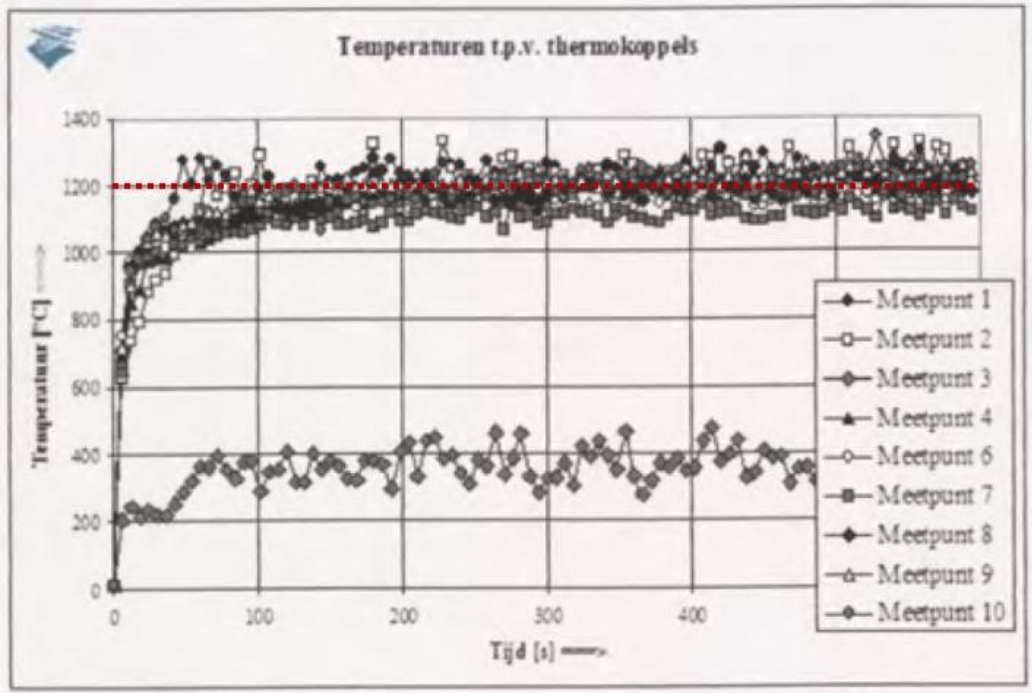


FIGURE 7.19 – TEMPERATURE DEVELOPMENT (WITH HOLES)
Adapted from RWS 2003 [90]

7.2.4.3 Effect of Holes

It is reported in RWS 2003 [90] that the holes on the wall had a significant impact on the temperature development inside the tunnel. Nonetheless, the results provided in Figure 7.20 indicate a difference only of around *100 °C* for the cases *with* (red line) and *without holes* (yellow line).

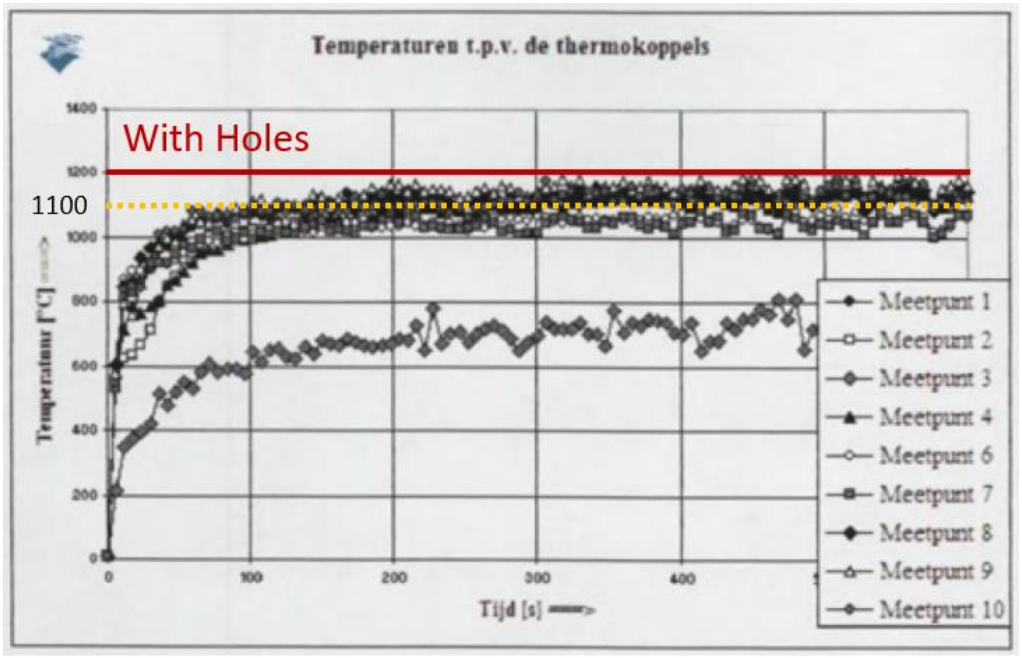


FIGURE 7.20 – TEMPERATURE DEVELOPMENT (WITHOUT HOLES)
Adapted from RWS 2003 [90]

Figure 7.21 shows the HRR in time for the simulation *without holes* (yellow line). As expected, there was a reduction of around 0.5 MW on the maximum HRR achieved when compared to the same case when including *holes* (red line).

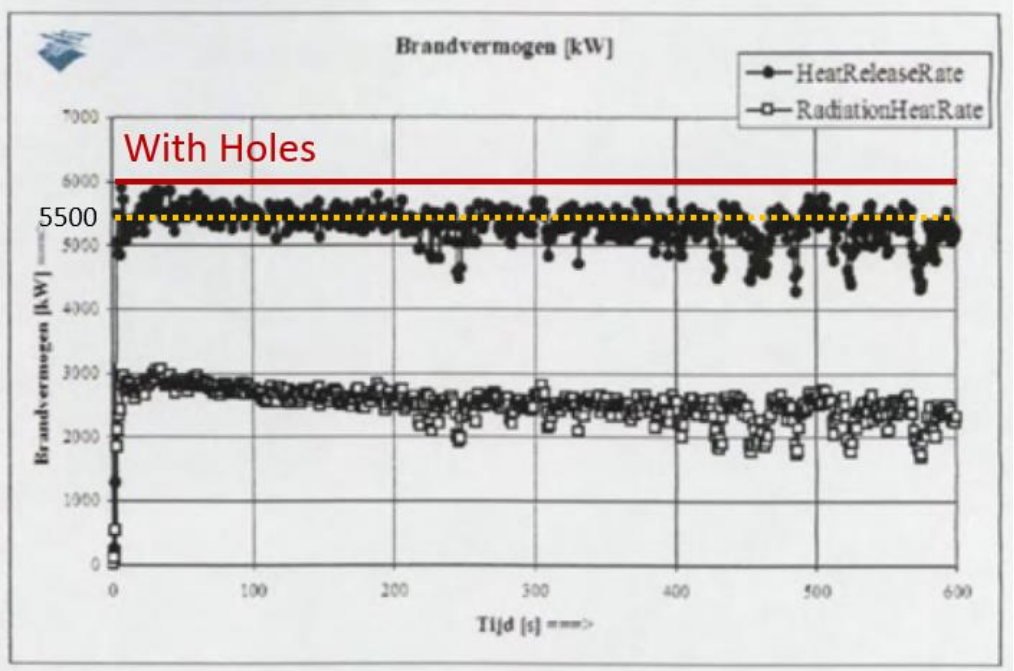


FIGURE 7.21 – HRR (WITHOUT HOLES)
Adapted from RWS 2003 [90]

7.3 Temperatures Measured during the RWS Tests

Considering the magnitude of temperatures measured during the RWS tests, we know that the radiation contribution was certainly governing the heat exposure to the ceiling of the tunnel (Section 5.1.3.2). Thus, to understand if those temperature measurements were really representative on describing the thermal exposure which was imposed onto the ceiling structure, it becomes fundamental to understand the kind of temperatures (gas or radiation) that were really collected during the test.

As described in Section 7.2.1.3 and shown in Figure 7.7, *wire thermocouples* were used during the RWS tests. Byström et al. [92] explain that this type of thermocouple consists of a very small body, often less than a few millimeters. According to basic heat transfer theory, such small bodies have large convection heat transfer coefficient (i.e. h in equation 5.5), and will be more susceptible to heat transferred through convection than radiation. In other words, the thermocouples used during the RWS tests are expected to reflect on the real gas temperatures achieved inside the tunnel. If this was indeed the case, then the RWS curve, which was derived out of those temperature measurements, might not be representative on describing the real heat exposure suffered by the structure during a tunnel fire. Moreover, at least from a structural point of view, the AST (Section 5.3.3.3) is the temperature that should have been tracked during the test, and as we know, for fires it is governed by the radiation component (the radiation temperature in equation 5.11).

It is possible to measure the AST in a test through the use of *plate thermometers* (PT), also described by Byström et al. [92]. It might be good to make a distinction between this type of thermometer and the one used during the RWS tests (Section 7.2.1.3), here entitled as TC.

Thus, the PT (Figure 7.22) consists of a *thin steel plate* (such that any heat transferred through conduction can be neglected), which is insulated on the back side. The temperature of the steel plate is recorded through a TC welded also to the back side of the plate. The PT should then be positioned parallel to the surface with its insulated back facing the surface of the structure, such that the radiation emitted from the structure itself will not affect the temperature measurements collected by this device.

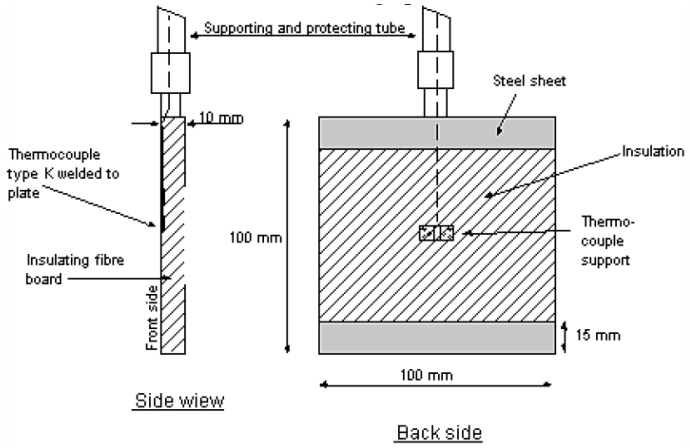


FIGURE 7.22 – PLATE THERMOMETER
Retrieved from Byström et al. [92]

In reality, both the PT and the TC are affected by heat transferred through radiation and convection within the enclosure. With that in mind, imagine the scenario in which a regular TC and a PT are placed side by side such that they suffer exactly the same exposure. Now, assume they both have the same emissivity, making them to be equally affected by radiation. As the TC is much smaller than the PT, it has a convection heat transfer coefficient much larger than that of the PT, making the TC to be much more affected by the gas temperatures (convection component) than the PT. In this hypothetical case, if the radiation temperature is identical to the gas temperature, then both devices should measure the same temperature. Nevertheless, if the radiation temperature is different from the gas temperature at that position, then the PT will approach the radiation temperature while the TC will approach correspondent gas temperature. In the end, both these devices are providing measurements of their own AST. The difference between them lies in the fact that the AST for the TC is closer to the gas temperature (T_g) while the AST for the PT is, as in a structure exposed to fire, will be closer to radiation temperature (T_r).

To prove the point presented in the last paragraph, FDS was used to compare TC and PT measurements with the correspondent T_g and T_{AST} values at the ceiling (Section 7.4.2.4 explains how FDS calculates these temperatures). The simulation performed here is focused on explaining the differences between those two measuring devices (TC and PT). Thus, despite considering the original setup of RWS 1980 [89], in accordance with the models developed in Section 7.4.3, the results shown here in Figure 7.23 and Figure 7.24 should not be compared to the temperature measurements obtained during the real test. This will be done later in Section 7.4.

In FDS, a TC is simulated by a small nickel sphere (Table 7.1) assigned to the position of interest. The temperatures achieved by this sphere during a simulation should represent the

temperatures collected by a TC used in a real test. Ideally, the temperature measured by a TC shall reflect the true gas temperature. Nonetheless, in reality, there is always a lag between those two, with the accuracy of the measurements being determined by the TC's bead diameter. In this sense, TCs of different diameters were studied and the results of their simulated measurements are provided in Figure 7.23 in comparison with the correspondent T_g, T_{AST} and T_r. At first, note that at such high temperatures, T_{AST} is practically the same as T_r, which is in perfect agreement with what was discussed previously in this thesis (Section 5.3.3.3). Now, notice that the measurements of the TCs are clearly more affected by convection heat transfer than the ceiling surface, as even for very big bead diameters (3 mm and 1 cm), the simulated temperatures are evidently above T_{AST}. Finally, notice that the bead diameter is indeed governing the accuracy of the TC measurements in comparison to the correspondent T_g. The results for the TCs with small bead diameters (0.25 mm and 0.50 mm) are basically the same, and deviate in less than 5% from the correspondent T_g at all times during the simulation. For increased bead diameters (3 mm and 1 cm), the predictions of the TCs deteriorate, but are still deviating in less than 10% from the actual T_g.

Parameter	Value
Density	8908 kg/m^3
Specific Heat	0.44 kJ/kg.K
Emissivity	0.85
Bead Diameter	0.25 mm; 0.50 mm; 3 mm; 1cm

TABLE 7.1 – TC'S THERMAL PROPERTIES USED IN FDS

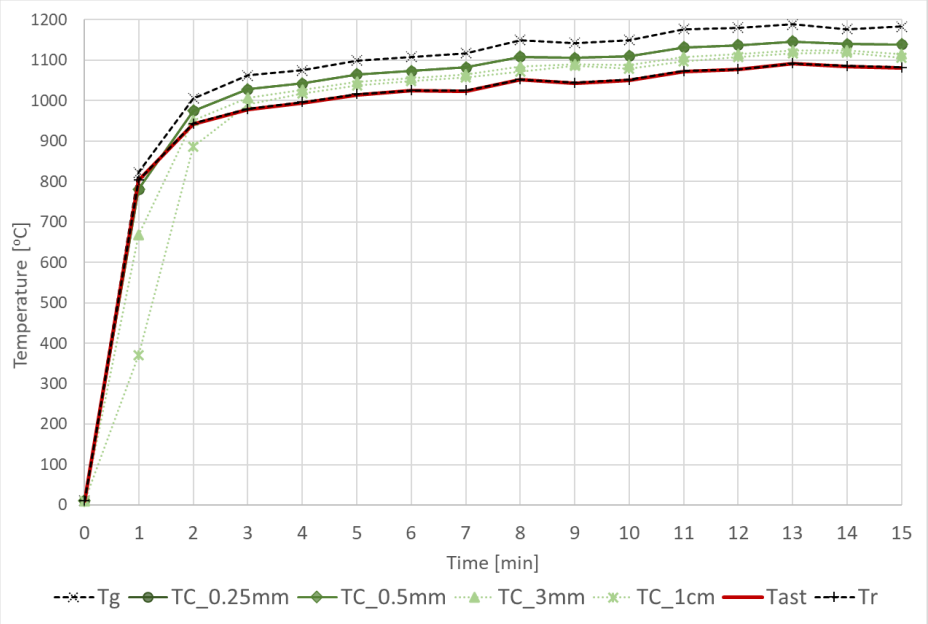


FIGURE 7.23 – SIMULATED TC MEASUREMENTS

Now, let us address the PT measurements for the same simulation. In this case, a PT was simulated in FDS through a thin layer of *Inconel* which was insulated on the back, and its measurements are expressed by the surface temperature of the Inconel plate during the simulation. This representation of a PT is depicted in Table 7.2, and is used for several cases given in *FDS Validation Guide* [93]. Differently from reality though, instead of having an area

of 100 mm *x* 100 mm, in the simulation performed here the PT area was changed to 250 mm *x* 250 mm, which is the minimum area feasible due to the grid size selected. For the purpose of the comparison between TC and PT developed here, this change in the PT area is not expected to have a significant impact on the results, as the trend of measurements obtained for this increased PT should still be representative to describe the temperatures that are measured by a real PT.

Inconel	
Parameter	**Value**
Density	8470 kg/m^3
Emissivity	0.8
Thickness	0.7 mm
Conductivity	
T = 20 ºC	14.9 W/m.K
T = 100 ºC	15.9 W/m.K
T = 200 ºC	17.3 W/m.K
T = 300 ºC	19.0 W/m.K
T = 400 ºC	20.5 W/m.K
T = 500 ºC	22.1 W/m.K
T = 600 ºC	23.9 W/m.K
T = 700 ºC	25.7 W/m.K
T = 800 ºC	27.5 W/m.K
Specific Heat	
T = 20 ºC	0.444 kJ/kg.K
T = 100 ºC	0.465 kJ/kg.K
T = 200 ºC	0.486 kJ/kg.K
T = 300 ºC	0.502 kJ/kg.K
T = 400 ºC	0.519 kJ/kg.K
T = 500 ºC	0.536 kJ/kg.K
T = 600 ºC	0.578 kJ/kg.K
T = 700 ºC	0.595 kJ/kg.K
T = 800 ºC	0.611 kJ/kg.K
T = 900 ºC	0.628 kJ/kg.K
Insulation	
Parameter	**Value**
Density	280 kg/m^3
Emissivity	0.8
Thickness	10 mm
Conductivity	0.1 W/m.K
Specific Heat	1.0 kJ/kg.K

TABLE 7.2 – PT'S THERMAL PROPERTIES USED IN FDS [8]

Figure 7.24 below provides the results for PT measurements in comparison with the correspondent T_g, T_{AST} and T_r. Note that the PT is assigned to the same position as the TCs shown in Figure 7.23. The PT is clearly more affected by heat transferred through radiation,

[8] https://github.com/firemodels/fds/blob/master/Validation/SP_AST/FDS_Input_Files/SP_Room_A1.fds

being able to capture the real heat exposure imposed onto the ceiling structure at the assigned position. Also, note that it takes a bit longer for the PT to react to the heat exposure, and thus start providing reliable measurements (Section 8.2.1). Even so, after *5 minutes* of fire, the PT temperatures are already deviating in less than 5% from the respective T_{AST}.

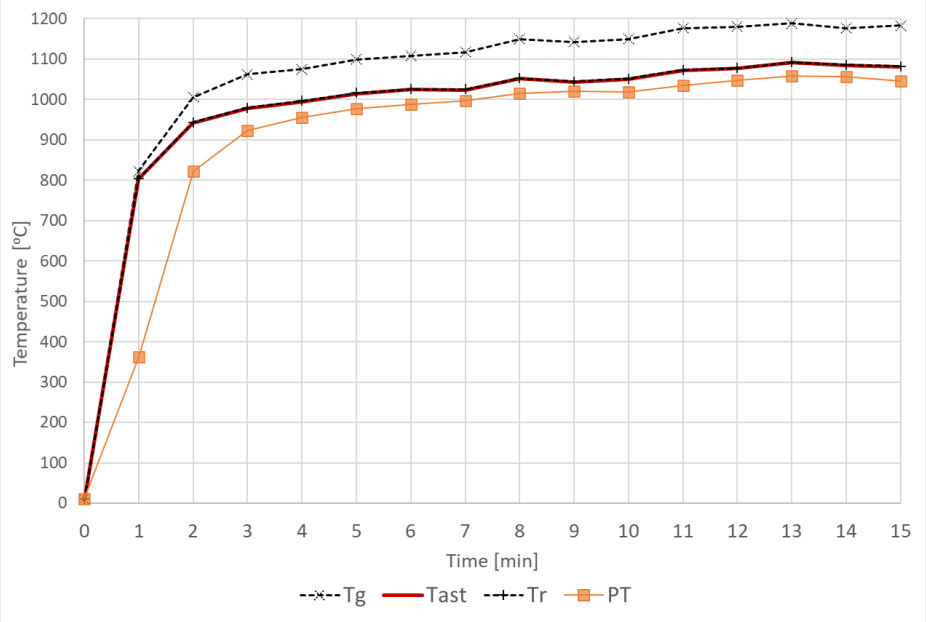


FIGURE 7.24 – SIMULATED PT MEASUREMENTS

The results shown in Figure 7.23 and Figure 7.24, prove that the temperatures collected during the RWS tests are representative in describing the true gas temperatures (T_g) achieved inside the tunnel during the test. Unfortunately, no information is provided about the bead diameter of the *wire thermocouples* used in those tests, making it impossible to make any claims about the accuracy of the temperatures measurements in RWS 1979 [88] and RWS 1980 [89]. Even so, it is confirmed here that the RWS curve is developed based in measurements which might not be representative to describe the heat exposure suffered by the structure during a tunnel fire. In essence, gas temperatures will only truly describe the thermal exposure imposed on a structure if *blackbody* behavior is achieved within the formed flames and/or smoke body (Section 5.1.3.1). For those cases, thermal radiation will be emitted at their maximum levels, and the gas temperature will be equivalent to the radiation temperature. A deeper investigation on this matter is addressed in Sections 7.4 and 7.5.

7.4 Numerical Simulations of RWS Tests

This section serves as an investigation of the RWS tests through numerical simulations in FDS. Here, it will become clear the limitations that are involved in the available test data and their effects on accurately modeling the original tests (Section 7.4.1). A description about FDS modeling is provided in Section 7.4.2, together with the assumptions made when constructing the models. Finally, the models developed here are described in Sections 7.4.3 and 7.4.4. Variations on the original RWS test setup are studied in Section 7.5.

7.4.1 Uncertainties involved in RWS Tests

Very few data are available regarding the RWS tests described in Section 7.2. Basically, the only valuable information that can be found in the original reports [88, 89] are: (1) the geometry of the tunnel; (2) the amount of fuel burned; (3) the total burning time; and (4) the gas temperature measurements in time.

The following uncertainties are worth mentioning:

1) *Type of fuel:* Regular gasoline is reported to be used in both RWS tests. Nonetheless, there is no information with regard to the *effective heat of combustion* (equation 4.2) of the fuel originally used. As depicted in Section 4.1.1, this parameter effectively changes the HRR in the simulation. Also, as shown in Figure 7.4, the burning area achieved in the tests is unknown, making it hard to define a boundary condition for the amount of fuel released into the model during the simulations.

2) *HRR:* The mass loss rate of fuel in time was not measured during the test. This makes it impossible to know the real development of HRR. Another important point here is regarding the early stage of fire growth. In RWS 1979 [88] the first temperature measurement is provided after *2.5 minutes* of fire, while for RWS 1980 [89] it is provided only after *5 minutes*. Thus, it is impossible to make any claims on how long it took for the pool fires used in the test to achieve their full capacity.

3) *Thermal and physical properties of the tunnel:* Excluding the density and moisture of the insulation layer applied on the concrete ceiling (Figure 7.11), the report lacks information regarding the thermal properties of all materials used in the RWS tunnel.

4) *Ventilation conditions:* The RWS tests did not apply any mechanical ventilation in the tunnel. Nonetheless, due to the local conditions where the test was performed, it is inherent that there was some sort of natural ventilation during the test. It is hard to assume any ventilation effects for the simulations, but as it was used in [89] to explain differences between measurements of T1_80 and T6_80 in Figure 7.16, most likely it had some effect on the final results.

Those uncertainties allied with limitations of the FDS code itself, make it a hard task to perform such simulations in a way that the exact same results are obtained. Nonetheless, the FDS simulations performed in this thesis, as summarized in Section 7.6, are able to provide deep insight into the development of the RWS curve.

7.4.2 FDS Modeling

As explained in Section 7.2.2 the RWS curve appears to be the result of temperature measurements obtained in RWS 1980 [89] (Figure 7.14). Thus, this section provides a brief description of the models developed in FDS to simulate this test. Here, it will become clear what assumptions were made to cover the uncertainties explained in the previous Section 7.4.1, and what were the boundary conditions involved in the simulations. The next subsections will discuss important aspects related to the models developed in FDS.

7.4.2.1 Combustion Process

As described previously in this thesis, regular gasoline was used in RWS 1980. This fuel is a mixture of different components, and therefore is not included in FDS database. Nonetheless, the properties of *N-OCTANE* are available, and this fuel can be used to represent a gasoline pool fire. Note that when studying the temperature development in a simulation, the type of fuel used was found to be less important than the prescribed HRR. Moreover, if the same heat of combustion is applied for different types of fuels, and the prescribed HRR function is fully achieved inside the domain of simulation, then, very similar gas temperatures will be obtained for different fuels.

The following combustion process was prescribed in all FDS simulations used in this chapter:

&REAC	FUEL = 'N-OCTANE'	(C_8H_{18})
	SOOT_YIELD = 0.034	(kg Soot/ kg Fuel)
	CO_YIELD = 0.010	(kg CO/kg Fuel)
	HEAT_OF_COMBUSTION = 43542.9812	(kJ/kg Fuel)
	RADIATIVE_FRACTION = 0.4	

Note that the yields of CO and Soot which were used in the models are tabulated values found in Hurley [94] for *fuel-controlled* fires. Based on the yields of those products of incomplete combustion, FDS calculated the *heat of combustion* shown above. As mentioned before (Section 7.4.1), the real *heat of combustion* of the gasoline used during the RWS tests is unknown. Nonetheless, the value used in the simulations agrees with the effective heat of combustion of gasoline (43.7 MJ/kg) that is reported in the literature (Hurley [94]). The radiative fraction is kept as default (Figure 5.13), and should be indeed at its maximum for those rather small pool fires.

7.4.2.2 Fire

FDS can simulate both liquid and solid fires. However, for the scope of this thesis, an even simpler model is assumed to suffice, and the pool fires used in RWS 1980 [89] (Section 7.2.1.2) are simulated simply through a boundary condition (Section 5.2.3.1). To prescribe this boundary condition, the user can either establish: (1) a fire function based on the heat release rate per unit area (HRRPUA); or (2) a fire function based on a mass loss rate per unit area (MLRPUA). In either case, a fire source is created once this fire function is assigned to a specific area inside the domain. The fire source will, according to the prescribed function, constantly release gasified fuel into the domain. As explained in Section 5.2.3.1, whenever this gas fuel encounters enough oxygen, it immediately combusts, thus creating a fire.

In FDS, the size of the elements (i.e. solid obstructions and pool fires) used in the simulation is constrained by the mesh size. This means that the dimensions of such obstacles need to be multiple of the grid size. Therefore, for reasons of simplicity and to easier the task of performing mesh refinements, the pool fires used in the RWS 1980 [89] (Section 7.2.1.2) were simulated by four pool fires of 1 m *x* 1 m. As the HRR function is unknown (Section 7.4.1), it was chosen to prescribe a mass loss rate per unit area (MLRPUA) function based on the total amount of fuel burned (*1500 liters*) and on the total burning time (*100 minutes*) of RWS 1980 [89]. This gives an average burning ratio of *3.75 liters/min per bin*. Accordingly:

$$MLRPUA = \frac{Mass\ Loss\ Rate\ x\ \rho_{gasoline}}{Pool\ Area}$$

$$MLRPUA = \left(3.75 \frac{L}{min} x \frac{m^3}{1000\ L} x \frac{720\ kg}{m^3} x \frac{min}{60\ s} \right) x \frac{1}{1\ m^2} = 0.045 \frac{kg}{m^2.s}$$

Therefore, based on the calculations shown above and unless specified otherwise, the following bi-linear fire function was used in all simulations performed in this chapter:

```
&SURF ID='Fire',MLRPUA=0.045, RAMP_Q='fire_function'/
&RAMP ID='fire_function', T=0.00,    F=0.00 /
&RAMP ID='fire_function', T=15.00,    F=1.00 /
&RAMP ID='fire_function', T=1500.00,    F=1.00 /
```

The code provided above prescribes that for all pool fires, a boundary condition was created in which the amount of fuel released into the domain grows linearly from zero up to a maximum at *15 seconds*, and then it is kept constant at full power (*0.045 kg/m^2.s*) until the end of simulation. As described previously, the conditions in which fire grew in reality are unknown, as the first temperature measurement in RWS 1980 [89] is provided only after *5 minutes* from the beginning of the test. Therefore, the idea here was to almost immediately insert fire at its full capacity, so that steady state conditions would be reached as fast as possible.

A final remark here concerns Section 4.1.1.2. Making use of equation 4.2 and the data provided in Figure 4.5, we can calculate an expected minimum burning rate ($\dot{m}''_{f,min}$) which should have been achieved by the pool fires during the original test. Accordingly:

$$\dot{m}''_{f,min} = \dot{m}''_{\infty}\left(1 - e^{-k\beta D}\right)$$

The constants $\dot{m}''_{\infty} = 0.055$ kg/(m^2.s) and $k\beta = 2.1$ m^{-1} are retrieved from Figure 4.5. The equivalent pool fire diameter is obtained according to:

$$D = \sqrt{\frac{4A_{max}}{\pi}}$$

From Figure 7.4 the maximum burning area of a single pool fire is $A_{max} = 0.88$ m^2, thus $D = 1.06$ m. Therefore, the minimum burning rate becomes:

$$\dot{m}''_{f,min} = 0.055\ x\ \left(1 - e^{-(2.1\ x\ 1.06)}\right) \rightarrow \dot{m}''_{f,min} = 0.0491 \frac{kg}{m^2.s}$$

Note that this minimum expected burning rate agrees quite well with the average value obtained in reality. In this case, the calculated *MLRPUA = 0.045 kg/(m^2.s)* should be divided by the maximum area of a single pool fire, or *0.88 m^2*. This yields in an average minimum burning rate of $\dot{m}''_{RWS\ 1980,min}$ *= 0.0511 kg/(m^2.s)* during the real test. This value deviates in less than 5% of the expected $\dot{m}''_{f,min}$ calculated above.

7.4.2.3 Thermal Properties of Solid Materials

The thermal properties of solid obstructions (i.e. conductivity, specific heat and density in equation 5.4) are assumed, in all simulations performed in this thesis, as constant in time. In

reality, conductivity and specific heat are often temperature dependent. Nonetheless, it is hard to find in the available literature reliable information about the variation of those parameters with temperature.

Three different kinds of material are involved in RWS 1980 [89]:

1) *Concrete gas-block bricks:*

As previously described (Section 7.2.1.1), the walls of the RWS tunnel were made of concrete gas-block bricks. Apparently, this type of concrete is known as *aerated concrete*, a porous lightweight concrete that provides a high degree of thermal insulation (Narayanan and Ramamurthy [95]). Table 7.3 below, gives the selected thermal properties for *aerated concrete*.

Parameter	Value	Reference
Density	600 kg/m^3	Narayanan and Ramamurthy [95]
Specific Heat	1.0 kJ/kg.K	Mathey and Rossiter [96]
Thermal Conductivity	0.17 W/m.K	Narayanan and Ramamurthy [95]
Emissivity	0.8	Wickström [67]
Thickness	0.24 m	RWS 1980 [89]

TABLE 7.3 – THERMAL PROPERTIES OF AERATED CONCRETE USED IN FDS

2) *Insulation*:

Figure 7.11 shows the types of insulation, with their respective thicknesses, applied to the ceiling of the tunnel used in RWS 1980 [89]. As reported, the average thickness achieved for the insulation layers varied slightly from the prescribed values and are provided below:

- *PYROK*:
  ρ = *705 kg/m^3*
  Slab 3 = *28.4 mm*
  Slab 4 = *39.8 mm*
  Slab 7 = *58.7 mm*

- *HOECO FII/I*:
  ρ = *290 kg/m^3*
  Slab 2 = *26.9 mm*
  Slab 5 = *33.1 mm*
  Slab 6 = *51.9 mm*

For the sake of simplicity, whenever an insulation layer was applied into the FDS models developed in this chapter, it was always considered to be *50 mm* thick, applied uniformly to the whole ceiling of the simulated tunnel. The density assigned to the material comes from a simple average density between PYROK and HOECO FII/I, calculated as shown below:

$$\rho_{Insulation,FDS} = \frac{(0.0284 + 0.0398 + 0.0587)\ x\ 705\ x\ 1\ x\ 2 + (0.0269 + 0.0331 + 0.0519)\ x\ 290\ x\ 1\ x\ 2}{0.05\ x\ 6\ x\ 2}$$

$$\rho_{Insulation,FDS} \cong 405\ kg/m^3$$

As depicted in Section 7.4.1, the thermal properties of the insulation layers originally used in RWS 1980 [89] are unknown. Therefore, based on Hurley [94] and considering the description

of the properties of those insulation materials, HOECO FII/I is assumed to be a *perlite or vermiculite plaster*, and PYROK is taken as a *high-density perlite or vermiculite plaster*. Table 7.4 below summarizes the assumed thermal properties for the insulation material used in the FDS models developed here.

Parameter	Value	Reference
Density	405 kg/m^3	Explained above
Specific Heat	1.2 kJ/kg.K	Hurley [94]
Thermal Conductivity	0.12 W/m.K	Hurley [94]
Emissivity	0.8	Wickström [67]
Thickness	0.05 m	Explained above

TABLE 7.4 – THERMAL PROPERTIES OF INSULATION USED IN FDS MODELS

3) *Concrete*:

The last material that involved in the simulations is concrete (Table 7.5). As described in Section 11.5, Eurocode 2 Part 1-2 [9] provides more elaborated functions for the development of specific heat and thermal conductivity of concrete in temperature. However, the FDS simulations presented in this chapter were among the first tasks accomplished during this thesis, and at that time, focus was related to learn the important aspects involved in fire modeling. With that in mind, Section 7.6 discusses the influences of the selected thermal properties on the obtained results.

Parameter	Value	Reference
Density	2300 kg/m^3	Wickström [67]
Specific Heat	1.0 kJ/kg.K	Wickström [67]
Thermal Conductivity	1.0 W/m.K	Wickström [67]
Emissivity	0.8	Wickström [67]
Thickness	0.15 m	RWS 1980 [89]

TABLE 7.5 – THERMAL PROPERTIES OF CONCRETE USED IN FDS MODELS

7.4.2.4 Temperature Measurements in FDS

There are several kinds of temperature which can be tracked during a FDS simulation. In general, they are calculated at the center of the cells. A brief description of those temperatures is given below:

1) *Gas temperatures* (T_g): Gas temperatures can be tracked in FDS through the use of two devices: (1) a *temperature* device, which gives true gas temperature at the center of the cell which it is assigned to; or (2) a *thermocouple* device, which yields the temperature a small nickel sphere would achieve if located in the assigned position. For *thermocouple* devices, reference is made to Section 7.3. In all FDS models developed here, gas temperatures were collected at the same positions of the thermocouples used in the real test (Figure 7.12). Moreover, the recorded value is computed *0.3 m* away from the walls, and at the center of the last gas cell located on the interface with the solid obstruction (i.e. the ceiling). There were no significant differences between the results of *temperature* devices and *thermocouple* devices for the simulations performed here. Thus, only the true gas temperatures will be used from now on.

2) *Surface temperatures at solid obstructions* ($T_{surface}$): In FDS, the surface temperature at the center of the surface of an obstruction cell is nominated as wall temperature, and can be tracked through a *wall temperature* device assigned to the desired position.

3) *Inside wall temperatures:* To record the temperature inside a solid obstruction, an *inside wall temperature* device should be used together with the specified *depth* in which the solid temperature is desired. The solid temperature is a function of the 1D heat conduction model used by FDS (Section 5.2).

4) *Adiabatic surface temperatures* (T_{AST}): FDS can also compute the AST at a desired position on the surface of a solid obstruction. It is tracked by a *adiabatic surface temperature* device which gives the wall temperature in case the sum of the convective and radiative heat flux would equal zero, as depicted by equation 5.27.

5) *Radiation temperatures* (T_r): Radiation temperatures are indirectly tracked in FDS either by an *incident heat flux* device, or through a *radiative heat flux* device assigned to the position of interest. In the former case, FDS provides the incident radiation $\dot{q}''_{inc}$ on the surface of the solid, and the radiation temperature (T_r) can be calculated as in:

$$T_r = \sqrt[4]{\frac{\dot{q}''_{inc}}{\sigma}} \qquad 7.1$$

where σ is the Stefan-Boltzmann constant (5.67 x 10^{-8} W/(m^2K^4)).

In the latter case, FDS provides the total radiation heat flux $\dot{q}''_{rad}$ to the structure, and T_r is given by:

$$T_r = \sqrt[4]{\frac{\dot{q}''_{rad}}{\varepsilon_s \sigma} + T^4_{surface}} \qquad 7.2$$

where ε_s is the surface emissivity and $T_{surface}$ is the absolute surface temperature (K).

Note that the solution of equations 7.1 and 7.2 will generate the same T_r values.

7.4.2.5 Mesh Resolution

In general, as in any computational modeling software, one should perform a mesh sensitivity analysis to ensure the level of accuracy obtained during a numerical simulation is sufficient to fulfill its purpose. Nonetheless, as described in *FDS User's Guide* [71], for simulations involving buoyant plumes, an indication of how well the flow field is resolved (Figure 1.1) is given by the non-dimensional parameter D^*/δ_x. Accordingly:

$$D^* = \left(\frac{\dot{Q}}{\rho_\infty \, c_p \, T_\infty \sqrt{g}} \right)^{\frac{2}{5}} \qquad 7.3$$

where D^* is the characteristic fire diameter (m), $\dot{Q}$ is the total HRR of the fire (kW), ρ_∞ is the ambient air density (kg/m^3), c_p is the specific heat of air (kJ/(kg.K)), T_∞ is the initial air temperature (K), g is the acceleration of gravity (m^2/s), and δ_x is the nominal size of a mesh cell (m).

In FDS, the resolution of the calculation increases with the number of cells spanning the fire. Note that here, fire is characterized by the characteristic fire diameter (D^*), which is independent on the physical size of the fire source. As a rule of thumb, a good starting point is to have between 8 to 10 cells in the characteristic diameter, and, at least, 6 to 8 cells across the burner.

The concept presented here will be used to address the accuracy of the calculated temperatures in the developed models. It is important to keep in mind that the uncertainties explained in Section 7.4.1 allied with the unknown accuracy of the thermocouples used during the test (Section 7.3), limit the comparison of results between the FDS simulations and the real test data. Not only that, there are also limitations regarding the software itself. In general, if the HRR is accurately specified by the user, the temperatures away from the fire are better predicted than those near it, as shown in Vigne and Jonsson [97] for a tunnel fire test. Note for the simulations performed here, as the RWS tunnel is very short and the ceiling is all covered in flames, the temperature measurements practically on top of the fire source, so differences between the predicted temperatures in FDS models and the temperature measurements in RWS 1980 [89] are already expected.

7.4.3 FDS Model I – Reduced Domain

As a starting point, due to shorter computational time and based on the CFD simulations performed by RWS itself (Section 7.2.4), FDS models of RWS 1980 [89] were first developed in a reduced domain. Basically, as shown in Figure 7.25, the computational domain was limited to the edges of the simulated RWS tunnel, with a box size of 3.5 m *x* 13.25 m *x* 3.5 m (width *x* length *x* height). Note that an *open* boundary condition was assigned to all faces defined by the outer black lines in Figure 7.25.

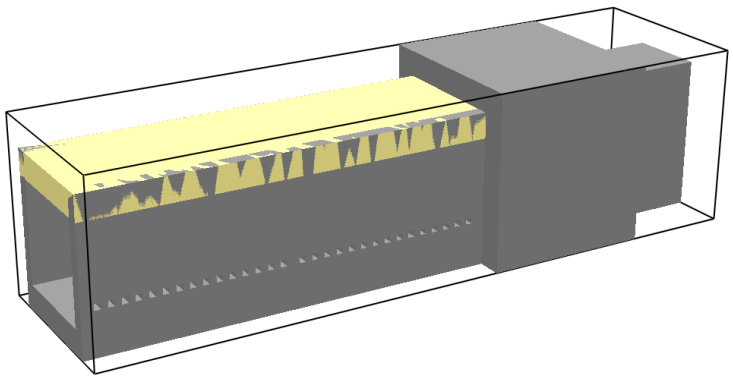


FIGURE 7.25 – FDS MODEL I

In FDS, this special boundary condition denotes a passive opening to the outside, where ambient conditions are assumed to exist beyond this boundary. *FDS User's Guide* [71] describes that this *open* boundary usually provides stable conditions for flows that are predominantly normal to it, moving mostly in or out of it. Note that this is not the case for the simulations performed here. Specially at the two *open* ends of the tunnel, the flow of gases through the boundaries, despite being mainly normal to it, occur in both directions. Moreover, there are hot gases flowing out of the domain, as well as, a bottom layer of fresh air being pushed inside the tunnel (Figure 7.26). Those flows impede each other, meaning that not necessarily enough space is present to sustain the outwards flow of hot gases and the inwards flow of air. Therefore, FDS models in an extended domain are also studied in Section 7.4.4.

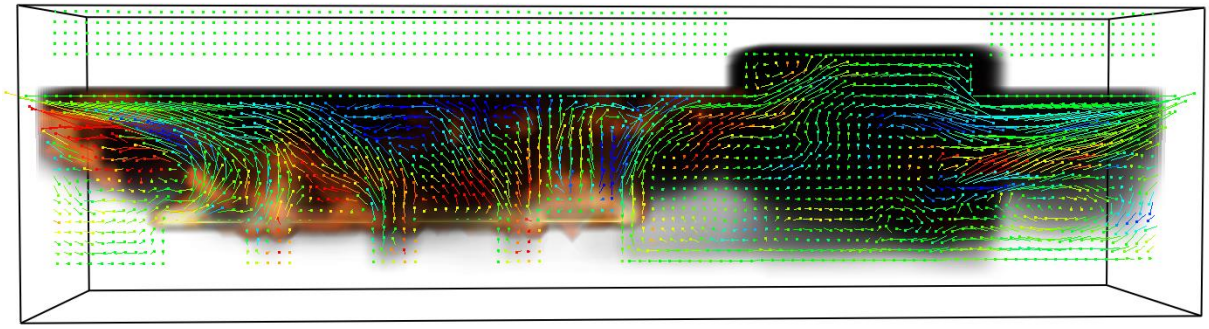


FIGURE 7.26 – GAS VELOCITIES PLOT FOR FDS MODEL I
(After 600s of Fire Simulation)

The FDS models studied in this section were developed in agreement with what was presented in Section 7.4.2 and with the geometry of the RWS tests described in Section 7.2.1.1. Thus, Table 7.6 provides the materials assigned to the obstructions.

Tunnel	Material	Thickness
Floor	Concrete	0.15 m
Walls	Concrete gas-block bricks	0.24 m
Ceiling	Insulation + Concrete	0.05 m + 0.15 m
Room and Corridor	**Material**	**Thickness**
Floor	Concrete	0.15 m
Walls	Concrete gas-block bricks	0.24 m
Ceiling	Concrete	0.15 m

TABLE 7.6 – GEOMETRY USED IN FDS MODEL I

The *30 openings* on the right wall (Section 7.2.1.1) were included in all simulations. As described before, the size of the elements in FDS is limited by the grid. Therefore, the holes on the RWS tunnel wall were simulated here by conserving the total opening area of *0.45 m^2*, or 30 times the area of each hole (*0.015 m^2*). This means: (1) *one single hole* on the wall, located according to the center of the pools, for a grid size of *0.5 m*; (2) *7 holes* uniformly distributed on the wall for a grid size of *0.25 m*; and (3) *30 holes* for the *0.125 m* mesh.

7.4.3.1 Mesh Refinement

A mesh refinement study was performed to define the grid size that should be used in the simulations on a reduced domain (Model I). Table 7.7 below summarizes the results obtained with the models studied here.

Mesh	Coarse	Medium	Fine
δx =	0.5 m	0.25 m	0.125 m
Number of cells =	1,512	10,388	83,104
HRR =	6.69 MW	6.07 MW	5.84 MW
D* =	2.09 m	2.01 m	1.98 m
D*/δX=	4	8	16

TABLE 7.7 – MESH REFINEMENT STUDY (FDS MODEL I)

As described in Section 7.4.2.4, gas temperatures were collected at the same locations as that of the thermocouples used in RWS 1980 [89] (Figure 7.12). Thus, Figure 7.27 provides the average gas temperatures tracked in the models in a comparison with the average gas temperature measurements of the real test.

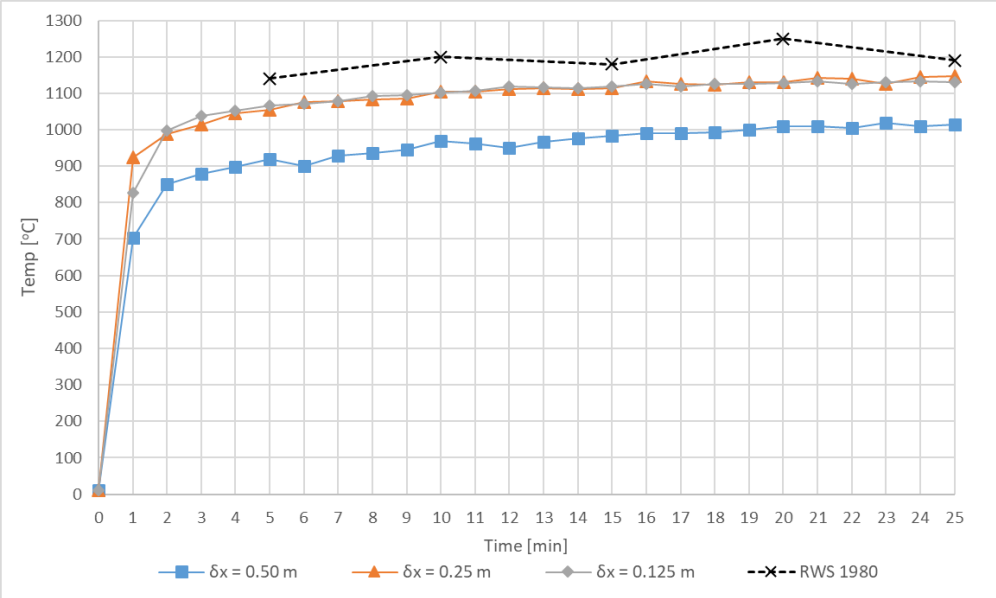


FIGURE 7.27 – AVERAGE GAS TEMPERATURE MEASUREMENTS (FDS MODEL I)

Some conclusions are drawn from the results provided in Figure 7.27. As expected, the *coarse* mesh does not provide reliable estimates. The gas temperatures measurements obtained by the medium and fine mesh are nearly identical, indicating that a grid size of *0.25 m* is enough to provide enough resolution of the numerical calculations performed within a reduced domain. As explained before, the first temperature measurement in RWS 1980 [89] is provided only after *5 minutes* of the beginning of the test, meaning that it is unknown how fast fire actually grew in the early stage of fire development. This highlights that the temperatures provided for the first *5 minutes* of fire simulation (Figure 7.27), should not be assumed to represent the real conditions achieved during RWS 1980. The calculated gas temperatures for the *medium* and *fine* meshes deviate in less than *10%* at all times from the temperatures measured in the test. Considering all the uncertainties involved in modeling those tests, and all assumptions made in the development of the models, the results are taken to be satisfactory.

When compared to the simulations performed by RWS itself (Section 7.2.4.2), the calculated average temperatures are around 100 °C lower, despite the fact that the achieved HRR is nearly the same (~6 MW). Nonetheless, this difference in temperature is not considered to be representative for the following reasons: (1) The simulations performed by RWS were developed in 2003 [90] in FDS 2.0, and a lot has improved in the FDS code since then. For

instance, this thesis is developed in FDS 6.7.3; and (2) the thermal properties of the solid obstructions used in the RWS simulations are unknown, but small differences in thermal conductivity, for instance, might already yield in a *100 ^{o}C* variation.

7.4.4 FDS Model II – Extended Domain

FDS User's Guide [71] describes that if the flow through a certain opening is of importance, then the domain of computation should be set a few meters away from this opening. According to this recommendation, the *open* boundary condition previously placed in the edges of the simulated tunnel (Section 7.4.3), should actually have been set far enough from the ends of the tunnel, such that they would not affect the flow pattern through these openings. Therefore, this section studies the effect of extended computational domains to understand if the previous models were indeed providing accurate predictions of the flow pattern conceived during the RWS test.

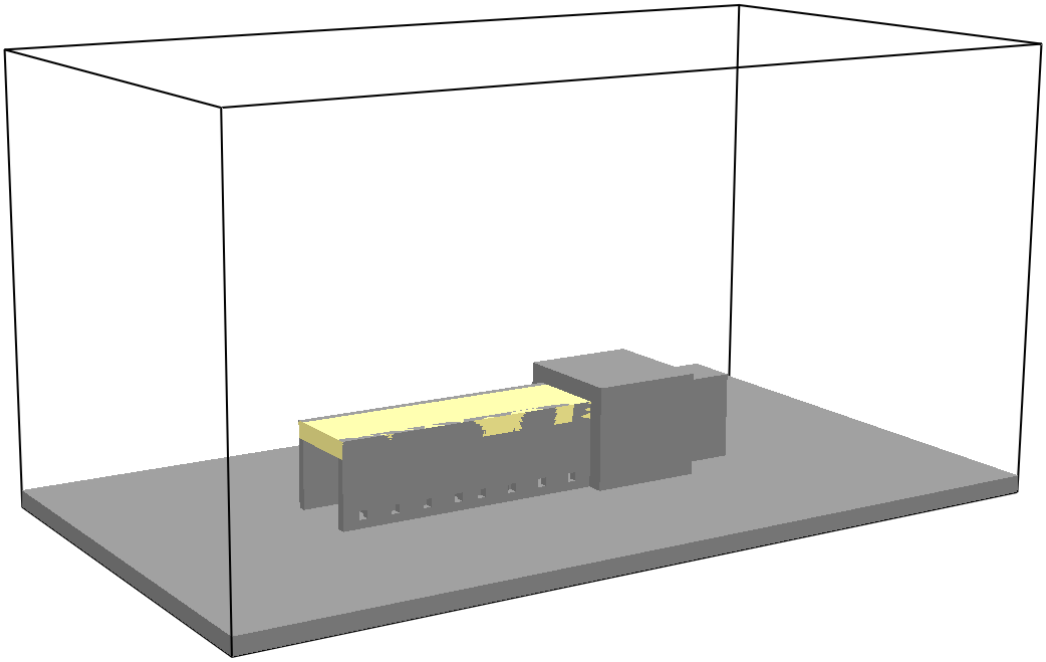


FIGURE 7.28 – FDS MODEL II

Four models with different extended domains (Figure 7.28) were studied here for grid sizes of *0.25 m* and *0.125 m*. The first two models consider an increase of the domain in longitudinal direction, and also in height. The second two models, besides the previous modifications, also include an increase of the domain in the transversal direction. The tunnel used here is exactly the same as the one used in the previous Section 7.4.3. Note that from now on, models in a reduced domain (Section 7.4.3) will be referred to as *MI* (Figure 7.25), and models in an extended domain (Figure 7.28) are described as *MII*. For the latter, another distinction is made between *MII.a* and *MII.b*, where *a* stands for an increase in the computational domain in both longitudinal and height direction, whereas *b* represents models extended in all directions.

Table 7.8 below provides a summary of the cases study in this section in a comparison with the correspondent reduced domain models. Note that the numbers accompanying the name of the models refer to the grid size (m) adopted in the simulation.

Model	MI – 0.25	MII.a – 0.25	MII.b – 0.25	MI – 0.125	MII.a – 0.125	MII.b – 0.125
Box =	3.5 x 13.25 x 3.5 m^3	3.5 x 19.25 x 7 m^3	13.5 x 25.25 x 13 m^3	3.5 x 13.25 x 3.5 m^3	3.5 x 19.25 x 7 m^3	11.5 x 19.25 x 7 m^3
δx =	0.25 m	0.25 m	0.25 m	0.125 m	0.125 m	0.125 m
Cells =	10,388	30,184	283,608	83,104	241,472	793,408
HRR =	6.07 MW	7.79 MW	7.81 MW	5.84 MW	7.82 MW	7.84 MW
D* =	2.01 m	2.22 m	2.22 m	1.98 m	2.22 m	2.22 m
D*/δX=	8	9	9	16	18	18

TABLE 7.8 – EXTENDED DOMAIN STUDY

Figure 7.29 provides the results for the average gas temperature measurements obtained for the models studied in this section in comparison with the results collected from the models studied in the previous Section 7.4.3. Note that the simulation time is limited to *10 minutes* of fire development due to the required computational time for Model II. For instance, the numerical calculations for *MII.b – 0.125* took near a week.

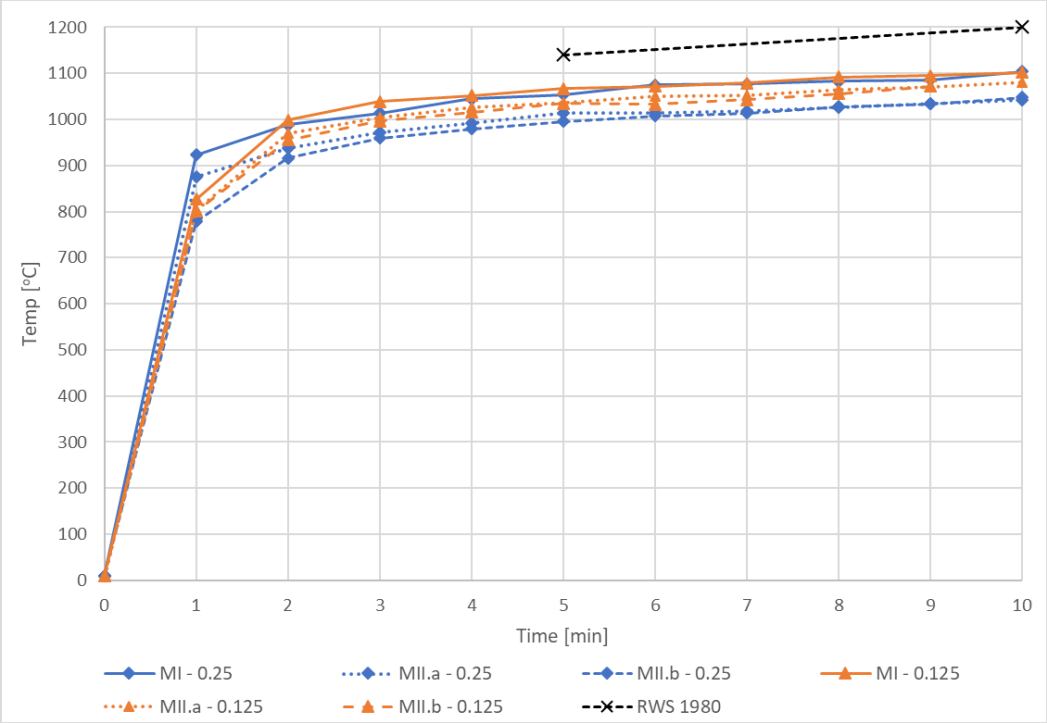


FIGURE 7.29 – MODEL I VS MODEL II

From Figure 7.29, it is clear that the location of the *open* boundaries has an influence on the calculated gas temperatures in FDS. For a grid size of *0.25 m* the average temperatures are near *100 °C* lower than the respective model in a reduced domain (*MI – 0.25*). For a cell size of *0.125 m*, this difference is always reduced to less than *50 °C*. This is explained by the complexity of the flow pattern shown in Figure 7.30. Differently from before, now the *finer mesh*, which is always better capturing the real flow, is able to provide more accurate results than the *medium mesh*. Also, note that the results of the extended domain models, despite being dependent on grid size, are nearly the same between *MII.a* and *MII.b* models for the same grid size. Moreover, once the chimney effect is covered within the simulation domain, the resolution of the pattern flow appears to be complete. This means that the extension of the domain in the

transversal direction had no influence on the outcome of the simulations. However, keep in mind that all models studied up to now include the holes on the right wall of the tunnel (Section 7.2.1.1), and that this transversal extension might be needed to capture the effect of those holes in fire development. The latter is dealt with in Section 7.5.1.

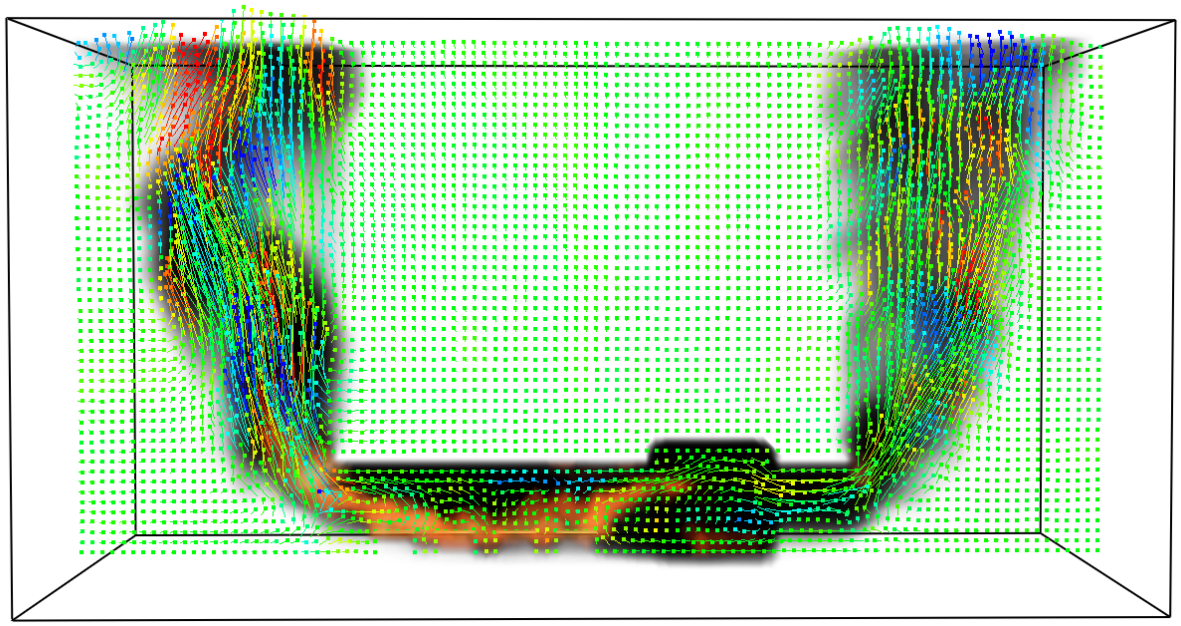


FIGURE 7.30 – GAS VELOCITIES PLOT FOR FDS MODEL II
(After 600s of Fire Simulation)

As described, the differences between the reduced and the extended models lie in the inclusion of the chimney effect on the solution of the second type of model. This effect is highlighted in Figure 7.30, where a gas velocity plot at the center section of the tunnel is given. In a comparison with the same plot for the reduced domain (Figure 7.26), it becomes clear that the *open* boundaries located at the edges of the tunnel in Model I are not able to fully capture the real flow pattern obtained during the RWS tests (Figure 7.31). Thus, the calculated gas temperatures in Model II are certainly representing the real scenario more accurately. Note that the average gas temperatures obtained for the *finer mesh* used in Model II deviate in approximately *10%* of that which was obtained by the temperature measurements of RWS 1980 [89] (Figure 7.28). Thus, we can conclude that despite all assumptions and limitations involved in developing these simulations, the models studied here are able to represent a very similar fire scenario as the one conceived during RWS test.

All that being said, notice that the simulations performed in a reduced domain still provide valuable results. Despite slightly overpredicting the simulated gas temperatures, the differences between the resolution of calculations achieved in Models I and II are limited to *5%*. Thus, aside from not being able to capture the flow of gases due to the chimney effect, the *open* boundary conditions at the ends of the RWS tunnel in Model I, are still able to represent the inflow of fresh air underneath the hot buoyant layer, which is required to sustain fire development inside the domain of simulation.



FIGURE 7.31 – CHIMNEY EFFECT IN RWS TEST
Retrieved from RWS 1979 [88]

A final remark here refers to the differences between the HRR output from Model I and Model II highlighted in Table 7.8. In the latter, flames are emerging out of the tunnel (Figure 7.30), but are still solved inside the domain of simulation. This means that the gas fuel which is burning outside the tunnel also contributes to the HRR outputted from FDS for the extended models. As a consequence, the HRR for Model II will be inherently higher.

7.5 Variations on the Original RWS Tests

This section covers variations on the RWS test setup. Here, the effect of the holes on the right wall of the tunnel will be studied (Section 7.5.1). Also, a comprehensive study over gas, wall AST, and radiation temperatures, considering the effects of the insulation applied on the ceiling, is provided (Section 7.5.2). Later, a hypothetical scenario in which the RWS tunnel is assumed to be completely made of concrete is also studied (Section 7.5.3).

7.5.1 Effect of Holes on the Wall

The effect of the holes on the right wall was studied for all models described in Sections 7.4.3 and 7.4.4. The only simulation that was able to capture differences between models *with* and *without holes* was *MII.b* (Figure 7.34). For all other models, the average gas temperatures calculated by FDS for cases *with* and *without holes* were nearly the same. This fact is explained by the solution of the flow field in the transversal direction. Comparing Figure 7.32 with Figure 7.33 it becomes clear that, for models with reduced length in transversal direction, the *open* boundary condition on the right end of the domain, is simply not able to provide the inner flow of oxygen at the level of the holes, which is only perceived for the models developed in a transversely extended domain.

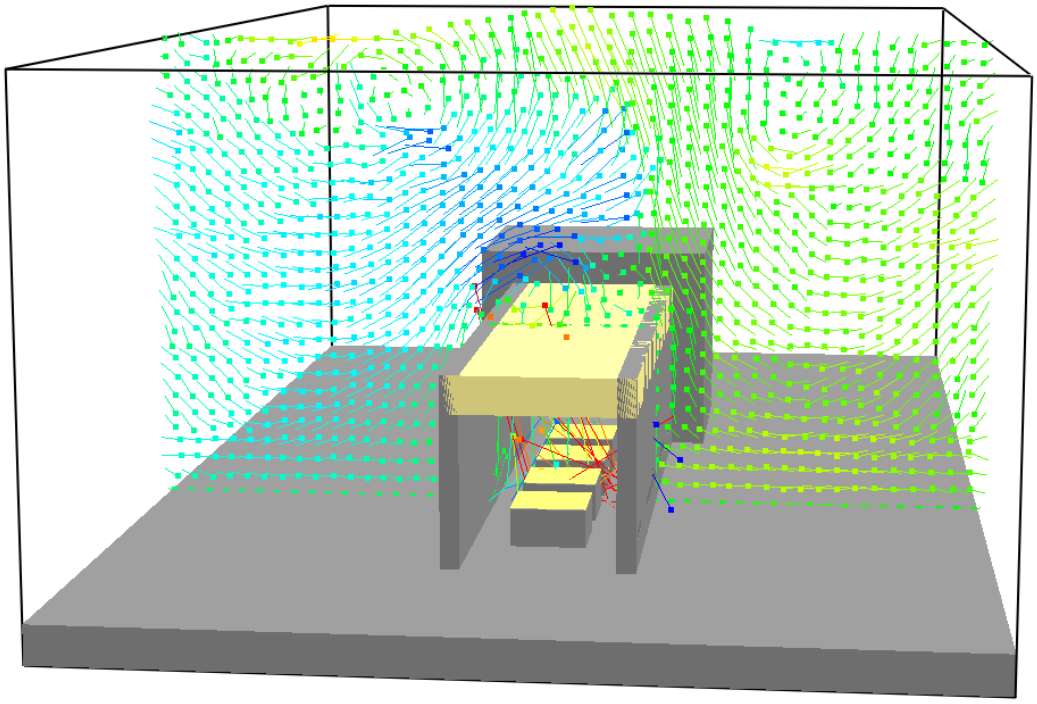


FIGURE 7.32 – GAS VELOCITIES PLOT IN FDS (MII.B – 0.125)
(After 540s of Fire Simulation)

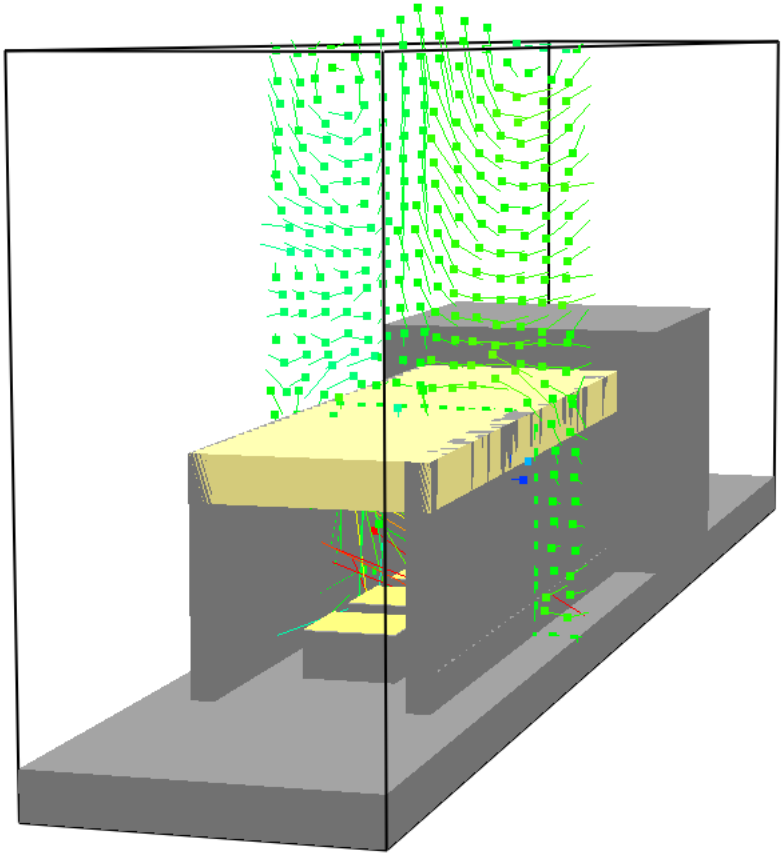


FIGURE 7.33 – GAS VELOCITIES PLOT IN FDS (MII.A – 0.125)
(After 540s of Fire Simulation)

Figure 7.34 below shows that, against what one might have expected, the holes on the walls appear to have had a rather limited effect on the gas temperatures achieved in RWS 1980 [89]. It is noticeable from the same figure that the presence of holes for *MII.b – 0.25* led to temperature differences of around *100 ºC* for the end of fire simulation, while for *MII.b – 0.125*, the differences for cases *with* and *without holes* are limited to approximately *50 ºC* at all times, which is half of that for the case of the simulation realized by RWS itself (Section 7.2.4.3). Thus, the effect of the holes appears to be overtaken by the pressure differences due to the hot buoyant gases originated by the fire, which are further amplified by the chimney effect at both ends of the tunnel (Figure 7.31).

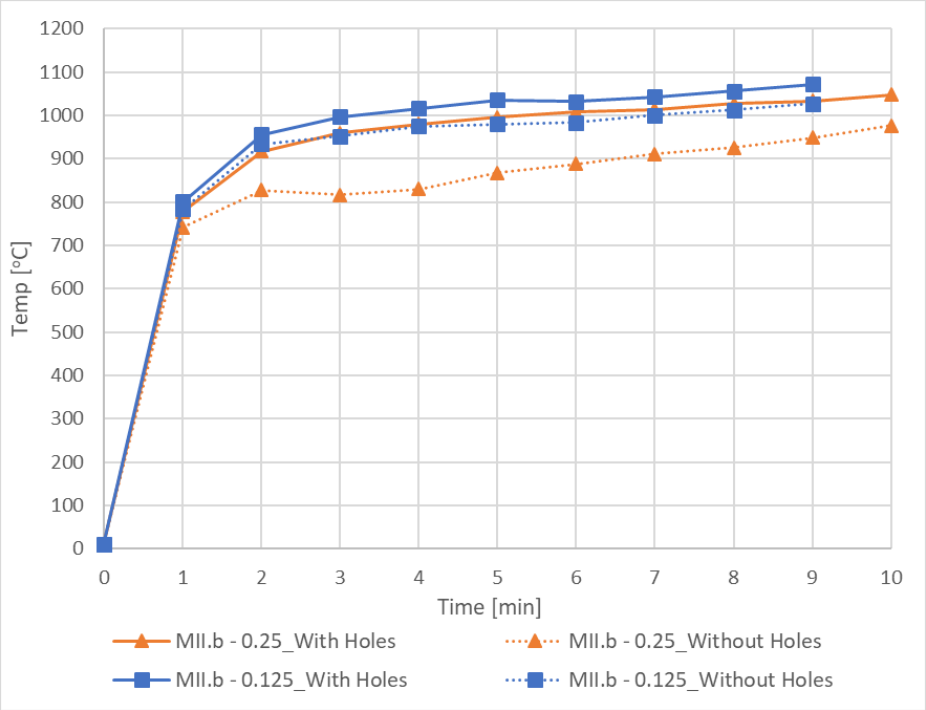


FIGURE 7.34 – EFFECT OF HOLES

In conclusion, for the simulations performed here, the bottom layer of fresh air that is constantly supplied to the fire due to pressure differences, appears to be enough to sustain the HRR development (Figure 7.35), thus limiting the effects of the extra air supplied through the holes. Nonetheless, it is important to have in mind that the simulation results depicted here can be somehow misleading. As described in Section 7.4.2.1, fire is modeled in FDS through a boundary condition that constantly releases fuel into the domain. This means that the development of a pressure difference inside the tunnel is inherently imposed in the model by the buoyant plume, even for those cases in which holes are removed from the wall. Moreover, we are making use of the results of RWS 1980 [89], which already intrinsically account for any effects the holes could have had during the test, and are imposing it to both simulations indistinctively (*with* and *without holes*). Thus, it is hard to ensure that the obtained fire development would also have happened in reality if the test would have been performed *without holes*. Hence, we are left with two options, either: (1) the holes had indeed very limited effect on fire development during the test, as indicated by the simulations performed here; or (2) the holes had a bigger effect on fire development than that shown by Figure 7.34, but, due to the assigned boundary conditions, we are not able to fully capture those.

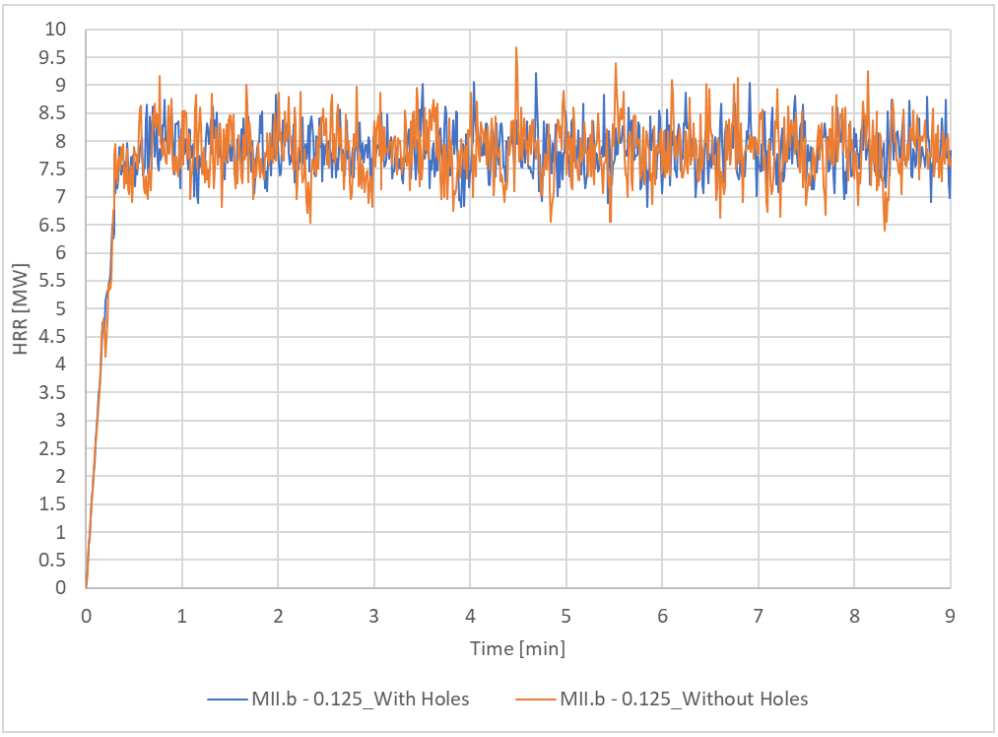


FIGURE 7.35 – HRR FOR CASES WITH AND WITHOUT HOLES (MII.B – 0.125)

7.5.2 Effects of Insulation on Temperature Development

To be able to simulate the original RWS test for a longer period, and thus having a fair comparison of the temperature development between models *with* and *without insulation*, model *MI – 0.25*, which considers the original RWS test setup in a reduced domain for a grid size of *0.25 m*, was used in all simulations studied in this section. Note that also some changes in the original test setup are studied for the section entitled as tunnel, marked by the red ellipse in Figure 7.36.

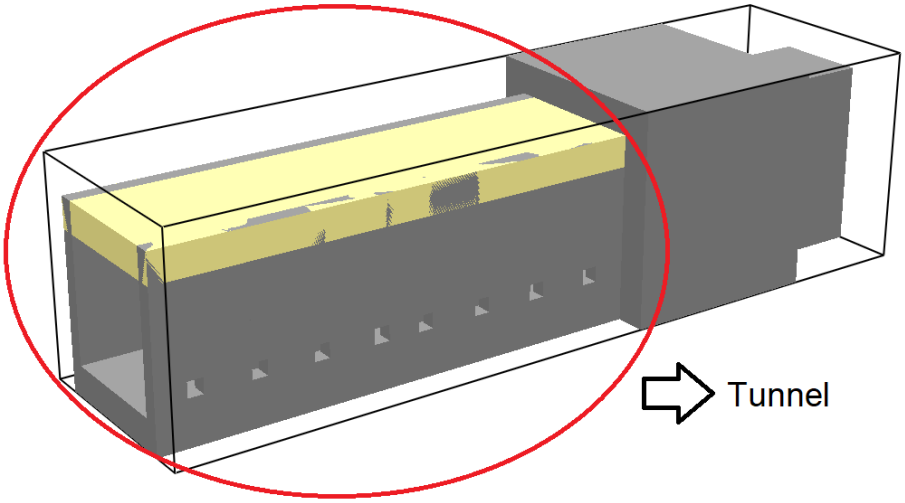


FIGURE 7.36 – TUNNEL

Those modifications are explained below together with a full description of the models and their respective terminology:

1) *MI_0.25_Adiabatic*:

This simulation refers to the upper bound gas temperature development that is achieved inside the tunnel. Therefore, as depicted in Table 7.9, adiabatic conditions are assigned to the walls and ceiling of the tunnel, while the rest of the test setup is kept identical to what was prescribed in Table 7.6. In FDS, assigning a solid obstruction as *adiabatic* means prescribing a boundary condition in which there is no net heat transfer (radiative and convective) from the gas to the solid phase. In other words, FDS creates an obstruction with NET_HEAT_FLUX=0 and EMISSIVITY=1, resembling a perfect insulation material.

Tunnel	Material	Thickness
Floor	Concrete	0.15 m
Walls	Adiabatic	-
Ceiling	Adiabatic	-

TABLE 7.9 – MODIFICATIONS USED IN MI_0.25_ADIABATIC

2) *MI_0.25_Insulation:*

In this case the ceiling of the tunnel is simulated only by the insulation layer (i.e. without a concrete slab on top). Table 7.10 summarizes the case.

Tunnel	Material	Thickness
Floor	Concrete	0.15 m
Walls	Concrete gas-block bricks	0.24 m
Ceiling	Insulation	0.05 m

TABLE 7.10 – MODIFICATIONS USED IN MI_0.25_INSULATION

An important remark for this case, and also for the following ones, is referring to the MLRPUA prescribed in the simulation. Here, differently from what is explained in Section 7.4.2.2, instead of reaching its full power at *15 seconds* of simulation, fire is set to reach its maximum capacity after *5 minutes* of fire simulation, and thus a linear temperature development up to the first temperature measurement of the RWS 1980 [89], is to be expected. Note that this is not valid for *MI_0.25_Adiabatic*, where the MLRPUA function was kept the same as described in Section 7.4.2.2.

3) *MI_0.25_Concrete:*

Here the tunnel ceiling is simulated only through a concrete slab (i.e. without any insulation material), which is directly exposed to fire (Table 7.11).

Tunnel	Material	Thickness
Floor	Concrete	0.15 m
Walls	Concrete gas-block bricks	0.24 m
Ceiling	Concrete	0.15 m

TABLE 7.11 – MODIFICATIONS USED IN MI_0.25_CONCRETE

4) *MI_0.25_RWS 1980:*

This case is kept identical to the original test setup adopted in RWS 1980 [89] (Table 7.6).

7.5.2.1 Gas Temperatures inside the Tunnel

Figure 7.37 provides the average gas temperature development inside the tunnel up to *50 minutes* of fire simulation. Firstly, notice that even when *adiabatic* conditions are assigned to the walls and ceiling of the tunnel, the gas temperatures predicted by the simulations still do not reach the measurements obtained during the RWS test for almost the whole simulation. That being said, it is noticeable that the differences between the actual measurements and the simulated results are reduced in time, and that the *MI_0.25_RWS 1980* model, even when considering all the limitations involved, provides a reasonable comparison with the scenario achieved during the RWS test.

Now, notice that the average gas temperatures obtained for *MI_0.25_Insulation* and *MI_0.25_RWS 1980* are nearly identical. This proves that the absence of a concrete slab in the simulations performed by RWS itself (Section 7.2.4) has not affected their results. It is also noticeable that the temperature development for *MI_0.25_Concrete* is lower than that for the *insulated* ceiling cases. Moreover, it is clear from Figure 7.37 that the insulation material applied to the ceiling is partially responsible for the gas temperatures measured during the original test. Basically, if the ceiling would have been made of concrete, the gas temperature development inside the tunnel, at least for the first *20 minutes* of fire, would not be so steep as that which was measured for an *insulated ceiling*. It is true that, with time, this difference practically vanishes, and all cases approach *adiabatic* conditions (i.e. thermal equilibrium). Even so, this confirms the expectation that the thermal properties of the obstructions in the enclosure are dictating the gas temperature development in the environment, raising the question of how different the temperature development inside the tunnel would have been in case it was completely made of concrete. This matter will be further investigated in Section 7.5.3.

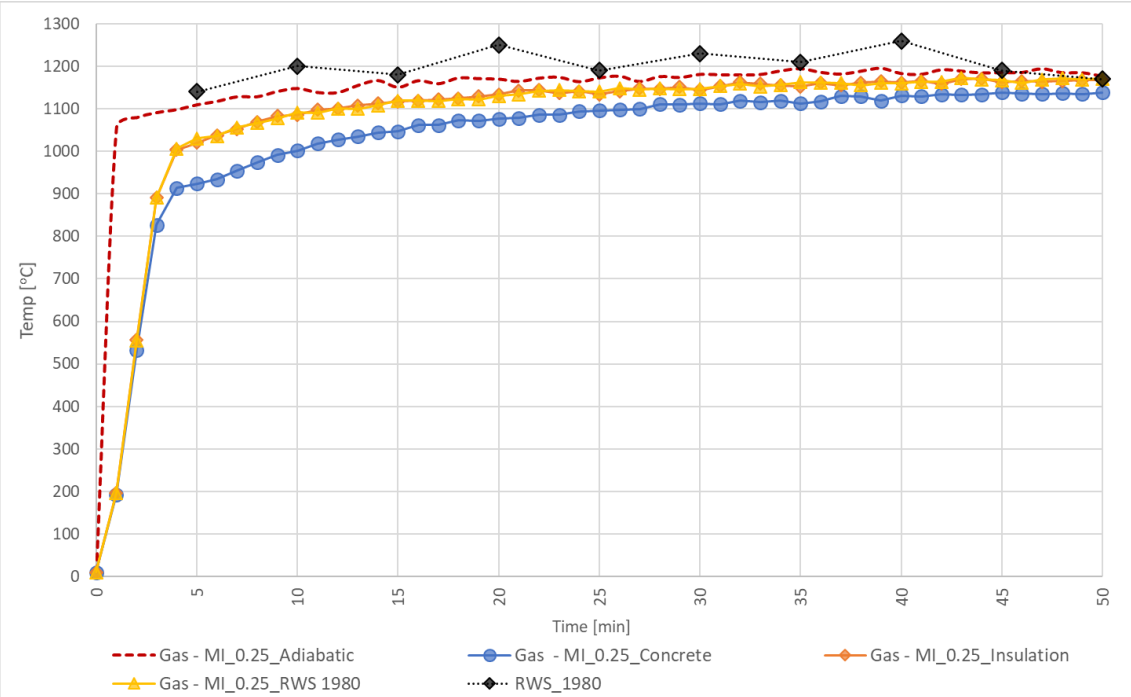


FIGURE 7.37 – AVERAGE GAS TEMPERATURE AT THE CEILING

7.5.2.2 AST, Radiation and Wall Temperatures

This section presents a comprehensive study regarding the structure exposure during the RWS test. Keep in mind the distinction between AST, radiation and wall temperatures as presented in Section 7.4.2.4. Accordingly, AST is obtained by the solution of equation 5.27 in time, radiation temperatures are given by the solution of equation 5.11, and wall temperatures (surface temperatures) are calculated in FDS as a function of the 1D heat conduction model adopted by the software (equation 5.14).

As previously discussed in Section 5.1.3.2, whenever a fire is generating hazardous conditions to a structure, high temperatures are inherently achieved in the enclosure, and the heat exposure will be governed by the radiation component. This is confirmed by Figure 7.38, where the average AST development at the ceiling for the simulation of the original RWS test setup (*MI_0.25_RWS 1980* in Section 7.5.2) is given in comparison with the average gas and radiation temperatures inside the tunnel. The results depicted here clearly show that for the conditions achieved during the RWS test, the average AST of the ceiling is practically the same as the correspondent average radiation temperature. Thus, as discussed in Section 7.3, at least from a structural point of view, the development of the RWS curve should have been based on AST measurements rather than on gas temperature measurements. This is the case because AST combines both radiation and convection effects, characterizing the highest temperature ever achievable by the structure during a given fire.

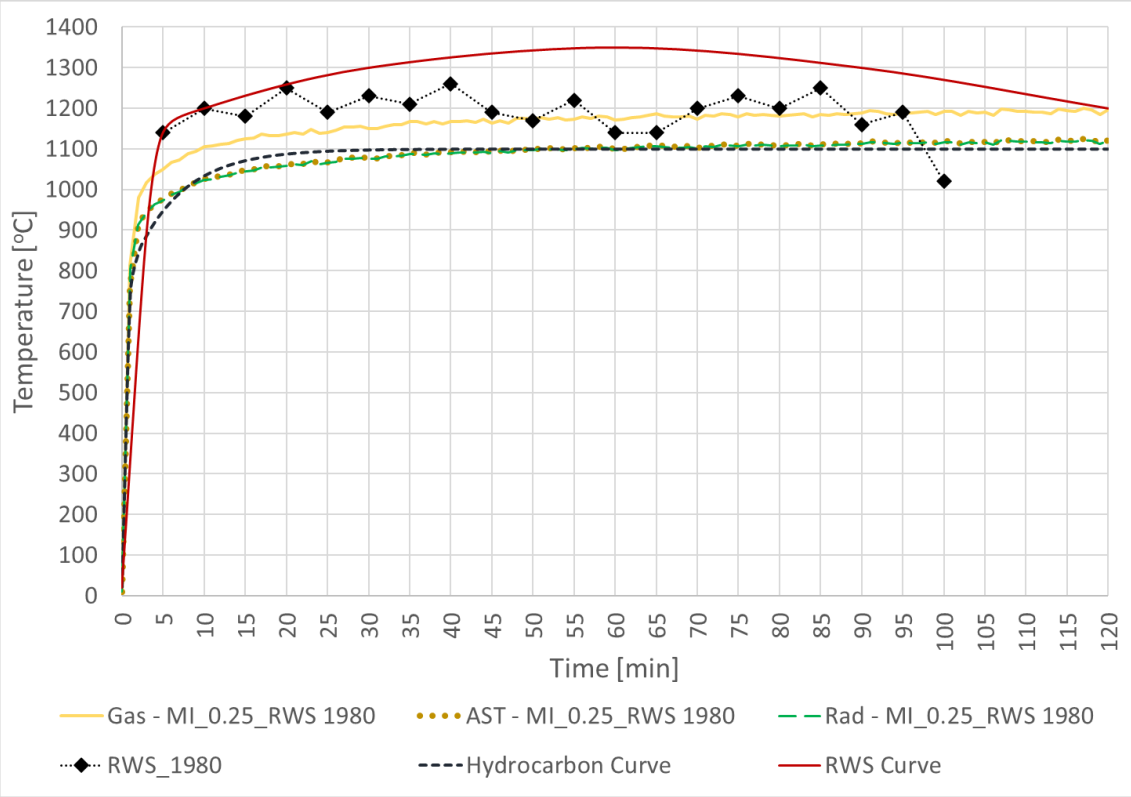


FIGURE 7.38 – AST AT THE CEILING FOR MI_0.25_RWS 1980

Figure 7.39 gives a comparison between the average gas, AST and wall temperatures for the same model. It is clear that the AST is around *100 °C* lower than the gas temperatures obtained in the simulation. Note also that for the insulation material applied on the ceiling, the wall

temperature is, since the beginning of the simulation, very close to its own AST. This means that *insulation* materials react almost immediately to a thermal exposure, rapidly reaching the equilibrium temperature.

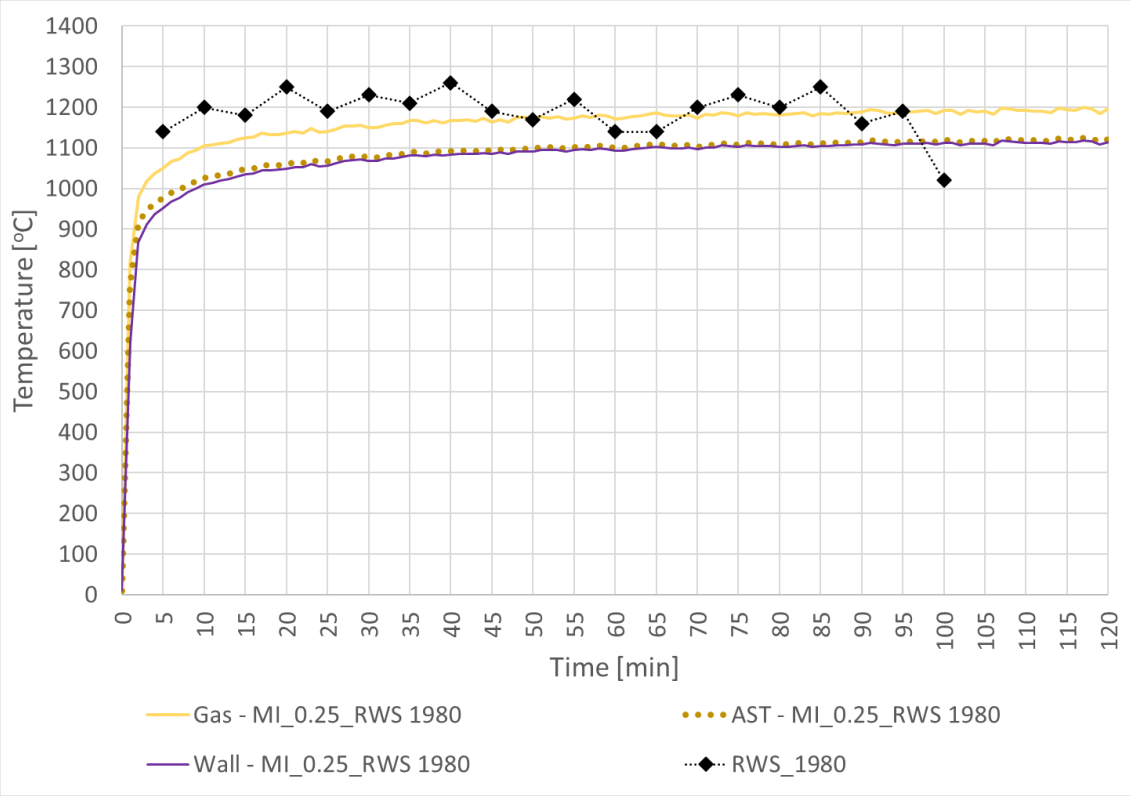


FIGURE 7.39 – AVERAGE TEMPERATURES AT THE CEILING FOR MI_0.25_RWS 1980

Now, consider the case of *MI_0.25_Concrete*, in which the ceiling of the tunnel is made solely of concrete, in a comparison with the simulation for the real test setup (i.e. *MI_0.25_RWS 1980*). As already discussed in Section 7.5.2.1, Figure 7.40 shows that the gas temperatures obtained for the *unprotected concrete* case are lower than those for the *insulated concrete* case. Similarly to the previous case (Figure 7.39), note that also here, the AST of *unprotected concrete* appears to be approximately *100 °C* lower than the correspondent gas temperature at all times. On the other hand, concrete's surface temperature (entitled as wall Figure 7.40) is lower than the correspondent AST during the whole simulation, but especially for the first *25 minutes* of fire. This is explained by the fact that *concrete* has a higher thermal inertia than the *insulation* material, thus taking much longer to react to an imposed thermal exposure and to reach the equilibrium temperature.

Figure 7.41 shows, as expected, that the AST for an *unprotected concrete* ceiling is also lower than the AST for the *insulated* ceiling, but the difference between them is vanished in time. Here it is important to remark that the walls of the tunnel are still being simulated by the thermal properties of *aerated concrete* (Section 7.4.2.3), which is also a material characterized by high insulation properties. For this reason, a fully *unprotected concrete* tunnel will be investigated in the next Section 7.5.3.

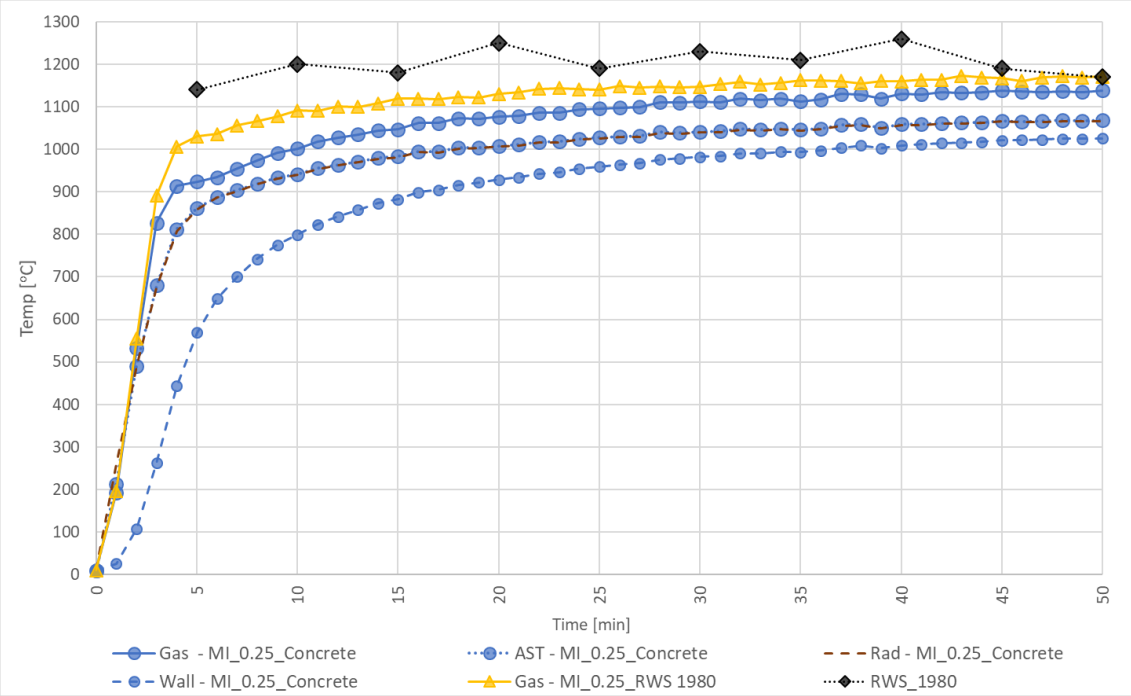


FIGURE 7.40 – AVERAGE TEMPERATURES AT THE CEILING FOR MI_0.25_CONCRETE

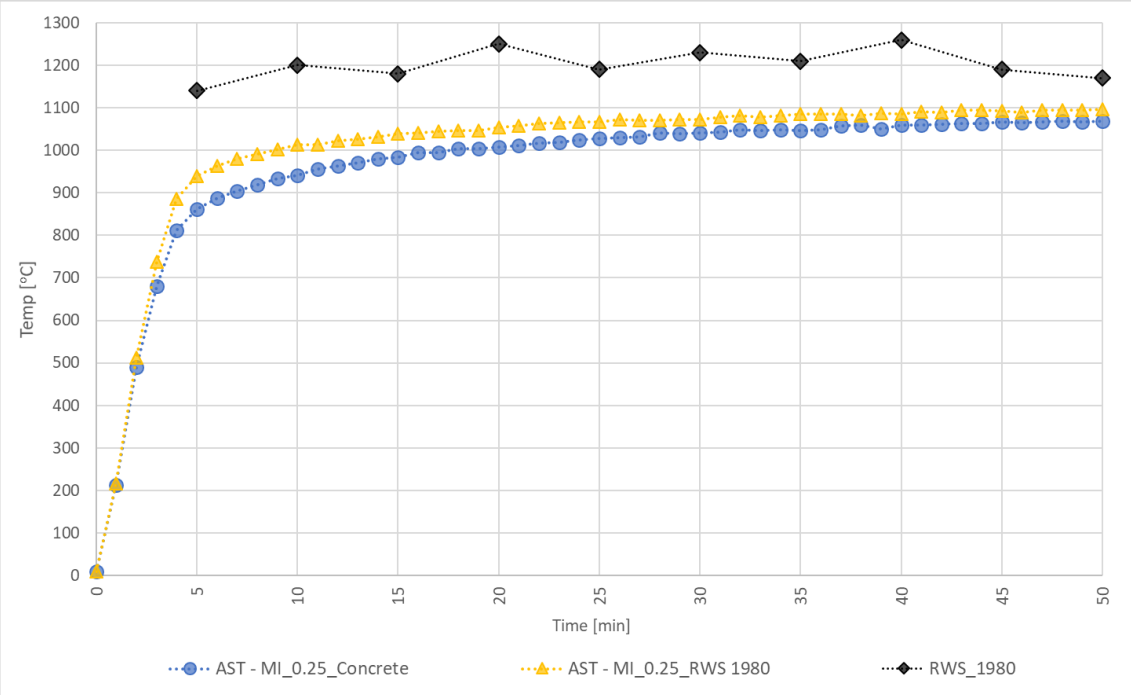


FIGURE 7.41 – COMPARISON OF AVERAGE AST IN FDS SIMULATIONS

Up to now, it was already proven that the RWS curve is based on gas temperature measurements collected during RWS 1980 [89] (Section 7.3). It was also confirmed that the thermal properties of the materials used to build the tunnel are partially responsible for achieving such high temperatures (Section 7.5.2.1). This section confirmed that the temperatures prescribed by the RWS curve might not be representative for the structure, and that a curve based on AST should be used instead. This raises the question if FDS could be a

reliable tool in developing such a curve. As described in Section 5.2.1, FDS applies an 1D heat conduction model for solid obstructions. This means that the solution for gas, wall and radiation temperatures are inherently a function of this 1D model. As AST is depends on both gas and radiation temperatures, it also becomes a function of the 1D heat conduction model adopted by the software. Thus, it is essential to understand whether this 1D model is representative to describe tunnel fires.

During the RWS 1980 [89], slab 8 (Figure 7.11) was left partially unprotected and one thermocouple was recording the surface temperature of this slab during the hole test [89]. Figure 7.42 below provides a comparison between the measurements of this thermocouple and the average wall temperatures obtained for *MI_0.25_Concrete* (Table 7.11). As it can be seen, they agree very well with each other, showing that the 1D heat conduction model performs well in describing the conditions achieved during the RWS tests. Note that in the RWS test setup, the tunnel is very short, and the pools are covering practically its whole length (Figure 7.3). Therefore, we can assume that a more or less uniform heating of the ceiling occurred in the simulation, and that the average wall temperature (surface temperature) shown in Figure 7.42 should indeed represent the general behavior of a concrete ceiling during the RWS test.

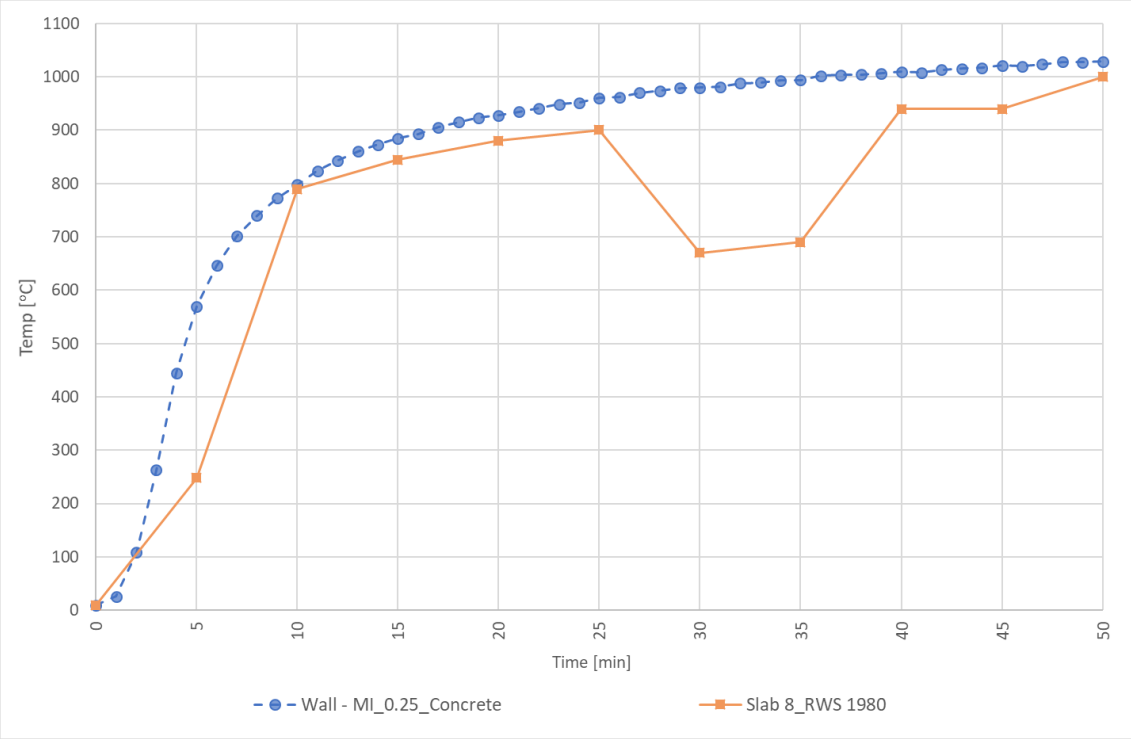


FIGURE 7.42 – WALL (FDS) AND REAL SURFACE TEMPERATURE (RWS 1980)

7.5.3 Concrete Tunnel

It was shown in Section 7.5.2.1, that the *insulation* used on the ceiling during the RWS tests is partially responsible for the gas temperature measurements obtained in the original test. Note that the walls of the tunnel used in the RWS test, were also built with a material of high thermal insulation properties, namely *aerated concrete* (Section 7.4.2.3). Thus, it becomes of interest to understand how the temperature development would be if the tunnel was completely made of concrete. In this sense, a *MI – 0.25* model of the full RWS 1980 test setup in a reduced

domain was again used here. This new model is entitled *MI_0.25_Concrete Tunnel* and is summarized in Table 7.12 below. Note that the fire function described in Section 7.4.2.1 is also used here, differently from the models presented in the previous Section 7.5.2. Therefore, one should avoid any comparison between the temperature measurements of different models before *5 minutes* of fire simulation for all results shown in this section.

Tunnel	Material	Thickness
Floor	Concrete	0.15 m
Walls	Concrete	0.24 m
Ceiling	Concrete	0.15 m

TABLE 7.12 – MODIFICATIONS USED IN MI_0.25_CONCRETE TUNNEL

Figure 7.43 below provides the average gas temperatures obtained for a *concrete tunnel* in comparison with the original test results and also with the FDS simulation for the real test setup (*MI_0.25_RWS 1980*). As described previously (Section 7.5.2.1), the *insulation* on the ceiling contributes to achieving higher gas temperatures inside the tunnel. The same behavior is noticed for the original walls (*concrete gas-block bricks*) as the gap between the gas temperatures for a *unprotected concrete* ceiling and an *insulated* ceiling (Figure 7.40) is significantly increased when the whole tunnel is assumed to be made of *unprotected concrete* (Figure 7.43). Moreover, the gas temperatures measurements obtained during the RWS test would be significantly reduced if the whole tunnel would have been made only of *concrete*. The magnitude of the differences is more remarkable during the first *15 minutes* of fire development, where the temperatures for the *unprotected concrete* case are around *200 ^{o}C* lower than that of the original setup. This difference in temperature is reduced in time, but the gas temperatures for the *concrete tunnel* appear to be at least *100 ^{o}C* lower, even when steady state conditions are reached. This confirms that the temperature development inside the tunnel during a fire is influenced by the thermal properties of the tunnel lining. Thus, if materials with insulation properties are applied to the tunnel, then higher gas temperatures are to be expected during a fire. Note that the temperature development inside the *concrete tunnel* is even lower than the well-known *hydrocarbon curve* (Section 8.1.1), while the temperature development for an *insulated tunnel* is still above this curve. This comparison basis an interesting conclusion:

Materials with high thermal insulation properties will warm up quite immediately during a tunnel fire (Figure 7.39). As we know, the radiation emitted by a surface is related to the fourth power of its own bulk temperature (equation 5.13). This means that insulation materials will contribute with important levels of radiation to the enclosure almost from the beginning of a tunnel fire, thus enhancing the maximum gas temperatures reached inside the tunnel. On the other hand, concrete not only takes more time to warm up (Figure 7.40), but it also requires much more energy to do so. In essence, before emitting relevant levels of radiation back to tunnel, concrete has to extract a lot of energy from the fire-induced gas phase to increase its own temperature. When those effects are put together, it appears that concrete actually contributes to reduce the high gas temperatures generated by a fire within an enclosure (Figure 7.43).

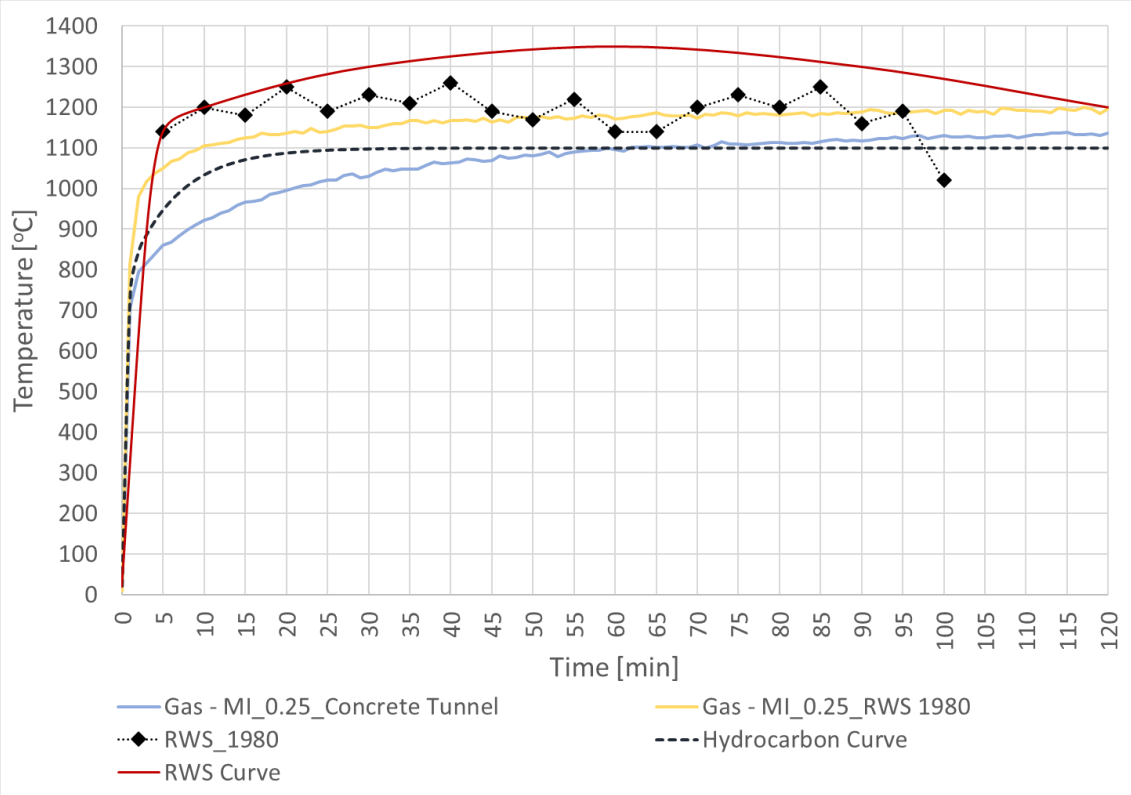


FIGURE 7.43 – AVERAGE GAS TEMPERATURE IN A CONCRETE TUNNEL

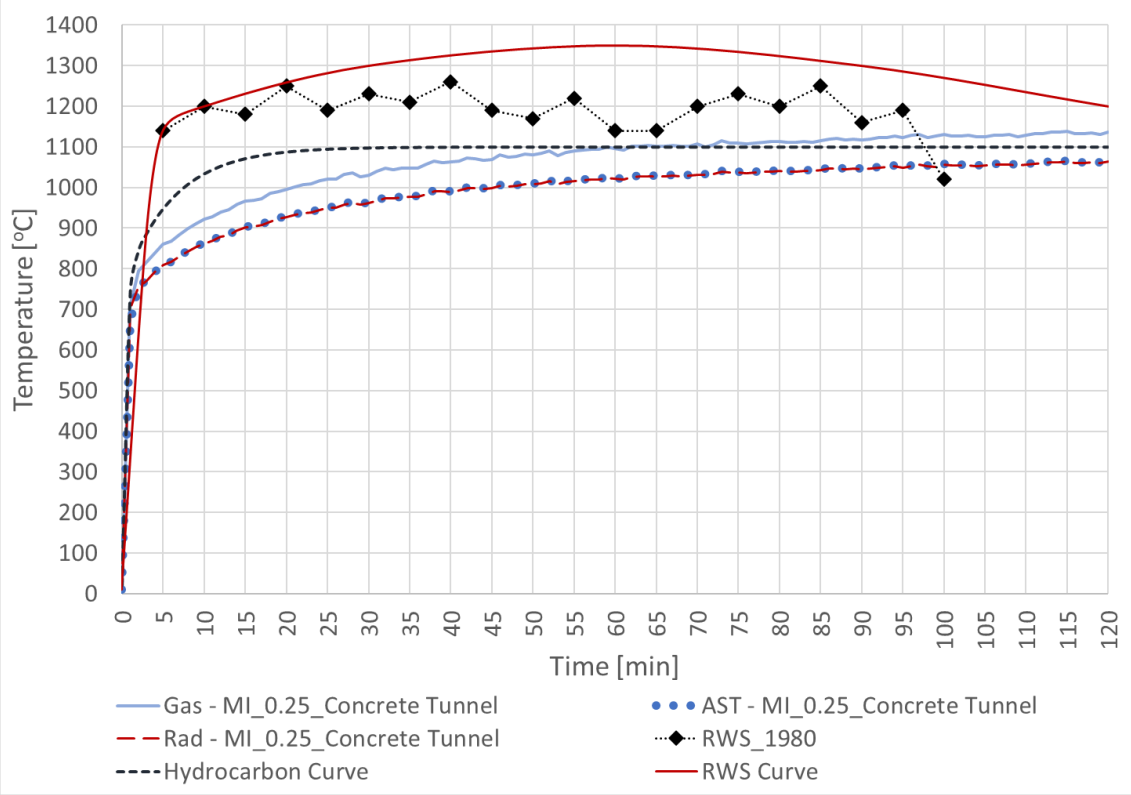


FIGURE 7.44 – AST AT THE CEILING FOR MI_0.25_CONCRETE TUNNEL

Now, let us address the heat exposure on the ceiling for the case of a *concrete tunnel*. First, notice from Figure 7.44, that even for the reduced gas temperatures obtained in this case, the AST is still practically the same as the radiation temperature. Once again, the results shown here are confirming that at high temperatures, the heat exposure to the structure is governed by radiation heat transfer.

Figure 7.45 provides an AST comparison between an *insulated* and an *unprotected concrete* tunnel. As in the gas temperature analysis, the same temperature differences between the scenarios are also noticed here when looking at the AST development on the ceiling. Here, it is important to reinforce the idea that the RWS curve is based on gas temperature measurements within an *insulated tunnel*. Thus, the application of this curve to those cases (*insulated tunnels*) should already be considered conservative, as the AST in the original test setup is clearly limited to *1200 ºC* (dotted yellow line in Figure 7.45).

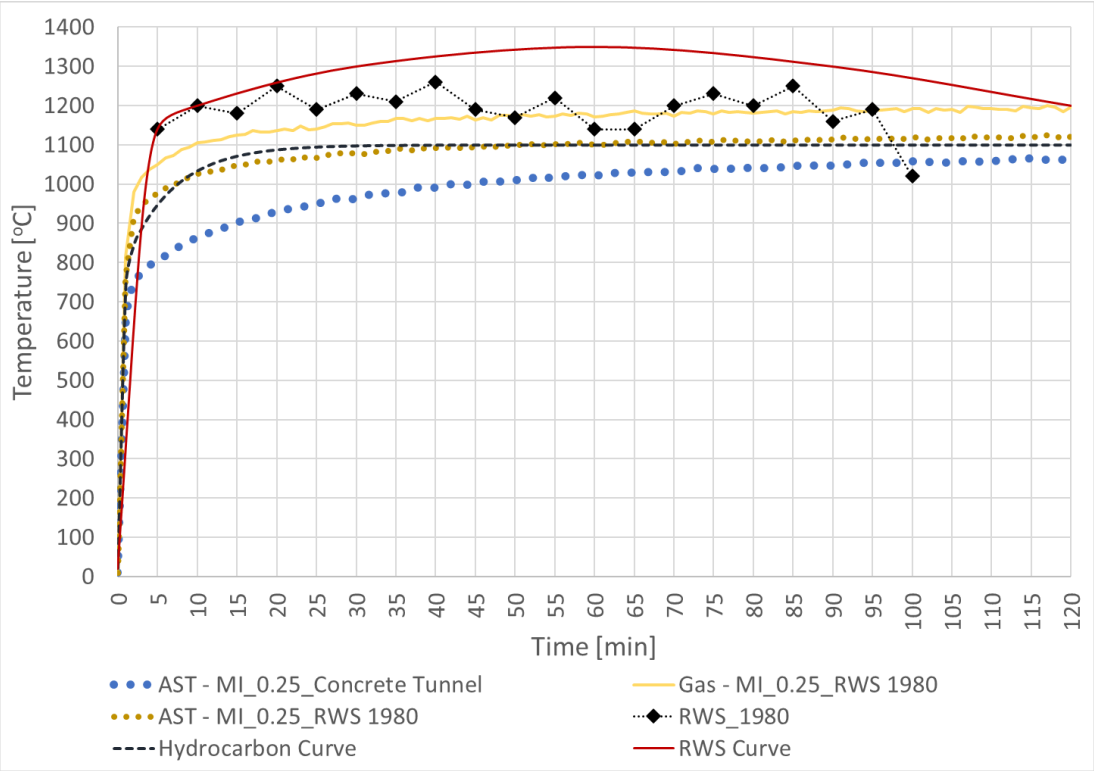


FIGURE 7.45 – AVERAGE AST IN A CONCRETE TUNNEL

The discussion goes even further if one considers the application of the RWS curve for *unprotected concrete tunnels*. As depicted in Figure 7.43, the gas temperatures developed inside a *concrete tunne*l are comparable to the *hydrocarbon curve*, but the thermal exposure imposed on the *concrete* ceiling is not. In essence, Figure 7.45 clearly shows that the maximum AST achieved for the *concrete* ceiling is at least *50 ºC* below the *hydrocarbon curve* for the total time of simulation. Therefore, the results provided in this topic indicate that the RWS curve can be conservatively applied to *insulated tunnels*, but that it seems mistakenly used to address *unprotected concrete tunnels*. Moreover, the maximum heat exposure imposed on a *concrete structure*, represented by the dotted blue line in Figure 7.45, is nearly *200 ºC* lower than the gas temperatures which based the development of the RWS curve (black line in Figure

7.45) at the end of simulation. In the early stages (up to *20 minutes*), this difference is even bigger, reaching approximately *300 °C*.

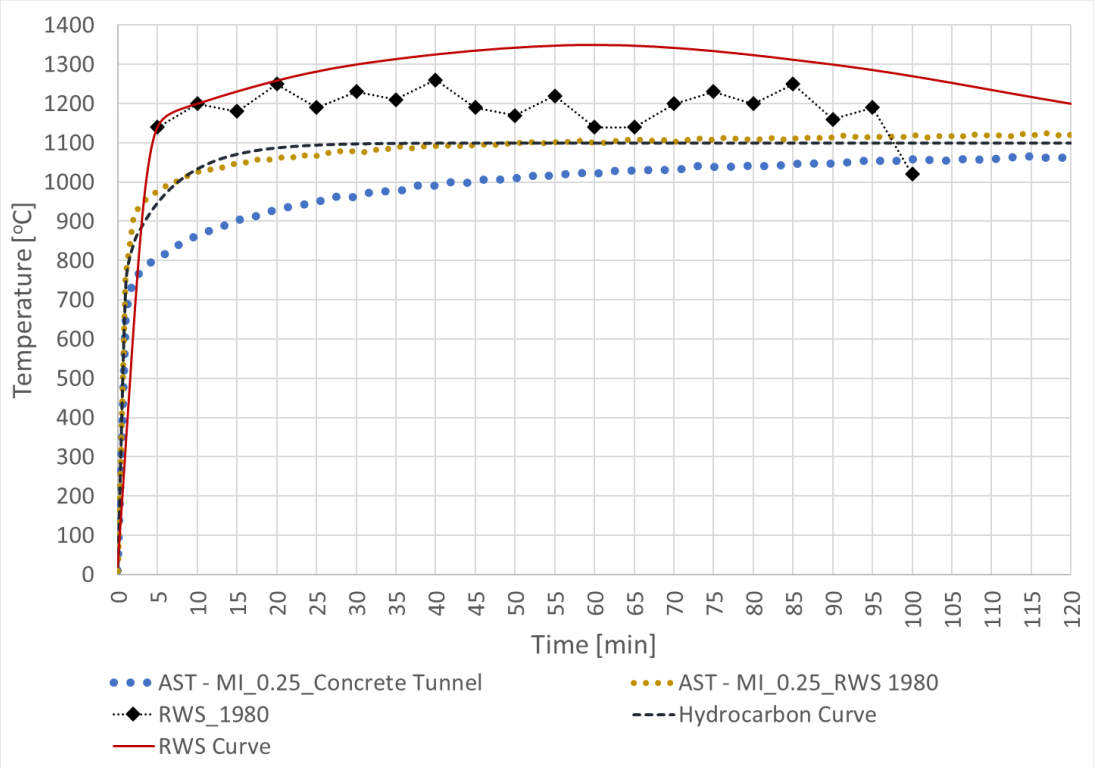


FIGURE 7.46 – THERMAL EXPOSURE IN PROTECTED AND IN UNPROTECTED CONCRETE TUNNELS

In conclusion, Figure 7.46 provides the structural thermal exposure of *insulated* and *unprotected concrete* tunnels in comparison with the RWS curve and the *hydrocarbon curve*. It is clear that the RWS curve is over conservatively applied to both types of tunnel. The *hydrocarbon curve* seems to accurately represent the thermal exposure of *insulated* tunnel linings, and could still be conservatively applied to *concrete* tunnels.

7.5.4 Fire Load

To conclude the investigation about the development of the RWS curve, it is important to understand if the temperature measurements obtained in the test were indeed the maximum temperatures that could ever be achieved inside the tunnel used in RWS 1980 [89]. In this sense, the *mass loss rate per unit area* (MLRPUA) described in Section 7.4.2.1 was varied between several models of the original RWS test setup (*MI_0.25_RWS 1980* in Section 7.5.2), yielding in different fire loads. Table 7.13 below summarizes the studied cases.

MODEL	MLRPUA (kg/(m².s))	HRR (MW)	% HRR RADIATION	D*/δX	DIFFERENCE Tgas – Trad (%)
MI_0.25_0.5 MLRPUA	0.0225	3.76	46	6.6	16
MI_0.25_0.75 MLRPUA	0.03375	5.22	50	7.6	10
MI_0.25_RWS 1980 (*)	0.045	6.01	51	8.0	8
MI_0.25_1.25 MLRPUA	0.05625	6.57	51	8.3	6
MI_0.25_1.5 MLRPUA	0.0675	6.68	48	8.3	5
MI_0.25_2 MLRPUA	0.09	6.53	41	8.3	4

TABLE 7.13 – FIRE LOAD

(*) The fire function used in MI_0.25_RWS 1980 (Section 7.5.2) is here modified to reach its' full power at *15 seconds* of fire simulation. This is also done for all models studied in this section.

Figure 7.47 provides a comparison between the average gas temperatures at the ceiling for all models studied here. It is noticeble that the gas temperature development in the tunnel is nearly the same for all cases within a *25%* variation on the original MLRPUA. The results shown here indicate that, at least for the test setup used in RWS 1980 [89], the thermocouples measurements obtained during the test are indeed representing the maximum gas temperatures which could ever occur inside that tunnel. It appears that if the fire load is sufficiently large to generate flame impingiment on the ceiling, forcing flames to spread longitudinally through it, then, the gas temperatures calculated in the simulations will reach a maximum level. For those cases, the temperatures outputted by FDS are actually representing the flame temperature, and thus a very similar temperature development at the ceiling is obtained even for different levels of HRR. Two important conclusions can be drawn here:

1) The temperature development at the ceiling obtained for *MI_0.25_0.75 MLRPUA* is already at the maximum level, indicating that the holes on the right wall of the tunnel should really have had a very limited effect on the temperature measurements of RWS 1980 [89], as shown in Section 7.5.1.

2) The results shown here also expose a limitation in the use of FDS to address tunnel fires. Moreover, in large scale fire simulations flame temperatures are usually not well-solved (Section 1.2), as this would require the use of very fine meshes which can be translated into unresonable computational time. Nonetheless, even for those cases in which flames impinge on the ceiling, FDS is still able to provide deep insight under fire development, and also on the heat exposure suffered by the structure.

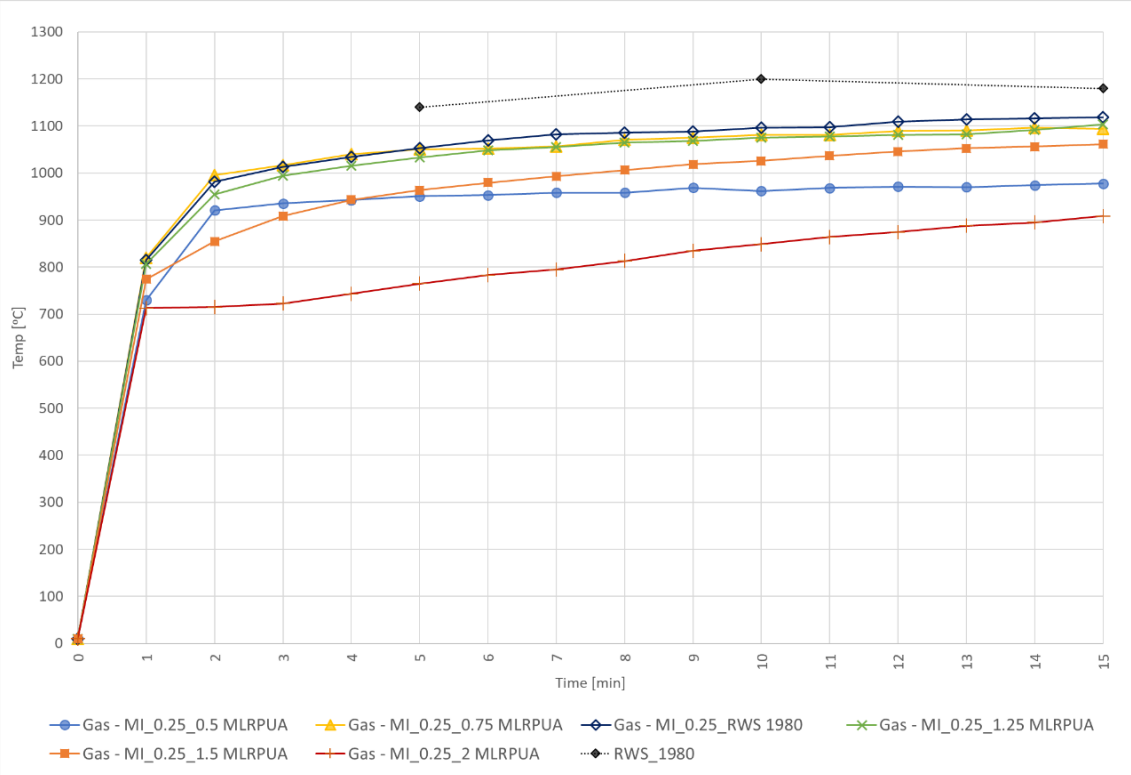


FIGURE 7.47 – AVERAGE GAS TEMPERATURES AT THE CEILING

Now, let us address the results of the last two simulations of Table 7.13. One might be intrigued by the fact that the HRR obtained for those cases is almost the same as for the original simulation of the test (*MI_0.25_RWS 1980*), while the temperature development is not (Figure 7.47). Note that the differences between the temperatures obtained in *MI_0.25_RWS 1980*, and those for *MI_0.25_1.5 MLRPUA* and *MI_0.25_2 MLRPUA* are reduced in time, and that *MI_0.25_1.5 MLRPUA* is already providing comparable temperatures by the end of the simulation. The different results are solely a function of the boundary condition used to define the fire for each one of the models. As explained previously in Section 7.4.2.1, a fire is created through a boundary condition which constantly releases vaporized fuel into the domain according to a specified rate. Combustion immediately occurs whenever fuel encounters sufficient oxygen in the domain of simulation.

One may distinct *fuel-controlled* or a *ventilation-controlled* fire based on the stoichiometric coefficient (r). This is described by Ingason [14] based on the chemistry below:

$$C_aH_bO_c + \left(a + \frac{b}{2} + \frac{c}{4}\right)(O_2 + 3.76N_2) \rightarrow aCO_2 + \frac{b}{2}H_2O + \left(a + \frac{b}{2} + \frac{c}{4}\right)3.76N_2$$

The stoichiometric coefficient r gives the air/fuel ratio required for stoichiometric combustion of fuel to occur. Accordingly:

$$r = \frac{137.8\left(a + \frac{b}{4} - \frac{c}{2}\right)}{12a + b + 16c} \qquad 7.4$$

A *fuel-controlled* condition is achieved in case the air/fuel mass ratio is greater or equal than r. On the other hand, if the air/fuel ratio is below r, then not enough oxygen is available to combust all the fuel and the combustion process is governed by the supply of oxygen, characterizing a *ventilation-controlled* fire. As described previously in Section 7.4.2.1, *N-OCTANE* (C_8H_{18}) was used to simulate the gasoline pool fire used during the RWS tests. Based on equation 7.4, the stoichiometric coefficient for *N-OCTANE* is $r = 15.1$, meaning that *15.1 kg* of air are required to completely burn *1 kg* of *N-OCTANE*. Thus, by comparing the mass fraction of fuel with the inverse of value of r, or $1/r = 0.0662$, we can analyze the differences in temperature shown in Figure 7.47 for the models with higher fire loads.

Hence, Figure 7.48 below provides the mass fraction of fuel for the different models studied in this section. Here, the maximum mass fraction in the plot was selected as the inverse of the stoichiometric coefficient ($1/r$), thus denoting excess fuel zones inside the domain (marked by the red regions in Figure 7.48). It becomes clear that this zone grows between the different models due to the increase of the MLRPUA boundary condition imposed to the models. Therefore, for the cases of *MI_0.25_1.5 MLRPUA* and *MI_0.25_2 MLRPUA*, the fire load applied inside the tunnel is so high, that the excess fuel zone grows tremendously and covers almost the whole tunnel. This makes the combustion inside the tunnel to be governed by the supply of oxygen, meaning that a local *ventilation-controlled* condition is achieved in the region above the pools. The lack of oxygen to combust the vaporized fuel inside the tunnel, specially near the ceiling, is the reason for the temperature drop of those two last models when compared to the maximum temperatures obtained for the previous cases.

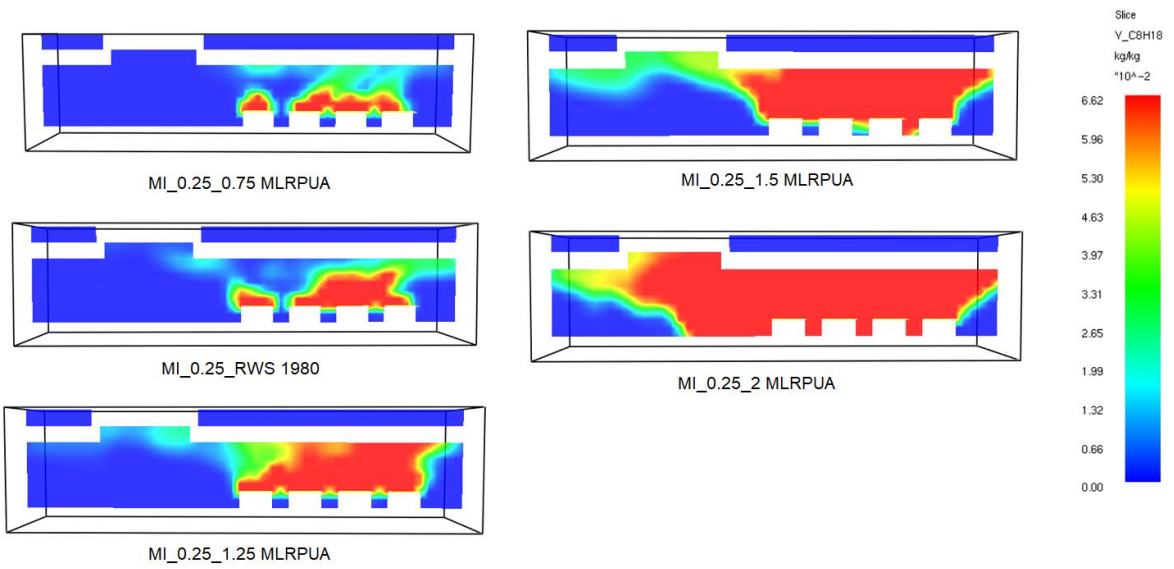


FIGURE 7.48 – MASS FRACTION OF UNBURNED FUEL FOR DIFFERENT MODELS
(AT *300 S* OF SIMULATION)

The models studied in this section indicate that the gas temperatures measured in RWS 1980 [93] were at the level of the maximum temperatures ever achievable inside the tunnel when considering the original setup of the test. Nevertheless, as explained previously in this chapter, we know that the gas temperatures are not governing the heat exposure to the structure. Thus, it becomes fundamental to understand if the radiation temperature development would also reach a maximum for different fire loads. First of all, notice from Figure 7.49 that for all cases studied here, the average radiation temperature at the ceiling (dotted lines in Figure 7.49) is always below the correspondent average gas temperature (continuous lines in Figure 7.49). However, the results also show that the gap between these two temperatures is reduced with the increase of MLRPUA. This reduction in differences between gas and radiation temperatures is also highlighted in the last column of Table 7.13. In FDS, as the flame temperatures are often not well-resolved, a fraction of the HRR is always assumed to be released in the form of thermal radiation (Section 5.2.3.2). This is the case because the radiation varies with the fourth power of the flame temperatures, and due this dependence, the source term in the radiation transport equation cannot be accurately predicted [71].

For *N-OCTANE* this radiation fraction is 0.4, meaning that *40%* of all energy released from fuel combustion is directly converted into radiation. Hence, by increasing the amount of fuel released inside the domain, and thus obtaining higher HRRs, we are also raising the levels of thermal radiation emitted from the fire. This should explain the reduction in the differences between gas temperatures and radiation temperatures for the several models (Figure 7.49). Note that it is not a simple task to evaluate the radiation solution in a fire simulation, as the radiation temperatures shown in Figure 7.49 are a function of radiation transported from every point inside the domain to the surface of the ceiling, and radiation is emitted not only from the combustion of fuel, but also from the smoke layer and walls within the tunnel. All that being said, Figure 7.50 provides a comparison for the radiation temperatures among all models studied in this section. An interesting aspect to notice here is that model *MI_0.25_0.75 MLRPUA* despite providing the same maximum gas temperatures as *MI_0.25_RWS 1980*

(Figure 7.47), does not generate an equivalent radiation temperature inside the tunnel (Figure 7.50). Actually, it is clear that the gas temperatures for *MI_0.25_0.75 MLRPUA* (Figure 7.47) are higher than that of *MI_0.25_1.5 MLRPUA* at all times, but the radiation temperature obtained for the latter overcome that of the former (Figure 7.50). Thus, differently from the gas temperatures, the radiation temperatures do not reach their maximum values for a reduced fire load. In essence, due to the use of a radiative fraction, the radiation temperature appears to be way more sensible to variations in the HRR than the correspondent gas temperature. Even so, as shown in Table 7.13, the maximum fire size achieved inside the tunnel is limited to approximately 6.70 MW due to the availability of oxygen to sustain combustion, and as depicted in Figure 7.50 the maximum radiation temperatures are already achieved for a 6 MW fire (*MI_0.25_RWS 1980*).

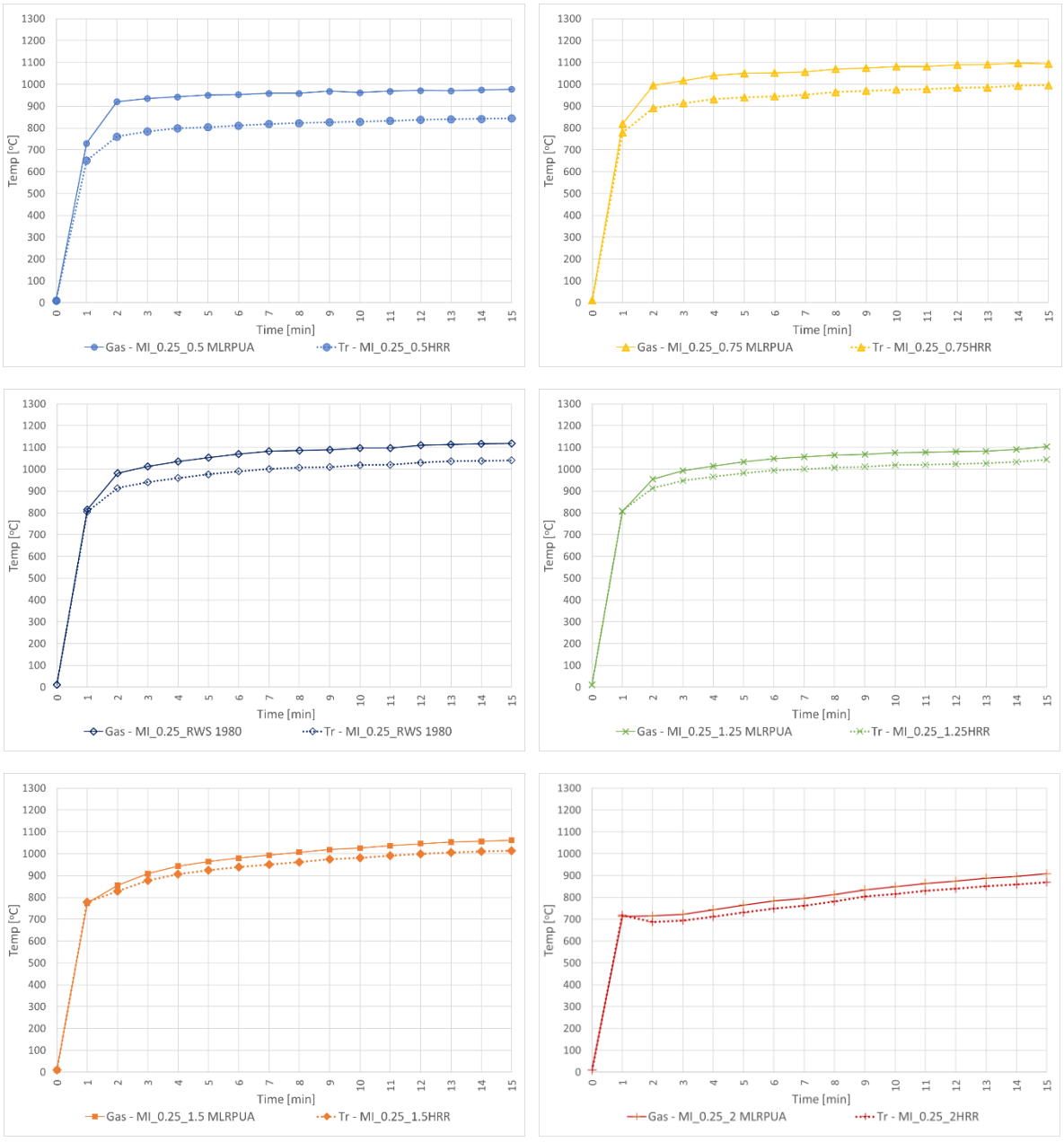


FIGURE 7.49 – DIFFERENCES BETWEEN GAS AND RADIATION TEMPERATURES

In conclusion, the results of the simulation of the original test, given by model *MI_0.25_RWS 1980,* appear to provide the maximum gas and radiation temperatures that could be achieved when considering the test setup used in RWS 1980 [89]. This reinforces the validity of the conclusions drawn in Sections 7.5.2.2 and 7.5.3 with respect to the use of the RWS curve.

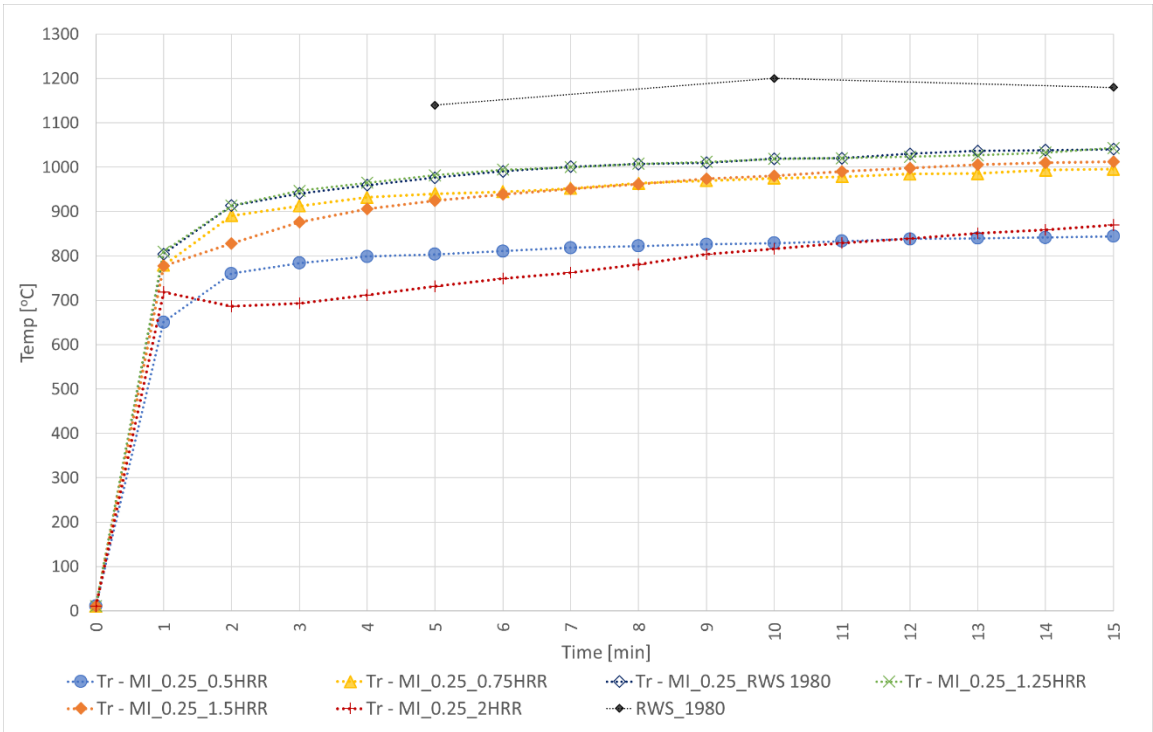


FIGURE 7.50 – AVERAGE RADIATION TEMPERATURES AT THE CEILING

7.6 Influence of Selected Concrete's Thermal Properties

As explained in Section 7.4.2.3, the work developed in this chapter was the among first tasks accomplished during this thesis. At that point, focus was mainly on understanding how to simulate fires and to learn what factors would mainly influence the results. For this reason, constant thermal properties were assigned to *concrete* (Table 7.5). In reality, however, both the thermal conductivity and the specific heat capacity (equation 5.4) are temperature dependent. Therefore, the simple model presented in Section 6.6 is once again used here, to compare the results of a thermal transient analysis for a *concrete structure* subjected to the RWS curve for two cases: (1) *concrete's* thermal properties according to Table 7.5, here entitled as '*Eurocode*'; and (2) *concrete's* thermal properties according to Table 6.1, here entitled as '*FDS_RWS Tests*'. They are also given in Table 7.14 below.

Parameter	Eurocode	FDS_RWS Tests
Density	2300 kg/m^3	2300 kg/m^3
Specific Heat	u = 0% (Figure 11.3)	1.0 kJ/kg.K
Thermal Conductivity	Lower Limit (Figure 11.2)	1.0 W/m.K
Emissivity	0.7	0.8

TABLE 7.14 – INFLUENCE OF SELECTED THERMAL PROPERTIES

Figure 7.51 provides the surface temperature development obtained in DIANA for both cases. As we can see, there is no significant difference among the surface temperature development between these two cases. Note, for instance, that this validates the comparison given in Figure

7.42. However, it must be noted that the solution of the heat conduction problem (equation 5.4) is not the same for both cases, as depicted in Figure 7.52. In fact, as in the work developed in this chapter, we made use of a higher thermal conductivity than that which is adopted by Eurocode 2 Part 1-2 [9] (Table 7.14), heat flows much more easily within the solid phase for a concrete described according to the thermal properties given by *'FDS_RWS Tests'*. This, however, do not harm the results of the fire simulations performed in this chapter when considering a *concrete tunnel* (Section 7.5.3). Basically, as we are focusing on the results of the fire-induced gas phase and also on the interface of heat transfer between *concrete* and fire, but not on the solution of heat flow within the solid phase itself, the results shown in Figure 7.44 for a *concrete tunnel* are still valid.

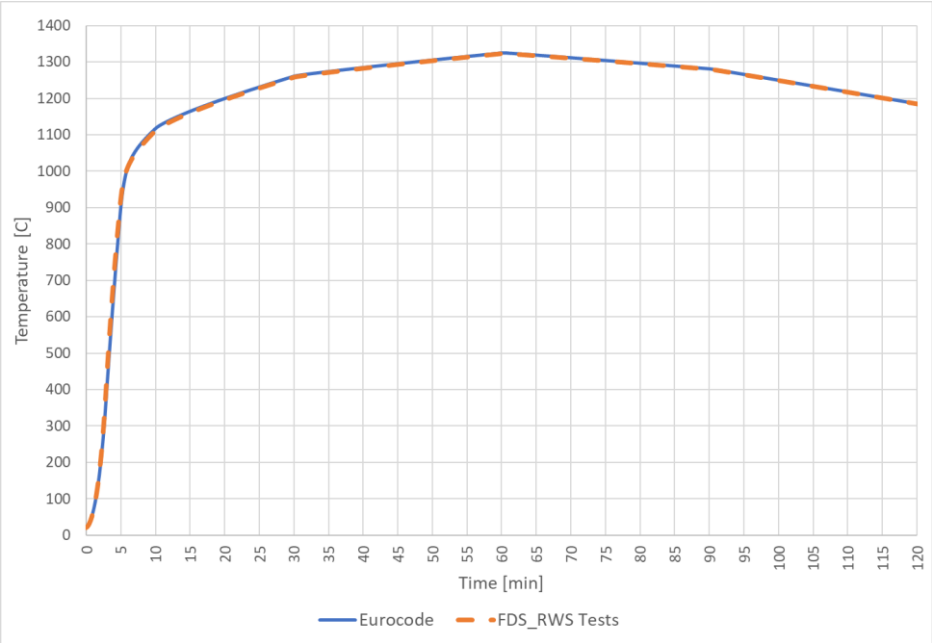


FIGURE 7.51 – SURFACE TEMPERATURE DEVELOPMENT

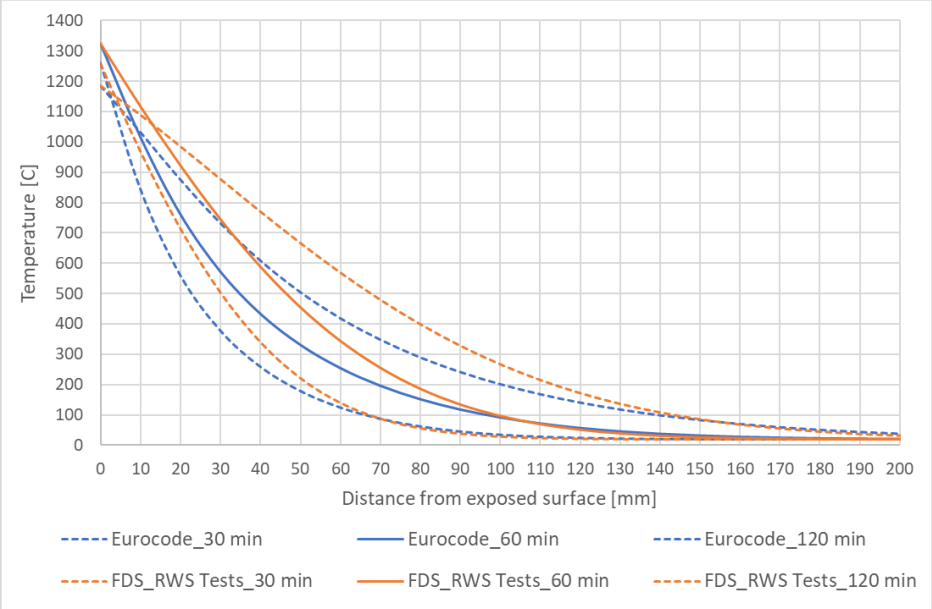


FIGURE 7.52 – EVOLUTION OF TEMPERATURE DISTRIBUTION IN TIME

7.7 Conclusions

Before addressing the final conclusions of this chapter, the following remark has to be made here:

- The work developed in this chapter proves that the RWS curve was derived based on gas temperature measurements. The real thermal exposure imposed on the ceiling of the RWS tunnel during the tests was however, as in any fire scenario, governed by the radiation temperature (fully characterized by the AST). In engineering practice, the use of the RWS curve according to Eurocode 1 Part 1-2 [9], given by equation 5.25, assumes a *blackbody* behavior for the fire-induced gas phase. In simple terms, this means that the gas and radiation temperatures are assumed equal, and are both described by the temperature development given by the RWS curve. In essence, this implies that the use of the RWS curve based on Eurocode 1 Part 1-2 [9], represents the AST for the structure in analysis. Numerous comparisons between the ASTs obtained for different models developed here and the RWS curve or the *hydrocarbon curve* were described during this chapter. Whenever this was the case, both the RWS curve and the *hydrocarbon curve* were assumed to be representing ASTs for the scenarios on analysis.

That being said, the following conclusions can be drawn based on the work developed in this chapter:

1) FDS models to reproduce the original RWS tests were developed here. There are numerous uncertainties involved in the original test data (Section 7.4.1), hardening the task of fully reproducing the original experiment numerically. Even with all those limitations, the FDS model (entitled *MI_0.25_RWS 1980*) created here was able to reproduce the original results fairly well (compare *Gas_MI_0.25_RWS 1980* with *RWS_1980* in Figure 7.43).

2) The RWS curve was derived based on *gas temperature measurements* from RWS 1980 [89] (Figure 7.14). Such temperature measurements are not necessarily representative to describe the thermal exposure generated to structures subjected to fire. Moreover, at such high temperatures as those achieved during any fire, the total heat transfer to the structure will be governed by the radiation component (Section 5.1.3.2), which can be translated in terms of a hypothetical radiation temperature (equation 5.11). For certain cases, gas temperatures are equivalent to the correspondent radiation temperatures, and only for those, the true gas temperatures will be representative to describe the thermal exposure imposed on the structure. Such condition characterizes a *blackbody* behavior for flames and/or smoke generated during a fire, meaning that the fire-induced gas phase emits thermal radiation at its maximum capacity (Section 5.1.3). Considering the simulations performed here, this condition was not achieved during the RWS test, as the radiation temperatures at the ceiling where somewhat lower than the correspondent gas temperatures (compare *Gas_MI_0.25_RWS 1980* with *Rad_MI_0.25_RWS 1980* in Figure 7.38). This indicates that the measurements obtained during the original test were not really representative to describe the thermal exposure imposed on the ceiling of the RWS tunnel during the that test.

3) The RWS curve was derived within a tunnel composed of materials with *insulation* thermal properties. Such materials warm up quite immediately when exposed to fire (compare *Wall_MI_0.25_RWS 1980* with *AST_MI_0.25_RWS 1980* in Figure 7.39), thus limiting the amount of heat transferred from a fire to the material itself. On the other hand, *concrete* requires much more energy to warm up, and also takes much longer to do so (compare *Wall_MI_0.25_Concrete* with *AST_MI_0.25_Concrete* in Figure 7.40). As a consequence, it appears that higher gas temperatures are achieved within an *insulated tunnel* when compared to that of an identical fire scenario in a *concrete tunnel* (compare *Gas_MI_0.25_RWS 1980* with *Gas_MI_0.25_Concrete Tunnel* in Figure 7.43). This aspect will be covered in more detail in Chapter 8.

4) The real exposure suffered by a structure during a fire is characterized by the AST (equation 5.27). This parameter has the added benefit of combining gas and radiation temperatures into a single term, being capable of fully describing the fire-phase in a structural analysis. With this at heart and assuming that the fire scenario achieved during the RWS tests is truly capable of describing the worst-case for a tunnel fire then two points are worth mentioning:

    a. The RWS curve appears to be conservatively applied even to *insulated tunnels* (compare *AST_MI_0.25_RWS 1980* with *RWS Curve* in Figure 7.46).

    b. The use of the RWS curve to describe *concrete tunnels* seems overconservative (compare *AST_MI_0.25_Concrete Tunnel* with *RWS Curve* in Figure 7.46). For those, the use of the hydrocarbon curve would still be conservative and appears to represent a more reasonable choice (compare *AST_MI_0.25_Concrete Tunnel* with *Hydrocarbon Curve* in Figure 7.46).

5) FDS is limited by the application of an 1D heat conduction model for solid obstructions (Section 5.2.1). The use of this model affects the solution of gas, wall (surface) and radiation temperatures (Section 7.4.2.4) within the computational domain, and thus will also affect the computed AST values. Nonetheless, if the goal is to develop a realistic *AST curve* for a specific tunnel based on an idealized fire scenario then, the use of this 1D model should not be a problem. In essence, the maximum thermal exposure imposed on the structure during a tunnel fire will cover relatively large areas more or less uniformly (Figure 9.41), and for such areas, the 1D heat conduction model should perform well in predicting the temperature development in depth.

8 The Prescriptive Approach and its Consequences

The structural design of Dutch tunnels in fire conditions is currently done according to a prescriptive-based approach, in which the RWS curve is used without any distinction among insulated and concrete tunnels. Thus, this chapter aims at clarifying the consequences of the use of such an approach. At first, the RWS curve is translated in terms of an imposed thermal loading and its magnitude is compared against other fire scenarios. Then, the differences in the thermal response of concrete and insulation to this curve are elaborated. Finally, the current testing methodology applied in fire safety (i.e. furnace tests) is investigated and the complexity involved in such tests is explained.

8.1 The Prescriptive Approach

As described by Maluk [74], the origin of the prescriptive approach dates back to the early 1900s with the introduction of the standard time-temperature curve (Figure 8.1) during an annual meeting of the National Fire Protection Association (NFPA). Even though the actual source behind the chosen temperature development remains unknown, this standard curve is assumed to represent a compartment fire involving combustible solids found inside buildings. It is largely adopted worldwide and still constitutes the basis for the assessment of fire resistance of building structures. The common approach in the building industry is to test single structural elements (i.e. columns, beams, slabs and walls) individually in furnace resistance tests (Figure 8.27), and thus quantify the time to failure of the specimen when subjected to the standard curve. In this case, the temperature of the gases inside the furnace is controlled to follow this curve and no distinction is made between tests of elements of different structural materials (e.g. concrete, steel or timber). Thus, the ability of a certain element to continue to perform its function as a barrier, surviving a certain fire duration, characterizes its fire resistance (Drysdale [65]).

The use of this methodology implies that the average gas temperature achieved inside the enclosure is assumed to fully represent the damaging potential of a fire. At heart, this implies that the boundaries of the enclosure are perceived as mere passive participants in the fire process, solely responding to the destructive conditions which are imposed upon them (Hamarthy and Mehaffey [98]). However, the nature of a fire is not only a result of the combustion process, it is also strongly affected by a complex interaction between fire gases and the enclosure, making the prescriptive approach of translating the characteristics of an enclosure fire only in terms of the state of the gases contained within this enclosure too simplistic. For instance, the effects of different enclosure lining materials in the dynamics of a fire are highlighted by the work of McCaffrey et al. [99], which is summarized in Figure 8.2. This figure provides the rate of heat release (Q_{FO}) necessary to achieve flashover in a compartment of predefined dimensions (*4 m* x *6 m* x *2.4 m* high) for different boundary materials: (1) brick; (2) chip board (CB); (3) plasterboard (PB); (4) fibre insulating board (FIB); and (5) expanded polystyrene (EPS). As it can be seen, the thermal properties of the walls are also an important aspect during the development of a compartment fire, but this is clearly not addressed by the use of the standard curve in a prescriptive-based approach.

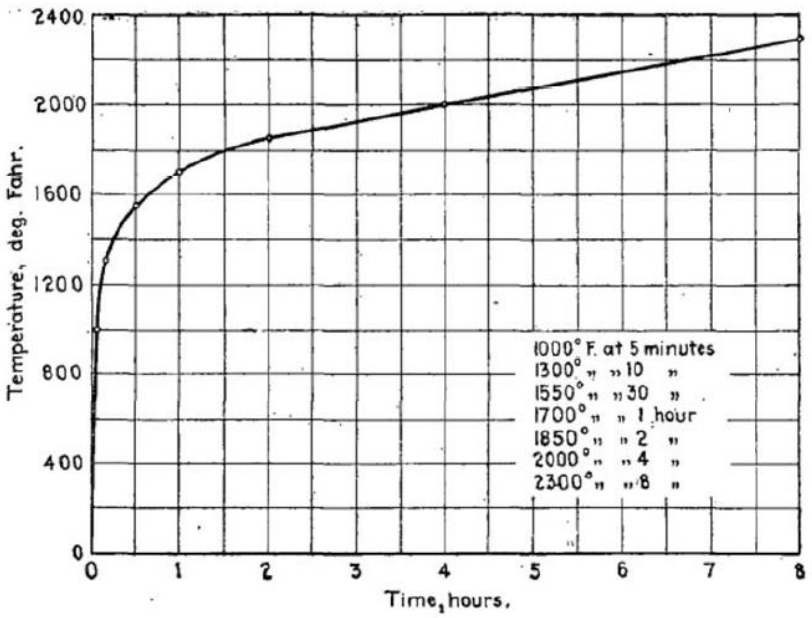


FIGURE 8.1 – STANDARD TIME-TEMPERATURE CURVE PRESENTED AT THE 1918 NFPA ANNUAL MEETING
Retrieved from Maluk [74]

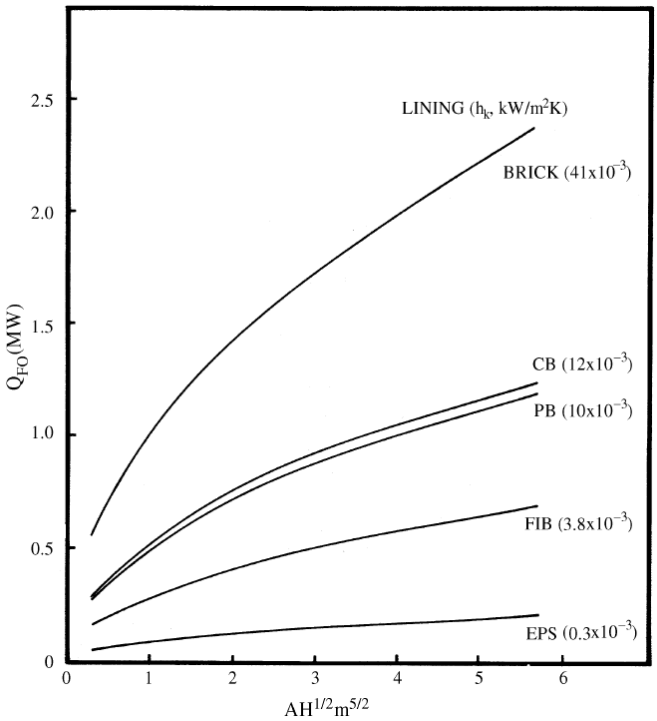


FIGURE 8.2 – FIRE LOAD NECESSARY FOR COMPARTMENT FLASHOVER FOR DIFFERENT LINING MATERIALS
Retrieved from McCaffrey et al. [99]

8.1.1 Tunnels

In case of tunnels, a fire is assumed to generate higher temperatures than those reached in a building. This is due to a more confined nature of the enclosure and an increased fire load. Not only that, due to limited fire-fighting possibilities, a tunnel fire is also expected to last longer

than a building fire, thus increasing the requirements for structural elements that most cope with a higher and longer fire exposure (often taken as two hours for the Dutch context). Different curves are used worldwide in the representation of a tunnel fire (Figure 8.3):

1) *Hydrocarbon Curve:* The hydrocarbon curve was derived by the petrochemical industry and is representative for liquid fuels burning in the open, which are known to achieve higher burning rates than the solid fuels present inside buildings. Accordingly, this curve provides a more rapid increase of air temperatures when compared to the standard-curve (Figure 8.1). Here, just *10 minutes* after the beginning of a fire, the prescribed temperature is already above *90%* of its maximum value or, *1100 ^{o}C*.

2) *RABT-ZTV:* This curve was developed in Germany and its applied to both highways and roadways in a distinct way. An interesting aspect is that this curve is the only one to account for a long cooling down phase during fire development.

3) *Modified Hydrocarbon Curve:* This curve is enforced by the new French regulation, which carefully revised the existing safety provisions for tunnels after some fire events led to real disasters, especially for the case of the Mont-Blanc tunnel (UPTUN [51]). The modified hydrocarbon curve is assumed to account for the enclosure effects on fire development and prescribes an increase in the temperatures originally provided by the hydrocarbon curve, which was derived for fires in the open.

4) RWS Curve: The RWS curve was developed in The Netherlands, but is largely used worldwide. Chapter 7 provides a full description of the tests behind the derivation of this curve.

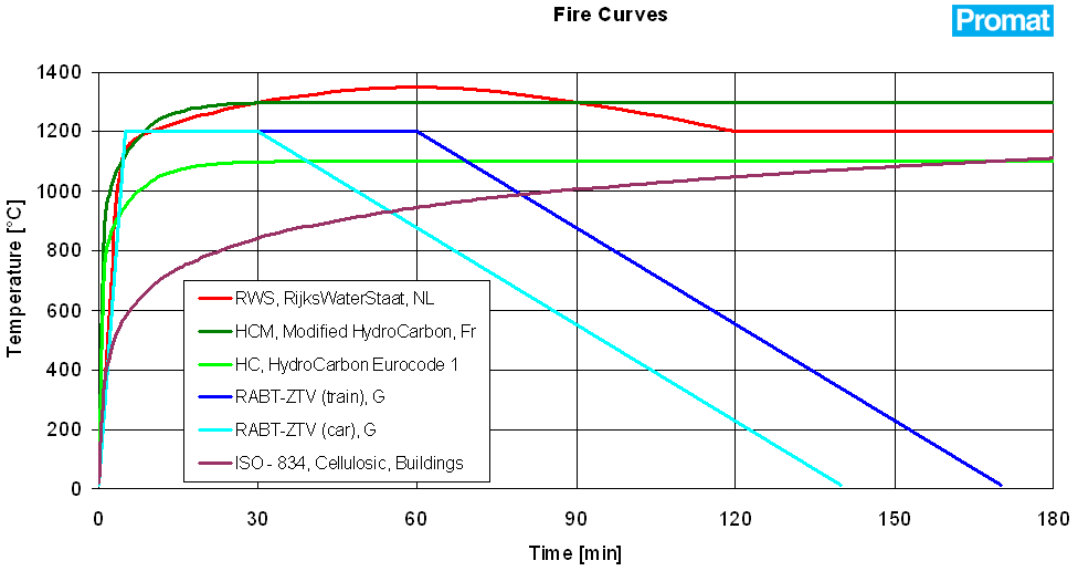


FIGURE 8.3 – TIME-TEMPERATURE CURVES ADOPTED IN TUNNEL FIRES[9]

[9] https://www.promat-tunnel.com/en/advices/fire-protection/fire%20curves

The occurrence of such high temperatures during a tunnel fire was amongst others verified during the Runehamar tests [5] in Norway. In total, four different mockups, designed to realistically represent HGV fire loads, were tested: (T1) wood and plastic pallets; (T2) wood pallets and mattresses; (T3) real furniture and tires; and (T4) plastic cups in cardboard cartons. As shown by Figure 8.4, the maximum temperatures measured at the ceiling during the Runehamar tests fit very well the RWS curve. Also, notice from the same figure that, in all tests, temperatures above *1200 ºC* were achieved.

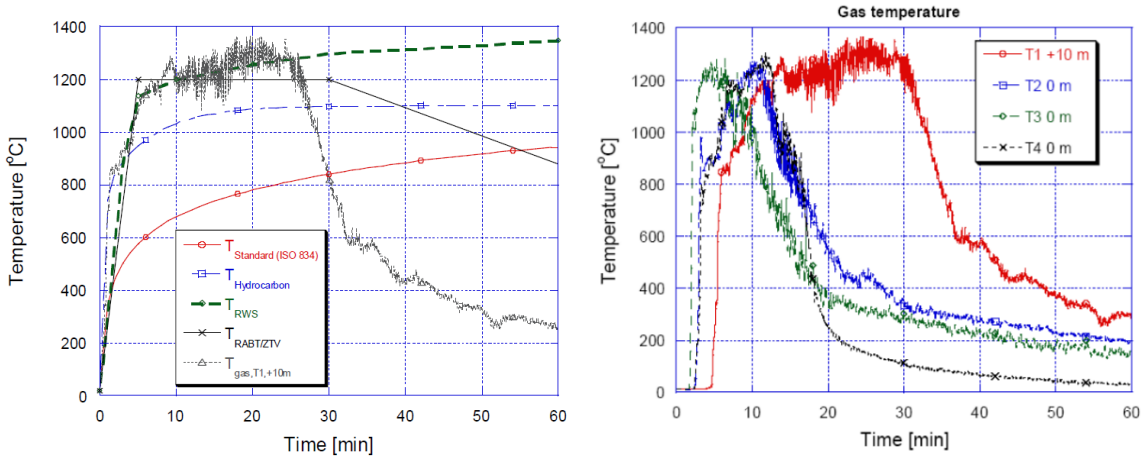


FIGURE 8.4 – MAXIMUM GAS TEMPERATURES AT THE CEILING (RUNEHAMAR TESTS)
Retrieved from Ingason et al. [5]

A more recent test series was perfomed in 2018 in the San Pedro de Anes tunnel test facility in Spain by VID Fire-Kill Aps (Jessen [100]). Intended to evaluate the performance of their low pressure water mist system (known as TUNPROTEC) in controlling the development of large HGV fires (*HRR* $\geq$ *250 MW*), full-scale tests with high longitudinal ventialtion velocities ($\geq$ *5 m/s*) were executed. A free-burn test was also performed in order to verify the the capacity of the fuel package (a mock up consisting of a combination of wood and plastic pallets) on representing a realistic HGV fire. As it can be seen from Figure 8.5, the gas temperatures achieved in the free-burn test were above *1100 ºC*, apparently nearly reaching *1300 ºC* in certain locations.

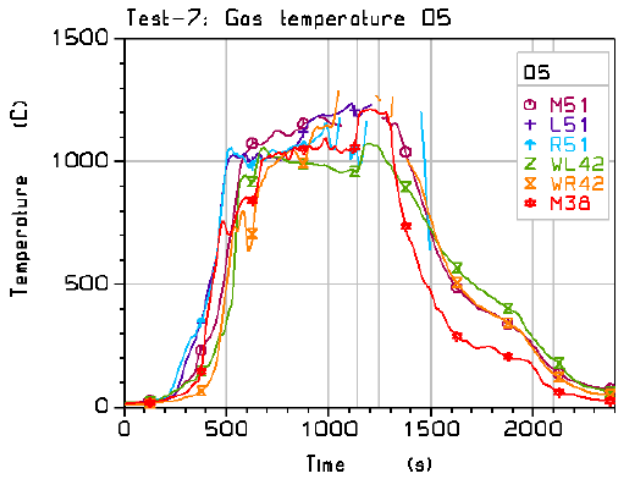


FIGURE 8.5 – GAS TEMPERATURES AT THE CEILING LOCATED 5 M DOWNSTREAM THE FIRE SOURCE (SAN PEDRO DE ANES TESTS)
Retrieved from Jessen [100]

8.1.2 The RWS Fire Scenario from a Different Perspective

As described in the previous section, the Runehamar test results are often taken as a confirmation of the applicability of the RWS fire curve to translate the severity of tunnel fires. For now, let us take this as a valid truth and assume that this curve is indeed representative to describe the most critical fire within a tunnel. If this is the case, then it becomes fundamental to have a clear idea of the magnitude of the fire load which is inherently prescribed by the use of this curve. As we know, radiation governs the heat exposure to a structure (Section 5.1.3.2) thus making the achieved gas temperatures to be of less importance when addressing the structural consequences of a fire. However, as explained in Section 5.3.3.2, Eurocode 1 Part 1-2 [75] defines that for elements which are completely surrounded by fire, the radiation temperature may be taken as equal to the gas temperature prescribed by the RWS curve (equation 5.25). Note that this assumption inherently characterizes a *blackbody* behavior for the fire-induced gas phase (Section 5.1.3). Keep also in mind that, at least with regard to the simulations of the RWS tests performed in Chapter 7, this appears to be a conservative assumption (compare gas and radiation temperatures in Figure 7.38). Even so, we can still use this principle from Eurocode 1 Part 1-2 [75] to define the amount of radiation which is inherently considered in the application of this fire scenario. This is done through the use of equation 5.13, but given the importance of such for the work developed in this chapter, this equation is rewritten below:

$$\dot{q}''_{rad,inc} = \varepsilon_f \sigma T^4_{RWS} \qquad \textbf{8.1}$$

where $\dot{q}''_{rad,inc}$ is the incident radiation heat flux (W/ m^2) prescribed by the use of the RWS curve, σ is the Stefan-Boltzmann constant (5.67 x 10^{-8} W/(m^{2}K^4)), T_{RWS} is the temperature development prescribed by the RWS curve (K) and ε_f is the flame emissivity that in this case is equal to 1 (Eurocode 1 Part 1-2), thus characterizing a blackbody behavior for the flames, in which radiation temperatures are equivalent to the correspondent gas temperatures.

Keep in mind that the heat flux prescribed by equation 8.1 is not the total heat flux to the structure, which is actually given by equation 5.25 and is the result of a complex solution involving all modes of heat transfer (i.e. radiation, convection and conduction). However, if we address the RWS curve in terms of a fire induced radiative heat flux, then we have a solid basis of comparison against different fire scenarios, making it easier to understand what level of fire severity we are imposing to our structures by the indiscriminate use of this curve in the design of tunnels. In this sense, Figure 8.6 below provides the incident radiation heat flux given by the solution of equation 8.1 in time. Notice that the peak heat flux nearly reaches *400 kW/m^2*, being grather than 350 *kW/m^2* for almost one hour and higher than *300 kW/m^2* for approximately 70% of the total exposure time.

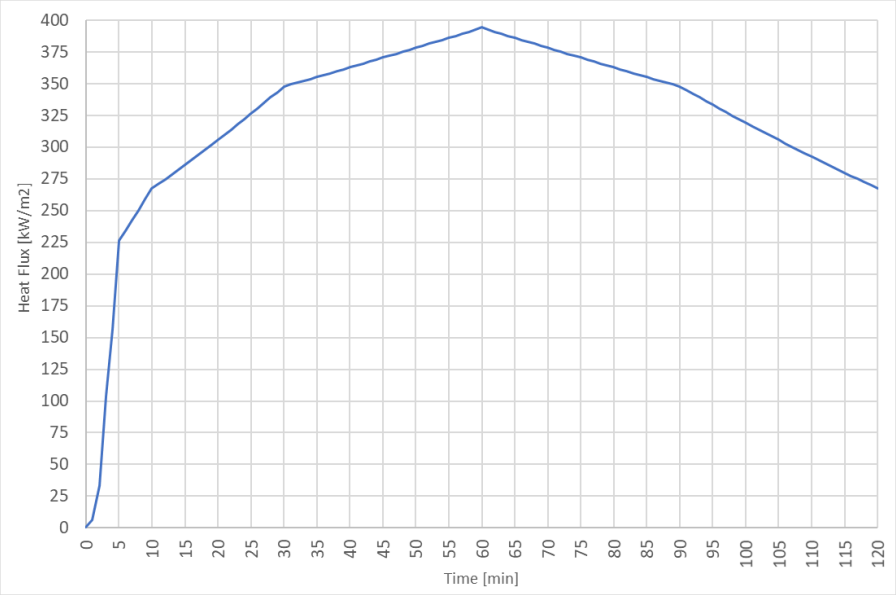


FIGURE 8.6 – FIRE-INDUCED RADIATIVE HEAT FLUX GIVEN BY THE USE OF THE RWS CURVE

Having rewritten the RWS fire scenario in terms of the amount of thermal radiation emitted by a fire, we can now investigate what other types of fire could actually generate such levels of radiative heat flux. Unfortunately, in literature, data regarding the level of radiation released from fires appear to be limited to the petrochemical industry, which is mainly focused in the occurrence of hydrocarbon fires in the open (e.g. pool fires, jet fires, fire balls, and vapor explosions). When considered both the destructive potential and the total duration of fire, two of those cases become of interest for the scope of this thesis, namely pool fires and jet fires.

8.1.2.1 Pool Fires

A pool fire is a turbulent diffusion fire that burns of a horizontal pool of vaporizing liquid fuel with low initial momentum, which limits the contribution of convection heat transfer in such fires. Ideally, the level of radiation generated by a pool fire could be determined based on the achieved flame temperature through equation 8.1. However, remember from Section 5.1.3.1 that, in reality, gas temperatures vary all over the flame body (Figure 5.14), and also that the common assumption that *luminous flames* always behave as *blackbodies* (i.e. taking $\varepsilon_f = 1$ in equation 8.1) is not necessarily true, as the emissive capacity of a flame is directly related to soot concentration within the flame body itself.

Several studies about heat transfer to targets within large-scale pool fires are reported by Beyler [72] and summarized in Figure 8.7. Note that most of the work presented here is based on measurements of objects centrally located within the lower portions of the flame and fully immersed in all sides or, in other words, the values reported here are expected to represent the maximum heat fluxes which are expected to occur within a pool fire (Figure 5.14). Another important aspect highlighted by the author refers to the size of the elements used to measure those heat fluxes. Accordingly, larger objects appear to effectively average the heat fluxes over their whole body, yielding in significant smaller measurements (*120 kW/m²*) than those provided by small calorimeters (*170 kW/m²*). This effect appears to grow even further for objects with comparable sizes to that of the diameter of the pool. For those cases, the maximum heat flux seems limited to *85 kW/m²*. As the measurements of such large objects are given by

only two studies (marked with superscription [a] in Figure 8.7), Beyler [72] reccomends the use of a maximum time-averaged heat flux of *120 kW/m²* as a conservative representation for targets located within pool fires.

Large calorimeters	kW/m²
Gregory et al. [72]	120
Wachtell and Langhaar [73]	85
Anderson et al. [68]	100
National Academy of Science [74] (average of data in the literature pre-1970)	110
Moodie [75]	100
Tunc and Venart [76]	105
McLain [71]	85[a]
Taylor et al. [70]	75[a]
Small calorimeters	kW/m²
Russell and Cansfield [66]	170
Gregory et al. [72]	160

[a]Object site comparable to pool fire

FIGURE 8.7 – MAXIMUM AVERAGE HEAT FLUX MEASUREMENTS OF LARGE-SCALE POOL FIRES
Retrieved from Beyler [72]

The value proposed by Beyler [72] is also in line with the requirements made by the Norwegian petroleum industry in NORSOK S-001 [101]. This standard adopts a global average heat load of *100 kW/m²* for the design of structures subjected to pool fire flames. It also considers a maximum local heat flux of *150 kW/m²*, but this value is assumed to be representative only for small areas and is recommended to be used to evaluate the rupture temperature of equipments or piping lines.

Higher heat flux values are proposed by the Fire and Blast Information Group (FABIG) in its *'Technical Note 13 – Design Guidance for Hydrocarbon Fires'* [102]. Accordingly, maximum radiative heat fluxes of *125 kW/m²* are expected in small hydrocarbon pool fires (*diameter < 5 m*) and values as high as *230 kW/m²* can be achieved for larger pools (*diameter > 5 m*). One important remark here is linked to the kind of fuel used. Apparently, for decreasing values of fuel molecular weight, the generated gases and soot particles become much hotter, thus leading to higher levels of radiation when compared to heavier hydrocarbon flames. For instance, while maximum radiative heat fluxes of kerosene pool fires appear to be limited to *160 kW/m²*, which is in line with the review given by Beyler [72], radiation levels generatred by natural gas (LNG) flames may even achieve *300 kW/m²* (Figure 8.8). In essence, the growing use of LNG as fuel in the transportation sector means an imminent increase on the expected levels of fire radiation, which will most likely require fundamental changes for the fire safe design of tunnel structures in the near future.

Organisation	Reference	Pool size, m	Fuel	Total heat flux, kW m^{-2}
AEA Winfrith	1	0.5 x 9.5	kerosene	150
US Dept of Transportation	2	see reference	kerosene	138
US Coast Guard	3	see reference	kerosene	110-142
US Dept of Transportation	4	see reference	kerosene	136-159
Sandia	5	see reference	kerosene	113-150
HSE Buxton	6	see reference	kerosene	130
Shell Research	7	4 x 7	kerosene	94-112
Hagglund	8	see reference	JP-4	120-150
Sandia	9	9 x 18	JP-4	90-164
Sandia	10	9 x 18	JP-4	80-120
Shell Research	11	35	LNG	250-300
Shell Research	12	12.5 x 15.5	Refrigerated Propane & Butane	230-270

References

1. C.J. Fry, "Pool Fire Testing at AEA Winfrith." CONF-8906331 PATRAM '89, 3, pp 1587-1594, 1989.

2 W. Townsend, C. Anderson, J. Cook, & G. Cowgill, "Comparison of Thermal Coated and Uninsulated Rail Tank Cars Filled with LPG Subjected to a Fire Environment", US Dept of Transportation Report No. FRA-OR&D, pp 75-32, December, 1974.

3 R.C. Richards and R.G. Vorthman, "Full-Scale Ship's Hull Exposure Fire Tests. Dept. of Transport US Coast Guard Report No. CG-D-97-76, June 1976.

4 T.I. Eklund, "Pool Fire Radiation Through a Door in a Simulated Aircraft Fuselage", US Dept of Transportation FAA, December, 1978.

5 J.A. Canfield & L.H. Russell, "Measurements of the Heat Flux within a Luminous Avaition Fuel Flame", Presented at the September Meeting of the Easter Section of the Combustion Institute, 1969.

6 K. Moodie, K. Billinge, & D.P. Culter, "The Fire Engulfment of LPG Storage Tanks", I. Chem E. Symp. Series no. 93, pp 87-106.

7 K. Moodie, L.T. Cowley, R.B. Denny, L.M. Small and I. Williams, "Engulfment Tests on a 5 Tonne LPG Tank", J. Hazardous Materials, 20, pp 55-71, 1988.

8 B. Hagglund and L. Persson, "The Heat Radiation from Petroleum Fires", FOA Raport, Forvarets, Forskningsanstalt, Stockholm, 1976.

9 J.J. Gregory, N.R. Keltner & R. Mata, Jr., "Thermal Measurements in Large Pool Fires", Trans ASME, J of Heat Transfer, Vol 111, pp 446-455, May 1989.

10 M.E. Schneider & L.A. Kent, "Measurement of Gas Velocities and Temperatures in a Large Open Pool Fire", Fire Technology, pp 51-80, Feb 1989.

11 D. Nedelka, J. Moorhouse and R.F. Tucker, "The Montoir 35m diameter LNG Pool Fire Experiments", Presented at 9th Int. Congress and Exposition of Liquified Natural Gas, LNG9, 17-20 October, Nice, France.

12 F.D. Wayne & K. Kinsella, "Spectral Emission Characteristics of Large Hydrocarbon Pool Fires", American Soc. of Mech. Engineers, 84-WA/HT-74, 1984.

FIGURE 8.8 – HEAT FLUXES GENERATED BY POOL FIRES
Retrieved from FABIG [102]

Limited information regarding the confinment effects in pool fires was found in literature. FABIG [102] describes that for *fuel-controlled* fires in *insulated* compartments, internal heat fluxes may reach *350 kW/m^2*, while for *ventilation-controlled* fires (also in *insulated* compartments) maximum values drop to *230 kW/m^2*, as the burning rate of fuel is reduced to adjust to the availability of oxygen. It is also described that the temperatures achieved inside

non-insulated compartment fires are in a range of *200 – 400 °C* lower than that of an *insulated* compartment. This also means a decrease in the expected levels of radiation heat flux achieved inside the enclosure for *non-insulated* boundaries. For instance, making use of equation 8.1 and considering the temperature achieved in an *insulated* compartment as the radiation temperature which leads to a heat flux of *350 kW/m²*, then a reduction of *200 °C* for the maximum temperature achieved in a *non-insulated* compartment would correpond to a maximum heat flux of *~205 kW/m²* or, a reduction of over 40% on the total level of exposure within the enclosure.

The data presented here is compiled in Table 8.1. As we can see, the RWS curve prescribes a fire scenario (Figure 8.6) which is much more destructive than that achieved by a pool fire in the open. When compared to pool fires confined in an enclosure, the RWS fire scenario is in line with that which is reported for an *insulated* compartment, but is still at least 1.7 times greather than that of a *non-insulated* compartment.

Reference	Recommended Heat Flux
Beyler [72]	120 kW/m²
NORSOK S-001 [101]	100 kW/m²
FABIG [102]	160 kW/m² – 300 kW/m² [a] 350 kW/m² [b]

TABLE 8.1 – MAXIMUM HEAT FLUXES FOR LARGE-SCALE POOL FIRES

[a] Apparently, the level of radiation generated by fuels of high molecular weight (e.g. gasoline) within pool fires, is limited to *160 kW/m²*. On the other hand, fuels with low molecular weight (e.g. LNG) achieve higher levels of radiation and may lead to heat fluxes as high as *300 kW/m²*. For a large hydrocarbon fire in the open, a total heat flux of 250 kW/m² is proposed, representing the added contribution of radiative heat flux of 230 kW/m² and an initial convective heat flux of 20 kW/m².

[b] Value representative for *fuel-controlled* pool fires in *insulated* compartments. Significant reduction is expected for the levels of radiation achieved in *non-insulated* compartments.

8.1.2.2 Jet Fires

According to Nolan [103], a jet fire (Figure 8.9) results from the combustion of a constant stream of pressurized flammable gases or atomized liquids, having considerable momentum in a specific direction. The high velocity of escaping gases provides more air entrainment into the jet, leading to a more efficient combustion than that which is achieved in a pool fire. Despite being very localized, jet fires are known to generate severe thermal exposure to anything inside or near the flame zone. One important remark regarding jet fires is that, differently from pool fires where the convection contribution is very limited, here, the total heat flux to objects located within the flames is actually a combination of highly radiative fluxes (due to optically thick flames) with very high convective heat fluxes. Moreover, the convective component is not negligible in jet fires and accounts for a significant percentage of the total heat flux to an object located within the flame. Essentially, this means that the exposure suffered by an object subjected to a purely radiative heat flux of *350 kW/m²* such as the prescribed by the RWS fire scenario (Figure 8.6) is more severe than the exposure suffered by an object imposed to a total heat flux of *350 kW/m²* in which *230 kW/m²* is radiative heat flux and *120 kW/m²* is convective heat flux. The difference of total thermal exposure for these two cases is highlighted in Figure 8.10 which is fully explained by Section 11.6.



FIGURE 8.9 – JET FIRE
Retrieved from Nolan [103]

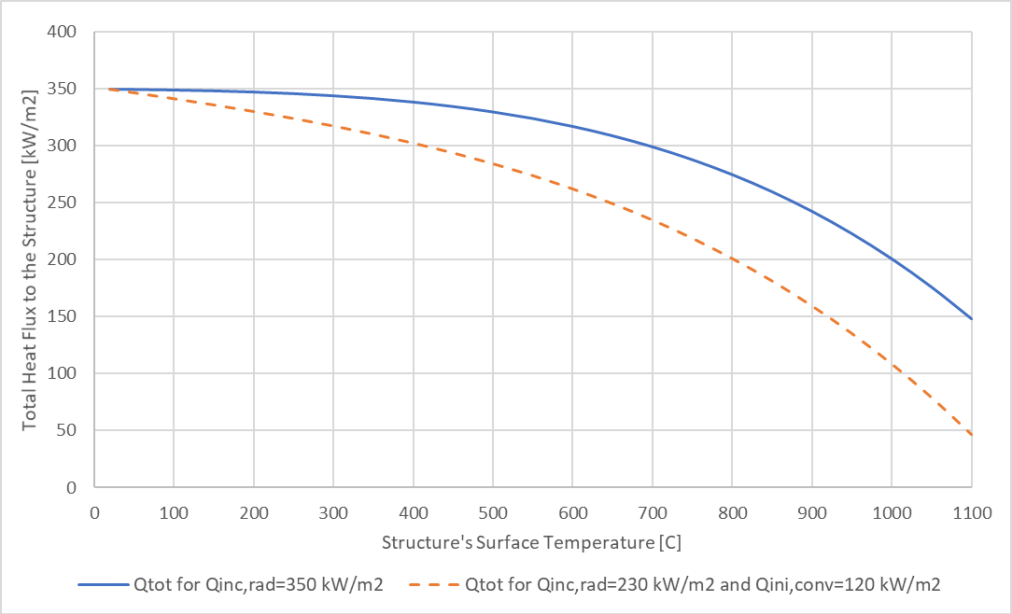


FIGURE 8.10 – COMPARISON OF THERMAL EXPOSURE

Beyler [72] summarizes some studies on the heat exposure generated by the impingement of jet fires. The maximum heat flux measurement reported is equal to *340 kW/m²*, but this value is reduced to *200 kW/m²* when averaged over the impingement area of a cylindrical target fully immersed in flames. NORSOK S-001 [101] recommends the use of *100 kW/m²* as a representative heat flux for the global average heat load to be used in structural design. It also suggets that the total heat flux can achieve local peaks of *350 kW/m²* in small areas. FABIG [102] proposes the use of maximum heat fluxes on engulfed objects in a range of *180 kW/m²* – *400 kW/m²* depending on the mass release rate of fuel. For the maximum level of exposure, the radiative component accounts for 70% of the total heat flux, which also agrees with what is reported by Beyler [72]. The radiation contribution to the total exposure is reduced to approximately 45% in smaller jet fires, characterized by lower levels of mass release rate of

fuel (*0.1 kg/s*). Note that such mass loss rate is still almost twice as big as the maximum loss rate obtained for a gasoline pool fire (Figure 4.5). In case of large jet fires confined in an enclosure, FABIG [102] describes typical values in the range of *290 kW/m^2 – 400 kW/m^2* with a maximum radiation contribution of 70% of the total heat flux.

The data presented here is summarized in Table 8.2. Now, consider the level of radiation heat flux which is inherently defined by the use of the RWS curve (Figure 8.6). Notice that for more than 70% of the total exposure time, the radiative heat flux prescribed by the RWS fire scenario is above *300 kW/m^2*. This means that, at least during this period, the thermal exposure prescribed to tunnel structures might even be more severe than that of the maximum exposure generated by the impingment of a jet fire, if considered that total heat flux of a jet fire is actually composed of *280 kW/m^2* of radiative heat flux and *120 kW/m^2* of convective heat flux (superscription [b] in Table 8.2), and we are still missing the convection contribution in the use of the RWS fire scenario. Therefore, in order to understand how severe the exposure imposed by the use of the RWS curve really is, Section 8.1.2.3 provides a comparison of the thermal response of a concrete structure subjected to the different fire scenarios investigated here (i.e. pool and jet fires) with that which is given by the use of the RWS curve.

Reference	Maximum Total Heat Flux	Averaged over a Large Impingement Area
Beyler [72]	340 kW/m^2 [a]	200 kW/m^2
NORSOK S-001 [101]	350 kW/m^2	100 kW/m^2
FABIG [102]	400 kW/m^2 [b]	Does not differentiate

TABLE 8.2 – TOTAL HEAT FLUXES FOR JET FIRES

[a] *Radiative heat flux accounts for approximately 2/3 of the total heat flux.*

[b] *280 kW/m^2 of radiative heat flux added to 120 kW/m^2 of initial convective heat flux, consideing a flame emissivity of 0.85 and a convective heat transfer coefficient of 95 W/(m^2.K).*

8.1.2.3 Comparison of Concrete's Thermal Response to Different Fire Scenarios

The review over the heat fluxes generated by pool and jet fires presented in Sections 8.1.2.1 and 8.1.2.2, respectively, has indicated that the use of the RWS curve according to Eurocode 1 Part 1-2 [75] (i.e. equation 5.25) might represent one of the most severe fire scenarios encountered in literature. To ensure that this is indeed the case, this section compares the thermal response of a concrete structure exposed to: (1) the RWS curve; (2) a pool fire; and (3) a jet fire. In this sense, the same model described in Section 6.6 (shown in Figure 6.13) is also used here to evaluate the differences between the selected fire scenarios. Here, the thermal properties of concrete are also selected according to Table 6.1, but the thermal boundary conditions are changed according to each fire scenario (Table 8.3). The development of such boundary conditions for the pool and jet fires is explained in Section 11.7.

Fire Scenario	Thermal Boundary Condition (T_{AST})	Convection Heat Transfer Coefficient (h)
RWS	RWS Curve (equation 5.5)	50 W/(m^2.K)
Pool Fire	1305 K	20 W/(m^2.K)
Jet Fire	1507 K	95 W/(m^2.K)

TABLE 8.3 – THERMAL BOUNDARY CONDITIONS

Figure 8.11 provides a comparison between the thermal boundary conditions used in DIANA and the solution of the evolution of concrete's surface temperature in time for each fire

scenario. Figure 8.12 compares the numerical solution of the total heat flux to the concrete structure, for which the integral in time provides the total amount of energy absorbed by the structure in each case (2527 kJ/m^2 for the RWS curve, 2092kJ/m^2 for the pool fire and 2485 kJ/m^2 for the jet fire). As it can be seen, the differences between the total amount of energy absorbed by concrete when exposed to the RWS curve and to the most destructive jet fire encountered in literature are negligible. When compared to an equivalent pool fire in the open, the use of the RWS curve represents an increase of ~20% in the total amount of energy transferred to the structure.

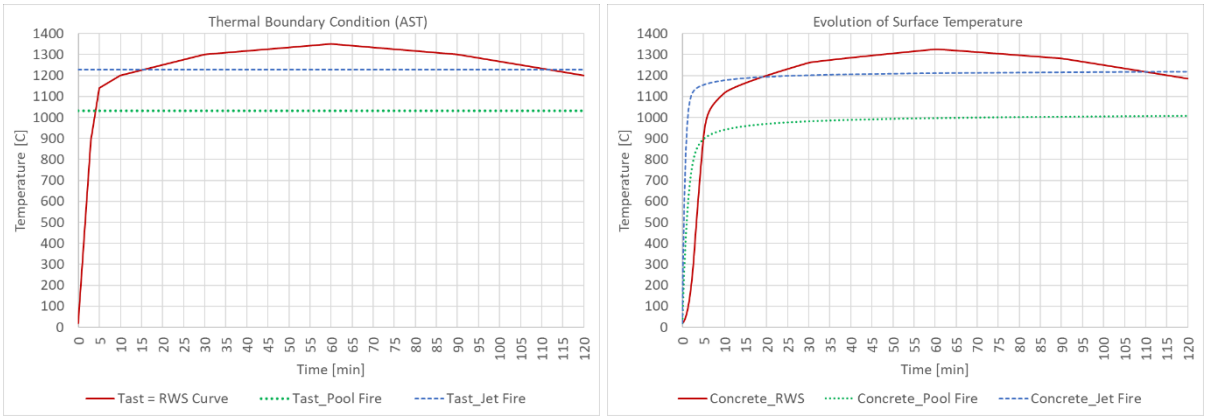


FIGURE 8.11 – THERMAL BOUNDARY CONDITIONS AND EVOLUTION OF SURFACE TEMPERATURE

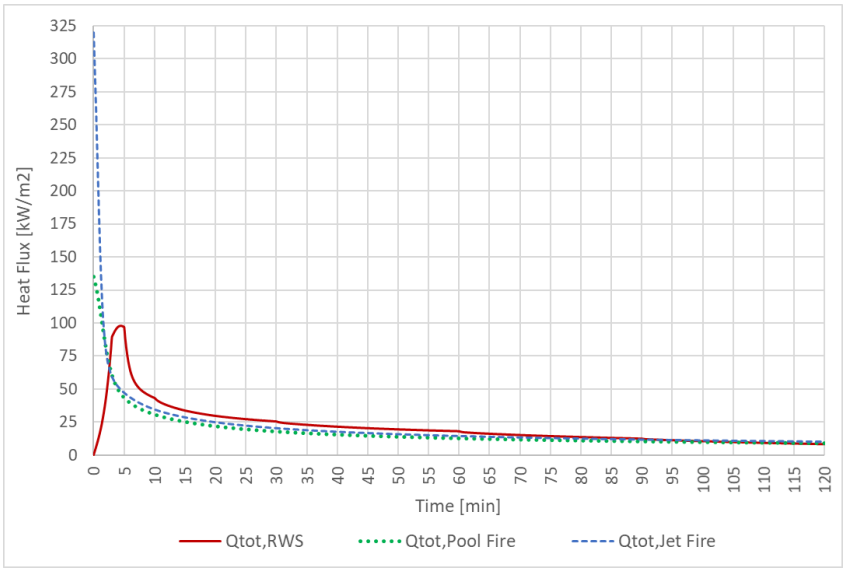


FIGURE 8.12 – COMPARISON OF THE TOTAL HEAT FLUX TO THE STRUCTURE

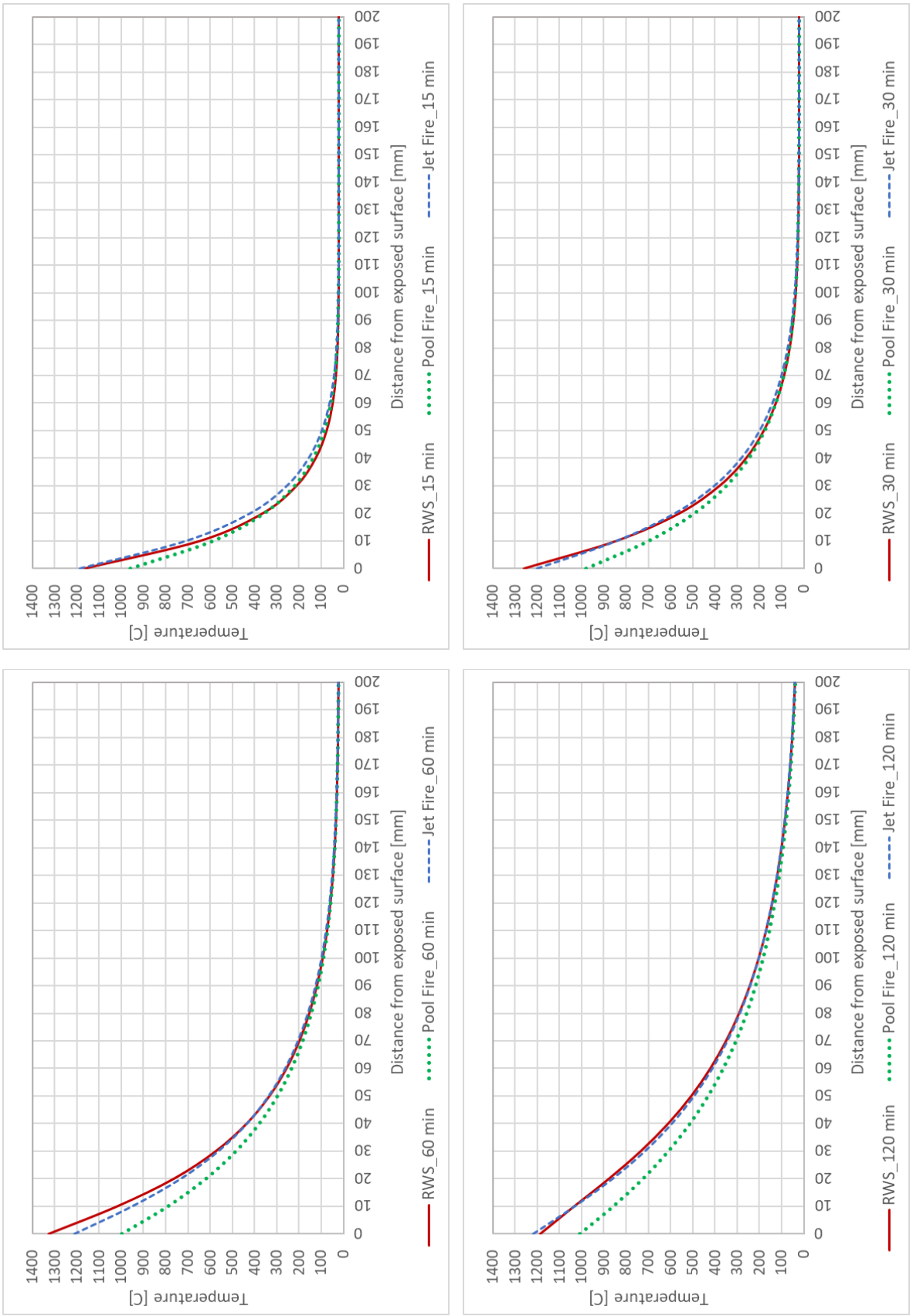


FIGURE 8.13 – COMPARISON OF TEMPERATURE DISTRIBUTION FOR DIFFERENT FIRE SCENARIOS

Figure 8.13 compares the evolution of the temperature distribution within the concrete structure for all cases studied here. It is once again clear that the thermal exposure imposed by the use of the RWS curve is more severe than that which can be expected for an equivalent gasoline pool fire in the open, being very similar to that of the most extreme jet fire encountered in literature. In fact, the thermal gradient formed within the concrete structure due to the use of the RWS curve will even surpass that generated by a jet fire for a certain period of time (look for instance at the maximum temperature distribution obtained by the use of the RWS curve, which occurs after one hour of fire).

8.1.2.4 Large-Scale Tunnel Fire Tests

The results of the previous section indicate that the use of the RWS curve prescribes, if not the most, one of the most critical fire scenarios encountered. This leaves us with two options, either: (1) due to the enclosed nature of tunnel fires the radiation feedback from the tunnel walls is actually sufficient to lead to such a magnitude of radiation heat flux in those fires; or (2) we are extremely overloading our structures in the fire safety design of tunnels. Hence, it becomes essential to gather real data into the radiation levels achieved in large-scale tunnel fire tests. Those latter are few in number and most of the data are often not fully available in literature. In this sense, heat fluxes measurements were found for only two of those large-scale tests:

- Runehamar Tests [5]:

Figure 8.14 provides the heat fluxes achieved during the Runehamar tests (briefly described in Section 8.1.1). Those measurements were obtained through the use of plate thermocouples (Section 7.3), centrally located at the ceiling of the tunnel and up to a distance of *40 m* from the fire source. As it can be seen, heat flux levels were above *300 kW/m^2* in the vicinity of fire for all tests performed. In case of tests T1 and T2, the maximum heat fluxes surpassed the level of *400 kW/m^2*, which is an even higher value than that which is prescribed by the use of the RWS curve (Figure 8.6). This seems to indicate that the destructive potential of a tunnel fire could indeed by represented by the RWS fire scenario. Nonetheless, a few remarks have to be made regarding the results presented here:

1. As described in Section 3.3.1, in large tunnel fires, flames will impinge on the ceiling propagating in the londitudinal direction (Figure 3.13). For the case of the Runehamar tests, the maximum heat fluxes at the ceiling were obtained within the flame zone, meaning that the plate thermocouples used in the tests were likely to have been fully engulfed in flames (Figure 8.15). According to Wickström et al. [104], this device should provide very robust measurements even within flame impigement zones. Nonetheless, we know that radiative heat fluxes are not uniform inside the flame body (Figure 5.14), and that the plate thermometer is very small (total exposure area of 0.01m^2) when compared to the achieved flame size (Figure 8.15). As described by Beyler [72], the effect of the size of the measuring device on the measured flame heat flux measurements is still not systematically studied, but it appears that larger objects tend to yield in smaller values than those obtained for smaller objects (Figure 8.7). If this would be valid, then the heat fluxes shown in Figure 8.14 could actually represent local peak values at the assigned positions rather than being representative values for

the whole ceiling structure at those locations. Hence, it is likely that the global average heat flux which is imposed by the fire on the ceiling would, in fact, be lower than that which is seen in Figure 8.14.

2. The cross-section of the tunnel was modified in the vicinity of the fire source. As shown by Figure 8.16, protection boards (PROMATEC-T) were applied to the ceiling and walls of the tunnel. According to Ingason et al. [5], the ceiling was fully protected for a total length of *75 m* (*21.5 m* upstream the centre of the fire and *53.5 m* downstream), while the walls were protected for *39 m* (*12.5 m* upstream the fire source and *26.5 m* downstream). To avoid hot gases from reaching the structure sustaining the ceiling protection, the remaining parts of unprotected wall were covered with ceramic curtains. The fire source was *10.45 m* long, meaning that the development of fire occurred inside an *insulated* tunnel. As indicated by the findings of Chapter 7, the results obtained at the Runehamar tests are in line with fires in *insulated tunnels*, which as shown by the same chapter and also by Section 8.2 appear not to be valid to describe *unprotected concrete tunnels*. Moreover, the thermal properties of the tunnel lining also play an important role in fire development, effectively changing fire dynamics. Thus, the heat flux levels achieved inside *insulated* tunnels are expected to be higher than that of *non-insulated* tunnels.

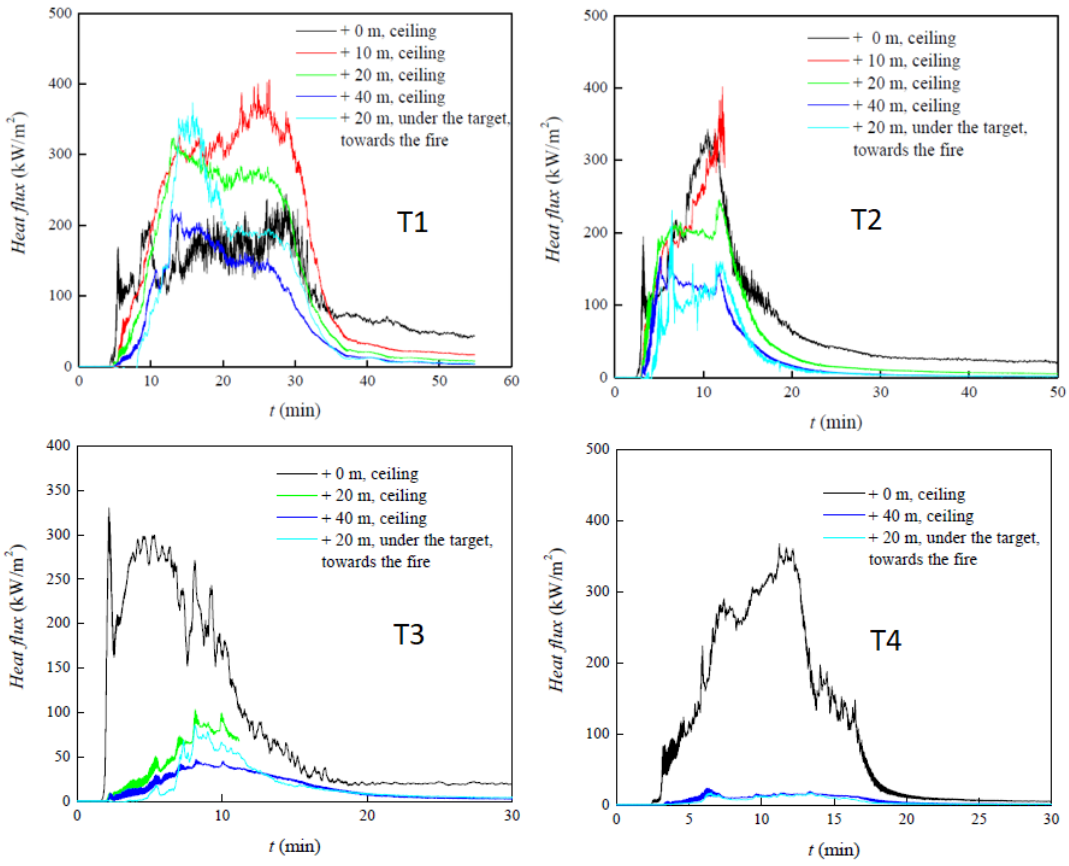


FIGURE 8.14 – RUNEHAMAR HEAT FLUXES MEASUREMENTS AT THE CEILING
Retrieved from Ingason et al. [5]



FIGURE 8.15 – FIRE DEVELOPMENT AFTER 5 MINUTES (RUNEHAMAR TESTS)
Retrieved from Lemaire [105]

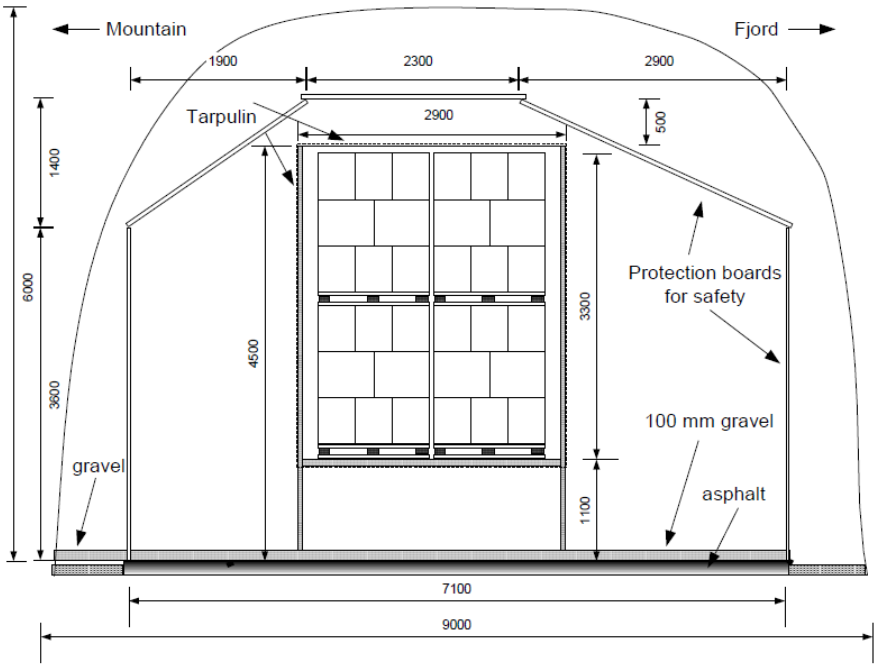


FIGURE 8.16 – TUNNEL CROSS SECTION (RUNEHAMAR TESTS)
Retrieved from Ingason et al. [5]

- San Pedro de Anes Tests [100]:

These tests were realized by private parties and the results available in literature are limited only to few collected measurements. Even so, high levels of incident heat flux were also

verified in the free-burn test (Section 8.1.1), reaching a peak value of *312 kW/m²*. Notice from Figure 8.17 that, in the overall, the heat fluxes obtained in this test are still smaller than the maximum values obtained for test T1 in the Runehamar tunnel [5], which reached a peak value of *402 kW/m²*, even though the achieved HRR is quite comparable between those two cases (Figure 8.18). In fact, the maximum HRR achieved in the San Pedro de Anes test was actually higher than that obtained in the Runehamar test (Figure 8.18). However, as there is only one single heat flux measurement available in literature for the free-burn test in the San Pedro de Anes tunnel and it was collected in a different position than those at the Runehamar tunnel, it is hard to make any definitive conclusions when comparing these two cases. A final remark here concerns the differences between the size of the flames and that of the measuring devices. As in the Runehamar tests, also here plate thermocouples were used to measure heat fluxes, meaning that the values presented in Figure 8.17 might also represent local maximums (see comment number 1 about the Runehamar tests).

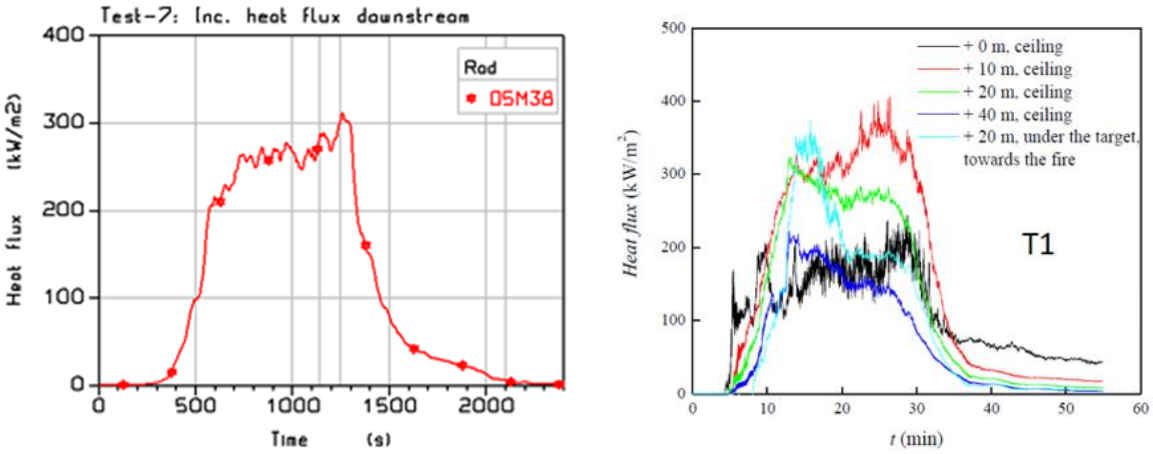


FIGURE 8.17 – COMPARISON OF MAXIMUM INCIDENT HEAT FLUX
Retrieved from Jessen [100]

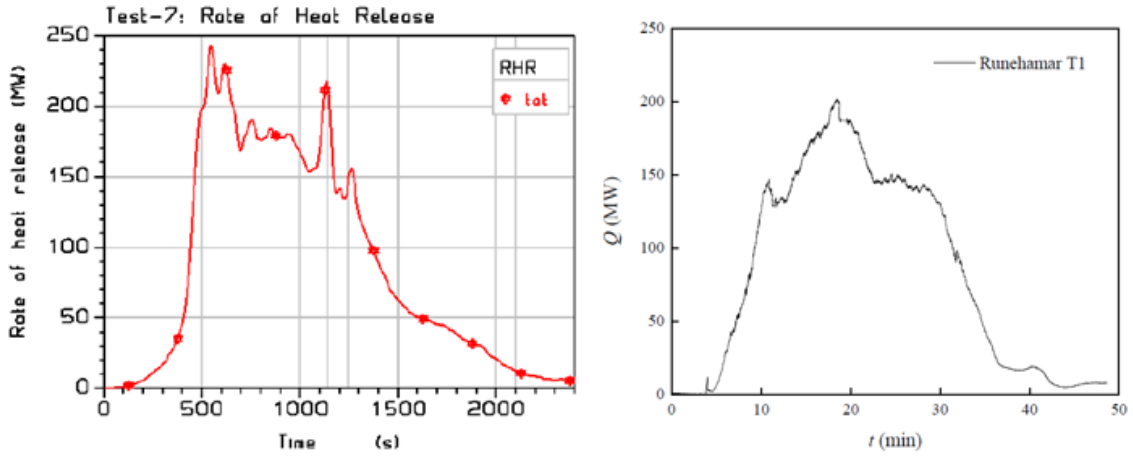


FIGURE 8.18 – HRR COMPARISON BETWEEN SAN PEDRO DE ANES AND RUNEHAMAR TESTS
Retrieved from Jessen [100] and Ingason et al. [5]

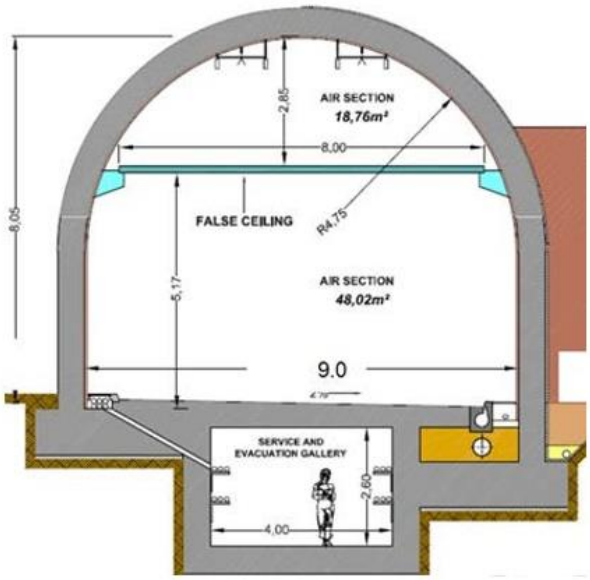


FIGURE 8.19 – TUNNEL CROSS SECTION (SAN PEDRO DE ANES TESTS)
Retrieved from Jessen [100]

In conclusion to this topic, we can say that the RWS curve represents one of the most critical fire scenarios, when considered both the destructive potential and the total fire duration. Therefore, it certainly imposes extreme conditions to any structure subjected to it. The results of large-scale tests, though limited, indicate that such a scenario can be attained inside a tunnel during the occurrence of large fires (Figure 8.6, Figure 8.14 and Figure 8.18). Even further, we can infer that, at least for the case of *insulated* tunnels, the achievable fire scenario might be even more destructive than that of fires in the open (i.e. pool and jet fires). Finally, large-scale tests performed in *unprotected concrete* tunnels simply do not exist. Regularly, studies under the development of a tunnel fire are reported in literature as if fire dynamics would be independent on the thermal properties of the boundaries of the enclosure. In essence, results collected for *insulated* tunnels (e.g. Runehamar tests) are simply taken as confirmation of the potential severity of a tunnel fire, reinforcing the use of the RWS curve as a valid truth for any type of tunnel (i.e. *insulated* and *unprotected concrete* tunnels). Nonetheless, the study performed in Chapter 7 indicates otherwise, as the thermal properties of the tunnel linning material, despite being often ignored, also play an important role in fire development. Therefore, the next section will provide a deeper view on this matter, elucidating the differences between the response of *insulated* and of *unprotected concrete* to the RWS fire scenario.

8.2 Thermal Response of Different Materials to the RWS Exposure

Heat transfer, thermal boundary conditions and the solution of Fourier's heat conduction equation in a transient thermal analysis were deeply discussed in Chapters 5 and 6 . However, given the importance of such equations into the analysis of the thermal response of structures subjected to fire, those will be shortly described here. In this sense, the use of the RWS curve according to Eurocode 1 Part 1-2 [75] defines the total exposure suffered by a structure in case of a tunnel fire. For structures which are surrounded by fire, Eurocode 1 Part 1-2 [75] indicates that the radiation temperature may be assumed as equal to the gas temperature. Based on this, the total heat flux from the gas phase to the specimen is simplified into the equation below:

$$\dot{q}''_{tot} = \varepsilon_s \sigma \left(T^4_{RWS} - T^4_{surface}\right) + h\left(T_{RWS} - T_{surface}\right) \quad \textbf{8.2}$$

where $\dot{q}''_{tot}$ is the total heat flux (W/ m^2), σ is the Stefan-Boltzmann constant (5.67 x 10^{-8} W/(m^{2}K^4)), T_{RWS} is the temperature development prescribed by the use of the RWS curve (K), h is the convection heat transfer coefficient which is assumed to be equal to 50 W/(m^2.K), $T_{surface}$ is the surface temperature achieved by the structure (K) and ε_s is the surface emissivity.

Equation 8.2 indicates that the total amount of heat absorbed by the structure depends on the development of its own surface temperature in time. Hence, $\dot{q}''_{tot}$ becomes a function of the capacity of the structure to conduct heat, which is evaluated according to the solution of Fourier's equation for thermal conductivity, shown below for a simple one-dimensional case:

$$\rho_s c_s \frac{\partial T_s(x,t)}{\partial t} = \frac{\partial}{\partial x}\left(k_s \frac{\partial T_s(x,t)}{\partial x}\right) \quad \textbf{8.3}$$

where ρ_s is the solid's density (kg/m^3), c_s is the solid's specific heat (kJ/(kg.K)), k_s is the solid's thermal conductivity (W/(m.K)) and $T_s(x,t)$ is the temperature development of the solid in time at a depth x, where x=0 represents the surface of the solid.

Equations 8.2 and 8.3 are coupled through a boundary condition determining the continuity of heat flux between the gas and the solid phases:

$$\dot{q}''_{tot} = -k_s \frac{\partial T_s(0,t)}{\partial x} \quad \textbf{8.4}$$

where $T_s(0,t)$ is the evolution of $T_{surface}$ in time.

The solution of equations 8.2 to 8.4 in a transient analysis is quite complex, often requiring the use of numerical methods. Even so, there are three distinct types of behavior which can be expected for the solid phase. According to Torero et al. [106], the development of thermal gradients within the structure is related to its own thermal properties and in particular with the conductivity. In essence, it determines whether or not the in-depth thermal gradients formed within the structure are sensitive or insensitive to the characteristics of the gas phase generated by a fire. Figure 8.20 below illustrates the three possibilities:

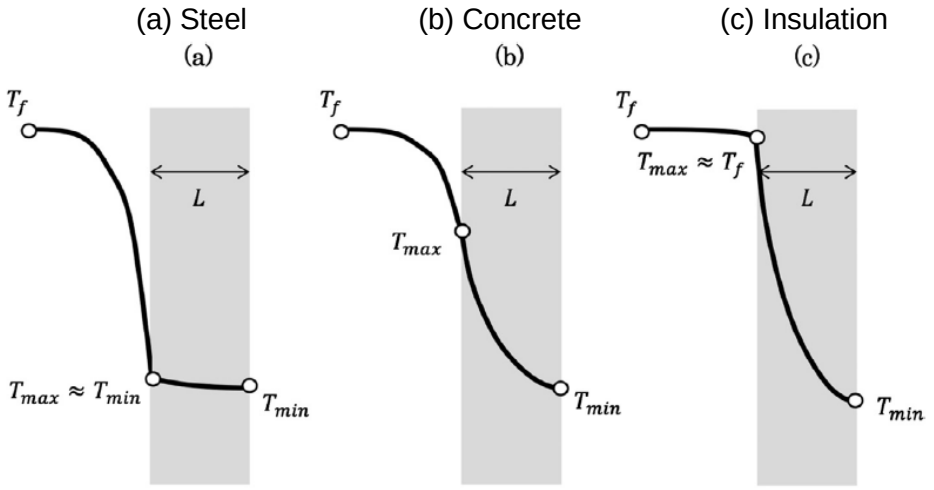


FIGURE 8.20 – TEMPERATURE DISTRIBUTION FOR DIFFERENT MATERIALS IN CASE OF FIRE
Adapted from Torero et al. [106]

8.2.1 Material Type (a): Steel

In materials with high thermal conductivity (e.g. steel), the energy will be rapidly diffused through its integrity. Fundamentally, the heat conduction within the material is faster than the heat transfer to the surface. In case the element is just a few millimeters thick, this allows us to assume a single temperature for the whole body and eliminates the need to resolve spatial temperature distributions within this specimen. A good example of this behavior is represented by a plate thermocouple. As explained in Section 7.3, this device is intended to measure the thermal exposure to a structure, being used to ensure that a standard curve (e.g. RWS curve) is followed during a furnace test. In essence, the working principle of this device is based on the assumption that the surface temperature of the thin steel plate (Figure 7.22) is equal to its back temperature (where a wire thermocouple is actually measuring the achieved solid temperature). Finally, the temperature measurements of the plate thermocouple should also follow a standard curve, ensuring the thermal exposure to a structure is controlled during the test. Figure 8.21 shows it to be true only a few minutes after the beginning of a test. We can understand this by looking at equation 8.3. As steel is a material of extremely high density, it takes time for it to react to the thermal exposure, making the temperature of the body to lag the '*imposed temperature*' in the early stages of the test. However, as the steel plate composing a plate thermocouple is very thin, shortly the temperature of the body reaches that of the fire phase (AST). On the other hand, if we would have a very thick steel body, then the temperature of the solid phase would lag significantly that of the fire phase for much longer than what is shown by Figure 8.21.

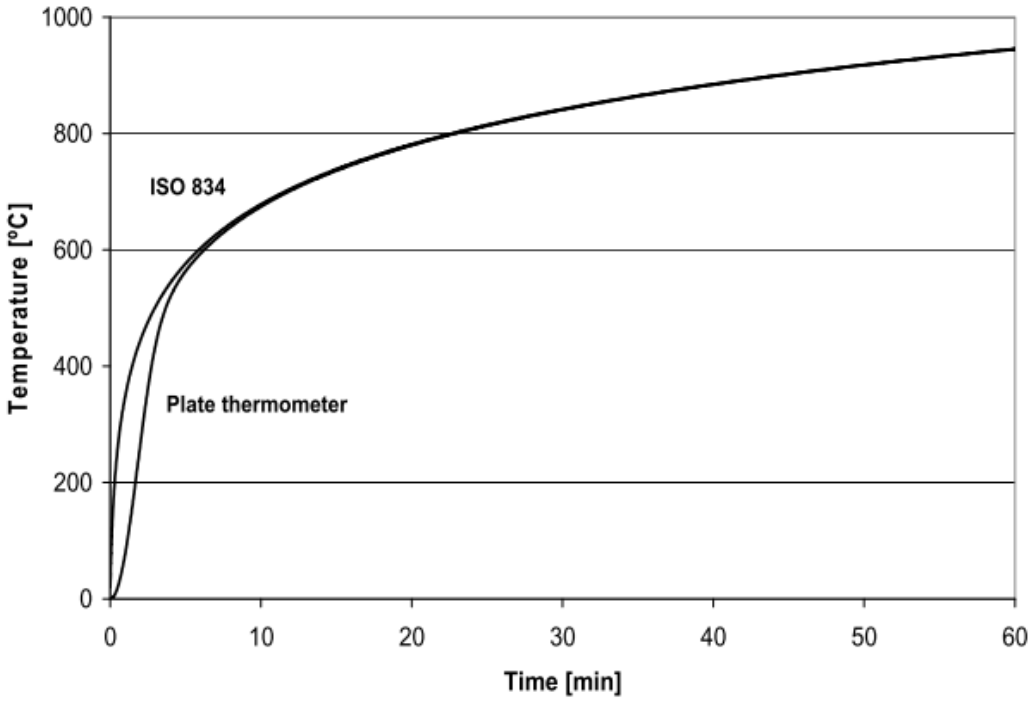


FIGURE 8.21 – RESPONSE OF A PT WHEN EXPOSED TO THE STANDARD CURVE
Retrieved from Wickström [76]

8.2.2 Material Type (c): Insulation

For materials characterized by low thermal conductivity (e.g. insulation), the surface temperature of the body may be taken as equal to its AST or, T_{RWS} in our case, meaning that the material behaves as a 'perfect' insulator. Keep in mind that this assumption is only intended for the calculation of the temperature development within the solid, but, as shown by Figure 7.39, it really seems valid. If equation 8.2 is taken into account, this assumption fundamentally means that there is no heat exchange between the fire induced gas phase and the solid phase or, in other words, that $\dot{q}''_{tot} = 0$. For sure this is not the case in a real fire, as the solid phase requires to absorb energy from a different source to increase its own temperature. Even so, just the possibility to make this assumption without any major errors already indicates that the heat exchange between fire and insulation materials should be extremely limited.

8.2.3 Material Type (b): Concrete

The problem gets more complicated for materials of type (b), which have neither low nor high conductivity (e.g. concrete). Essentially, it means that no simplifications can be made in the solution of the heat conduction equation 8.3. This makes the thermal gradients developed inside the structure to be fully dependent on $\dot{q}''_{tot}$. On one hand, the surface temperature development of the solid determines the amount of heat transferred from the fire to the element. On the other, the increase of its body temperature depends upon the amount of heat which is absorbed by the material. As a result, the development of the surface temperature of the structure in time will lag behind that of the fire induced temperature (AST) for a significant amount of time, as shown by Figure 7.40. Therefore, a full resolution of the heat conduction problem is required to evaluate the thermal gradients which will develop within a concrete structure exposed to fire.

For the scope of this thesis, this difference in the behavior of *concrete* and *insulation* is of special interest as it is/was common practice in The Netherlands to make use of partially insulated tunnels. Hence, the solution of equation 8.2 for these two materials when subjected to a same thermal exposure (i.e. RWS curve) is addressed more carefully in the next subsection.

8.2.4 Differences between Concrete and Insulation

As described before, the complete resolution of the heat conduction problem (equations 8.2 to 8.4) in a transient fire analysis is of complex nature. This is the case not only for the interdependence of $\dot{q}''_{tot}$ and $T_{surface}$ on each other, but also because the thermal properties of the material (i.e. density, specific heat capacity and thermal conductivity) are often temperature dependent and will vary in time. Commonly, this requires the use of a FEM-based program (for which DIANA FEA is chosen) to achieve a numerical solution of the problem.

8.2.4.1 Concrete

At first, to ensure that the solution obtained in DIANA for a transient heat transfer analysis was reliable, the mesh size and time step used in this study were calibrated to provide results which were in line with the temperature profiles available in Annex A of Eurocode 1 Part 1-2 [75] for a concrete slab exposed to the standard curve (see Section 11.5). Once this step was completed, the model described in Table 8.4 was created in DIANA to analyze the thermal response of a concrete structure to the RWS fire scenario.

Thermal Properties	
Conductivity	Lower Limit (Figure 11.2)
Specific Heat	u = 0% (Figure 11.3)
Density	2300 kg/m^3
Convection Heat Transfer Coefficient	50 W/m^2.K
Emissivity	0.7
Geometry	
Internal Dimensions	2 m x 2 m
Wall Thickness	1 m
Boundary Conditions	
Internal Edges	Exposed to RWS Curve
External Edges	External Temperature = 20 ^{o}C
Initial Body Temperature	20 ^{o}C
Numerical Solution	
Mesh Size (Figure 8.22)	0.01 m up to a wall thickness of 0.1 m (green section in Figure 8.22); Adaptive size for the remaining 0.9 m (yellow section in Figure 8.22)
Time Step	10 seconds
Iteration Process	Newton-Raphson
Convergence Tolerance	1E-6

TABLE 8.4 – CONCRETE MODEL USED IN DIANA

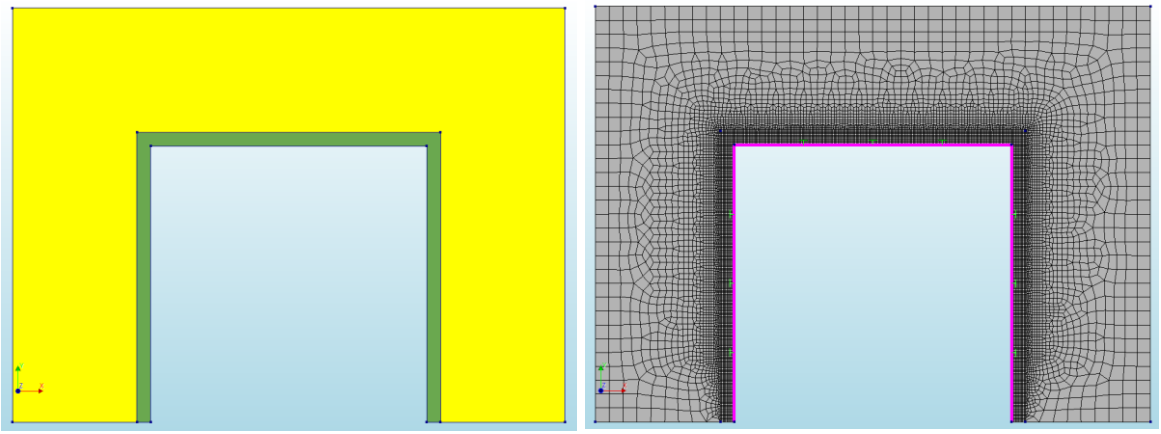


FIGURE 8.22 – GEOMETRY AND MESH

Figure 8.23 provides the numerical solution of the total heat flux to a concrete structure subjected to the RWS evaluated for the middle node at the bottom of the ceiling in Figure 8.22. Here, it is important to mention that DIANA solves a more complex form of equation 8.3, accounting for a two-dimensional heat conduction thus affecting the solution of $\dot{q}''_{tot}$. However, in our case, the thermal load was uniformly applied to the whole length of the internal parts of the walls and ceiling (pink lines in Figure 8.22), making the numerical solution shown here (Figure 8.23) to approach that of a one-dimensional thermal analysis. Moreover, except for a small region at the vicinity of the corners (where the walls meet the ceiling), the resolution of our problem can be fully described by the one-dimensional heat conduction equation 8.3. For instance, if you take the development of $T_{surface}$ in time for the middle node at the bottom of the ceiling (Figure 8.25) and solve equation 8.2 for $\dot{q}''_{tot}$, you will notice that if the radiation (blue line in Figure 8.23) and convection (orange line in Figure 8.23) parcels are combined, then the result will deviate in less than 0.5% from the total heat flux obtained with DIANA (dashed line in Figure 8.23).

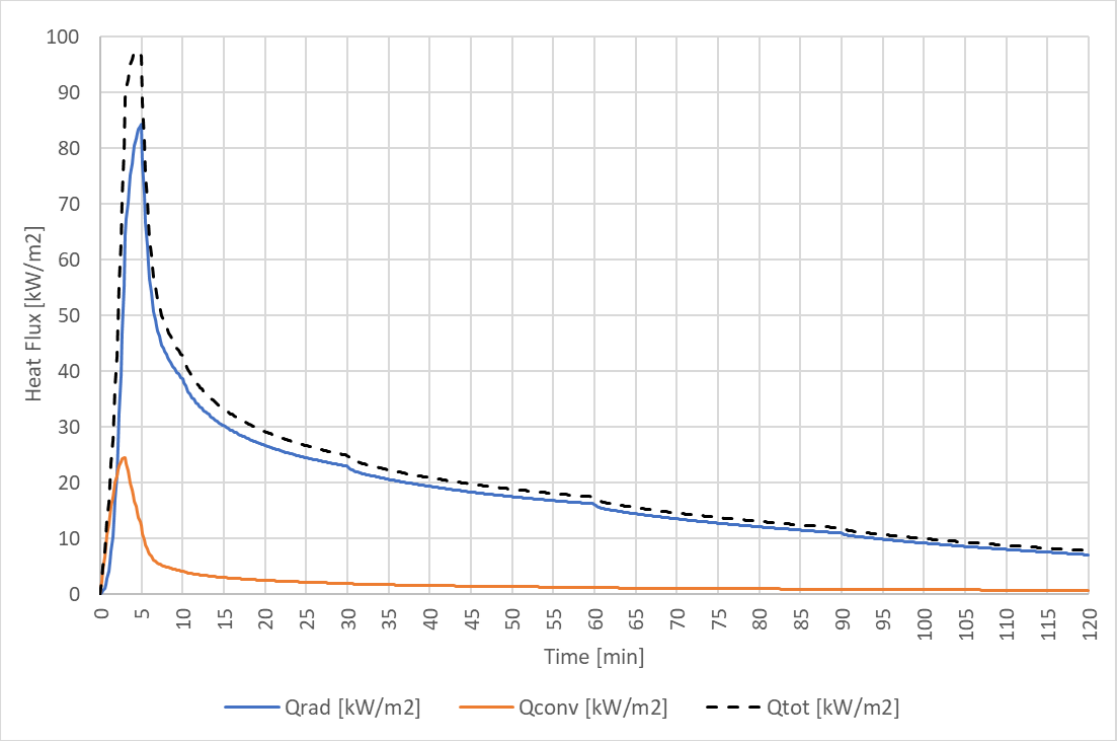


FIGURE 8.23 – TOTAL HEAT FLUX TO A CONCRETE STRUCTURE SUBJECTED TO THE RWS CURVE

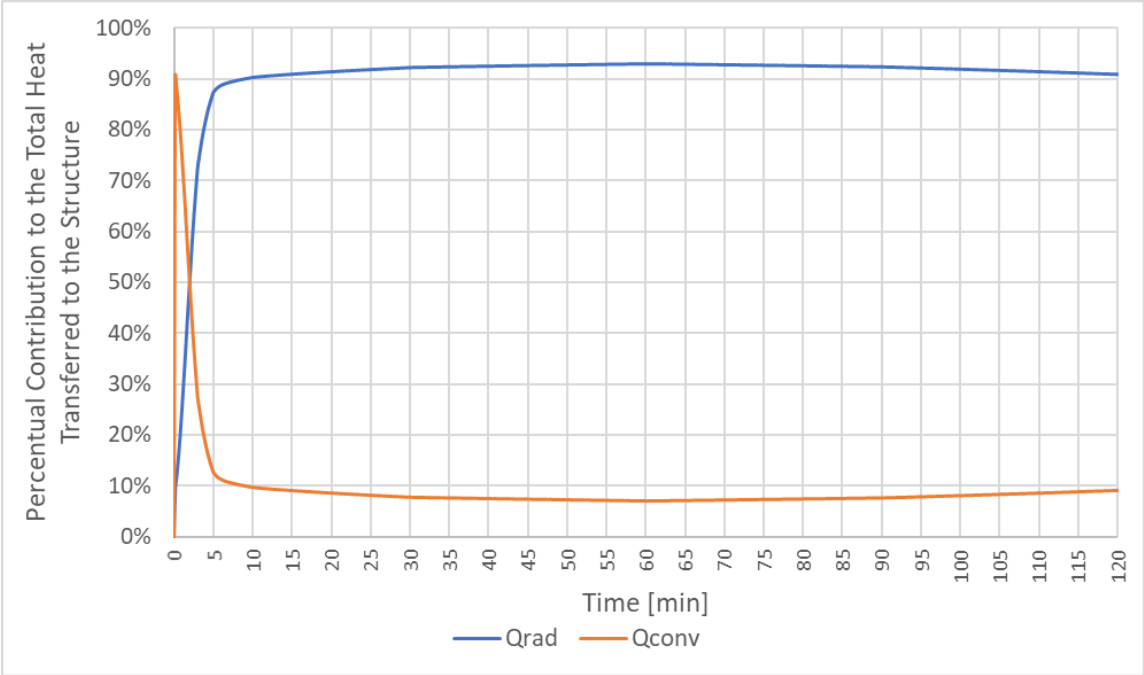


FIGURE 8.24 – PERCENTUAL CONTRIBUTION TO TOTAL HEAT FLUX

Considering an analogue line of thinking, the obtained $T_{surface}$ is used to calculate the contributions of radiation and convection to $\dot{q}''_{tot}$ (Figure 8.23). These results are then used to build Figure 8.24, which shows the percentual contribution of each mode of heat transfer (i.e. radiation and convection) to the total heat flux to the structure. As it can be seen, as soon as a fire starts generating high temperatures within an enclosure (Figure 7.1), the amount of heat transferred to the structure becomes governed by the radiation contribution. For the case of the

RWS fire scenario, it accounts for more than 90% of $\dot{q}''_{tot}$ for almost the total duration of fire. Note that this is the reason for which the RWS curve was translated in terms of a fire induced radiative heat flux in Section 8.1.2. This radiation dominance in fire events has also a practical consequence for the current approach adopted in fire resistance testing of specimen. However, let us avoid this discussion for now as this will be covered in detail in Section 8.3.2.

8.2.4.2 Insulation

To highlight the different behavior of *protected* and *unprotected concrete* tunnels when exposed to a same fire scenario (i.e. RWS curve), the study performed for *concrete* was also done for an *insulated* case. The same model shown in Figure 8.22 was used, but the finer mesh (i.e. the green part in Figure 8.22) is now changed to represent an *insulation* layer. To be in line with a realistic case for tunnels, PROMATECT-T was selected as the *insulation* material. According to the manufacture (Promat), this product consists of a calcium silicate-aluminate fire protective board, designed to protect structures subjected to severe fire scenarios, such as that of the RWS curve. The capacity of PROMATECT-T on protecting tunnel structures was confirmed during the Runehamar tests (Section 8.1.2), for which the final report (Ingason et al. [5]) provides the thermal properties used in the study performed here (Table 8.5).

Thermal Properties (PROMATECT-T)	
Conductivity	0.212 W/m.K
Specific Heat	1100 J/kg.K
Density	900 kg/m^3
Convection Heat Transfer Coefficient	50 W/m^2.K
Emissivity	0.8
Geometry	
Internal Dimensions	2 m x 2 m
Wall Thickness	1 m
Boundary Conditions	
Internal Edges	Exposed to RWS Curve
External Edges	External Temperature = 20 ^{o}C
Initial Body Temperature	20 ^{o}C
Numerical Solution	
Mesh Size (Figure 8.22)	0.01 m up to a wall thickness of 0.1 m (*Insulation*); Adaptive size for the remaining 0.9 m (*Concrete*)
Time Step	10 seconds
Iteration Process	Newton-Raphson
Convergence Tolerance	1E-6

TABLE 8.5 – INSULATION MODEL USED IN DIANA

Figure 8.25 provides the development of the surface temperature for both *concrete* and *insulation* in comparison with the RWS curve. Once again, remember that due to the assumption made in Eurocode 1 Part 1-2 [75] of considering the radiation temperature to be equal to the gas temperature (i.e. *blackbody* behavior), the RWS curve fundamentally represents the AST for the structure. Also, notice that the results obtained here are in line with what was described in Section 8.2.2. Moreover, we can see from Figure 8.25 that since the beginning of the heat flow analysis, the temperature development of the surface of the *insulation* approaches the maximum temperatures induced by the fire (i.e. RWS curve). In essence, this allow us to assume that the surface temperature of an *insulated* tunnel will be equal to the RWS curve, making the heat conduction problem independent of $\dot{q}''_{tot}$ and fully

resolved only by the use of equation 8.3. This is not the case for *concrete* tunnels, where the surface temperature will lag the AST development in time (i.e. RWS curve), thus requiring a full resolution of the heat conduction problem.

The numerical solution of $\dot{q}''_{tot}$ is affected by this different behavior. As shown by Figure 8.26, the total heat flux to a *concrete* structure subjected to the RWS curve is much higher than that of an *insulated* structure exposed to the same conditions. If $\dot{q}''_{tot}$ is integrated in time, we can conclude that the total amount of energy absorbed by a *concrete* structure exposed for two-hours to the RWS curve is approximately equal to *2530 kJ/m^2*, which is almost three times the amount of energy which would be absorbed by an *insulated* structure (*~ 900 kJ/m^2*) if subjected to the same fire scenario. Thus, as a *concrete tunnel* will absorb much more energy than an *insulated tunnel* during the occurrence of an identical fire, we cannot expect the temperature development within the *concrete tunnel* to be equal to that which would be achieved inside an *insulated tunnel*. At heart, the use of the RWS curve in a prescriptive-based approach neglects this difference by avoiding to consider any interaction between the boundaries of the tunnel and the fire. Hence, the indiscriminate use of this curve without any distinction among *concrete* and *insulated tunnels* inherently means that we are considering two different fire scenarios between those cases. Not only that, if we are to achieve the same level of thermal exposure for both types of tunnel (i.e. RWS curve), this fire scenario has to be more severe for a *concrete tunnel*. However, in reality, the maximum expected fire load for a certain tunnel is independent on whether this tunnel is *insulated* or *not*. Thus, if we are to assume that a time-temperature curve can represent the worst-case fire scenario in a prescriptive-based approach, this curve cannot be identical for *concrete* and *insulated tunnels*, otherwise we will be overloading the *concrete structure*.

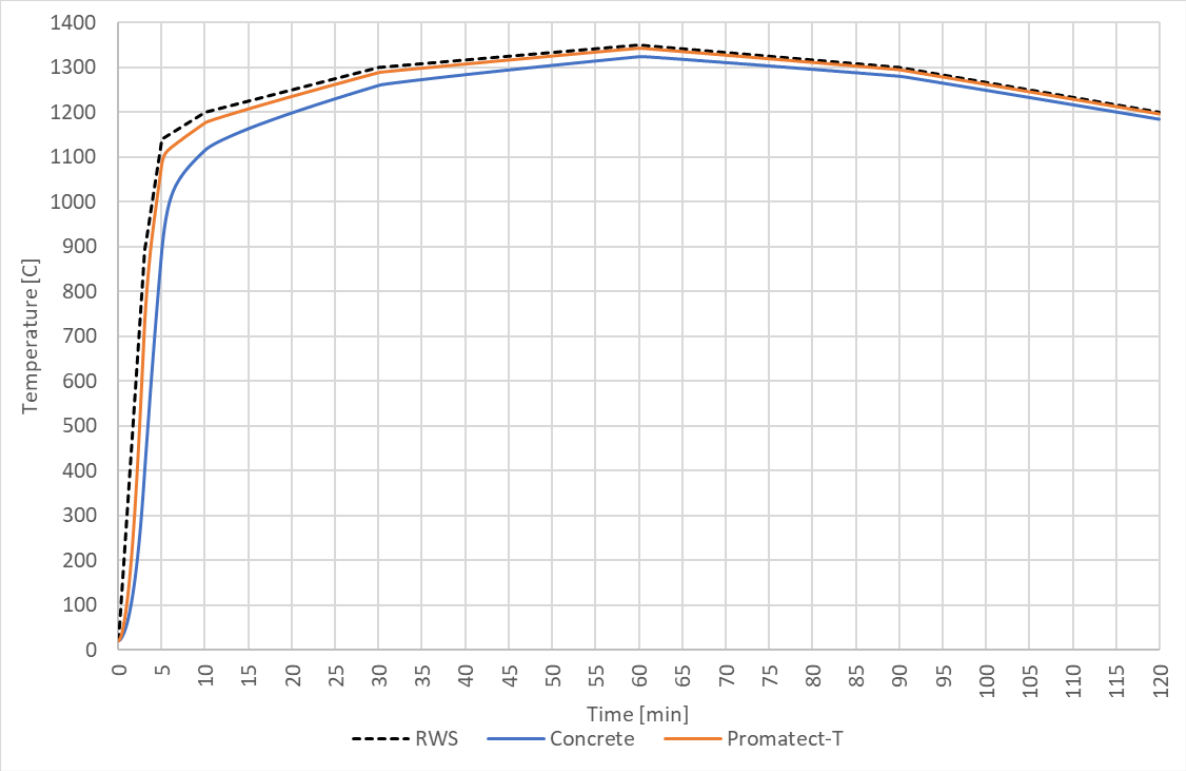


FIGURE 8.25 – EVOLUTION OF SURFACE TEMPERATURE IN TIME

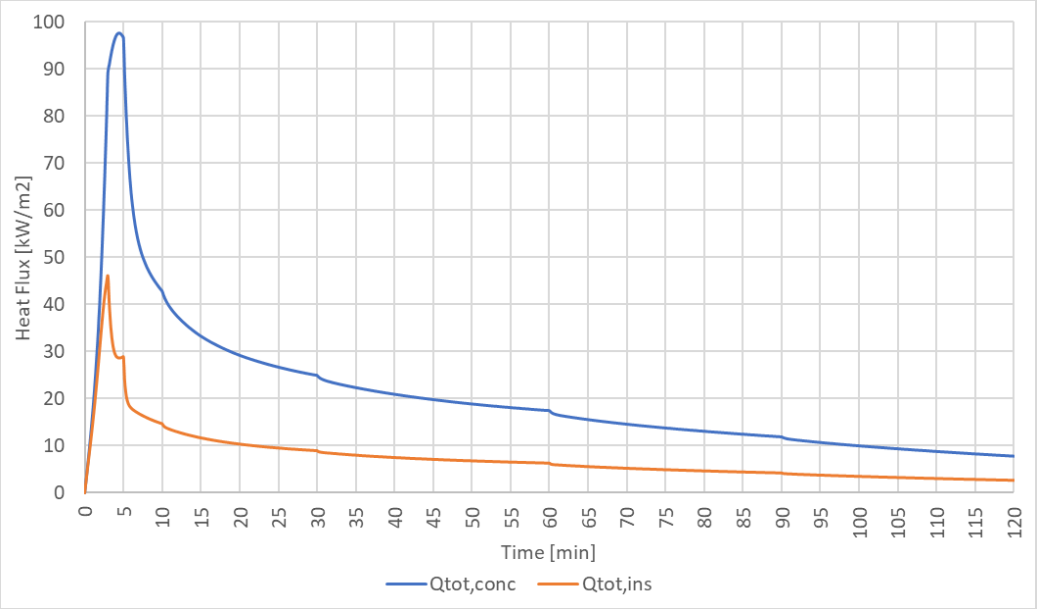


FIGURE 8.26 – COMPARISON OF THE TOTAL HEAT FLUX TO THE STRUCTURE

In conclusion, the study performed here is in line with the findings of Chapter 7. As the RWS curve was developed within an *insulated tunnel*, it cannot represent the temperature development which would be achieved for an identical *concrete tunnel* when subjected to the same fire scenario. In essence, we can conclude that the use of *insulation* promotes heat accumulation in the enclosure which leads to the occurrence of higher gas temperatures inside the tunnel when compared to an equivalent case for a *concrete tunnel*.

8.3 Furnace Resistance Tests

As described in Węgrzyński et al. [107], the origin of furnace resistance tests dates back to the beginning of the 20th century as a response to the urgent demand of the building industry on having a means of quantifying the fire resistance of different elements in a reliable and repeatable manner. This happened in a time where the complex dynamics of fire development where still unknown, and its effects could only be evaluated based on temperatures. Thus, this test provided a way of assessing the performance of building structures by rating the time to failure of simple structural elements (i.e. columns, beams, walls and slabs) when subjected to an environment in which the temperatures in the enclosure would be controlled to follow a standardized curve (Figure 8.27). Hence, the capacity of an element to withstand the imposed temperatures for a certain amount of time would serve as proof of reaching the required level of fire safety so that it could be used in a building. Nowadays, our understanding of fire dynamics has grown tremendously. Even so, furnace tests still constitute the main means of characterizing the fire resistance of any structural specimen.

In a different manner, such tests are also applicable to tunnel structures. For concrete tunnels in The Netherlands, they are required by the Ministry of Infrastructure (RWS) for two cases: (1) to assess the suitability of an *unprotected concrete structure* for application in practice (i.e. *spalling test*); or (2) to confirm the insulation capacity of an external fire protection system (i.e. *thermal insulation test*). These tests are often performed in laboratories according to specific testing guidelines, such as the *"Fire testing procedure for concrete tunnel linings"* [11], before

the construction of new tunnels. This section will, therefore, be focused on understanding the working principle of such furnace tests and to evaluate the thermal exposure which is imposed onto the structure during those tests. Thus, Section 8.3.1.1 will discuss the consequences of using a same time-temperature curve for the two different tests (i.e. the *spalling test* and the *thermal insulation test*), while Section 8.3.2 covers the effects of the controlling mechanism, used to measure temperatures during the test, on the achieved level of thermal exposure to the structure. Finally, Section 8.3.3 will introduce a new methodology for fire testing of structures. However, before addressing all those topics, the next Section 8.3.1 provides a short introduction of the current in-situ furnace tests performed in the Netherlands.



FIGURE 8.27 – FURNACE TEST [10]

8.3.1 On-site Tunnel Fire Resistance Testing

After several tests performed in previously considered *non-spalling concrete* demonstrated the occurrence of severe progressive spalling in such mixtures (van der Waart and van Gulik [12]), existing *unprotected concrete tunnels* also became a concern in The Netherlands. To cope with the need of being able to investigate such existing structures and allow to evaluate the necessity or performance of passive fire protection systems, *Efectis* developed a mobile fire resistance oven (known as MobiFiRe [108]), providing an option of testing tunnel in-situ (Figure 8.28). This small oven is designed to test surfaces of *1* m^2, making it easy for transportation and installment on site, and is assumed large enough to capture reliable results, while also being small enough not to compromise the tested structure. It can be used to test either the walls or ceiling of an existing tunnel, for both the *spalling test* and the *thermal insulation test* (Figure 8.29).

[10] https://www.europages.co.uk/FIRE-RESISTANCE-TEST-FURNACES/BTF/cpid-5750886.html



FIGURE 8.28 – MOBIFIRE (EFECTIS) [11]



FIGURE 8.29 – SPALLING AND THERMAL INSULATION TESTS PERFORMED WITH THE MOBIFIRE[12]

[11] https://www.efectis.com/en/references/fire-safety-in-the-northsouth-line/
[12] *Spalling* and *thermal insulation tests* performed by Efectis in the Stadsbaantunnel (Utrecht).

To perform the in-situ test, first the MobiFiRe is placed on the assigned location. Then, an operator is responsible for controlling the burner and will regulate the amount of fuel supplied to the oven, such that the temperatures achieved in the enclosure are controlled to follow the RWS curve within a certain error margin (red lines in Figure 8.30). Temperature measurements are given by the use of a few *wire thermocouples*, located inside the oven and close to the surface of the specimen (Figure 8.31).

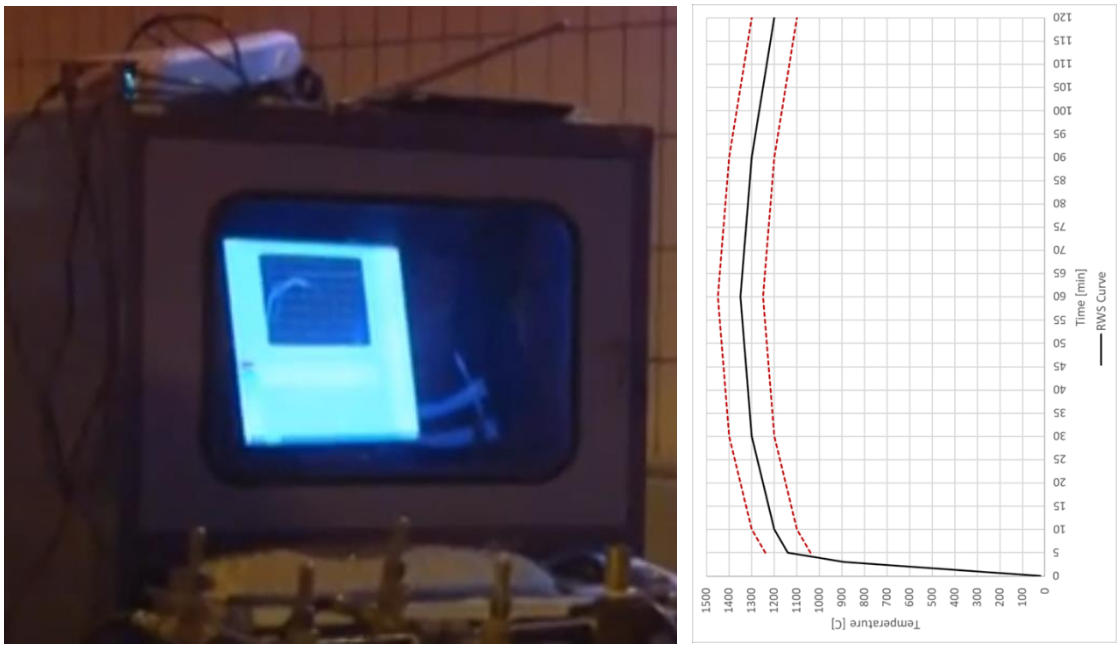


FIGURE 8.30 – TEMPERATURE DEVELOPMENT INSIDE THE OVEN[13]



FIGURE 8.31 – WIRE THERMOCOUPLES USED TO MEASURE TEMPERATURES INSIDE THE OVEN[14]

[13] *Spalling test* performed by Efectis in the Maastunnel (Rotterdam): https://www.youtube.com/watch?v=m4zcB9JmHx4

[14] *Spalling test* performed by Efectis in the Stadsbaantunnel (Utrecht).

8.3.1.1 Energy Balance

To understand the working principle of a furnace test we have to address the energy balance within the enclosure. Maluk et al. [109] explains this in a simplified way based on Figure 8.32. During a furnace test, heat is produced through the combustion of gasified fuel, which generates an inflow of hot gases in the enclosure ($\dot{q}''_{inflow}$). As air and fuel are continuously supplied to the furnace during the whole test, Węgrzyński et al. [107] points out that exhaustion vents are often used in furnaces to limit the pressure development within the enclosure. Thus, part of the heat supplied to the furnace is lost with the outflow of hot gases through the extraction vent ($\dot{q}''_{outflow}$). The remaining amount of heat will then be divided into the total heat flux to the furnace lining ($\dot{q}''_{net,lining}$), the total heat flux to the specimen ($\dot{q}''_{net,s}$) and the energy stored within the gas phase ($V_g \rho_g c_g \frac{\partial T}{\partial t}$).

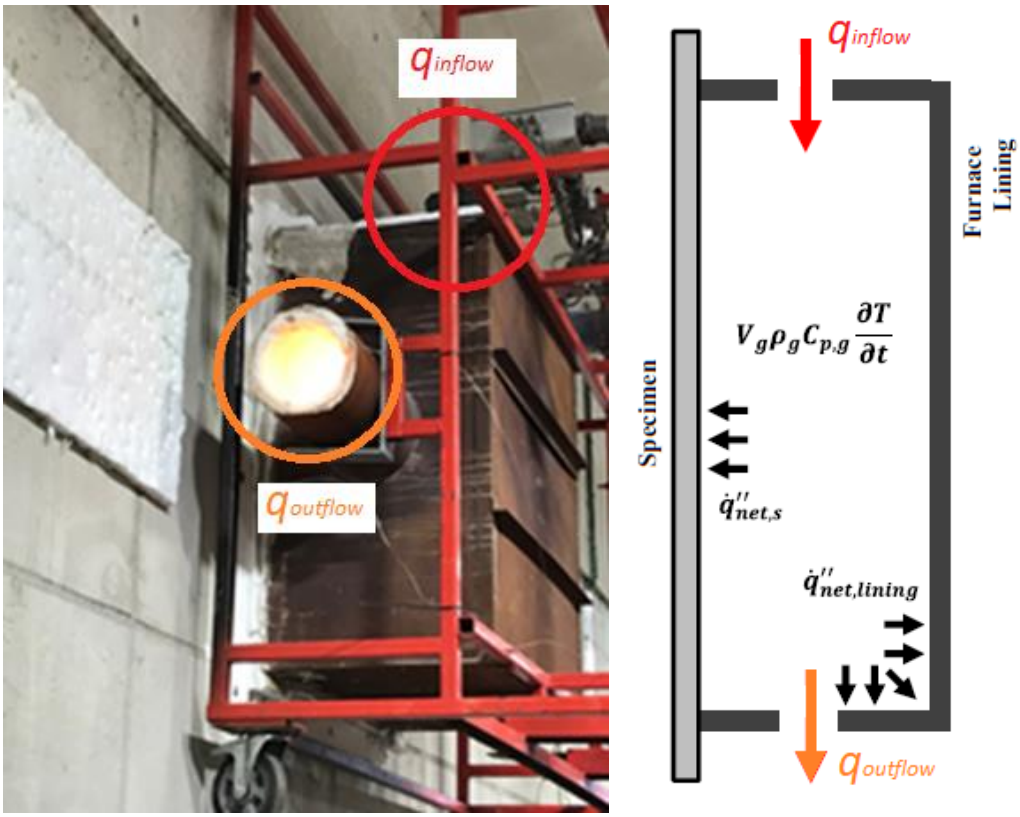


FIGURE 8.32 – ENERGY CONSERVATION IN A FURNACE TEST
Adapted from Maluk et al. [109]

Thus, conservation of energy within the furnace implies that:

$$\Delta \dot{Q} = \dot{q}''_{net,lining} A_{lining} + \dot{q}''_{net,s} A_s + V_g \rho_g c_g \frac{\partial T}{\partial t} \qquad 8.5$$

where $\Delta \dot{Q}$ is the total amount of energy provided to the furnace (essentially the differential between $\dot{q}''_{inflow}$ and $\dot{q}''_{outflow}$), $\dot{q}''_{net,lining}$ is the total heat flux to the furnace lining, A_{lining} is the total exposed surface area of the furnace lining, $\dot{q}''_{net,s}$ is the total heat flux to the specimen and A_s is the total exposed area of the specimen. The product $V_g \rho_g c_g \frac{\partial T}{\partial t}$ represents the total enthalpy associated with the gases contained within the furnace, where V_g is the total volume of the furnace, ρ_g is the gas density, c_g is the specific heat of the gases and $\frac{\partial T}{\partial t}$ is the change of temperature in time.

If we now assume that the mass flow of gases entering and leaving the furnace are equal each other, then we can define $\Delta\dot{Q}$ as:

$$\Delta\dot{Q} = m_f \Delta H_{c,f} - m_g c_g (T_{out} - T_{in}) \qquad \textbf{8.6}$$

where m_f is the mass flow of fuel consumed in the furnace, $\Delta H_{c,f}$ is the heat of combustion of the fuel, m_g is the mass flow of gases leaving and entering the furnace, c_g is the specific heat of gases, T_{out} is the temperature of gases leaving the furnace and T_{in} is the temperature of gases entering the furnace.

Note that the discussion presented here is only valid with the following assumptions:

- The temperature within the control volume is homogeneous.
- The net heat fluxes at the exposed surfaces (i.e. furnace linings and specimen) is also homogeneous.
- Kinetic and potential energy related to the transient mass transfer of the gases inside the control volume are neglected.

In a furnace test, the primary idea is to monitor $\frac{\partial T}{\partial t}$ such that it follows a standardized curve or, in our case, the RWS curve (Figure 8.30). To be able to maintain the temperature development within the enclosure as intended, the furnace operator controls m_f such that the energy provided to the enclosure ($\Delta\dot{Q}$) can compensate for any changes in the thermodynamic system. Therefore, the thermal exposure to the test specimen during such a test will depend on several factors, as: (1) the thermal properties of the lining material; (2) the thermal properties of the specimen; (3) the type of fuel used in the test (e.g. sooty or not), which is related to the emissivity of the gas phase (equation 5.13). Węgrzyński et al. [107] describe that the furnace walls are usually covered with materials of very low thermal inertia (i.e. low density and conductivity), which minimizes the thermal losses to the furnace lining. This means that, in practical situations, the losses to the furnace walls are often assumed to be neglectable as they will be much smaller than the heat losses to the specimen and through the exhaustion vent. If that would really be the case, then equation 8.5 shows us that the dominant factor for the heat transfer within the furnace is the thermal response of the specimen itself.

To understand this go back to Figure 8.26 where the total heat flux to a *concrete structure* is compared to the total heat flux to an *insulated structure* when subjected to the RWS curve. Now imagine that these two specimens are to be tested in identical furnaces such as the one shown in Figure 8.32. Due to its thermal properties, the *concrete specimen* will extract more energy from the enclosure than the *insulation specimen*. Thus, if $\frac{\partial T}{\partial t}$ is to follow the RWS curve for both tests, then the amount of energy ($\Delta\dot{Q}$) supplied to the *concrete test* has to be higher than that of an *insulation test*. Hence, at least in theory, the consumption of fuel during a *spalling test* should be higher than that on a *thermal insulation test*. In reality, however, due to the furnace dimensions and the complexity involved in all terms of equation 8.5, we might not notice a significant difference among the fuel consumption between these two cases. For instance, it could be that the energy loss through the exhaustion vent is of such magnitude that it minimizes the different behavior between the specimens (i.e. *concrete* and *insulation*), thus leading to a similar amount of fuel consumption in both tests. Also, considering the acceptable error margin when following the temperatures of the RWS curve (which is shown by the red lines in Figure 8.30), it is unlikely that two different tests will identically follow the prescribed

curve. Altogether, these aspects might limit the comparison of fuel consumption among furnace tests of different specimens.

Even so, recent studies support the discussion presented here. For instance, the works of Barlett et al. [110] and Lange et al. [111] prove that remarkable differences in the total fuel consumption of furnace tests of different specimens occur when testing combustible (i.e. wood) and non-combustible (i.e. concrete) construction materials. For these cases, the combustible specimen itself becomes an extra source of heat to the furnace gases, significantly reducing the amount of fuel required for the temperatures within the enclosure to follow the prescribed curve. Unfortunately, literature lacks studies comparing furnace tests of *insulation* materials and *concrete*. Still, Węgrzyński et al. [107] were able to prove that less energy is required to sustain the same thermal exposure to sandwich panels walls (highly insulating material) than to gypsum plasterboard walls in identical furnace tests (Figure 8.33).

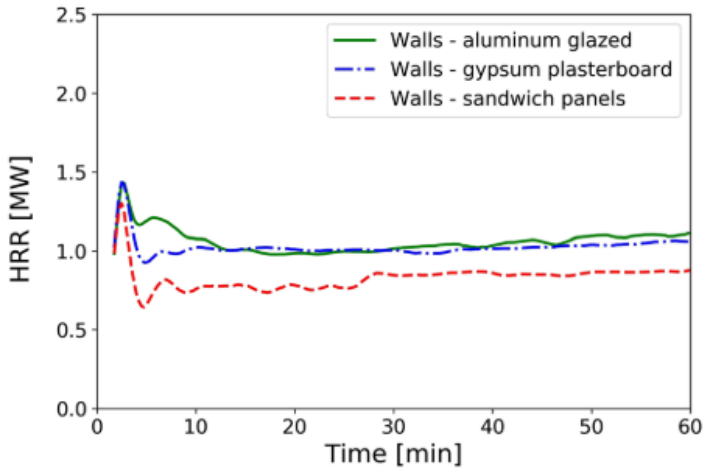


FIGURE 8.33 – DIFFERENCES IN FUEL CONSUMPTION FOR IDENTICAL FURNACE TESTS
Retrieved from Węgrzyński et al. [107]

In conclusion, let us focus on both types of tests which are performed for tunnels (i.e. the *spalling test* and the *thermal insulation test*). Evidently, despite providing the same thermal exposure (i.e. RWS curve) to both specimens, we are essentially analyzing two distinct fire scenarios (HRR). Not only that, but this fire scenario will also be more severe for the *concrete* specimen. It might also be good to point out that if the differences in the heat losses to *concrete* and *insulation* are scaled to the real size of a tunnel, it reinforces the idea that we cannot expect to achieve the same temperature development within *insulated* and *concrete tunnels* when considering an identical fire scenario. Hence, it is this difference that the prescriptive approach fails to include, as by evaluating the performance of different materials to the same exposure we neglect to consider the effects of the tunnel lining material itself in the achieved level of exposure.

8.3.2 Furnace Types and Controlling Mechanism

Problems with furnace tests are not only related to the use of a same time-temperature curve to test and rate materials with different thermal properties. Another particularly important factor influencing the results of a furnace test is the controlling mechanism (i.e. the type of thermocouple) applied to regulate the temperature development inside the enclosure. In

essence, the whole idea behind performing furnace tests is that the thermal exposure to the structure could be characterized solely by the conditions achieved by the gas phase or, in other words, the average gas temperature within the enclosure.

8.3.2.1 Furnace Types

During a test, the actual thermal exposure suffered by the structure is the result of the contribution of several sources of heat in a complex process. As we know, heat is transferred to the structure through convection and radiation (Section 5.1). The convection parcel is solely dependent on the state of gases within the furnace (i.e. the flow conditions near the surface and the gas temperatures) and is given by equation 5.5. However, as for structures subjected to fire, in a furnace test, radiation will also be the governing mode of heat transfer (Figure 8.24) to the specimen. As described by van de Leur and Twilt [112], it is here that the problem gets complex, as the radiative heat flux to the structure (equation 5.12) is not only resulting from the state achieved by the furnace gases, but is also affected by the radiation contributions from the walls of the furnace itself to the specimen. To understand what this means, first assume that uniform temperatures are achieved by both the furnace lining surface and the gas phase. Now, consider that in a furnace test, the inflow of hot gases constitutes the primary source of heat (Figure 8.32). In essence, this makes the temperature of the gas phase to be always higher than the surface temperature of the furnace lining. With this in mind, van de Leur and Twilt [112] distinguishes two types of furnaces (Figure 8.34):

1. *Optically Shallow Furnaces:* In this case, the total radiative heat flux to the specimen is governed by the contribution from the opposing wall. It happens in furnaces where the gas phase is transparent to thermal radiation, meaning that the amount of soot inside the furnace is extremely limited, and/or when the distance from the specimen to the opposing wall is rather small. As a result, the radiation temperature will be lower than the gas temperature ($T_{convection}$ in Figure 8.34) during the whole test.

2. *Optically Deep Furnaces:* Here, the total radiative heat flux to the specimen is governed by the contribution of the furnace gases. It will occur in furnaces where the gas body is opaque to thermal radiation (i.e. high soot generation) and/or the distance from the specimen to the opposing wall can be considered large. Not that in essence, this will characterize a *blackbody* behavior for the gas phase (Section 5.1.3), meaning that the radiation temperature inside the furnace will approach that of the gases ($T_{convection}$ in Figure 8.34).

No matter what kind of furnace is to be used for a test, the thermal exposure to the structure will always be governed by the radiation temperature, look for instance in Section 5.3.3.3 where the concept of AST is presented. Then, go back to Figure 7.38 and Figure 7.44 and compare the AST temperature for the specimens to the radiation temperature achieved within the enclosure. Therefore, unless a *blackbody* behavior is achieved by the gas phase (in which radiation and gas temperatures are equal), it becomes of primary importance in a furnace test to track the radiation temperature (in fact, to track the AST) and not the gas temperature. In this sense, there are two types of devices which are commonly used to measure temperatures in fire tests: (1) *wire thermocouples* (i.e. TC in Figure 8.34); and (2) *plate thermocouples* (i.e. PT in Figure 8.34). As explained in Section 7.3, a TC is more affected by convection heat

transfer than by radiation and will provide measurements which are representative to the achieved gas temperatures at the measuring position. A PT, on the other hand, perceives the exposure in the same way as the structure and will provide measurements which are equivalent to the radiation temperature achieved inside the furnace.

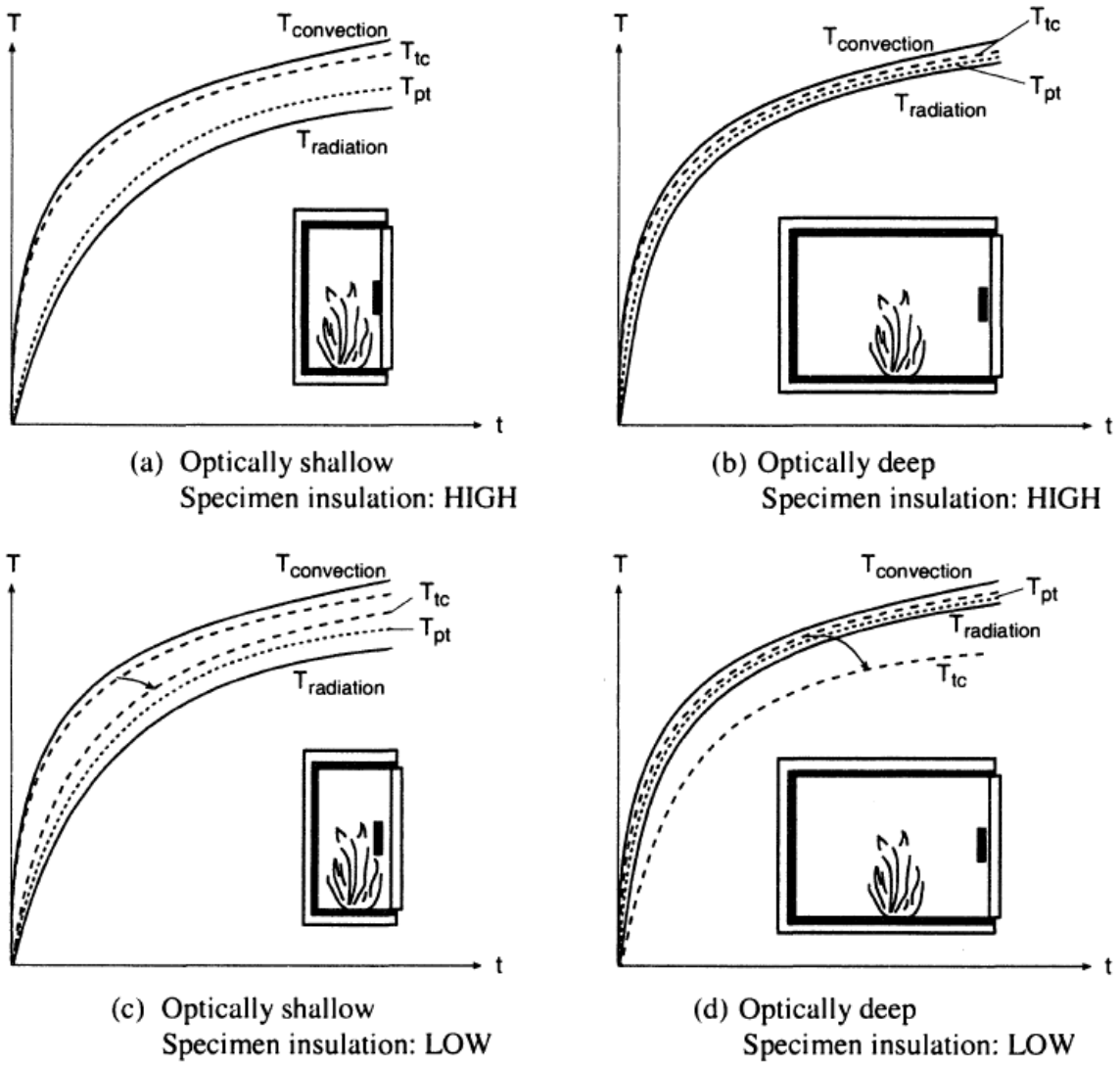


FIGURE 8.34 – EFFECT OF THE CHARACTERISTICS OF FURNACES ON THE ACHIEVED THERMAL EXPOSURE OF SPECIMENS
Retrieved from van de Leur and Twilt (1999) [112]

Once we have a clear definition of the types of furnaces (i.e. *optically shallow* and *optically deep*) and measuring devices (i.e. TC and PT), we can address what kind of behavior is to be expected for different conditions within a furnace test. In this sense, Figure 8.34 distinguishes four cases:

(a) Optically shallow furnaces applied to high insulation specimens: As explained before, for optically shallow furnaces there will be a significant difference between the higher gas temperatures and the lower radiation temperatures. If the specimen has a high level of insulation (i.e. low conductivity in equation 5.4), then the surface temperature of the specimen will approach the radiation temperature from the beginning of the test (Figure

8.25). In this condition, TC measurements will significantly deviate from PT measurements, as the TC will approach the gas temperature within the enclosure.

(b) Optically deep furnaces applied to high insulation specimens: Here, as the gas temperature is essentially the same as the radiation temperature, TC measurements shall be very close to PT measurements.

(c) Optically shallow furnaces applied to low insulation specimens: When optically shallow furnaces are applied to low insulation specimens, we will achieve a different scenario. As the measuring device is located close to the surface of the specimen, TC measurements will be influenced by this relatively cold structure and will decrease if compared to case *(a)*, meaning that they will also deviate from the true gas temperatures. On the other hand, PT measurements remain unchanged. This is the case because the PT is insulated on the back (Figure 7.22), which prevents it to be affected by the radiation emissions from the specimen.

(d) Optically deep furnaces applied to low insulation specimens: In this case, as the gas temperature and the radiation temperature are virtually the same, due to the proximity of the measuring device to the surface of the tested specimen, the TC measurements will drop below the measurements of a PT.

Therefore, for *optically deep furnaces*, the use of TCs to regulate the thermal exposure imposed onto the structure should also suffice in providing accurately controlled tests. An example of such a case is given by the furnace which was used to investigate different passive protection systems to be used in the Western Scheldt Tunnel (Figure 8.35). As it can be seen from Figure 8.36, during those tests, the temperature measurements obtained from TCs and from PTs were practically identical.

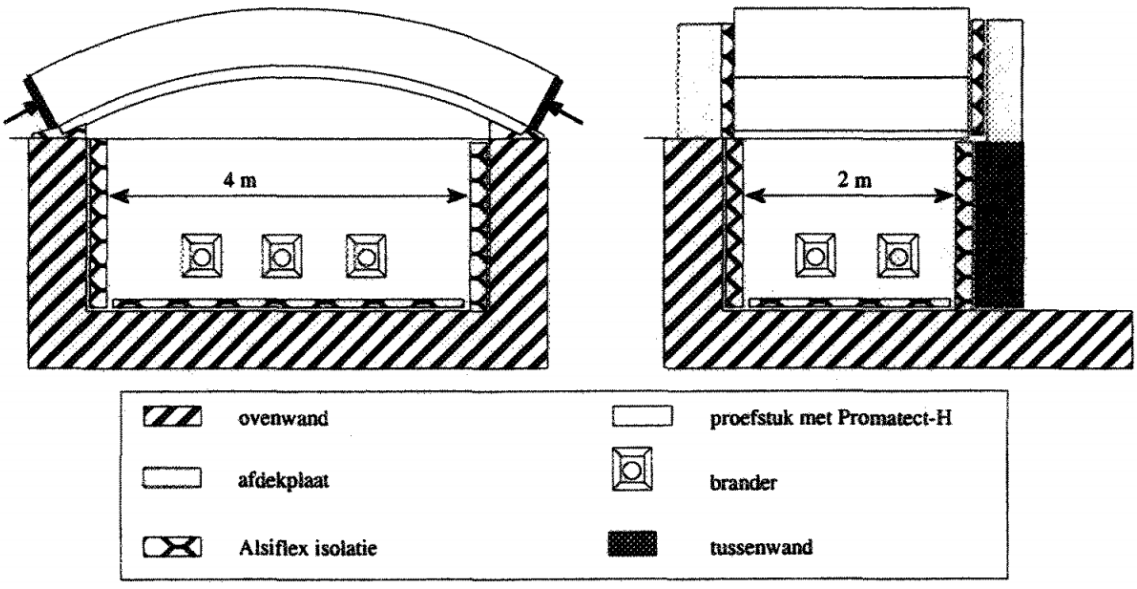
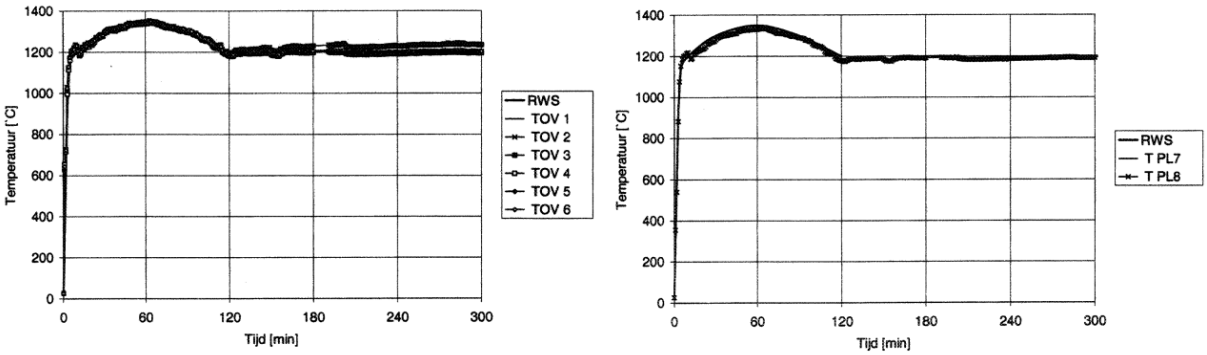


FIGURE 8.35 – PASSIVE PROTECTION TESTS FOR THE WESTERN SCHELDT TUNNEL (OPTICALLY DEEP FURNACE)
Retrieved from Both [113]



TC Measurements PT Measurements

FIGURE 8.36 – TEMPERATURES INSIDE THE FURNACE (OPTICALLY DEEP FURNACE)
Retrieved from Both [113]

However, when dealing with *optically shallow furnaces*, the use of TCs in controlling the thermal exposure imposed on the specimen might be misleading. For those cases, there will always be a difference between the gas temperature and the radiation temperature achieved within the furnace, and the use of PTs will be required if the level of thermal exposure is to be properly controlled during the test. An example of an *optically shallow furnace* is given by the small oven (0.5 *x* 0.4 *x* 0.525 m^3) used in the work of Jasson and Boström [114] to evaluate the occurrence of spalling in small slabs subjected to the standard curve. Figure 8.37 provides a comparison between TC measurements (green line) and PT measurements (red line) within this furnace, highlighting the difference of gas and radiation temperatures in such cases.

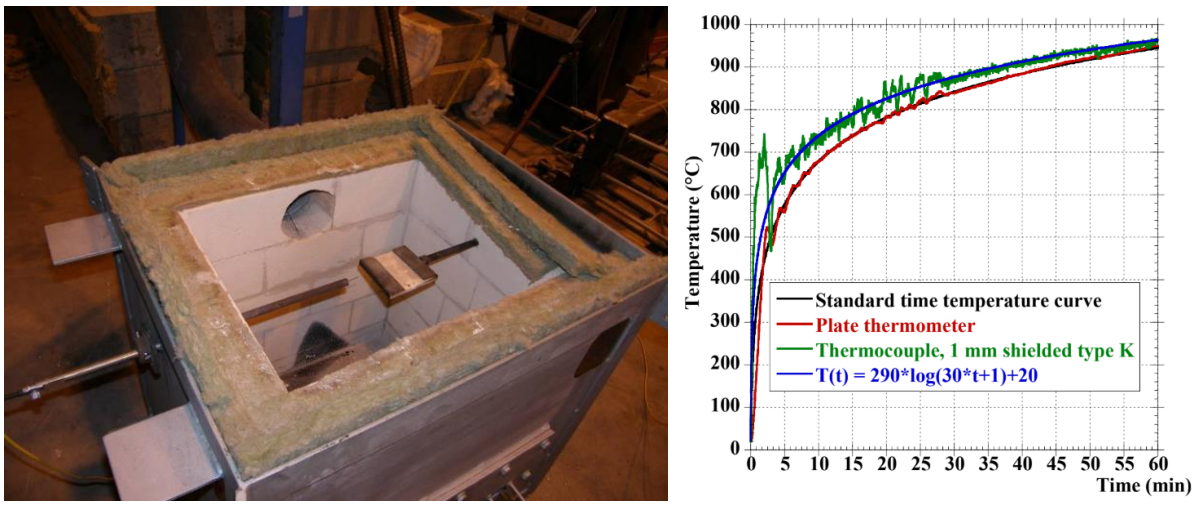


FIGURE 8.37 – OPTICALLY SHALLOW FURNACE

The MobiFire (Figure 8.28) used in in-situ testing of tunnel structures also appears to characterize an *optically shallow furnace*. This is the case because this furnace is also of relatively small dimensions and seems to make use of a non-sooty burner[15]. If this is indeed the case, then, the *spalling test* in this furnace will lead to a situation similar to that of type *(c)* in Figure 8.34, whereas a *thermal insulation test* would correspond to a scenario of type *(a)* in

[15] Maastunnel - Camera inside the MoBiFire (Efectis): https://www.youtube.com/watch?v=m4zcB9JmHx4

the same figure. As the MobiFiRe makes use of several TCs to control the temperatures during the test, the real thermal exposure imposed on the specimen (which is governed by the radiation component) might not be properly controlled during both types of fire tests performed inside this oven. In fact, as the TC measurements will be higher than the PT measurements, the real thermal exposure achieved inside the MobiFiRe should actually be lower than that which is desired by the test (i.e. RWS curve). Note also, that even if the MobiFiRe was somehow pre-calibrated to be controlled by the use of TCs in a similar process as that which is depicted in Figure 8.37, it is likely that the conditions achieved within this calibration will be specimen dependent, meaning that the calibrated TC curve (blue line in Figure 8.37) would probably only be representative to regulate the furnace in tests of a given material and not to regulate tests for a given furnace. Thus, given the importance of such tests in evaluating existing tunnel structures, it would be reasonable to use PTs as the controlling mechanism instead of TCs. Keep in mind that the use of PT as the controlling mechanism in furnace tests is required by EN 1363-1 [115] (the European standard for fire resistance tests).

8.3.2.2 Consequences of Temperature Control

A final remark here concerns the shape of the RWS curve and also the mechanism of controlling furnace tests through temperature measurements. Assume for instance that the measurements shown in Figure 8.30 are actually very representative in describing the thermal exposure to the structure. If this is the case, they should essentially follow the RWS curve during the whole test. However, this is not necessarily the case when performing a test in reality, and the temperature measurements are controlled to be within a certain margin error (marked by the dashed red lines in Figure 8.30). During the MobiFiRe test, for instance, this tolerance appears to be equal to $100\ ^oC$ above or below the RWS curve. Now, consider that the incident heat flux to the structure could be simply calculated according to equation 8.1, which should indeed be the case if gas and radiation temperatures would be assumed equivalent (*blackbody* behavior). Following this line of thinking, Figure 8.38 shows the accepted temperature margin of error translated in terms of an equivalent error range for the incident heat flux to the structure. At the peak temperature ($1350\ ^oC$), the margin tolerance (i.e. $100\ ^oC$) represents an approximate error of 7% in temperature. Due to the fourth power dependence of radiation on temperature, however, this tolerable error actually translates in an acceptable deviation of ~25% on the level of exposure imposed to the structure. Note also that this value is actually representing the minimum percentual error for the incident heat flux. For instance, the same allowable error ($100\ ^oC$) in a temperature level of $1200\ ^oC$ would represent a percentual error of ~30% in the level of incident radiation to the structure. Therefore, whereas such variations might not seem that representative in terms of global temperatures, they can significantly affect the level of thermal exposure imposed on structures during a furnace test, thus contribution to increasing the variability of test results for similar test specimens (look at shaded grey area in Figure 8.40). Also, it seems that the shape of the RWS curve (Figure 1.1) makes it inadequate to be used during furnace tests. Moreover, its constant variations in temperature development appear to harden the task of following this curve during an in-situ test with the MobiFiRe, where, due to the limited size of the oven, temperatures within the furnace are hardly uniform. This might lead to a different temperature development than that which is idealized by the use of the RWS curve, thus contributing to increase even further the variability of uncontrolled thermal exposure among different tests.

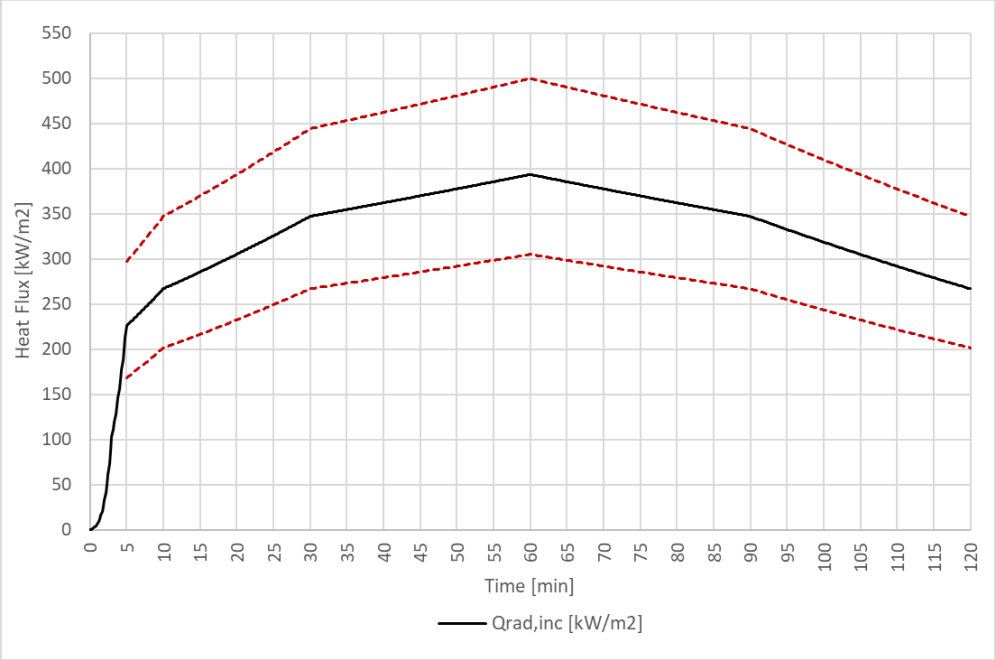


FIGURE 8.38 – MARGIN OF ERROR DURING A FURNACE TEST (INCIDENT RADIATION)

8.3.3 H-TRIS

Considering the issues of uncontrolled and non-uniform thermal exposure within furnace tests, Maluk [74] proposed a novel test method, entitled as *Heat-Transfer Rate Inducing System* (H-TRIS) and illustrated in Figure 8.39. Through this innovative test methodology, one is able to directly control the thermal exposure imposed on a test specimen, by regulating the incident radiant heat flux onto the exposed surface of the structure according to any desired function (which can, for instance, be equivalent to the exposure idealized by the use of a standard fire curve). In essence, during this test, one will make use of a thermal boundary condition of type 2 (Section 5.3.2), while directly controlling $\dot{q}''_{inc}$ in equation 5.22. This is done through the use of radiant panels. Apparently, when compared to identical conditions for conventional fire resistance furnace tests (shaded grey area in Figure 8.40), this innovative test has proven to reduce the variability of the results, and thus, to improve the repeatability of different tests of correspondent specimens (black lines in Figure 8.40).

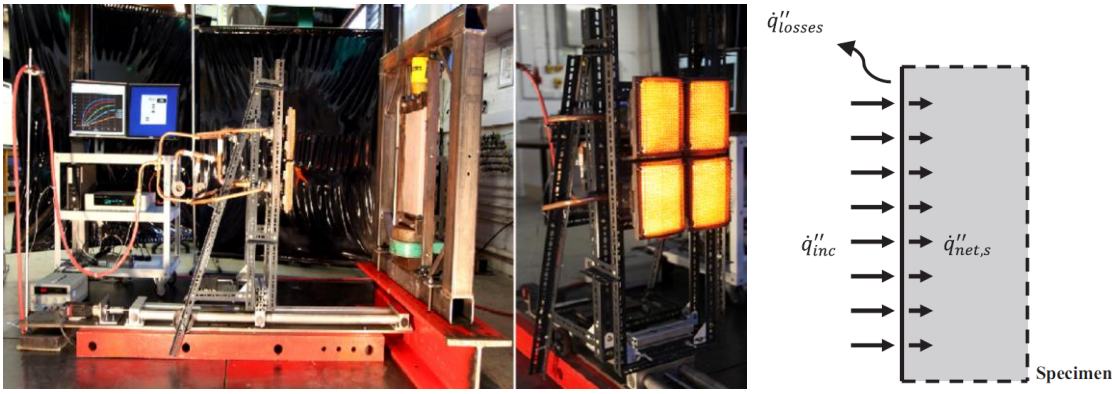


FIGURE 8.39 – H-TRIS
Retrieved from Maluk et al. [109]

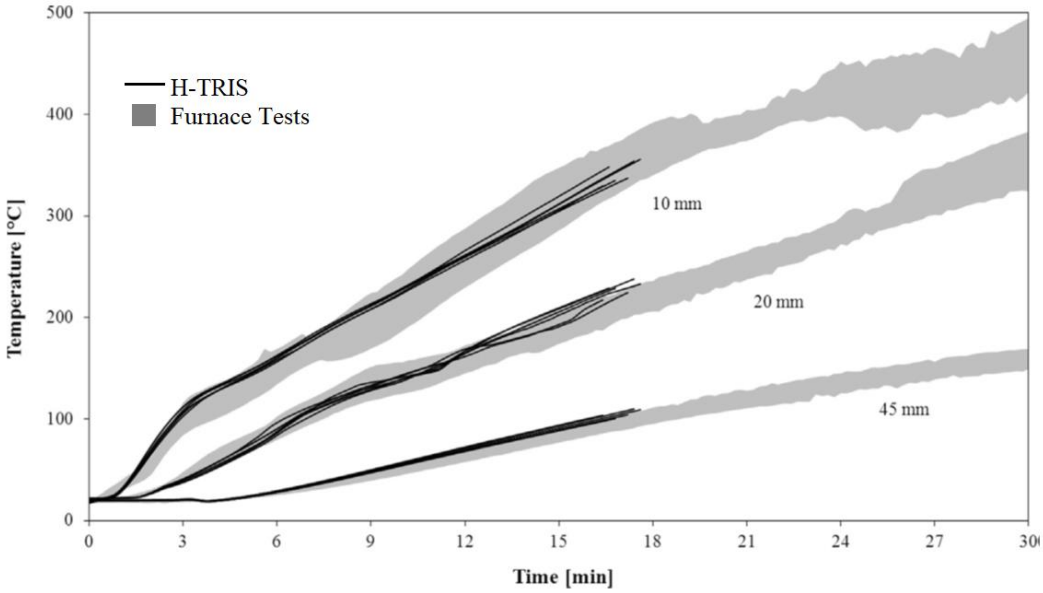


FIGURE 8.40 – COMPARISON OF THE TEMPERATURE DEVELOPMENT INSIDE CONCRETE SPECIMENS FOR H-TRIS AND FURNACE TESTS
Adapted from Maluk et al. [109]

8.4 Conclusions

Based on the study performed in this chapter the following conclusions apply:

1) The RWS curve represents, if not the most, one of the most severe fire scenarios encountered in literature, being as destructive as the most severe jet fires (Figure 8.13).

2) The Runehamar test results are often taken as an indication that such an extreme scenario (RWS curve) is indeed conceivable during a tunnel fire (Figure 8.4). However, the study developed in this chapter indicates that such high temperatures were only measured during that test due to the use of *insulation* on protecting the whole cross-section of the Runehamar tunnel (Figure 8.16). Effectively, as also shown in Chapter 7, the same fire scenario is unlikely to generate the same exposure in identical *protected* and *unprotected concrete tunnels.*

3) Materials with different thermal properties react differently to the same thermal exposure (Section 8.2). The thermal properties of the boundaries of an enclosure will also effectively change fire dynamics, thus also affecting the thermal exposure suffered by the structure itself. The current methodology of applying the same time-temperature curve to different types of material neglects this completely.

4) When addressing tunnels, for instance, the use of the RWS curve indiscriminately among *concrete* and *insulation* inherently defines the analysis of two distinct fire scenarios between each case, but with *concrete* being subjected to the more severe one. As the most critical fire scenario within a certain tunnel should not be dependent on whether or not this tunnel is *protected* or *unprotected*, the use of the RWS curve should be limited to describe only *insulated tunnels*.

5) Furnace fire resistance tests were conceived in a period where society's need surpassed the past engineering knowledge over fire dynamics. Thus, such tests were based on the sole assumption that the thermal exposure imposed on a structure could be fully characterized by the average gas temperatures achieved within the enclosure. Nowadays, we know this not to be the case. In a furnace test, the thermal exposure on the structure is actually the result of the added contribution of several different sources (i.e. furnace linings, gases, and the specimen itself) to the specimen. As a consequence of this complex interaction, it appears that for some situations the thermal exposure achieved inside the furnace during a test is often not properly controlled (Figure 8.34).

6) If *wire thermocouples* (TC) are replaced by the use of *plate thermocouples* (PT), then significant improvement is achieved on controlling the thermal load to the structure, increasing the level of reliability of the furnace test. Nonetheless, radiation heat transfer governs the total heat flux to the structure (Figure 8.24), and it depends on temperatures to the fourth power. Thus, despite homogenizing the level of exposure among different furnaces (i.e. making a test to be furnace independent), the use of PT will not change the fact that rather "small" temperature variations (Figure 8.30) might represent significant changes on the level of thermal exposure imposed on the structure (Figure 8.38).

7) Maluk et al. [109] propose an alternative fire testing method (H-TRIS) in which the thermal exposure to the structure can be directly controlled based on a time-history of incident radiant heat flux (i.e. $\dot{q}''_{inc}$ in equation 5.22) on the structure. When compared to furnace tests, the use of this new methodology should reduce the variability among different tests of similar specimens and improve the overall quality of the test results (Figure 8.40). Note that basing the design on heat fluxes is already common in other fields, such as the oil industry (Table 8.1 and Table 8.2).

9 Performance-Based Approach: A Case Study for the Piet Hein Tunnel

To conclude the work developed in this thesis, this chapter addresses a case study. At first, the development of the idealized RWS fire scenario (i.e. 200 MW gasoline pool fire) is studied within a real tunnel. Then, the development of a smaller fire scenario (i.e. 30 MW gasoline pool fire) is also included. For both, the effects of ventilation and the generated thermal exposure are thoroughly investigated. In the end, the process of coupling CFD calculations for the fire phase with the FE model for the structural analysis is explained.

9.1 Introduction

In Chapter 5 important aspects related to fire and to the resulting thermal exposure on structures were introduced. In essence, heat is transferred from a fire to the structure through convection and radiation. Convection heat transfer refers to the amount of heat supplied to the structure due to the temperature difference between that of the gases surrounding this structure and that of the surface of the structure itself. This process occurs at a rate which is dependent on the conditions of the flow in the vicinity of the solid (equation 5.5). Radiation heat transfer describes the net result of thermal radiation absorbed and emitted by the structure during a fire. We learned that the amount of radiation emitted by a body is related to the fourth power of its own bulk temperature (Section 5.1.3). This relationship allows us to rewrite the incident radiative heat flux on a structure in terms of a hypothetical radiation temperature (equation 5.10). Based on this, we are able to describe the rate of radiation heat transfer in terms of the difference between the fourth power of this fire-induced radiation temperature and that of the fourth power of the surface temperature of the structure (equation 5.12). Therefore, the total amount of heat absorbed by the structure during a fire becomes the added contribution of each one of these modes of heat transfer. However, for fire-related exposures, the rate through which heat will be transferred to the structure is always governed by the radiation component (Section 5.1.3.2). This makes the achieved radiation temperature to be more important than the true gas temperatures inside an enclosure.

In Chapter 7 the derivation of the RWS curve was investigated thoroughly. As we know, this curve is used indistinctively among *protected* and *unprotected concrete tunnels* and is assumed to represent a severe fire scenario, in which a large hydrocarbon pool fire would burn at a constant HRR of *200 MW* for a total of two hours (Section 7.1). The curve was, however, derived based on gas temperature measurements within a very short and narrow *insulated tunnel*, where oxygen supply was practically unlimited. As described in the previous paragraph, such gas temperatures might not necessarily be representative to describe the thermal exposure imposed on a structure during a fire. In fact, gas temperatures will only truly represent the exposure if the resulting gas phase of a fire behaves like a *blackbody* (Section 5.1.3.1). For such cases, the gas temperatures will equal the radiation temperature, meaning that the gas body will emit thermal radiation at its maximum potential. Although this is a comm678on assumption for *luminous flames* (Figure 5.9), it is not necessarily true. When considering the scenario achieved within the tunnel during the RWS tests, for instance, it appears that the real thermal exposure on the ceiling was somewhat smaller than that which is described by the use of the RWS curve (compare AST with gas temperatures in Figure 7.38).

Besides this previous point, it was also noted in Chapter 7, and later explained in Section 8.2.4, that *concrete tunnels* and *insulated tunnels* behave differently when subjected to a same fire scenario. In essence, due to its thermal properties, *concrete* extracts much more energy from a fire than *insulation*. As in tunnels, the boundaries of the enclosure are really close to the fire source, this difference in the thermal behavior of *concrete* and *insulation* contributes to reducing the maximum temperatures that are to be achieved within a *concrete tunnel* when compared to those which are achieved for an equivalent *insulated tunnel* when subjected to an identical fire scenario (compare AST for *concrete* with AST for *insulation* in Figure 7.46). Hence, as the RWS curve was derived in an *insulated tunnel*, it appears that this curve is not realistically representing the thermal exposure reached inside *concrete tunnels*. In reality, however, the situation is quite different from that which based the development of the RWS curve. On one hand, the cross-section of real tunnels is much larger than that of the tunnel used during RWS tests (2 m *x* 2 m). On the other, the expected fire size also grows tremendously. There is also a new factor in play, which complicates the matter even further. As explained in Section 3.2, tunnels often make use of longitudinal ventilation systems to provide users with a smoke-free route upstream of the fire source. The use of such systems is known to affect fire dynamics, but the reported effects of ventilation in tunnel fires vary considerably in the available literature (Section 4.2.2).

Therefore, to conclude this thesis, a case study will be addressed. Here, a real tunnel is selected, and different fire scenarios are used to investigate the possible benefits of elaborating the design in a performance-based approach rather than in the use of prescriptive measurements. As a starting point we are going to look at the RWS fire scenario or, in other words, a *200 MW* gasoline pool fire burning for a total of two hours. Then, a smaller pool fire (*30 MW*) is also investigated, exposing the differences on the achieved thermal exposure for a reduced fire size. For both cases, the effects of ventilation are also investigated. However, before moving further to the work developed in this chapter, the next paragraph will briefly describe the selected case study.

For almost 25 years, the Piet Hein tunnel has been one of the main arteries of the Amsterdam road network, serving approximately 30.000 vehicles every day[16]. It also provides a rail connection from the Amsterdam's Central Station to the IJburg district. This tunnel is partially immersed and has a total length of *1.900 m*. The part underwater is *1.265 m* long and is made of 8 reinforced concrete tunnel sections of approximately *160 m* each. The Piet Hein tunnel will be renovated in the next years to comply with the new tunnel regulations imposed by the Dutch government (Section 1.1), which are also in line with the European-directive 2004/54/EC[17]. Considering this context, this partially immersed tunnel serves as an ideal case study for the scope of this thesis, providing a realistic example for the use of a prescriptive-based approach.

[16] https://www.amsterdam.nl/projecten/tunnels/deelprojecten/piet-heintunnel/
[17] https://eur-lex.europa.eu/legal-content/EN/TXT/HTML/?uri=CELEX:32004L0054&from=EN

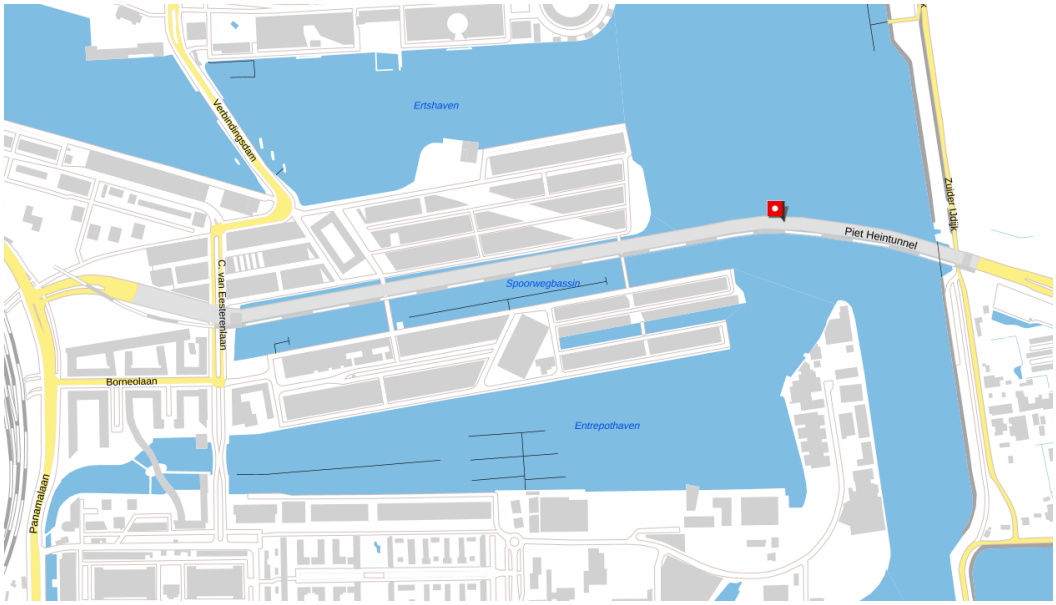


FIGURE 9.1 – PIET HEIN TUNNEL[18]

9.2 Model I – RWS Fire Scenario (200 MW)

The first type of fire investigated here refers to the idealized RWS fire scenario or, in other words, a 200 MW gasoline fire burning for two hours. For this, three different models were studied in FDS, namely (1) 200 MW – v=0 m/s, (2) 200 MW – v=3 m/s, and (3) 200 MW – v=6 m/s. The first model accounts for the occurrence of the RWS fire scenario within a *concrete tunnel* and without any ventilation effects. Although, this would probably never happen in reality (as ventilation will most likely be applied on smoke control), this scenario is important to understand if a fire as big as this one would be sustained within a tunnel even without ventilation. The expectation is that due to the limited oxygen availability, such a large fire would not be sustained for that long. The second and third models are intended to evaluate the effects of ventilation in mainly two ways: (a) enhancing combustion; and (b) controlling the temperature development within the tunnel. The ventilation velocities were selected to be approximately equal to: (1) the critical velocity (3 m/s), thus representing the minimum ventilation velocity adopted within a tunnel to avoid backlayering of smoke (Section 3.2.1.1); and (2) the maximum ventilation capacity which appears to be currently available in most Dutch tunnels (6 m/s). Therefore, the next topic will discuss how the correspondent FDS models were constructed for each one of those cases, clarifying important aspects and highlighting fundamental assumptions.

9.2.1 FDS Models

9.2.1.1 Geometry and Thermal Properties

Figure 9.2 below provides the original cross-section of the Piet Hein tunnel. To create the FDS model, this geometry had to be adapted. For once, only one road tube was modelled to perform the fire simulation. Also, in FDS, the geometry of solid obstructions is mesh depend, thus only

[18] https://www.amsterdam.nl/projecten/tunnels/deelprojecten/piet-heintunnel/?bigmap=true

allowing obstructions whose dimensions are multiple of the selected grid size. For the RWS fire scenario a grid size of *0.5 m* was used (Section 9.2.2). Following this line, Figure 9.3 provides the cross-section of the model used in FDS (squares in Figure 9.3) in comparison to that of the Piet Hein tunnel (hidden line in Figure 9.3). The hatched squares on the bottom mark the position of the pool fires within the model, and the tagged circles highlight the positions of the devices used to collect AST (Section 5.3.3.3), gas temperatures and/or incident thermal radiation on the cross-section. Note that the correspondent gas temperatures are actually collected at the center of the last gas cell located in the interface with the solid obstruction.

Although the geometry of the object is tied to the mesh size, different thicknesses may be applied to each solid obstruction individually. Therefore, the solution of the heat conduction model used in FDS (Section 5.2.1) is not dependent on the grid size. Even so, the thinnest concrete element in the Piet Hein tunnel cross-section is already *0.5 m* thick, and this is more than enough to avoid heat from surpassing from the exposed side of the obstruction to the other. Therefore, for simplicity, all elements used in the FDS simulations performed here are also set to be *0.5 m* thick.

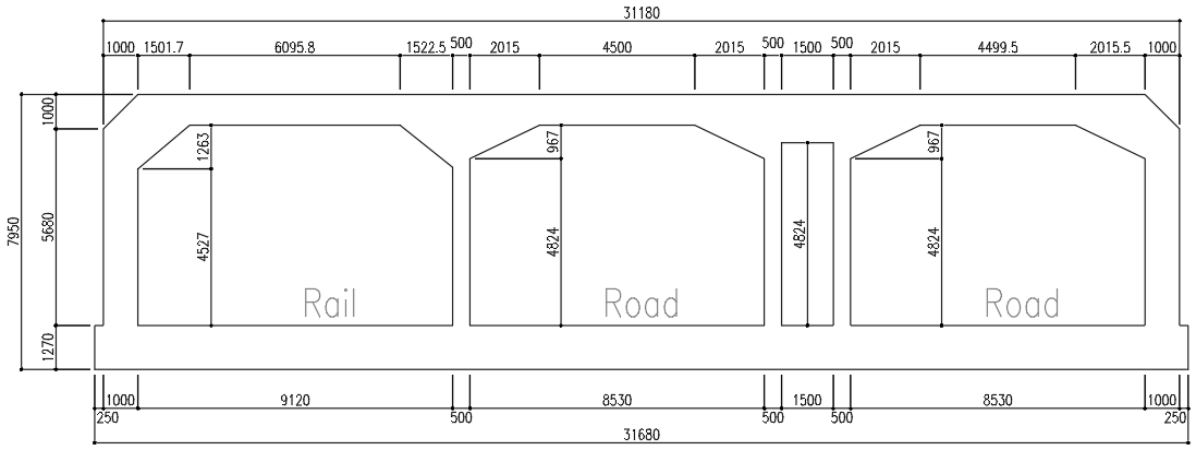


FIGURE 9.2 – PIET HEIN TUNNEL (CROSS SECTION)

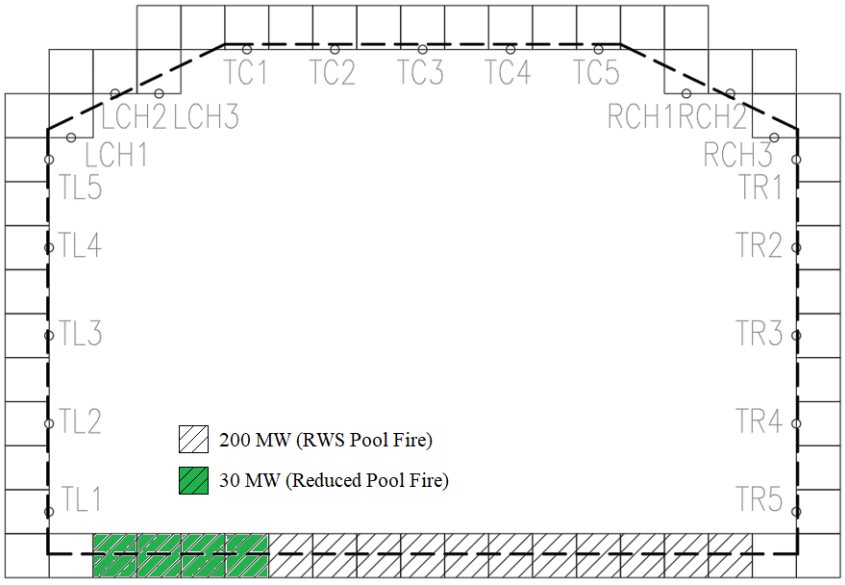


FIGURE 9.3 – CROSS SECTION IN FDS

As it can be seen from Figure 9.1, the profile of the Piet Hein tunnel has a really long straight section ending, on both sides, in curved sections. The longitudinal linear section is approximately *930 m* long and has an inclination of *0.763%*. In the models developed here, only part of this linear section was included in the simulation, and the inclination was not considered. This, however, is not assumed to affect the results significantly, as the slope of the tunnel is rather small for this straight section. The modelled longitudinal dimension varied among cases *with* and *without* ventilation. For model (1) 200 MW – v=0m/s, a length of *300 m* was simulated in a grid size of *0.5 m*, with the fire source being assigned to the center of this section. This middle section was connected on both ends to linear sections of *150 m* (simulated in a grid size of *1 m*), yielding in a total length of *600 m*. Both extremities of the tunnel were assigned as *open* boundaries (Figure 9.4). For models (2) and (3), the longitudinal dimension of the tunnel was shorted due to the use of ventilation. A section of *240 m* was simulated in a grid size of *0.5 m*, with the center of the fire source being located *30 m* ahead from one of its extremities. Upstream the fire source, the simulated domain ended in a *ventilation* boundary condition, meaning that FDS constantly supplies air to the tunnel according to the prescribed ventilation velocity. Downstream of the fire source, the tunnel was connected to a *90 m* long section simulated in a grid size of *1 m*. The latter ended in an *open* boundary condition (Figure 9.5). Table 9.1 summarizes the geometry used in each one of the models studied in this section and provides the considered concrete's thermal properties.



FIGURE 9.4 – FDS MODEL WITHOUT VENTILATION

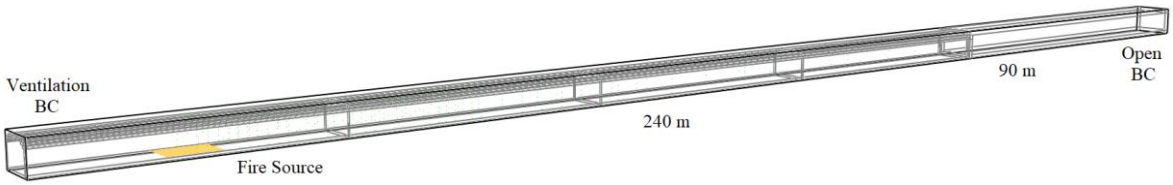


FIGURE 9.5 – FDS MODEL WITH VENTILATION

Thermal Properties of Concrete (EC1992-1-2)	
Density	2300 kg/m³
Thermal Conductivity	Lower Limit (Figure 11.2)
Specific Heat	u = 0% (Figure 11.3)
Emissivity	0.7
Thickness	0.5 m
Cross Section in FDS Compared to (Real Dimension)	
Maximum Internal Width in FDS	8.5 m (8.53 m)
Maximum Internal Height in FDS	5.5 m (5.59 m)
Tunnel Length	
200 MW – v=0m/s	300 m in 0.5 m grid + 2 x 150 m in 1 m grid
200 MW – v=3m/s	240 m in 0.5 m grid + 90 m in 1 m grid
200 MW – v=6m/s	240 m in 0.5 m grid + 90 m in 1 m grid

TABLE 9.1 – MODEL GEOMETRY

9.2.2 Pool Fire and Mesh Size

The pool fire used to represent the RWS fire scenario was created according to what is described in Section 5.2.3.1. This means that fire was simulated through the use of a boundary condition that constantly releases gasified fuel to the domain of simulation according to a prescribed fire function. From Section 4.1.1.2, we know that pool fires burn with a well-defined and constant mass loss rate. For small pool fires, the burning rate grows with the diameter of the pool up to a maximum value, which is then kept unchanged for any further increases in the size of the pool (Figure 4.4). For gasoline, the maximum mass loss rate equals *0.055 kg/m^2.s* (Figure 4.5), thus defining the burning area required for a gasoline pool fire to achieve the intended HRR (200 MW). Such a huge liquid pool is here assumed to occupy the whole width of the Piet Hein tunnel. However, due to modelling related restrictions, the limits of the pool fire were set to be one grid cell away from the walls of the tunnel (hatched squares in Figure 9.2). For this reason, a pool fire of 7.5 m *x* 11 m was selected. Table 9.2 summarizes the boundary condition assigned to FDS to represent the fire source. Note that the mesh size is related to the HRR of the fire and is determined in accordance with what was explained in Section 7.4.2.5.

Pool Fire	
Fuel	N-OCTANE
Dimensions (Width x Length)	7.5 m x 11 m
Mass Loss Rate per Unit Area	0.055 kg Fuel/m^2.s
Radiative Fraction	0.4 (Figure 5.13)
Soot Yield	0.034 kg Soot/kg Fuel (Section 7.4.2.1)
CO Yield	0.010 kg CO/kg Fuel (Section 7.4.2.1)
Heat of Combustion (FDS)	43.5 MJ/kg Fuel (Section 7.4.2.1)
Total HRR	0.055 x 7.5 x 11 x 43.5 = 197.4 MW
Burning Function	
Time	HRR
0 s	0 MW
15 s	197.4 MW
7200 s	197.4 MW
Mesh Size	
Characteristic Fire Diameter (D*)	7.97 m (Equation 7.3)
Mesh Size (δ_x)	0.5 m
D*/ δ_x	16

TABLE 9.2 – RWS FIRE SCENARIO

As described in Section 5.2.3.2, a particularly important parameter when performing fire simulations in FDS is the radiative fraction. It defines the percentage of the HRR which is released inside the domain in the form of thermal radiation. Here, it is conservatively selected as 0.4, which is the default radiative fraction for N-OCTANE in FDS. In open fires, this radiative fraction decreases significantly for large pool fire diameters, as a consequence of radiation reabsorption within the flame body itself. For instance, in the open, a gasoline pool fire of the same size as the one used here, would have a radiative fraction of approximately 0.1 (Figure 5.15), which is one fourth of the value that we are using here. However, we do not actually know to what extent this fraction could be altered when dealing with fires in tunnels. Basically, for a large tunnel fire, flames will impinge on the ceiling and spread longitudinally through it (Section 3.3.1). This could, for instance, reduce the levels of thermal radiation reabsorption within the flame corpse. For this reason, it was decided to conservatively stick to

the maximum radiative fraction for the selected fuel. Note that this fraction is representative of very small flames (i.e. pool diameter < 1 m in Figure 5.15), where radiation reabsorption is minimum. For this reason, the selected radiative fraction is considered as the maximum fraction for the fuel used here. Thus, at least in theory, the results presented here should be rather conservative.

9.2.3 Temperature Development at the Ceiling

In this section, we are going to study the temperature development only at the center of the ceiling. Here, correspondent gas, AST (equation 5.27) and radiation temperatures (equation 5.11) will be first addressed for each model individually. Then, the effects of ventilation on controlling the maximum temperatures achieved within the tunnel are also evaluated by comparing the different cases among each other.

9.2.3.1 200 MW – v = 0 m/s

Figure 9.6 provides the evolution of gas temperatures in time at the center of the ceiling (i.e. TC3 in Figure 9.2) for several positions downstream the fire source, whose center marks the reference point (*0 m*). What we clearly see here is that a fire this big simply cannot be sustained within a tunnel without some extra source of oxygen supply. This is also highlighted by the HRR output of this fire which was obtained from FDS (Figure 9.7).

Another important aspect when performing fire simulations is highlighted here. If you look at Figure 9.6 you will see that the temperatures at the ceiling rapidly grow to a peak in the vicinity of the fire source (i.e. up to *10 m*) and then, immediately start decaying afterward. Further ahead (i.e. from *10 m* to *150 m*), the gas temperatures also grow to a certain level, remaining approximately steady at this temperature for a longer period of time. Then, they raise again up to a second peak, but also decay afterward. This highlights a limitation when modeling fires through the use of a boundary condition. Basically, independent of the availability of oxygen within the model, during the whole simulation, FDS will continuously provide fuel to the domain (according to the rate described in Table 9.2). At the beginning of simulation, as soon as fuel enters the domain, it will just immediately combust. This leads to an increase in the gas temperatures at the ceiling right on top of the fire source. As combustion continuous to occur, the availability of oxygen at the fire source is reduced tremendously. Once there is not enough oxygen to sustain combustion anymore, the remaining unburned fuel starts to travel longitudinally within the tunnel, pushing the combustion zone (see the definition of reacting zone in Section 5.2.3.1) towards the extremities, where oxygen is still plenty available. However, as FDS keeps providing fuel to the domain unstoppably, a zone of unburned fuel forms on top of the boundary condition (i.e. pool fire). As there is lack of oxygen, this zone will continuously grow during the whole fire simulation, always pushing the combustion zone even further down the tunnel. This is what explains the second peak in temperature for locations which are away from the fire source, thus indicating that combustion is now occurring at those places within the tunnel.

In reality, however, this would not occur. As soon as there is lack of oxygen to sustain full combustion, a fire will become *ventilation-controlled* (Section 3.1), characterizing a scenario in which it equates its own burning rate to the availability of oxygen. Therefore, what we could actually expect from a fire scenario like the one simulated here, is that a lower HRR would be

achieved, but the total burning time would be increased. This indicates, for instance, that the maximum temperatures at the ceiling right on top of the pool fire would actually last for much longer than 5 minutes.

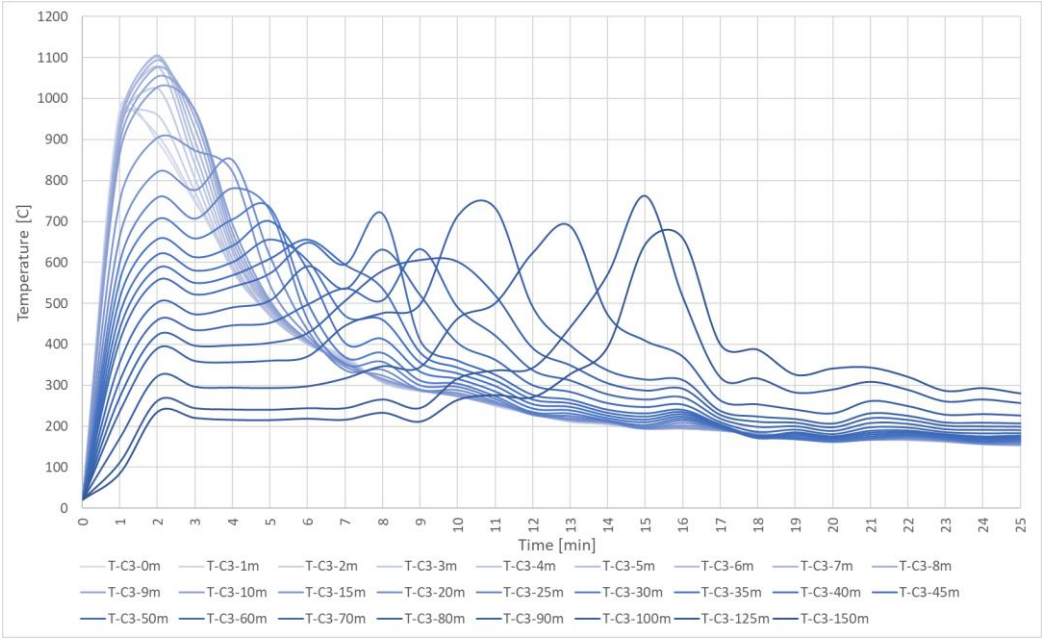


FIGURE 9.6 – EVOLUTION OF GAS TEMPERATURES AT THE CEILING (200 MW – V = 0 M/S)

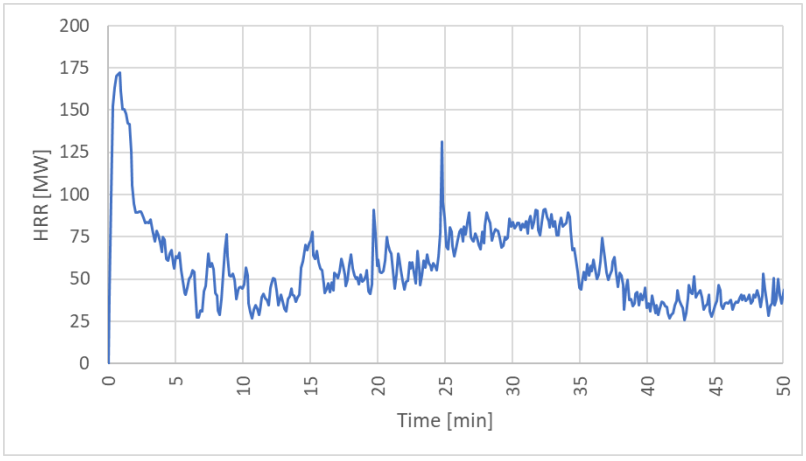


FIGURE 9.7 – HRR (200 MW – V = 0 M/S)

In conclusion, the results obtained for a 200 MW fire without ventilation have no value whatsoever in terms of design purposes. They simply serve to prove that a such a large fire simply cannot be sustained inside the Piet Hein tunnel if there is no extra source of oxygen supply (e.g. longitudinal ventilation systems).

9.2.3.2 200 MW – v = 3 m/s

Now, the use of longitudinal ventilation provides the means to fully sustain the RWS fire scenario at its maximum capacity and for the total period of fire simulation (Figure 9.8). Accordingly, Figure 9.9 provides the longitudinal gas temperature evolution at the center of the ceiling (i.e. TC3 in Figure 9.2) together with an illustration of the conceived pool fire. As it can be seen, gas temperatures grow in time during the whole fire simulation, with maximum

temperatures occurring in between *20 m* to *40 m* downstream the fire source. This is also due to the use of ventilation, which forces the flames towards the floor of the tunnel, while also promoting mixing of cooler air with the hot buoyant smoke at the ceiling. This contributes to limit the maximum gas temperatures in the vicinity of the fire source up to a certain point.

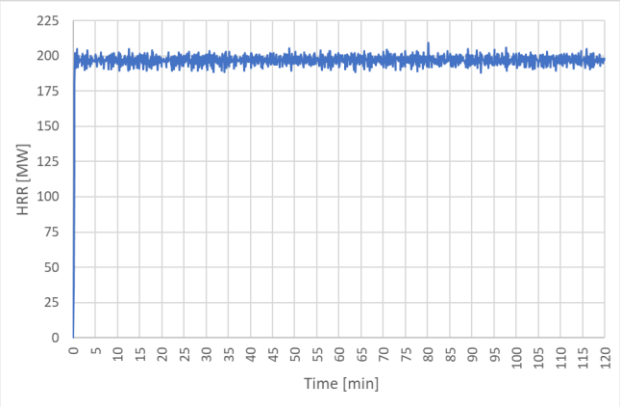


FIGURE 9.8 – HRR (200 MW – V = 3 M/S)

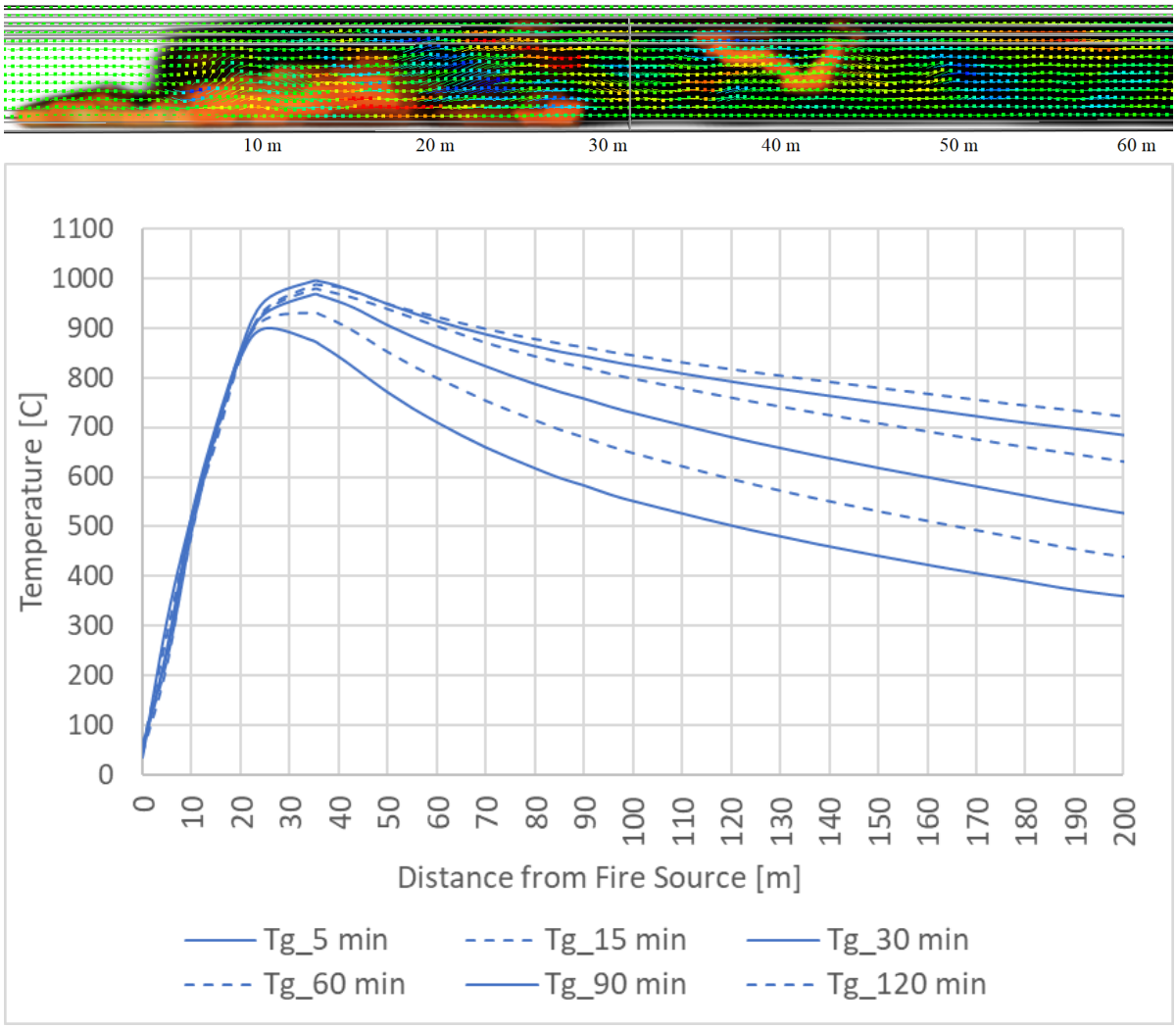


FIGURE 9.9 – LONGITUDINAL GAS TEMPERATURE EVOLUTION IN TIME (200 MW – V = 3 M/S)

As we know, the thermal exposure imposed on the ceiling structure is actually governed by the radiation component. Therefore, Figure 9.10 provides the longitudinal evolution of gas temperatures in comparison with the correspondent AST (equation 5.27) and radiation temperatures (equation 5.11) for *30*, *60*, *90* and *120 minutes* of fire simulation. An identical pattern is noticed among all images, with radiation temperatures being higher than the gas temperatures up to a distance of *~60 m* from the fire source. Also, it can be seen that AST is, as definition, in between the gas and radiation temperatures, tending towards the latter.

As previously explained, ventilation contributes to limit the maximum gas temperatures at the ceiling up to a certain distance from the fire source. For instance, gas temperatures are limited to less than *500 ºC* up to *10 m*. However, combustion still occurs near the floor of the tunnel, on the assigned pool fire, and based on Section 5.1.3.1 we know that pure air is practically invisible to thermal radiation. Therefore, the radiation released from the flames at ground level will still impinge on the ceiling above the flames (Figure 9.9), characterizing the occurrence of high radiation temperatures (*~700 ºC*) right above the fire source (*0 m*). As the reacting zone (highlighted by the flames in Figure 9.9) grows downstream the pool fire, so does the levels of emitted thermal radiation, contributing to further increase the radiation temperatures at the ceiling and leading to a peak somewhere in between *20 m* to *30 m* from the fire source. Note from Figure 9.9, that the reacting zone seems to decrease significantly after surpassing the mark of *30 m*.

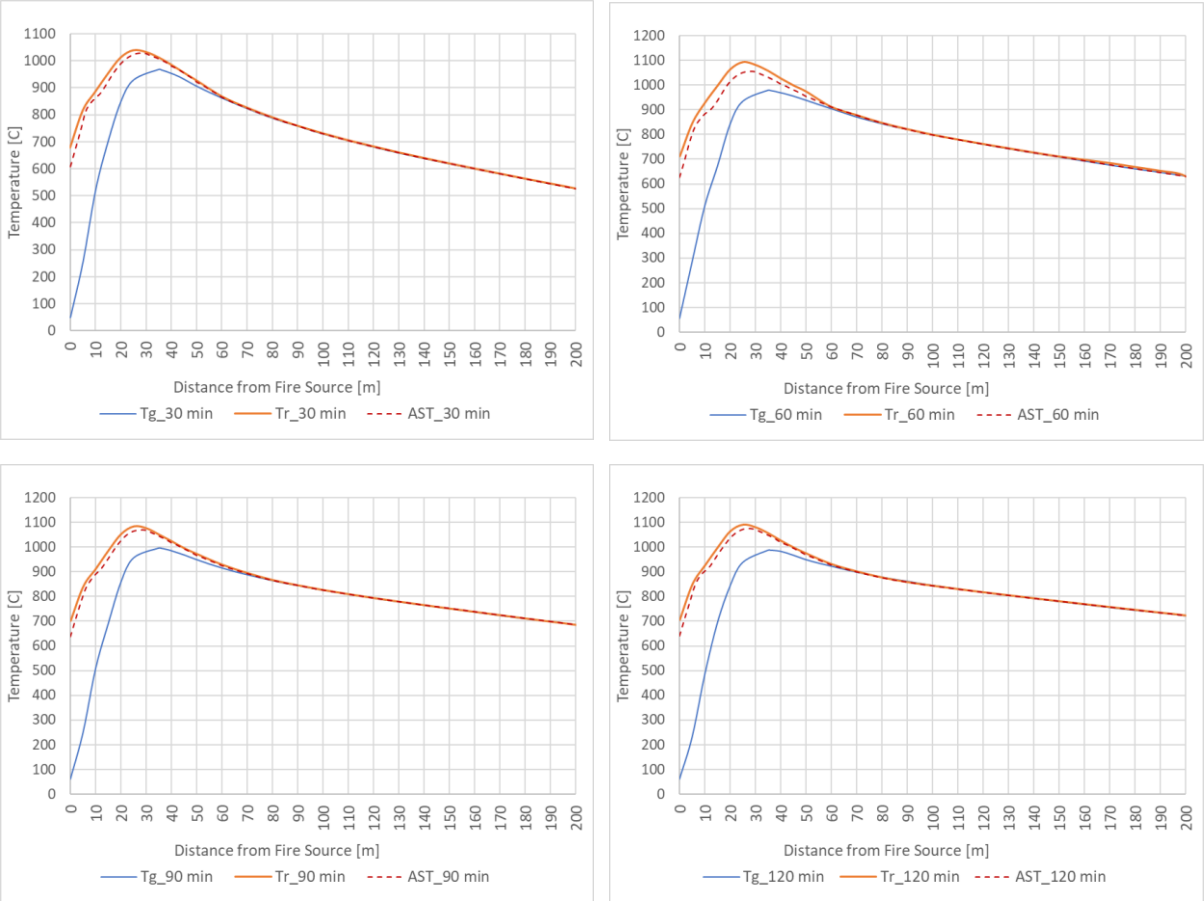


FIGURE 9.10 – LONGITUDINAL GAS, AST AND RADIATION TEMPERATURES (200 MW – V = 3 M/S)

Another interesting aspect to notice from Figure 9.10 is that from *60 m* onwards, correspondent gas and radiation temperatures at the center of the ceiling become equivalent for the remaining length of the tunnel. This indicates that the level of soot concentration within the smoke body located at the ceiling is sufficiently large to characterize a *blackbody* behavior for this mass of gas or, in other words, that the emissivity of the smoke body (i.e. ε_f in equation 5.13) becomes equal to 1. As a consequence, thermal radiation is emitted at its maximum capacity according to the bulk temperature achieved by the smoke layer at such positions. In the next section, we will see that this is not necessarily true for every fire scenario.

9.2.3.3 200 MW – v = 6 m/s

Figure 9.11 provides the evolution of longitudinal gas temperatures at the ceiling for the RWS fire scenario under high ventilation velocity (*6 m/s*). Although the maximum temperatures are significantly reduced, when compared to the previous case (Figure 9.9), being limited to less than *700 ºC* at all times, the general behavior is quite similar to that of a reduced ventilation velocity (*3 m/s*). Also here, due to the use of ventilation, the occurrence of maximum gas temperatures at the ceiling is pushed further away from the center of the fire source. However, as the ventilation velocity is higher, the maximum temperature zone will now be somewhere in between *50 m* to *60 m* down the tunnel.

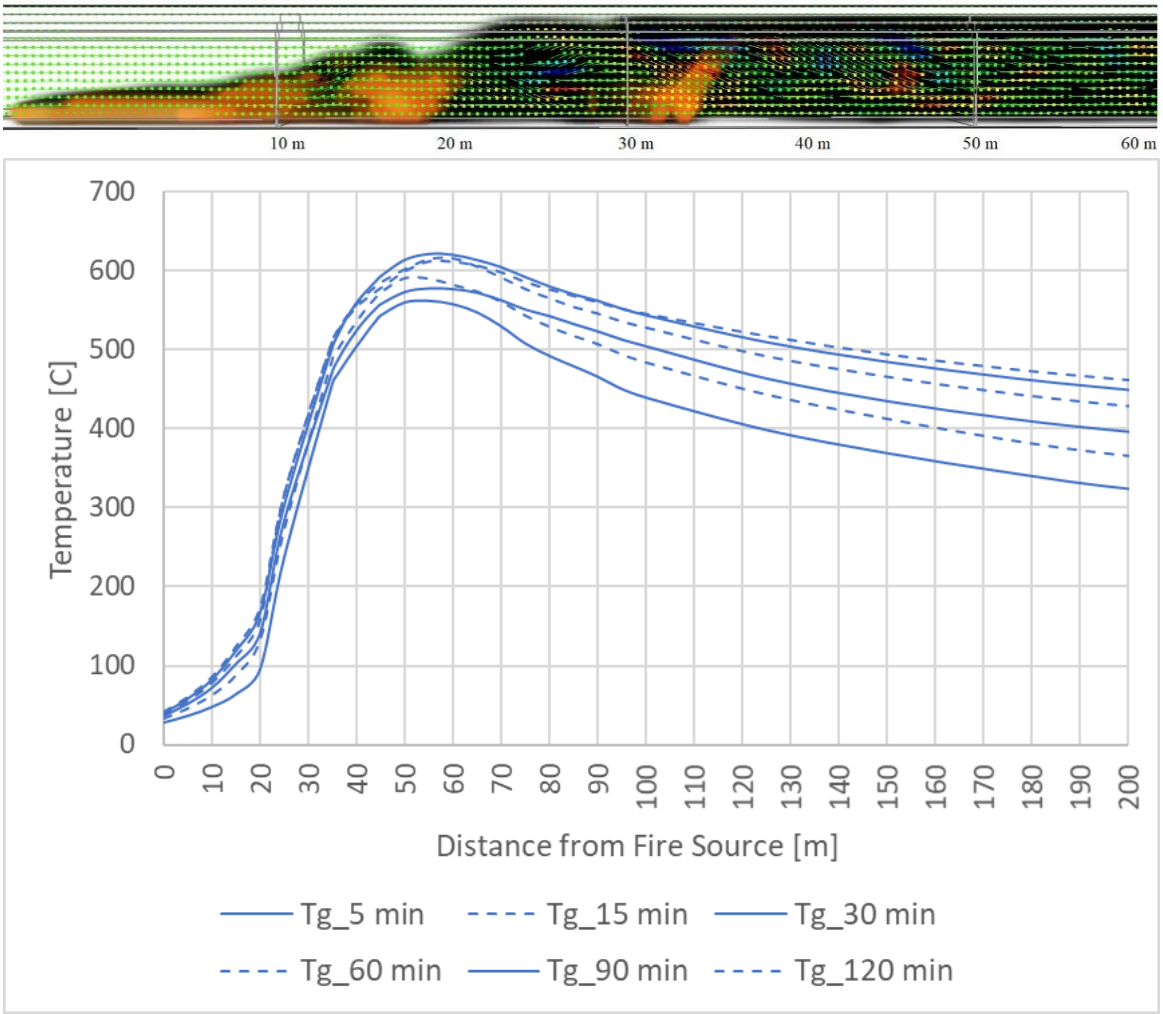


FIGURE 9.11 – LONGITUDINAL GAS TEMPERATURE EVOLUTION IN TIME (200 MW – V = 6 M/S)

Figure 9.12 provides the longitudinal evolution of gas temperatures in comparison with the correspondent AST (equation 5.27) and radiation temperatures (equation 5.11) for *30*, *60*, *90* and *120 minutes* of fire simulation. Once again, the same behavior pattern from the previous case (Figure 9.10) is noticed here, with radiation temperatures being higher than gas temperatures until *~70 m* downstream the fire source and with AST being in between both, but tending to the correspondent radiation temperature. Here, however, it is interesting to highlight that after *70 m*, gas temperatures surpass the equivalent radiation temperatures, indicating that for this case, the smoke layer at the ceiling does not achieve *blackbody* behavior. This is probably related to the fact that for a higher ventilation velocity, more air is pushed to the cross section of the tunnel, but the combustion process is kept unchanged, as it was identically defined for both cases (Table 9.2). This means that the amount of soot generation does not change among these models (3 m/s and 6 m/s), as in both of them full fire capacity was achieved (Figure 9.18). Accordingly, as the case with higher ventilation velocity imposes more air entrainment into the smoke layer, soot concentration is reduced. This could explain why, for this case, a *blackbody* behavior for the smoke layer at the ceiling was not achieved.

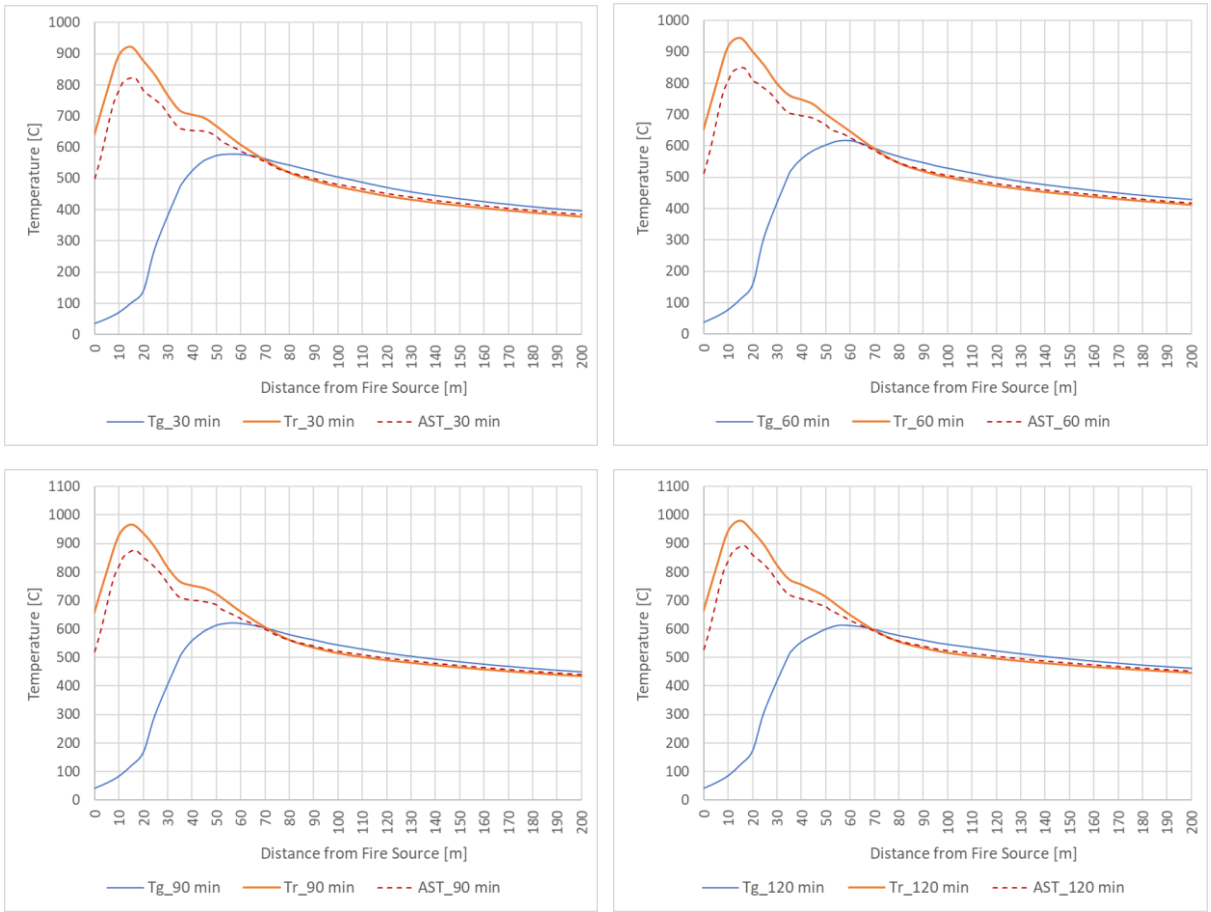


FIGURE 9.12 – LONGITUDINAL GAS, AST AND RADIATION TEMPERATURES (200 MW – V = 6 M/S)

9.2.3.4 Effects of Ventilation

In the previous Sections 9.2.3.2 and 9.2.3.3, we treated the cases with ventilation individually. Now, we are going to compare the results of both to understand the effects of applying a higher ventilation velocity during a tunnel fire. In this sense, Figure 9.13 provides a comparison of the

longitudinal gas temperatures at the ceiling, achieved after *60* and *120 minutes* of fire for both cases studied here. As we can see, the use of a higher ventilation velocity promotes a significant reduction on the maximum gas temperatures at the ceiling, which move from *~1000 ºC* for a ventilation velocity of *3 m/s* to around *600 ºC* for a ventilation velocity of *6 m/s*. This appears to be related to the levels of cool air entrainment into the hot buoyant smoke layer generated by combustion, that is enhanced at a higher ventilation velocity. Such a high mass flow of air improves convection heat transfer within the gas phase (Figure 9.14) where, apparently, heat is lost from the hot gases generated by combustion to the cooler masses of air that are entraining the smoke body. This contributes to limit the gas temperatures achieved within the tunnel as a whole.

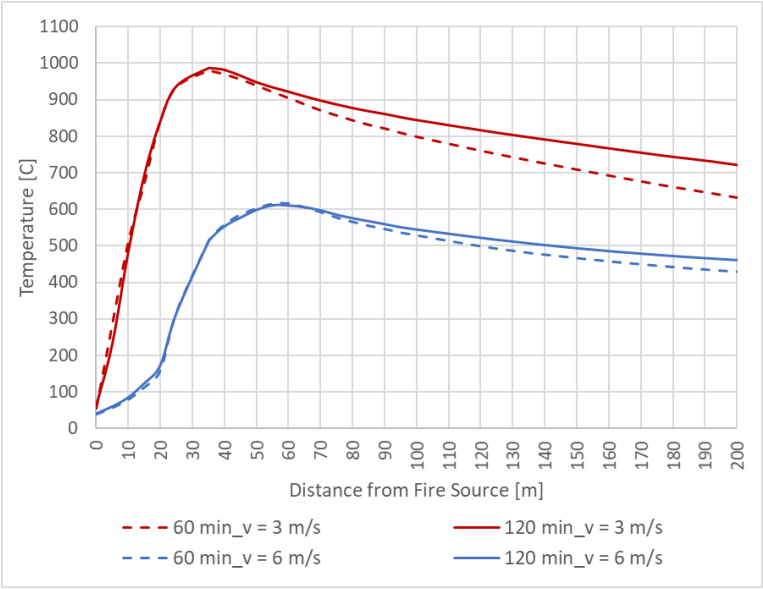


FIGURE 9.13 – COMPARISON OF LONGITUDINAL GAS TEMPERATURES (RWS FIRE SCENARIO)

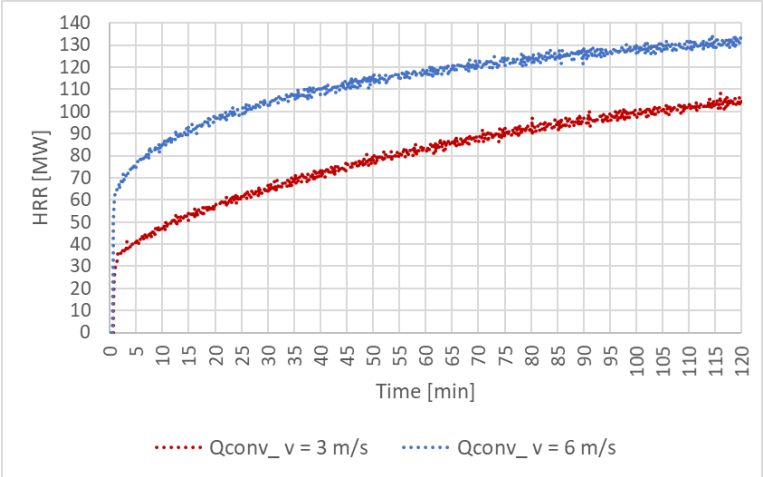


FIGURE 9.14 – HRR TRANSPORTED THROUGH CONVECTION (RWS FIRE SCENARIO)

Figure 9.15 compares the longitudinal radiation temperatures at the ceiling for both cases. Here, the differences in the maximum temperatures among different cases is reduced, and vary from *1100 ºC* for a ventilation velocity of 3 m/s to *1000 ºC* for a ventilation velocity of 6 m/s. This maximum radiation temperature, however, seems to be localized in the vicinity of the reacting

zone (highlighted by the flames in Figure 9.10 and Figure 9.12). Further ahead down the tunnel, the use of higher ventilation velocity also to contributes to reduce the radiation temperatures at the ceiling significantly. Basically, for both scenarios, longitudinal ventilation promotes convection within the gas phase (Figure 9.14) and reduces the amount of total HRR which is transported by radiation (Figure 9.16), but this effect appears to be even further magnified for higher levels of ventilation.

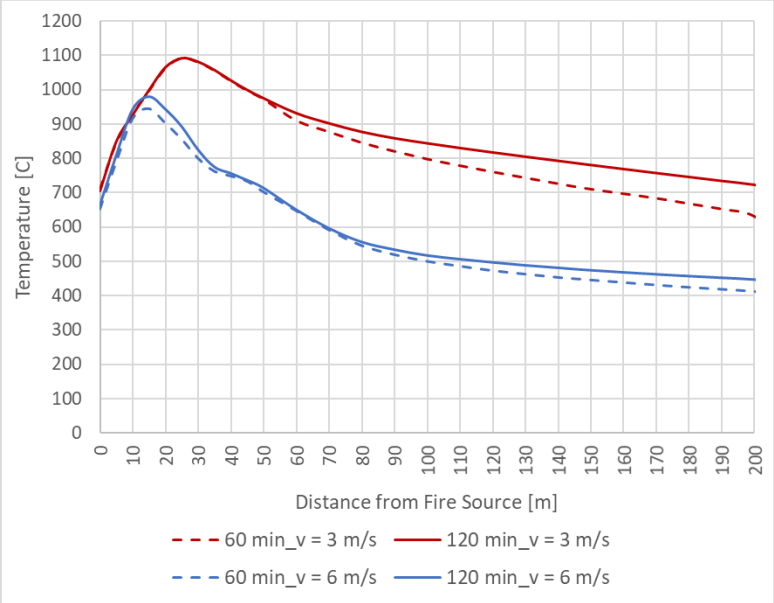


FIGURE 9.15 – COMPARISON OF LONGITUDINAL RADIATION TEMPERATURES (RWS FIRE SCENARIO)

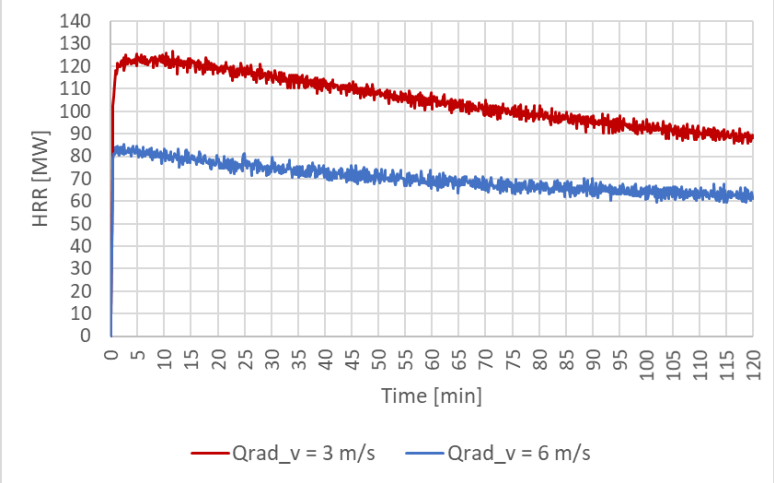


FIGURE 9.16 – COMPARISON OF HRR TRANSPORTED THROUGH RADIATION (RWS FIRE SCENARIO)

Figure 9.17 below, summarizes the percentage of HRR that is transported through convection and through radiation within the computational domain. As it can be seen, the amount of energy transported through convection grows in time, while the opposite is noted for radiation. Remember from Table 9.2 that the selected radiative fraction is equal to 0.4, ensuring that 40% of the total amount of heat generated through combustion is released in terms of thermal radiation. Elsewhere within the domain, radiation is absorbed or emitted by products of

combustion (e.g. soot and water vapor) and solid obstructions. With this in mind, notice that for a ventilation velocity of *3 m/s* the amount of thermal radiation transported within the domain, despite reducing in time, surpasses that which is released through combustion (i.e. *40%*). This indicates that for this case the smoke body within the tunnel achieves sufficiently high temperatures to contribute even further to the total amount of thermal radiation transported within the domain. However, by increasing the ventilation velocity, gas temperatures appear to be reduced to such a level, that the smoke body instead of becoming an extra source of thermal radiation to the domain, is now absorbing big parcels of thermal radiation generated by combustion of fuel, thus contributing to reduce the total amount of thermal radiation transported within the domain to levels below that which is ensured through combustion (i.e. 40%).

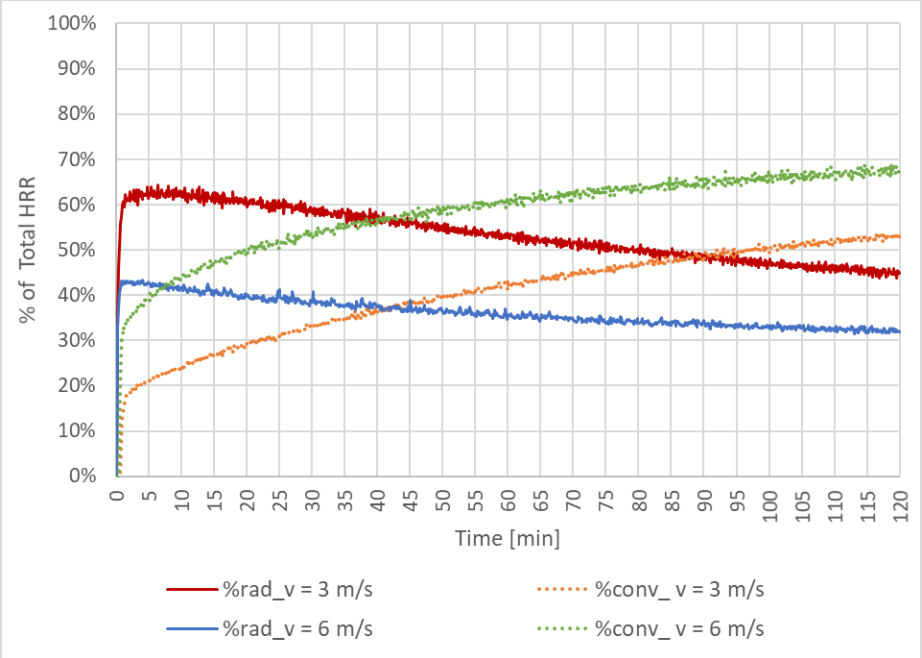


FIGURE 9.17 – PERCENTAGE OF HRR TRANSPORTED THROUGH CONVECTION AND RADIATION (RWS FIRE SCENARIO)

In conclusion, it seems that the use of higher ventilation velocities is very beneficial in terms of controlling the gas temperature development within the tunnel during a fire. It also appears to reduce the overall thermal exposure induced onto the structure (Section 9.2.4). However, a few remarks must be made here, as they might play a role in the achieved results:

1) The use of longitudinal ventilation will enhance combustion for fires that are burning in an environment lacking oxygen (i.e. *ventilation-controlled* fires). Note, for instance, that the sole reason for which the RWS fire scenario was sustained within the Piet Hein tunnel is the extra source of oxygen supply (Figure 9.18).

2) We do not know the real fire capacity that would have been achieved by the RWS fire scenario without the use of longitudinal ventilation (Section 9.2.3.1). This highlights an important limitation when modeling fires, where, most often, a fire is prescribed rather than predicted. Basically, the true development of *ventilation-controlled fires* will not

be accurately predicted if a fire is to be prescribed by the use of a boundary condition that constantly releases fuel into the domain of simulation.

3) The RWS fire scenario reaches its full capacity (200 MW) for a total of two hours for both ventilation velocities selected here (Figure 9.18), indicating that the fire has become *fuel-controlled*. For those scenarios, the use of higher ventilation velocities appears to be beneficial on controlling the temperature development within the tunnel. However, it must be noted that the combustion process here is well defined (Table 9.2), and that a pool fire burns very differently from a solid fire (Sections 4.1.1.1 and 4.1.1.2). This means that the results shown here are not necessarily representative for the latter, where flames are expected to be even closer to the ceiling and both the burning rate and burning area vary significantly in time.

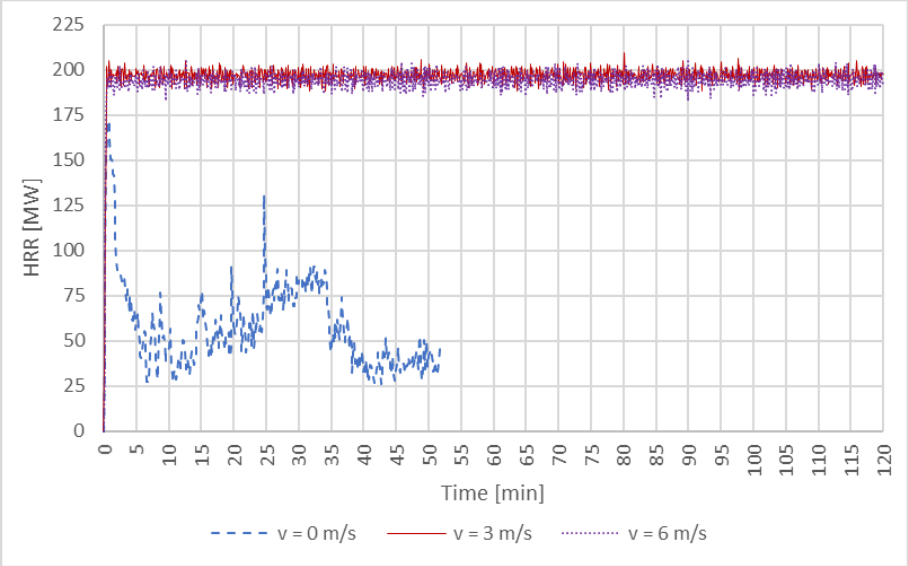


FIGURE 9.18 – HRR (RWS FIRE SCENARIO)

9.2.4 Thermal Exposure

As described in Section 5.3.3.3, the AST (Figure 5.17) is a parameter which combines both the convection and radiation contributions to the total heat transfer to the structure, into a single term, being capable of fully characterizing the exposure induced by the fire-related phase to the structure. This parameter is easily outputted from FDS and can be used to define a boundary condition in a FEA software (e.g. DIANA). Here, the thermal exposure imposed by the RWS fire scenario on the Piet Hein tunnel structure is studied based on measurements of several AST devices, placed on the surface of the cross-section at the locations assigned in Figure 9.2. Those measuring points are also longitudinally distributed downstream the fire source according to what is described below:

- Every 2 m up to a distance of *60 m* from the fire source.
- Every 5 m from *60 m* to *100 m* downstream the fire source.
- Every 10 m from *100 m* to *150 m* downstream the fire source.
- Every 25 m from *150 m* to *200 m* downstream the fire source.

9.2.4.1 200 MW – v = 3 m/s

Due to the use of longitudinal ventilation it was explained that the flames are pushed towards the floor and that the gas temperatures at the ceiling are rather limited right on top of the fire source (Figure 9.9). This also induces a difference on the achieved levels of thermal exposure along the cross section. Basically, from the center of fire source and up to a distance of *~14 m*, the thermal exposure at the bottom of the walls of the Piet Hein tunnel is higher than that which is imposed on the top parts of the cross section (i.e. upper part of walls and ceiling). The magnitude of the exposure (*~800 ^{o}C* on the bottom of the walls and limited to *~600 ^{o}C* on the ceiling at section *0 m*) grows longitudinally from the fire source, reaching a maximum value on the bottom of the walls of *~1200 ^{o}C* after two hours of fire exposure. This occurs in a section *12 m* ahead from the fire source (Figure 9.19). Note that for the same section, the maximum thermal exposure on the ceiling is limited to *~1000 ^{o}C*.

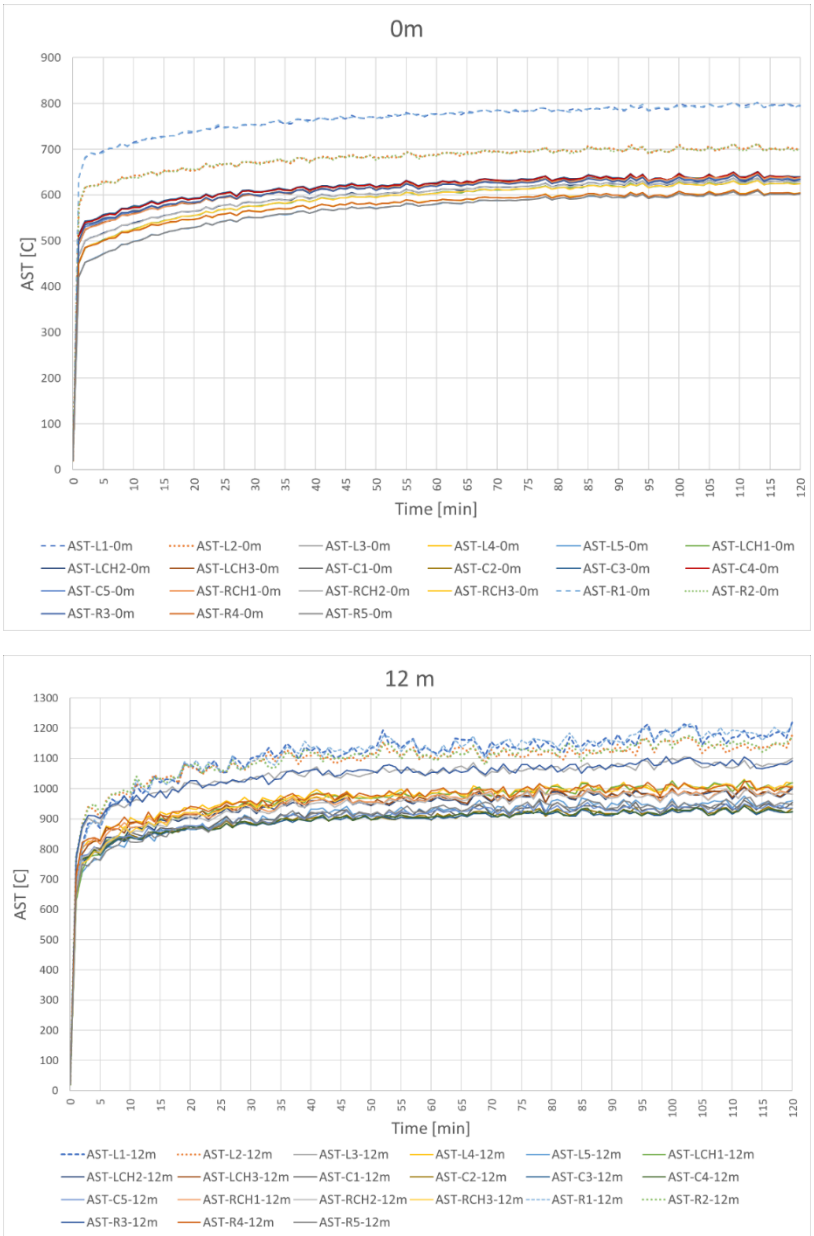


FIGURE 9.19 – THERMAL EXPOSURE IN THE VICINITY OF THE FIRE SOURCE (200 MW – V = 3M/S)

At a distance of *14 m*, the exposure at ground level starts to decrease, whereas the AST at the ceiling level keeps increasing. As a result, a rather homogeneous exposure of the whole cross-section is achieved up to a distance of *22 m*. This exposure is maximum at *20 m*, and is shown in Figure 9.20 in comparison with the hydrocarbon and RWS curves.

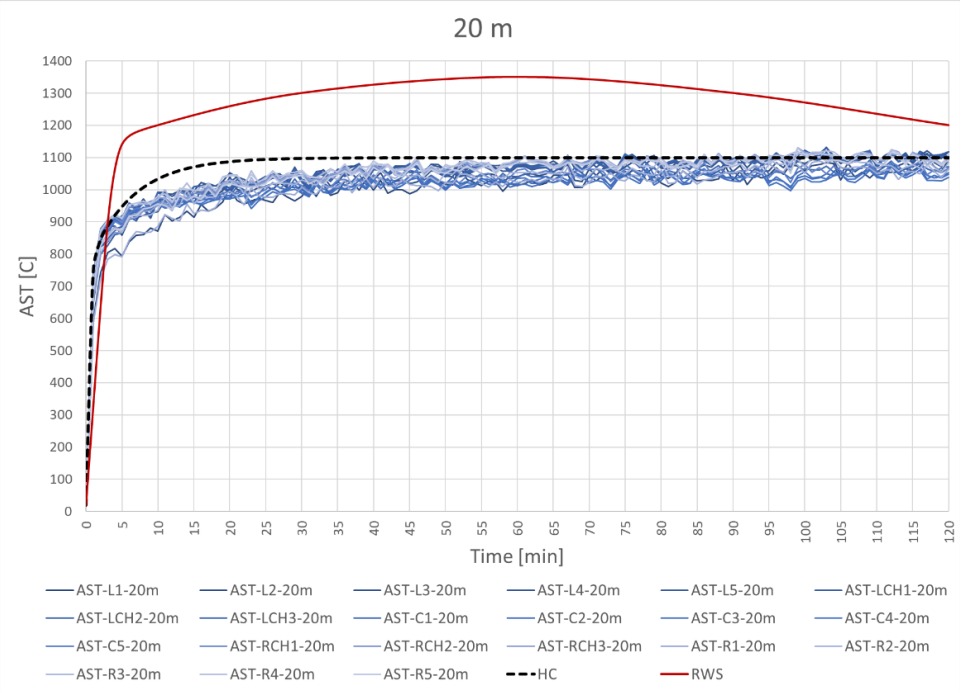


FIGURE 9.20 – MAXIMUM HOMOGENEOUS THERMAL EXPOSURE (200 MW – V = 3 M/S)

From *22 m* up to *60 m*, the thermal exposure appears to become buoyancy driven, being higher at the ceiling than at the bottom of the walls (Figure 9.21), but with both decaying in magnitude for increasing distances from the fire source. From *60 m* up to *200 m*, although the thermal exposure on the ceiling is still always slightly higher than that at the ground level, for growing distances, it becomes once again more and more homogeneous for the whole cross-section of the tunnel. For those sections (after *60 m*), the level of homogeneous exposure is well described by the longitudinal AST development for the center of the ceiling (Figure 9.12). Table 9.3 summarizes the thermal exposure along the Piet Hein tunnel for the RWS fire scenario in a ventilation velocity of *3 m/s*.

Section	Thermal Exposure	Reference
0 m – 14 m	Higher at the bottom walls	Figure 9.19
14 m – 22 m	Homogeneous	Figure 9.20
22 m – 60 m	Higher at the ceiling	Figure 9.21
60 m – 200 m	Homogeneous	Figure 9.10

TABLE 9.3 – THERMAL EXPOSURE ALONG THE TUNNEL (200 MW – V = 3 M/S)

Before moving further to the next case, Figure 9.22 highlights the maximum thermal exposure imposed by the RWS fire scenario on the Piet Hein tunnel at a ventilation velocity of *3 m/s*. It can be seen that the maximum homogenous exposure on the cross-section (i.e. blue lines in Figure 9.22) is practically limited to the boundaries of the hydrocarbon curve, which is in line with the findings of Chapter 7. Locally, an even higher thermal exposure is achieved for the bottom of the walls, located in the vicinity of the flames (i.e. orange lines in Figure 9.22). At

this zone, however, the exposure on the ceiling is limited to approximately *1000 °C* (look at the AST distribution at *12 m* in Figure 9.19). Finally, it must be noticed that the maximum exposure is always below that which is defined by the use of the RWS curve. Therefore, if a 200 MW hydrocarbon pool fire can be assumed as a worst-case fire scenario for a tunnel, then the results provided here reinforce the idea that this curve is not representative to describe *concrete tunnels*.

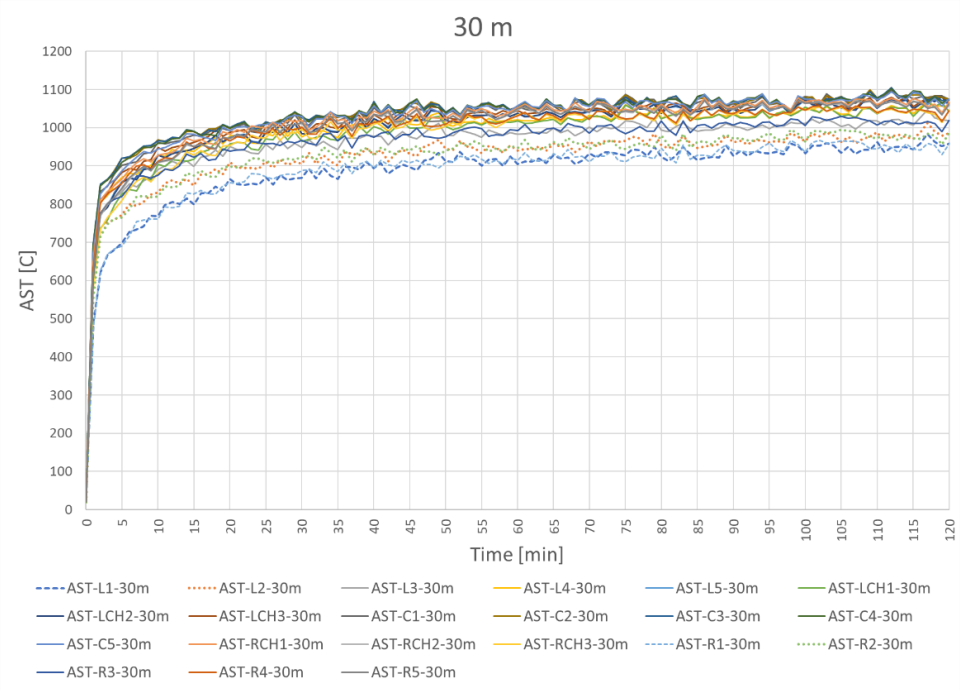


FIGURE 9.21 – EXAMPLE OF A SECTION WITH HIGHER THERMAL EXPOSURE ON THE CEILING

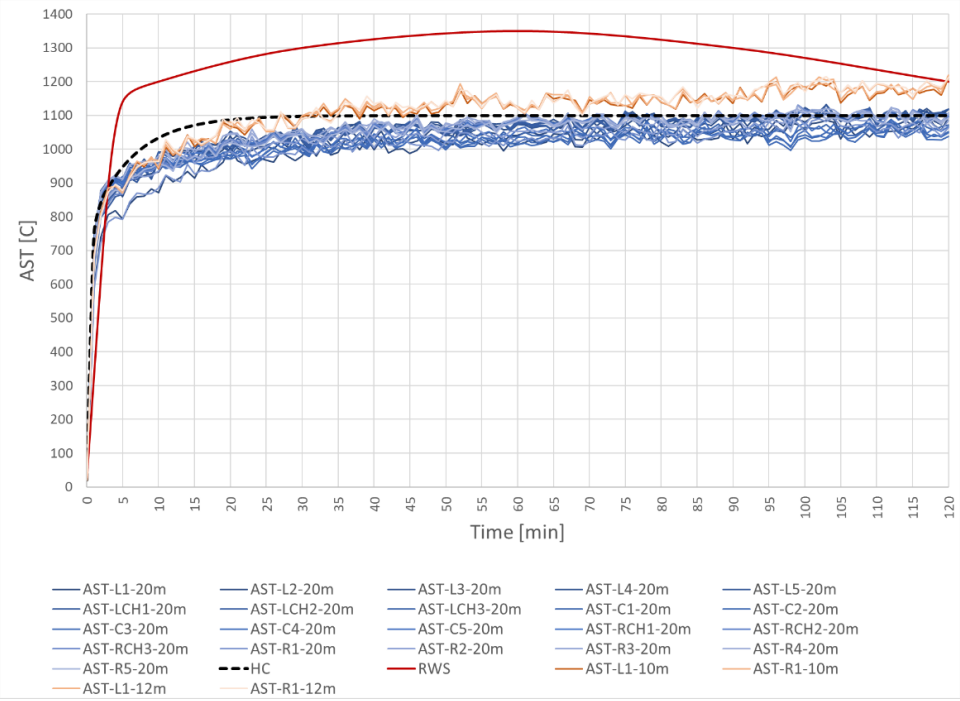


FIGURE 9.22 – MAXIMUM THERMAL EXPOSURE ON THE PIET HEIN TUNNEL (200 MW – V = 3 M/S)

9.2.4.2 200 MW – v = 6 m/s

Generally speaking, the longitudinal distribution of the thermal exposure for a higher ventilation velocity has the same pattern as that which was presented in Section 9.2.3.2. Here, however, the differences in magnitude of the exposure at the bottom of the walls and at the ceiling are more pronounced. Accordingly, the exposure is higher on the bottom of the walls up to a distance of *32 m* from the fire source. From *0 m* up to *16 m* the exposure grows in magnitude for the cross-section as a whole, achieving its peak (*~1200 ºC* after two hours of fire exposure) on the bottom of the walls at *16 m* (Figure 9.23). Note that at the same section, the exposure imposed on the ceiling is limited to *~900 ºC*. From that point downwards, the level of exposure at ground level starts to reduce while the exposure at the ceiling continuous to grow until a more or less uniform exposure of the cross-section as a whole is achieved at a distance of *32 m*.

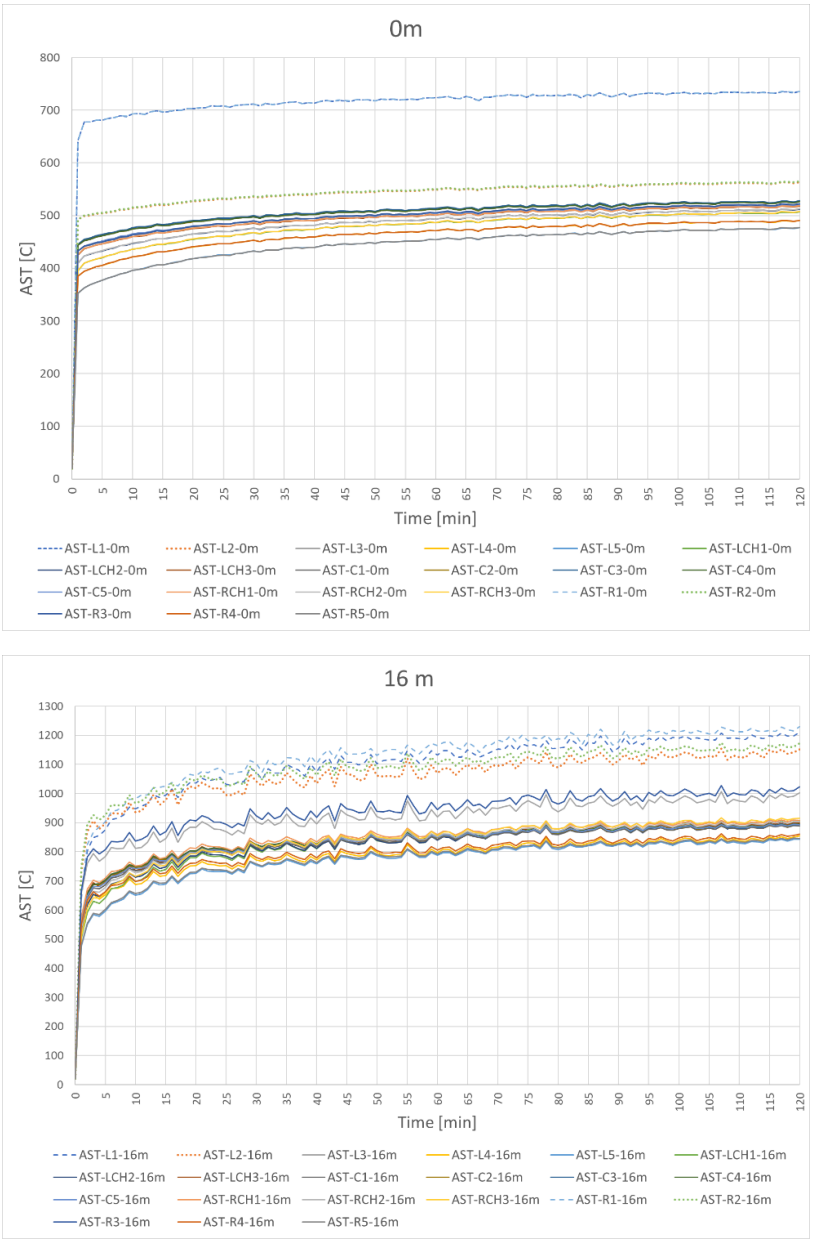


FIGURE 9.23 – THERMAL EXPOSURE IN THE VICINITY OF THE FIRE SOURCE (200 MW – V = 6 M/S)

From *32 m* up to *40 m* the exposure remains more or less homogeneous for the whole cross-section, reaching a maximum of *~700 ºC* at *34 m* (Figure 9.24). At *40 m* the exposure becomes buoyancy driven and will be higher at the ceiling than at the bottom of the walls up to a distance of *100 m*, always decaying for increasing distances from the fire source (Figure 9.25). Then, the thermal exposure becomes once again more or less uniform for the whole cross-section up to the end of the tunnel. Table 9.4 summarizes the thermal exposure along the Piet Hein tunnel for the RWS fire scenario exposed to a ventilation velocity of 6 m/s.

One important remark here is that, differently from the previous case, the maximum exposure on the ceiling does not occur at the section of maximum homogeneous exposure (Figure 9.24). In fact, for a ventilation velocity of 6 m/s, the maximum thermal exposure on the ceiling will occur at the same position of the maximum exposure on the bottom of the walls (at *16 m* in Figure 9.23), even though it is considerably smaller than that which is achieved at ground level.

Section	Thermal Exposure	Reference
0 m – 32 m	Higher at the bottom walls	Figure 9.23
32 m – 40 m	Homogeneous	Figure 9.24
40 m – 100 m	Higher at the ceiling	Figure 9.25
100 m – 200 m	Homogeneous	Figure 9.12

TABLE 9.4 – THERMAL EXPOSURE ALONG THE TUNNEL (200 MW – V = 6 M/S)

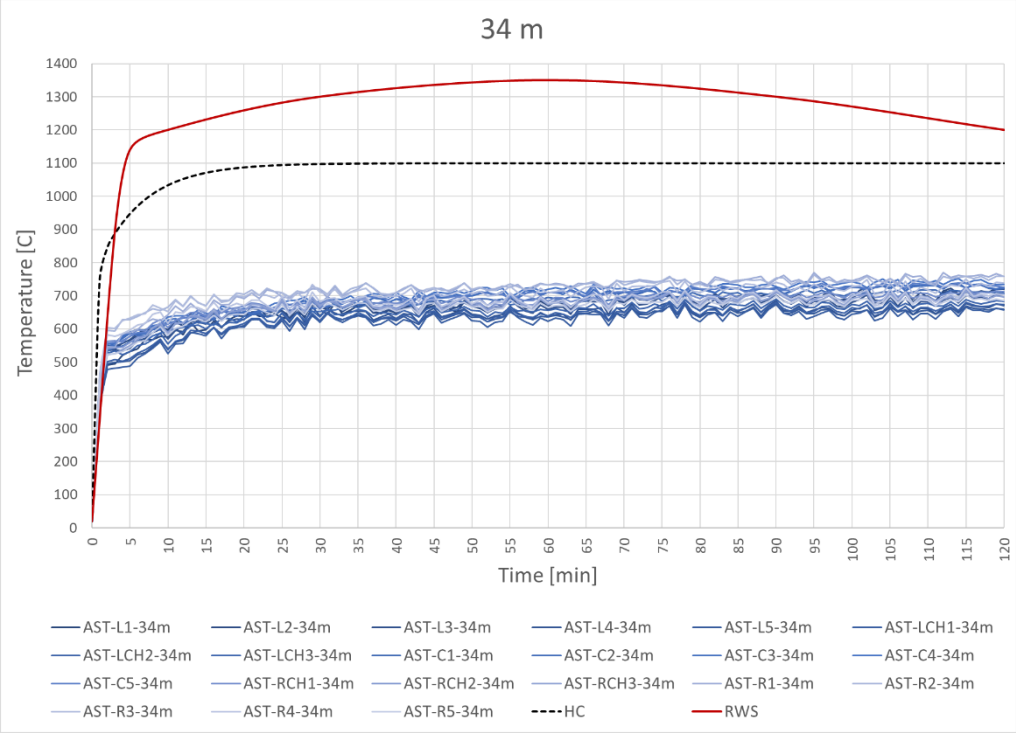


FIGURE 9.24 – MAXIMUM HOMOGENEOUS THERMAL EXPOSURE (200 MW – V = 6 M/S)

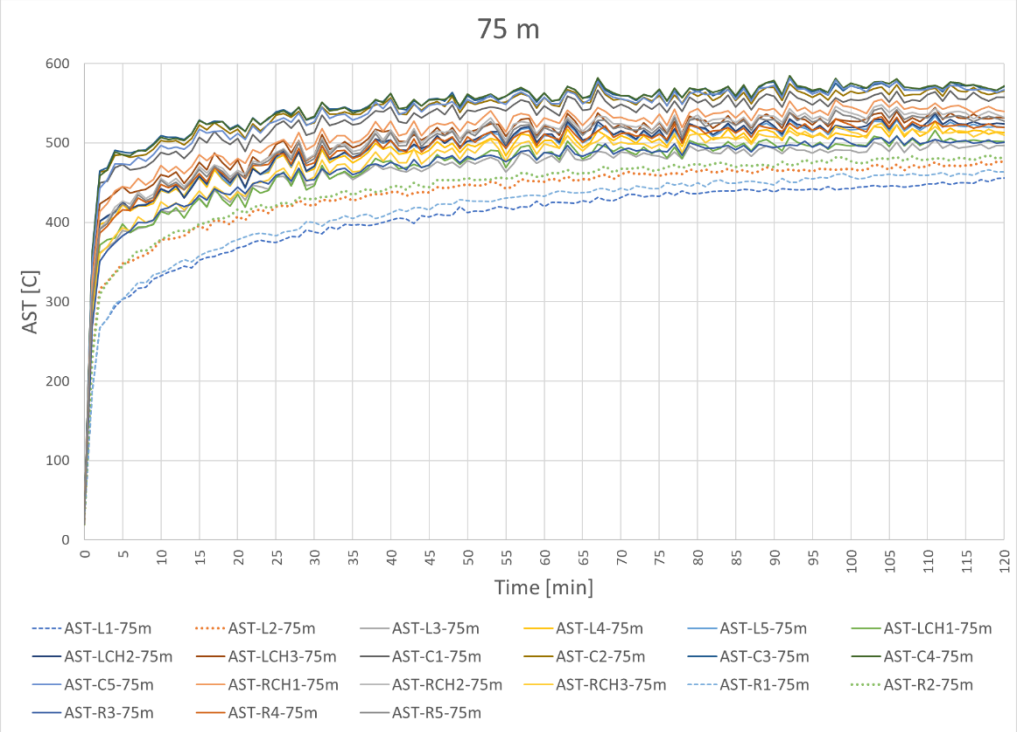


FIGURE 9.25 – EXAMPLE OF A SECTION WITH HIGHER THERMAL EXPOSURE ON THE CEILING

Figure 9.26 highlights the maximum thermal exposure imposed by the RWS fire scenario on the Piet Hein tunnel for a ventilation velocity of 6 m/s. It can be seen that the maximum homogenous exposure on the cross-section (blue lines in Figure 9.26) is approximately limited to *700 ºC*, and is significantly smaller than that which was achieved for a ventilation velocity of 3 m/s (i.e. *~1100 ºC* as shown by the blue lines in Figure 9.22). This shows that the use of higher ventilation velocities is indeed beneficial in terms of controlling the maximum overall thermal exposure achieved during a tunnel fire. However, at least when considering such big fires as the RWS fire scenario, the use of a high ventilation velocity still does not avoid the occurrence of high local thermal exposures. For instance, when looking at the maximum exposure on the bottom of the walls, the AST achieved for a ventilation velocity of 6 m/s (orange lines in Figure 9.26) is even higher than that for the same case at a velocity of 3 m/s (orange lines in Figure 9.22). For the ceiling structure, the use of a high ventilation velocity is still advantageous, although the differences with the previous case are considerably reduced if considering that a maximum AST of *~900 ºC* is still achieved for a ventilation of 6 m/s (compare green lines in Figure 9.26 with blue lines in Figure 9.22). Note that this peak in the maximum thermal exposure on the ceiling occurs in the vicinity of the flames, somewhere between *10 m* and *20 m* (Figure 9.11), where high levels of thermal radiation are inherently emitted by the flames of the pool fire. Finally, it is important to highlight that, also here, the maximum exposure generated inside the tunnel is still below the RWS curve, except for the last 5 minutes of fire on the very low positions of the walls that are located very close to the flames. Once again, except for the bottom of the walls in the vicinity of the fire source, the maximum exposure within the tunnel is fully contained within the boundaries of the hydrocarbon curve.

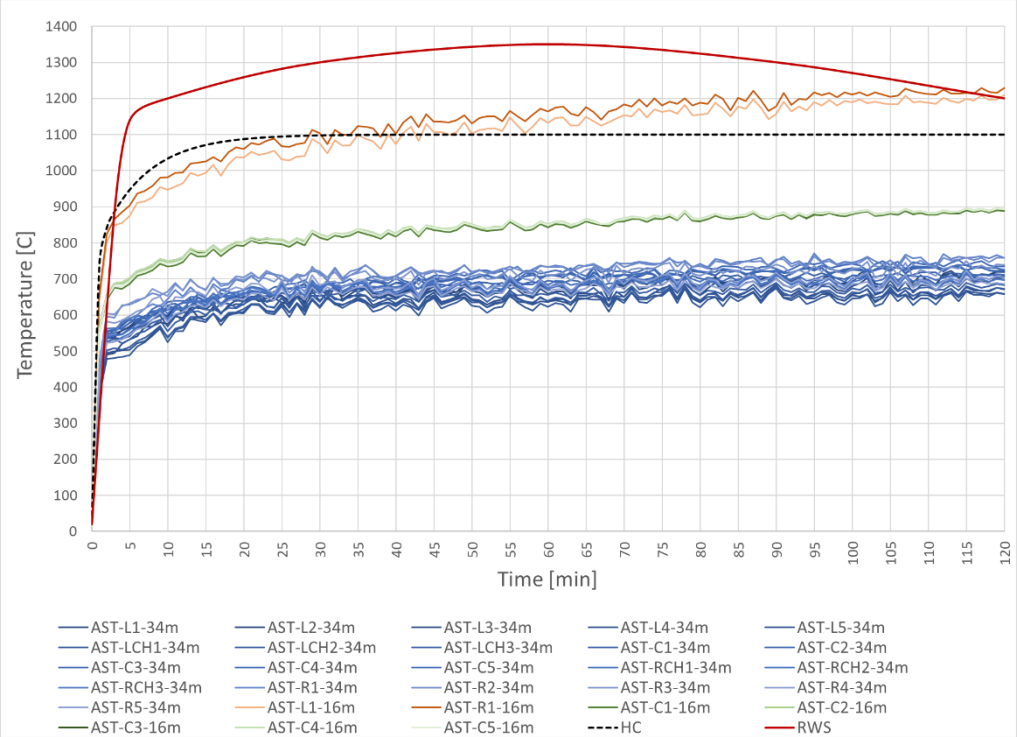


FIGURE 9.26 – MAXIMUM THERMAL EXPOSURE ON THE PIET HEIN TUNNEL (200 MW – V = 6 M/S)

9.3 Model II – Reduced Pool Fire Scenario (30 MW)

In the previous Section 9.2, we studied the thermal exposure imposed by the idealized RWS fire scenario on the structure of the Piet Hein tunnel. However, when considering the restrictions applied to the traffic of vehicles within this tunnel (classified as category D in Section 4.3.1), the occurrence of such a large fire as that imposed by the RWS fire scenario is not likely to happen. For this reason, the thermal exposure generated by a smaller pool fire is also addressed for three distinct cases, namely (1) 30 MW – v=0 m/s, (2) 30 MW – v=3 m/s, and (3) 30 MW – v=6 m/s.

The reduced fire scenario was idealized based on the propositions of the *New French Regulation* (UPTUN [51]) depicted in Figure 4.3. In this regulation, a 30 MW HGV fire with a total energy content of 125 GJ is indicated as the worst-case fire scenario for a tunnel in which dangerous goods are not allowed. Here, this proposed HGV fire was translated in terms of an equivalent gasoline pool fire by considering both the maximum HRR and the total energy content. The required burning area (A_b) is calculated based on the HRR, the maximum mass loss rate achieved by a gasoline fire (i.e. *0.055 kg/m^2.s* as shown in Figure 4.5), and the heat of combustion of gasoline (i.e. 43.5 MJ/kg as explained in Section 7.4.2.1). Accordingly:

$$A_b = \frac{HRR}{MLRPUA\ x\ \Delta H_c} = \frac{30}{0.055\ x\ 43.5} = 12.54\ m^2$$

As described earlier, the geometry of the fire source is mesh dependent. Considering this, the reduced pool fire is assumed to be of 2 m *x* 6.5 m (width *x* length), and is placed closer to one of the walls of the tunnel (Figure 9.2). The total burning time (t_b) was also originally defined based on the proposed energy content (125 GJ) and maximum HRR (30 MW), as depicted below:

$$t_b = \frac{125000\ MJ}{30\ MW} = 4167\ seconds \rightarrow t_b \cong 70\ minutes.$$

However, to achieve reliable results in FDS, this reduced fire size required the use of a finer mesh for the reacting zone (Section 5.2.3.1), which increased the total computational time significantly. Due to this, it was only feasible to simulate *60 minutes* of fire. Table 9.5 below summarizes the FDS models for the reduced pool fire scenario.

Pool Fire	
Fuel	N-OCTANE
Dimensions (Width x Length)	2 m x 6.5 m
Mass Loss Rate per Unit Area	0.055 kg Fuel/m^2.s
Radiative Fraction	0.4 (Figure 5.13)
Soot Yield	0.034 kg Soot/kg Fuel (Section 7.4.2.1)
CO Yield	0.010 kg CO/kg Fuel (Section 7.4.2.1)
Heat of Combustion (FDS)	43.5 MJ/kg Fuel (Section 7.4.2.1)
Total HRR	0.055 x 2 x 6.5 x 43.5 = 31.1 MW
Burning Function	
Time	HRR
0 s	0 MW
15 s	31.1 MW
3600 s	31.1 MW
Mesh Size	
Characteristic Fire Diameter (D*)	3.75 m (Equation 7.3)
Mesh Size (δ_x)	0.25 m
D*/ δ_x	15
Tunnel Geometry	
30 MW – v=0m/s	12 m in 0.25 m grid (Fire Source) + 2 x 102 m in 0.5 m grid + 2 x 192 m in 1 m grid
30 MW – v=3m/s	30 m in 0.25 m grid (Fire Source) + 190 m in 0.5 m grid + 90 m in 1 m grid
30 MW – v=6m/s	30 m in 0.25 m grid (Fire Source) + 190 m in 0.5 m grid + 90 m in 1 m grid

TABLE 9.5 – REDUCED POOL FIRE SCENARIO

As in for the RWS fire scenario, also here, the temperature development at the center of the ceiling will be studied first (Section 9.3.1). Then, the thermal exposure imposed on the tunnel structure is also discussed for each case individually (Section 9.3.2).

9.3.1 Temperature Development at the Ceiling

At first, this section studies the correspondent gas, AST (equation 5.27) and radiation (equation 5.11) temperatures at the center of the ceiling (i.e. TC3 in Figure 9.2) for each case in a reduced pool fire scenario. Then, a comparison of all cases is provided, exposing the effects of the use of longitudinal ventilation (Section 9.3.1.4). Finally, the temperature development at the ceiling for the reduced pool fire scenario is compared to that of the RWS fire scenario (Section 9.3.1.5).

9.3.1.1 30 MW – v = 0 m/s

Differently from the previous case (Section 9.2.3.1), here, fire reaches its full capacity for the total time of simulation even without the use of longitudinal ventilation (Figure 9.33). However, it is important to highlight that the Piet Hein tunnel is in fact *1.900 m* long and only a section of *600 m* with open boundaries at both ends (Figure 9.4), was used in the FDS model.

Thus, in reality, we cannot ensure that this reduced pool fire scenario would truly be sustained within the Piet Hein tunnel without any extra source of oxygen supply. Even so, the results of the fire simulation performed here are still valid to foment a discussion about fire dynamics, thermal exposure, and the effects of longitudinal ventilation for a reduced pool fire scenario. In this sense, Figure 9.27 provides the longitudinal gas temperature evolution at the center of the ceiling together with an illustration of the conceived pool fire. It is clear that the temperatures are at their maximum levels right on top of the center of the fire source, decaying in the longitudinal direction. Note that the gas temperatures are limited to less than *1000 ^{o}C* at the center of the ceiling.

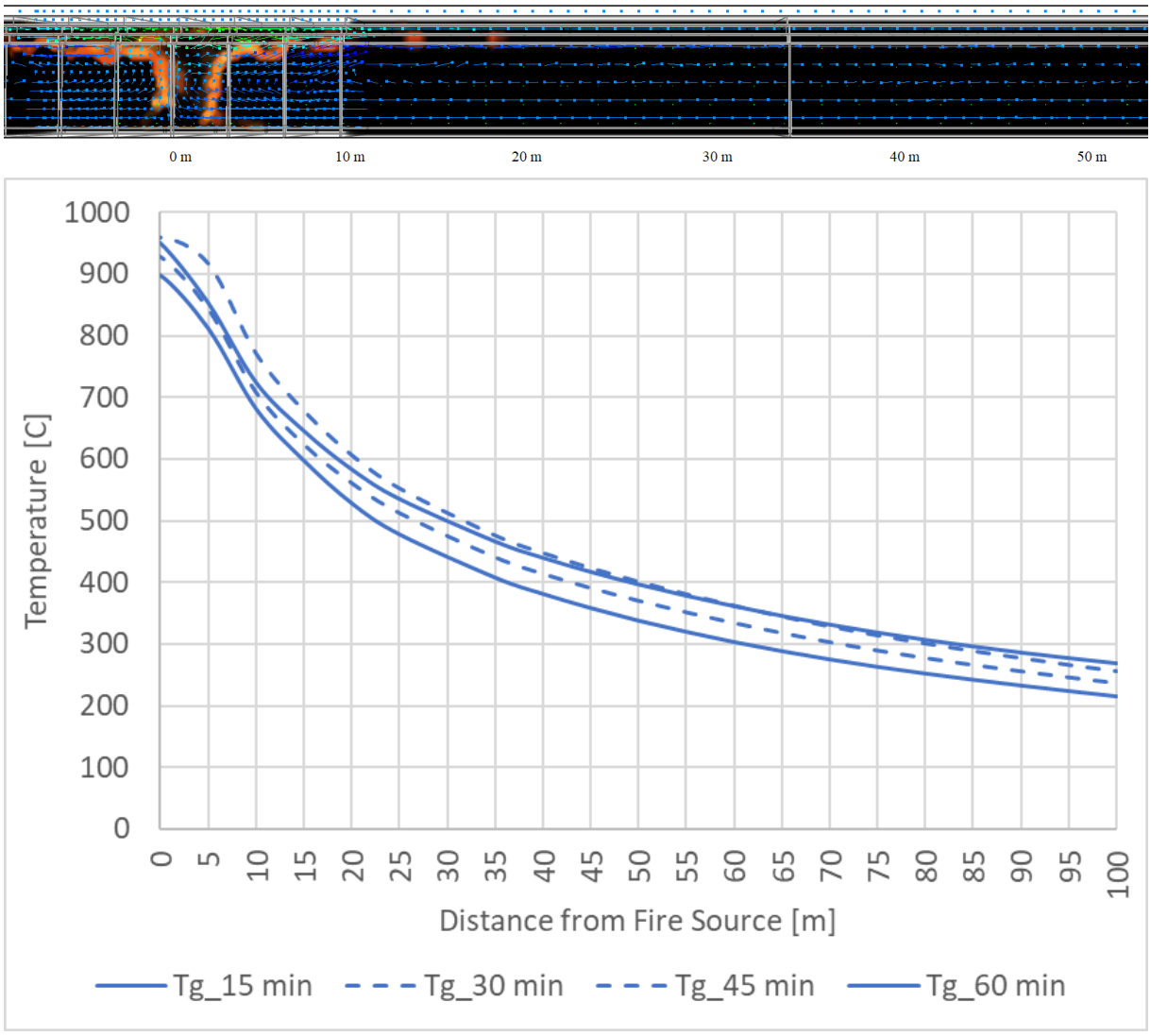


FIGURE 9.27 – LONGITUDINAL GAS TEMPERATURE EVOLUTION IN TIME (30 MW – V = 0 M/S)

Figure 9.28 compares the evolution of longitudinal gas, AST (equation 5.27), and radiation (equation 5.11) temperatures for *15*, *30*, *45* and *60 minutes* of fire simulation. There are a few aspects which are worth mentioning here. First of all, remember that, by definition, the AST should be in between the correspondent gas and radiation temperatures. This is clearly not the case for sections up to *~10 m* from the fire source, where the AST is actually slightly below the correspondent radiation temperatures (Figure 9.28). This is probably related to the measuring

points used to plot those curves. In essence, as a reduced pool fire required the use of a smaller mesh size for the reacting zone (Table 9.5), the measurements used to plot the AST curve were collected in slightly different positions than those used to plot gas and radiation temperatures. Even so, the differences are practically negligible, and it is still clear that the AST tend towards the radiation component at such high temperatures.

The second aspect that is interesting to notice is that the radiation temperatures are smaller than the correspondent gas temperatures at all times, indicating that soot concentration within the smoke body, formed due to the combustion of fuel, is not sufficient to generate *blackbody* behavior for this mass of gas. Hence, thermal radiation is not emitted at its maximum level or, in other words, the emissivity (i.e. ε_f in equation 5.13) of the smoke body is somewhat smaller than 1. Also, note that the radiation temperature is at least *100 ^oC* smaller than the correspondent gas temperature right above the fire source, but this difference is reduced further ahead in the longitudinal direction, as the soot concentration increases on the smoke layer at the top.

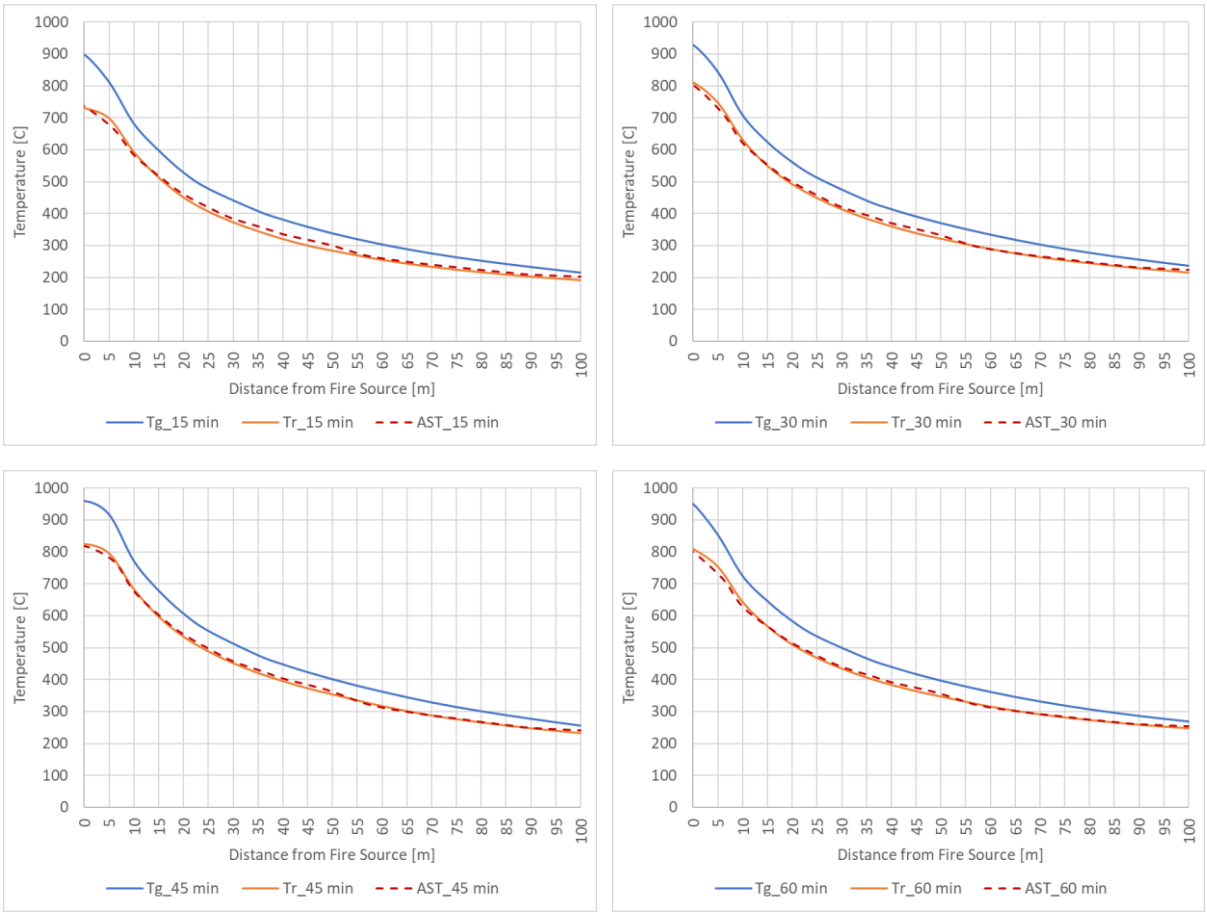


FIGURE 9.28 – LONGITUDINAL GAS, AST AND RADIATION TEMPERATURES (30 MW – V = 0 M/S)

9.3.1.2 30 MW – v = 3 m/s

Figure 9.29 provides the longitudinal gas temperature evolution at the center of the ceiling for the reduced pool fire scenario considering a ventilation velocity of *3 m/s*. The maximum temperatures at the ceiling are significantly reduced when compared to the same fire scenario without the use of longitudinal ventilation (Figure 9.27), being limited to *~500 ^oC* at all times.

As for the same case when considering the RWS fire scenario (Section 9.2.3.2), also in here, the use of longitudinal ventilation bends the flames towards the ground level, promoting mixing of cooler air with the hot buoyant smoke. As a consequence, the zone of maximum gas temperatures at the ceiling occurs somewhere in between *5 m* to *15 m* ahead from the fire source.

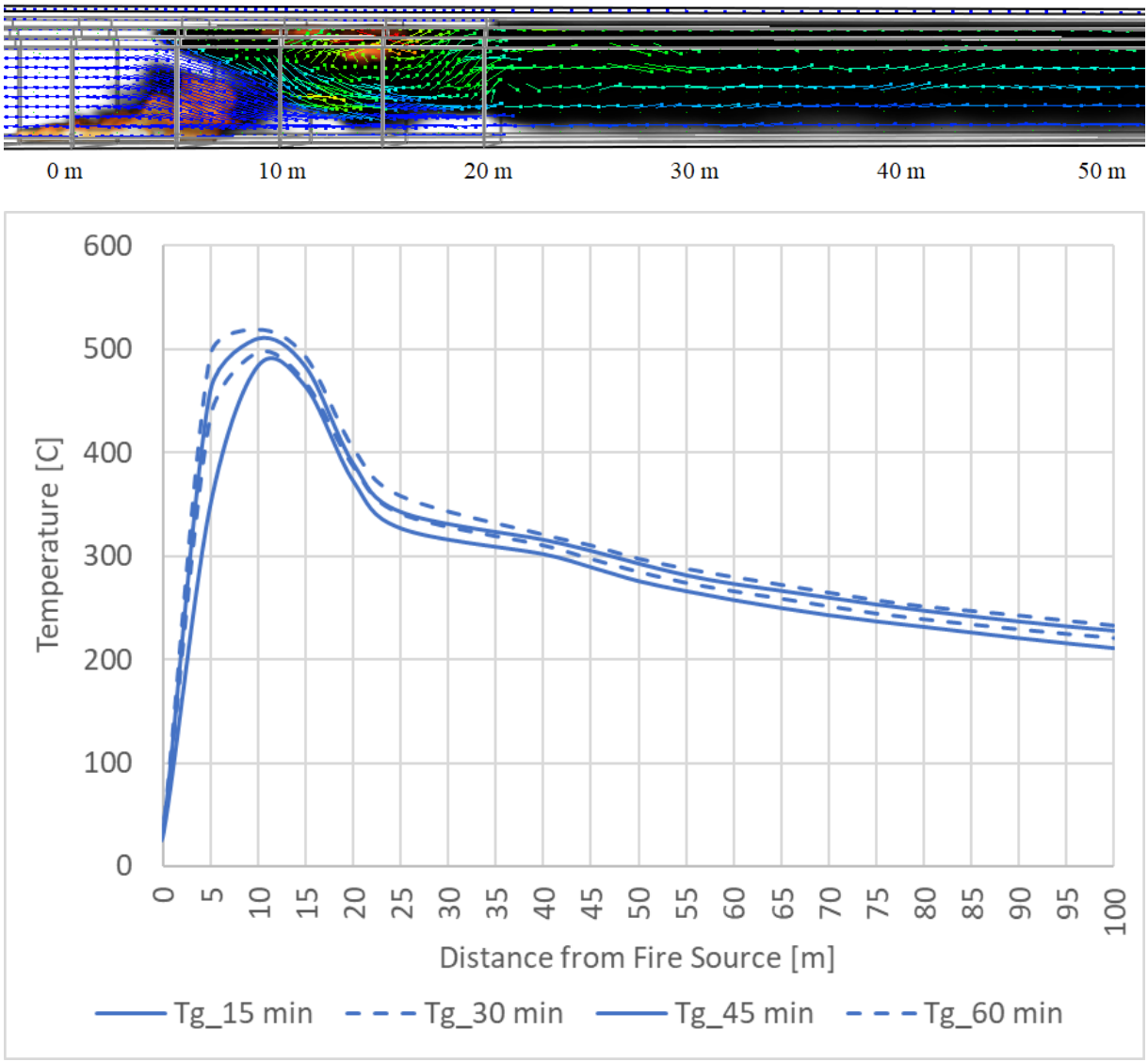


FIGURE 9.29 – LONGITUDINAL GAS TEMPERATURE EVOLUTION IN TIME (30 MW – V = 3 M/S)

Figure 9.30 compares the evolution in time of gas, AST, and radiation temperatures at the center of the ceiling. First of all, notice that the AST is always in between the correspondent gas and radiation temperatures. Once again, notice from Figure 9.30, that the use of longitudinal ventilation, despite significantly reducing the gas temperatures at the ceiling, does not avoid the occurrence of high radiation temperatures in sections surrounding the flames (Figure 9.29). For instance, when compared to the previous case (reduced pool fire without longitudinal ventilation), the maximum gas temperatures at the ceiling drop from *~950 ºC* to *~500 ºC*, whereas the maximum radiation temperatures are reduced from *~800 ºC* to *~600 ºC*.

There is also an interesting aspect that is worth mentioning here. Basically, as explained thoroughly during this thesis, we know that the radiation component will govern the thermal exposure imposed by a fire on the structure (Section 5.1.3.2), and that this exposure is fully characterized by the AST (Section 5.3.3.3). Therefore, by comparing AST with the correspondent gas and radiation temperatures up to a distance of *30 m* (Figure 9.30), one can clearly see that the AST will tend towards the radiation component. From that moment onwards, however, the convection component is clearly increasing its contribution to the total thermal exposure (AST). At heart, for low radiation temperatures (i.e. below *200 ^{o}C*), convection also becomes of importance when addressing the thermal exposure imposed on the structure. Notice from Figure 9.32 that for very low radiation temperatures (*~100 ^{o}C*), the AST will actually tend towards the correspondent gas temperatures or, in other words, the convection component.

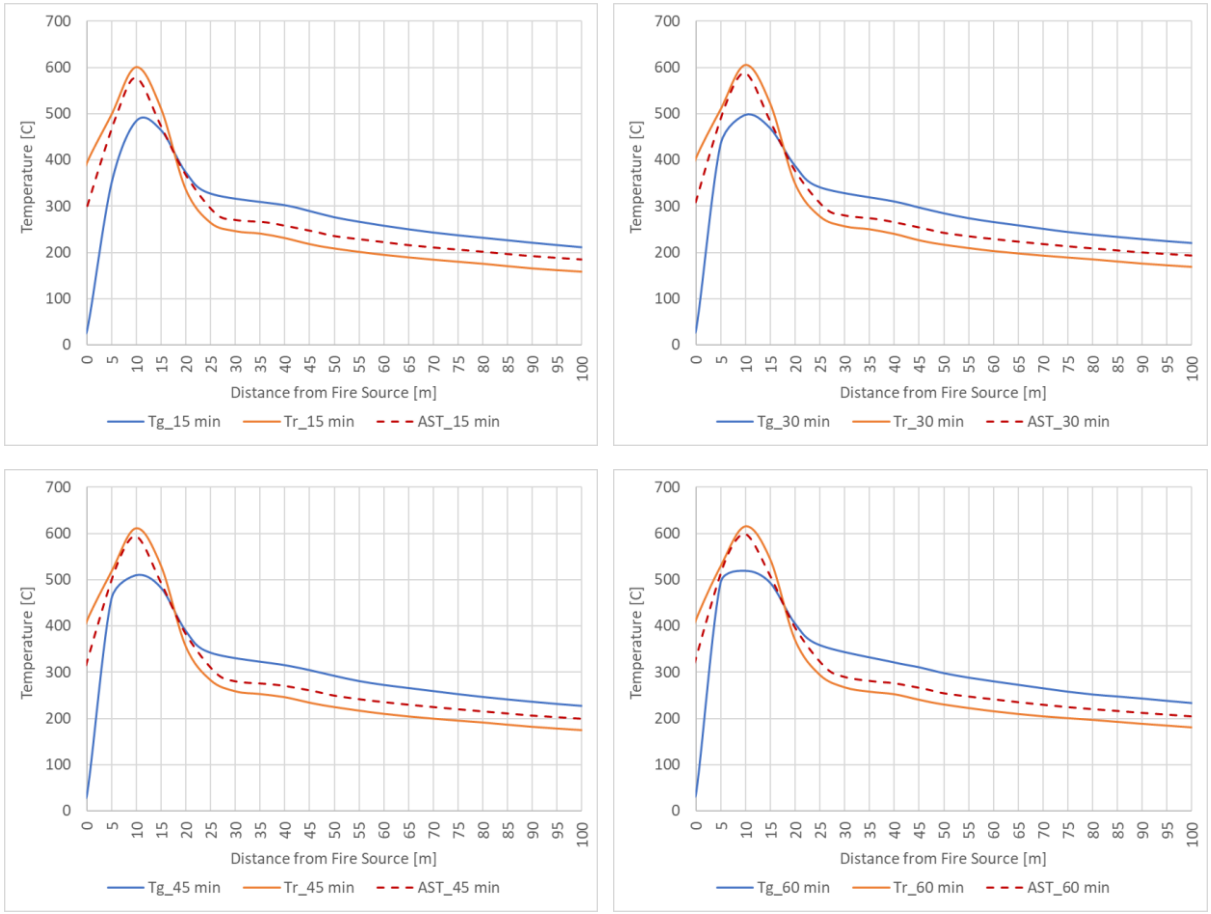


FIGURE 9.30 – LONGITUDINAL GAS, AST AND RADIATION TEMPERATURES (30 MW – V = 3 M/S)

9.3.1.3 30 MW – v = 6 m/s

Figure 9.31 provides the evolution of longitudinal gas temperatures at the ceiling for the reduced pool fire scenario at a ventilation velocity of 6 m/s, while Figure 9.32 compares gas, AST, and radiation temperatures for the same case. Also here, the same pattern noticed for all cases considering the use of longitudinal ventilation is achieved, and both gas and radiation temperatures are reduced when compared to the previous case (at a ventilation velocity of 3 m/s), but with a more significant reduction being noticed for the maximum gas temperatures.

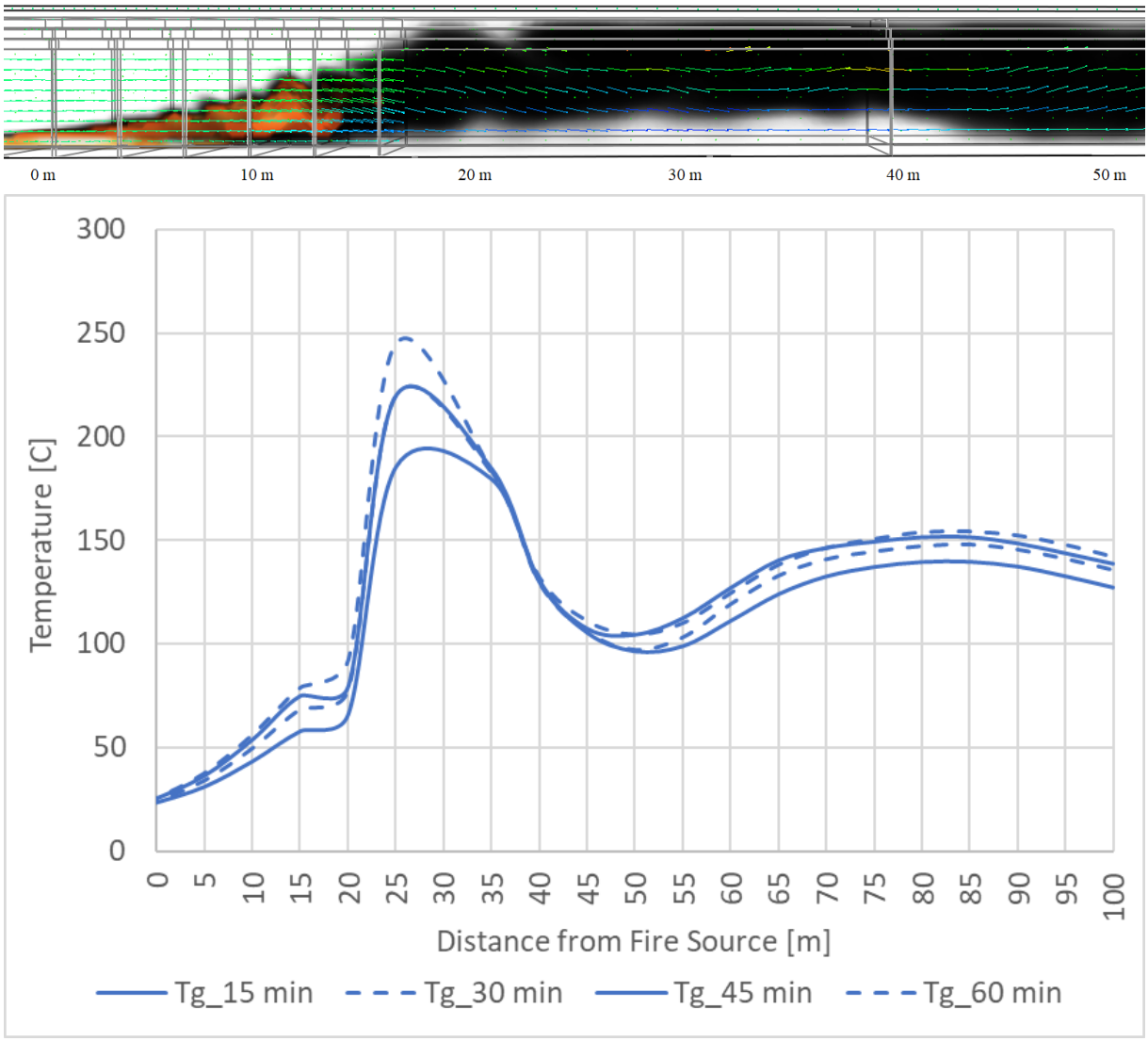


FIGURE 9.31 – LONGITUDINAL GAS TEMPERATURE EVOLUTION IN TIME (30 MW – V = 6 M/S)

Among all cases studied here, this is the only one in which the ceiling of the tunnel is completely free of smoke for the total length of the reacting zone (i.e. the flames shown in Figure 9.31). Such a scenario is very elucidative to visualize the effects of longitudinal ventilation. Basically, as the ceiling section on top of the flames is smoke-free, the gas temperature development within this section is quite limited. In fact, gas temperatures will start to be significantly increased when the hot smoke layer reaches the ceiling at *~20 m* from the fire source (Figure 9.31). The opposite is noticed for the development of radiation temperatures. In essence, high levels of thermal radiation are emitted by the flames, making the tunnel sections surrounding the flame body to experience high radiation temperatures. As a consequence, the radiation temperature at the ceiling is already significant from the center of the fire source, growing to a peak in a section still within the total length of the flame (Figure 9.32). A parenthesis here is that this peak appears to occur at *10 m* from the fire source, but this is not necessarily the case. In fact, the evolution of radiation temperature shown in Figure 9.32 is based on measurements collected only every 5 m. As the flame body clearly extends further than *10 m* from the fire source but does not reach *15 m* in length, it could actually be that the

maximum radiation temperatures would occur in a section a bit further ahead from *10 m*, where the flame body is slightly larger (Figure 9.31). That being said, it is noticeable that the radiation temperatures on the ceiling decay considerably for sections located after the end of the reacting zone (flames).

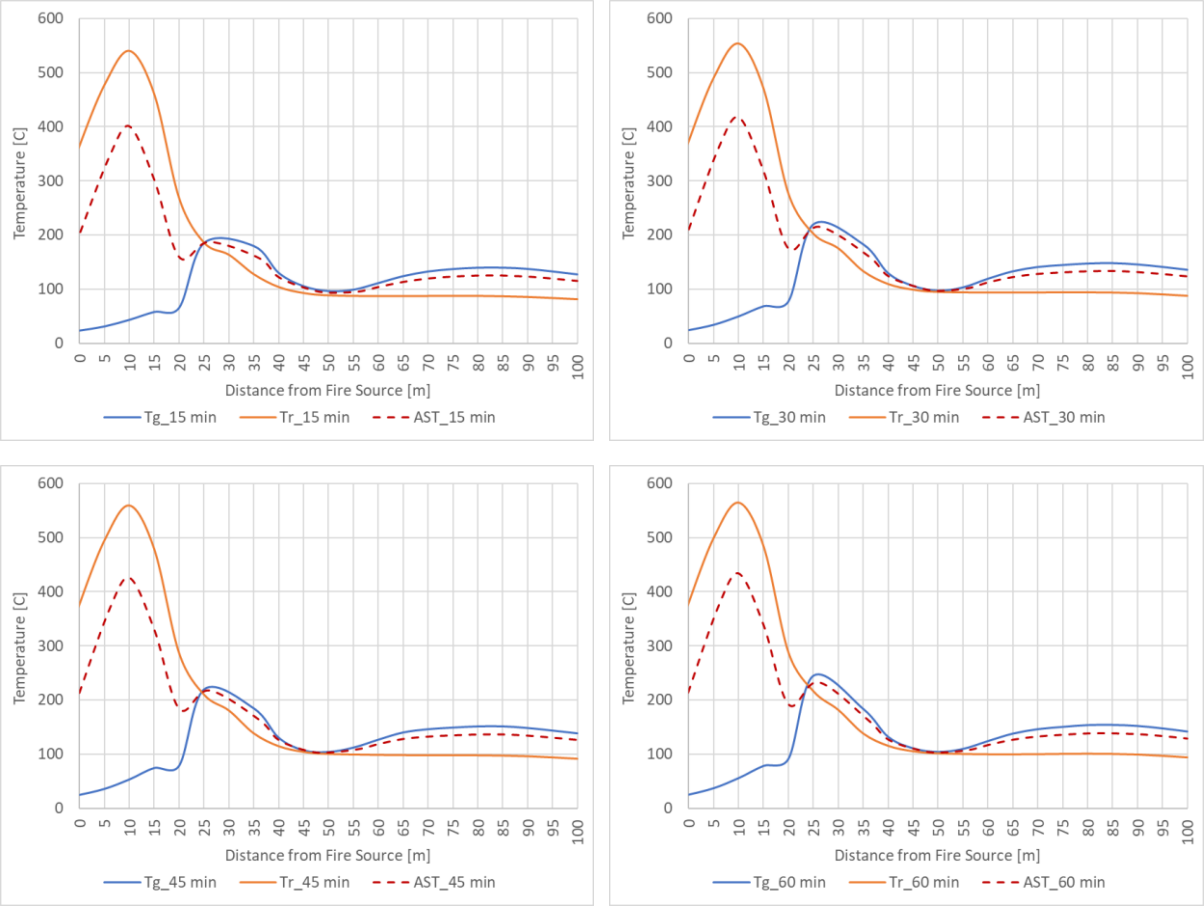


FIGURE 9.32 – LONGITUDINAL GAS, AST AND RADIATION TEMPERATURES (30 MW – V = 6 M/S)

Therefore, we can characterize the effects of longitudinal ventilation in the total level of thermal exposure generated by *fuel-controlled* pool fires based on two different zones, here entitled as (1) *flame zone*, and (2) *after-flame zone*. The *flame zone* describes all sections of the tunnel which are either surrounding or being impinged by the flames of a fire. For this zone, we can infer that the use of longitudinal ventilation pushes the flames towards the ground and contribute to reducing the maximum gas temperatures at the ceiling up to a certain point. However, as soon as the hot smoke body or the flames itself impinge on the ceiling, high gas temperatures are expected to occur (Figure 9.9, Figure 9.11, Figure 9.29, and Figure 9.31). Also, the use of ventilation will not avoid the occurrence of high radiation temperatures within the *flame zone*, as high levels of thermal radiation will always be emitted by the flame body independently from the ventilation conditions. As the total exposure to the structure is governed by the radiation component, we can expect the occurrence of high thermal exposure for sections within the *flame zone*.

The *after-flame zone* describes all sections of the tunnel which are ahead from the *flame zone* and will only experience the propagation of smoke. For this zone, the use of longitudinal

ventilation contributes significantly to reduce the thermal exposure imposed on the structure. Basically, ventilation promotes mixing of cooler air with the hot buoyant smoke, effectively reducing the temperature of the smoke body. This enhances radiation absorption within the smoke layer, contributing to decrease the total amount of thermal radiation transported inside the domain (Figure 9.16 and Figure 9.36).

9.3.1.4 Effects of Ventilation

Figure 9.33 shows the HRR outputted from FDS for the reduced pool fire scenario. As it can be seen, for all cases studied here, the prescribed fire load (~30 MW as described in Table 9.5) was fully achieved within the model for the total time of fire simulation. However, when compared to the cases including the use of longitudinal ventilation (blue and orange lines in Figure 9.33), it is clear that the variability of the HRR is much larger for the case without ventilation (red line in Figure 9.33). Also, notice that this variability is growing in time, indicating that the oxygen availability inside the tunnel is being reduced as fire develops. As only a section of 600 m was included in the fire simulation for the case without ventilation, this corroborates with what was earlier described in Section 9.3.1.1 or that, if considered the real length of the tunnel is approximately *2000 m* then, most likely, not even this reduced pool fire would be sustained within the Piet Hein tunnel without the use of some extra source of ventilation.

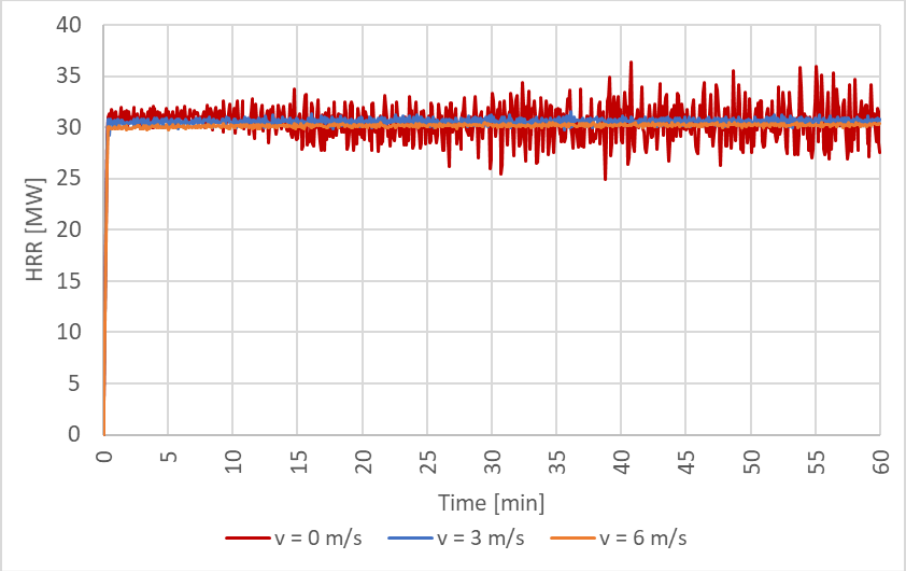


FIGURE 9.33 – HRR (REDUCED POOL FIRE)

Figure 9.34 compares the longitudinal gas temperatures at the center of the ceiling for the three different scenarios studied for the reduced pool fire. Accordingly, the use of longitudinal ventilation has shown to significantly reduce the maximum gas temperatures inside the tunnel. At a ventilation velocity of 3 m/s, maximum temperatures on the ceiling will already drop from *~950 ^{o}C* (without ventilation) to *~500 ^{o}C*. This reduction is further potentialized by the use of a high ventilation velocity (6 m/s), where maximum gas temperatures are approximately limited to *~250 ^{o}C*. When looking at the maximum radiation temperatures (Figure 9.35), also an overall reduction is noted due to the use of ventilation. However, this reduction is rather limited when compared to that which was obtained for the gas temperatures, with maximum

radiation temperatures varying from *~800 °C* for the case without ventilation to *~600 °C* at a ventilation velocity of 3 m/s and to *~550 °C* at a ventilation velocity of 6 m/s.

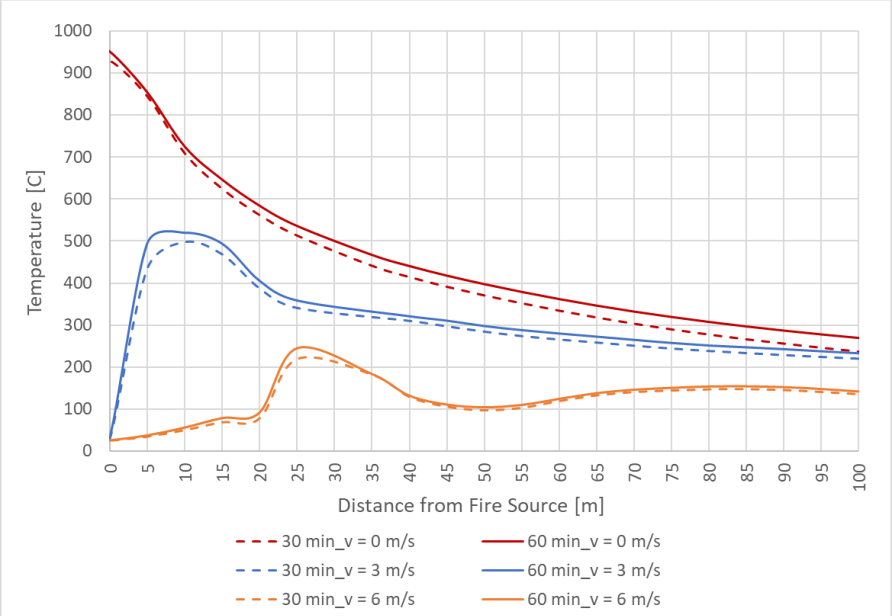


FIGURE 9.34 – COMPARISON OF LONGITUDINAL GAS TEMPERATURES (REDUCED POOL FIRE SCENARIO)

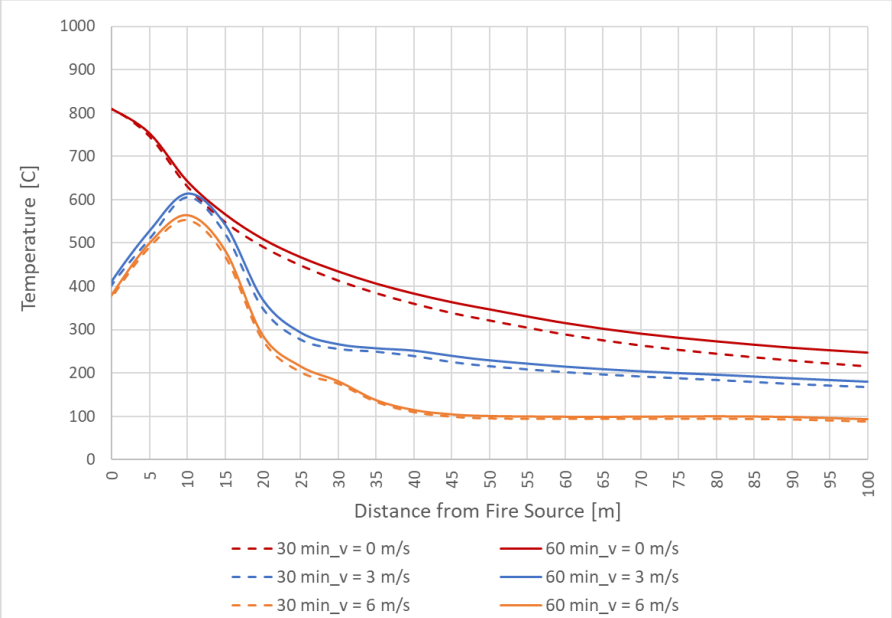


FIGURE 9.35 – COMPARISON OF LONGITUDINAL RADIATION TEMPERATURES (REDUCED POOL FIRE SCENARIO)

The reasoning behind the different temperature developments (Figure 9.34 and Figure 9.35) obtained for the cases studied here is essentially the same as that described in Section 9.2.3.4, when considering the RWS fire scenario. In essence, as depicted in Figure 9.36, the use of longitudinal ventilation enhances cool air entrainment into the hot buoyant smoke, promoting convection heat transfer within the gas phase (compare dotted red, blue, and orange lines in Figure 9.36) and thus significantly reducing the gas temperatures within the tunnel.

This reduction in the total gas temperature state of the smoke body also contributes to significantly reduce the total amount of thermal radiation that is transported within the domain of simulation (compare continuous red, blue, and orange lines in Figure 9.36). Firstly, remember that the emissions of thermal radiation from the smoke layer are related to the fourth power of the gas temperatures within the smoke layer (equation 5.13). Thus, by reducing such, we are inherently reducing the levels of thermal radiation emitted from the smoke body. Secondly, while the amount of radiation emitted by the reacting zone (flames) is corrected by FDS to correspond to the radiative fraction (Section 5.2.3.2), elsewhere within the domain, radiation is emitted and absorbed by smoke and solid obstructions according to their own temperatures. Therefore, depending on the extent of which the gas temperatures are reduced (due to the use of ventilation) within the tunnel, the smoke released from the fire, instead of becoming an extra source, adding to the total amount of thermal radiation transported within the domain, might contribute to partially reabsorb the thermal radiation emitted through combustion, thus reducing the total percentage of the HRR which is transported through radiation. That being said, notice that the radiative fraction adopted in this study corresponds to 40% of the total HRR. For the case without ventilation, it is clear that the total amount of radiation transported within the domain surpasses this value, reaching approximately 60% of the total HRR (continuous red line in Figure 9.36), clearly indicating that the smoke generated through combustion reaches sufficiently high temperatures to become an extra source of thermal radiation inside the domain of simulation. On the other hand, for the cases with ventilation, but in especial at a high ventilation velocity (continuous orange line in Figure 9.36), the total percentage of HRR transported through radiation is below that which is released through combustion. So, for those cases, the formed smoke body is partially reabsorbing the emissions of thermal radiation from the flames.

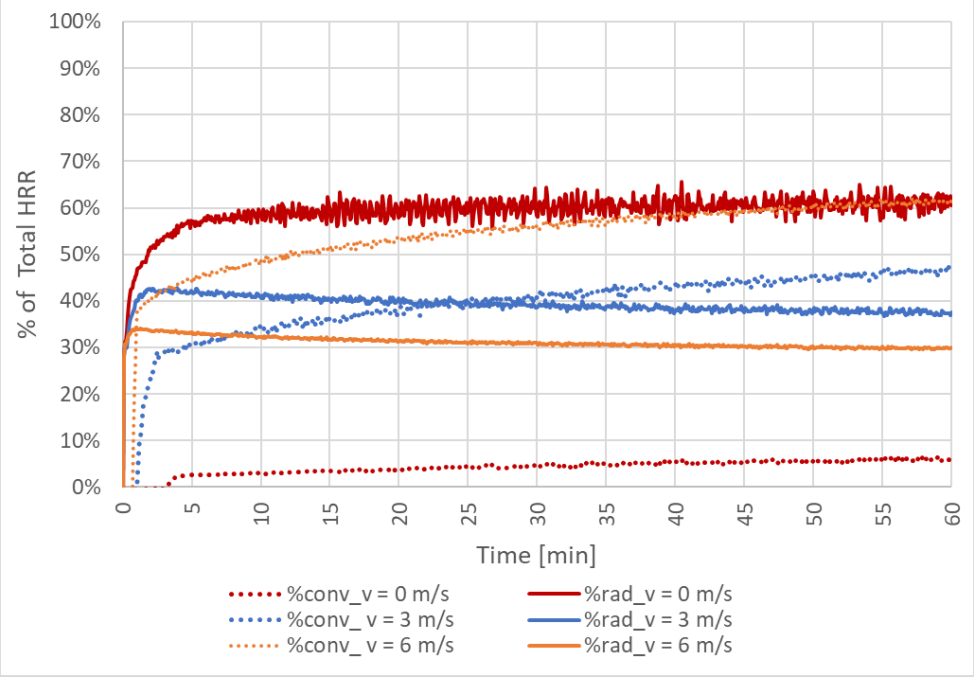


FIGURE 9.36 – PERCENTAGE OF HRR TRANSPORTED THROUGH CONVECTION AND RADIATION (REDUCED POOL FIRE SCENARIO)

In conclusion, we can state that the use of longitudinal ventilation has once again shown to be beneficial in reducing both gas and radiation temperatures within the tunnel as a whole. It appears that the higher the ventilation velocity is, the higher the temperature reductions will be. Still, it must be said that the use of longitudinal ventilation will not avoid the occurrence of high radiation temperatures for tunnel sections near the fire source, which are either surrounding or being impinged by flames.

9.3.1.5 Comparison with the RWS Fire Scenario

Here, the temperature development at the center of the ceiling (i.e. TC3 in Figure 9.2) for the Reduced Pool Fire Scenario (Section 9.3) is compared to that obtained for the RWS Fire Scenario (Section 9.2). Bear in mind that, differently from the RWS pool fire (200 MW), the reduced pool fire (30 MW) was not placed at the center of the cross-section. As a consequence, the temperature developments for the reduced pool shown in Figure 9.37, Figure 9.38, and Figure 9.39 are not necessarily representing the maximum temperatures achieved at the ceiling. Basically, as the reduced pool fire is placed closer to the left wall (see green squares in Figure 9.2), especially for sections located in the vicinity of the fire source, maximum temperatures at the ceiling will occur on the junction between the left wall and the ceiling (i.e. LCH3/TC1 in Figure 9.2). However, the results shown here are still elucidative to highlight the differences in the magnitude of the temperature development within the tunnel for an extremely large fire (RWS pool fire) and a relatively large fire (reduced pool fire).

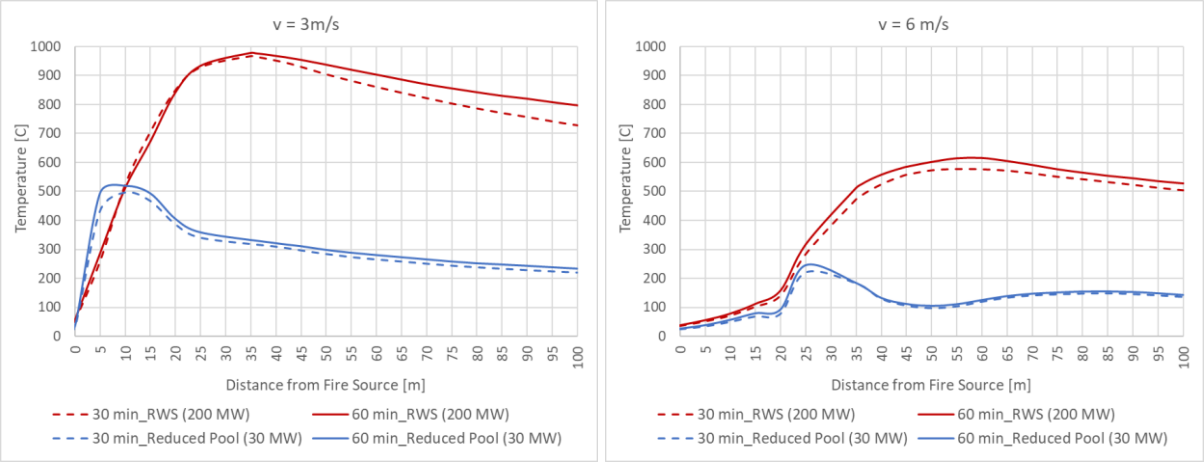


FIGURE 9.37 – LONGITUDINAL GAS TEMPERATURES AT THE CENTER OF THE CEILING

Figure 9.37 compares the development of longitudinal gas temperatures at the ceiling for both fire scenarios studied here. Cleary, the temperatures achieved for the larger pool fire (200 MW) are much higher than that for the reduced pool fire (30 MW). For a longitudinal ventilation velocity of 3 m/s, the maximum gas temperature for the RWS fire is *~1000 ^{o}C*, whereas for the reduced pool fire it is limited to less than *~550 ^{o}C*. When the ventilation is increased to 6 m/s, the maximum gas temperature at the center of the ceiling will significantly decay for both cases, being close to *~600 ^{o}C* for the larger pool fire and *~250 ^{o}C* for the smaller one.

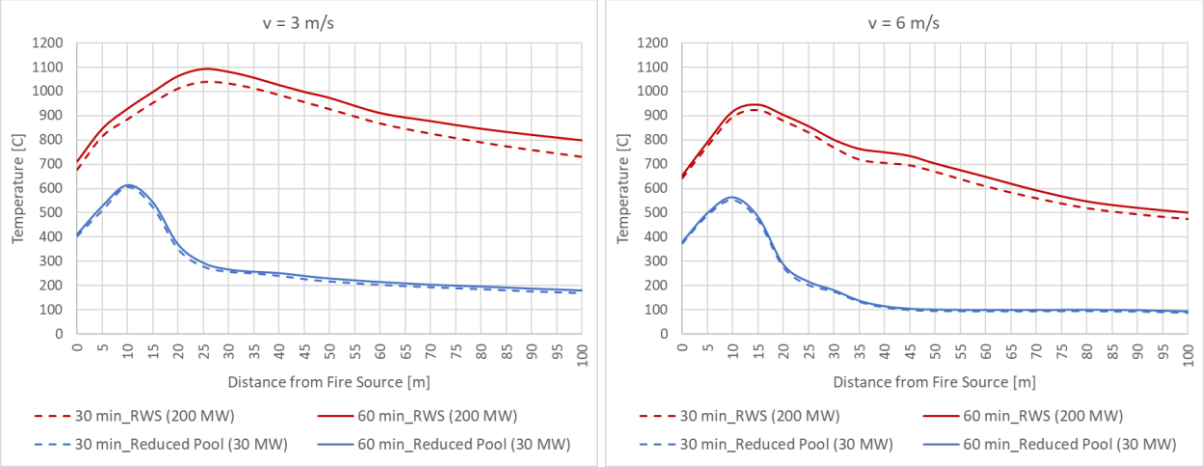


FIGURE 9.38 – LONGITUDINAL RADIATION TEMPERATURES AT THE CENTER OF THE CEILING

Figure 9.38 provides the same comparison for the radiation temperatures at the center of the ceiling. Once again, a significant difference between the maximum temperatures achieved for both cases is noted. Here, for a ventilation velocity of 3 m/s, the maximum radiation temperature for the RWS fire scenario and for the reduced pool fire scenario are *~1100 ºC* and *~600 ºC*, respectively. For a higher ventilation velocity (6 m/s), the radiation temperature is only slightly altered for both cases, being reduced to *~950 ºC* for the larger pool fire, and to *~550 ºC* for the reduced pool.

Figure 9.39 compares the longitudinal distribution of the AST at the center of the ceiling. As thoroughly explained along this thesis, due to the high temperatures achieved in any fire, the AST will always tend towards the correspondent radiation temperature (Section 5.3.3.3). Remember also that the AST combines the contribution of radiation and convection into a single term which fully characterizes the thermal exposure imposed by a fire on the structure. That being said, notice that for a ventilation velocity of 3 m/s the maximum AST at the center of the ceiling is equal to *~1050 ºC* for the RWS fire (200 MW) and to *~600 ºC* for the reduced pool fire (30 MW), being marginally equal to the correspondent radiation temperatures of each case. When the longitudinal velocity is increased to 6 m/s, the maximum AST is reduced to *~850 ºC* in the former case, and to *~450 ºC* in the latter. Although the differences from the correspondent radiation temperatures are now slightly increased, if considered that at the location of maximum AST the gas temperatures are clearly limited to less than *100 ºC* for both fire scenarios (look at the gas temperature development up to *15 m* from the fire source for a ventilation velocity of 6 m/s in Figure 9.37), it is still clear that the AST is much more influenced by the radiation component.

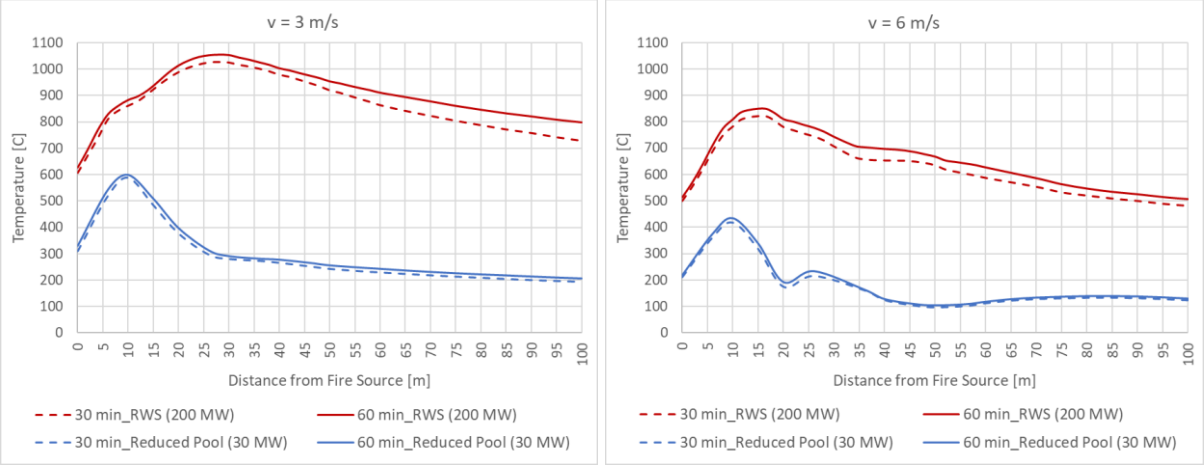


FIGURE 9.39 – LONGITUDINAL AST AT THE CENTER OF THE CEILING

To conclude this topic, it must be pointed out that, in the overall, the thermal exposure imposed on the structure of the Piet Hein tunnel by the RWS fire scenario is much more severe than that which is imposed by the reduced pool fire scenario. Notice, however, that the differences for the maximum thermal exposure obtained for both fire scenarios for different levels of ventilation will be later compared against each other in Section 9.4.

9.3.2 Thermal Exposure

Similarly from the work developed in Section 9.2.4 for the RWS fire scenario, this section addresses for each one of the cases studied in a reduced pool fire (i.e. without ventilation, and ventilation velocities of 3 m/s and 6 m/s), the thermal exposure imposed onto the structure of the Piet Hein tunnel as whole (Sections 9.3.2.1 to 9.3.2.3). The exposure is evaluated based on measurements collected from several AST devices, which are placed on the surface of the cross-section of the tunnel according to Figure 9.2. Those measuring points are also longitudinally distributed downstream the fire source as described below:

- Every *2 m* up to a distance of 60 m from the fire source.
- Every *5 m* from 60 m to 100 m downstream the fire source.

9.3.2.1 30 MW – v = 0 m/s

If longitudinal ventilation is not used inside the tunnel, flames from the reduced pool fire will impinge on the ceiling right on top of the fire source, propagating longitudinally both in the upstream and in the downstream directions (Figure 9.40). As the fire source is located closer to the left wall in the cross-section of the Piet Hein tunnel (see green squares in Figure 9.2), the thermal exposure imposed on the tunnel structure for a section located at the center of the fire source is rather inhomogeneous (Figure 9.41). The maximum exposure will occur on the junction of the left wall and the ceiling (i.e. LCH1 to C2 in Figure 9.2), and except for the first five minutes of fire, it will be limited to *~1000 ºC* for the total fire time. Also, the AST of the cross-section is continuously reduced from the left side of the ceiling up to the bottom of the right wall (Figure 9.41).

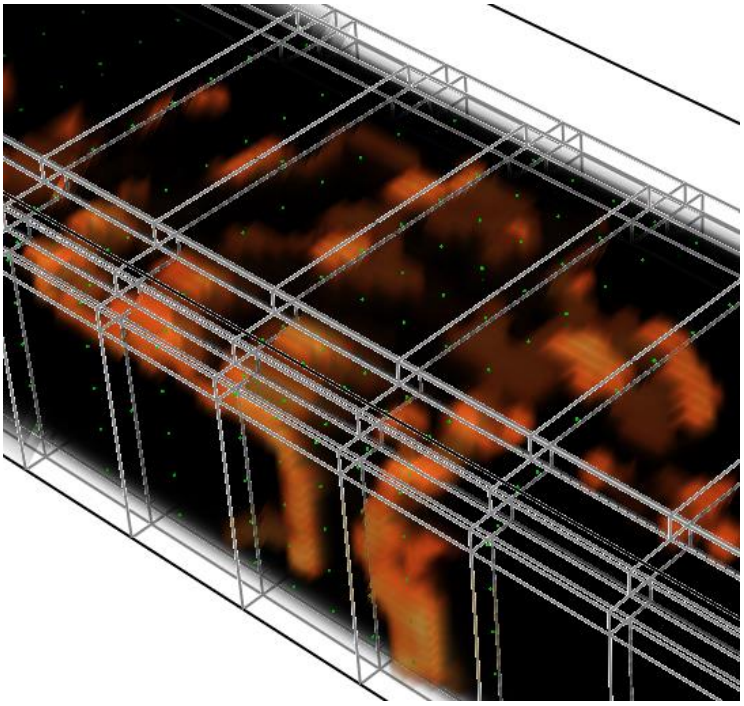


FIGURE 9.40 – FLAME IMPINGEMENT ON THE CEILING (30 MW – V = 0 M/S)

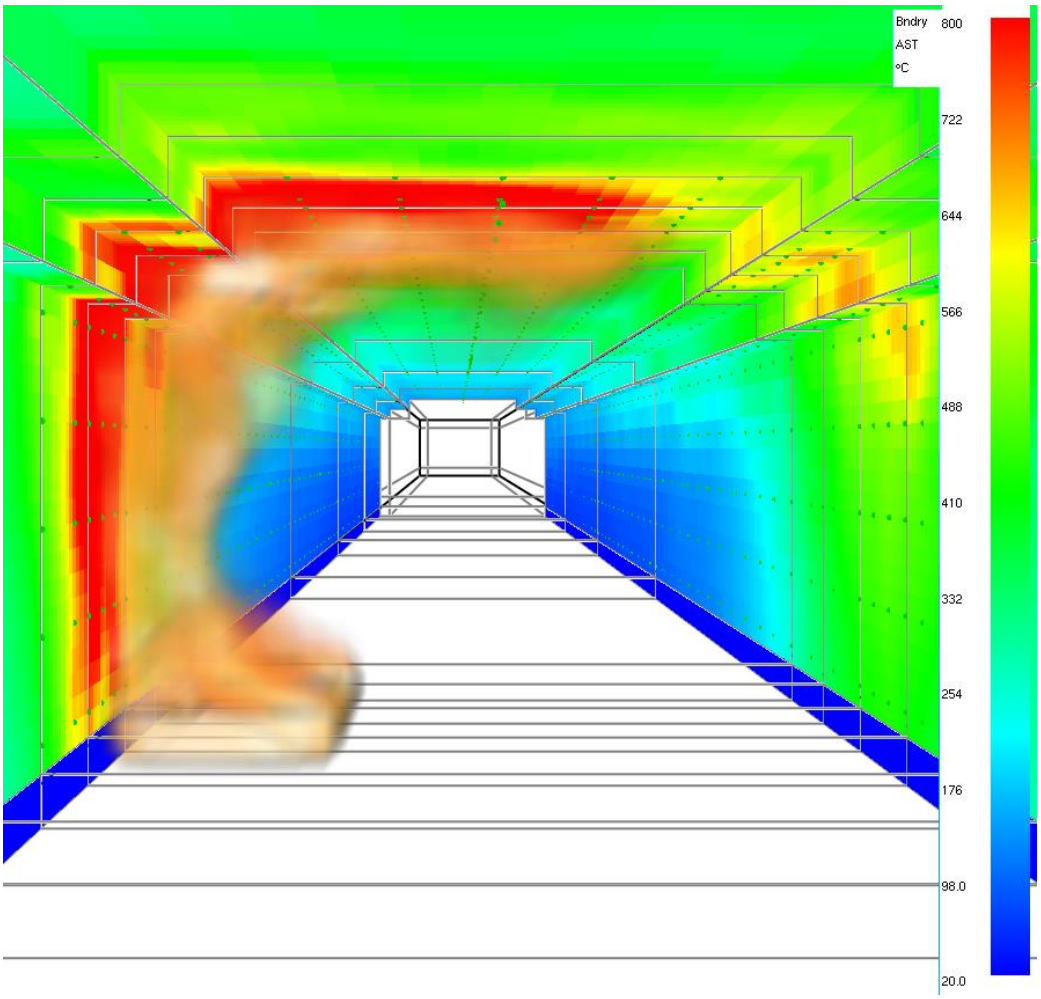


FIGURE 9.41 – THERMAL EXPOSURE (AST) ON THE TUNNEL LINING (30 MW – V = 0 M/S)

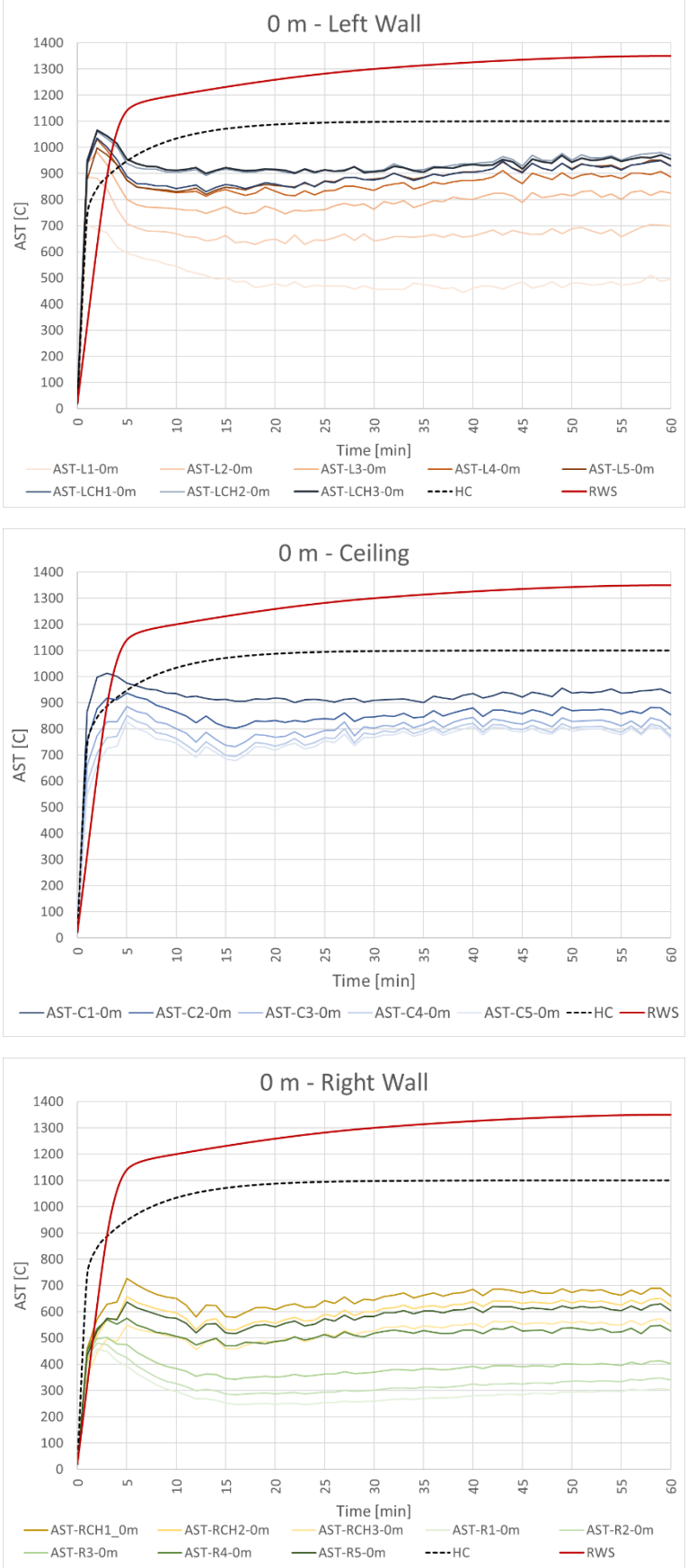


FIGURE 9.42 – THERMAL EXPOSURE AT THE CENTER OF THE FIRE SOURCE (30 MW – V = 0 M/S)

Moving away from the center of the fire source, with flames spreading on the ceiling and with the hot buoyant smoke propagating in the longitudinal direction of the tunnel, the thermal exposure on the ceiling starts to be more and more uniform. At *10 m* from the fire source, the thermal exposure on the ceiling becomes homogeneous within a range of *600 ºC* to *700 ºC* (Figure 9.43). Note that from this point onwards, the thermal exposure on the ceiling is already well-characterized by the longitudinal AST curves shown in Figure 9.28. Also from *10 m*, due to the propagation of hot buoyant smoke along the tunnel, the thermal exposure on the cross-section as a whole starts to become well stratified, continuously reducing from the ceiling of the tunnel up to the bottom of the walls (look at *18 m* in Figure 9.43). This stratification in the thermal exposure on the cross-section of the tunnel will continue to exist at least until the last AST measuring point, located *100 m* away from the fire source.

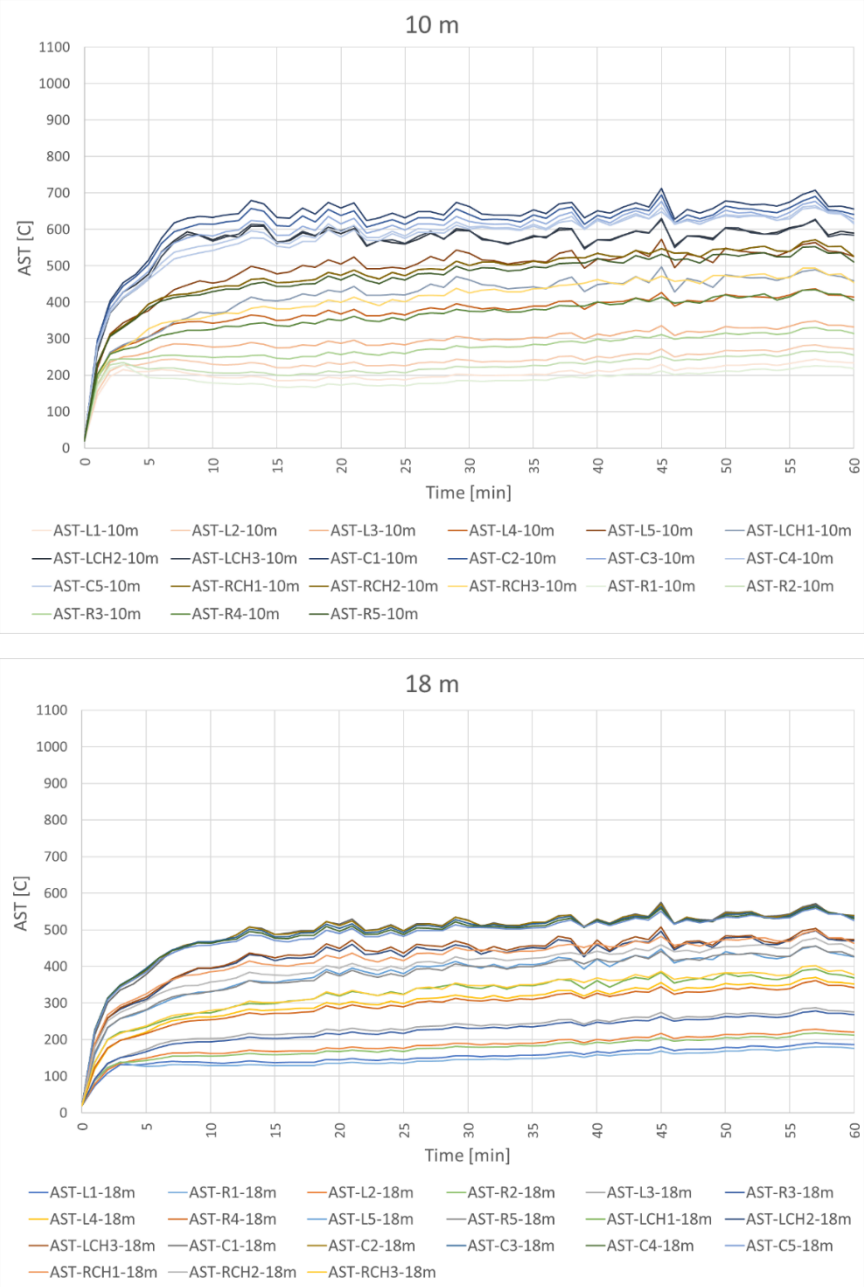


FIGURE 9.43 – STRATIFIED THERMAL EXPOSURE (30 MW – V = 0 M/S)

Figure 9.44 compares the thermal exposure achieved within the Piet Hein tunnel with the hydrocarbon and RWS curves. The maximum thermal exposure of the tunnel as a whole (blue lines in Figure 9.44) occurs at the center of the fire source on the left parts of the ceiling and, besides the very early stage of fire development (up to 5 minutes), is fully contained within the boundaries of the hydrocarbon curve. The maximum thermal exposure at the ceiling (orange lines in Figure 9.44) also occurs for a cross-section located at the center of the fire source, being higher on the left corner (limited to *~1000 °C*) and decaying considerably on the right corner (limited *~800 °C*). Note that the maximum homogeneous exposure on the ceiling as a whole (green lines in Figure 9.44) is significantly smaller than that of the maximum exposure on the tunnel and will be limited to *~700 °C*.

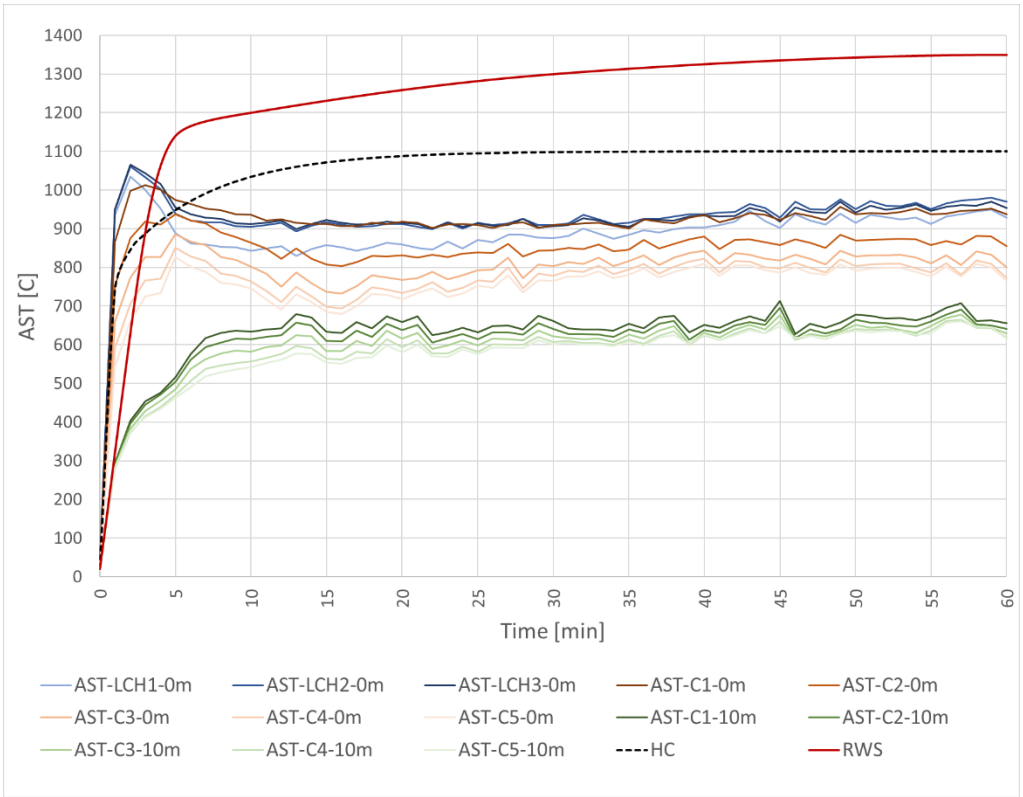


FIGURE 9.44 – MAXIMUM THERMAL EXPOSURE (30 MW – V = 0 M/S)

Table 9.6 below summarizes the thermal exposure along the Piet Hein tunnel for the reduced pool fire scenario without the use of longitudinal ventilation.

Section	Thermal Exposure	Reference
0 m – 10 m	Higher on the left corner of the ceiling	Figure 9.42
10 m – 18 m	Homogeneous at the ceiling	Figure 9.43 and Figure 9.28
18 m – 100 m	Higher on the ceiling and well-stratified on the cross-section	Figure 9.43 and Figure 9.28

TABLE 9.6 – THERMAL EXPOSURE ALONG THE TUNNEL (30 MW – V = 0 M/S)

9.3.2.2 30 MW – v = 3 m/s

Due to the use of longitudinal ventilation, flames are pushed towards ground level (Figure 9.45) and the gas temperature development on the ceiling is significantly reduced (compare cases *with* and *without* ventilation in Figure 9.34). However, as flames represent the primary source

of thermal radiation in a fire and the radiation component governs the total thermal exposure imposed onto the structure, cross-sections located in the vicinity of the flames will still experience high levels of thermal exposure. That being said, the thermal exposure for a section located at the center of the fire source (at *0 m* in Figure 9.46) is higher on the bottom of the left wall, close to the fire source. For the remaining parts of the cross-section, the thermal exposure is contained within a range of *200 ºC* to *400 ºC*. Further ahead from the fire source, the reacting zone (flames in Figure 9.45) grows in size and, so does, the level of thermal exposure imposed by the fire on the tunnel lining. At *6 m* (Figure 9.47), the AST will reach its maximum value at the bottom of the left wall (limited to *~1000 ºC*). At the same section, the thermal exposure is very inhomogeneous as a whole, being limited to less than *700 ºC* on the left corner of the ceiling, and equal to *~400 ºC* on the right wall.

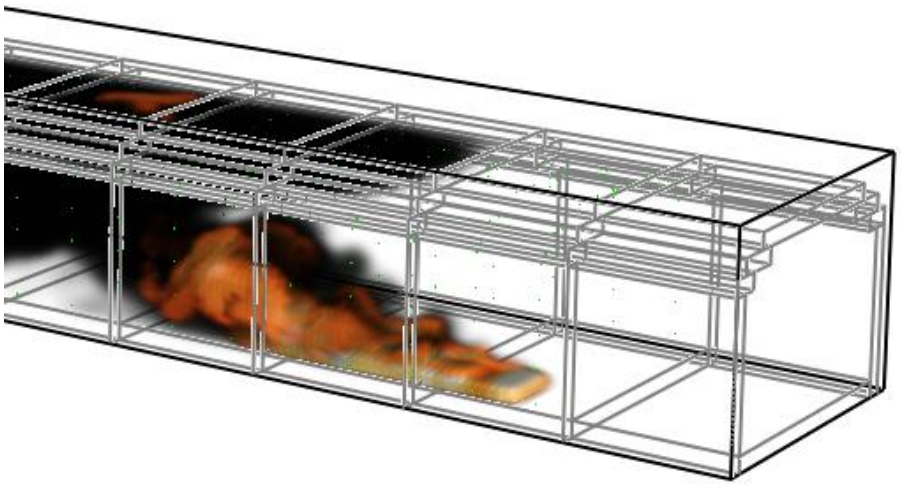


FIGURE 9.45 – EFFECTS OF VENTILATION ON FLAME PROPAGATION (30 MW – V = 3 M/S)

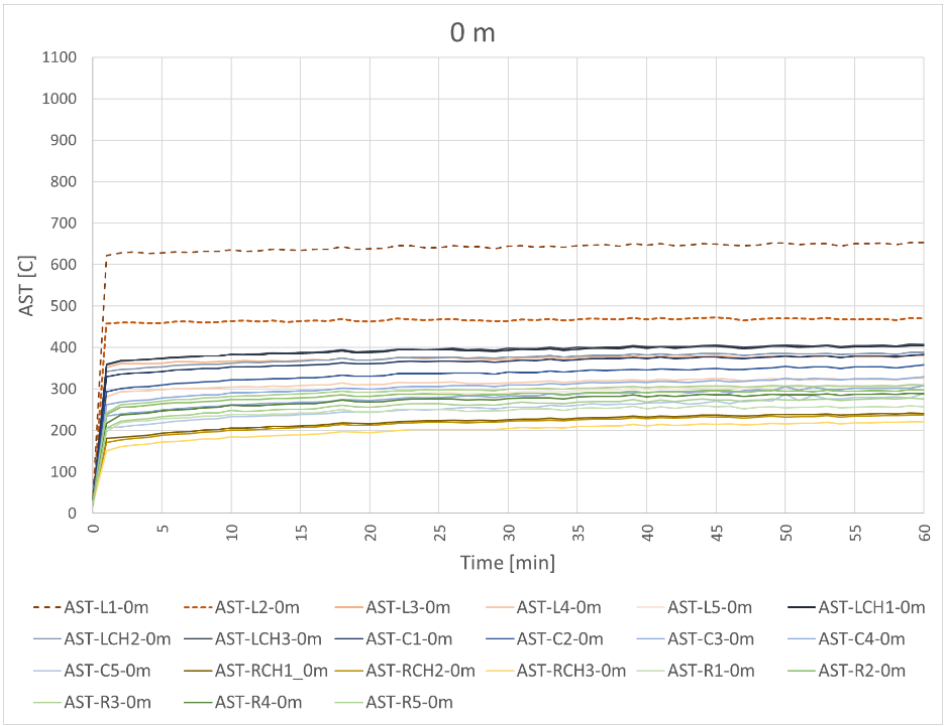


FIGURE 9.46 – THERMAL EXPOSURE AT THE CENTER OF THE FIRE SOURCE (30 MW – V = 3 M/S)

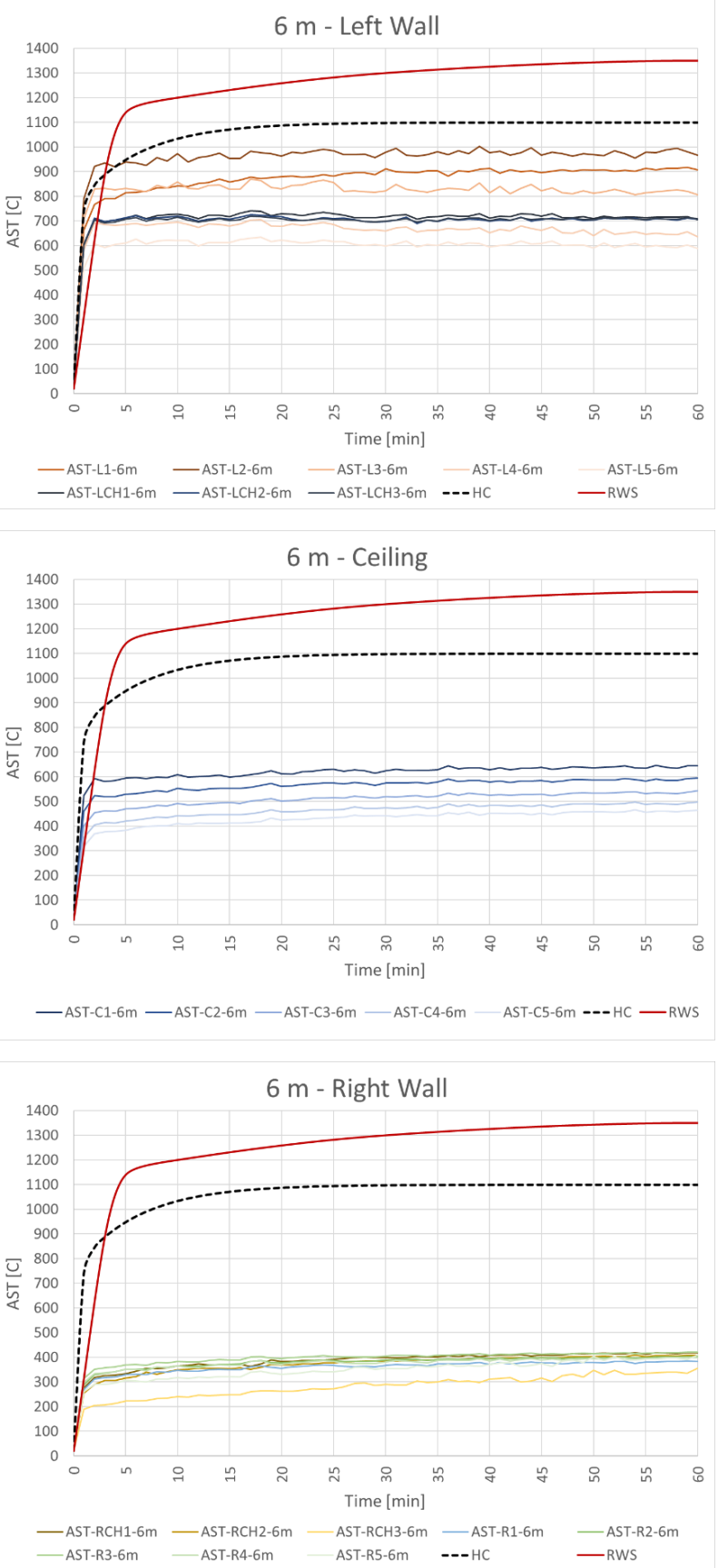


FIGURE 9.47 – THERMAL EXPOSURE IN THE VICINITY OF THE FIRE SOURCE (30 MW – V = 3 M/S)

The maximum exposure on the ceiling will occur at *10 m* from the fire source, but will still be very stratified (Figure 9.48). In this section, the AST for the left corner of the ceiling is limited to *~800 ºC* decaying to less than *500 ºC* on the right corner. From this point onwards, the thermal exposure on the ceiling, despite decaying for growing distances from the fire source, becomes more and more uniform. Homogenous thermal exposure on the ceiling is achieved for a section located at *18 m* from the fire source, but will already be around *~400 ºC* (Figure 9.49). It is also important to mention that at this section, the thermal exposure on the ceiling has already surpassed that which is imposed by the hot smoke layer on the walls of the tunnel. From *18 m* onwards, the thermal exposure on the ceiling of the tunnel is well described by the longitudinal AST curves shown in Figure 9.30.

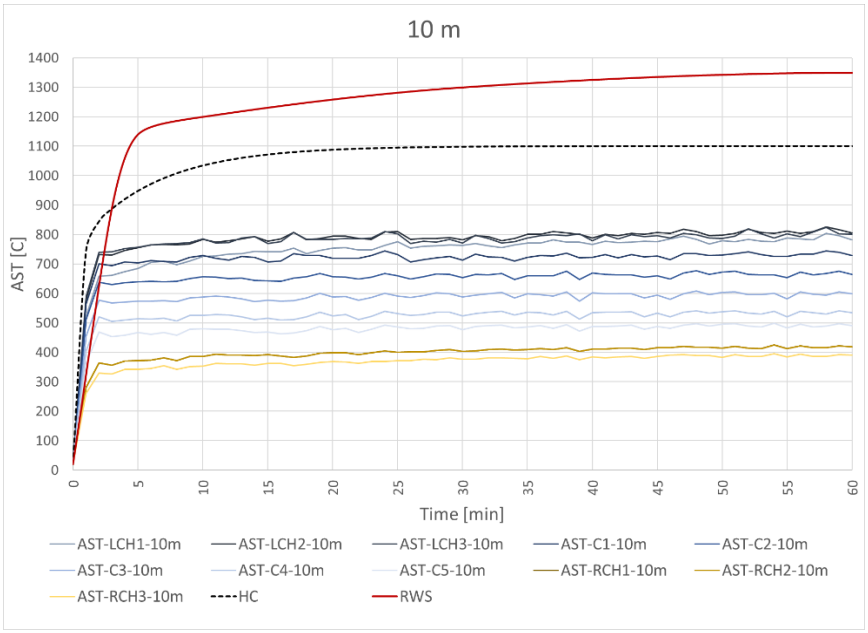


FIGURE 9.48 – MAXIMUM THERMAL EXPOSURE ON THE CEILING (30 MW – V = 3 M/S)

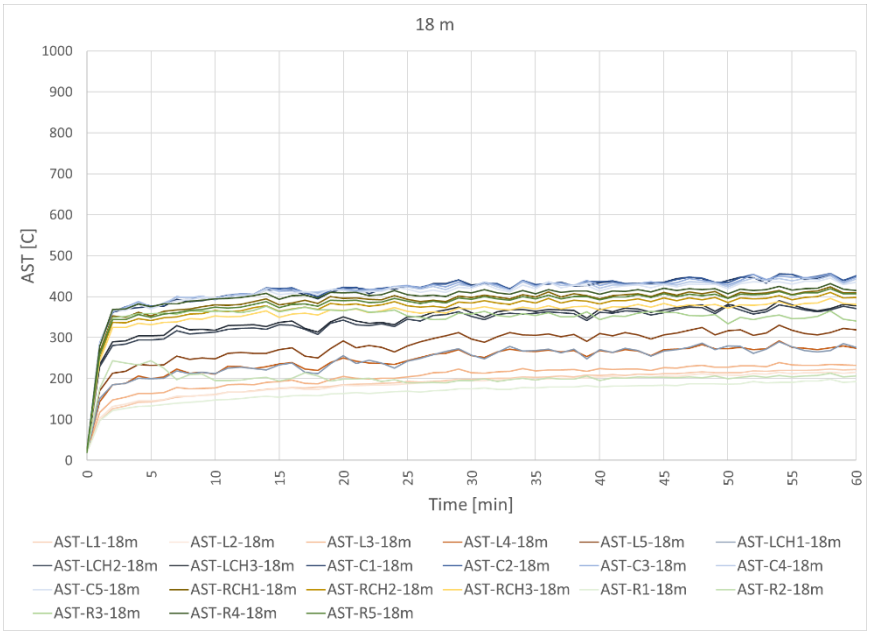


FIGURE 9.49 – MAXIMUM HOMOGENEOUS EXPOSURE ON THE CEILING (30 MW – V = 3 M/S)

Figure 9.50 compares the thermal exposure achieved within the Piet Hein tunnel for the reduced pool fire scenario at a ventilation velocity of 3 m/s to the hydrocarbon and RWS curves. The maximum thermal exposure (orange lines in Figure 9.50) occurs at the bottom of the left wall and is practically fully contained within the boundaries of the hydrocarbon curve. The maximum exposure on the ceiling (blue lines in Figure 9.50) is localized at the left corner, being limited to *800 ºC*. Note that the maximum homogeneous exposure on the ceiling (green lines in Figure 9.50) is much lower than that, and will be less than *500 ºC*.

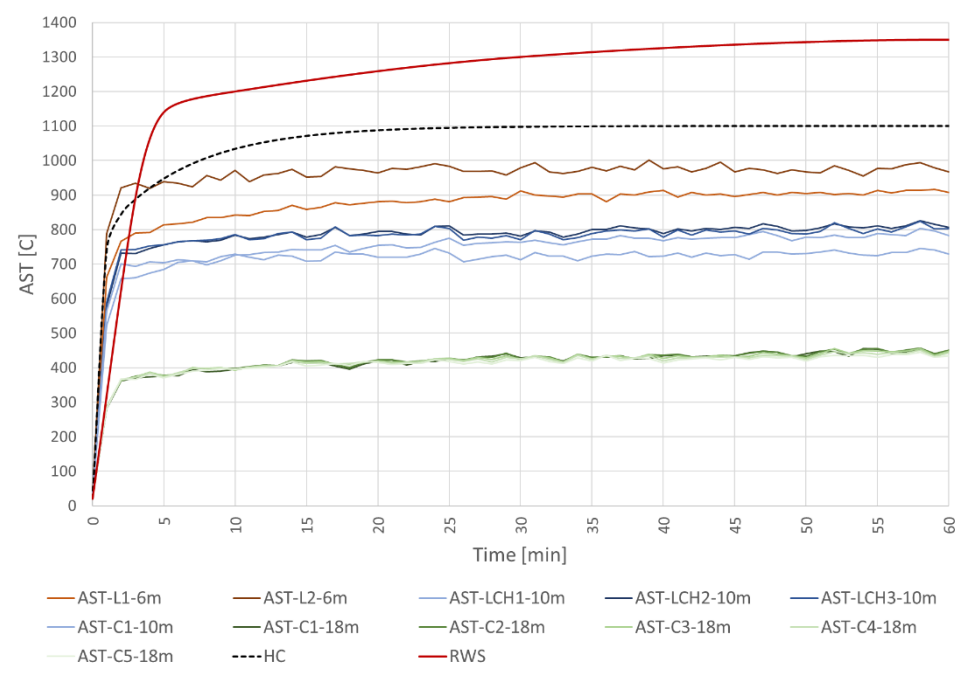


FIGURE 9.50 – MAXIMUM THERMAL EXPOSURE (30 MW – V = 3 M/S)

Table 9.7 below summarizes the thermal exposure along the Piet Hein tunnel for the reduced pool fire scenario at a ventilation velocity of 3 m/s.

Section	Thermal Exposure	Reference
0 m – 6 m	Higher on the bottom of the left wall	Figure 9.47 and Figure 9.42
6 m – 18 m	Higher on the left corner of the ceiling	Figure 9.48
18 m – 100 m	Higher on the ceiling	Figure 9.49 and Figure 9.30

TABLE 9.7 – THERMAL EXPOSURE ALONG THE TUNNEL (30 MW – V = 3 M/S)

9.3.2.3 30 MW – v = 6 m/s

Generally speaking, the thermal exposure imposed by the reduced pool fire at a ventilation velocity of 6 m/s on the Piet Hein tunnel follows the same trend from the previous case. Here, however, flames pushed even further towards the ground of the tunnel (Figure 9.51). As a consequence, the thermal exposure imposed on the bottom of the left wall in the vicinity of the flames will be higher than that for the remaining parts of the cross-section. In this sense, Figure 9.52 provides the thermal exposure imposed by the fire on the cross-section located at the center of the fire source. As it can be seen, the AST on the bottom of the left wall is *~600 ºC* for a very localized section. For the remaining parts, the thermal exposure is limited to less than *400ºC*.

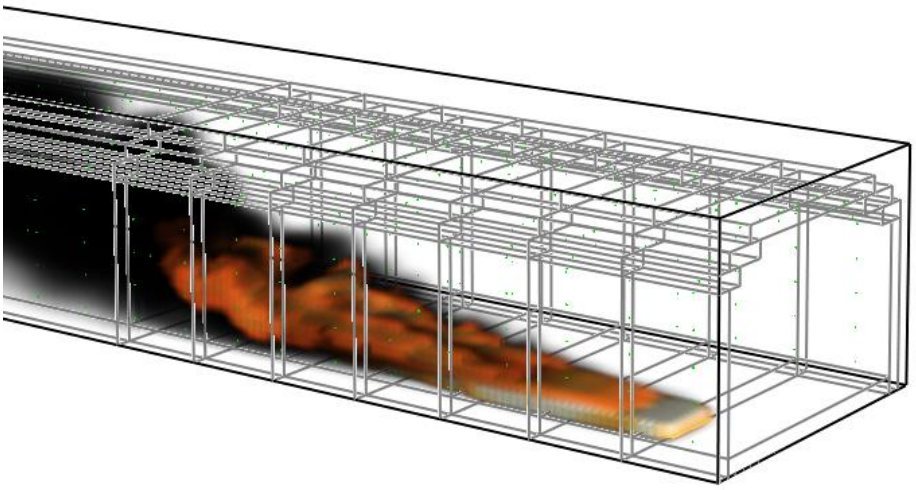


FIGURE 9.51 – EFFECTS OF VENTILATION ON FLAME PROPAGATION (30 MW – V = 6 M/S)

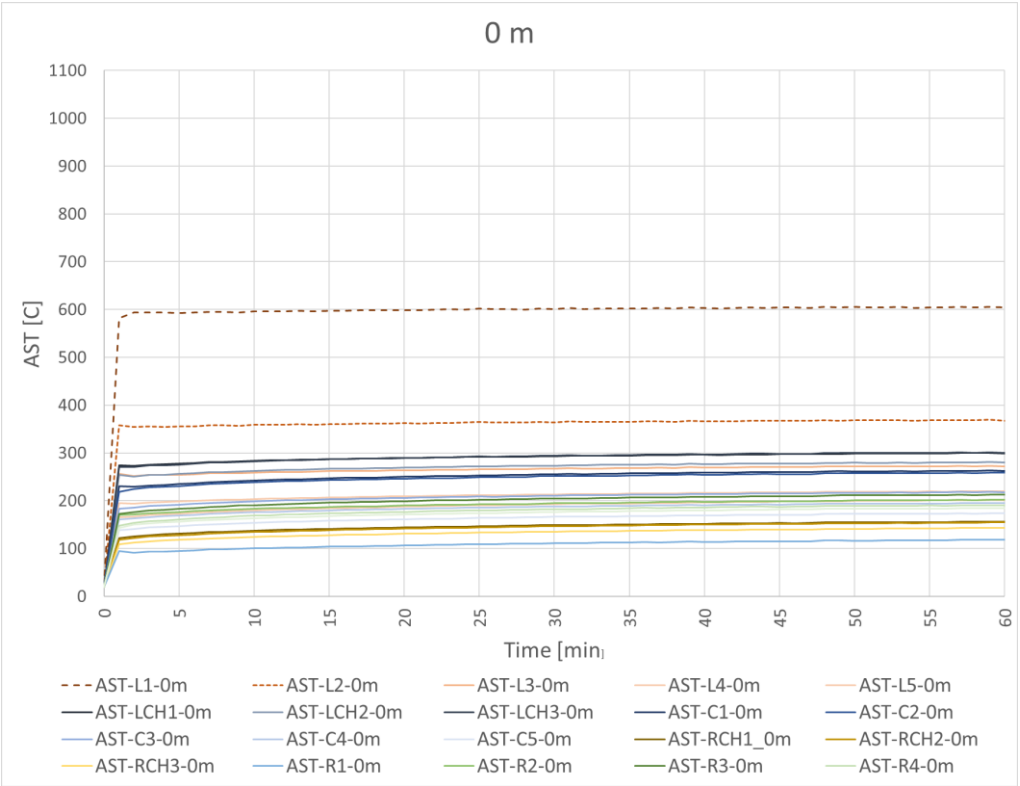
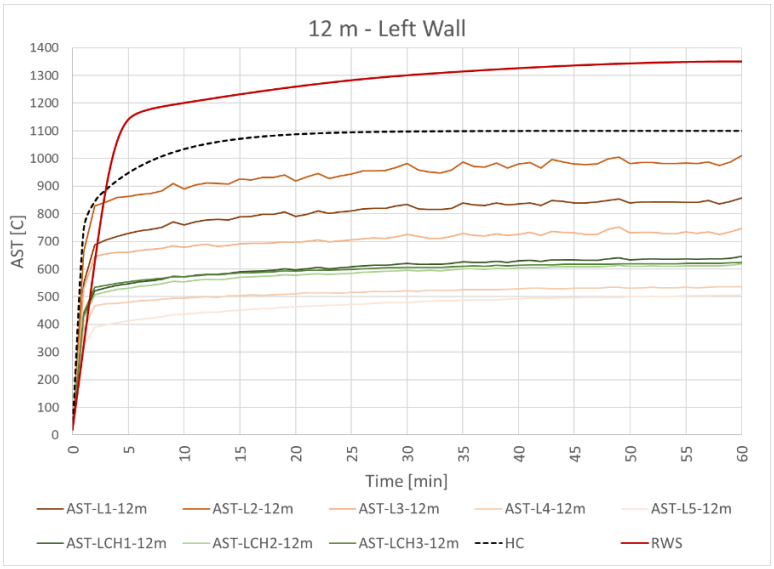
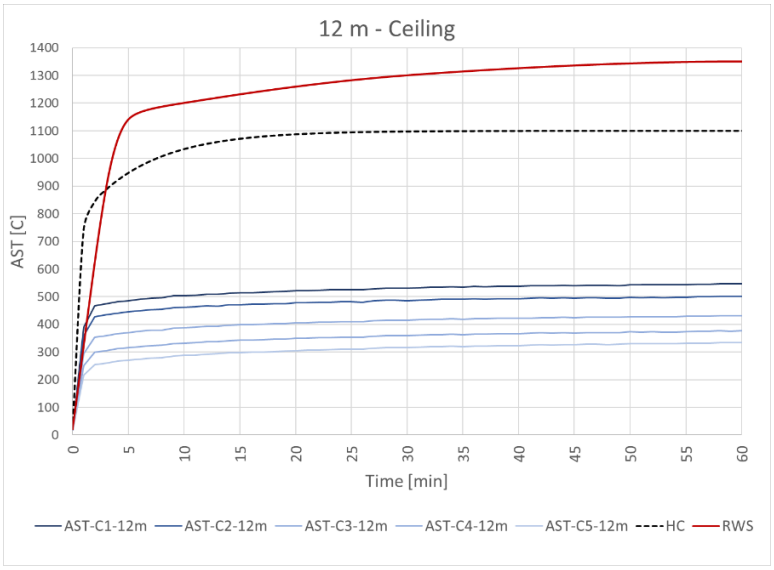


FIGURE 9.52 – THERMAL EXPOSURE AT THE CENTER OF THE FIRE SOURCE (30 MW – V = 6 M/S)

The flame body grows as we move further down the tunnel (Figure 9.51), leading to a section of maximum thermal exposure at *12 m* from the fire source (Figure 9.53). Here, the thermal exposure on the bottom of the left wall reaches a level of *~1000 ^{o}C*. The maximum thermal exposure on the ceiling, although still quite inhomogeneous, also occurs in this section. It approaches *~600 ^{o}C* on the left corner of the ceiling, and decays to *~400 ^{o}C* at the right corner. From this point onwards, the total magnitude of the thermal exposure will be continuously reduced for growing distances from the fire source.





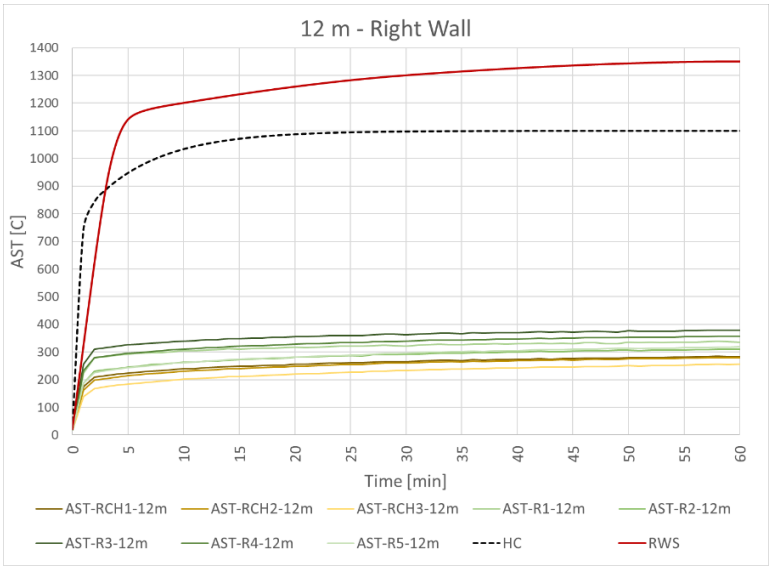


FIGURE 9.53 – MAXIMUM THERMAL EXPOSURE (30 MW – V = 6 M/S)

For such a high ventilation velocity (6 m/s), homogeneous exposure on the ceiling will not be reached and some level of stratification will always exist. However, as shown by Figure 9.54, at a section *22 m* away from the fire source, the level of thermal exposure imposed on the cross-section of the Piet Hein tunnel as a whole is already limited to *~300 ºC*. Therefore, for this fire scenario, asides from a short section in the vicinity of the flames (up to *~15 m* from the fire source), where high AST occurs either on the bottom of the left wall or on the left corner of the ceiling, the total exposure imposed on the Piet Hein tunnel is rather limited in the overall.

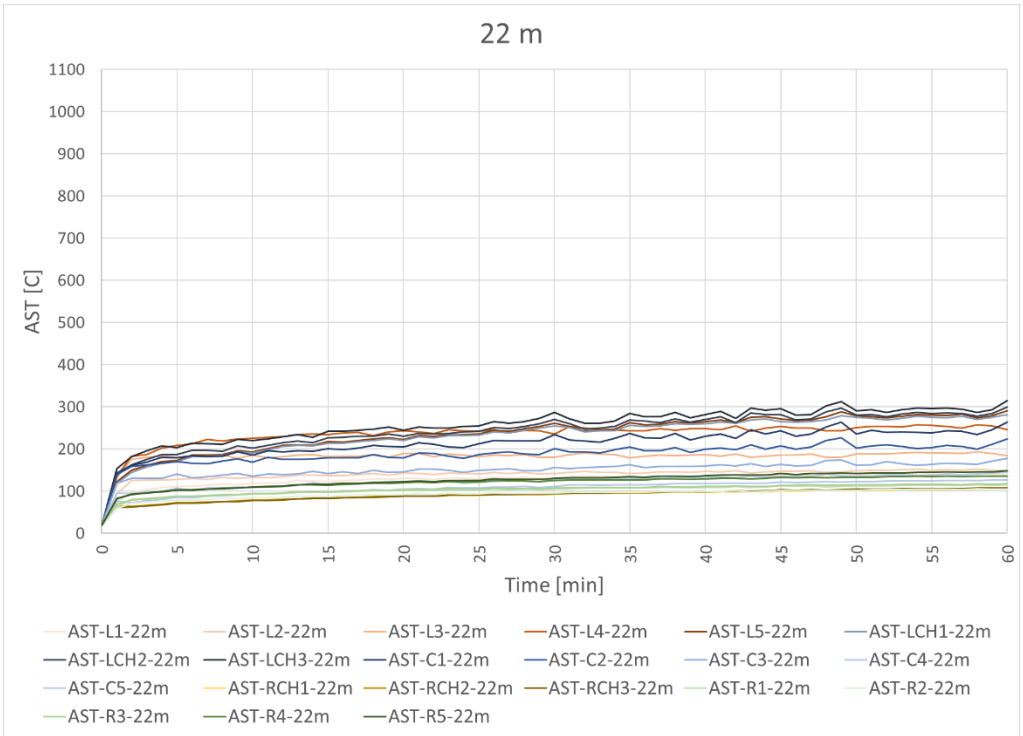


FIGURE 9.54 – REDUCED THERMAL EXPOSURE DOWNSTREAM THE TUNNEL (30 MW – V = 6 M/S)

Table 9.8 below summarizes the thermal exposure along the Piet Hein tunnel for the reduced pool fire scenario at a ventilation velocity of 6 m/s.

Section	Thermal Exposure	Figure
0 m – 12 m	Higher on the bottom of the left wall	Figure 9.53 and Figure 9.42
12 m – 22 m	Higher on the left corner of the ceiling	Figure 9.54
22 m – 100 m	Higher on the ceiling, but still stratified	Figure 9.32

TABLE 9.8 – THERMAL EXPOSURE ALONG THE TUNNEL (30 MW – V = 6 M/S)

9.4 Thermal Exposure Imposed on the Piet Hein Tunnel Structure

In Sections 9.2.4 and 9.3.2 the thermal exposure generated by the RWS fire scenario (200 MW) and by the reduced pool fire (30 MW) were described individually according to each case (i.e. without ventilation and with ventilation velocities of 3 m/s and 6 m/s). This section compares all cases studied in this thesis and summarizes the total state of thermal exposure imposed by each one of those fire scenarios on the Piet Hein tunnel structure.

In this sense, Figure 9.55 provides the maximum thermal exposure obtained inside the Piet Hein tunnel for both fire scenarios (i.e. reduced pool and RWS), and Table 9.9 summarizes the results. For all cases, the maximum thermal exposure occurs only in limited parts of the cross-

section, which are either impinged by flames or located in the vicinity of them. This makes the AST curves shown here (Figure 9.55) not to be representative in describing the total state of thermal exposure imposed on the cross-section as a whole. Also, there are two aspects which are worth mentioning here. Firstly, notice that the maximum thermal exposure imposed by a larger fire (bottom image in Figure 9.55) is higher than that which is achieved for the smaller one (top image in Figure 9.55), but high levels of exposure are still achieved for the reduced pool. Secondly, notice that the maximum exposure achieved for the whole tunnel is, for all cases, considerably smaller than that which is prescribed by the use of the RWS curve (equation 5.25). This is the case even for the two-hours exposure to the idealized RWS fire scenario (look at orange lines in Figure 9.22 and Figure 9.26).

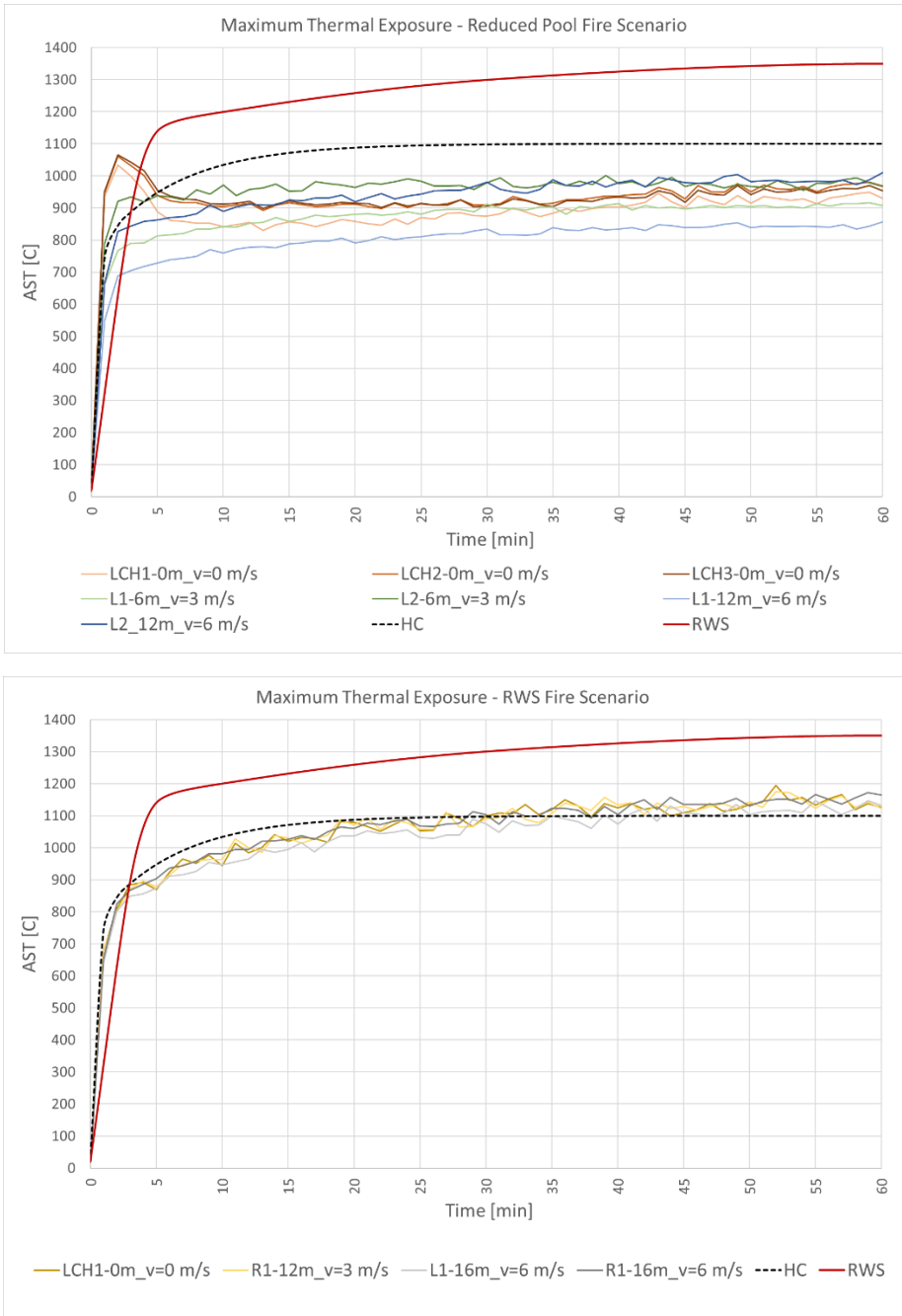


FIGURE 9.55 – MAXIMUM THERMAL EXPOSURE ON THE PIET HEIN TUNNEL

Fire Scenario	Zone of Maximum AST	Maximum AST
30 MW – v = 0m/s	Left Ceiling Corner	Limited to 1000 ºC with a short peak of 1100 ºC during the first 5 minutes of fire (orange lines in Figure 9.55)
30 MW – v = 3 m/s	Bottom of the Left Wall	Limited to 1000 ºC (green lines in Figure 9.55)
30 MW – v = 6m/s	Bottom of the Left Wall	Limited to 1000 ºC (blue lines in Figure 9.55)
200 MW – v = 3 m/s	Bottom of both Walls	Limited to 1100 ºC after 1 hour (yellow lines in Figure 9.55) Limited to 1200 ºC after 2 hours (orange lines in Figure 9.22)
200 MW – v = 6 m/s	Bottom of both Walls	Limited to 1100 ºC after 1 hour (grey lines in Figure 9.55) Limited to 1250 ºC after 2 hours (orange lines in Figure 9.26)

TABLE 9.9 – MAXIMUM THERMAL EXPOSURE ON THE PIET HEIN TUNNEL

Table 9.10 summarizes the maximum thermal exposure achieved on the ceiling (Figure 9.56). For the reduced fire scenario, the AST on the ceiling is not homogeneous for the cross-section subjected to the maximum thermal exposure achieved inside the tunnel. Basically, as the reduced pool fire is located closer to the left wall (look at green squares in Figure 9.2), the AST will be higher at the left corner of the ceiling, and will decay considerably up to the right corner. Further away from the fire source, the exposure on the ceiling will become homogeneous for the cases without ventilation and at a ventilation velocity of 3 m/s. This homogeneous exposure is much smaller than that which is locally achieved for the left corner of the ceiling at the cross-section of maximum exposure (Table 9.10).

Fire Scenario	Maximum Stratified Thermal Exposure on the Ceiling (AST)	Maximum Homogeneous Exposure on the Ceiling (AST)
30 MW – v = 0m/s	Goes from 1000 ºC on the left corner (orange lines in Figure 9.56) to 700 ºC on the right corner (blue lines in Figure 9.56)	Limited to 700 ºC (yellow lines in Figure 9.56)
30 MW – v = 3 m/s	Goes from 800 ºC on the left corner (orange lines in Figure 9.56) to 400 ºC on the right corner (blue lines in Figure 9.56)	Limited to 400 ºC (yellow lines in Figure 9.56)
30 MW – v = 6m/s	Goes from 600 ºC on the left corner (orange lines in Figure 9.56) to 300 ºC on the right corner (blue lines in Figure 9.56)	Does not reach, but the thermal exposure on the ceiling is already limited to 300 ºC at a section 22 m away from the fire source (Figure 9.54)
200 MW – v = 3 m/s	Does not occur	Limited to 1100 ºC after 1 hour (orange lines in Figure 9.55) Limited to 1100 ºC after 2 hours (blue lines in Figure 9.22)
200 MW – v = 6 m/s	Does not occur	Limited to 800 ºC after 1 hour (green lines in Figure 9.55) Limited to 900 ºC after 2 hours (green lines in Figure 9.26)

TABLE 9.10 – MAXIMUM THERMAL EXPOSURE ON THE CEILING

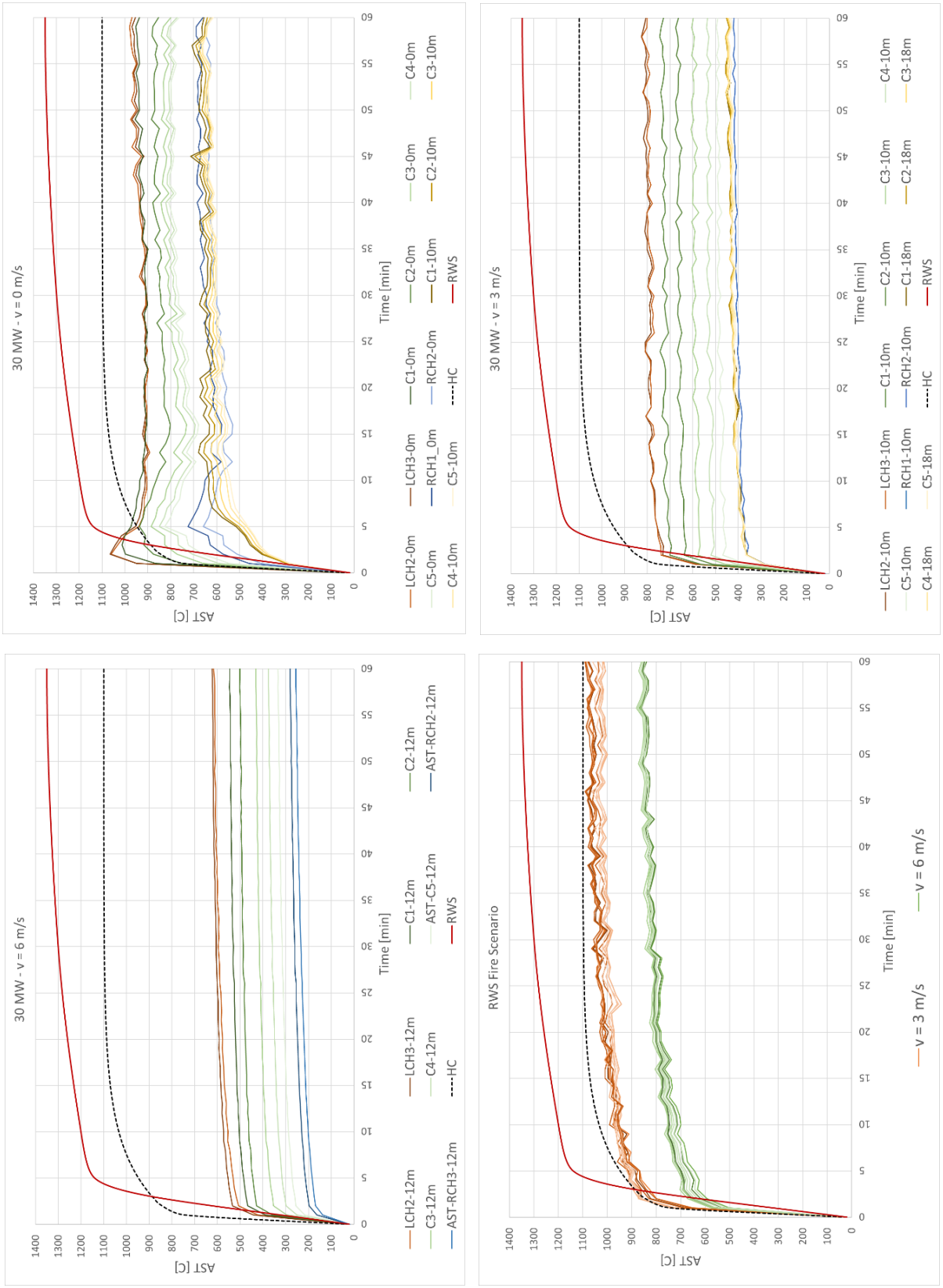


FIGURE 9.56 – MAXIMUM THERMAL EXPOSURE ON THE CEILING

For the RWS fire scenario, as the fire source covers practically the whole width of the tunnel (look at hatched squares in Figure 9.2), the maximum thermal exposure imposed on the ceiling will be quite homogeneous for both cases considered here (i.e. ventilation velocities of 3 m/s and 6 m/s). Note that for a ventilation velocity of 3 m/s, the maximum thermal exposure on the ceiling is actually quite representative for the whole cross-section (look at blue lines in Figure 9.22), whereas for a ventilation velocity of 6 m/s it is not. For the latter case, the maximum AST on the ceiling, although uniform (look at green lines in Figure 9.26), is still smaller than the AST achieved on the bottom of the walls (look at orange lines in Figure 9.26). Keep in mind that the maximum homogenous exposure imposed by the RWS fire scenario onto the whole cross-section of the Piet Hein tunnel for both ventilation velocities will be compared in Section 9.5, where the numerical calculations for the fire phase in FDS are coupled with the thermal analysis in DIANA.

In conclusion, two different fire scenarios were studied here (pool fires of 200 MW and 30 MW) for three conditions: (1) without ventilation; (2) longitudinal ventilation of 3 m/s (approximately equal to the critical velocity, explained in Section 3.2.1.2); and (3) longitudinal ventilation of 6 m/s (i.e. high ventilation velocity). A brief summary of the total state of thermal exposure generated by those fire scenarios along the tunnel is provided below:

1) For all cases studied here, the maximum thermal exposure achieved within the tunnel (Figure 9.55) is only representative in describing very localized parts of the cross-section of the tunnel, and thus, should not be used to characterize the total exposure imposed on the cross-section as a whole. For the cases with longitudinal ventilation, it occurs at the bottom of the wall(s), while for the case without ventilation (30 MW) it happens on the left corner of the ceiling. Table 9.9 summarizes the results.

2) Even when looking at the maximum AST achieved within the Piet Hein tunnel for all cases studied here (Figure 9.22, Figure 9.26 and Figure 9.55), the thermal exposure is still considerably smaller than that which is prescribed by the use of the RWS curve according to Eurocode 1 Part 1-2 [75] (i.e. equation 5.25). This reinforces the expectation that this curve should not be used to address *unprotected concrete tunnels* subjected to fire.

3) As the 200 MW pool fire occupies almost to the entire width of the cross-section of the tunnel (Figure 9.2), for the RWS fire scenario, the thermal exposure imposed on the ceiling is rather uniform since the center of the fire source, being reasonably well described by the red lines in Figure 9.10 and Figure 9.12 for ventilation velocities of 3 m/s and 6 m/s, respectively.

    a) Note that for the RWS fire scenario at a ventilation velocity of 3 m/s, from a section *14 m* away from the fire source, those red lines in Figure 9.10 are also representative to describe the total state of the thermal exposure along the tunnel for the cross-section as a whole. Note, however, that this exposure will be slightly higher on the ceiling from a section *22 m* downstream the fire source.

b) For the RWS fire scenario subjected to a higher ventilation velocity (6 m/s), the red lines in Figure 9.12 will only represent the total state of the thermal exposure for the cross-section as a whole for a section in between *32 m* and *40 m*. Up to *32 m* the thermal exposure will be higher at the bottom of the walls, and after *40 m* it will be higher at the ceiling. Therefore, for sections located after *40 m* those red lines in Figure 9.12 will be representative only on describing the maximum level of exposure on the cross-section along the tunnel.

4) Note that for the reduced fire scenario, homogeneous thermal exposure for the total cross-section of the tunnel is not achieved, at least up to *100 m* from the fire source. For the case without ventilation, the thermal exposure on the ceiling will always be higher than that of other parts of the cross-section. For the cases with longitudinal ventilation, the thermal exposure on cross-sections located in the vicinity of the fire/flames will be higher at the left wall. However, as soon as it becomes higher for the ceiling as a whole, in sections characterized by the propagation of smoke, it will remain like that for the rest of the tunnel.

5) For the reduced pool fire scenario, as the fire source is located closer to the left wall of the tunnel (Figure 9.2) and the conceived fire size is much smaller than that of a larger pool, the maximum exposure on the ceiling is quite stratified, being higher at the left corner and reducing tremendously up to the right corner (Table 9.10).

   a) For the reduced fire scenario without the use of longitudinal ventilation, the thermal exposure on the ceiling becomes rather homogenous for a cross-section *10 m* away from the fire source. From this section onwards, the red lines in Figure 9.28 are representative to describe the maximum thermal exposure on the remaining cross-sections along the tunnel.

   b) When considering the same case but at a ventilation velocity of 3 m/s, the thermal exposure on the ceiling will only become homogenous for a cross-section *18 m* ahead from the fire source. From this section onwards, the red lines in Figure 9.30 are characterizing the maximum thermal exposure on the remaining cross-sections along the tunnel.

   c) At a ventilation velocity of 6 m/s the thermal exposure will never become uniform for the ceiling. However, as indicated by the red lines in Figure 9.32, the total thermal exposure imposed on the tunnel as a whole will be quite limited. Table 9.10 summarizes the maximum thermal exposure on the ceiling for all cases studied here.

6) In the overall, the total thermal exposure induced by the RWS fire scenario on the Piet Hein tunnel is much more severe than that which is achieved for the reduced pool fire scenario (compare red and blue lines in Figure 9.39). When considered that the RWS fire scenario is not likely to occur within the Piet Hein tunnel (due to traffic restrictions), this comparison clearly indicates how one may benefit from a prescriptive-based approach.

9.5 Coupling FDS and DIANA

To illustrate the process of coupling CFD calculations and the FEA of structures, the maximum homogeneous exposure achieved for the RWS fire scenario, considering ventilation velocities of 3 m/s (Figure 9.22) and 6 m/s (Figure 9.24), is used here.

9.5.1 200 MW – v = 3 m/s

A time-temperature curve, here entitled as *AST_DIANA_v = 3m/s*, was created based on the AST measurements retrieved from the FDS fire simulation. This curve is shown in Figure 9.57 in comparison with the maximum homogeneous exposure obtained for the cross-section of the Piet Hein tunnel for the case in question.

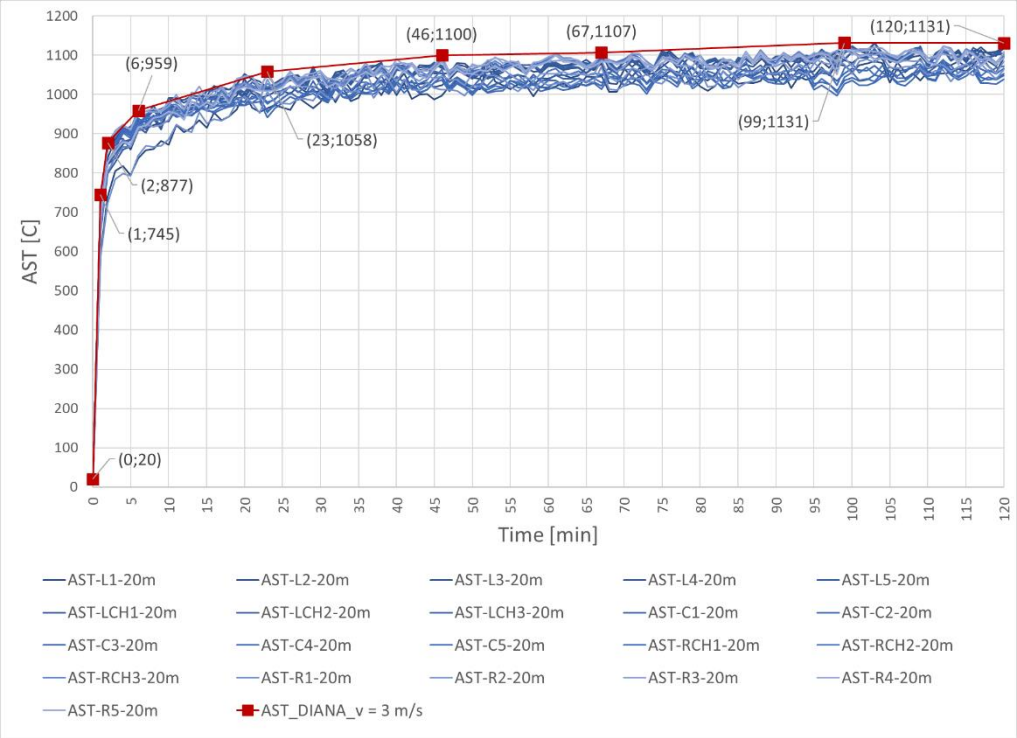


FIGURE 9.57 – AST _DIANA_V = 3 M/S

In DIANA, convection and radiation contributions have to be defined separately. However, when creating a combined thermal boundary condition, if both of them are assigned to a same edge (Figure 9.58), then DIANA only accepts one single temperature development to describe them both. Moreover, despite selecting the components individually, we are, in fact, making use of an AST boundary condition (equation 5.27), as this term represents the unique temperature development that combines the individual contributions of convection and radiation in a single equivalent term. This process is exemplified in Figure 9.59 for the case in question. In this figure, the pink lines mark the edges exposed to fire. For those, thermal boundary conditions are defined to describe the interface of heat transfer between a fire and the structure. The first step in this process, is to define a heat flow boundary interface for such edges, for which the types of discharge (i.e. convection and/or radiation) that are to be included in the FE model have to be selected, and their respective thermal parameters have to be defined (Figure 9.58). Those parameters are the emissivity of the surface (i.e. ε_s in equation 5.27) and the convection heat transfer coefficient (i.e. h in equation 5.27). Once the conditions describing

the process of heat exchange are specified, the next step is to prescribe the fire phase that will be used during the transient thermal calculation. To include the effects of convection, we need to assign an *external temperature* boundary condition to all edges exposed to fire. For radiation, we have to prescribe a *radiation temperature* to those same edges (Figure 9.59). Finally, a fire is characterized based on a single temperature curve that represents the evolution of both the *external temperature* and the *radiation temperature* in time (Figure 9.59).

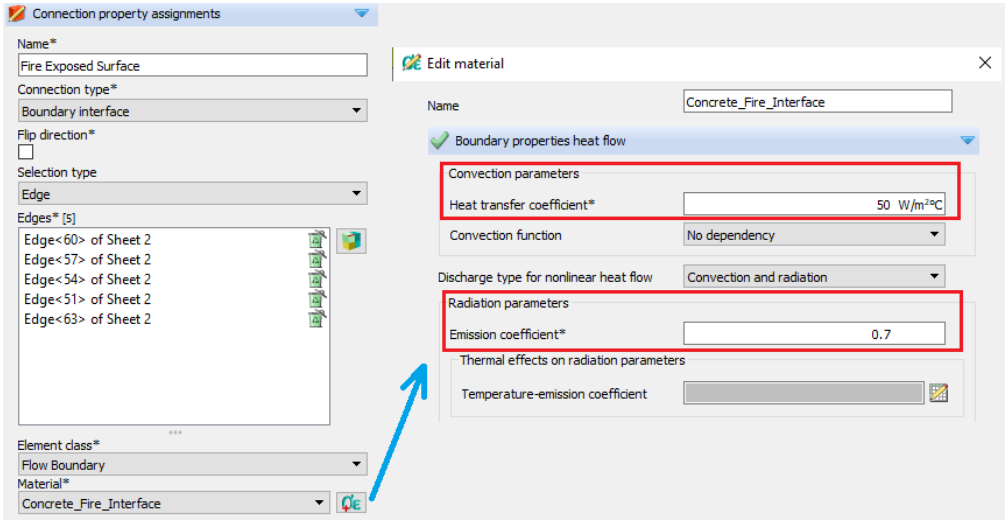


FIGURE 9.58 – DEFINING A FLOW INTERFACE AND ASSIGNING THERMAL PARAMETERS

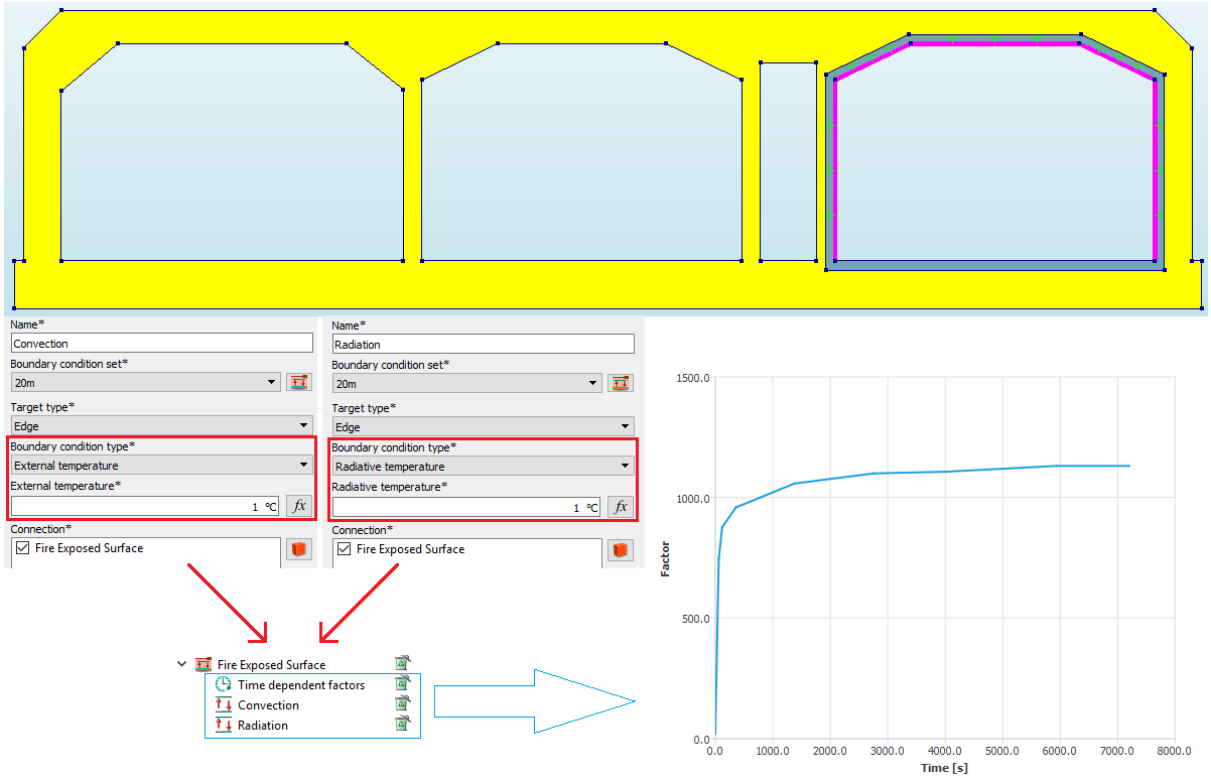


FIGURE 9.59 – CREATING A THERMAL BOUNDARY CONDITION IN DIANA

In essence, this process can be replicated for any section of the tunnel. Note that, ideally, we would define an AST development for different parts of the cross-section based on the

individual measurements of each one of the devices shown in Figure 9.2. These would allow us to differentiate the thermal exposure for several parts of the cross-section (e.g. bottom of the walls, ceiling, etc.). Even further, based on the use of *AST boundary files* in FDS, we are actually able to describe the AST evolution for the surface of every solid cell inside the computational domain of a fire simulation. This would let us couple the CFD model with the FE model for each finite element on the surface individually. However, in reality, thermal calculations in DIANA failed to produce reliable results when different time-temperature curves were assigned to two consecutive sections (Problem A in Figure 9.60). Problems with the numerical solution in DIANA were also perceived when the time-temperature curve is defined in its natural form, continuously varying between peaks and valleys (Problem B in Figure 9.60). Those are the reasons for which a continuously growing time-temperature curve, englobing the maximum AST values obtained in FDS, was created and applied homogeneously to the cross-section of the tunnel (Figure 9.57).

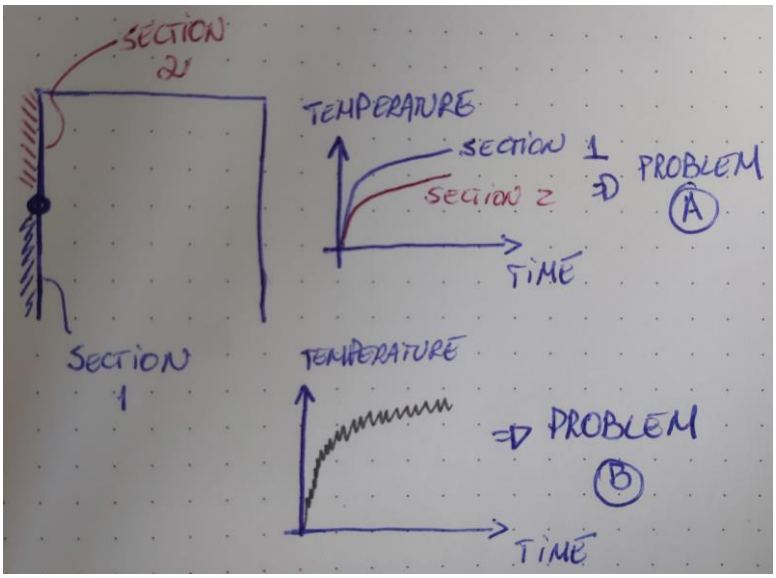


FIGURE 9.60 – PROBLEMS WHEN PERFORMING THERMAL CALCULATIONS IN DIANA

For the transient thermal analysis performed in DIANA, the thermal properties of concrete are, as in the FDS calculation, defined according to Table 9.1. A remark here concerns the convection heat transfer coefficient (i.e. h in equation 5.27). As it can be seen from Figure 9.58, a value of *50 W/m.K* is used (Eurocode Part 1-2 [75]). Note, however, that this parameter actually varies in time, being calculated by FDS at every time step during a fire simulation (Section 5.2.2). Thus, in practice, we could also define this parameter based on CFD results. Nevertheless, the total heat transfer to the structure is governed by the radiation component (Section 5.1.3.2), and assuming a constant, and rather conservative, convection heat transfer coefficient will not have a big effect on the results of the thermal transient analysis in FEA. Note, for instance, that the convection heat transfer coefficient calculated in FDS for the fire scenario in question, appears to be limited to less than 30 *W/m.K* along the tunnel (Figure 9.61). Peak values of ~40 *W/m.K* are achieved in small areas close to the fire source, but only for a limited amount of time (less than a minute).

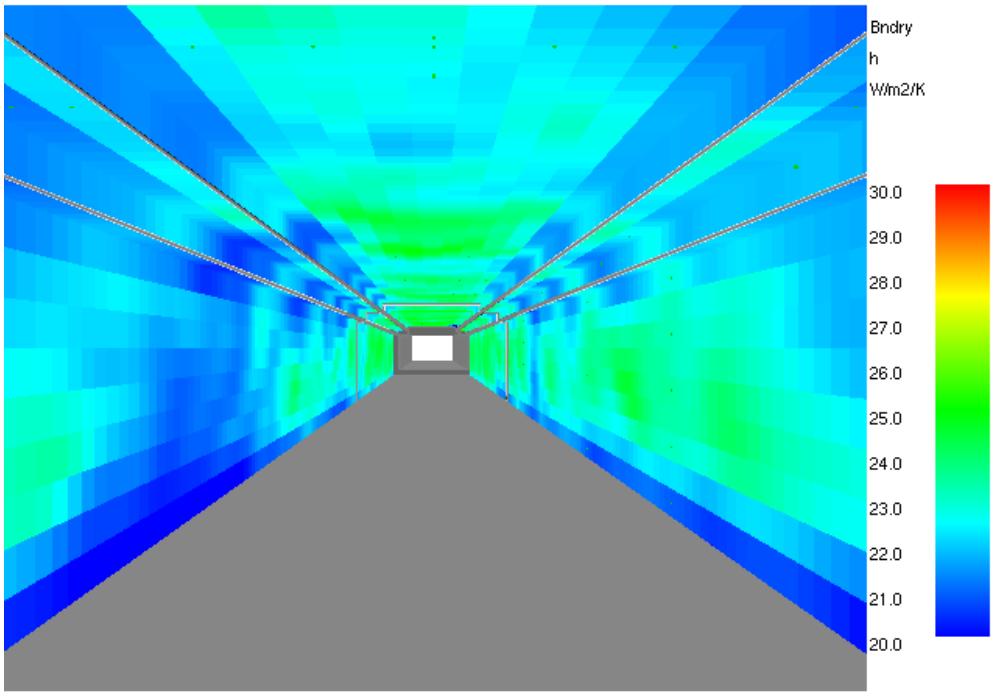


FIGURE 9.61 – CONVECTION HEAT TRANSFER COEFFICIENT IN FDS

Figure 9.62 provides the temperature development of the concrete tunnel at the cross-section of maximum homogeneous exposure (at *20 m* from the center of the fire source). The results of this transient thermal analysis are based on a mesh size of *0.01 m* up to a wall depth of *250 mm* (blue surface in Figure 9.59) and an adaptive mesh size of *0.1 m* for the remaining cross-section of the tunnel (yellow surface in Figure 9.59), for a time step of *10 seconds*. They are evaluated at the center of the ceiling, but are also representative on describing the temperature evolution of the cross-section as a whole, since the same time-temperature curve was uniformly applied to the tunnel surfaces.

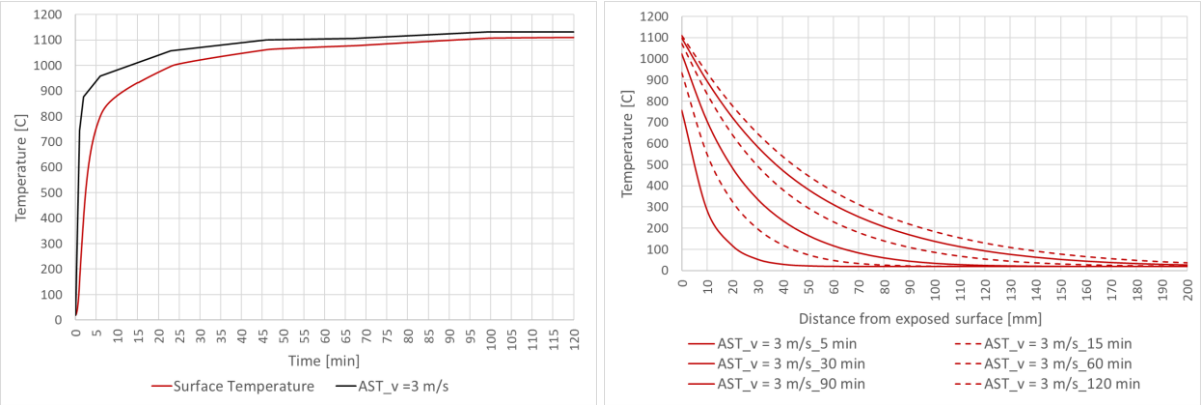


FIGURE 9.62 – TRANSIENT THERMAL ANALYSIS (200 MW – V = 3 M/S)

9.5.2 200 MW – v = 6 m/s

The exact same procedure was also followed here to analyze the temperature development of the Piet Hein tunnel structure at the position of maximum homogeneous exposure for the RWS pool fire in a ventilation velocity of *6 m/s*. The constructed AST curve is shown in Figure 9.63, and the results of the transient thermal analysis are depicted in Figure 9.64.

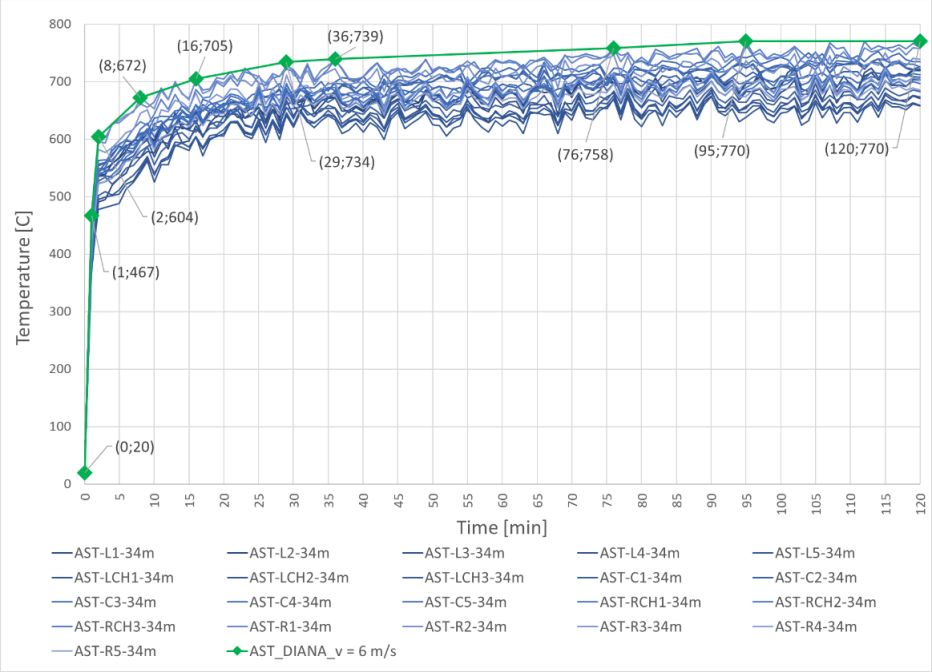


FIGURE 9.63 – AST _DIANA_V = 6 M/S

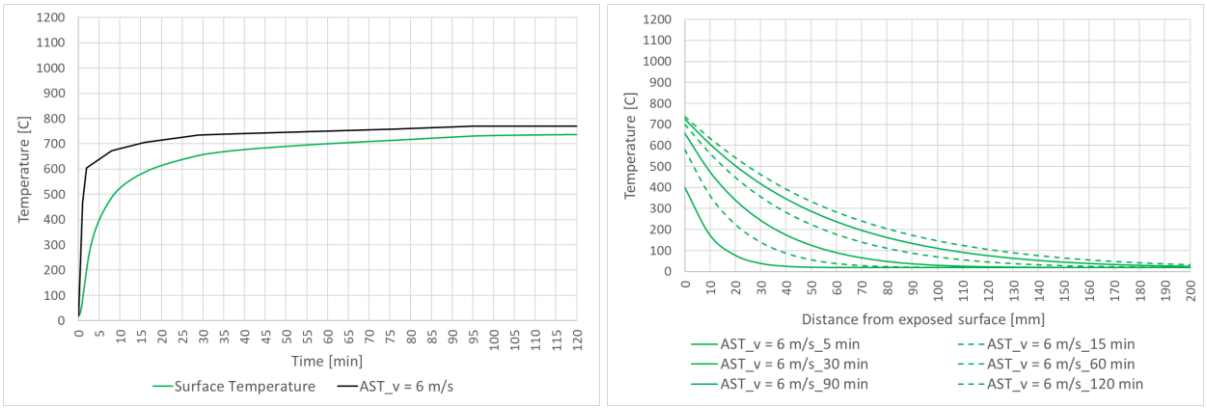


FIGURE 9.64 – TRANSIENT THERMAL ANALYSIS (200 MW – V = 6 M/S)

It is important to highlight that the convection heat transfer coefficient appears to increase at higher ventilation velocities. Even so, in this case it is still limited to a range of *20* to *40 W/m.K* along the tunnel, only reaching *50 W/m.K* in really small areas in the vicinity of the fire, which also only happens for an extremely limited time span (less than a minute).

9.5.3 Comparison with the RWS Curve

This section compares the temperature developments obtained in Sections 9.5.1 and 9.5.2, which are based on CFD calculations in a performance-based approach, against that which is obtained through the use of the RWS curve in a prescriptive-based approach. In this sense, Figure 9.65 below compares the surface temperature development in time among the three cases studied here, while Figure 9.66 compares the evolution of the thermal gradients formed within the structure.

First of all, remember that the lines shown here for the FDS simulations of the RWS fire scenario (i.e. $v = 3$ *m/s* and $v = 6$ *m/s* in Figure 9.65) do not represent the response of the

concrete structure to the maximum thermal exposure which was obtained in FDS for each one of those cases. Moreover, in both fire simulations, the maximum AST within the whole tunnel is given on the bottom of the walls located near the fire source (look at the orange lines in Figure 9.20 and Figure 9.26). Here, the red line shown in Figure 9.65 represents the response of the concrete structure to the maximum homogenous exposure obtained at the Piet Hein tunnel for a ventilation velocity of 3 m/s, which in this case also represents the maximum thermal exposure imposed on the ceiling of the tunnel. On the other hand, the green line in Figure 9.65, despite also providing the response to the maximum homogeneous exposure for a ventilation velocity of 6 m/s, does not represent neither the highest values at the ceiling nor at the walls of the Piet Hein tunnel (look at green and orange lines in Figure 9.26). That being said, those curves were selected as such to indicate how to couple CFD-based calculations in FEA and to highlight the possible benefits one may get by following a performance-based approach.

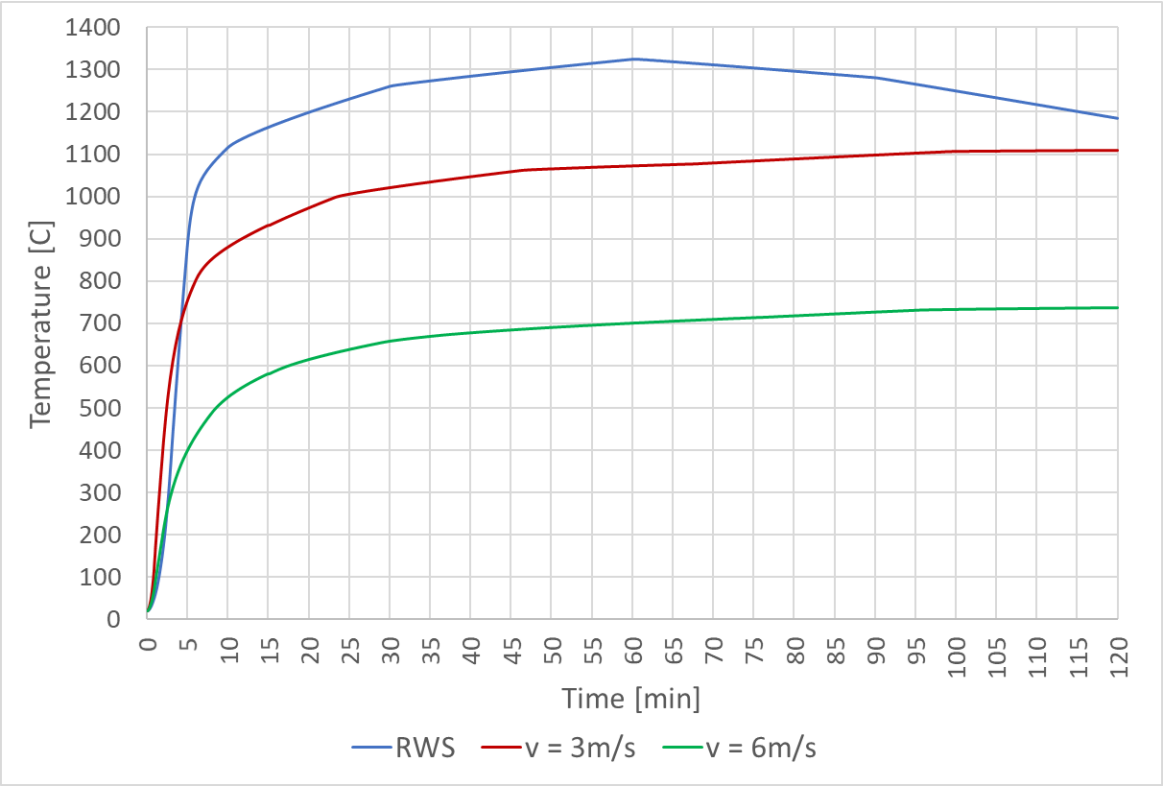


FIGURE 9.65 – COMPARISON OF SURFACE TEMPERATURE DEVELOPMENT IN TIME

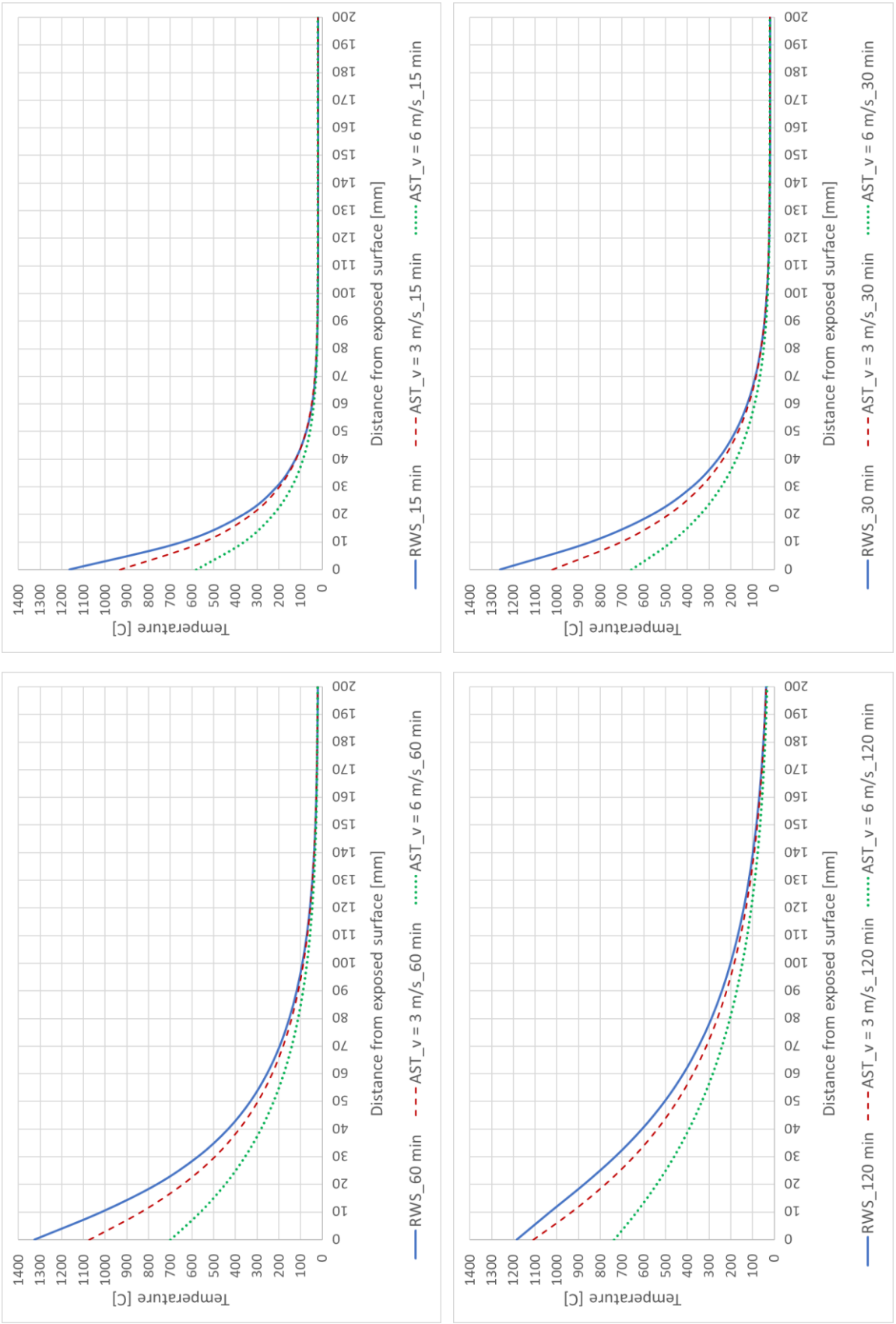


FIGURE 9.66 – COMPARISON OF THE EVOLUTION OF TEMPERATURE DISTRIBUTION

As it can be seen from Figure 9.65 and Figure 9.66, a reduced temperature development for the structure can be obtained when a more elaborated analysis is performed. It is clear that the idealized RWS fire scenario (200 MW gasoline pool fire), when addressed in a more realistic manner by considering both the geometry of the tunnel and the minimum ventilation velocity often adopted in smoke control (3 m/s), is not as destructive as that which is indicated by the use of the RWS curve (compare red and blue lines in Figure 9.65 and Figure 9.66). Also, even for such large fires as that conceived by the RWS fire scenario, which occupies almost the whole width of the cross-section of the tunnel (Figure 9.2), the use of high ventilation velocities has proven to be beneficial. Although it does not totally prevent the occurrence of zones characterized by high thermal exposure (look at AST for *16 m* in Figure 9.23), in the overall, it considerably reduces the achieved levels of thermal exposure in the tunnel as a whole (compare green lines with red and blue lines in Figure 9.65 and Figure 9.66), significantly limiting the temperature development within the concrete structure.

9.6 Conclusions

9.6.1 Limitations

Bear in mind that the work developed here, and the conclusions that are described the next Section 9.6.2, are bounded by the following limitations:

1) For the reduced pool fire scenario without ventilation only a section of *600 m* was modeled when performing the fire simulation. Therefore, when considering that the real length of the Piet Hein tunnel is approximately *2000 m*, even this reduced pool fire might not be sustainable in reality without an external source of ventilation.

2) Only a reduced straight section of the tunnel was used to perform the fire simulations presented here, and the slope of the tunnel was not included in the models.

3) The results presented here, especially when concerning the added benefits of using high ventilation velocities in controlling the temperature development within the tunnel, are limited by the conditions used when performing the fire simulations. Therefore, they are only intended to describe *fuel-controlled* pool fires and only for cases where the combustion process is kept unaltered at higher levels of ventilation.

4) For cases including the effects of ventilation, it must be pointed out that the longitudinal ventilation was uniformly applied, at constant velocity, to the cross-section of the tunnel through the use of a boundary condition.

9.6.2 Conclusions

The following conclusions are drawn based on the study developed here:

1) Due to lack of oxygen, the idealized RWS fire scenario (i.e. a 200 MW gasoline pool fire burning for a total of two hours) is not sustainable within the Piet Hein tunnel (Figure 9.7). Therefore, without the use of longitudinal ventilation, such a large pool fire will develop as *ventilation-controlled*. Note that, in this case, the real HRR evolution remains unknown, but the use of ventilation will enhance combustion.

2) For both levels of longitudinal ventilation investigated here (3 m/s and 6 m/s), the RWS fire scenario reached its full capacity (200 MW) for the total period of fire simulation (Figure 9.18). For those cases, fire developed as *fuel-controlled*.

3) For *fuel-controlled* tunnel fires, the use of longitudinal ventilation has shown to be highly effective in controlling the maximum gas temperatures within the tunnel (Figure 9.13 and Figure 9.34). Ventilation pushes the flames towards the ground and promotes mixing of cooler air with the hot buoyant smoke, significantly reducing the temperature of the smoke body. In essence, the higher the ventilation velocity the higher the reduction on gas temperatures within the tunnel.

4) In the overall, the use of longitudinal ventilation has also shown to reduce the radiation temperatures within the tunnel (Figure 9.15 and Figure 9.35), but this effect is more pronounced for sections located further away from the fire source, after the end of the reacting zone. In essence, as flames constitute the primary source of thermal radiation in any fire, independently from the level of ventilation applied inside the tunnel, sections located in the vicinity of the flame body will still experience high radiation temperatures. Further away, for sections subjected only to the propagation of smoke, as the use of ventilation significantly reduces the temperature of the smoke body, naturally, it also contributes to limit the radiation temperatures along the tunnel. This is the case because the thermal radiation emitted by the smoke layer is related to the fourth power of its own bulk temperature (equation 5.13).

5) As we know, the thermal exposure imposed by a fire on the structure of the tunnel is fully characterized by the AST (Section 5.3.3.3), which is governed by the radiation component (compare AST and correspondent gas and radiation temperatures in Figure 9.10 and Figure 9.12, for instance). As consequence, the use of longitudinal ventilation, despite not avoiding the occurrence of high thermal exposure in certain zones of the cross-section which are either subjected to flame impingement or are located in the vicinity of flames (Figure 9.55), has shown to be very beneficial in reducing the total state of thermal exposure imposed by the fire on the tunnel structure (Table 9.10). This, however, should be limited to describe *fuel-controlled* pool fires.

6) It must be pointed out that, for all cases studied here, the maximum thermal exposure achieved within the Piet Hein tunnel is only representative to describe the exposure imposed on very localized parts of the cross-section of the tunnel (Figure 9.55). Accordingly, it should not be used to characterize the total state of thermal exposure imposed on the cross-section as a whole. Note that even if we would assume otherwise, meaning that the maximum AST achieved for a rather small part of the cross-section could be used on describing the maximum homogeneous exposure on the tunnel as a whole, it would still be considerably smaller than that which is prescribed by the use of the RWS curve according to Eurocode 1 Part 1-2 (i.e. equation 5.25). This confirms the expectations raised in Chapters 7 and 8 or, in other words, that the RWS curve should not be used to describe the thermal exposure within *concrete tunnels* subjected to fire.

7) Among all cases studied here, the maximum homogeneous thermal exposure imposed on the cross-section of the Piet Hein tunnel as a whole, happens for the RWS fire scenario at a ventilation velocity of 3 m/s. It is practically fully contained within the boundaries of the hydrocarbon curve for a total burning time of two-hours (look at blue lines in Figure 9.26). Therefore, as indicated by the findings of Chapter 7, the hydrocarbon curve appears to be a better choice to describe a worst-case scenario for *concrete tunnels* subjected to fire.

8) As summarized in Table 9.10 and reinforced by the longitudinal development of the AST at the ceiling (Figure 9.39), the thermal exposure imposed by the reduced pool fire scenario (30 MW) is much smaller than that which is imposed by the idealized RWS fire (200 MW). Note that if considered the traffic restrictions applied to the Piet Hein tunnel, the latter is unlikely to occur. Therefore, if the reduced pool fire would have been taken as the worst-case fire scenario for this tunnel, the benefits of adopting a performance-based approach in the design phase are clearly elucidated by the study performed here, exposing the added benefit of adopting such an approach in the design phase.

9) Through a performance-based approach, one will benefit from considerably smaller thermal gradients within the concrete structure exposed to fire (compare blue with red and green lines in Figure 9.66). However, such reductions in the temperature distribution within the concrete structure are not linearly translated into a reduced thermal stress state inside the structure. For instance, the study developed in Section 6.6.3, showed that two completely distinct temperature developments for the same concrete structure yielded in practically equivalent levels of thermal stresses. This matter has to be further investigated if the performance-based approach is to truly be achieved in the near future of tunnel fire safety engineering.

10 Conclusions and Recommendations

In this chapter conclusions related to the main research question and proposed objectives (Chapter 2) are presented. Here, they will be given according to four different categories: (1) Fires and Fire Modeling in FDS (Section 10.1.1); (2) Fire-Structure Interface (Section 10.1.3); (3) RWS Curve and The Prescriptive-Based Approach (Section 10.1.3); and (4) Concrete Structures and The Performance-Based Approach (Section 10.1.4). In the end, recommendations for engineering practice and future research are provided (Section 10.2).

10.1 Conclusions

10.1.1 Fires and Fire Modeling in FDS

The conclusions presented below refer to fundamental aspects related to fire and their consequences when performing fire simulations in FDS:

1) Solid and liquid fires burn in a very different manner. For both cases, the development of HRR is related to the product between the mass loss rate of fuel ($\dot{m}_f''$ in equation 4.1) and the total area contributing to combustion (A_f in equation 4.1). Liquid (pool) fires will achieve a constant $\dot{m}_f''$ (Figure 4.4) shortly after ignition, making the development of HRR to be easily quantifiable based on the area of the pool. On the other hand, for solid fires, not only the exposed burning area varies in time, but also the burning rate of the material itself will not be constant. These together, make it practically impossible to predict how a solid fire will develop (Figure 4.1).

2) For the reason stated above, and considering the time span dedicated to this thesis, it was not feasible to model solid fires in FDS. Thus, any further discussion about such fires is beyond the scope of this thesis, and the more interested reader is referred elsewhere (Cheong et al. [116]; Wang [117]; Trelles and Mawhinney [118]).

3) In its simplest form, pool fires are easily characterized in FDS by the use of a boundary condition, which constantly releases fuel to the domain of simulation according to a prescribed function (Section 5.2.3.1). When dealing with *ventilation-controlled* fires, where the burning rate of the fuel equates the availability of oxygen inside the enclosure, the use of such boundary conditions in FDS will be deeply misleading (Figure 9.6). This exposes a limitation in fire modeling, where, most often, a fire is prescribed rather than predicted. Accordingly, the use of this type of boundary condition in fire modeling should be limited to the study of *fuel-controlled* fires.

4) A fire losses heat through convection and radiation. The former is associated with the motion of fluids in the environment in analysis, whereas the latter refers to the propagation of electromagnetic waves in the speed of light. It is the production of soot within the flame corpse (Figure 5.8) which provides the main means for the high emissions of thermal radiation normally achieved during a fire, differentiating highly emissive *luminous flames* (sooty) from low emissive *non-luminous flames* (non-sooty) (Figure 5.9).

5) If soot is not fully consumed by the oxidative regions within the flame corpse, it will eject at the top parts to form what we know as smoke (Figure 5.8). It is due to the presence of soot that we are able to describe such smoke bodies as either *grey* or *blackbodies* (Figure 5.5), exposing their high interaction with thermal radiation during a fire.

6) The radiation temperature achieved by this fire-induced gas phase will only equate the correspondent gas temperature if this mass of gas achieves *blackbody* behavior, marking a scenario in which thermal radiation is emitted at its maximum levels. Note that achieving such a condition is related to soot production during a fire.

7) If a *grey body* state is achieved instead then, the radiation temperature will be at a lower level than that of its correspondent gas temperature, meaning that the emissivity (ε_f in equation 5.13) will be smaller than one.

8) As the gas temperatures achieved within the flame corpse are highly inhomogeneous (Figure 5.14), the total amount of thermal radiation emitted from a fire is more often quantified in terms of a radiative fraction (Section 5.2.3.2) or, in other words, the percentual amount of HRR of a fire that is released through radiation. This radiative fraction is at its maximum value for small flame bodies and decays considerably for larger flames (Figure 5.15), where radiation reabsorption within the flame corpse itself is significantly larger. Therefore, there is simply no single value of radiative fraction which is representative to describe all fire scenarios related to a given fuel.

9) Due to limited computational capacity, in daily fire safety engineering practice, CFD fire simulations in FDS are most often performed in LES (Section 1.2.1). In this mode, the numerical resolution of gas temperatures within the reacting zone (Figure 5.11) is not reliable. Thus, in FDS, gas temperatures are better predicted further away from the fire source.

10) Given the importance of thermal radiation in fire analysis and considering that the emissions of radiation from a fire are related to the fourth power of flame temperatures (equation 5.13), FDS applies the radiative fraction to correct the emissions of thermal radiation from a fire (Section 5.2.3.2). Therefore, provided a correct value for this parameter is selected by the user, one can still expect an accurate resolution of the radiation field. For this reason, the thermal exposure imposed on structures surrounding or impinged by flames should still be properly characterized by FDS, even though the gas temperatures at such locations are not reliable.

10.1.2 Fire-Structure Interface

Heat is transferred from a fire to the structure through convection (Section 5.1.2) and radiation (Section 5.1.3). Convection heat transfer refers to the amount of heat that is supplied to the structure according to the temperature difference between that of the gases located in the vicinity of this structure and that of the structure itself, at a rate regulated by the conditions achieved by the flow (equation 5.5). Radiation heat transfer describes the net result of thermal

radiation absorbed and emitted by the structure during a fire. The total heat supplied through radiation can be simplified in terms of a hypothetical radiation temperature (Figure 5.6), and occurs according to the difference between the fourth power of this radiation temperature and that of the fourth power of the surface temperature of the structure (equation 5.12). Thus, the total heat transfer to the structure becomes the added contribution of these two terms (equation 5.1). With this at heart, the following conclusions regarding the interface between a fire and a structure hold:

1) AST combines the individual contributions of convection and radiation to the total heat transferred to the structure into a single term (equation 5.27), being able to fully characterize the thermal exposure imposed by a fire onto the structure. Note that this parameter will always assume a value in between its correspondent gas and radiation temperatures.

2) When assessing the response of structures subjected to fire, AST is the correct term to couple CFD-based calculations for the fire phase to the structural analysis of elements in FEA. The process of linking FDS and DIANA is highlighted in Section 9.5 of this master thesis.

3) Given the different dependency of convection and radiation on temperatures, as soon as a fire starts generating high temperatures within an enclosure, the radiation contribution to the heat transfer to the structure will take over convection, becoming the governing mode of heat supply from a fire to the structure (Figure 5.10). In practical terms, whenever a fire is imposing hazardous conditions on a structure, radiation is the primary term of concern (Figure 8.24).

4) As AST fully represents the fire-phase for the structural analysis, and considering that radiation heat transfer regulates the total amount of heat supplied to the structure, the AST will always tend towards the radiation temperature induced by a fire (look at the AST value, given by the grey line in Figure 5.18, for a gas temperature of $1000\ ^oC$ and a radiation temperature of $700\ ^oC$).

5) Note that very often structural engineers appear to be unaware of this radiation governance in fires. For this reason, it seems quite common to define the thermal boundary condition in a fire analysis for the structure solely based on convection heat transfer. In this case, the temperature development of the structure will be severely underpredicted (Figure 6.21 and Figure 6.22).

10.1.3 RWS Curve and The Prescriptive-Based Approach

The conclusions presented here are aimed at the development of the RWS curve and on the consequences of its use in a prescriptive-based approach:

1) The RWS curve appears to be the result of only two gas temperature measurements (Figure 7.14) from a test performed in a very narrow and short tunnel, where oxygen supply was practically unlimited. Note also, that the walls and ceiling of this tunnel were characterized by the use of materials with *insulation* thermal properties.

2) Despite the numerous uncertainties and limitations involved in reproducing the RWS tests through numerical simulations (Section 7.4.1), the FDS model developed in this thesis was able to replicate the original results fairly well (compare *Gas – MI_0.25_RWS 1980* with *RWS_1980* in Figure 7.39).

3) The results of this model also indicate that the fire-induced gas phase produced during the RWS test did not achieve *blackbody* behavior (compare *Gas – MI_0.25_RWS 1980* with *Rad – MI_0.25_RWS 1980* in Figure 7.38). As a consequence, it appears that the thermal exposure induced on the ceiling of the tunnel during the actual test was considerably smaller than that which is described by the use of the RWS curve (compare *AST – MI_0.25_RWS 1980* with *RWS Curve* in Figure 7.38). Note that the results of the study performed in Section 7.5.4 indicate that both gas and radiation temperatures, given in Figure 7.38, appear to be at their maximum values for the tunnel in question.

4) *Concrete* and *insulation materials* have completely distinct thermal properties (in special the thermal conductivity) and will react very differently to the same thermal exposure (Figure 8.24). In simple terms, *concrete* will extract much more energy from a fire than *insulation* (Figure 8.23). For this reason, the use of *insulation* on protecting tunnels also promotes heat confinement within the gas phase trapped inside the tunnel, contributing to enhancing the temperatures within the enclosure (compare *Gas – MI_0.25_Cocrete Tunnel* with *Gas – MI_0.25_RWS 1980* in Figure 7.43).

5) The conclusion presented above highlights the main flaw of the prescriptive-based approach. In essence, especially in the context of tunnel fires, where the boundaries of the enclosure are well defined and the structure of the tunnel is inherently located close to the fire source, applying the same time-temperature curve (e.g. RWS curve) to address *protected* and *unprotected concrete tunnels* necessarily mean that we are analyzing two distinct fire scenarios between those cases. Not only that, but this fire scenario has also to be more severe for the *unprotected concrete tunnel*. Therefore, if the RWS curve (which was developed for an *insulated tunnel*) can be assumed as being representative of the worst-case tunnel fire scenario then, it **should not be used** to describe *unprotected concrete tunnels*. Note that all fire simulations performed in this thesis support this claim (Figure 7.45; Figure 9.22; Figure 9.26; Figure 9.44; Figure 9.50; Figure 9.55).

6) Among all fire simulations performed for the case study of this thesis (Chapter 9), the maximum homogeneous thermal exposure of the cross-section of the tunnel as a whole, happened for the RWS fire scenario (200 MW gasoline fire) at a ventilation velocity of 3 m/s (i.e. approximately the critical velocity), and it is practically limited to the boundaries of the *hydrocarbon curve* during the total period of fire simulation (Figure 9.20). This reinforces the idea that if a prescriptive-based approach is to be used for the design of *unprotected concrete tunnels* then, the *hydrocarbon curve* represents a more reasonable choice.

7) The use of the RWS curve according to Eurocode 1 Part 1-2 [9] presupposes a *blackbody* behavior (i.e. gas and radiation temperatures are assumed equal) for the fire-induced gas phase. In practical terms, this means that the RWS curve is assumed to represent the AST for the structure under analysis (equation 5.25).

8) When considering this assumption in Eurocode 1 Part 1-2 [9], the RWS curve has shown to represent, if not the most, one of the most hazardous fire scenarios encountered in the literature (Section 8.1.2). The use of this curve prescribes a thermal exposure, at least, as severe as that which is generated by the most damaging jet fires (compare continuous red lines with dashed blue lines in Figure 8.13).

9) Furnace resistance tests constitute the primary means of testing structural elements in fire safety engineering. The following conclusions refer to these tests:

    a. There are two types of devices used to measure temperatures in fire safety tests, namely *wire thermocouples* (Figure 7.7) and *plate thermocouples* (Figure 7.22). The first type is more affected by convection heat transfer and will approach the true gas temperatures at the measuring position (Figure 7.23). The second type perceives the exposure in the same manner as the structure and will approach the AST at the measuring position (Figure 7.24). Thus, whenever the thermal exposure to the structure is to be controlled, *plate thermocouples* represent the correct choice.

    b. There are two types of furnaces, namely *optically shallow* and *optically deep* (Figure 8.34). For the former case, gas temperatures will be higher than the radiation temperatures within the furnace (Figure 8.37), whereas for the latter they will equal each other (Figure 8.36). If *wire thermocouples* are used to control the temperature development within *optically shallow* furnaces then, the thermal exposure imposed on the structure during the test will not be properly controlled. Note that this scenario appears to represent that which is achieved by tests performed by the use of the MobiFiRe [108] (Section 8.3.1) in the investigation of existing tunnel structures, indicating that the thermal exposure imposed on the structure during those tests might not be properly controlled.

10.1.4 Concrete Structures and The Performance-Based Approach

The conclusions drawn below are related to the response of concrete structures subjected to fire and to the use of a performance-based approach when assessing concrete tunnels:

1) Fire imposes one of the most hazardous conditions for concrete structures, leading to irreversible chemical and physical changes in the composition of the material. The main concerns are: (1) the severe thermal degradation of mechanical properties (i.e. compressive strength, tensile strength, and elastic modulus), as depicted in Section 6.2; (2) the development of thermal strains (Section 6.3.1); and (3) the occurrence of spalling (Figure 6.9).

2) Steep thermal gradients will form within concrete structures subjected to fire (Figure 6.14), inherently leading to the occurrence of eigen temperatures (Figure 6.12). As a consequence, thermal stresses will always develop inside the concrete structure during a fire (Figure 6.15).

3) Numerous parameters will have an influence on the total thermal stress state developed within the structure. Among those, we can state: (1) the support conditions (Figure 6.18); (2) the elastic modulus (Figure 6.19); and (3) the geometry of the structure (Figure 6.26). Note, for instance, that due to the nature of restrained deformations, the use of Eurocode 2 Part 1-2 [9] to describe normal strength concrete (Figure 6.4) might lead to unconservative results (compare blue and red lines in Figure 6.19).

4) Due to the occurrence of spalling, a new surface of the material (at a cooler temperature) is exposed to fire. As the heat exchange between a fire and the structure also depends on the temperature of the structure itself, a new boundary condition will be formed as soon as a piece of the structure spalls off the section, enhancing, once again, the amount of heat supplied to the structure (Figure 6.28). This means that the driving force for the occurrence of spalling is always renewed every time a large piece is spalled from the structure, which probably explains the continuous nature of the phenomenon.

5) Unless some external source of ventilation is applied, the idealized RWS fire scenario (i.e. a 200 MW gasoline pool fire burning for two hours) was found not to be sustainable within the case study of this thesis (Figure 9.7). For those cases (i.e. *ventilation-controlled* fires), the use of longitudinal ventilation will enhance the HRR.

6) Given the limitations involved on the case study (Section 9.6.1), the use of high ventilation velocities (for *fuel-controlled* fires) has shown to significantly reduce the overall gas temperatures (Figure 9.13 and Figure 9.34) and radiation temperatures (Figure 9.15 and Figure 9.35) along the tunnel, thus contributing to limit the total state of thermal exposure achieved within the tunnel (Figure 9.39). However, it must be pointed out that ventilation will not avoid the occurrence of zones of high thermal exposure for parts of the cross-section that are either impinged by flames or located really close to them (Figure 9.55).

7) The added benefit of the adoption of a performance-based approach is elucidated when both fire scenarios studied for the Piet Hein tunnel (i.e. 200 MW and 30 MW pool fires) are compared against each other. As shown by the longitudinal AST development at the ceiling (Figure 9.39), by accounting for the specific characteristics of a given tunnel (traffic restrictions, for instance) and selecting a more realistic fire scenario, one might considerably reduce the thermal exposure (AST) for the structural analysis.

8) One may expect to obtain a reduced temperature development for the structure in analysis when making use of a performance-based approach (green and red lines in Figure 9.66) in replacement to the conventional prescriptive-approach (blue line in Figure 9.66).

10.2 Recommendations

1) When assessing existing tunnels or in the design of new ones through a prescriptive-based approach, the use of the RWS curve should be limited to *insulated tunnels*. For *unprotected concrete tunnels*, the *hydrocarbon curve* should be used instead. Note that for both cases, the temperatures prescribed by the curve in question describe the AST for the structure under analysis, meaning that equation 5.25 must be applied to characterize the fire-structure interface.

2) Implement *plate thermocouples* as the controlling device for the MobiFiRe (Figure 8.28 and Figure 8.31).

3) Given the radiation governance when addressing structures subjected to fire, the focus of the tunnel fire community should move towards measuring the maximum heat fluxes generated by tunnel fires, rather than measuring the maximum gas temperatures achieved within the enclosure. In this sense, the work of Shaw et. al [119] might present a starting point. Also, notice that basing the structural design on heat fluxes rather than on temperatures is already common practice in other fields, such as the oil production industry (Table 8.1 and Table 8.2).

4) Practically equivalent levels of thermal stresses (Figure 6.24) were obtained for two completely distinct temperature evolutions within the same structure (Figure 6.22). This matter has to be further investigated by the inclusion of other types of physical nonlinearities (cracking and crushing) and even geometrical nonlinearities into the structural analysis of concrete tunnels subjected to fire. Note that properly characterizing the differences in the structural response of concrete under different temperature distributions is a primary concern if a performance-based approach is to be achieved in the near future.

5) A fundamental parameter when performing fire simulations in FDS is the radiative fraction for the selected fuel (fire scenario). Due to radiation reabsorption within the flames, for fires in the open, this radiative fraction is known to decrease for increasing fire sizes. However, especially when dealing with large tunnel fires where flames impinge on the ceiling propagating longitudinally along it, the heat feedback from the walls and ceiling might have an effect on the emissions of radiation from a fire. Therefore, the possible effects of the enclosure on the radiative fraction of tunnel fires is also a matter of interest.

6) Evaluating the differences in fuel consumption (HRR) between furnace tests of *concrete* and of *insulation* materials should also be an object of research.

7) Performing a parametric study to evaluate the influences of selecting different (1) radiative fractions and (2) soot yields into the numerical solution of the radiation field in FDS. Note that, in a performance-based approach, the resolution of the radiation field will determine the thermal exposure (AST) to be used for the structural analysis. Therefore, evaluating and quantifying the parameters that may affect the numerical

solution of the radiation transport equation in FDS is also of extreme importance for the use of a performance-based approach.

8) Given the importance of concrete's elastic modulus when analyzing the development of thermal stresses due to restrained imposed deformations, a proper characterization of the evolution of this mechanical property with temperature is required. For such a study, the use of H-TRIS (Figure 8.39) is recommended to ensure full control of the thermal exposure imposed on the specimen.

11 Appendices

11.1 Smoke Stratification

In the methodology proposed by Newman [16], Fr stands for the Froude number which is given by:

$$Fr = \frac{{u_{avg}}^2}{\sqrt{\frac{\Delta T_{cf}}{T_{avg}} gH}} \; ; \; u_{avg} = \frac{u\, T_{avg}}{T_a}$$

where u is the air velocity upstream the fire (m/s), ΔT_{cf} is the temperature difference between the floor and the ceiling (K), T_{avg} is the average temperature in the cross-section (K), T_a is the ambient temperature (K), g is acceleration of gravity (m/s^2) and H is the ceiling height (m).

Newman [16], also suggested equations to calculate the temperatures at the ceiling for regions I and II, which are needed in the calculation of the Froude number. In a later study, Nyman and Ingason [17] investigated the use of those equations to describe the results of large and model-scale tests. They claimed that the equations below provide a better fit to evaluate tunnels:

$$\Delta T_{ca} = 1.06 \left[\frac{gH}{T_{avg}{u_{avg}}^2}\right]^{0.23} \Delta T_{avg}^{1.23} \; ; \; \Delta T_{cf} = 0.225 \left[\frac{gH}{T_{avg}{u_{avg}}^2}\right] \Delta T_{avg}^2$$

where ΔT_{ca} is the temperature difference between the ceiling and the ambient temperature (K). Also a more reasonable value for the interface of Regions II and III should be given by Fr > 3.2.

Once T_{avg}, ΔT_{avg} and u_{avg} are known, the ceiling and floor temperatures can be calculated by the equations above. It is important to highlight that those are purely empirical and are only to be used in the estimation of the Froude number to define the level of smoke stratification. Moreover, they should not be considered as the real ceiling temperatures. Models to predict those temperatures are presented on Section 3.3.2.1.

11.2 Flame Length

According to Qiu et al. [37], the flame length can be calculated separately for cases *with* or *without* ventilation, according to:

1) Correlation for the flame length in tunnels **without** longitudinal air flow:

Note that the proportionality between the dimensionless flame length and the second term of the righthand side of the equation below is assumed to hold at all times. The coefficient was determined through the experiment results. Also, the flame density (ρ_f) is assumed to be equal 0.32 kg/m^3 considering a flame temperature of *1100 K*.

$$\frac{l_{f,0}}{D} = 10.20\left[\frac{\left(\frac{H_f - H_{ef}}{H_f}\right)}{\sqrt{\frac{2\Delta\rho_f}{\rho_a}}}\right] Q^{**}$$

with

$$H_f = -1.02D + 0.235Q^{\frac{2}{5}};\ Q^{**} = \frac{Q}{3013\rho_a\sqrt{gH_{ef}}WD}$$

where $l_{f,0}$ is the flame length without longitudinal airflow (m), D is the equivalent diameter of the fire source (m), H_{ef} is the effective height from the fire source to the tunnel ceiling (m), $\Delta\rho_f$ is the density difference between flame (ρ_f) and ambient air (ρ_a) (kg/m^3), and W is the tunnel width (m).

2) Correlation for flame length of tunnels **with** longitudinal air flow:

The following formulae is valid for $0.199 \leq Q^{**} \leq 0.427$ *and* $0.3 \leq u \leq 1.8$.

- *Flame length upstream the fire source* ($l_{f,us}$):

$$\frac{l_{f,us}}{D} = 60.24\left(\frac{H_f - H_{ef}/\cos\theta}{H_f}\right)\left[\frac{\sqrt{\frac{2\Delta\rho_f}{\rho_a}gH_{ef}} - u}{2\sqrt{\frac{2\Delta\rho_f}{\rho_a}gH_{ef}}}\right] Q^{**}$$

with

$$H_f = -1.02D + 0.235Q^{\frac{2}{5}};\ Q^{**} = \frac{Q}{3013\rho_a\sqrt{gH_{ef}}WD}$$

- *Flame length downstream the fire source* ($l_{f,ds}$):

$$\frac{l_{f,ds}}{D} = 43.78\left(\frac{H_f - H_{ef}/\cos\theta}{H_f}\right)\left[\frac{\sqrt{\frac{2\Delta\rho_f}{\rho_a}gH_{ef}} - u}{2\sqrt{\frac{2\Delta\rho_f}{\rho_a}gH_{ef}}}\right] Q^{**}$$

- *Total flame length* ($l_{f,t}$):

Is given by the simple summation of the equations above, but can be simplified by the equation provided below:

$$\frac{l_{f,t}}{D} = 104.02\left(\frac{H_f - H_{ef}/\cos\theta}{H_f}\right) Q^{**}$$

In the above equations, u_a is the longitudinal air flow speed (m/s) and θ is the flame tilt angle (degree), which is given by:

$$\theta = arctan\left[9.1\left(\frac{800\rho_a c_p u^5}{Q}\left(\frac{T_a}{800g}\right)^2\right)^{\frac{1}{5}}\right]$$

where $l_{f,0}$ is the flame length without longitudinal airflow (m), D is the equivalent diameter of the fire source (m), H_{ef} is the effective height from the fire source to the tunnel ceiling (m), $\Delta\rho_f$ is the density difference between flame (ρ_f) and ambient air (ρ_a) (kg/m^3), and W is the tunnel width (m).

11.3 Variation of AST with Radiation Temperatures for Fixed Gas Temperatures

Figure 5.18 is constructed based on the solution of T_{AST} for four fixed levels of T_g and varying levels of T_r according to the equation below:

$$\varepsilon_s\sigma(T_r^4 - T_{AST}^4) + h(T_g - T_{AST}) = 0$$

where σ is the Stefan-Boltzmann constant (5.67 x 10^{-8} W/(m^{2}K^4)), T_r is the radiation temperature (K), T_g is the gas temperature (K), T_{AST} is the adiabatic surface temperature (K), h is the convection heat transfer coefficient which is assumed to be equal to 50 W/(m^2.K), and ε_s is the surface emissivity which is here taken as 0.7. Both levels are described in Eurocode 1 Part 1-2 as representative for concrete structures subjected to tunnel fires.

The results are provided by Table 11.1 below.

	$T_g = 20\ ^oC$	$T_g = 100\ ^oC$	$T_g = 500\ ^oC$	$T_g = 1000\ ^oC$
$T_r\ [^oC]$	$T_{AST}\ [^oC]$	$T_{AST}\ [^oC]$	$T_{AST}\ [^oC]$	$T_{AST}\ [^oC]$
0	19	91	369	581
100	29	100	375	585
200	51	121	388	593
300	92	158	411	608
400	156	217	448	632
500	246	299	500	666
600	356	399	567	712
700	478	511	646	770
800	604	628	734	839
900	727	746	830	916
1000	849	863	929	1000
1100	967	978	1030	1089
1200	1082	1091	1133	1182
1300	1195	1202	1237	1277
1400	1306	1312	1340	1374
1500	1415	1420	1444	1473

TABLE 11.1 – EVOLUTION OF AST WITH RADIATION TEMPERATURE FOR FIXED GAS TEMPERATURES

11.4 Radiation Governance in Fire Analysis

Due to the high temperatures achieved in fires, radiation will be the governing mode of heat transfer to the structure. As explained previously, the total heat flux to the structure is given by the equation below:

$$\dot{q}''_{tot} = \varepsilon_s \sigma \left(T_r^4 - T_{surface}^4\right) + h(T_g - T_{surface})$$

where $\dot{q}''_{tot}$ is the total heat flux (W/ m^2), σ is the Stefan-Boltzmann constant (5.67 x 10^{-8} W/(m^{2}K^4)), T_r is the radiation temperature (K), T_g is the gas temperature (K), h is the convection heat transfer coefficient which is assumed to be equal to 50 W/(m^2.K), $T_{surface}$ is the surface temperature achieved by the structure (K) and ε_s is the surface emissivity which is here taken as 0.2, 0.7 and 1.0.

The first term on the right-hand side is related to the radiation contribution ($\dot{q}''_{rad}$) to the total heat flux, while the second term provides the convection parcel ($\dot{q}''_{con}$). To understand why radiation is the governing mode of heat transfer to the structure, the equation above was solved for three fixed levels of surface temperature (i.e. 20 ºC, 500 ºC and 1000 ºC), while varying the values of temperature exposure from the reference surface temperature up to a maximum value of 1500 ºC. Note that equivalent levels of gas and radiation temperatures (i.e. $T_g = T_r$) were considered in this study. The results are provided by Table 11.2 to Table 11.4 and plotted in Figure 5.10.

$T_g = T_r$ [^oC]	$T_{surface} = 20\ ^oC$			
	$\dot{q}''_{con}$ [kW/m^2]	$\dot{q}''_{rad_}\varepsilon_s = 0.2$ [kW/m^2]	$\dot{q}''_{rad_}\varepsilon_s = 0.7$ [kW/m^2]	$\dot{q}''_{rad_}\varepsilon_s = 1.0$ [kW/m^2]
20	0.0	0.0	0.0	0.0
50	1.5	0.0	0.1	0.2
100	4.0	0.1	0.5	0.7
150	6.5	0.3	1.0	1.4
200	9.0	0.5	1.7	2.4
250	11.5	0.8	2.7	3.8
300	14.0	1.1	4.0	5.7
350	16.5	1.6	5.7	8.1
400	19.0	2.2	7.8	11.2
450	21.5	3.0	10.6	15.1
500	24.0	4.0	13.9	19.8
550	26.5	5.1	17.9	25.6
600	29.0	6.5	22.8	32.5
650	31.5	8.1	28.5	40.7
700	34.0	10.1	35.3	50.4
750	36.5	12.3	43.2	61.7
800	39.0	14.9	52.3	74.7
850	41.5	18.0	62.8	89.8
900	44.0	21.4	74.8	106.9
950	46.5	25.3	88.5	126.4
1000	49.0	29.7	103.9	148.5
1050	51.5	34.7	121.3	173.3
1100	54.0	40.2	140.8	201.1
1150	56.5	46.4	162.4	232.1
1200	59.0	53.3	186.6	266.5
1250	61.5	60.9	213.2	304.6
1300	64.0	69.3	242.7	346.7
1350	66.5	78.6	275.1	393.0
1400	69.0	88.8	310.6	443.8
1450	71.5	99.9	349.5	499.3
1500	74.0	112.0	391.9	559.9

TABLE 11.2 – RADIATION AND CONVECTION CONTRIBUTIONS TO THE TOTAL HEAT FLUX TO THE STRUCTURE FOR TSURFACE = 20 ºC

$T_g = T_r$ [^oC]	$T_{surface} = 500\ ^oC$			
	$\dot{q}''_{con}$ [kW/m^2]	$\dot{q}''_{rad_}\varepsilon_s = 0.2$ [kW/m^2]	$\dot{q}''_{rad_}\varepsilon_s = 0.7$ [kW/m^2]	$\dot{q}''_{rad_}\varepsilon_s = 1.0$ [kW/m^2]
500	0.0	0.0	0.0	0.0
550	2.5	1.2	4.0	5.8
600	5.0	2.5	8.9	12.7
650	7.5	4.2	14.6	20.9
700	10.0	6.1	21.4	30.6
750	12.5	8.4	29.3	41.9
800	15.0	11.0	38.4	54.9
850	17.5	14.0	49.0	69.9
900	20.0	17.4	61.0	87.1
950	22.5	21.3	74.6	106.6
1000	25.0	25.7	90.1	128.7
1050	27.5	30.7	107.4	153.5
1100	30.0	36.3	126.9	181.3
1150	32.5	42.4	148.6	212.2
1200	35.0	49.3	172.7	246.7
1250	37.5	57.0	199.4	284.8
1300	40.0	65.4	228.8	326.9
1350	42.5	74.6	261.2	373.2
1400	45.0	84.8	296.8	423.9
1450	47.5	95.9	335.6	479.5
1500	50.0	108.0	378.0	540.1

TABLE 11.3 – RADIATION AND CONVECTION CONTRIBUTIONS TO THE TOTAL HEAT FLUX TO THE STRUCTURE FOR TSURFACE = 500 °C

$T_g = T_r$ [^oC]	$T_{surface} = 1000\ ^oC$			
	$\dot{q}''_{con}$ [kW/m^2]	$\dot{q}''_{rad_}\varepsilon_s = 0.2$ [kW/m^2]	$\dot{q}''_{rad_}\varepsilon_s = 0.7$ [kW/m^2]	$\dot{q}''_{rad_}\varepsilon_s = 1.0$ [kW/m^2]
1000	0.0	0.0	0.0	0.0
1050	2.5	5.0	17.4	24.8
1100	5.0	10.5	36.8	52.6
1150	7.5	16.7	58.5	83.6
1200	10.0	23.6	82.6	118.0
1250	12.5	31.2	109.3	156.2
1300	15.0	39.6	138.8	198.2
1350	17.5	48.9	171.2	244.5
1400	20.0	59.1	206.7	295.3
1450	22.5	70.2	245.6	350.8
1500	25.0	82.3	288.0	411.4

TABLE 11.4 - RADIATION AND CONVECTION CONTRIBUTIONS TO THE TOTAL HEAT FLUX TO THE STRUCTURE FOR TSURFACE = 1000 °C

11.5 Calibration of DIANA's Heat Conduction Solution

Annex A of Eurocode 2 Part 1-2 [9] provides the developed temperature profiles within concrete slabs which are subjected to the standard-curve exposure (Figure 8.1) for a total exposure time in a range of *30 – 240 minutes*. The calculated temperature profiles consider the following properties:

- Lower limit of thermal conductivity (Figure 11.2).
- Specific heat capacity of concrete with a moisture content of 1.5% (*u=1,5%* in Figure 11.3).
- Concrete's density variation due to water loss as depicted in Figure 11.4.
- Concrete's emissivity = 0.7
- Convection heat transfer coefficient = 25 W/m^2.K

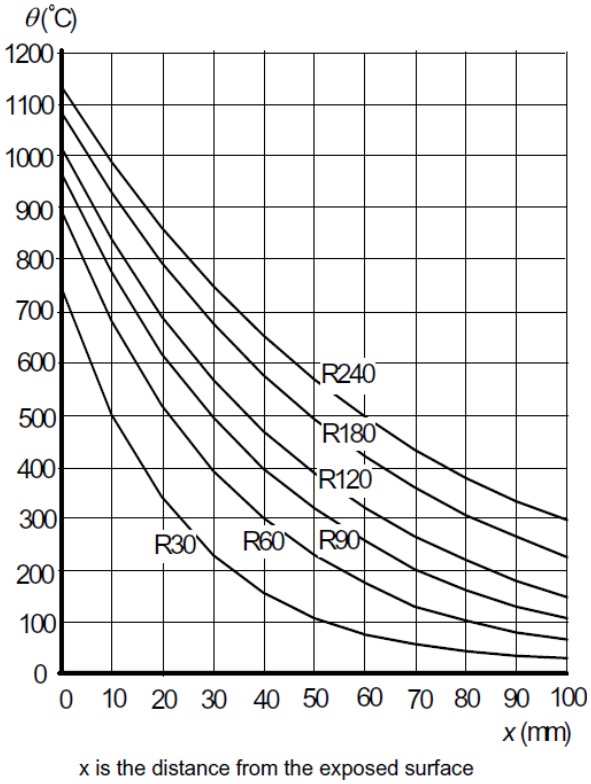


FIGURE 11.1 – TEMPERATURE PROFILES FOR CONCRETE SLABS EXPOSED TO THE STANDARD CURVE
Retrieved from Eurocode 2 Part 1-2 [9]

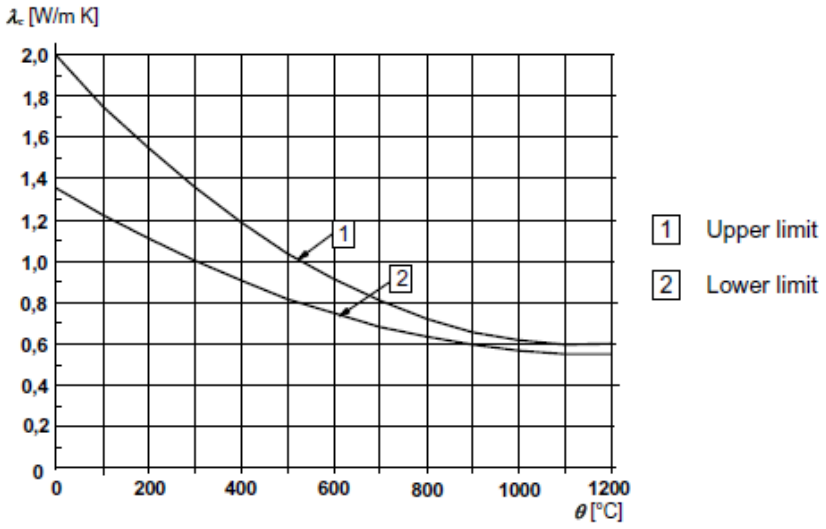


FIGURE 11.2 – THERMAL CONDUCTIVITY OF CONCRETE
Retrieved from Eurocode 2 Part 1-2 [9]

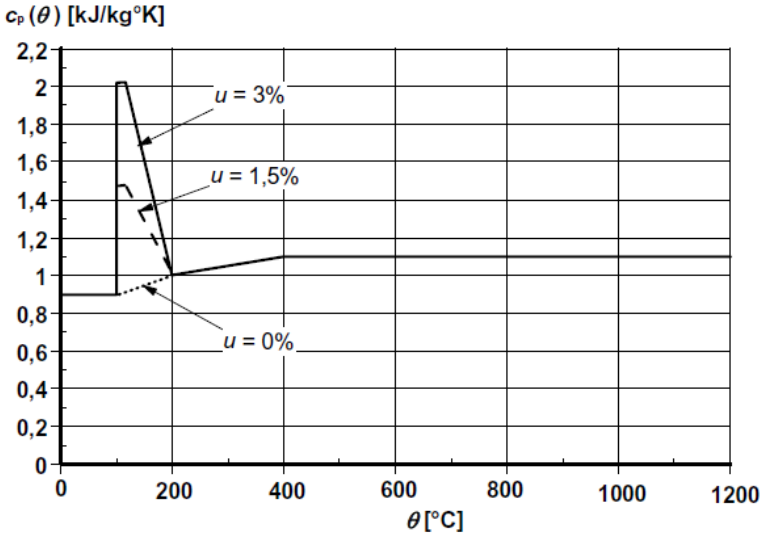


FIGURE 11.3 – SPECIFIC HEAT OF CONCRETE
Retrieved from Eurocode 2 Part 1-2 [9]

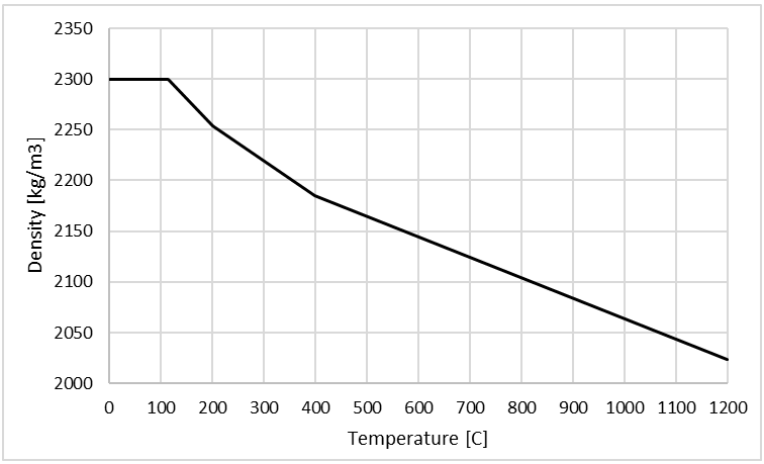


FIGURE 11.4 – VARIATION OF CONCRETE'S DENSITY WITH TEMPERATURE DUE TO WATER LOSS
Based on Eurocode 2 Part 1-2 [9]

To ensure that the results of the heat flow analyses performed in DIANA for the study developed in Section 8.2.4 (i.e. concrete and insulation response to the RWS exposure) were reliable, first the mesh size and time step chosen for the models had to be calibrated. Thus, the temperature profiles provided by Figure 11.1 were used as reference to analyze the quality of the numerical solution. As it can be seen by looking at Figure 11.5, a mesh size of *0.01 m* with a time step of *10 seconds* were found to provide enough resolution for the problem, as the temperature profiles obtained in DIANA were quite comparable to those of Eurocode 2 Part 1-2 [9] (Figure 11.5), when considering exactly the same conditions.

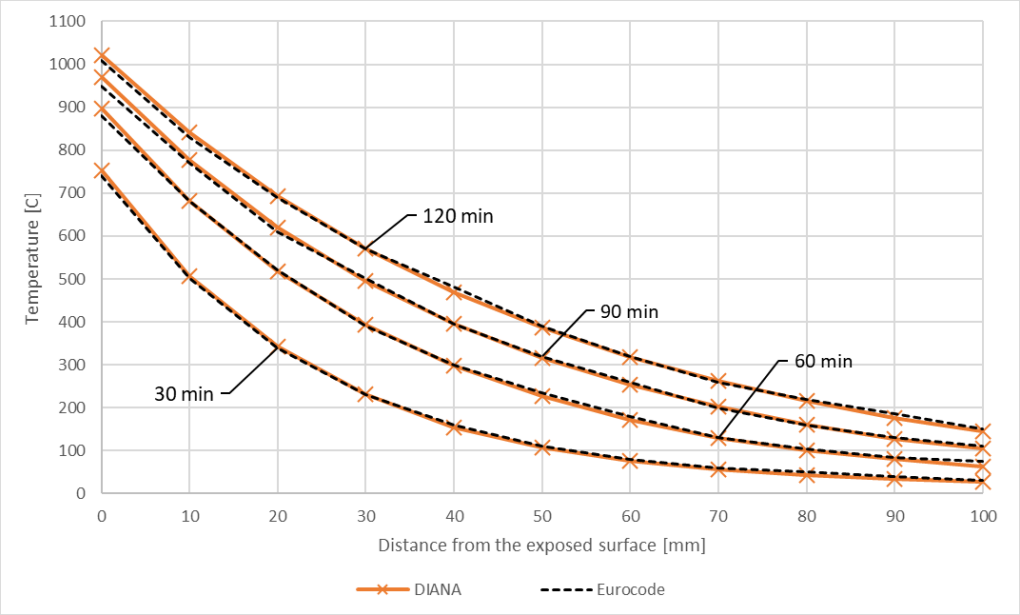


FIGURE 11.5 – TEMPERATURE PROFILES (DIANA VS EUROCODE)

11.6 Comparison of Thermal Exposure

In order to prove that the thermal exposure imposed by a scenario in which the incident heat flux of *350 kW/m²* is purely radiative is more aggressive than the thermal exposure generated by an initial heat flux of *350 kW/m²* in which the incident radiation equals *230 kW/m²* and the initial convective heat flux is *120 kW/m²* consider the following:

- *Case I: Hypothetical case of a structure subjected to a constant radiative heat flux* $(\dot{q}''_{inc,rad})$ *of* $350\ kW/m^2$

In this case the total heat flux to the structure can be calculated according to the equation below:

$$\dot{q}''_{tot,Case\ I} = \varepsilon_{surface}\left(\dot{q}''_{inc,rad} - \sigma T^4_{surface}\right)$$

If we assume $\varepsilon_{surface} = 1$, then we can solve $\dot{q}''_{tot,Case\ I}$ for different values of $T_{surface}$. The results are shown in Table 11.5.

- *Case II: Maximum gas jet fire as described in FABIG (2014) [102]*

  - Initial $T_{surface} = 293\ K$
  - $h = 95\ kW/m^2K$
  - $T_{flame} = 1560\ K$
  - $\dot{q}''_{initial,conv} = 0.095\ x\ (1560 - 293) = 120\ kW/m^2$
  - $\varepsilon_{flame} = 0.7$
  - $\dot{q}''_{inc,rad} = 0.7\ x\ 5.67\ .10^{-8}\ x\ 1560^4 = 230\ kW/m^2$

Thus the total heat flux to the structure can be calculated based on equation below:

$$\dot{q}''_{tot,Case\ II} = \varepsilon_s\left(\dot{q}''_{inc,rad} - \sigma T^4_{surface}\right) + h(T_f - T_{surface})$$

Also here if we assume $\varepsilon_{surface} = 1$, then we can solve $\dot{q}''_{tot,Case\ II}$ for different values of $T_{surface}$. The results of *Case II* are shown in comparison with *Case I* in Table 11.5. Note that the values given by this table are used to plot the graphs shown in Figure 8.10.

$T_{surface}\ [^oC]$	$\dot{q}''_{tot,Case\ I}\ [kW/m^2]$	$\dot{q}''_{tot,Case\ II}\ [kW/m^2]$
20	349.6	349.9
50	349.4	346.9
100	348.9	341.7
150	348.2	336.2
200	347.2	330.4
250	345.8	324.3
300	343.9	317.7
350	341.5	310.5
400	338.4	302.6
450	334.5	294.0
500	329.8	284.5
550	324.0	274.0
600	317.1	262.3
650	308.8	249.4
700	299.2	234.9
750	287.9	218.9
800	274.8	201.1
850	259.8	181.3
900	242.7	159.4
950	223.2	135.2
1000	201.1	108.4
1050	176.3	78.8
1100	148.5	46.3

TABLE 11.5 – TOTAL HEAT FLUX TO THE STRUCTURE

11.7 Thermal Boundary Conditions for Pool and Jet Fires

Section 8.1.2.3 compares the thermal response of a concrete structure subjected to three different fire scenarios, namely (1) the RWS curve, (2) a pool fire and (3) a jet fire. The recommendations given in FABIG [102] were used in order to create thermal boundary conditions to express the maximum exposure generated by pool and jet fires. According to this guideline, the total heat flux to the structure can be calculated based on the equation below:

$$\dot{q}''_{tot} = \varepsilon_s \sigma \left(\varepsilon_f T_f^4 - T_{surface}^4\right) + h(T_f - T_{surface})$$

where $\dot{q}''_{tot}$ is the total heat flux to the structure (W/m^2), ε_s is the surface emissivity (0.7 for concrete), σ is the Stefan-Boltzmann constant (5.67 x 10^{-8} W/(m^{2}K^4)), ε_f is the flame emissivity, T_f is the flame temperature (K), $T_{surface}$ is the development of the surface temperature in time (K), and h is the convective heat transfer coefficient (W/(m^2.K)).

The recommended values to represent the worst-case for pool and jet fires are given in Table 11.6.

Fire Scenario	Flame Emissivity (ε_f)	Flame Temperature (T_f)	Convection Heat Transfer Coefficient (h)
Pool Fire	0.9 (Modified to 0.62)	1460 K	20 W/(m^2.K)
Jet Fire	0.85	1560 K	95 W/(m^2.K)

TABLE 11.6 – MAXIMUM THERMAL EXPOSURE EXPECTED FROM POOL AND JET FIRES
Retrieved from FABIG [102]

Note that the product of the Stefan-Boltzmann constant (σ), the flame emissivity (ε_f), and the fourth power of the flame temperature (T_f) represents the amount of thermal radiation which is generated by the considered fire scenario. When looking at the values proposed for the maximum exposure expected for a large hydrocarbon pool fire, we can see that the use of FABIG [102] imposes an incident radiative heat flux of *~230 kW/m²*. However, as described in the same guideline, the maximum heat flux generated by hydrocarbon liquid fuels of high molecular weight seems to be limited to *~160 kW/m²* (Figure 8.8). Therefore, as the use of the values described in FABIG [102] appear to be too conservative to represent a gasoline pool fire in the open, the flame emissivity (ε_f) of the pool is reduced to 0.62 in Table 11.6 in order to consider an incident radiative heat flux of *160 kW/m²* in replacement to what is originally proposed by this guideline. With this in mind and based on the concept of AST, which was introduced in Section 5.3.3.3, one may calculate an equivalent thermal boundary condition to represent each one of those fire scenarios (i.e. pool and jet fire) when performing a transient thermal analysis for the structure in a FEA software. This is done by solving the equation below for T_{AST}:

$$\varepsilon_s \sigma \left(\varepsilon_f T_f^4 - T_{AST}^4 \right) + h \left(T_f - T_{AST} \right) = 0$$

Accordingly, Table 11.7 below provides the thermal boundary conditions used in DIANA to express pool and jet fires in the study performed in Section 8.1.2.3.

Fire Scenario	Adiabatic Surface Temperature (T_{AST})	Convection Heat Transfer Coefficient (h)
Pool Fire	1305 K	20 W/(m².K)
Jet Fire	1507 K	95 W/(m².K)

TABLE 11.7 – THERMAL BOUNDARY CONDITIONS

12 References

1. *Guidelines for structural fire resistance for road tunnels*. 2004, (ITA) International Tunneling Association.
2. Ingason, H., Li, Y. Z., and Lönnemark, A., *Tunnel Fire Dynamics*. 2015: Springer.
3. Haack, A., *Fire Protection in Traffic Tunnels : General Aspects and Results of the EUREKA Project.* Tunnelling and Underground Space Technology, 1999. **13**(4): p. 377-381.
4. *Memorial Tunnel Fire Ventilation Test Program*. 1995, Massachusetts Highway Department.
5. Ingason, H., Lönnermark, A. and Li, Y. Z., *Runehamar Tunnel Fire Tests*. 2011, SP Technincal Research Institute of Sweden.
6. *National Annex to NEN-EN 1991-1-2+C1: Eurocode 1 - Actions on structures - Part 1-2: General actions - Actions on structures exposed to fire*, (NEN) Nederlands Normalisatie-instituut, 2011.
7. *Richtlijnen Ontwerp Kunstwerken*, Rijkswaterstaat, 2017, Ministerie van Infrastructuur en Milieu.
8. Rijkswaterstaat, *Basisspecificatie TTI RWS Tunnelsysteem*, Ministerie van Infrastructuur en Milieu, 2016.
9. *NEN-EN 1992-1-2 Eurocode 2: Design of concrete structures - Part 1-2: General rules - Structural fire design*, (NEN) Nederlands Normalisatie-instituut, 2006.
10. *National Annex to NEN-EN 1992-1-2 Eurocode 2: Design of concrete structures - Part 1-2: General rules - Structural fire design*, (NEN) Nederlands Normalisatie-instituut, 2011.
11. *Fire testing procedure for concrete tunnel linings*. 2008, Efectis.
12. van der Waart van Gulik, T. G., et al., *Spalling behaviour of a non-spalling qualified concrete*. 2014.
13. McGrattan, K. and Milles, S., *In: Hurley, M. J. In the SFPE Handbook of Fire Protection Engineering*. 5th ed. 2016: Springer.
14. Ingason, H., *In: Beard A. N. and Carvel R.O.; In The Handbook of Tunnel Fire Safety*. 2nd ed. 2012, London: ICE Publishing.
15. Karlsson, B. and Quintiere, J., *Enclousure Fire Dynamics*. 1st ed. 2000, Boca Raton, USA: CRC Press.
16. Newman, J. S., *Experimental evaluation of fire-induced stratification.* Combustion and Flame, 1984. **57**(1): p. 33-39.
17. Nyman, H. and Ingason, H., *Temperature stratification in tunnels.* Fire Safety Journal, 2012. **48**: p. 30-37.

18. Thomas, P. H., *The movement of buoyant fluid against a stream and the venting of underground fires.* Fire Research Station, 1958.

19. Vantelon, J. P., et al., *Investigation of fire-induced smoke movement in tunnels and stations: An application to the paris metro.* Fire Safety Science: Proceedings of the Third International Symposium, 1991: p. 907-918.

20. Li, Y. Z., Lei, B. and Ingason, H., *Study of critical velocity and backlayering length in longitudinally ventilated tunnel fires.* Fire Safety Journal, 2010. **45**(6-8): p. 361-370.

21. Gannouni, S. and Maad, R. B., *Numerical study of the effect of blockage on critical velocity and backlayering length in longitudinally ventilated tunnel fires.* Tunnelling and Underground Space Technology, 2015. **48**: p. 147-155.

22. Meng, N., et al., *Effect of blockage ratio on backlayering length of thermal smoke flow in a longitudinally ventilated tunnel.* Applied Thermal Engineering, 2018. **132**: p. 1-7.

23. Ingason, H., *State of the Art of Tunnel Fire Research.* Fire Safety Science, 2008. **9**: p. 33-48.

24. Thomas, P. H., *The movement of smoke in horizontal passages against an air flow.* Fire Research Station, 1968(723).

25. Oka, Y. and Atkinson, G. T., *Control of Smoke Flow in Tunnel Fires.* Fire Safety Journal, 1996. **25**: p. 305-322.

26. Wu, Y. and Bakar, M. Z. A., *Control of smoke flow in tunnel fires using longitudinal ventilation systems - a study of the critical velocity.* Fire Safety Journal, 2000. **35**(4): p. 363-390.

27. Kunsch, J., *Simple model for control of fire gases in a ventilated tunnel.* Fire Safety Journal, 2002. **37**(1): p. 67-81.

28. Li, Y. Z. and Ingason, H., *Effect of cross section on critical velocity in longitudinally ventilated tunnel fires.* Fire Safety Journal, 2017. **91**: p. 303-311.

29. Hwang, C. C. and Edwards, J. C., *The critical ventilation velocity in tunnel fires—a computer simulation.* Fire Safety Journal, 2005. **40**(3): p. 213-244.

30. Vauquelin, O. and Wu, Y., *Influence of tunnel width on longitudinal smoke control.* Fire Safety Journal, 2006. **41**(6): p. 420-426.

31. Tsai, K. C., Chen, H. H. and Lee, S. K., *Critical ventilation velocity for multi-source tunnel fires.* Journal of Wind Engineering and Industrial Aerodynamics, 2010. **98**(10-11): p. 650-660.

32. Carvel, R. O., Beard, A. N., and Jowitt, P. W., *Fire Spread Between Vehicles in Tunnels: Effects of Tunnel Size, Longitudinal Ventilation and Vehicle Spacing.* Fire Technology, 2005. **41**(4): p. 271-304.

33. Lönnermark, A. and Ingason, H., *Fire Spread and Flame Length in Large-Scale Tunnel Fires.* Fire Technology, 2006. **42**(4): p. 283-302.

34. de Poli, M., *Fire dynamics and spalling mechanism in tunnel infrastructures*, MSc Thesis. 2018, Delft University of Technology.

35. Rew, C. and Deaves, D., *Fire spread and flame length in ventilated tunnels—a model used in Channel tunnel assessments*. in *in: Proceedings of the International Conference on Tunnel Fires and Escape from Tunnels*. 1999. Lyon, France.

36. Ingason, H. and Li, Y. Z., *Model scale tunnel fire tests with longitudinal ventilation.* Fire Safety Journal, 2010. **45**(6-8): p. 371-384.

37. Qiu, A., et al., *Flame extension lengths beneath a confined ceiling induced by fire in a channel with longitudinal air flow.* Fire Safety Journal, 2018. **97**: p. 29-43.

38. Wang, H. Y., *Numerical and theoretical evaluations of the propagation of smoke and fire in a full-scale tunnel.* Fire Safety Journal, 2012. **49**: p. 10-21.

39. Li, Y. Z. and Ingason, H., *The maximum ceiling gas temperature in a large tunnel fire.* Fire Safety Journal, 2012. **48**: p. 38-48.

40. Kurioka, H., et al., *Fire properties in near field of square fire source with longitudinal ventilation in tunnels.* Fire Safety Journal, 2003. **38**(4): p. 319-340.

41. Hu, L. H., et al., *On the maximum smoke temperature under the ceiling in tunnel fires.* Tunnelling and Underground Space Technology, 2006. **21**(6): p. 650-655.

42. Li, Y. Z. and Ingason, H., *Maximum Ceiling Temperature in a Tunnel Fire*. 2010, SP Technical Research Institute of Sweden: Sweden.

43. Li, Y. Z., Lei, B. and Ingason, H., *The maximum temperature of buoyancy-driven smoke flow beneath the ceiling in tunnel fires.* Fire Safety Journal, 2011. **46**(4): p. 204-210.

44. Lönnermark, A. and Ingason, H., *The Effect of Cross-sectional Area and Air Velocity on the Conditions in a Tunnel during a Fire*. 2007, SP Techinical Reseach Institute of Sweden: Sweden.

45. Ji, J., et al., *Experimental investigation on influence of different transverse fire locations on maximum smoke temperature under the tunnel ceiling.* International Journal of Heat and Mass Transfer, 2012. **55**(17-18): p. 4817-4826.

46. Fan, C. G., et al., *Effect of tunnel cross section on gas temperatures and heat fluxes in case of large heat release rate.* Applied Thermal Engineering, 2016. **93**: p. 405-415.

47. Zhao, X., et al., *An extended model for predicting the temperature distribution of large area fire ascribed to multiple fuel source in tunnel.* Tunnelling and Underground Space Technology, 2019. **85**: p. 252-258.

48. Fan, C. G., et al., *Experimental study on transverse smoke temperature distribution in road tunnel fires.* Tunnelling and Underground Space Technology, 2013. **37**: p. 89-95.

49. Ingason, H., *Fire development in large tunnel fires*. in *Fire Safety Science - Proceedings of the eight international symposium*. 2005.

50. Hansen, R. and Ingason, H., *Heat release rates of multiple objects at varying distances.* Fire Safety Journal, 2012. **52**: p. 1-10.

51. (UPTUN) Upgrading of existing tunnels for fire safety, *Fire scenarios and accidents in the past*. 2008.

52. (UPTUN) Upgrading of existing tunnels for fire safety, *Design fire scenarios*. 2008.

53. Lönnermark, A., *On the Characteristics of Fires in Tunnels, Department of Fire Safety Engineering and Systems Safety*. 2005, Lund University.

54. Ingason, H., *Effects of Ventilation on Heat Release Rate of Pool Fires in a Model Tunnel*. 1995, SP Techinical Research Institute of Sweden: Sweden.

55. Carvel, R. O., et al., *Variation of heat release rate with forced longitudinal ventilation for vehicle fires in tunnels.* Fire Safety Journal, 2001. **36**: p. 569-596.

56. Li, Y. Z. and Ingason, H., *The Fire Growth Rate in a Ventilated Tunnel Fire.* Fire Safety Science, 2011. **10**: p. 347-258.

57. Carvel, R. O., et al., *The influence of tunnel geometry and ventilation on the heat release rate of a fire.* Fire Technology, 2004. **40**: p. 5-26.

58. Li, Y. Z., et al., *Effect of cross section and ventilation on heat release rates in tunnel fires.* Tunnelling and Underground Space Technology, 2016. **51**: p. 414-423.

59. Li, L., et al., *Effect of longitudinal ventilation on heat release rate of tunnel fires.* Tunnelling and Underground Space Technology, 2012. **30**: p. 230-232.

60. Roh, J. S., et al., *Critical velocity and burning rate in pool fire during longitudinal ventilation.* Tunnelling and Underground Space Technology, 2007. **22**(3): p. 262-271.

61. Davidson, M. T., Harik, I. E. and Davis, D. B., *Fire Impact and Passive Fire Protection of Infrastructure: State of the Art.* Journal of Performance of Constructed Facilities, 2013. **27**(2): p. 135-143.

62. Tomar, M. S. and Khurana, S., *Impact of passive fire protection on heat release rates in road tunnel fire: A review.* Tunnelling and Underground Space Technology, 2019. **85**: p. 149-159.

63. Kim, H. K., Lönnermark, A. and Ingason, H., *Effective Firefighting Operations in Road Tunnels*. 2010, SP Techinical Research Institute of Sweden: Sweden.

64. Waterstaat, I.V.e., *Vervoer gevaarlijke stoffen en tunnels*, Ministerie van Infrastructuur en Milieu. 2011.

65. Drysdale, D., *An Introduction to Fire Dynamics*. 3rd ed. 2011: Wiley.

66. Wickström, U., *Temperature Calculation in Fire Safety Engineering*. 2016: Springer.

67. Wickström, U., *In: Hurley, M. J. In the SFPE Handbook of Fire Protection Engineering*. 5th ed. 2016: Springer.

68. Tien, C. L., Lee, K. Y., and Stretton, A. J., *In: Hurley, M. J. In the SFPE Handbook of Fire Protection Engineering*. 5th ed. 2016: Springer.

69. Kholghy, M. R., *The Evolution of Soot Morphology in Laminar Co-Flow Diffusion Flames of the Surrogates for Jet-A-1 and Synthetic Kerosene*, in *Department of Mechanical and Industrial Engineering*. 2012, University of Toronto.

70. *Fire Dynamics Simulator Technical Reference Guide Volume 1: Mathematical Model*. 2019, National Institute of Standards and Technology (NSIT).

71. *Fire Dynamics Simulator User's Guide*. 2019, National Institute of Standards and Technology (NSIT).

72. Beyler, C. L., *In: Hurley, M. J. In the SFPE Handbook of Fire Protection Engineering*. 5th Ed. ed. 2016: Springer.

73. Munoz, M., et al., *Analysis of the geometric and radiative characteristics of hydrocarbon pool fires.* Combustion and Flame, 2004. **139**(3): p. 263-277.

74. Maluk, C., *Development and Application of a Nove Test Method for Studying the Fire Behaviour of CFRP Prestressed Concrete Structural Elements*. 2014, The University of Edinburgh.

75. *NEN-EN 1991-1-2+C1 Eurocode 1: Actions on structures - Part 1-2: General actions - Actions on structures exposed to fire*, (NEN) Nederlands Normalisatie-instituut, 2011.

76. Wickström, U., *Adiabatic Surface Temperature and the Plate Thermometer for Calculating Heat Transfer and Controlling Fire Resistance Furnaces.* Fire Safety Science, 2008. **9**: p. 1227-1238.

77. Kodur, V., *Properties of Concrete at Elevated Temperatures.* ISRN Civil Engineering, 2014. **2014**: p. 1-15.

78. Buchanan, A. H. and Abu, A. K., *Structural Design for Fire Safety*. 2nd ed. 2017: John Wiley & Sons.

79. Fletcher, I., et al., *Behaviour of concrete structures in fire.* Thermal Science, 2007. **11**(2): p. 37-52.

80. *Model Code for Concrete Structures*, (*fib*) The International Federation for Structural Concrete, *2010*.

81. Hager, I. and Krzemień, K., *An Overview of Concrete Modulus of Elasticity Evolution with Temperature and Comments to European Code Provisions*, in *IFireSS - International Fire Safety Symposium*. 2015.

82. Khoury, G. A. and Anderberg, Y., *Fire Safety Design - Concrete Spalling Review*. 2000: Report submitted to the Swedish National Road Administration.

83. Lottman, B. B. G., *The Spalling Mechanism of Fire Exposed Concrete*, Doctoral Dissertation. 2017, Delft University of Technology.

84. Harmathy, T. Z., *Effect of moisture on the fire endurance of building materials.* ASTM Special Technical Publication, 1965(385): p. 74-95.

85. Dougill, J. W., *Modes of failure of concrete panels exposed to high temperatures.* Megazine of Concrete Research, 1972(24(79)): p. 71-76.

86. van Breugel, K., *Concrete Structures under Imposed Thermal and Shrinkage Deformations*. 2016, Delft.

87. Timoshenko, S. P. and Goodier, J. N., *Theory of Elasticity*. 1970: Mcgraw-Hill Book Company.

88. *Beproeving van het gedrag bij verhitting van twee isolatiematerialen ter bescherming van tunnels bij brand*. 1979, Instituut TNO voor Bouwmaterialen en Bouwconstructies.

89. *Betreffende de beproeving van het gedrag van twee isolatiematerialen ter bescherming van tunnels tegen brand*. 1980, Instituut TNO voor Bouwmaterialen en Bouwconstructies.

90. *CFD predictie- en postpredictieberekeningen, Brandproeven 2e Beneluxtunnel*. 2003, Ministerie van Verkeer en Waterstaat (RWS).

91. Goldstein, R. J., Chen, P. H. and Chiang, H. D., *In: Rohsenow, W. M.; Hartnett, J. P.; Cho, Y. L.; In the Handbook of Heat Transfer*. 3rd Ed. ed. 1998: McGraw-Hill.

92. Byström, A., Wickström, U. and Veljkovic, M., *Use of Plate Thermometers for Better Estimate of Fire Development.* Applied Mechanics and Materials, 2011. **82**: p. 362-367.

93. *Fire Dynamics Simulator Technical Reference Guide Volume 3: Validation*. 2019, National Institute of Standards and Technology (NIST).

94. Hurley, M. J., *SFPE Handbook of Fire Protection Engineering*. 5th ed. 2016: Springer.

95. Narayanan, N. and Ramamurthy, K., *Structure and properties of aerated concrete: a review*. Cement and Concrete Composites, 2000. **22**(5): p. 321-329.

96. Mathey, R. G., Rossiter, W. J., Jr., *A Summary of the Manufacture, Uses, and Properties of Autoclaved Aerated Concrete.* Insulation Materials, Testing and Applications, 1990. **SPT1030**: p. 15-37.

97. Vigne, G., Jonsson, J., *Experimental Research - Large-Scale Tunnel Fire Tests and the use of CFD modelling to predict Thermal Behaviour*. 2009, ArupFire.

98. Harmathy, T. Z. and Mehaffey, J. R., *Normalized Heat Load: A Key Parameter in Fire Safety Design.* Fire and Materials, 1982. **6**(1).

99. McCaffrey, B. J., Quintiere, J. G. and Harkleroad, M. F., *Estimating Room Temperatures and the Likelihood of Flashover Using Fire Test Data Correlations.* Fire Technology, 1981.

100. Jessen, J., *VID Fire-Kill and their TUNPROTEC® active fire fighting solution for tunnels underwent one of the most comprehensive full-scale tunnel fire test series in recent times in Pedro de Anes Test tunnel in Spain in 2018.* 2019, TUNPROTEC.

101. *NORSOK standard S-001*, Standards Norway, 2008.

102. *Techincal Note 13 - Design Guidance for Hydrocarbon Fires*, (FABIG) Fire and Blast Information Group, 2014.

103. Nolan, D. P., *Handbook of Fire and Explosion Protection Engineering Principles for Oil, Gas, Chemical, and Related Facilities*. 2019, Gulf Professional Publishing. p. xv-xvi.

104. Wickström, U., Anderson, J. and Sjöström, J., *Measuring incident heat flux and adiabatic surface temperature with plate thermometers in ambient and high temperatures.* Fire and Materials, 2019. **43**(1): p. 51-56.

105. Lemaire, T., *Runehamar Tunnel Fire Tests: Radiation, Fire Spread and Back Layering*, in *Proceedings of the International Symposium on Catastrophic Tunnel Fires*. 2003, SP Fire Technology.

106. Torero, J. L., Law, A. and Maluk, C., *Defining the thermal boundary condition for protective structures in fire.* Engineering Structures, 2017. **149**: p. 104-112.

107. Węgrzyński, W., Turkowski, P. and Roszkowski, P., *The discrepancies in energy balance in furnace testing, a bug or a feature?* Fire and Materials, 2019.

108. Efectis. *Mobile furnace - Cost-effective on-site fire resistance test*.; https://www.efectis.com/wp-content/uploads/2019/03/Mobile_furnace.pdf.

109. Maluk, C., et al., *A Heat-Transfer Rate Inducing System (H-TRIS) Test Method.* Fire Safety Journal, 2019. **105**: p. 307-319.

110. Bartlett, A. I., et al., *Comparative energy analysis from fire resistance tests on combustible versus noncombustible slabs.* Fire and Materials, 2019.

111. Lange, D., et al., *A Comparison of the Conditions in a Fire Resistance Furnace When Testing Combustible and Non-combustible Construction.* Fire Technology, 2020.

112. van de Leur, P. H. E. and Twilt., L., *Thermal Exposure in Fire Resistance Furnaces*. in *Fire Safety Science - Proceedings of the Sixth International Symposium*. 1999. International Association for Fire Safety Science.

113. Both, C., *Experimenteel onderzoek naar passieve brandveiligheidsvoorzieningen voor de Westerschelde tunnel uitgaande van de RWS brandkromme - Deel 2: Fendolite MII*. 2000, TNO.

114. Jansson, R. and Boström, L., *Spalling of concrete exposed to fire*. 2008.

115. *NEN-EN 1363-1 Fire resistance tests - Part 1 : General requirements*, (NEN) Nederlands Normalisatie-instituut, 2020.

116. Cheong, M .K., Spearpoint, M. J. and Fleischmann, C. M., *Calibrating an FDS Simulation of Goods-vehicle Fire Growth in a Tunnel Using the Runehamar Experiment.* Journal of Fire Protection Engineering, 2009. **19**(3): p. 177-196.

117. Wang, X., *Fire Dynamics Simulator (FDS) Pyrolisis Model Analysis of Heavy Goods Vehicle Fires in Road Tunnels*, in *Department of Civil and Natural Resources Engineering*. 2017, University of Canterbury.

118. Trelles, J. and Mawhinney, J. R., *CFD Investigation of Large Scale Pallet Stack Fires in Tunnels Protected by Water Mist Systems.* Journal of Fire Protection Engineering, 2010. **20**(3): p. 149-198.

119. Shaw, T., et al., *Experimental evaluation of the heat flux induced by tunnel fires.* Tunnelling and Underground Space Technology, 2016. **60**: p. 49-55.